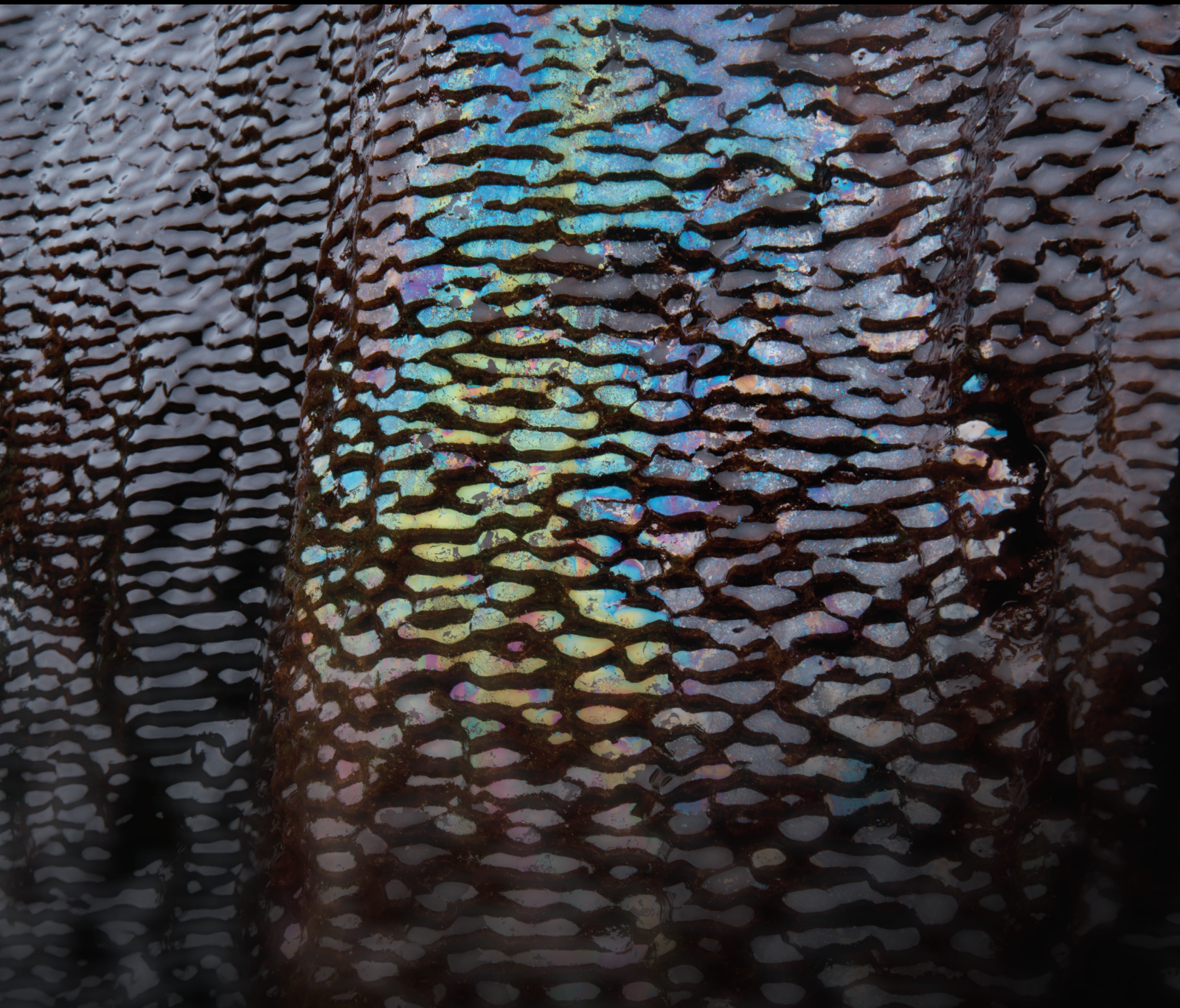# Numerical and Experimental Methods in Hydraulic Fracturing

Lead Guest Editor: Haojie Lian
Guest Editors: Chensen Ding and Zhenghe Liu

Numerical and Experimental Methods in Hydraulic Fracturing

Numerical and Experimental Methods in Hydraulic Fracturing

Lead Guest Editor: Haojie Lian
Guest Editors: Chensen Ding and Zhenghe Liu

Bisheng Wu, China
Da-yang Xuan, China
Yi Xue, China
HE YONGLIANG, China
Fan Yang, China
Zhenyuan Yin, China
Sohrab Zendehboudi, Canada
Zhixiong Zeng, Hong Kong
Yuanyuan Zha, China
Keni Zhang, China
Mingjie Zhang, China
Rongqing Zhang, China
Xianwei Zhang, China
Ye Zhang, USA
Zetian Zhang, China
Ling-Li Zhou, Ireland
Yingfang Zhou, United Kingdom
Daoyi Zhu, China
Quanle Zou, China
Martina Zucchi, Italy

Contents

Contents

WILEY | Hindawi

Research Article

Analysis of Hydrogeochemical Characteristics of Tunnel Groundwater Based on Multivariate Statistical Technology

Chen Peng,[1] Yuanming Liu ●,[1] Huiyu Chen,[1] Qiaowei Yuan,[1] Qingzhi Chen ●,[1] Shilong Mei,[2] and Zhonghu Wu ●[1]

[1]School of Civil Engineering, Guizhou University, Guiyang 550000, China
[2]School of Architecture and Urban Planning, Guizhou University, Guiyang 550000, China

Correspondence should be addressed to Yuanming Liu; liuym_2021@163.com

Following tunnel excavation, which is influenced by hydraulic fracturing and geological structure, a series of hydrochemical reactions occur in the karst aquifer, which has a significant impact on groundwater hydrology and the earth process. Based on five sets of 38 samples collected in the Tongzi Tunnel in 2020 and 2021, the main geochemical processes and water quality conditions of the karst aquifer system during tunnel construction were revealed by multivariate statistical analysis and graphical methods. The results showed that water-rock action is the main mechanism controlling groundwater chemistry in the study area; HCO_3^-, Ca^{2+}, and Mg^{2+} are associated with the widely distributed carbonate rocks in the study area. SO_4^{2-} is derived from gypsum and sulfate rocks and special strata, which are another important source of Ca^{2+}. Sodium-containing silicates and reverse cation exchange as the causal mechanisms of Na^+ whereas F^- is derived from fluorite. According to the mineral saturation index calculations, the dissolution and precipitation of minerals such as alum, gypsum, calcite, dolomite, and salt rock have an important influence on the main chemical components in water. The 38 samples were subjected to cluster analysis, and the results could be classified into seven categories. The representative clusters 1, 3, and 5 were selected for principal component analysis. Clusters 1 and 5 of groundwater represent weathering, dissolution, and ion exchange of carbonate and sulfate rocks and are closely related to the lithologic limestone, limestone intercalated with carbonaceous mudstone, carbonaceous mudstone, and coal-measure strata in the aquifer. Cluster 3 is dominated by upper surface river water and characterizes the geochemistry in natural water bodies dominated by the dissolution of carbonate, sulfate, and salt rocks. Finally, groundwater quality is mostly found in Class IV, with NO_3^- and F^- being the main contaminants in the water.

1. Introduction

In the karst areas of southwest China, tunneling is the main way to improve transportation due to the special topographical features. When tunnels pass through geological units of different lithological formations, there will inevitably be a significant impact on the karst aquifer system, especially in deeply buried tunnels with high ground stresses. Tunnel excavation usually creates a hydraulic fracturing effect, in which cracks in the surrounding rock sprout and expand under the action of hydraulic splitting, creating new drainage channels and causing significant changes in groundwater [1]. Hydraulic fracturing has become a central mechanism for water damage in some high water pressure tunnels. At the

same time, hydraulic fractures and water pressure also provide sites and conditions for aquifer water-rock action, leading to a series of hydrochemical reactions that affect the groundwater chemical field.

Relevant studies have shown that the construction of underground works has a significant impact on the hydrogeochemical processes and groundwater quality of aquifers. Chae et al. analyzed 72 sets of tunnel seepage samples collected from 43 underground stations in Korea and found that hydrogeological interactions caused by underground construction altered water chemistry and led to the deterioration of groundwater quality [2]. Based on a study of groundwater flow conditions around the Chienberg Tunnel, Butscher et al. found that groundwater from different

aquifers mixed after tunnel excavation and that coupled hydraulic-mechanical and geochemical effects altered the pore water chemistry and caused swelling of the gypsum salt rock [3]. Piña et al. modeled the path of surface water into the tunnels using hydrochemical analyses and isotopic techniques and found that the depth of burial of the tunnels affects the intensity and timing of water-rock action and that carbon dioxide and oxygen in the air react with the exposed minerals [4]. This type of alteration of the dissolution state of minerals due to the renewal of aquifers by tunnel drainage, resulting in hydrogeochemical imbalances, is common in all types of rock formations [5]. The impact on water quality and water chemistry is even more pronounced if the tunnel passes directly through underground karst aquifers and fracture zones [6].

Along with the natural chemical reactions caused by the hydraulic fracturing effect of tunnels and groundwater exchange, explosive residues used in tunnel construction by blasting can also directly affect groundwater quality, the most significant effect being a surge in NH_4^+ and NO_3^- in groundwater [7]. Contaminated groundwater can also damage the surrounding rock and tunnel structure, Ghobadi et al. investigated the groundwater chemistry of Iranian metro line 2, finding that the gypsum, hard gypsum, and coal contained in the strata after the construction of the tunnels had a significant impact on groundwater quality, and the sulfates and chlorides produced by the reaction make the groundwater corrosive to the tunnel linings [8]. Howladar and Rahman conducted a study on the quality of tunnel drainage, and the results showed that water quality has an impact on biology and drinking. Natural processes and human activities are the main control factors for water pollution sources [9]. It can be seen that the influence of tunnel water-rock action on groundwater chemistry and water quality cannot be ignored. It is related to multiple factors such as stratum lithology, groundwater storage conditions, hydraulic strength, and tunnel construction.

Multivariate statistical analysis has been successfully applied to hydrogeochemical studies in many fields. Megherfi et al. applied multivariate statistical analysis to group the groundwater chemistry in the study area and revealed the main controlling processes of the hydrochemical characteristics [10]. Engle and Rowan used multivariate analysis to study the geochemical data of injected water and produced water during hydraulic fracturing of shale gas wells [11]. Pan et al. evaluated the irrigating properties of groundwater near landfills through multiple statistical methods [12]. Kumar et al. introduced principal component analysis and cluster analysis in water quality evaluation, and the results showed that multivariate statistical methods can reasonably explain large data sets and reduce the cost of water quality monitoring [13]. Prusty and Farooq used multivariate statistical methods to reveal the mechanism of seawater's influence on groundwater and surface water, providing a basis for water resource management [14].

The karst area has a complex geological structure, widespread faults and caves, and rich mineral resources, and the karst groundwater system is extremely sensitive to tunnel construction. Although some scholars have studied the hydrogeochemical processes induced by mining activities in the karst areas of Southwest China [15, 16], however, there are no reports on groundwater chemistry in the karst tunnel fracture zone; the existing research on groundwater related to tunnel mainly focuses on the influence of groundwater level decline and water pressure on the safety of lining structure, lack of understanding of groundwater and surrounding rock matrix water-rock interaction. As a result, it is critical to conduct groundwater chemical processes and water quality research for karst tunnels. The Tongzi Tunnel, an extralong highway tunnel under construction in Guizhou Province, serves as the research material in this study. Through indoor experiments, combined with hydrochemical methods and multivariate statistical methods, the Tongzi Tunnel groundwater chemical characteristics and water quality are evaluated, aiming to understand the water-rock interaction and hydrochemical evolution mechanism caused by tunnel construction.

2. Overview of the Study Area

2.1. Location. The Tongzi Tunnel is 10.5 km long and is located at the deflection extension of Dalou Mountain. It is an important part of the expansion project of the Chongqing-Zunyi section of the Lanzhou-Haikou Expressway. Geographically, the tunnel is located in two towns in Tongzi County, Guizhou Province. With the watershed in the middle of the tunnel as the boundary, the Chongqing side is under the jurisdiction of Dahe Township, while the Zunyi side is under the jurisdiction of Mazong Township. Construction of the tunnel started in June 2018 and is expected to be completed and commence traffic by the end of 2022. The location of the study area is shown in Figure 1(a).

2.2. Hydrology. The surface basins of the tunnel belong to the Qijiang River system, Chishui River system, and Wujiang River system in the Yangtze River Basin. There is no perennial surface runoff around the tunnel. The rivers are mainly supplied by precipitation, or shallow short streams are formed due to springs exposed in gullies. With the surface watershed as the boundary, the surface runoff of the Chongqing section flows into the Songkan River, and the surface runoff of the Zunyi section flows into the Tongzi River. Figure 1(b) shows the monthly average rainfall in Tongzi County from 1990 to 2011. May-August is the rainy season, the rainfall peaks in June, and the rainfall gradually decreases from August with a short peak in October. Groundwater flow and water level lag for several or tens of days after rainfall and the overall change are coordinated with precipitation.

2.3. Stratum Lithology and Bad Geology. The Tongzi Tunnel has a large buried depth, complex geological structure, and diverse lithology. The overlying Quaternary soil layer is scattered. The geological section is shown in Figure 1(c). The maximum horizontal principal stress value of the cave body measured by the hydraulic fracturing test in the

(a)

(b)

(c)
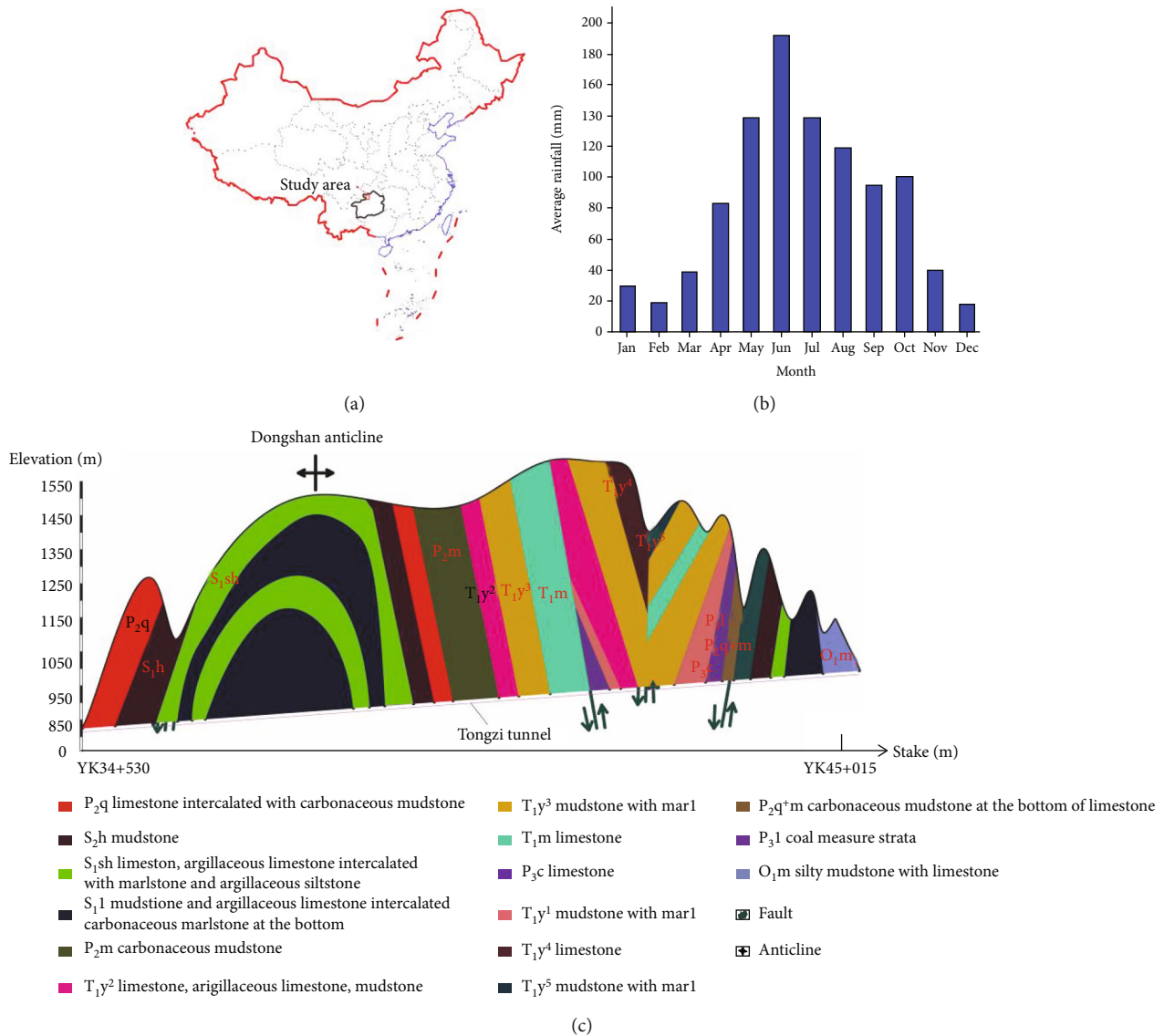
Figure 1: (a) Location of the study area. (b) Monthly average rainfall in the study area from 1995 to 2011. (c) Geological profile of Tongzi Tunnel.

deeply buried section is 9.43~21.84 MPa; at the same time, it also traverses the Kaijianpu fault, Linghujiayakou fault, water outlet fault, and Yemaodong fault. The exit section of the tunnel passes through the mine boundary of Tuanyuan Coal Mine in Mazong Township, and the old kiln water may collude through the preset roadway. During the geological prospecting stage, a water quality test was performed on the S1 spring point water in the T_1m formation and the P_3l coal measure formation water in the Tuanyuan coal mine coal tunnel. The test results show that the water quality of the groundwater within T_1m and the stream water at the exit of the tunnel is made up of calcium carbonate. Surface water and groundwater are slightly corrosive to reinforced concrete structures. The underground water of Tuanyuan Coal Mine (P_3l) constitutes potassium sodium sulfate, whereby groundwater in coal-bearing strata is weakly corrosive to reinforced concrete structures.

3. Materials and Methods

3.1. Experimental Sampling. The groundwater outflow point of the tunnel is mainly located in the fault fracture zone. According to research purpose, the sampling was carried out mainly on the Yemaodong fault, the water outlet fault, and the Linghujiayakou fault. 34 groundwater samples were collected in July 2020 (group I), October 2020 (group II), December 2020 (group III), March 2021 (group IV), and April 2021 (group V). They are secondary lining water outlets or leakage without lining after excavation and are not mixed with other water samples. Four surface glasses of water were collected in July 2020 (group S-I), October 2020 (group S-II), and March 2020 (group S-IV). The river is located on the surface of the upper part of the tunnel, and its flow is affected by rainfall, but there is no cut-off in the dry season which allows water to flow uniformly. Figure 2 depicts the distribution of sampling point locations.
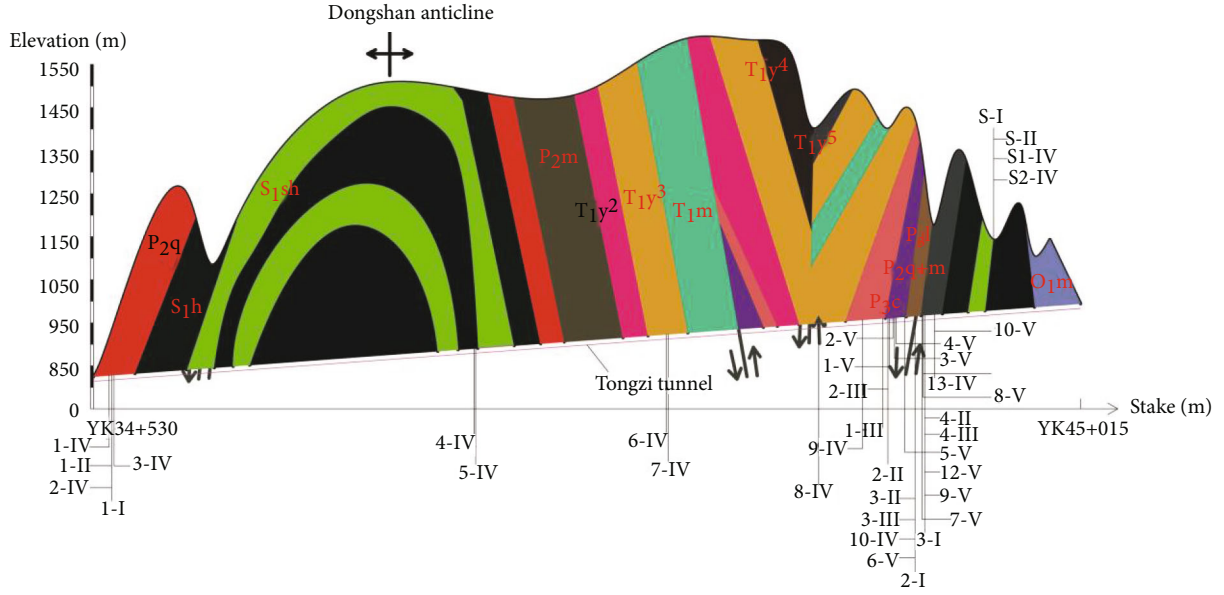
Figure 2: Location and number of sampling points.

Table 1: Conventional indexes and limits of groundwater quality (mg/L).

Class	pH	TDS	SO_4^{2-}	Cl^-	Fe	Al	NH_4^+	Na^+	NO_3^-	F^-	As
I	8.5	300	50	50	0.1	0.01	0.02	100	2	1	0.001
II	8.5	500	150	150	0.2	0.05	0.1	150	5	1	0.001
III	8.5	1000	250	250	0.3	0.2	0.5	200	20	1	0.01
IV	9	2000	350	350	2	0.5	1.5	400	30	2	0.05
V	9	2000	350	350	2	0.5	1.5	400	30	2	0.05

3.2. Experimental Method. The sampling bottle was cleaned with deionized water before sampling and rinsed with sample water more than three times during sampling. After sampling, the sample water was fitted with 0.22 μm and 0.45 μm membranes and put into a 150 mL polyethylene bottle. pH, TDS, and EC are measured by a portable pH meter and composite electrode. The concentration of HCO_3^- is determined by titration, cationic (K^+, Ca^{2+}, Na^+, and Mg^{2+}) samples are acidified with nitric acid dropwise, and the concentration is determined by flame atomic absorption spectrophotometry with TAS-990 instrument whereas anions (SO_4^{2-}, NO_3^-, Cl^-, and F^-) are analyzed by ion chromatography with ICS-1100 instrument. NH_4^+ was determined by Na's reagent spectrophotometry. The metal elements are determined by inductively coupled plasma mass spectrometry by ICP-MS instruments. The experiment process strictly follows the relevant specifications.

3.3. Analysis Method

3.3.1. Hydrochemical Methods. Common water chemistry analysis methods include Piper's three-line diagram, Gibbs model, and ion scatter diagram. The Piper three-line diagram consists of two triangles representing the percentages of the main anions and cations in milligram equivalents. Two triangles are integrated into the middle diamond-

shaped part to form a point for identifying the groundwater chemical phase [17]. The Gibbs model is divided into three regions by TDS and Na + /($Na^+ + Ca^{2+}$) and Cl^-/($Cl^- + HCO_3^-$), revealing the chemical control factors of groundwater, namely, atmospheric precipitation, rock weathering, and evaporative crystallization [18]. The concentration relationship between the main ions can determine the source of solute and the chemical process of groundwater.

The chloride alkalinity index can be used to determine whether there is cation cross-adsorption in groundwater. As shown in formulas (1) and (2), if CAI 1 and CAI 2 are both positive, it indicates that Na^+ and K^+ in groundwater exchange with Ca^{2+} and Mg^{2+} in the surrounding rock, and if they are negative at the same time, the reverse direction exchange occurs [19].

$$CAI\,1 = \frac{[Cl^- - (Na^+ + K^+)]}{Cl^-}, \tag{1}$$

$$CAI\,2 = \frac{[Cl^- - (Na^+ + K^+)]}{HCO_3^- + SO_4^{2-} + NO_3^- + CO_3^{2-}}. \tag{2}$$

3.3.2. PHREEQC Simulation. PHREEQC simulation is an important method to identify water chemical reactions and physical processes. One of them is the calculation of the

Table 2: Evaluation score of single index and comprehensive evaluation score.

Class	I	II	III	IV	V
Evaluation score of single index F_i	0	1	3	6	10
Comprehensive evaluation score F	<0.80	0.80~2.50	2.50~4.25	4.25~7.20	>7.20

Table 3: Statistics of hydrochemical parameters (mg/L).

	pH	EC	TDS	HCO_3^-	SO_4^{2-}	Cl^-	NO_3^-	F^-	Ca^{2+}	Mg^{2+}	Na^+	K^+	NH_4^+	Fe	Al
1-I	8.12	354.00	176.00	68.27	5.16	2.55	27.80	0.31	29.68	31.80	14.50	4.10	0.12	0.35	0.05
2-I	8.12	260.00	129.00	53.05	26.34	1.32	3.48	0.33	19.54	60.68	12.74	15.50	0.13	0.21	0.09
3-I	8.06	633.00	315.00	112.11	203.09	1.32	6.58	0.27	55.16	142.60	8.36	5.02	0.97	0.62	0.04
1-II	8.33	268.00	134.00	92.09	25.76	3.15	41.25	0.24	43.00	6.14	19.19	2.28	0.00	0.20	0.09
2-II	8.31	238.00	120.00	108.08	31.89	0.83	2.85	0.34	56.20	3.64	8.37	0.90	0.00	0.21	0.03
3-II	8.34	367.00	183.00	82.08	135.40	1.26	0.88	0.25	50.62	14.64	16.03	6.74	0.11	0.26	0.04
4-II	8.31	404.00	203.00	134.13	124.12	1.29	0.89	0.28	84.36	12.96	10.44	2.07	0.03	0.41	0.02
1-III	8.56	252.00	126.00	190.69	30.58	1.01	3.41	0.53	37.68	2.02	14.66	0.82	0.37	0.54	0.03
2-III	8.57	315.00	157.00	202.13	68.67	0.97	1.76	0.62	39.37	4.04	16.83	1.97	0.05	0.71	0.06
3-III	8.57	472.00	238.00	175.43	220.15	1.66	0.68	0.12	53.85	7.22	18.99	13.14	0.14	0.68	0.03
4-III	8.58	441.00	220.00	175.43	159.70	1.18	4.60	0.20	56.69	6.19	15.79	3.31	0.00	0.67	0.02
1-IV	8.57	305.00	152.00	122.04	56.30	4.09	41.78	2.56	36.69	4.05	33.34	9.84	0.00	0.46	0.06
2-IV	8.58	297.00	148.00	122.04	51.21	3.80	38.77	2.20	35.70	4.60	30.69	4.70	0.05	0.28	0.06
3-IV	8.58	293.00	145.00	122.04	51.62	3.91	38.67	2.17	37.90	4.54	32.04	5.17	0.00	0.43	0.07
4-IV	8.67	298.00	149.00	156.36	14.43	1.12	2.38	0.87	0.02	0.88	89.00	3.75	0.07	0.00	0.27
5-IV	8.67	294.00	147.00	183.06	14.47	1.22	1.59	0.81	0.00	0.53	90.68	1.09	0.05	0.00	0.05
6-IV	8.57	315.00	158.00	194.50	62.26	1.43	0.27	1.49	31.13	7.11	48.43	2.03	0.08	0.29	0.02
7-IV	8.61	298.00	149.00	160.18	66.19	1.42	0.74	1.46	25.15	6.86	47.95	3.18	0.00	0.24	0.05
8-IV	8.65	170.00	84.00	106.79	24.09	0.36	0.11	0.33	0.23	0.02	52.22	0.94	0.00	0.00	0.04
9-IV	8.64	290.00	144.00	91.53	76.48	0.97	1.57	2.46	0.85	0.12	83.37	3.44	0.00	0.00	0.28
10-IV	8.62	234.00	116.00	0.00	90.59	1.98	9.05	0.60	7.65	2.83	44.79	14.60	0.00	0.09	0.25
11-IV	8.56	476.00	240.00	221.20	162.81	1.85	4.65	0.20	75.34	6.49	16.47	3.63	0.00	1.08	0.01
12-IV	8.59	433.00	215.00	198.32	141.64	1.92	6.62	0.24	62.01	5.95	17.00	3.49	0.00	0.87	0.01
13-IV	8.58	419.00	209.00	179.25	139.84	1.97	6.06	0.24	67.54	5.99	17.86	3.93	0.00	0.56	0.02
1-V	8.69	213.00	156.00	190.69	57.54	1.12	1.61	0.50	62.90	3.82	13.07	1.38	0.00	0.40	0.01
2-V	8.65	383.00	191.00	202.13	97.13	1.89	0.64	0.11	70.51	7.58	14.04	2.95	0.00	0.53	0.02
3-V	8.63	381.00	191.00	217.38	94.90	1.95	0.41	0.12	70.89	7.54	13.25	2.43	0.01	0.51	0.02
4-V	8.62	400.00	200.00	217.38	100.10	1.97	0.47	0.13	72.13	7.60	13.93	2.43	0.00	0.81	0.02
5-V	8.63	386.00	193.00	163.99	129.53	1.59	1.17	0.13	55.96	6.19	18.30	12.70	0.00	0.65	0.09
6-V	8.60	419.00	210.00	205.94	131.90	1.77	4.37	0.16	78.28	6.12	13.64	3.89	0.00	0.55	0.02
7-V	8.60	458.00	229.00	205.94	151.62	1.54	3.24	0.11	84.14	6.36	11.52	3.02	0.00	0.97	0.00
8-V	8.60	385.00	192.00	171.62	123.51	2.04	4.48	0.22	73.58	6.04	14.65	2.83	0.00	0.49	0.01
9-V	8.09	403.00	201.00	198.32	123.57	1.85	4.58	0.22	71.67	5.90	14.43	3.38	0.00	0.50	0.01
10-V	8.60	408.00	204.00	186.87	122.01	1.98	4.82	0.23	60.44	5.51	13.69	3.27	0.00	0.76	0.02
S-II	8.09	205.00	102.00	85.69	1.23	0.40	2.27	0.22	25.78	18.48	3.84	2.60	0.08	0.24	0.01
S-III	8.32	188.00	94.00	100.10	9.78	0.64	2.71	0.25	51.30	2.06	2.51	0.74	0.00	0.17	0.05
S1-IV	8.59	204.00	101.00	152.55	14.39	0.45	2.10	0.07	46.65	1.91	2.59	0.89	0.00	0.43	0.01
S2-IV	8.59	197.00	98.00	152.55	14.24	0.46	1.55	0.05	51.53	2.02	2.72	0.88	0.00	0.43	0.01

Note: pH is dimensionless.
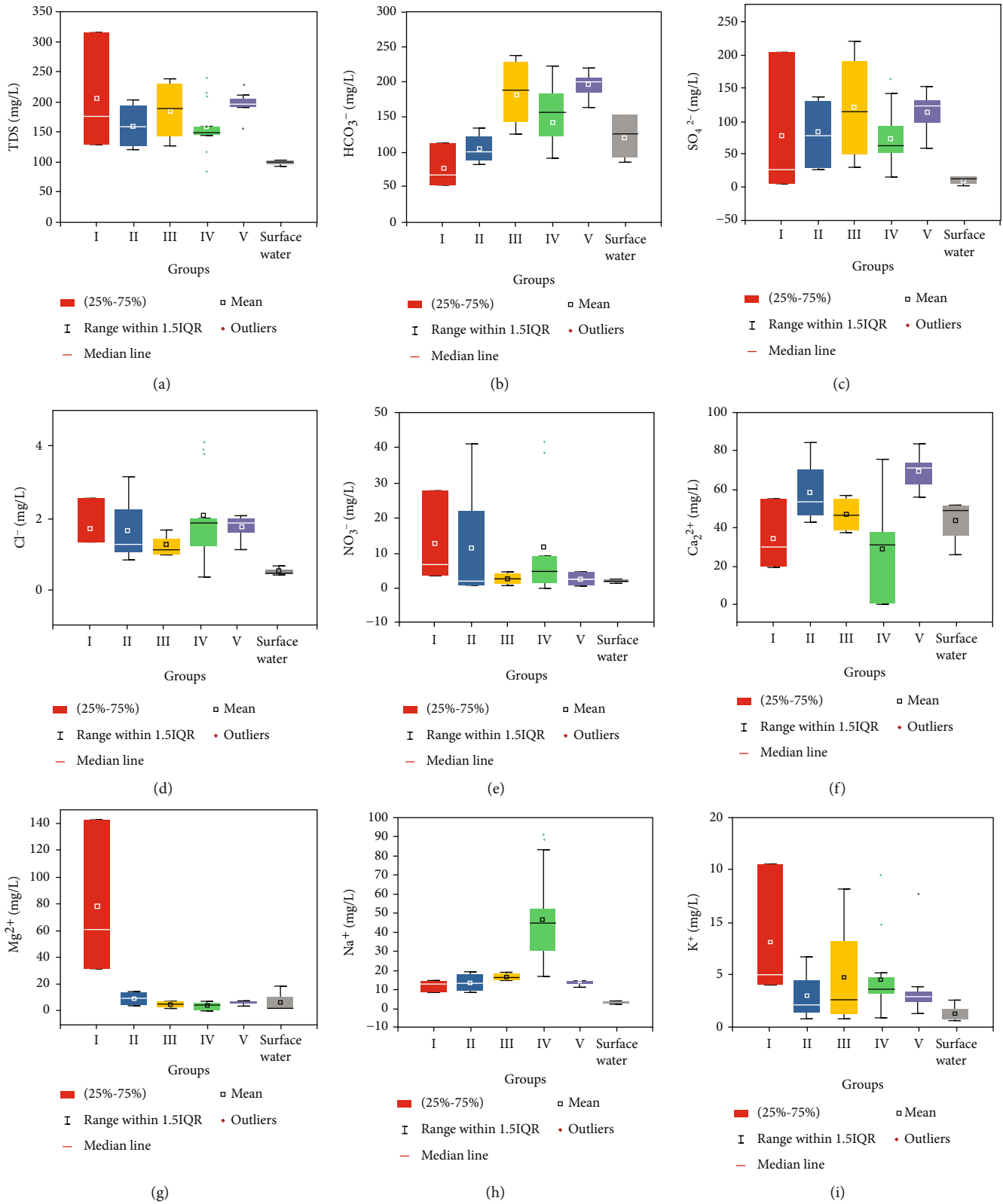
FIGURE 3: Box diagram of main ion concentration in the study area.

saturation index SI of mineral dissolution through the PHREEQC software, as shown in formula (3). IAP is the active product of mineral water ions, and K_{ep} represents the equilibrium constant at a certain temperature. If SI is positive, it means that the mineral dissolution is in a saturated state; otherwise, the mineral dissolution is unsaturated.

$$SI = \log \frac{IAP}{K_{ep}}. \qquad (3)$$

3.3.3. Cluster Analysis. Cluster analysis is based on multiple analysis target indicators. Find statistics that can measure the degree of similarity between indicators and use them to classify types. A dendrogram classification system is formed based on the degree of similarity between the variables, and only one cluster is left at the end [20].

3.3.4. Principal Component Analysis. The principal component analysis is one of the main multivariate statistical methods for analyzing hydrochemical data, simplifying the data structure by reducing the dimensionality of the research object indicators. The principal component after dimensionality reduction is a linear combination of the original data, compared with the 2-variable scatter diagram, which can only describe the relationship between two variables. The principal component analysis can describe the chemical process of groundwater from a multivariate perspective [21].

3.3.5. Groundwater Quality. The F value method recommended by the "Groundwater Quality Standard of the People's Republic of China" is employed. Evaluate the groundwater quality in the study area. As shown in Table 1, the code divides the quality of groundwater into I~V categories. Refer to Table 2, first, a single index is scored, and then, according to formulas (4) and (5), the individual index evaluation score F_i and the comprehensive evaluation score F are obtained, and the water quality category is obtained [22].

$$F = \sqrt{\frac{\bar{F}^2 + F_{max}^2}{2}}, \qquad (4)$$

$$\bar{F} = \frac{1}{n} \sum_{1}^{n} F_i. \qquad (5)$$

In the formula, $\bar{F}$ is the average value of each single index score F_i, F_{max} is the maximum value of single index score F_i, and n is the number of evaluation index items.

4. Results and Discussion

4.1. Statistics of Experimental Results. The water chemical indicators analyzed in this study are pH, TDS, EC, HCO_3^-, SO_4^{2-}, Cl^-, NO_3^-, F^-, Ca^{2+}, Mg^{2+}, K^+, Na^+, NH_4^+, Fe, and Al; the experimental results are listed in Table 3. The time trend of the concentration of main ions is shown in box plot 3.

Figures 3(a)–3(i) show the time changes of TDS, HCO_3^-, SO_4^{2-}, Cl^-, NO_3^-, Ca^{2+}, Mg^{2+}, K^+, and Na^+ concentrations during 5 samplings. TDS characterizes the total amount of dissolved components in water and is an important parameter for evaluating water salinity. It can be seen from Figure 3(a) that the average TDS in the samples in April 2021 is the largest. The TDS content in the surface water is lower than the underground water content in the tunnel
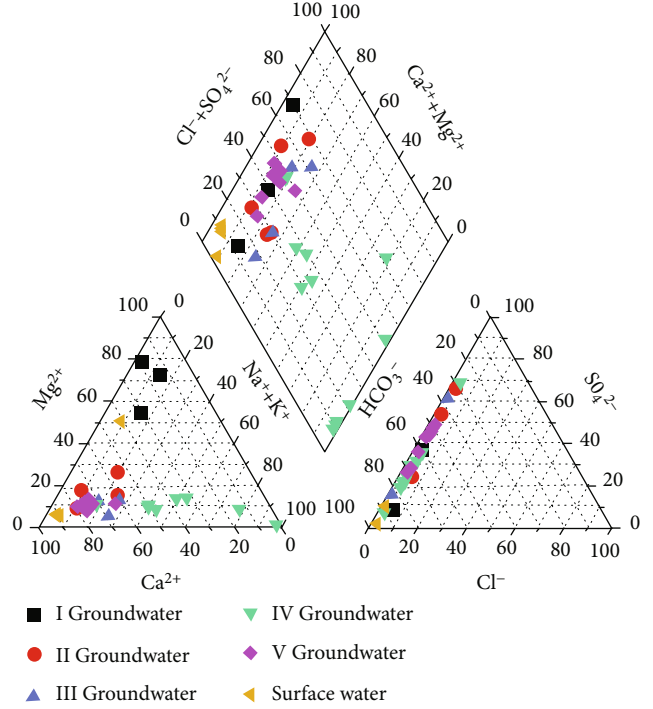
FIGURE 4: Pipper three-line diagram of the study area.

which indicates that after the excavation of the tunnel, the groundwater circulation is accelerated, and the water-rock interaction time increases due to the influence of stratum lithology and construction. HCO_3^- is the most common anion in the study area, the HCO_3^- concentration of surface water is much greater than other anions, and this is also the characteristic of ion content in natural river water in karst areas, which is related to the widespread distribution of carbonate rocks. Ca^{2+}, Mg^{2+}, K^+, and Na^+ in the karst zone mainly come from the dissolution of carbonate rocks, silicate rocks, and salt rocks. It is also a common cation in karst areas; the content of cations in different groups of groundwater varies greatly, which may be affected by the different intensity of water and rock action. The geochemical behavior of Cl^- is simple, it does not participate in the oxidation-reduction reaction and mainly comes from atmospheric precipitation and salt rock [23], NO_3^- is a common pollutant in surface water, and SO_4^{2-}, Cl^-, and NO_3^- all have abnormal values in the underground water in the tunnel. The surface water, on the other hand, has no abnormal value and very low content, indicating that the natural surface water in the study area is of good quality and less polluted, and groundwater is more sensitive to tunnel construction.

4.2. Water Chemistry Characteristics. As can be seen from Figure 4, the dominant cations of the water samples of group I are Mg^{2+}, and the dominant cations of the water samples of other groups are Ca^{2+}, K^+, and Na^+. The anions of all samples are distributed on the HCO_3^- side; the overall performance is $HCO_3^- > SO_4^{2-} > Cl^-$. Groundwater and surface water of groups I, II, III, and V are distributed on the upper left side of the diamond shape, and the main types of water chemistry are HCO_3-Ca·Mg type and SO_4·Cl -Ca·Mg type.
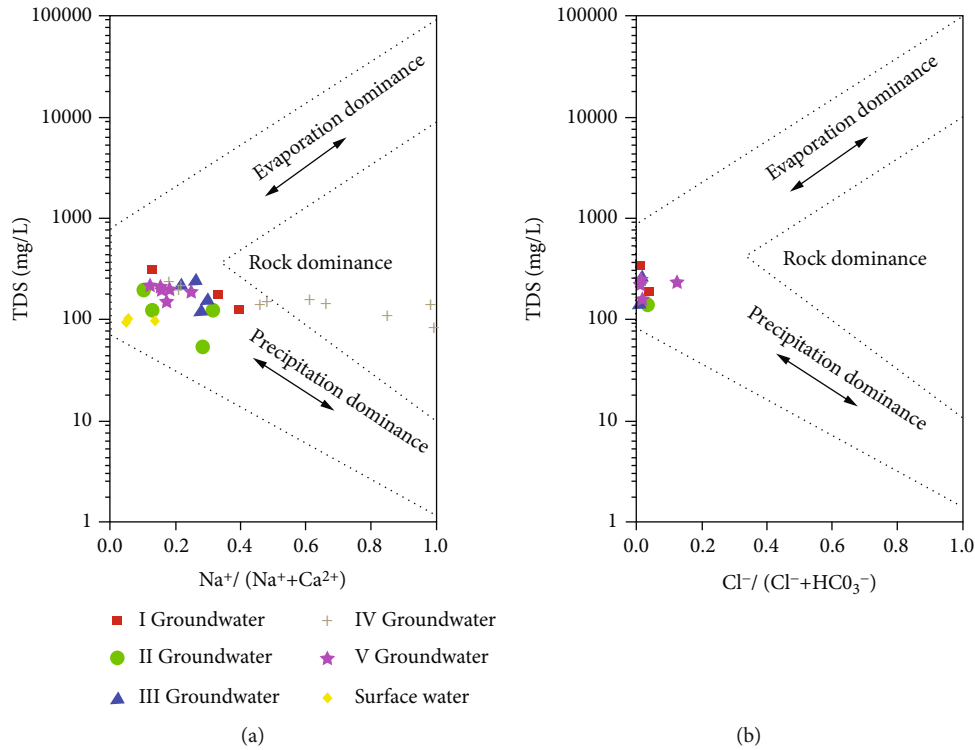
FIGURE 5: Gibbs model of the study area.

The groundwater of group IV is distributed in the middle and lower right side of the rhombus, and the water chemistry type is mainly $HCO_3 \cdot Na \cdot K$ type. The surface water sample is carbonate calcium water, and the sampling point is in the downstream of the surface river, which is consistent with the hydrochemical type of spring point at the tunnel outlet in the geological exploration stage before construction. The water samples of group IV and group V were taken in March and April 2021, respectively. They are in the dry season; the water samples of group IV are mainly from YK38+621 to YK43+730, interspersed with coal-measure strata; it can be seen that the water chemical phase transition of the water samples of group IV is related to the formation lithology.

As shown in Figure 5, groundwater and surface water samples from various periods are distributed in the middle of the Gibbs model. It reveals that rock weathering controls the chemical composition of the water in the study area, and the effects of atmospheric precipitation, evaporation, and crystallization are negligible. Water-rock interaction is the main hydrogeochemical process in the study area.

4.3. Relationship between Main Ions in Groundwater. The relationship of ion ratio in the water further illustrates the water-rock interaction in the study area. In karst areas, carbonate rocks are generally the main source of HCO_3^-, Ca^{2+}, and Mg^{2+} in the study area. In Figures 6(a) and 6(b), the 4 samplings of surface river water all fall on the 1:1 line, which is consistent with the weathering and dissolution of carbonate rocks in the natural water bodies of the study area. Most of the groundwater samples of groups I, II, and V are located in the upper part of the 1:1 line; it shows that in

addition to typical carbonate dissolution such as calcite and dolomite, other minerals are containing Ca^{2+} dissolved in groundwater. The equivalent ratio of Ca^{2+} to Mg^{2+} is usually used to explain the source of Ca^{2+}, except for the first group of water samples; the equivalent ratio of Ca^{2+} to Mg^{2+} is greater than 2:1; it shows that the dissolution of gypsum and sulfate rock minerals has a great contribution to Ca^{2+} [24]; Ca^{2+} in the study area is affected by the dissolution of carbonate rock, silicate rock, gypsum, etc. However, the intensities of the interaction between carbonate rock and gypsum are different in different sampling periods.

It can be seen from Figure 6(c) that the equivalent ratio of Ca^{2+}, Mg^{2+}, and HCO_3^- in the groundwater and surface water samples of groups I, II, and V is greater than 1:1; it depicts that in addition to the HCO_3^- produced by the reaction of H_2CO_3 in the carbonate rock, other anions are needed to balance it; the anion in groundwater and surface water next to HCO_3^- is SO_4^{2-}. SO_4^{2-} equivalent accounted for 51.2% of the anions in group I, 45.8% in group II, 44.0% in group III, 36.5% in group IV, 41.5% in group V, and 9.05% in surface water. It can be seen that SO_4^{2-} cannot be neglected in the interaction between groundwater and surrounding rocks, and carbonic acid is dominant in surface water. Since the Tongzi Tunnel is a mountain tunnel with a large buried depth, there are no human settlements on the overlying, so industrial activities will not affect SO_4^{2-}. It is preliminarily judged that SO_4^{2-} comes from gypsum and sulfate rock and special formations. The equivalent ratio of Ca^{2+}, Mg^{2+}, and HCO_3^- in the water samples of groups III and IV is less than 1:1, which means that the cations are mainly balanced by HCO_3^-.
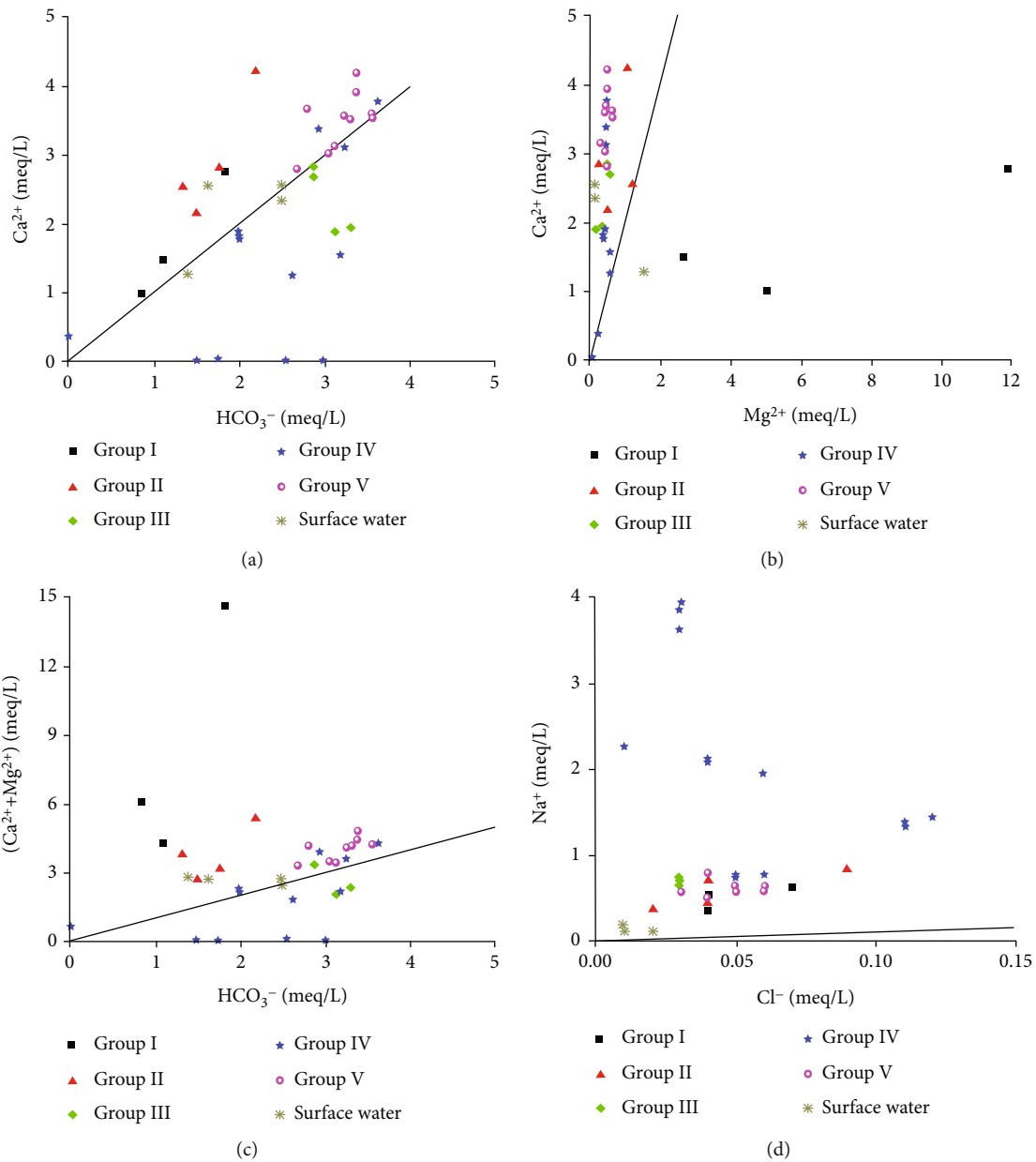
FIGURE 6: Ratio of main ions in the study area.

If Na^+ and Cl^- mainly come from the dissolution of salt rock, the equivalent ratio of Na^+ and Cl^- is 1:1. When the ratio of Na^+ to Cl^- is greater than 1:1, silicate rocks contribute more to Na^+ [25]. From Figure 6(d), the surface water sample is closest to the 1:1 line, and there is a large excess of Na^+ in the groundwater since the atmospheric precipitation in the study area has no obvious control effect on the source of ions; then, the sodium-containing silicate rock and cation exchange may be the main cause of Na^+.

4.4. Cation Exchange. As can be seen from Figures 7(a) and 7(b), about 77% of the water samples of group IV are on the -1:1 line, and CAI1 and CAI2 are both negative, which shows that reverse cation exchange occurred in the IV water sample. The dissolved Ca^{2+} and Mg^{2+} in the carbonate rock

in the groundwater exchanged with the Na^+ and K^+ in the surrounding rock of the tunnel. The adsorption of Ca^{2+} and the release of Na^+ explain the increase of Na^+ in the IV water sample, which also leads to changes in the chemical composition of the water. The lithology of group IV mainly includes coal-measure strata, carbonaceous mudstone, and mudstone intercalated with limestone. There are silicate minerals and clay minerals such as feldspar and quartz in these rock formations. According to the geological survey before the construction of the tunnel, the chemical type of underground aquifer water in the coal tunnel of Tuanyuan Coal Mine is sulfate potassium sodium water. It is speculated that SO_4^{2-} comes from sulfate rock and gypsum, and Na^+ and K^+ come from reverse cation exchange. After the construction of the tunnel, the frequent exchange and flow of
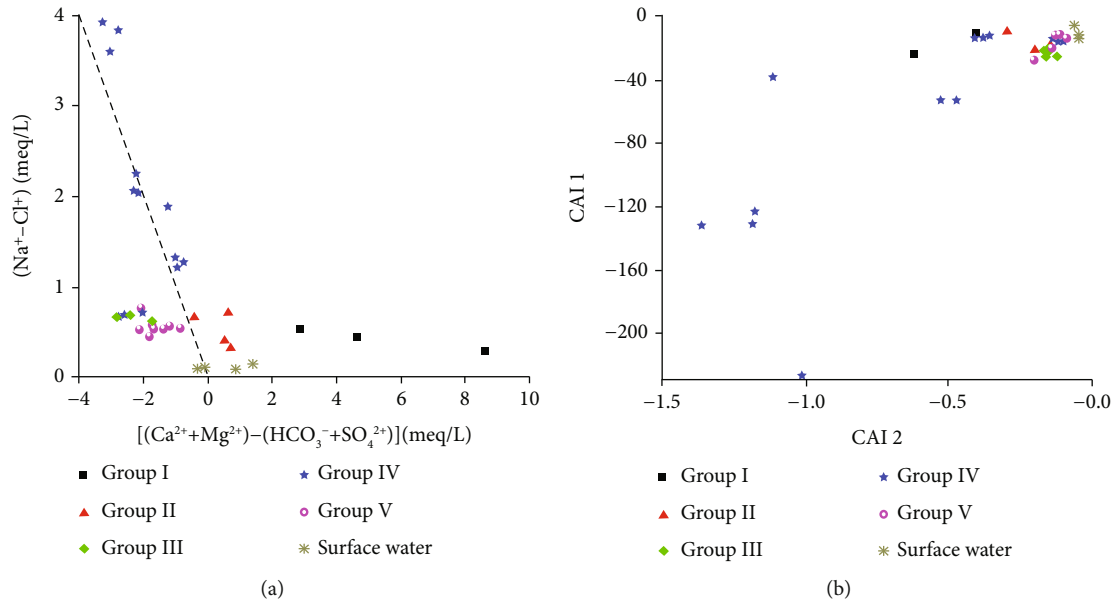
FIGURE 7: Cation reverse exchange.

groundwater accelerate this cation exchange behavior. According to the size of the chlor-alkali index, the intensity of cation adsorption alternate action in the groundwater of group IV is greater than that of other groups of water samples, and the ion exchange intensity of groundwater is greater than that of surface water.

4.5. Hydrogeochemical Simulation. The main ion genesis mechanisms in the study area are water-rock interaction, as well as rock weathering and dissolution. To ascertain the dissolution and precipitation processes of the major minerals influencing groundwater chemistry [26]. Alum, calcite, dolomite, fluorite, gypsum, rock salt, hematite, and dissolved carbon dioxide saturation index were calculated using PHREEQC software. The scatter plot of saturation index and TDS is shown in Figure 8.

It can be seen that the saturation index of alunite in the study area is less than 0, which is unsaturated; the saturation index of alunite in surface river water is the smallest. The SI value of gypsum containing SO_4^{2-} is also less than 0, which verifies the hypothesis that SO_4^{2-} in water comes from sulfate minerals and gypsum. In karst areas, pyrite in coal-measure strata also has higher SO_4^{2-}. The saturation index of mostly calcite and dolomite is greater than 0. Also, in a saturated state, only a small part of the water samples of group IV is unsaturated. Due to the independence of the SI value of calcite and dolomite from TDS, the supersaturated carbonate minerals produce precipitation and contribute chemical components to the groundwater [27, 28].

The physical and chemical properties of fluorite and calcite are indistinguishable. In addition to the replenishment of surface runoff and infiltration by atmospheric precipitation, the F$^-$ in surface water and groundwater mainly comes from the dissolution of fluorite. It can be seen from Figure 8(d) that the dissolution of fluorite in the study area is unsaturated. The saturation index of hematite in most

water samples is greater than 0, indicating that the hematite has been dissolved and saturated. Hematite and pyrite are the main sources of Fe in groundwater. After the tunnel is excavated, the original aquifer's closed state is broken, and the CO_2 may come from the dissolution of CO_2 in the atmosphere. Figure 8 shows that as CO_2 dissolves, the pH value decreases and produces carbonic acid to participate in water-rock action [29].

4.6. Cluster Analysis. Figure 9 indicates that the water samples in the study area can be divided into 7 categories. The first cluster is dominated by group IV water, including 3 water samples near the entrance of the tunnel at ZK34 +715 during the dry season and 5 water samples at the exit of the tunnel between YK38+621 and YK43+025, respectively. The lithology of the aquifer group is dominated by limestone intercalated with carbonaceous mudstone, carbonaceous mudstone, and coal-measure strata representing the weathering and dissolution of sulfate rock and ion exchange. The second cluster is the water samples of group I ZK34+715 in the wet season. The third cluster includes surface river water and groundwater in groups 1-III, 1-V, 2-II, and 8-IV, representing the chemical characteristics of natural water bodies in the study area. The fourth cluster is the water sample of YK43+650 in the abundant and dry water periods. The fifth cluster is dominated by water samples of group V, concentrated between YK43+613 and YK43+730; the lithology of the aquifer group is dominated by limestone and coal-measure strata. The reverse cation exchange behavior of this group of water samples is weaker than that of group IV, due to the difference in stratum lithology. Various minerals such as calcite and other carbonate rocks, gypsum, and silicate rocks are dissolved and precipitated. The sixth and seventh clusters have only one water sample, and the water chemistry characteristics are relatively independent.

(a)

(b)

(c)

(d)

(e)

(f)
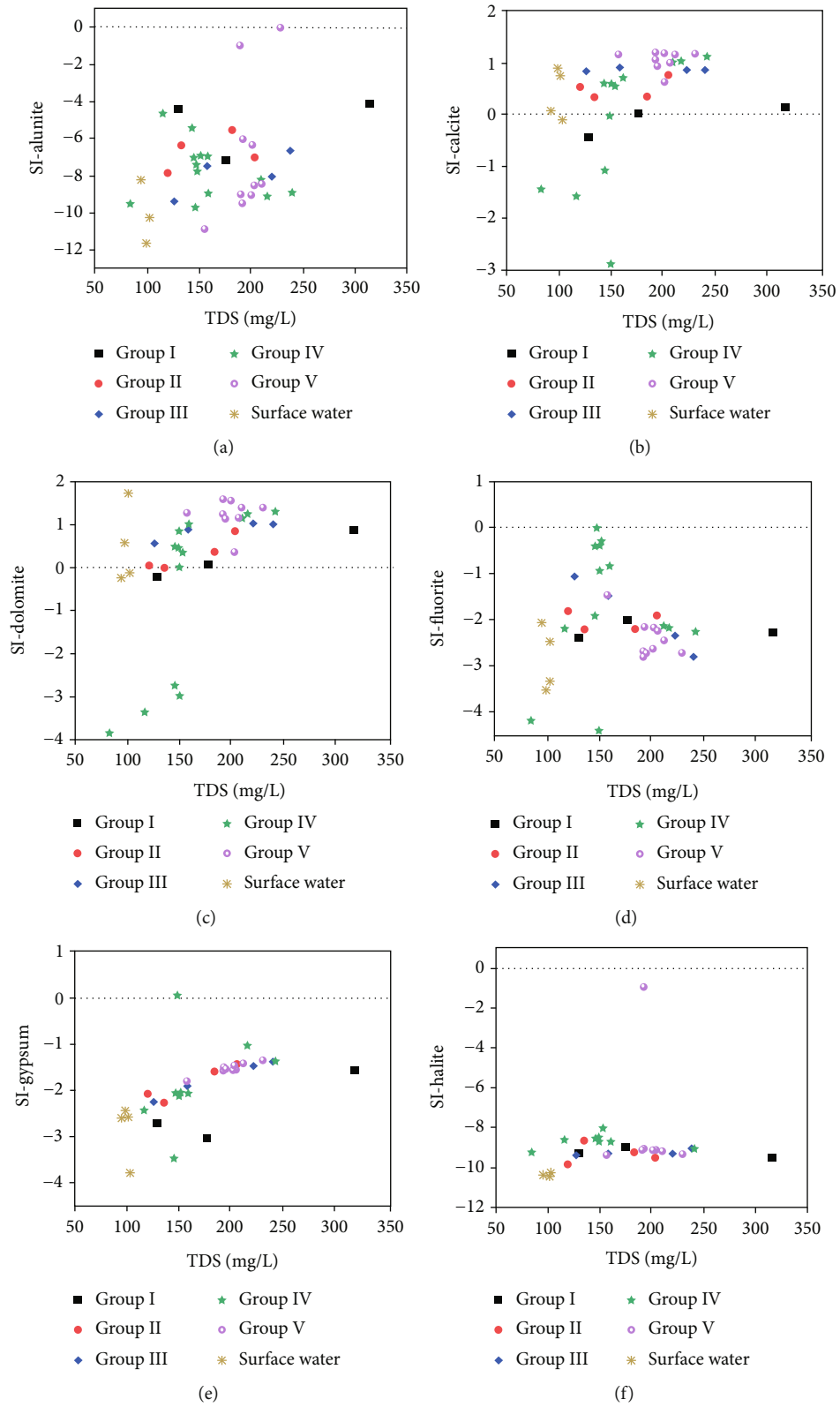
FIGURE 8: Continued.

(g)

(h)
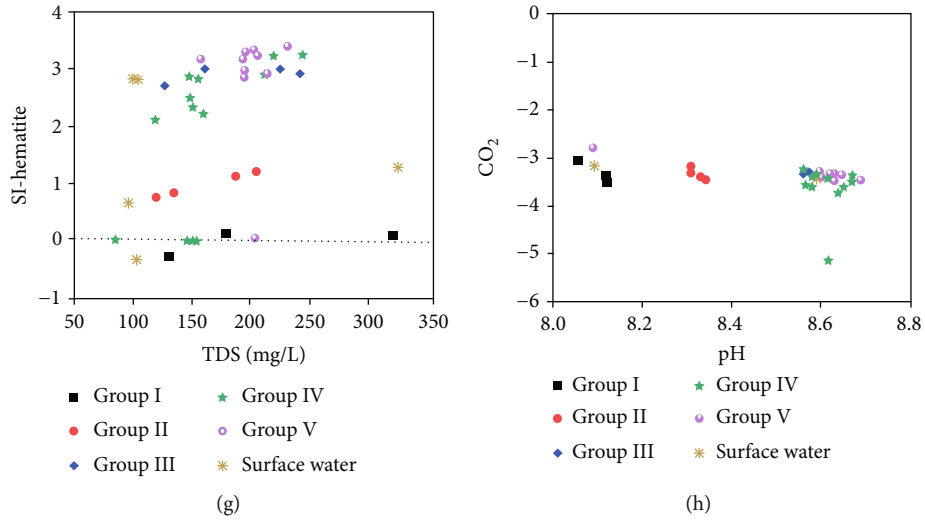
FIGURE 8: Saturation index of main minerals.

According to the clustering results, surface river water has a lower impact on groundwater, and the groundwater is consistent with the potassium-sodium water chemistry of the sulfate rock drilled in the Tuan Yuan coal mine (coal formation) before construction. It shows that the karst fissure pipeline is relatively developed in fault and goaf. Under the disturbance of tunnel construction and the action of water pressure, the groundwater in the Tuanyuan coal mine boundary mixed with bedrock fissure water into the tunnel.

4.7. Principal Component Analysis. According to the cluster analysis results, the first, third, and fifth clusters with the most samples were chosen for principal component analysis as shown in Figure 10. The KMO value of the sample passed the test. Figures 10(a) and 10(b) are the load distribution diagrams of the three principal components of the first type of samples. The total variance contribution rate was 82.56%, and the variance contribution rate of principal component 1 was 37.46%, which showed a strong positive correlation with Ca^{2+}, Mg^{2+}, and Fe and a strong negative correlation with Na^+, Al, and pH. The variance contribution rate of principal component 2 is 27.82%, which is positively correlated with EC, TDS, HCO_3^-, and NH_4^+. The variance contribution rate of principal component 3 is 17.28%, which is positively correlated with K^+, Cl^-, F^-, and NO_3^-. It can be seen that the aquifer originally contained more Ca^{2+} and Mg^{2+}. The excavation of the tunnel opens the closed coal-measure aquifer and causes the oxidation-reduction reaction of minerals such as pyrite in the coal-measure strata. Therefore, the Fe load value is higher, and because it is negatively correlated or not correlated with Na^+ and HCO_3^-. It indicates that the carbonate rock is saturated with dissolution and Ca^{2+} has other sources, which should be reversed in cation adsorption alternately.

Figures 10(c) and 10(d) are the three principal component loading distribution diagrams of the third cluster sample. The variance contribution rate of principal component 1 is 45.18%, which shows a strong positive correlation with TDS, SO_4^{2-}, Cl^-, F^-, and Na^+. The variance contribution rate
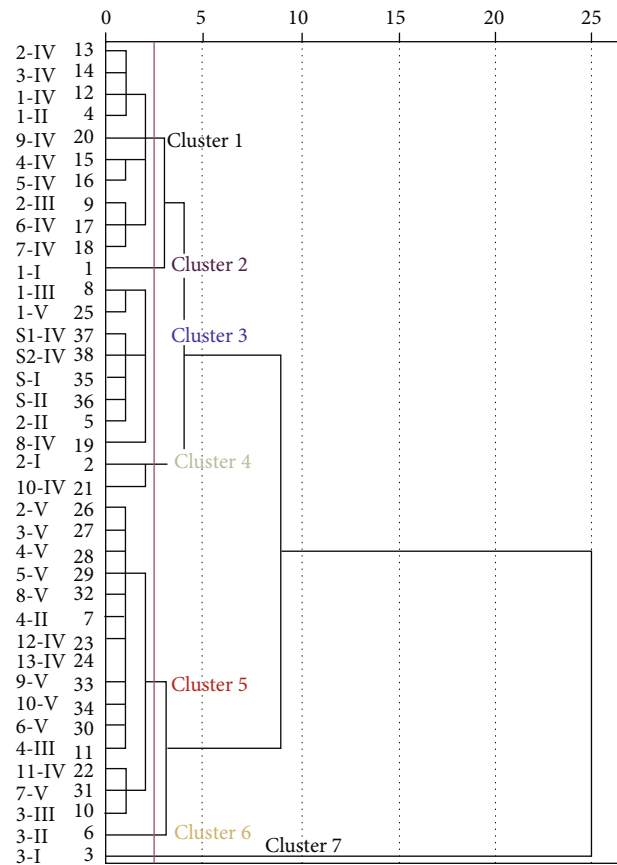
FIGURE 9: Sample clustering diagram.

of principal component 2 is 22.63%, which is positively correlated with Ca^{2+} and negatively correlated with Mg^{2+} and K^+. The variance contribution rate of principal component 3 is 16.56%, which shows a strong positive correlation with NO_3^- and NH_4^+. It shows that the water-rock action in this type of water sample is the dissolution of sulfate rock and salt rock. Cl^- has stable chemical characteristics, mainly from atmospheric precipitation. The surface river water and the
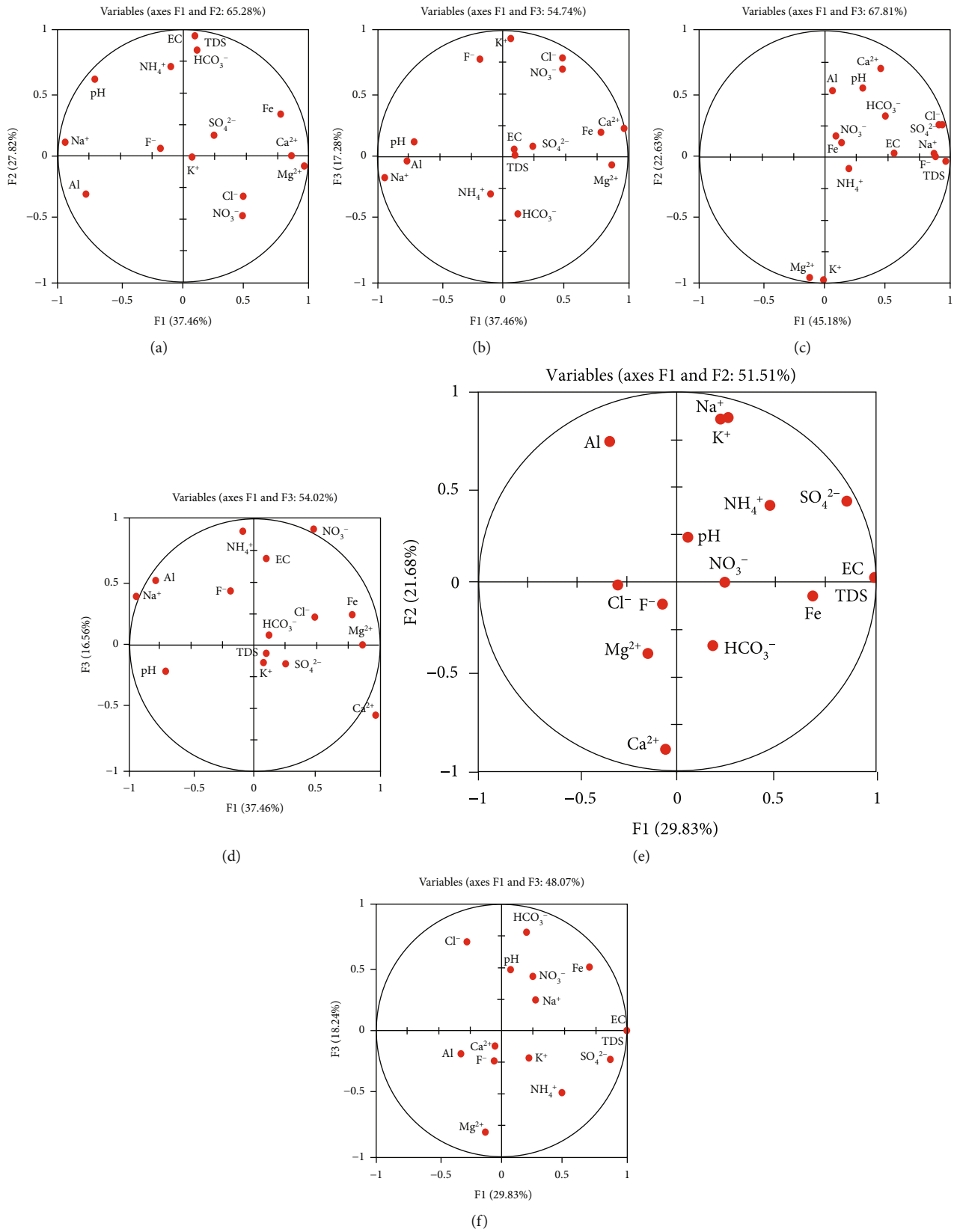
Figure 10: Principal component analysis results.

TABLE 4: Water quality evaluation results in the study area.

Sample number	F value	Quality type	Sample number	F value	Quality type	Sample number	F value	Quality type
1-I	6.2	IV	3-IV	10.5	V	3-V	6.1	IV
2-I	3.1	III	4-IV	6.3	IV	4-V	6.1	IV
3-I	6.3	IV	5-IV	6.1	IV	5-V	6.1	IV
1-II	10.1	V	6-IV	6.2	IV	6-V	6.2	IV
2-II	3.0	III	7-IV	6.2	IV	7-V	6.2	IV
3-II	3.1	III	8-IV	6.1	IV	8-V	6.1	IV
4-II	6.1	IV	9-IV	10.3	V	9-V	6.0	IV
1-III	6.2	IV	10-IV	6.2	IV	10-V	6.2	IV
2-III	6.2	IV	11-IV	6.2	IV	S-I	3.0	III
3-III	6.2	IV	12-IV	6.2	IV	S-II	1.0	II
4-III	6.2	IV	13-IV	6.2	IV	S1-IV	6.1	IV
1-IV	10.5	V	1-V	6.1	IV	S2-IV	6.1	IV
2-IV	10.5	V	2-V	6.1	IV			

groundwater of this group are recharged and infiltrated by atmospheric precipitation and are characterized by natural hydrogeochemical effects.

Figures 10(e) and 10(f) are the load distribution diagrams of the three principal components of the fifth cluster of samples. The variance contribution rate of principal component 1 is 29.83%, which shows a strong positive correlation with EC, TDS, SO_4^{2-}, and Fe. The variance contribution rate of principal component 2 is 21.68%, which is positively correlated with Na^+, K^+, and Al and strongly negatively correlated with Ca^{2+}. The variance contribution rate of principal component 3 is 18.24%, which is positively correlated with HCO_3^- and Cl^- and strongly negatively correlated with Mg^{2+}. The three main components of this type of groundwater have a low variance contribution rate and large differences, and the water chemical composition is influenced by multiple water-rock interactions.

4.8. Groundwater Quality. According to the evaluation criteria and methods, the water quality category of the study area is obtained. As shown in Table 4, the best water quality is the surface river water of group S-II Grade II. There are 4 groups for Grade III water quality, 28 groups for Grade IV water quality at most, accounting for 73.6%, and there are 5 groups for Grade V water quality. The worst water quality is the 4 groups of water samples near the ZK34+715 section, which are caused by high concentrations of NO_3^- and F^-, and a group of water samples of the YK43+025 section, due to high F^- concentration which is derived from Ca_2F dissolution. Since NO_3^- has no known lithological source, there is almost no agricultural activity over the tunnel. During the construction period, the sewage outside the tunnel is also strictly prohibited to enter the tunnel. Therefore, the human activities represented by NO_3^- will pollute the groundwater; it is most likely to come from tunnel construction residues.

The water quality type of groundwater in the coal stratigraphic section is mainly IV water, and the factors determining the water quality category are Fe and pH, and the water quality is influenced by iron-bearing minerals. Conventional ions such as SO_4^{2-}, K^+, and Na^+ in coal aquifers

have little effect on water quality. The F value method highlights the maximum pollution factors, and the analysis of pollution sources is more targeted than other groundwater quality evaluation methods.

5. Conclusion

This research adopts methods such as water chemistry, multivariate statistical analysis, and geochemical simulation. The evolution process of groundwater in the Tongzi Tunnel and the formation mechanism of main ions are analyzed. The main conclusions are as follows:

(1) HCO_3^- is the dominant anion in the research area while Ca^{2+} is the dominant cation in the research area. The type of water chemistry is related to the lithology of the formation. The natural water body is mainly carbonate calcium water, while the content of SO_4^{2-}, Na^+, and K^+ in the groundwater of coal strata increases, and the water chemical type tends to sulfate sodium water. It is essentially consistent with the chemical characteristics of the water intake drilled in the Tuanyuan Coal Mine during the tunnel's early stages; tunnel construction uses karst fractures and hydraulic fracturing effects to bring coal aquifers into the tunnel

(2) Water-rock interaction is the main genetic mechanism of ions. The dissolution of carbonate minerals reaches saturation, which has contributed most of the HCO_3^-, Ca^{2+}, and Mg^{2+} in the water. The sulfate rock minerals such as alum and gypsum are not saturated in dissolution and are the main sources of Ca^{2+}, Mg^{2+}, and SO_4^{2-} in the later stage. F^- is mainly from fluorite. After the tunnel construction, CO_2 in the air dissolves in the water, which has an important influence on the pH adjustment of the water

(3) Except for the dissolution of silicate rock, Na^+ and K^+ mainly come from the reverse exchange of cations. The strong reverse exchange of cations in

coal-measure formations is also the cause of the transformation of cations from Ca^{2+} and Mg^{2+} to Na^+ and K^+ in the water samples of group IV

(4) Clustering and principal component analysis show that the 38 groups of samples can be divided into 7 clusters; the water samples are concentrated in clusters 1, 3, and 5. The first cluster is dominated by group IV. The lithology of the aquifer is limestone intercalated with carbonaceous mudstone, carbonaceous mudstone, and coal-measure strata, which represents the weathering and dissolution of sulfate rock and ion exchange. The third cluster is dominated by surface river water, representing the action of water-rock in natural water bodies. The fifth cluster is dominated by water samples of group V, the aquifer lithology is limestone and coal-measure strata, and the reverse cation exchange behavior is weaker than that of group IV

(5) The groundwater quality is mostly Grade IV, with 28 groups, accounting for 73.6%, and there are 5 groups of Class V water; NO_3^- and F^- are the main pollution factors. Followed by Fe, pH, conventional ions in groundwater have little effect on water quality. There is no agricultural activity over the tunnel, and pollution may be caused by special ground or tunnel construction. Hydrochemical evidence indicates that aquifer has hydraulic connection

Data Availability

The data used to support the findings of this study are available from the corresponding author upon request.

Conflicts of Interest

The authors declare that they have no conflicts of interest.

Acknowledgments

References

[1] Q. Zhang, B. X. Huang, M. C. He, and S. Guo, "A numerical investigation on the hydraulic fracturing effect of water inrush during tunnel excavation," *Geofluids*, vol. 2020, Article ID 6196327, 2020.

[2] G. T. Chae, S. T. Yun, B. Y. Choi et al., "Hydrochemistry of urban groundwater, Seoul, Korea: the impact of subway tunnels on groundwater quality," *Journal of Contaminant Hydrology*, vol. 101, no. 1-4, pp. 42–52, 2008.

[3] C. Butscher, P. Huggenberger, and E. Zechner, "Impact of tunneling on regional groundwater flow and implications for swelling of clay-sulfate rocks," *Engineering Geology*, vol. 117, no. 3-4, pp. 198–206, 2011.

[4] A. Pina, L. D. Donado, S. Blake, and T. Cramer, "Compositional multivariate statistical analysis of the hydrogeochemical processes in a fractured massif: La Linea tunnel project, Colombia," *Applied Geochemistry*, vol. 95, pp. 1–18, 2018.

[5] F. Mossmark, K. K. Annertz, L. O. Ericsson, and M. Norin, "Hydrochemical impact of construction of the western section of the Hallandsås rail tunnel in Sweden," *Bulletin of Engineering Geology & the Environment*, vol. 76, no. 2, pp. 751–769, 2017.

[6] M. Ćuk, I. Jemcov, A. Mladenović, and M. Ilić, "Hydrochemical impact of the hydraulic tunnel on groundwater in the complex aquifer system in Pirot, Serbia," *Carbonates and Evaporites*, vol. 35, no. 2, 2020.

[7] F. Mossmark, L. O. Ericsson, L. M. Norin, and L. O. Dahlström, "Hydrochemical changes caused by underground constructions – a case study of the Kattleberg rail tunnel," *Engineering Geology*, vol. 191, pp. 86–98, 2015.

[8] M. H. Ghobadi, M. Firuzi, and E. Asghari-Kaljahi, "Relationships between geological formations and groundwater chemistry and their effects on the concrete lining of tunnels (case study: Tabriz metro line 2)," *Environmental Earth Sciences*, vol. 75, no. 12, pp. 987.1–987.14, 2016.

[9] M. F. Howladar and M. M. Rahman, "Characterization of underground tunnel water hydrochemical system and uses through multivariate statistical methods: a case study from Maddhapara Granite Mine, Dinajpur, Bangladesh," *Environmental Earth Sciences*, vol. 75, no. 24, p. 1501, 2016.

[10] K. Megherfi, M. Maza, A. Saou, and J. L. Seidel, "Hydrochemical and statistical study of karstic spring waters of Bejaia coastal area (North Algeria)," *Arabian Journal of Geosciences*, vol. 13, no. 11, pp. 1–19, 2020.

[11] M. A. Engle and E. L. Rowan, "Geochemical evolution of produced waters from hydraulic fracturing of the Marcellus Shale, northern Appalachian Basin: a multivariate compositional data analysis approach," *International Journal of Coal Geology*, vol. 126, pp. 45–56, 2014.

[12] C. Pan, K. Ng, and A. Richter, "An integrated multivariate statistical approach for the evaluation of spatial variations in groundwater quality near an unlined landfill," *Environmental Science and Pollution Research*, vol. 26, no. 6, pp. 5724–5737, 2019.

[13] A. Kumar, G. Matta, and S. Bhatnagar, "A coherent approach of water quality indices and multivariate statistical models to estimate the water quality and pollution source apportionment of River Ganga System in Himalayan region, Uttarakhand, India," *Environmental Science and Pollution Research*, vol. 28, no. 31, pp. 42837–42852, 2020.

[14] P. Prusty and S. H. Farooq, "Application of water quality index and multivariate statistical analysis for assessing coastal water quality," *Environmental Processes*, vol. 7, no. 3, 2020.

[15] X. Li, P. Wu, Z. Han, X. Zha, H. Ye, and Y. Qin, "Effects of mining activities on evolution of water quality of karst waters in Midwestern Guizhou, China: evidences from hydrochemistry and isotopic composition," *Environmental Science and Pollution Research*, vol. 25, 2018.

[16] H. Huang, Z. H. Chen, and T. Wang, "Characteristics and processes of hydrogeochemical evolution induced by long-term mining activities in karst aquifers, southwestern China," *Environmental Science and Pollution Research*, vol. 26, no. 29, pp. 30055–30068, 2019.

[17] R. Sarikhani, A. G. Dehnavi, Z. Ahmadnejad, and N. Kalantari, "Hydrochemical characteristics and groundwater quality assessment in Bushehr Province, SW Iran," *Environmental Earth Sciences*, vol. 74, no. 7, pp. 6265–6281, 2015.

[18] M. Abbas, S. L. Shen, H. M. Lye, A. N. Zhou, and S. Rashid, "Evaluation of the hydrochemistry of groundwater at Jhelum Basin, Punjab, Pakistan," *Environmental Earth Sciences*, vol. 80, no. 8, 2021.

[19] F. Touhari, M. Meddi, M. Mehaiguene, and M. Razack, "Hydrogeochemical assessment of the Upper Cheliff groundwater (North West Algeria)," *Environmental Earth Sciences*, vol. 73, 2015.

[20] T. G. Alharbi and F. K. Zaidi, "Hydrochemical classification and multivariate statistical analysis of groundwater from Wadi Sahba area in central Saudi Arabia," *Arabian Journal of Geosciences*, vol. 11, no. 20, 2018.

[21] M. A. Ansari, A. Deodhar, and U. S. Kumar, "Modeling of geochemical processes and multivariate statistical analysis for hydrochemical assessment of spring water of the Outer Himalaya, India," *Environmental Earth Sciences*, vol. 78, no. 24, 2019.

[22] D. D. Wang, C. D. Yang, and L. M. Shao, "The spatiotemporal evolution of hydrochemical characteristics and groundwater quality assessment in Urumqi, Northwest China," *Arabian Journal of Geosciences*, vol. 14, no. 3, 2021.

[23] H. Y. Wei, X. J. Liang, S. H. Liu, M. J. Liu, and C. L. Xiao, "Hydrochemical evolution of groundwater in Dehui, China," *Water*, vol. 12, no. 12, p. 3378, 2020.

[24] J. Xiao, Z. D. Jin, F. Zhang, and W. Jin, "Major ion geochemistry of shallow groundwater in the Qinghai Lake catchment, NE Qinghai-Tibet Plateau," *Environmental Earth Sciences*, vol. 67, no. 5, pp. 1331–1344, 2012.

[25] J. Mallick, C. K. Singh, M. K. AlMesfer et al., "Hydro-geochemical assessment of groundwater quality in Aseer Region, Saudi Arabia," *Water*, vol. 10, no. 12, 2018.

[26] I. Hassen, F. Hamzaoui-Azaza, and R. Bouhlila, "Application of multivariate statistical analysis and hydrochemical and isotopic investigations for evaluation of groundwater quality and its suitability for drinking and agriculture purposes: case of Oum Ali-Thelepte aquifer, central Tunisia," *Environmental Monitoring and Assessment*, vol. 188, no. 3, pp. 135.1–135.20, 2016.

[27] Y. Rafighdoust, Y. Eckstein, R. M. Harami, M. H. M. Gharaie, and A. Mahboubi, "Using inverse modeling and hierarchical cluster analysis for hydrochemical characterization of springs and Talkhab River in Tang-Bijar oilfield, Iran," *Arabian Journal of Geosciences*, vol. 9, no. 3, p. 241, 2016.

[28] F. Liu, S. Wang, T. J. Yeh, P. Zhen, L. Wang, and L. Shi, "Using multivariate statistical techniques and geochemical modelling to identify factors controlling the evolution of groundwater chemistry in a typical transitional area between Taihang Mountains and North China Plain," *Hydrological Processes*, vol. 34, no. 8, pp. 1888–1905, 2020.

[29] M. Maghraby, "Hydrogeochemical characterization of groundwater aquifer in Al-Madinah Al-Munawarah City, Saudi Arabia," *Arabian Journal of Geosciences*, vol. 8, no. 6, pp. 1–16, 2015.

WILEY | Hindawi

Research Article

Evolution of the Oil Shale Permeability under Real-Time High-Temperature Triaxial Stress in the Jimusar Area, Xinjiang

Lusheng Yang [1] **and Peng Li** [2]

[1]*College of Basic Courses, Shanxi Institute of Energy, Jinzhong 030600, China*
[2]*Department of Mining Engineering, Shanxi Institute of Energy, Jinzhong 030600, China*

Correspondence should be addressed to Peng Li; lipeng@sxie.edu.cn

This paper adopts a real-time high-temperature triaxial seepage test system to study the permeability evolution of oil shale in the Jimusar area, Xinjiang, with the temperature, pore pressure, and volumetric stress. The results indicate that (1) the variation process of the oil shale permeability with the temperature can be divided into three stages: slow growth stage from 20 to 350°C, rapid growth stage from 350 to 500°C with a threshold temperature of 400°C, and growth deceleration stage from 500 to 600°C. (2) With increasing pore pressure, the permeability gradually decreases. Under a volumetric stress of 17 MPa, the permeability decreases the most rapidly from 1 to 2 MPa, and under a volumetric stress of 34 MPa, the permeability decreases the fastest from 1 to 3 MPa. (3) The oil shale permeability decreases with increasing volumetric stress. At room temperature, the decrease magnitude of the permeability is small and increases with increasing temperature. The results can provide a theoretical reference for the analysis of the seepage process of thermal fluids and pyrolysis oil and gas in oil shale.

1. Introduction

Oil shale is a kind of sedimentary rock containing organic matter (kerogen) with a low permeability. After heating, kerogen can be converted into shale oil and gas and can be used as fuel and chemical raw materials. The proven oil shale reserves in China reach approximately 719.9 billion tons, which can be converted into 47.6 billion tons of shale oil [1–3], which is much higher than the recoverable oil resources of 26.8 billion tons. Oil shale is mainly located in Liaoning, Jilin, Xinjiang, Guangdong, and other areas [4]. As a very large proportion of unconventional oil and gas resources, the efficient and green development and utilization of oil shale could be of great importance to improve the energy security in China and the strategic reserves of oil and gas resources.

The utilization of oil shale can be divided into two types: ground dry distillation furnace pyrolysis and in situ thermal injection pyrolysis. Among these methods, ground dry distillation faces the environmental problems involving the three waste materials, including wastewater, waste gas and waste residue, and the economic problem of a low mining efficiency [5]. In situ thermal injection oil shale mining can effectively solve the above environmental problems [6], which have attracted the attention of a large number of scholars in China and abroad. Among these scholars, Zhao et al. of the Taiyuan University of Technology proposed the method of in situ steam injection for oil shale production [7]; the core of which entails the efficient injection of high-temperature superheated steam via thermal injection wells into oil shale layers. Then, the oil and gas fluids produced by pyrolysis in the oil shale layers are produced with extraction wells. The evolution of the oil shale permeability at high temperatures can affect the flow of superheated water vapor and pyrolytic oil and gas in oil shale layers and can thus affect the efficiency of in situ pyrolysis. Therefore, studying the evolution law of the oil shale permeability under real-time high-temperature conditions is helpful to determine how to efficiently inject high-temperature steam into oil shale layers.

Under the action of a high temperature, organic matter pyrolysis in oil shale and heterogeneous expansion of

inorganic minerals generate a large number of pores and fracture structures in oil shale. Pore fracture structures are the flow channels of high-temperature fluids, and new pore fractures at high temperatures can affect the oil shale permeability. Thus, a large number of scholars have performed much research on the change in the pore fracture structure and permeability of oil shale at high temperatures. Kang et al. [8] carried out scanning experiments and permeability tests of oil shale after dry distillation with computed tomography (CT) and triaxial percolation equipment, respectively. A large number of cracks along the parallel bedding direction occurred beyond 400°C, and the oil shale permeability sharply increased at 400°C. Tiwari et al. [9] conducted a scanning experiment of the fracture structure in the Green River basin, United States, at high temperatures with CT equipment and obtained the variation law of the permeability with the temperature by analyzing the collected pore fracture structure data. It was found that with increasing temperature, the number of pore fracture structures in oil shale greatly increased, and the permeability increased from 173 to 2199 D. Rabbani et al. [10] calculated the permeability of connected seepage channels in an oil shale digital core at different temperatures with CT scanning technology and digital core technology. Beyond 400°C, the oil shale permeability increased sharply to 1 D. The change in oil shale permeability was slightly related with the pore size but attained a notable relationship with the pore connectivity. Yang et al. [11, 12] studied the change law of the oil shale permeability under the action of high-temperature steam and found that the increase in oil shale permeability was closely related to the change in fracture structures under the action of high-temperature steam. Geng et al. [13] examined the change law of the permeability along the vertical bedding direction of Fushun oil shale after high-temperature treatment. The permeability rapidly increased from 300 to 400°C, and the increase declined from 400 to 600°C. Zhao and Kang [14] investigated the permeability change law of Fushun oil shale at a 200 m buried depth under real-time high-temperature conditions and found that the oil shale permeability continued to increase from 350 to 600°C.

Most of the above studies on the oil shale permeability were carried out after high-temperature heating. Only the study of Zhao and Kang [14] was executed under real-time high-temperature conditions, but only the oil shale permeability in the Fushun area was studied, while the influence of the ground stress was not considered. However, the mineral composition of Fushun oil shale is obviously different from that of Xinjiang oil shale, of which Liaoning Fushun oil shale is mainly composed of clay mineral kaolinite, while Jimusar oil shale largely consists of quartz and feldspar, with few clay minerals. The variation in the oil shale permeability with the temperature in Xinjiang is likely different due to the difference in mineral composition. However, few scholars have studied the oil shale permeability in the Jimusar area of Xinjiang under real-time high-temperature conditions.

Therefore, this paper employs a real-time high-temperature permeability testing system independently developed by the Taiyuan Institute of Technology to determine the oil shale permeability in the Jimusar area of

Figure 1: Oil shale specimen.

Xinjiang under real-time high-temperature triaxial stress conditions. The variation in the oil shale permeability at different temperatures, pore pressures, and volumetric stresses was obtained. The evolution law of the oil shale permeability under real-time high-temperature conditions determined in this paper could provide a theoretical reference for the analysis of the flow behavior of heated fluids and pyrolytic oil and gas in oil shale deposits.

2. Experimental Methods and Steps

2.1. Specimen Preparation. The test specimens in this paper originate from the Jimusar area in Xinjiang, and all oil shale specimens are sealed and transported to the laboratory for sample processing. Oil shale is cut into $\Phi 50$ mm × 100 mm cylindrical standard specimens with a CNC sand wire cutting machine. As shown in Figure 1, the specimens are cut parallel to the bedding direction. The parallelism and smoothness of the samples meet the standards of the International Society of Rock Mechanics. The color of the sample is brown. The results of industrial and elemental analysis and mineral analysis are listed in Tables 1 and 2, respectively.

2.2. Test Equipment and Test Process

(1) Determination of study temperature

According to the TG-DSC curve, the weight loss of oil shale mainly occurs at 400-600°C, as shown in Figure 2. Moreover, kerogen in oil shale begins to be pyrolyzed into flowable oil and gas after 400°C, so the research temperature selected in this paper is 20-600°C.

(2) Test equipment

The in situ high-temperature seepage test is carried out with the real-time high-temperature triaxial stress seepage system independently developed by the Taiyuan Institute of Technology, as shown in Figure 3. The test system includes a dynamic loading system, which can apply a pressure up to 32 MPa with an accuracy of ±0.1 MPa, a temperature control system, which can generate a temperature up

TABLE 1: Elemental and industrial analysis.

Sample	Elemental analysis						Industrial analysis			
	N%	C%	H%	O%	H/C	O/C	Moisture content	Ash content	Volatile matter	Fixed carbon
Jimusar, Xinjiang	1.56	8.27	2.98	9.865	2.57	0.82	5.38	79.22	11.46	3.94

TABLE 2: Mineral composition of the oil shale.

Sample origin	Types and contents of minerals (%)							
	Quartz	Pyrite	Clay minerals	Feldspar	Plagioclase	Calcite	Dolomite	Gypsum
Jimusar, Xinjiang	36.3	0.4	5.2	8.0	25.8	4.6	18.8	0.9
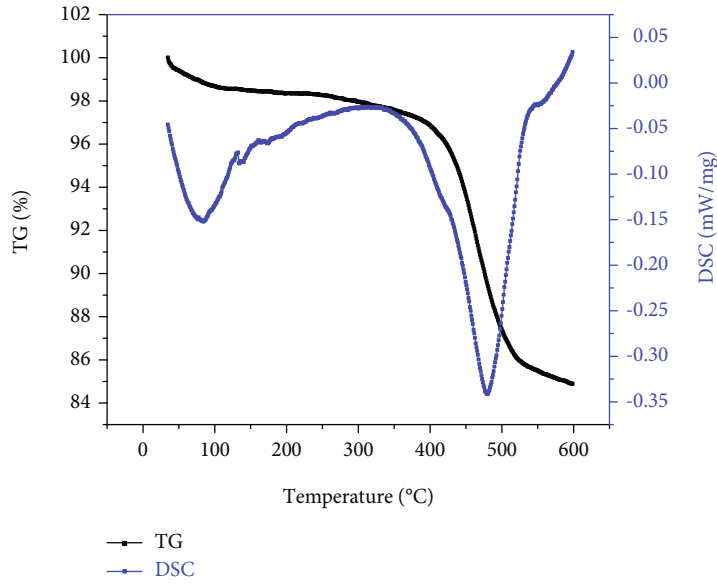
FIGURE 2: TG-DSC curve.
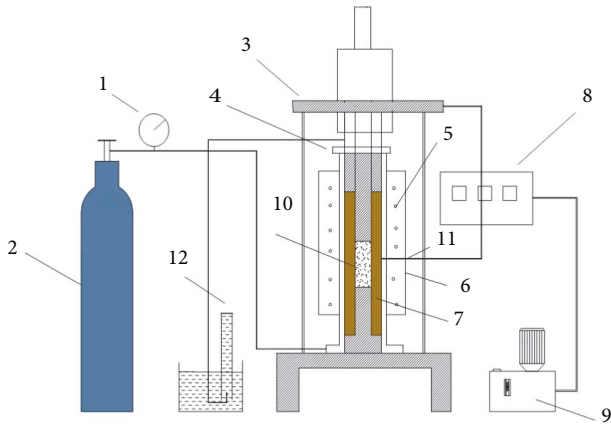
FIGURE 3: Real-time high-temperature triaxial stress seepage penetration testing system. (1) Pressure-reducing valve, (2) cylinder, (3) loading system, (4) triaxial stress chamber, (5) heating sleeve, (6) insulated box, (7) sealing packing, (8) temperature control system, (9) hydraulic system, (10) sample, (11) thermocouple, and (12) air flow measuring equipment.

to 700°C at a heating rate of 1°C/min, and a confining pressure transmission device, which employs the solid pressure transmission technique to convert axial pressure into lateral

TABLE 3: Parameters of the axial, confining, and pore pressures.

Buried depth	Axial compression (MPa), σ_x	Confining pressure (MPa), σ_y	Volumetric stress (MPa), $\sigma_x + 2\sigma_y$	Pore pressure (MPa), P_m
200 m	5	6	17	1 2 3
400 m	10	12	34	1 2 3 4 5

pressure and further applies a confining pressure to the specimen.

(3) Test process

The in situ high-temperature permeability testing process is as follows: (1) different axial and confining pressures are loaded according to the buried depth of oil shale in the Jimusar area of Xinjiang (Table 3). (2) The permeability is tested under different pore pressures (Table 3) at room temperature, nitrogen is permeated under the different pressures, each pore pressure test interval lasts 20 min to prevent the influence of the last pore pressure interval on the test results, and the lower flow rate Q is recorded under each pore pressure. (3) The heating system is activated, the specimen is then heated to the preset temperature (100°C,

(a) $\Theta = 17\,\text{MPa}$ (b) $\Theta = 34\,\text{MPa}$
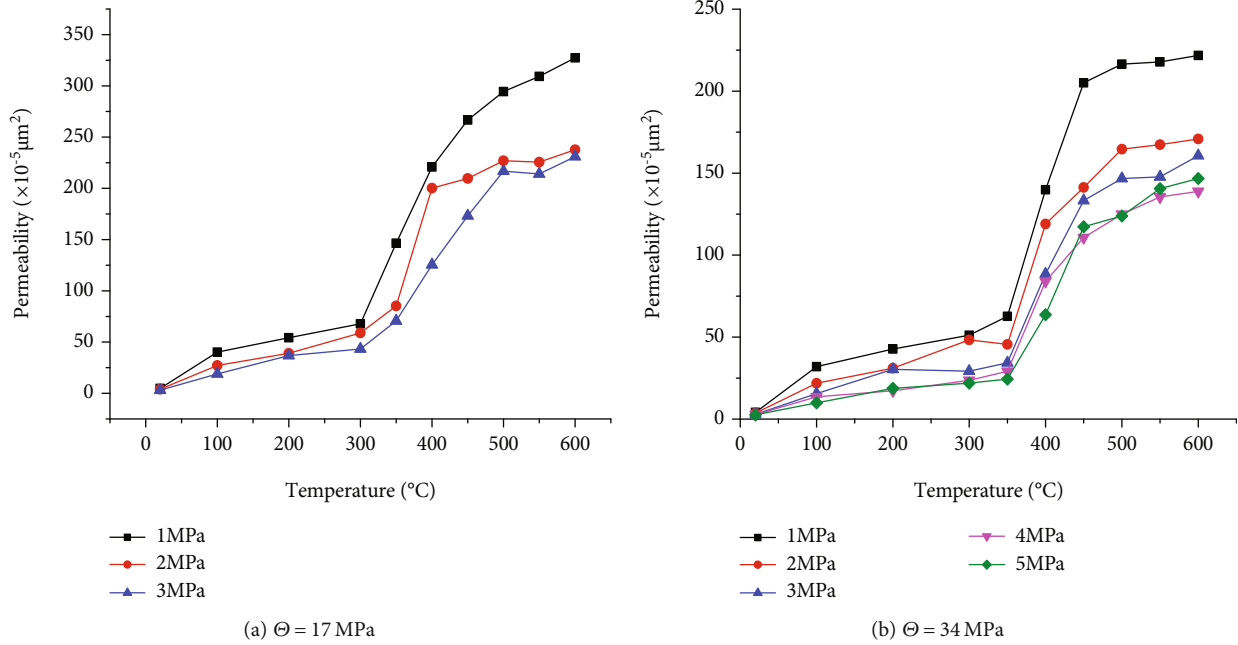
FIGURE 4: Variation in the permeability with the temperature.

200°C, 300°C, 350°C, 400°C, 450°C, 500°C, 550°C, or 600°C) at a heating rate of 1°C/min, and finally, the oil shale permeability is determined under the different pore pressures, as indicated in Table 3, with the same method as that in step 2.

The permeating medium used in this paper is N_2, which conforms to Darcy's law, so Equation (1) is applied to calculate the permeability.

$$k = \frac{2QP_{\text{down}}L\mu}{\left(P_{\text{up}}^2 - P_{\text{down}}^2\right)A}, \tag{1}$$

where k is the permeability, m^2; Q is the flow rate, m^3/s; $P0$ is the atmospheric pressure, at 0.1 MPa; L is the specimen length, m; μ is the gas dynamic viscosity, MPa·s; P_{up} is the inlet pressure, MPa; P_{down} is the outlet pressure, MPa; and A is the cross-sectional area of the specimen, m^2.

3. Test Results

3.1. Permeability Changes with the Temperature. Figure 4 shows the variation of oil shale permeability with the temperature under the different volumetric stresses. The permeability is very low at room temperature and reaches $3.01 \times 10^{-5}\,\mu m^2$ under a pressure of 2 MPa. The permeability gradually increases with increasing temperature. Although different stresses are applied to the oil shale specimen, the permeability exhibits a similar transformation pattern under the different volumetric stresses. Therefore, according to Figure 3, the variation trend of the permeability with the temperature is divided into three stages, and these three stages are analyzed with the permeability data obtained under a volumetric stress of 17 MPa and a pore pressure of 2 MPa.

From 20 to 350°C, the permeability increases slowly. At 100°C, the permeability increases from 4.7×10^{-5} to $18.9 \times 10^{-5}\,\mu m^2$, which is 6.3 times higher than that at 100°C. This occurs because the loss of free water at 100°C results in small cracks [15] parallel to the bedding direction in the oil shale specimen, causing an increase in permeability. Wang et al. studied the thermal fracture evolution law of oil shale under high temperature and found that there are connected fractures in the direction parallel to bedding at 100°C, as shown in Figure 5 [16], which verified the increase of oil shale permeability at 100°C. As the temperature is continuously increased, the oil shale permeability continues to slowly increase, which is attributed to the loss of the volatile oil shale fraction at high temperatures.

At 350 and 500°C, the permeability increases rapidly. The oil shale permeability increases sharply at 400°C, which is 23 times higher than that at room temperature. This occurs due to the initiation of kerogen pyrolysis in the oil shale specimen at 400°C [9, 10], resulting in the connection of a large number of pores and cracks in the oil shale specimen, which leads to a sharp increase in the oil shale permeability. It can be seen from Figure 5 that a large number of oil shale fractures are developed after 400°C, which also verifies that the permeability of oil shale will rise rapidly after 400°C. Therefore, 400°C can be defined as the threshold temperature in terms of the evolution of permeability of Jimusar oil shale. With increasing temperature to 500°C, kerogen pyrolysis continues, and the permeability continuously increases.

At 500 and 600°C, the permeability stabilizes and then increases, respectively. Kerogen pyrolysis in the oil shale specimen is basically completed beyond 500°C, and the permeability increase rate of the oil shale specimen begins to stabilize, but the permeability still increases because feldspar

(a) 20°C (b) 100°C (c) 300°C

(d) 350°C (e) 400°C (f) 450°C

(g) 500°C (h) 550°C (i) 600°C
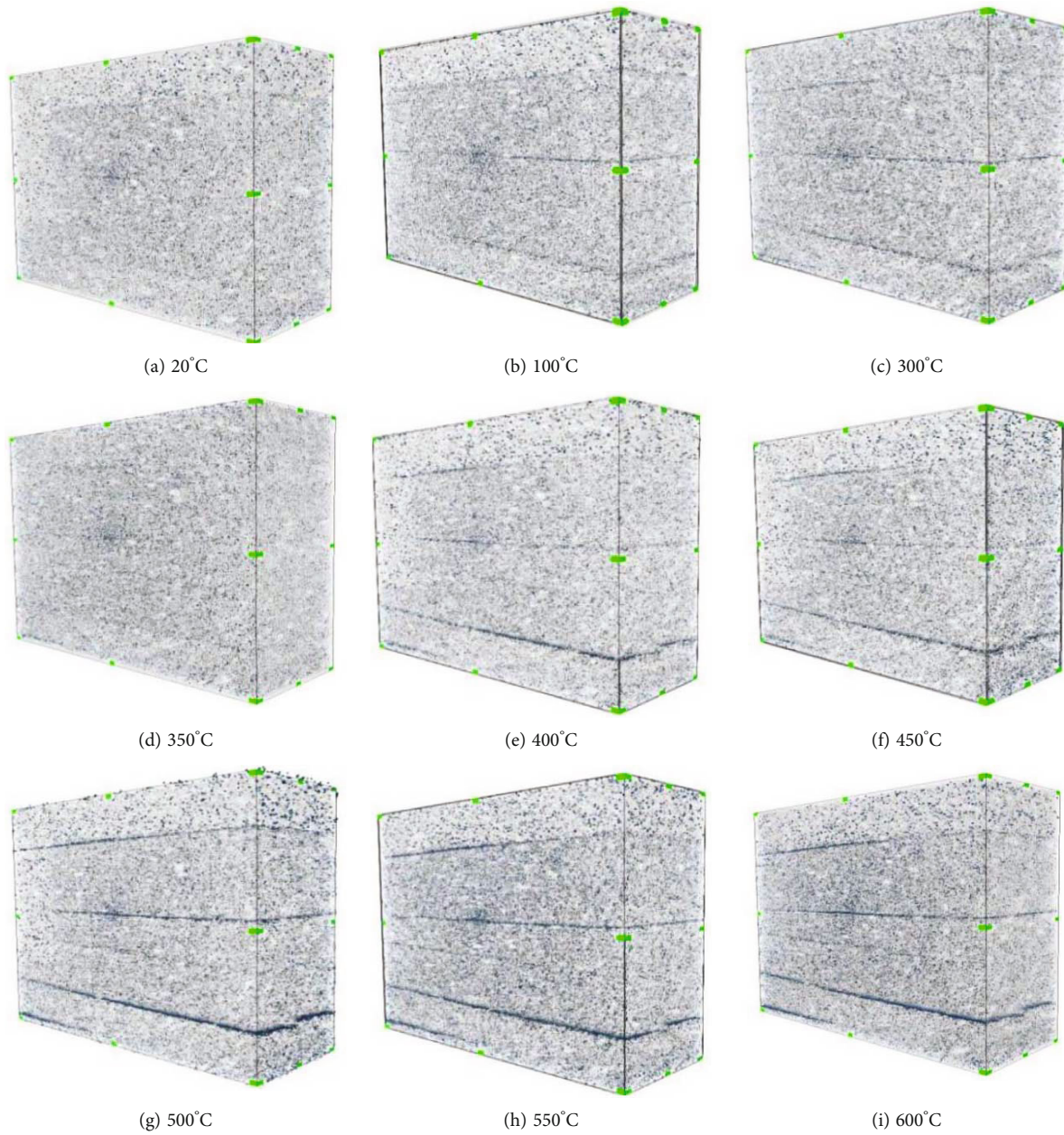
Figure 5: Anisotropic thermal cracking of oil shale [16].

in the oil shale specimen begins to decompose at 500°C, resulting in an increase in the permeability. It can also be seen from Figure 5 that fractures will continue to increase after 500°C, so the permeability at 500°C continues to increase compared with that at 400°C. At 600°C, the fracture growth rate slows down, so the permeability will not increase at 600°C. In addition, it can be found that the permeability rise rate at 600°C is smaller under 34 MPa volumetric stress, because the thermal fracture of oil shale will be closed under high stress. Then, under the combined action of thermal stress and high ground stress, the permeability of oil shale will no longer increase.

3.2. Permeability Changes with the Pore Pressure. The variation trend of the oil shale permeability with the pore pres-

sure is shown in Figure 6. Regardless of the volumetric stress or temperature, the oil shale permeability decreases with increasing pore pressure, but the decrease in permeability differs between the different volumetric stresses.

When the volumetric stress is 17 MPa, the permeability decreases greatly when the pore pressure ranges from 1 to approximately 2 MPa. This occurs because the Klinkenberg effect is notable at the low pore pressure stage [17, 18], which leads to the maximum oil shale permeability under 1 MPa. With increasing pore pressure to 2 MPa, the effective stress on the oil shale specimen decreases obviously, which leads to a decrease in the permeability, but the Klinkenberg effect still plays a leading role.

Under a volumetric stress of 34 MPa, the permeability greatly decreases when the pore pressure ranges from 1 to

(a) $\Theta = 17$ MPa

(b) $\Theta = 34$ MPa
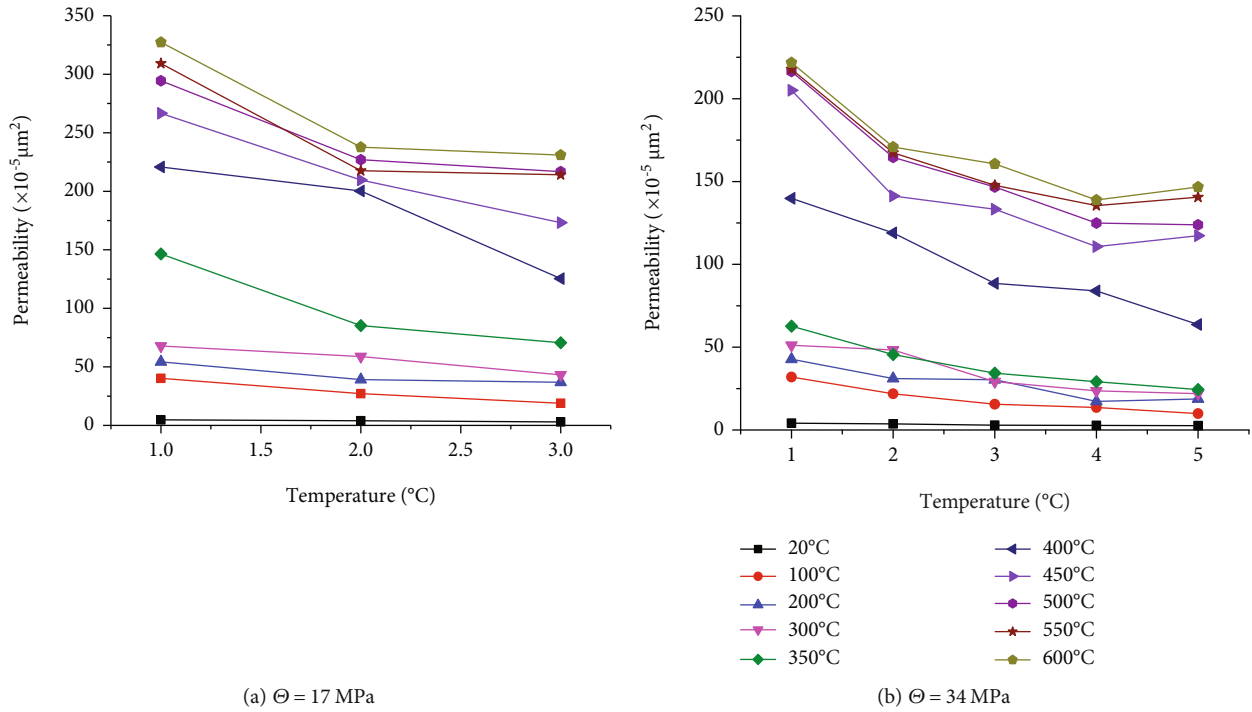
FIGURE 6: Effect of the pore pressure on the permeability.

approximately 3 MPa, which is still attributable to the obvious Klinkenberg effect at lower pore pressures, which leads to a higher oil shale permeability under lower pore pressures than that under higher pore pressures. However, when the volumetric stress reaches 34 MPa, the increase in pore pressure to 3 MPa is not enough to notably reduce the effective stress, overcome the Klinkenberg effect, and constrain the decrease in oil shale permeability.

3.3. Variation in the Permeability with the Volumetric Stress. The permeability under pore pressures of 2 and 3 MPa are chosen as an example to study the influence of the cumulative stress on the oil shale specimen at the different temperatures on the change in permeability. Permeability histograms under volumetric stresses of 17 and 34 MPa at the different temperatures are drawn based on the test data, as shown in Figure 7.

At the same temperature, the oil shale permeability decreases with increasing volumetric stress. However, the oil shale permeability decrease amount varies between the different temperatures. At 20°C, the pore pressure decreases by 8% and 3% under 2 and 3 MPa, respectively. As the temperature continues to rise, the permeability increasingly decreases with increasing volumetric stress, reaching 46% and 51%, respectively, at 350°C, because solid organic matter is first converted into fluid asphaltene [19] at 350°C. Oil shale is more likely to deform when the volumetric stress is higher, thus blocking seepage channels. At 400°C, a high degree of organic matter pyrolysis occurs in the oil shale specimen, resulting in more pyrolysis-induced pore fracture structures. Under high volumetric stresses, the pore fracture structures are closed, resulting in a larger decrease of 40%

and 39%, respectively. The oil shale strength is higher at lower temperatures, and the permeability decreases little with increasing volumetric stress. With increasing temperature, the pore fracture structures produced by oil shale softening and pyrolysis causes oil shale to deform more easily under high volumetric stresses [20], and the internal pore fissures in the oil shale specimen more readily collapse, which leads to a decrease in permeability with increasing volumetric stress, which is consistent with the variation in the Fushun oil shale permeability with the volumetric stress obtained by Geng [13].

4. Discussion

4.1. Mechanism of Permeability Evolution with the Temperature. In Section 2.1, it was mentioned that the variation in the oil shale permeability with the temperature is closely related to the decomposition of organic matter and inorganic minerals in oil shale. In this section, a weight loss curve of the oil shale specimen in the temperature range from 20°C to 600°C is obtained in thermogravimetric experiments. Figure 8 shows the curve of the weight loss and permeability of the oil shale specimen with the temperature. The ratio of the oil shale permeability (K) at the different temperatures to the oil shale permeability (K_0) at room temperature under a pressure of 2 MPa is indicated on the left axis, for theta = 17 MPa. The diagram reveals that the weight loss curve exhibits the first decrease point at 100°C, where the oil shale specimen begins to lose its internal free water, resulting in the first increase in the oil shale permeability. The main stage of oil shale weight loss ranges from 400 to 500°C, which further suggests that a large amount of kerogen

(a) $P_m = 2$ MPa

(b) $P_m = 3$ MPa
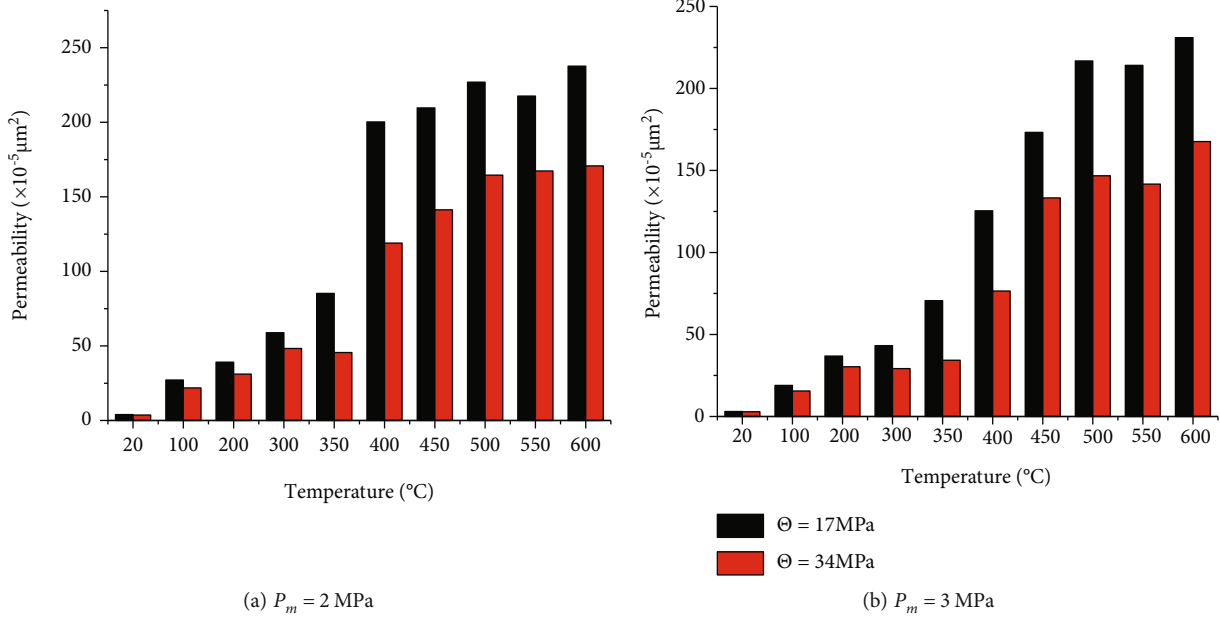
FIGURE 7: Effect of the volumetric stress on the permeability.
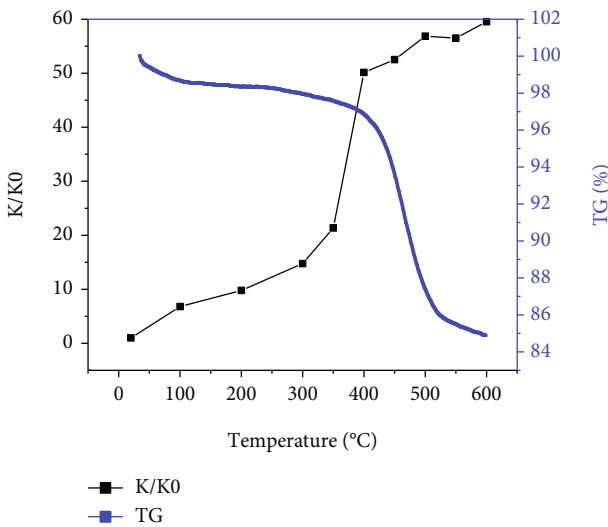
FIGURE 8: Variation in the weight loss rate with the temperature.

in the oil shale specimen is pyrolyzed at this temperature, resulting in a sharp increase in the oil shale permeability at this temperature. When the temperature is higher than 500°C, the weight loss rate begins to decrease, which is the stage of growth rate deceleration of the oil shale permeability.

The release of gas products indicates that there are connected seepage channels in the oil shale specimen, which causes these products to be released. Therefore, the variation in gas products due to kerogen pyrolysis with the temperature can effectively explain the variation in the permeability with the temperature. As can be seen in Figure 9, only a small amount of gas products is produced from 100 to 350°C, mainly free water and volatile matter. When the tem-

perature rises to 400°C, a large number of gas products is produced, which indicates that a large number of connected pores and fracture channels are generated in the oil shale specimen so that the gas products can be released from the matrix. This temperature point indicates the threshold temperature of oil shale permeability variation with the temperature. Beyond 500°C, the gas products begin to decrease, which indicates that the kerogen pyrolysis process in the oil shale specimen is basically completed, while the connected pores no longer increase, which is also the stage of slow permeability growth.

4.2. Comparative Analysis of the Evolution of the Oil Shale Permeability with the Temperature in the Different Areas. As the evolution of the oil shale permeability with the temperature plays a very important role in the in situ exploitation process of oil shale, predecessors have assessed the oil shale permeability in the Fushun area. Wang et al. [16] and Zhao and Kang [14] both measured the oil shale permeability at a depth of 200 m and obtained the change rules of the oil shale permeability with the temperature. The variation in permeability with the temperature under a pore pressure of 2 MPa obtained by predecessors and that determined in this experiment are compared and analyzed in the same diagram, as shown in Figure 10.

Figure 8 shows that the variation trend of the oil shale permeability with the temperature is similar between the Jimusar area of Xinjiang and the Fushun area of Liaoning Province. However, the oil shale permeability in the Jimusar area of Xinjiang is obviously higher than that in the Fushun area of Liaoning Province. This occurs because the clay mineral content in the oil shale of the Fushun area reaches 42.6 [21] at room temperature, while the clay mineral content in the oil shale of the Jimusar area reaches only 5%. As a result, the oil shale in the Fushun area of Liaoning Province is
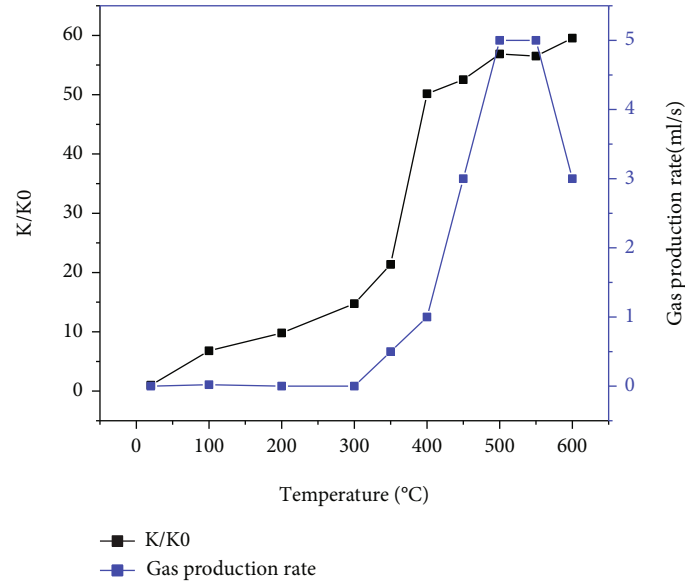
FIGURE 9: Variation in the production quantity with the temperature.
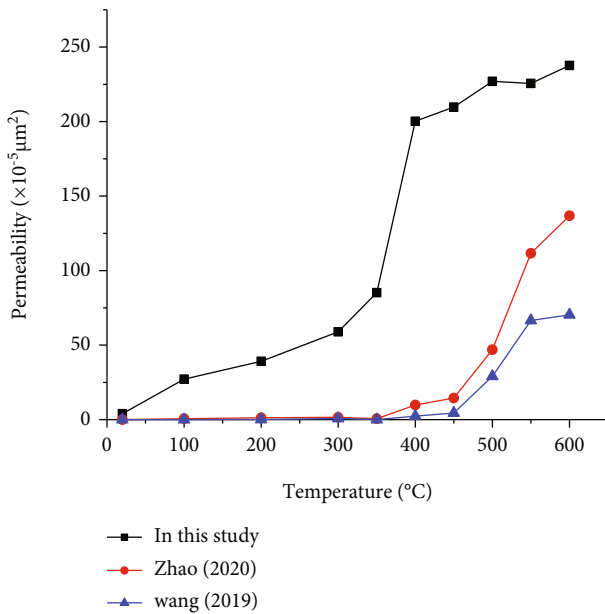
FIGURE 10: Comparison of the oil shale permeability between the different areas.

denser at room temperature, and the permeability is lower. With increasing temperature, the oil shale of the Jimusar area is subject to not only internal kerogen pyrolysis but also heterogeneous expansion deformation of minerals such as quartz (36.3%) and plagioclase (25.8%). As a result, the oil shale permeability in the Jimusar area of Xinjiang is relatively high.

4.3. Practical Application. In the process of in situ heating shale for oil production, high-temperature steam shall be injected into the oil shale seam through the injection well, as shown in Figure 11 [22]. In the process of injection, the

permeability evolution of oil shale will not only affect the injection efficiency of high-temperature steam but also affect the migration speed of oil and gas from oil shale to pumping wells after pyrolysis. In this paper, the real-time seepage experiment under high-temperature triaxial stress can truly reflect the seepage evolution law of oil shale under the combined action of in situ stress and temperature. It is found that the permeability of oil shale increases obviously at 400°C, that is, the injection temperature should be higher than 400°C in the process of injecting high-temperature steam. The permeability of oil shale decreases with the increase of in situ stress. The increase of in situ stress weakens the permeability, but the permeability of oil shale still increases at high temperature, indicating that the temperature still strengthens the permeability of oil shale under high ground stress. Therefore, the experimental results of this paper can provide data and theoretical support for in situ thermal injection and shale production.

5. Conclusion

In this paper, a real-time high-temperature triaxial permeability testing system independently developed by the Taiyuan Institute of Technology is employed to simulate the in situ high-temperature oil shale environment, and the variation in the oil shale permeability with the temperature in the Jimusar area of Xinjiang under real-time high-temperature triaxial stress conditions is obtained. The conclusions are as follows:

(1) The variation in the oil shale permeability with the temperature can be divided into three stages: the slow growth stage ranges from 20 to 350°C. This stage of the permeability change process is mainly caused by the loss of free water and volatiles. The rapid growth stage occurs from 350 to 500°C. The

(a)

(b)
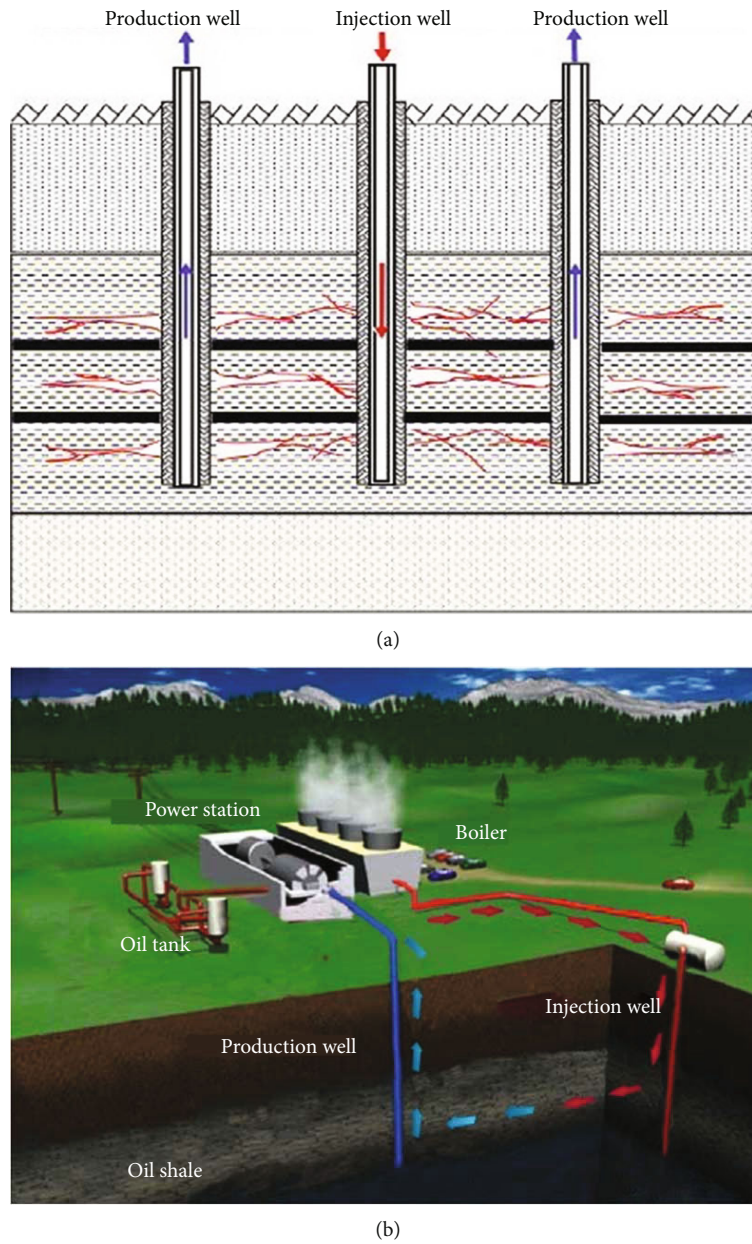
FIGURE 11: The oil shale in situ convection technology using injected superheated steam (MTI): (a) hydraulic fracturing and (b) schematic of the MTI system [22].

growth at this stage is mainly caused by the pyrolysis of oil shale kerogen, and 400°C is the threshold temperature. From 500 to 600°C, the growth process decelerates

(2) Under the same volumetric stress, with increasing pore pressure, the oil shale permeability first rapidly decreases and then slowly decreases. However, the change trend differs between the different volumetric stresses. Under the 17 MPa volumetric stress, the permeability decreases rapidly and then slowly from 1 to approximately 2 MPa. Under the 34 MPa volumetric stress, when the pore pressure ranges from 1 to approximately 3 MPa, the permeability first rapidly decreases and then slowly decreases

(3) At the same temperature, the oil shale permeability continuously decreases with increasing volumetric stress. However, the decrease amount varies between the different temperatures, the decrease amount is the smallest at room temperature, and the permeability decrease amount increases gradually with increasing temperature, which is attributed to oil shale softening and pyrolysis of the internal organic matter, which results in easier oil shale deformation under the action of external stress, resulting in pore fissure closure

(4) The oil shale permeability in the Jimusar area is obviously higher than that in the Fushun area because the oil shale in the Jimusar area contains

higher contents of quartz and feldspar and fewer clay minerals, which makes it easier to produce more thermal cracks at high temperatures to form more seepage channels

Data Availability

All data used to support the study is included within the article.

Conflicts of Interest

The authors declare that there is no conflict of interest regarding the publication of this paper.

Acknowledgments

References

[1] Z. J. Liu, Q. S. Dong, S. Q. Ye et al., "Current situation of oil shale resources in China," *Journal of Jilin University (Earth Science Edition)*, vol. 36, no. 6, pp. 869–879, 2006.

[2] Z. Liu, Q. Meng, Q. Dong et al., "Characteristics and resource potential of oil shale in China," *Oil Shale*, vol. 34, no. 1, pp. 15–41, 2017.

[3] D. Li, D. Tang, and Y. Yang, "Research, development and utilization of oil shale resources," *Petroleum Exploration and Development*, vol. 33, no. 6, pp. 657–661, 2006.

[4] J. Wang, L. Feng, M. Steve, X. Tang, T. E. Gail, and H. Mikael, "China's unconventional oil: a review of its resources and outlook for long- term production," *Energy*, vol. 82, pp. 31–42, 2015.

[5] Z. Li and X. Wang, "Ecological environment problems in the development and utilization of oil shale resources," *Petrochemical Environmental Protection*, vol. 3, pp. 8–12, 1991.

[6] Y. Tang, Y. Bai, and W. Wu, "New energy in Northwest China-typical characteristics of oil shale and several issues in its development and utilization," *China Geology*, vol. 38, no. 3, pp. 731–741, 2011.

[7] Y. S. Zhao, Z. C. Feng, and D. Yang, "The method for mining oil & gas from oil shale by convection heating," China Patent, CN200510012473.4, 5, 2010.

[8] Z. Kang, D. Yang, Y. Zhao, and Y. Hu, "Thermal cracking and corresponding permeability of Fushun Oil Shale," *Oil Shale*, vol. 28, no. 2, pp. 273–283, 2011.

[9] P. Tiwari, M. Deo, C. Lin, and J. D. Miller, "Characterization of oil shale pore structure before and after pyrolysis by using X-ray micro CT," *Fuel*, vol. 107, pp. 547–554, 2013.

[10] A. Rabbani, T. G. Baychev, S. Ayatollahi, and A. P. Jivkov, "Evolution of pore-scale morphology of oil shale during pyrolysis: a quantitative analysis," *Transport in Porous Media*, vol. 119, no. 1, pp. 143–162, 2017.

[11] D. Yang, J. Xue, Z. Kang, and Z. H. Liu, "Dry distillation and seepage experiments of Fushun oil shale," *Journal of Xi'an Petrol University*, vol. 22, no. 2, pp. 23–25, 2007.

[12] Z. Liu, D. Yang, J. Xue, and Y. S. Zhao, "Experimental study on the Seepage Lawof Distilied Oil Shale," *Journal of Taiyuan University*, vol. 37, no. 4, pp. 414–416, 2006.

[13] Y. Geng, "Experimental study on physical and mechanical properties of oil shale underground in-situ fracturing and pyrolysis," *Journal of Taiyuan University*, 2018.

[14] J. Zhao and Z. Kang, "Permeability of oil shale under in situ conditions: Fushun Oil Shale (China) experimental case study," *Natural Resources Research*, vol. 30, no. 1, pp. 753–763, 2021.

[15] F. Bai, Y. Sun, Y. Liu, and M. Guo, "Evaluation of the porous structure of Huadian oil shale during pyrolysis using multiple approaches," *Fuel*, vol. 187, pp. 1–8, 2017.

[16] G. Wang, D. Yang, Y. Zhao, Z. Kang, J. Zhao, and X. Huang, "Experimental investigation on anisotropic permeability and its relationship with anisotropic thermal cracking of oil shale under high temperature and triaxial stress," *Applied Thermal Engineering*, vol. 146, pp. 718–725, 2019.

[17] M. Firouzi, K. Alnoaimi, A. Kovscek, and J. Wilcox, "Klinkenberg effect on predicting and measuring helium permeability in gas shales," *International Journal of Coal Geology*, vol. 123, pp. 62–68, 2014.

[18] T. Chen, X. Feng, and Z. Pan, "Experimental study of swelling of organic rich shale in methane," *International Journal of Coal Geology*, vol. 150-151, pp. 64–73, 2015.

[19] T. Saif, Q. Lin, K. Singh, B. Bijeljic, and M. J. Blunt, "Dynamic imaging of oil shale pyrolysis using synchrotron X-ray microtomography," *Geophysical Research Letters*, vol. 43, no. 13, pp. 6799–6807, 2016.

[20] E. Eseme, R. Littke, and B. M. Krooss, "Factors controlling the thermo-mechanical deformation of oil shales: Implications for compaction of mudstones and exploitation," *Marine and Petroleum Geology*, vol. 23, no. 7, pp. 715–734, 2006.

[21] Z. Liu, "Study on the evolution law of pore structure and permeability characteristics of oil shale under temperature," *Journal of Taiyuan University*, 2018.

[22] Z. Kang, Y. Zhao, and D. Yang, "Review of oil shale in-situ conversion technology," *Journal of Applied Energy*, vol. 269, article 115121, 2020.

WILEY | Hindawi

Research Article

3D Morphology Distribution Characteristics and Discrete Element Simulation of Sand-Gravel Mixtures

Wu Qi,[1] Sun Suyu,[1] Gao Guangliang,[2] Fang Yi [iD],[1,3] and Chen Guoxing[1]

[1]*Institute of Geotechnical Engineering, Nanjing Tech University, Nanjing 210009, China*
[2]*BGI Engineering Consultants LTD., Beijing 100038, China*
[3]*National Institute of Natural Hazards, Ministry of Emergency Management of China, Beijing 100085, China*

Correspondence should be addressed to Fang Yi; yifang@ninhm.ac.cn

Sand-gravel mixtures are typical binary materials, exhibiting highly heterogeneous, discontinuous, and significant structural effects. The contact state between sand and gravel particles has a significant influence on the mechanical properties of the mixtures. This article focused on the complex internal structure and its mesostructural behavior of the mixtures, and a systematic statistical analysis was carried out to study the shape, size, and angularity of the coarse particles. The three-dimensional (3D) shapes of coarse aggregates were approximated to be hexahedron, pentahedron, and tetrahedron. An indicator called angularity and surface texture (AT) index was developed to characterize the combined effect of the coarse aggregate angularity and surface texture. Based on the screening testing and digital image processing, the particle size and AT index of aggregates were extracted, and their means, standard deviations, and statistical distributions were studied. An algorithm for generating 3D aggregates was developed based on the statistical results of the coarse aggregate 3D morphology. The coarse aggregate generating code was written using the fish language in PFC3D. The numerical model was then applied to conduct three typical monotonic or cyclic triaxial test simulations. Retrospective simulation of the laboratory tests using the proposed model showed good agreement, and the reliability of the model is effectively verified. The results interpreted well the mechanism of particle motion and the distribution of interparticle contact force during shearing from mesoscale of the mixtures, which can give better understanding and modeling of the nonlinear behavior of the sand-gravel mixtures.

1. Introduction

Hydraulic fracturing is a promising method for increasing the production of oil and gas wells. Hydraulic fracturing is currently the main form of natural gas extraction. It requires a large amount of water mixed with chemicals to be poured into the shale layer for hydraulic fracturing to release natural gas. At present, most of the world's natural gas and oil wells are drilled by hydraulic fracturing [1–4]. Due to the characteristics of deep underground drilling operation of hydraulic fracturing, it often crosses undesirable engineering geology such as a sandy gravel mixture layer [5, 6]. It is of great significance to guide the construction of engineering to establish a set of fast and effective methods to analyze the mechanical behavior of sandy gravel mixtures.

Sand-gravel mixtures are a special engineering geological material between the soil and the fractured rock; the sand-gravel mixture structure presents the mesostructure between sand particles and gravel particles [7]. The contact state and particle morphology of the mixtures have a significant contribution to their mechanical properties [8–12]. If the heterogeneous and discontinuous structural characteristics of the sandy gravel mixtures are ignored and the particle morphology and particle distribution are not considered, the authenticity of the mesostructure characteristic simulation of the material will be reduced, and it is difficult to describe the microscopic mechanical behavior between the particles [13].

Kennedy and Lin [14] constructed polygons to approximate the shape of particles and found that the number of

sides of the polygon is proportional to the circumference and inversely proportional to the length of the sides. This relationship is linear in double logarithmic coordinates, and the slope indicates the irregularity of the particles. Bowman et al. [15] use the Fourier transform and analysis theory to describe the particle morphology of sand. According to the research of Sukumaran and Ashmawy [16], the surface texture reflects the fine morphology of the particle surface and can be used to describe the roughness of the particle surface and the angular microscale. Cho et al. [17] described the particle morphology based on three aspects: sphericity, edge angle, and roughness. Ferellec and Mcdowell [18] replaced the average radius of curvature of the corners with the average radius of all inscribed circles on the projection contour of the particles, which improved the reproducibility of this parameter.

With the development of computer technology and the emergence of the discrete element method, numerical simulation has gradually become an important method to analyze the particle shape; the elastoplastic finite element method (FEM) was introduced in the initial stage. However, due to the discontinuity of sand, FEM based on continuous medium theory cannot reflect the influence of material parameters such as particle size and particle morphology on the simulation results [19, 20]. Therefore, the discrete element method (DEM) based on discontinuous medium mechanics has been widely used in the numerical simulation of granular media [21]. This method is low in cost and easy to operate and is very suitable for numerical simulation of discrete media such as sand and gravel.

Mcdowell and Harireche [22] found that adjusting the percentage of pellets empirically reflects the size effect of individual pellet strength. For the particle cluster model, when the particle interaction force exceeds the connection strength, the small particles are detached, which can simulate local or whole fracture. Cheng et al. [23] conducted a simulation of the particle flow of crushable soil, in which the crushed particles used a cluster model of particles formed by the bonding of several small particles, and the randomness of single particle strength was reflected by randomly deducting a certain percentage of small balls. Deluzarche and Cambou [24] used the discrete element code PFC2D and considered breakable clusters of 2D balls. The different parameters were determined from experimental data obtained from laboratory tests performed on rock blocks. The model was validated by comparing the results of the simulation of shearing tests with actual triaxial tests on rockfill material published in the literature. Alaei and Mahboubi [25] focused on numerical modelling of rockfill material with the discrete element method (DEM). Because the DEM models the interaction of separate elements, it was capable of modelling discrete structures of granular materials and particle breakage. Alonso et al. [26] established a distinct element method model developed in which grains were characterized in the clump model. The resulting particle shape approaches real geometries and allows a reasonable breakage evolution, and the particle breakage criterion involves the subcritical propagation of fissures in the grain.

In this study, taking the sand-gravel mixtures distributed at the project site of Binjiang Subway Station of Metro Line 3 in Chengdu as an example, using discrete element numerical simulation and digital image processing technology, the 3D form and distribution of gravel particles are systematically analyzed. Based on the PFC3D particle flow software, a 3D discrete element simulation method for sand-gravel mixtures was proposed. The triaxial numerical test and actual triaxial tests were compared to verify the accuracy of the method and discuss the mesomechanical behavior of the sand-gravel mixtures.

2. Basic Physical Properties of Sand-Gravel Mixtures

The sand-gravel mixture samples were taken from Binjiang Subway Station of Metro Line 3, Chengdu. The soil layers in this site from top to bottom are Quaternary Holocene (Q_h) artificial fill, alluvial silt, sand and pebble (medium sand lenticel sandwiched in some sections), Quaternary Pleistocene (Q_p) alluvial pebbles, and Upper Cretaceous (K_2) Guankou Formation mudstone. Three groups of sand-gravel mixtures at different depths are used for the particle-size analysis test, and the gradation curve is shown in Figure 1. According to the Unified Soil Classification System (ASTM D2487 [27]), the sand-gravel mixtures belong to poorly graded gravel (GP) with the minimum or maximum dry density of 1.437 or 1.740 g/cm^3, the specific gravity is 2.68, mean particle size $d_{50} = 6.31$ mm, coefficient of uniformity $C_u = 34.5$, and coefficient of curvature $C_c = 0.37$.

3. The 3D Morphological Characteristics of Sand-Gravel Mixtures

3.1. Test Materials and Test Methods. Gravel particle morphology is an important parameter of mesophysical and mechanical properties of the sand-gravel mixtures. 110 particles with the diameter range from 50 to 20 mm, 117 particles with the diameter from 20 to 10 mm, and 128 particles with the diameter from 10 to 5 mm were selected as the research objects. The 3D shape of gravel particles was captured by digital image processing technology. In order to distinguish the aggregate from the image background more accurately, the background was set to white, and the gravel particles were blackened with ink, as shown in Figure 2.

3.2. 3D Morphological Evaluation Parameters of Particles. The important size parameters of gravel particles include the length of the long axis, the length of the central axis, and the length of the short axis. In order to measure the size of the particles accurately, first, the particles should be neatly arranged on the white paper and a high-definition image was taken. Then, the particles were tiled in situ at a different angle and photographed again. The detailed steps are as follows:
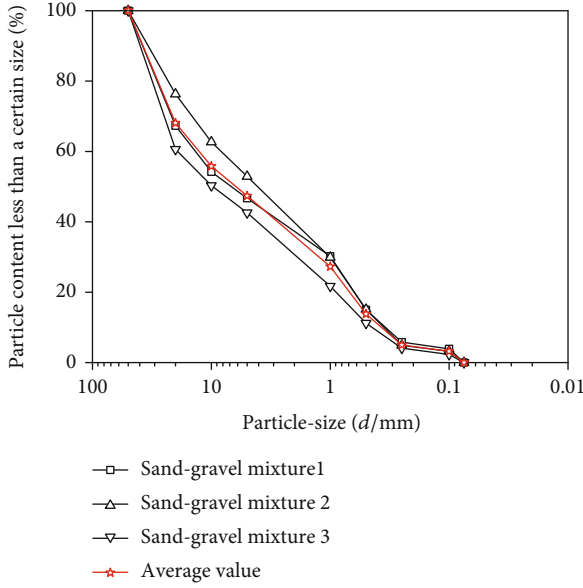
FIGURE 1: Gradation curve of sandy gravel.
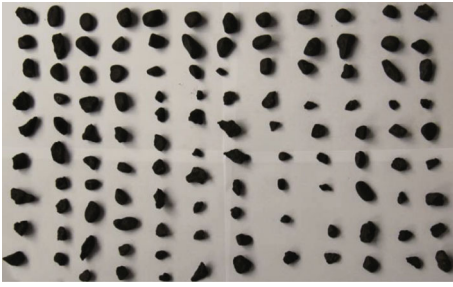
FIGURE 2: Image of blackened gravel particles with the diameter of 5~50 mm.

(1) Select gravel particle samples of all kinds of particle sizes

(2) Soak gravel particle samples with a certain proportion of ink and put them into the oven for full drying

(3) Arrange gravel particle samples on the white paper neatly, and use a digital camera to take high-definition sample images

(4) Replace the particles in situ at a different angle and take a picture again

(5) Use graphics software to sort out the particle images and extract 3D morphological parameters. The specific parameter determination method will be described in detail below

The size characteristics of the gravel particles are reflected by the aspect ratio, the short axis length, the central axis length, and the long axis length of particles. To be specific, the long axis length L is the relatively large diameter in the 3D dimension of the particles, the central axis length W is the maximum size of the vertical elevation with the long axis in the three-dimensional image of the particles, and

the short axis length t is the minimum diameter in the 3D diameter, which means t is the longest diameter perpendicular to both the long axis and the central axis. The details are exhibited in Figure 3. The size ratio between the long axis and the short axis (aspect ratio, L/t) is selected to reflect the shape characteristics of the particles.

In the particle image, the angular characteristics of gravel particles are represented by the smoothness of the contour lines. As shown in Figure 4, on the contour line of the particle image, the perimeter of the contour line increases with the increase of the number of fluctuations. Based on this, a two-dimensional angular coefficient (AC_{2D}) is proposed to characterize the angularity of particles. The angular coefficient AC_{2D} is defined as the ratio of the difference in the surface contour circumference (SCC) and convex contour circumference (CCC) of the particles to the convex contour circumference (CCC) in the image, as shown in

$$AC_{2D} = \frac{SCC - CCC}{CCC}, \tag{1}$$

in which SCC and CCC denote all the boundary lines of the particles themselves and the boundary line with high flatness that is obtained by ignoring the concave parts on the surface contour line, and the curve of the concave part of the particle surface is directly replaced by a straight line as the convex contour circumference.

In order to more realistically reflect the angular coefficient of a single particle, AC_{2D} of each side image is calculated, and the three-dimensional angular coefficient (AC_{3D}) of the particle is obtained by area weighted average, as shown in

$$AC_{3D} = \frac{\sum_1^n A_i \times AC_i}{\sum_1^n A_i}, \tag{2}$$

where n is the number of particles, A_i is the area of the image i, and AC_i is the angular coefficient of the image i.

3.3. Results and Analysis. Figure 5 shows the frequency histograms and normal distribution P-P graph of L, W, and t for particle size gravel of 20~10 mm. The horizontal axis and vertical axis of the frequency histogram of the 3D morphological parameters with different particle sizes represent the value interval and value frequency of the statistic, respectively. The P-P graph is a statistical graph that detects the degree of conformity of distribution types. If the P-P graph is displayed as a straight line from the origin of the vertical axis to the upper right, it means that the variable values follow a normal distribution [28]. In order to obtain the statistical distribution characteristics of L/t and AC, the P-P graphs of Laplace, Logistic, lognormal, Pareto, Student t, Weibull, and uniform distribution of L/t and AC are explored, respectively. Figure 6 shows that L/t and AC satisfy the lognormal distribution.

Using the same method, the probability statistics of the remaining two groups of gravel particles are performed, and the statistical parameter results are shown in Table 1. The three groups of gravel particles L, W, and t
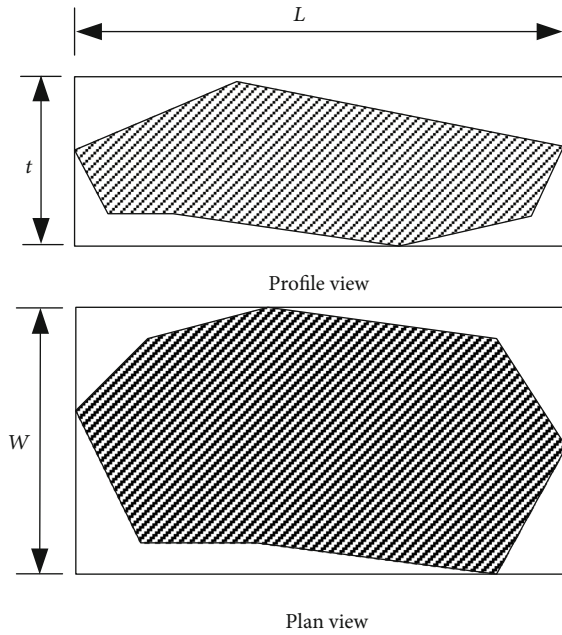
FIGURE 3: Plan and profile views of the particles.
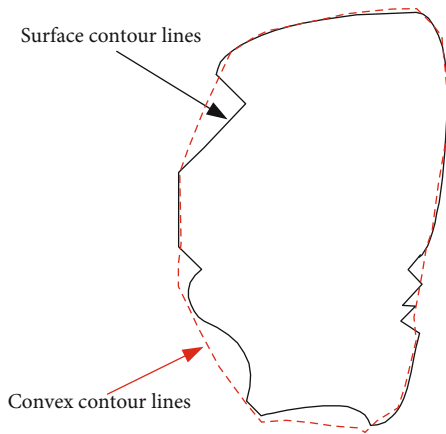
FIGURE 4: Surface contour lines and convex contour lines of the particle image.

approximately follow the normal distribution, while L/t and AC approximately follow the lognormal distribution.

4. The 3D Discrete Element Simulation of Sand-Gravel Mixtures

4.1. Gravel Particle Simulation. The above research shows that the three-dimensional morphological distribution characteristics of gravel particles are obvious. Spherical particles, as the basic unit of the calculation model in PFC3D, differ greatly from the actual gravel particles. In this article, polyhedral particles are used as the basic unit to simulate the target material. Clump logic in the PFC3D software can generate super particles composed of a large number of spherical elements with diverse shapes and nondeform-

able boundary conditions. At the same time, the effect of internal particles is ignored during calculation, so it can be regarded as a rigid whole for calculation. Zhang et al. [29] used clump super particles to simulate coarse aggregates based on PFC3D and proposed an algorithm for randomly generating the 3D morphology of coarse aggregate particles. The results showed that clump super particles can effectively make up the difference between traditional spherical particles and real materials. In order to improve the calculation accuracy and calculation efficiency, the author referred to reference [30, 31], focusing on the simulation of the 3D shape of gravel particles (greater than 5 mm), using the equal-size particles with a diameter of 5 mm to simulate the sand particles, which reached the balance of accuracy and efficiency.

In order to better reflect the morphological characteristics of gravel particles, polyhedron (hexahedron, pentahedron, or tetrahedron) and angular coefficient were adopted to describe the 3D form of gravel particles. Hexahedron, pentahedron, or tetrahedron was used to reflect the main shape of particles. Meanwhile, the angular coefficient was introduced to describe the local morphological characteristics (smoothness of particle contour). As shown in Figure 7(a), the 3D shape of gravel particles was simulated approximately through hexahedron, pentahedron, or tetrahedron in the model. The 3D size of gravel particles was determined by the length of perpendicular edges AB, AD, and AE; meanwhile, the corner angle characteristic of particles was controlled by changing the angle of angle ADH, angle ABF, and angle ABC. Through the change of the above six parameters, the particles in different sizes and sharp edges could be generated. According to the statistical results, L, W, and t of gravel particles with different particle sizes satisfied normal distribution, and L/t and AC satisfied logarithmic normal distribution. The mean value and standard deviation are shown in Table 2. According to the normal distribution, the model randomly selected the size parameters and angular parameters of particles to generate gravel grains with particle sizes of 50~20 mm, 20~10 mm, and 10~5 mm, as shown in Figure 7(b).

4.2. Sand Particle Simulation. The model simulated the sand particles with equal particle size with a minimum particle size of 5 mm. The specific generation process is as follows:

(1) Calculate the number N of spheres to be generated according to volume V, soil porosity n, and sphere radius R

(2) Use command "gen" in PFC3D to generate N spheres with a radius of $0.2r$ in the specimen, and assign the parameters of density and stiffness to the spheres. When the "gen" command is used to generate the spheres, the spheres are randomly generated within the sample and do not overlap each other, which ensures the uniformity of the sample

(3) Use command "mult" to enlarge the radius of the sphere by 5 times. There is a certain amount of overlap between the spheres

(a) Frequency histogram

(b) Normal distribution *P-P* figure
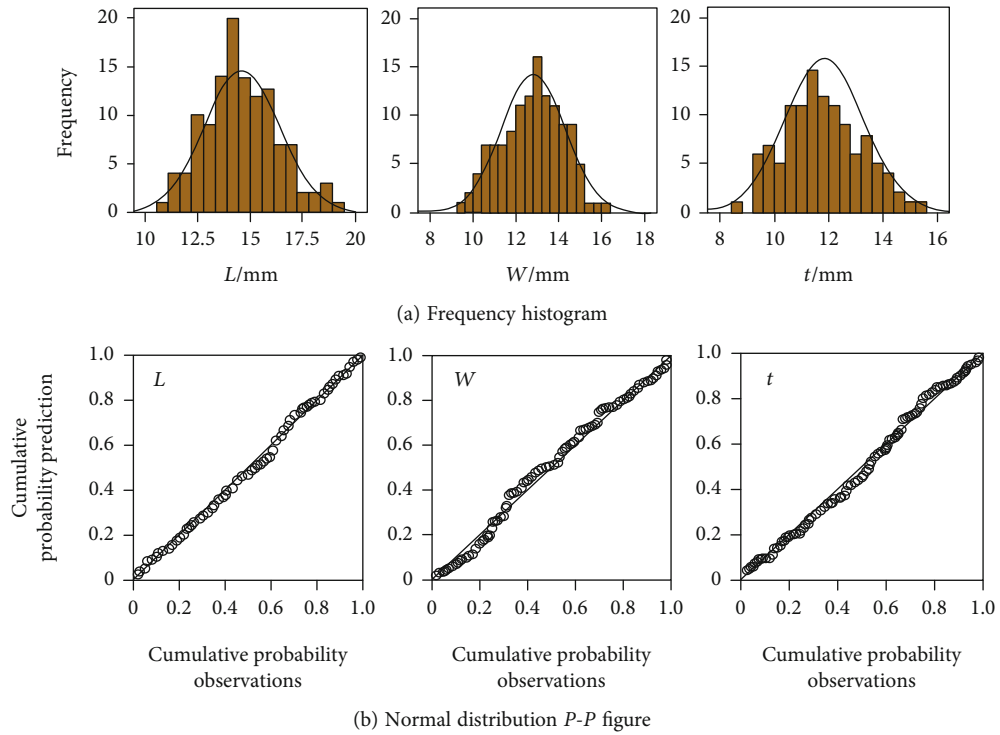
FIGURE 5: Frequency histogram and normal distribution *P-P* figure of *L*, *W*, *t*, *L/t*, and AC.
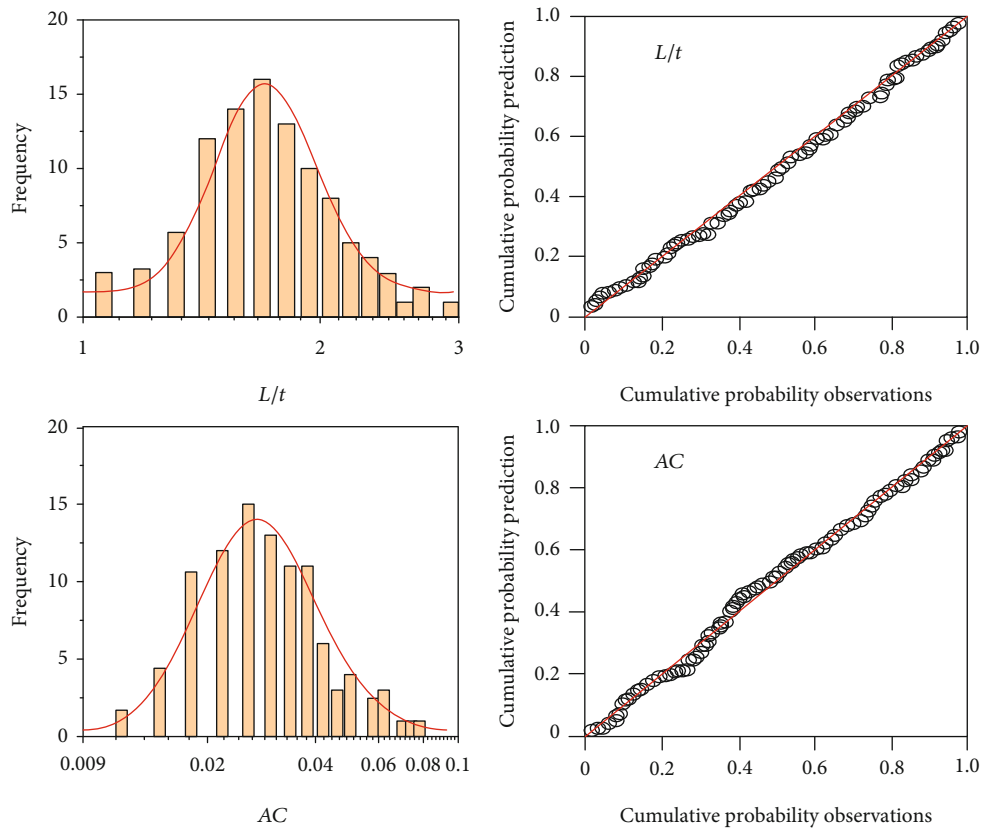
FIGURE 6: Frequency histogram and lognormal distribution *P-P* figures of *L/t* and AC.

TABLE 1: Statistical parameters of L, W, t, L/t, and A for different particle size gravel.

d (mm)	L (mm)		W (mm)		t (mm)		L/t		AC	
	Mean	Standard deviation	Mean	Standard deviation	Mean	Standard deviation	Mean	Standard deviation	Mean	Standard deviation
50~20	43.12	10.16	30.34	7.75	25.53	6.81	1.72	0.30	0.026	0.011
10~20	23.78	5.33	17.02	3.70	14.55	3.63	1.69	0.39	0.030	0.013
10~5	12.14	2.35	8.70	1.70	7.82	1.63	1.59	0.32	0.019	0.007

(a) Schematic drawing of the hexahedron   (b) Three-dimensional clump particle model
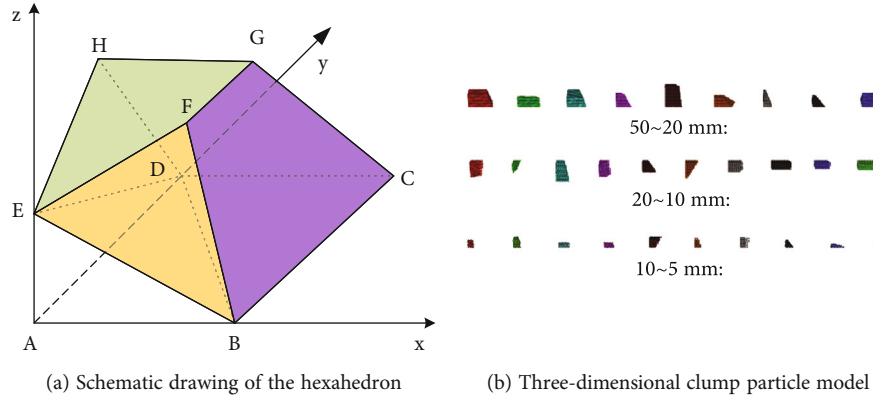
FIGURE 7: 3D clump particle model.

TABLE 2: Mesoparameters of particle for gravel-sand mixtures.

Parameter	Value
Normal stiffness (Pa)	$1e8$
Tangential stiffness (Pa)	$1e7$
Coefficient of friction	0.5
Normal bond strength (Pa)	0
Tangential bond strength (Pa)	0
Unidirectional/cyclic shear rate	001%/min
Density (g/cm^3)	1709

FIGURE 8: Discrete element sample of triaxial test.

(4) Use command "cycle" to run the program to eliminate the overlap between the particles, so as to obtain a uniformly distributed sand-gravel soil

4.3. Triaxial Mesoscopic Simulation Test and Analysis. After the sample is generated, there will be overlap between the particles. The model will judge whether the sand particles and gravel particles overlap one by one. If the two coincide, delete the former. Figure 8 shows the discrete element samples of the triaxial test of the sand-gravel mixtures obtained by the above method. In order to simulate the loading process of the triaxial shear test, a square wall simulation loading indenter was generated at the upper and lower ends of the sample; a cylindrical wall used to simulate the confining pressure was generated on the side of the sample; during the test simulation, the wall at the upper and lower ends was controlled to apply an axial load to the sample at a certain speed, and the change in the radius of the side wall was controlled so that the surrounding pressure around the sample remained unchanged; the radial speed of the side wall was

automatically controlled using "numerical servomechanism." The method can realize the application of confining pressure and the loading of the test sample. Through repeated adjustments, the values of the mesoscopic parameters of sand-gravel mixtures are basically consistent with the test results. In this article, a set of ideal mesoscopic parameters of sand-gravel mixture models were calibrated, as shown in Table 2.

Figure 9 shows the drained shear test results and numerical simulation results of saturated sandy gravel mixtures when the initial effective confining pressure is 300 kPa. In the initial stage of loading, the deviatoric stress increases rapidly with the increase of the axial strain. As the axial strain further increases, the deviatoric stress slowly increases until the peak deviatoric stress is reached, and the volume

(a)

(b)
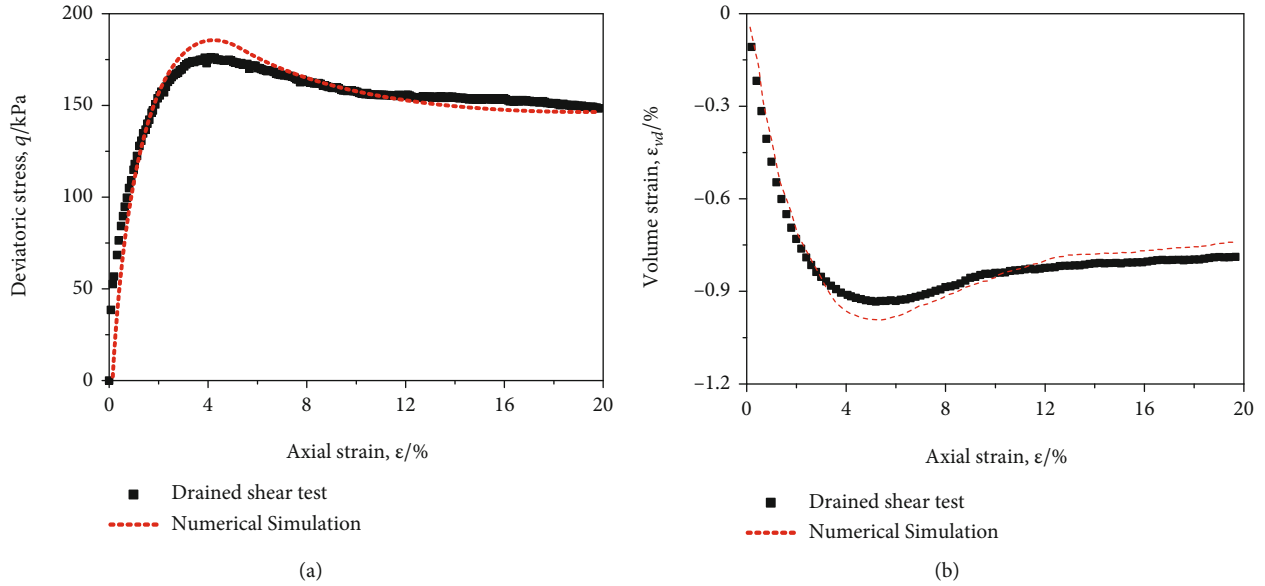
FIGURE 9: Deviatoric stress-axial strain and volume strain-axial strain curves of drained shear test.

(a)

(b)
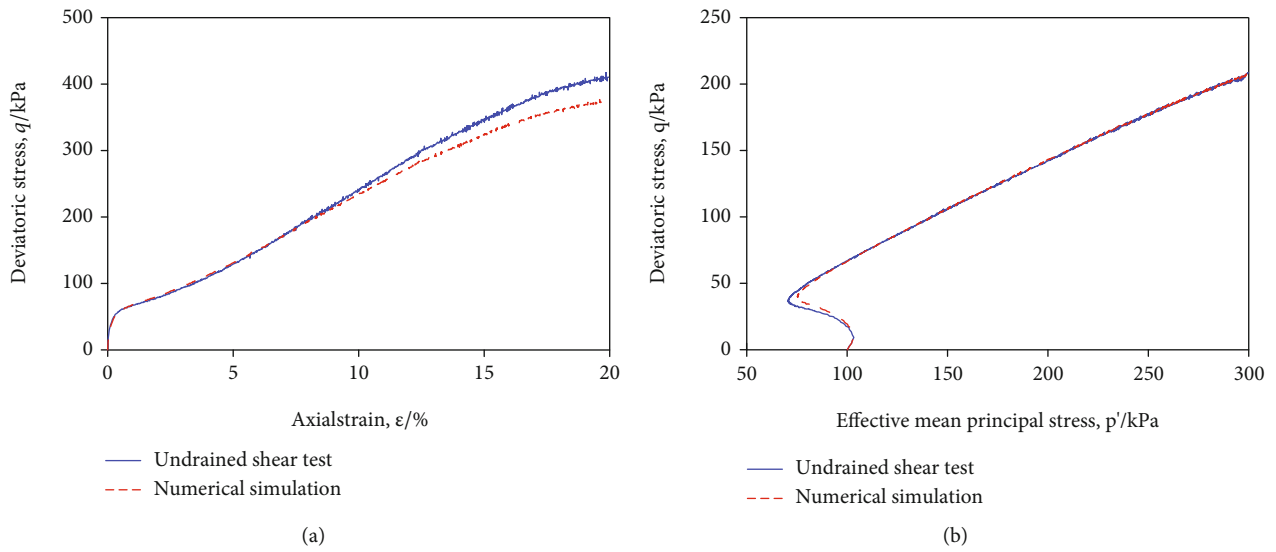
FIGURE 10: Deviatoric stress-axial strain curves and effective stress path of undrained shear test.

strain decreases with the increase of the axial strain; the soil appears to shrink. After that, the stress-strain relationship curve has obvious softening characteristics. As the axial strain increases, the deviatoric stress decreases. At this time, the axial strain-volume strain curve shows obvious shear expansion characteristics. It can be seen from Figure 9 that the numerical test results are in good agreement with the drained shear test results.

Figure 10 shows the undrained shear test results and numerical simulation results of saturated sandy gravel soil mixtures when the initial effective confining pressure is 300 kPa. It can be seen from the figure that when $\varepsilon < 10\%$, the difference between the numerical test results and undrained shear test results is very small. When $\varepsilon > 10\%$, the numerical test results is different from the undrained

shear test results, and the difference increases with the increase of axial strain. This is because the sample is not completely stable when it is in large deformation, and the numerical simulation results cannot fully reflect the mechanical properties of the soil. It is worth noting that the effective stress path of the numerical test and the undrained shear test is basically the same.

Figure 11 shows the undrained cyclic triaxial test results and numerical simulation results of saturated sandy gravel mixtures when the initial effective confining pressure is 100 kPa. The pore pressure ratio R_u of gravel-sand mixtures presents a "fast-steady" growth pattern, which is basically consistent with the typical test results of gravel-sand mixtures. The stress-strain curve of the triaxial test and the numerical test can maintain good consistency before
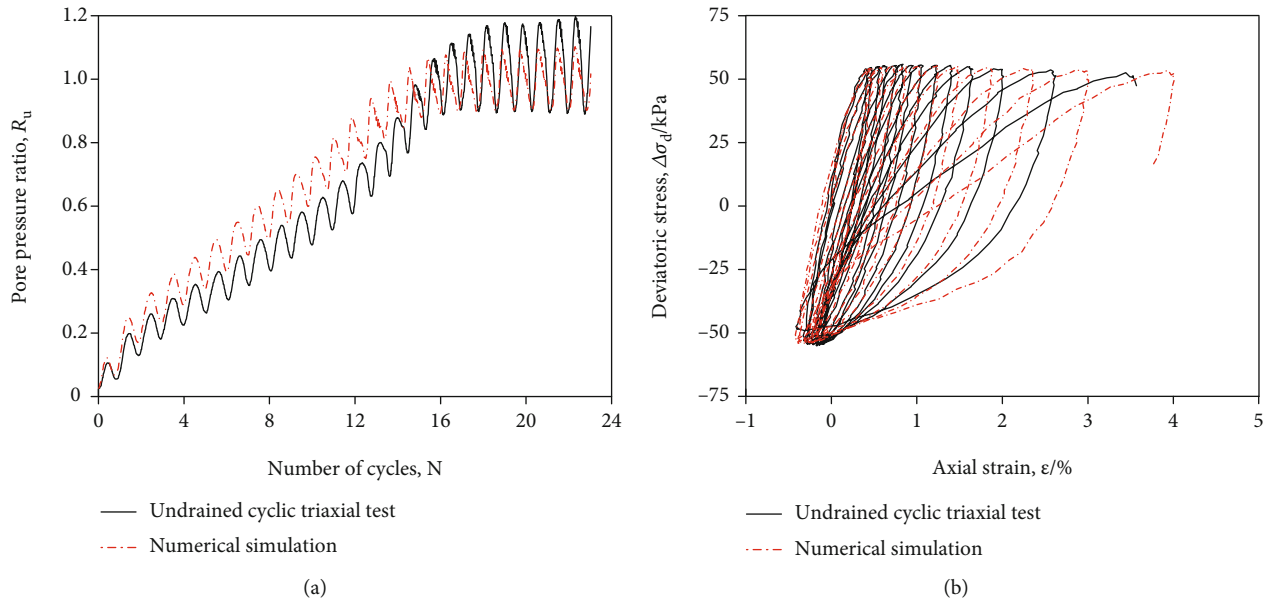
FIGURE 11: Pore pressure ratio-number of cycles and stress path of undrained cyclic triaxial test.
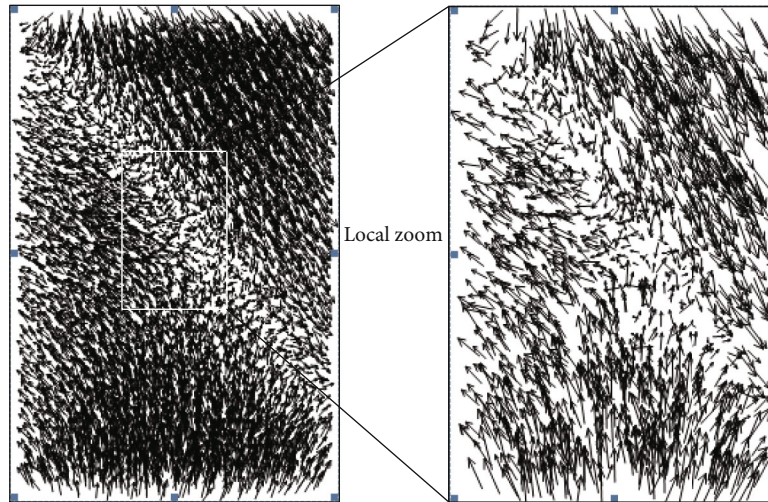
FIGURE 12: Distribution particle displacements.

liquefaction, and when the sample is liquefied, the sample no longer has shear strength. Meanwhile, it is difficult for the numerical test to accurately and effectively apply axial stress and reflect the true state of the sample, resulting in a certain difference in the stress-strain curve after liquefaction.

Because the particle flow sample is composed of discrete particles, similar to the actual coarse-grained soil, the interaction of the particles in the PFC3D numerical model can better reflect the mesomechanical properties of the actual sandy gravel mixtures. In the undrained shear numerical test, PFC3D provides the display of the force between particles. From the force between particles, the mesoscopic working mechanism can be analyzed. In order to study the particle movement law of the sandy gravel mixture sample, Figure 12 shows the particle displacement vector diagram of the numer-

ical sample under shear failure when the initial effective confining pressure is 100 kPa. When shear failure occurs, the directional movement of the particles is obvious, the upper particles move downward and the lower particles move in the opposite direction, and obvious shear bands appear, indicating that structural damage occurs inside the sample.

Figures 13(a) and 13(b) show the distribution of sand particle contact force and gravel particle contact force, respectively. The soil composed of sand and gravel with obvious differences in particle size has a skeleton structure jointly undertaken by sand and gravel. However, in the case of this test, the distribution of the contact force between the sand particles is scattered, and the contact force between the gravel particles can form a complete contact force, so the gravel particles are mainly stressed particles.

(a) Sand particle contact force diagram

(b) Gravel particle contact force diagram
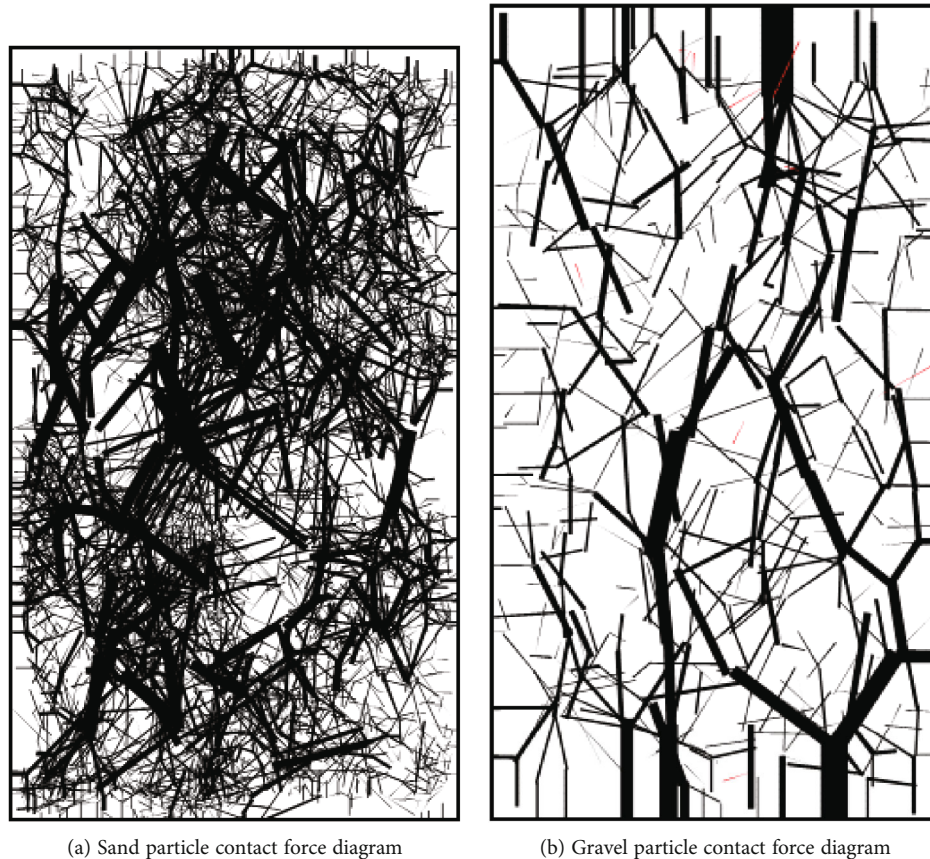
Figure 13: Particle contact force diagram.

The mechanical constitutive model of sand-gravel mixture established based on the 3D morphological distribution characteristics presents good applicability. The research results will provide an important scientific basis for the analysis of the stability and seismic performance of hydraulic fracturing drilling through crossing the sandy gravel mixture layer.

5. Conclusions

This article comprehensively used digital image processing technology and discrete element numerical simulation to study the mesoscopic structural characteristics and the PFC3D particle flow simulation method of the sand-gravel mixtures taken from the Chengdu metro area in China. According to the statistical characteristics of the 3D form and distribution of the particles, a 3D discrete element simulation method for sandy gravel mixtures is proposed. The discrete element method was used to analyze the particle movement law of the sand-gravel mixtures during the shear test process. The main conclusions are as follows:

(1) The long axis length L, the middle axis length W, and the short axis length t of the gravel particles in accordance with the normal distribution and the aspect ratio L/t and the angular coefficient AC satisfy the lognormal distribution. The PFC3D particle flow model can well simulate the 3D morphological distribution characteristics of gravel particles to form uniformly distributed sand-gravel mixtures

(2) The deviatoric stress-axial strain curves obtained from the simulated drained shear test, undrained shear test, and undrained cyclic triaxial test are in good agreement with the test results, which verifies the applicability of the model

(3) From the particle contact force diagram between the particles, it is concluded that the gravel particles in the sand-gravel mixtures are forced particles during the drained shear process

Data Availability

The data are generated from experiments and can be available from the corresponding author upon request.

Conflicts of Interest

The authors declare that there are no conflicts of interest regarding the publication of this paper.

Acknowledgments

References

[1] L. Chen, Z. Wang, X. Peng, J. Yang, P. Wu, and H. Lian, "Modeling pressurized fracture propagation with the isogeometric BEM," *Geomechanics and Geophysics for Geo-Energy and Geo-Resources*, vol. 7, no. 3, 2021.

[2] J. F. Yang, H. Lian, and L. Li, "Fracturing in coals with different fluids: an experimental comparison between water, liquid CO_2, and supercritical CO_2," *Scientific Reports*, vol. 10, no. 1, 2020.

[3] Z. H. Liu, J. Yang, L. S. Yang, X. Ren, X. Peng, and H. Lian, "Experimental study on the influencing factors of hydraulic fracture initiation from prefabricated crack tips," *Engineering Fracture Mechanics*, vol. 250, 2021.

[4] Z. H. Liu, X. K. Ren, X. Lin, H. Lian, L. Yang, and J. Yang, "Effects of confining stresses, pre-crack inclination angles and injection rates: observations from large-scale true triaxial and hydraulic fracturing tests in laboratory," *Rock Mechanics and Rock Engineering*, vol. 53, no. 4, pp. 1991–2000, 2020.

[5] H. Zhuang, R. Wang, G. Chen, Y. Miao, and K. Zhao, "Shear modulus reduction of saturated sand under large liquefaction-induced deformation in cyclic torsional shear tests," *Engineering Geology*, vol. 240, pp. 110–122, 2018.

[6] B. Ruan, K. Zhao, S. Y. Wang, G. X. Chen, and H. Y. Wang, "Numerical modeling of seismic site effects in a shallow estuarine bay (Suai Bay, Shantou, China)," *Engineering Geology*, vol. 260, 2019.

[7] M. D. Evans and S. Zhou, "Liquefaction behavior of sand-gravel composites," *Journal of Geotechnical and Geoenvironmental Engineering*, vol. 121, no. 3, pp. 287–298, 1995.

[8] Y. R. Li, R. Q. Huang, L. S. Chan, and J. Chen, "Effects of particle shape on shear strength of clay-gravel mixture," *KSCE Journal of Civil Engineering*, vol. 17, no. 4, pp. 712–717, 2013.

[9] T. D. O'Rourke, S. J. Druschel, and A. N. Netravali, "Shear strength characteristics of sand-polymer interfaces," *Journal of Geotechnical Engineering*, vol. 116, no. 3, pp. 451–469, 1990.

[10] L. E. Vallejo, "Interpretation of the limits in shear strength in binary granular mixtures," *Canadian Geotechnical Journal*, vol. 38, no. 5, pp. 1097–1104, 2011.

[11] W. J. Chang, "Evaluation of liquefaction resistance for gravelly sands using gravel content-corrected shear-wave velocity," *Journal of Geotechnical & Geoenvironmental Engineering*, vol. 142, no. 5, 2016.

[12] K. Zhao, Q. Z. Wang, Q. Chen, H. Zhuang, and G. Chen, "Simplified effective stress simulation of shear wave propagation in saturated granular soils," *Géotechnique Letters*, vol. 11, no. 1, pp. 1–22, 2021.

[13] S. Zhang, H. M. Tang, H. B. Zhan, G. Lei, and H. Cheng, "Investigation of scale effect of numerical unconfined compression strengths of virtual colluvial-deluvial soil-rock mixture," *International Journal of Rock Mechanics and Mining Sciences*, vol. 77, pp. 208–219, 2015.

[14] S. K. Kennedy and W. H. Lin, "A comparison of fourier and fractal techniques in the analysis of closed forms," *Journal of Sedimentary Research*, vol. 62, no. 5, pp. 842–848, 1992.

[15] E. T. Bowman, K. Soga, and W. Drummond, "Particle shape characterisation using Fourier descriptor analysis," *Géotechnique*, vol. 51, no. 6, pp. 545–554, 2001.

[16] B. Sukumaran and A. K. Ashmawy, "Quantitative characterisation of the geometry of discret particles," *Géotechnique*, vol. 51, no. 7, pp. 619–627, 2001.

[17] G. C. Cho, J. Dodds, and J. C. Santamarina, "Closure to 'particle shape effects on packing density, stiffness, and strength: natural and crushed sands' by Gye-Chun Cho, Jake Dodds, and J. Carlos Santamarina," *Journal of Geotechnical and Geoenvironmental Engineering*, vol. 133, no. 11, pp. 1474–1474, 2007.

[18] J. F. Ferellec and G. R. Mcdowell, "A simple method to create complex particle shapes for dem," *Geomechanics and Geoengineering*, vol. 3, no. 3, pp. 211–216, 2008.

[19] A. Cividini and G. Gioda, "A finite element analysis of direct shear tests on stiff clays," *International Journal for Numerical & Analytical Methods in Geomechanics*, vol. 16, no. 12, pp. 869–886, 1992.

[20] J. Tejchman, "FE analysis of shearing of granular bodies in a direct shear box," *Particulate Science and Technology*, vol. 23, no. 3, pp. 229–248, 2005.

[21] P. Mora and D. Place, "A lattice solid model for the nonlinear dynamics of earthquakes," *International Journal of Modern Physics C*, vol. 4, no. 6, pp. 1059–1074, 1993.

[22] G. R. Mcdowell and O. Harireche, "Discrete element modelling of soil particle fracture," *Géotechnique*, vol. 52, no. 2, pp. 131–135, 2002.

[23] Y. P. Cheng, Y. Nakata, and M. D. Bolton, "Discrete element simulation of crushable soil," *Geotechnique*, vol. 53, no. 7, pp. 633–641, 2003.

[24] R. Deluzarche and B. Cambou, "Discrete numerical modelling of rockfill dams," *International Journal for Numerical & Analytical Methods in Geomechanics*, vol. 30, no. 11, pp. 1075–1096, 2006.

[25] E. Alaei and A. Mahboubi, "A discrete model for simulating shear strength and deformation behaviour of rockfill material, considering the particle breakage phenomenon," *Granular Matter*, vol. 14, no. 6, pp. 707–717, 2012.

[26] E. E. Alonso, M. Tapias, and J. Gili, "Scale effects in rockfill behaviour," *Géotechnique Letters*, vol. 2, no. 3, pp. 155–160, 2012.

[27] ASTM, "Standard practice for classification of soils for engineering purposes (unified soil classification system)," in *ASTM D2487*, ASTM, West Conshohocken, PA, 2011.

[28] W. J. Xu, Z. Q. Yue, and R. L. Hu, "Study on the mesostructure and mesomechanical characteristics of the soil-rock mixture using digital image processing based finite element method," *International Journal of Rock Mechanics & Mining Sciences*, vol. 45, no. 5, pp. 749–762, 2008.

[29] D. Zhang, X. M. Huang, and Y. L. Zhao, "Algorithms for generating three-dimensional aggregates and asphalt mixture samples by the discrete-element method," *Journal of Computing in Civil Engineering*, vol. 27, no. 2, pp. 111–117, 2013.

[30] B. W. Flemming, "A revised textural classification of gravel-free muddy sediments on the basis of ternary diagrams," *Continental Shelf Research*, vol. 20, no. 10-11, pp. 1125–1137, 2000.

[31] I. López, L. Aragonés, Y. Villacampa, P. Compañ, and R. Satorre, "Morphological classification of microtidal sand and gravel beaches," *Ocean Engineering*, vol. 109, pp. 309–319, 2015.

Research Article

Rockburst Inducement Mechanism and Its Prediction Based on Microseismic Monitoring

Yongsong Li [ID][1] and Chao Zhou [ID][2]

[1]*School of Architecture Engineering, Huanghuai University, Zhumadian, China*
[2]*Key Laboratory of Geotechnical Mechanics and Engineering of Ministry of Water Resources, Yangtze River Scientific Research Institute, Wuhan, China*

Correspondence should be addressed to Chao Zhou; zhouchao@mail.crsri.cn

The rockburst disaster in the hard rock caused by excavation and unloading of deep underground caverns threatens the safety of engineering construction. In recent years, the microseismic monitoring technology, which can dynamically monitor the whole process of progressive failure of rock mass in real time, has been widely used in rockburst monitoring and early warning of underground engineering. In view of the slight rockburst in local surrounding rock during the excavation of underground powerhouse of Huanggou Pumped Storage Power Station, a rockburst microseismic monitoring system is constructed. And through the analysis of the temporal and spatial activity of microseisms during the monitoring period, the potential risk areas of rockbursts are identified and delineated. The monitoring results show that the microseismic system can effectively capture the blasting and microseismic signals during construction. The microseismic activity is closely related to the intensity of field blasting disturbance. The potential risk areas of rockburst are the upstream side arch shoulder and the intersection between lower drainage corridor and workshop installation room. The research results can provide technical support for later excavation and support of underground powerhouse caverns of Huanggou Hydropower Station.

1. Introduction

Rockburst is a phenomenon of rockmass dynamic instability such as fracture, spalling, ejection, and even throwing, caused by sudden release of elastic strain energy stored therein due to excavation and load removal in underground projects in high ground stress circumstances. Rockburst often occurs in hard and brittle rock masses, and they are accompanied by different degrees of cracking noises [1–4]. As underground projects go deeper, rockbursts occur more frequently. Frequent rockburst disasters during the excavation of deep underground caverns directly threaten the safety of construction personnel and equipment and delay the construction progress, especially, in severe cases. For example, on November 28, 2009, the drainage tunnel of the Jinping II Hydropower Station on the Yalong River in China's Sichuan province suffered a strong rockburst during

construction, and its supporting system was seriously damaged, resulting in seven persons killed and one person injured. The rescue and cleaning work lasted for more than one month, and the direct and indirect economic losses caused by the accident were immeasurable [4, 5].

At present, the rockburst prediction methods applied in engineering practice at home and abroad mainly include microseismic, microgravity, electromagnetic radiation, seismology, drilling cuttings, moisture, photoelasticity, rheological method, and rebounding [6]. Among them, the microseismic method can dynamically monitor the whole process of progressive failure of rock mass in real time, effectively delineate the potential risk area of rockburst in the monitoring area, and timely evaluate and predict the stability of surrounding rock. Compared with other on-site rockburst monitoring methods, the microseismic method has obvious advantages and has been widely promoted and applied in engineering practice in recent years.

Advanced microseismic monitoring systems have been installed in most of the deep underground projects in developed countries such as Canada, South Africa, the United States, and Australia and have been successfully applied in analyzing and determining the fracture distribution, damage state, and rockburst risk prediction [7]. In 1986, the Mentougou Coal Mine in Beijing used the 8-channel microseismic monitoring system imported from Poland to monitor the microseismic activity in the coal mining area, which was the beginning of the application of the microseismic monitoring system in China [8, 9]. Li et al. [10] established a 16-channel microseismic monitoring system in the Fankou Lead-Zinc Mine in Guangdong province and preliminarily analyzed the microseismic activity of large blasting in deep mining area. In recent years, Feng and other scholars introduced the microseismic system into rockburst monitoring and early warning of underground caverns of such hydropower projects as Jinping, Dagangshan, and Houziyan [11–14]. Ma and other scholars applied the microseismic monitoring system to slope engineering, in order to delineate the possible rock mass fracture zone and potential slip plane of slope and provide a basis for slope engineering support [15–17]. Practices have proved that the microseismic monitoring technology has laid a good foundation for the prediction and protection of rockburst disasters in deep underground engineering.

In this paper, the microseismic monitoring system of underground powerhouse of the Huanggou Pumped Storage Hydropower Station is constructed, and based on the monitoring data of two months from the beginning, the microseismic activities induced by blasting excavation of powerhouse caverns are analyzed.

2. General Situation of Underground Powerhouse Area of the Huanggou Hydropower Station

The Huanggou Pumped Storage Power Station is located in Sandaohezi Town, Hailin, Mudanjiang, Heilongjiang province. Its installed capacity is $4 \times 300,000$ kW. The main structures include an upper reservoir, a water transmission system, an underground powerhouse system, a ground switch station, and a lower reservoir. The excavation size of the main and auxiliary powerhouse caverns is $163.20 \times 25.00 \times 53.80$ m ($L \times W \times H$), and the top arch elevation is 178.60 m. The excavation size of the main transformer room is $127.10 \times 21.20 \times 22.40$ m ($L \times W \times H$), and the top arch elevation is 175.10 m. The excavation size of the tail gate chamber is $94.90 \times 11.40 \times 20.30$ m ($L \times W \times H$), and the top arch elevation is 159.20 m. The axial direction of the powerhouse is N49°W, and the main transformer chamber and tailgate chamber are arranged parallel to the powerhouse. The center distance between the main powerhouse and main transformer chamber is 61.30 m, and that between the main transformer chamber and tailgate chamber is 44.35 m.

The area occupied by the power station is topographically a small tectonic basin in the low and medium-height mountains and river valleys formed by tectonic erosion.

The underground powerhouse area has a hilly terrain which has been mildly cut, with the elevation of hills between 470 and 530 m and the ground surface slope between 20° and 40°. The underground powerhouse is 350~400 m in burial depth, and its surrounding rock is mainly hard and complete alaskite. The geological structure of such surrounding rock is not well developed, and two small faults, f_{33} and f_{34}, with steep dip angles, 3-5 mm in width and modest extension, are found therein. The main transformer chamber passes through two steeply inclined faults, f_{31} and f_{32}. The f_{31} fault is 0.3~1.10 m wide, and the latter is 0.05 m wide. Their fillings are mainly cataclastic rock and rock fragments. In this area, there are three groups of steep-dip joints (NWW, NE, and NEE, respectively) and a group of NEE-direction gentle-dip joints in the rock mass. The joint spacing is generally 0.5~2.5 m, and most of them are in a closed state. The surrounding rocks of the powerhouse are mostly type II surrounding rocks, and their integrity is relatively complete to complete (see Figure 1). According to the measurement of the in situ stress and the analysis of the regression inversion results of the stress field, the maximum principal stress in the underground powerhouse area is 11.0~15.0 MPa, which is a medium stress.

In the initial stage of excavation of the underground powerhouse of the hydropower station, the surrounding rocks of various locations have experienced different degrees of slab and rockburst (see Figure 2). In order to understand the stability of the surrounding rock in the subsequent excavation process, the microseismic monitoring system is introduced to monitor the underground powerhouse in real time, so as to identify and delineate the potential instability hazard areas that affect the stability of the surrounding rock and provide guidance for safe construction.

3. Microseismic Monitoring System in Underground Powerhouse Area

3.1. Principles of Microseismic Monitoring and Positioning. When the rock mass is disturbed by external forces, microcracks will occur in the rock mass, which is usually accompanied by elastic waves, releasing strain energy and generating microseismic events. If a certain number of sensors are arranged in the rock mass around the seismic source to form a spatial array, when a microseismic event occurs in the monitoring body, the elastic wave generated by it will propagate outward through the surrounding medium and be received by sensors installed in the hole close to the rock wall. The sensor converts microseismic signals into electrical signals and sends them to the signal acquisition instrument through cables. The signal acquisition instrument converts the electrical signals into digital signals and transmits them to the analysis computer. By analyzing and processing microseismic events with waveform processing software and demonstrating them with 3D visualization software, the time, space position, and intensity information of rock microseismic events can be obtained, that is, the three elements of "time, space, and intensity" of rock microfracture [18]. Figure 3 is a schematic diagram of the principle of microseismic monitoring.
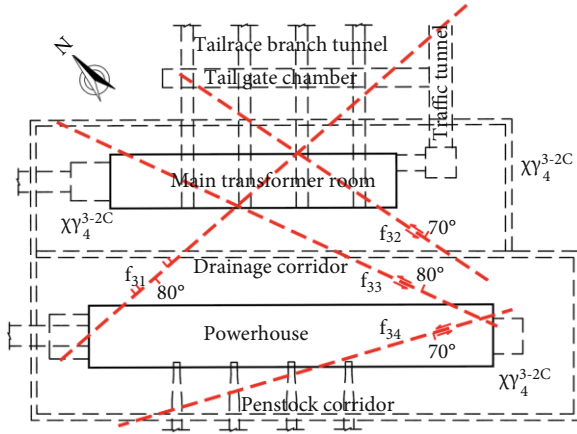
FIGURE 1: Planar graph of underground powerhouse area at elevation 172.60 m.

FIGURE 2: Rockburst at the intersection between lower drainage corridor and tailrace branch tunnel no. 1.
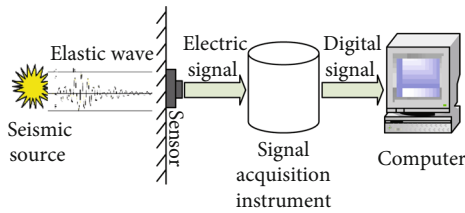
FIGURE 3: Schematic diagram of the principle of microseismic monitoring.

Microseismic source positioning is a method to determine the location of the rock fracture source according to the elastic wave propagation speed in the rock medium by monitoring the arrival of the elastic wave generated by the rockmass fracture. The principle of source location is shown in Figure 4. Microseismic positioning methods can be divided into regional positioning method and point positioning method (time difference positioning method). At present, several commonly used positioning methods mainly include the least square method, Bayesian positioning method, relative positioning method (ATD), slowness dispersion method, simplex positioning method, and Geiger positioning method [19–22]. The Geiger positioning method is an application of the Gauss-Newton method. It is suitable
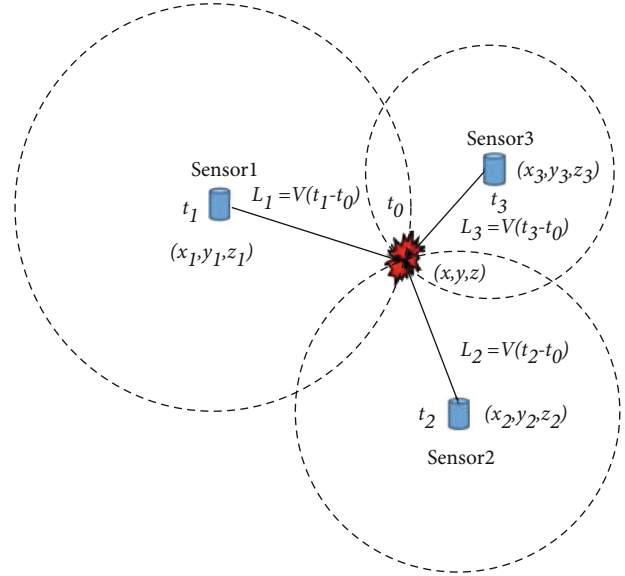
FIGURE 4: Schematic diagram of the source location principle.

for small-area seismic events with high positioning accuracy, and this method requires relatively loose positioning conditions for events, and there are more reasonable positioning events. The Canadian ESG microseismic monitoring system used in this article uses the Geiger positioning method based on the time difference positioning principle to locate the source event. In the sensor array arranged around the microseismic source monitoring area, the relative distance between the sensors is known. The difference in the arrival time of the elastic wave picked up by each sensor in the array is called the time difference. The time difference provides the distance information between the source event and the sensor array, and the location of the source event can be determined by selecting a suitable seismic wave velocity model.

Geiger positioning method is to approach the final result through iteration from a given test point $O(x, y, z, t)$. In each iteration, a correction vector $\Delta\theta(\Delta x, \Delta y, \Delta z, \Delta t)$ is calculated based on the least square method, and the vector $\Delta\theta$ is added to the result of the previous iteration (test point) to obtain a new test point and then judge this whether the new test point meets the requirements, if it meets the requirements. If it meets the requirements, the coordinates of this point will be the source position. If not, continue iteration. The result of each iteration is generated by the following time distance equation (1) (where x, y, z, and t are known numbers generated by artificial setting or iteration).

$$(x_i - x)^2 + (y_i - y)^2 + (z_i - z)^2 = v_p^2(t_i - t)^2, \qquad (1)$$

where (x, y, z) are the coordinates of the test point, the initial value of which is set manually; t is the time when the event occurs, and its initial value is set manually; (x_i, y_i, z_i) is the spatial position of the i-th sensor coordinates; t_i is the time of the P wave signal received by the i-th sensor; v_p is the propagation speed of the P wave in the rock mass.

For the arrival time $t_{o,i}$ of the P wave received by the i-th sensor, the first-order Taylor expansion of the arrival time calculated by the test point coordinates can be expressed as

$$t_{o,i} = t_{c,i} + \frac{\partial t_i}{\partial x} \Delta x + \frac{\partial t_i}{\partial y} \Delta y + \frac{\partial t_i}{\partial z} \Delta z + \frac{\partial t_i}{\partial t} \Delta t, \qquad (2)$$

where $t_{c,i}$ is the time for the P wave calculated from the test point coordinates to reach the i-th sensor. In equation (2),

$$\begin{aligned} \frac{\partial t_i}{\partial x} &= \frac{x_i - x}{v_p R}, \\ \frac{\partial t_i}{\partial y} &= \frac{y_i - y}{v_p R}, \\ \frac{\partial t_i}{\partial z} &= \frac{z_i - z}{v_p R}, \\ \frac{\partial t_i}{\partial t} &= 1, \end{aligned} \qquad (3)$$

$$R = \sqrt{(x_i - x)^2 + (y_i - y)^2 + (z_i - z)^2}. \qquad (4)$$

For N sensors, N equations can be obtained and written in the form of matrix.

$$A \Delta \theta = B, \qquad (5)$$

where

$$A = \begin{bmatrix} \frac{\partial t_1}{\partial x} & \frac{\partial t_1}{\partial y} & \frac{\partial t_1}{\partial z} & 1 \\ \frac{\partial t_2}{\partial x} & \frac{\partial t_2}{\partial y} & \frac{\partial t_2}{\partial z} & 1 \\ \vdots & \vdots & \vdots & \vdots \\ \frac{\partial t_n}{\partial x_1} & \frac{\partial t_n}{\partial v} & \frac{\partial t_n}{\partial z} & 1 \end{bmatrix},$$

$$\Delta \theta = \begin{bmatrix} \Delta x \\ \Delta y \\ \Delta z \\ \Delta t \end{bmatrix}, \qquad (6)$$

$$B = \begin{bmatrix} t_{o1} - t_{c1} \\ t_{o2} - t_{c2} \\ \vdots \\ t_{on} - t_{cn} \end{bmatrix}.$$

The modified vector is obtained by solving equation (3) with Gaussian water elimination method.

$$A^T A \Delta \theta = A^T B, \qquad (7)$$

$$\Delta \theta = \left(A^T A \right)^{-1} A^T B. \qquad (8)$$

After the correction vector is obtained from equation (5), the iteration is continued with $(\theta + \Delta \theta)$ as the new test point until the error requirement is met.

3.2. Establishment of Microseismic Monitoring System. A high-precision microseismic monitoring system of Canada's ESG (Engineering Seismology Group) is adopted in the project, which includes acceleration sensors, cables, Paladin signal collection system, and HANS data processing system. The underground powerhouse area in the project is formed by excavation by 7 layers, with the thicknesses of 10 m, 8 m, 8.1 m, 6.6 m, 7.4 m, 7.5 m, and 6.2 m from top to bottom. When the microseismic system is being set up, the excavation of the third layer has finished, the tailgate chamber and busbar tunnel have reached their middle point of excavation, and the main transformer chamber, upper/middle/lower drainage corridors, ventilation tunnel, and traffic tunnel have all been excavated to full capacity. According to the excavation status of the underground powerhouse area, 18 sensors are arranged in the excavated upper/middle drainage corridors to form a spatial array, focusing on monitoring and analyzing the influence of further excavation disturbance on the stability of the surrounding rock of the powerhouse roof arch and upstream side wall. Figure 5 is a schematic diagram of the layered excavation of the underground powerhouse and the location of the sensors.

Figure 6 is a schematic diagram of the spatial arrangement of sensors. Six and eight uniaxial sensors are, respectively, arranged in the upper and middle drainage corridors of the underground powerhouse system, three uniaxial sensors are arranged in the main transformer room, one uniaxial sensor is arranged in the traffic tunnel between the powerhouse and the main transformer room, and the monitoring center is placed in the traffic tunnel. The sensor mounting hole has a diameter of 50 mm and a depth of about 4 m. When being installed, the front end of the sensor is fixed at the bottom of the hole with anchor resin. The sensor is in point contact with the rock mass and can receive elastic wave signals from all directions. After the microseismic system is in position, the operation of the sensor was verified by a manual percussion test.

3.3. Selection of Velocity Model. The effective selection of the velocity model is very important to the positioning accuracy of the source event and thus the positioning error. After the installation of the system, a total of 10 manual knocking experiments are carried out in the upper and middle drainage corridors to decide the speed model. According to the available information, the average wave velocity in the rock mass in the underground powerhouse area is 4700~5100 ms^{-1}. The system wave speed adopts 17 different wave speed values between 4700 and 5100 ms^{-1}. With reference to the principle of event location and capture and the method of waveform processing discussed in reference [19], ten experimental points of manual percussion are systematically located, and the average error of location results is obtained. The correlation analysis of wave velocity and event location error is
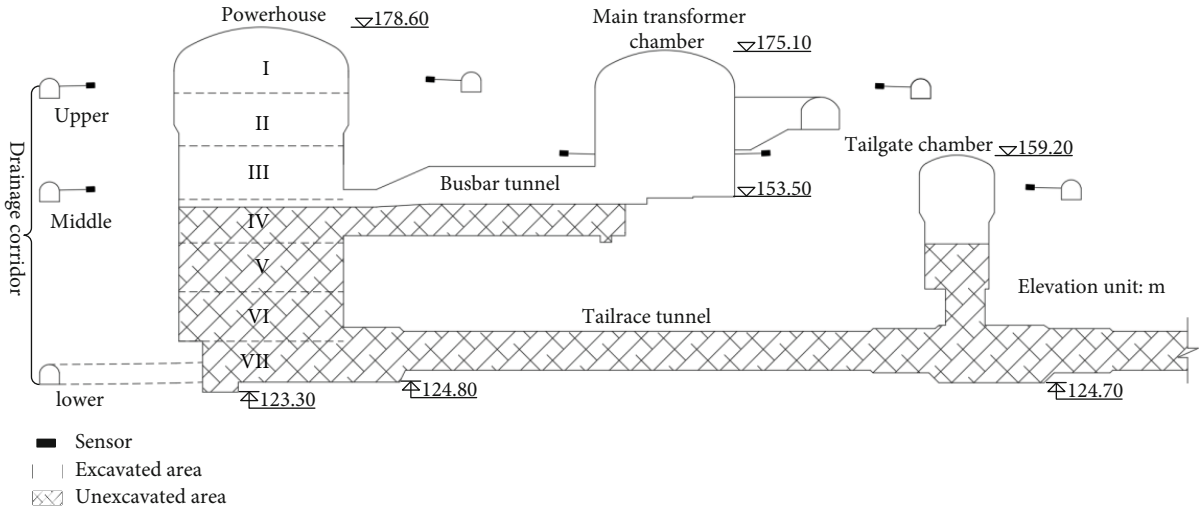
FIGURE 5: Schematic diagram of layered excavation of underground powerhouse and sensor positions.
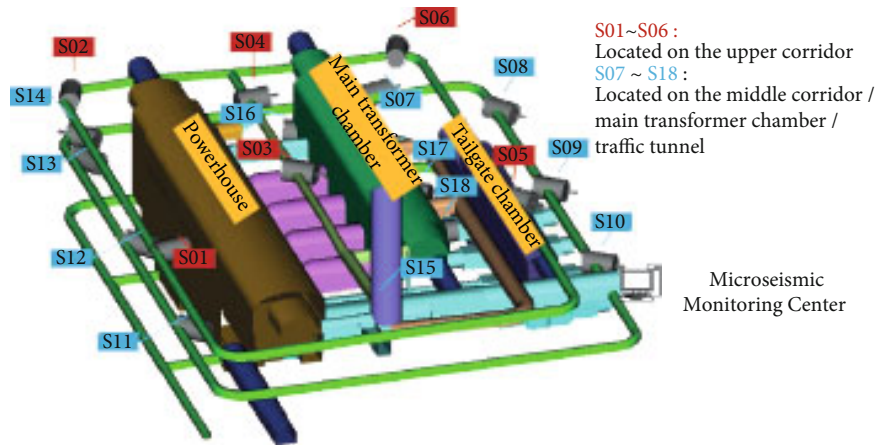
FIGURE 6: Schematic diagram of sensor layout in underground powerhouse area.

carried out, and the results are shown in Figure 7. Finally, the optimal P wave velocity of rock mass in the monitoring area is $5150 \, ms^{-1}$, at which the minimum positioning error is 5.4 m, and the positioning accuracy of the system meets the requirements of monitoring [11].

4. Analysis of Microseismic Monitoring Results

Between September 30, 2017, and November 30, 2017, the microseismic monitoring system has captured 123 microseismic events, two occurrences per day on average, and 54 blasting events, roughly one per day on average. Figure 8 shows the typical microseismic and blasting event signal wave monitored by the system. The microseismic signal has unique wave component and short duration, its amplitude is mostly concentrated between tens and hundreds of millivolts, and its frequency is mainly distributed in the middle- and low-frequency bands below 500 Hz. The blasting wave has multiple waveforms superimposed on each other in a window, with a long duration, large amplitude, and high frequency.
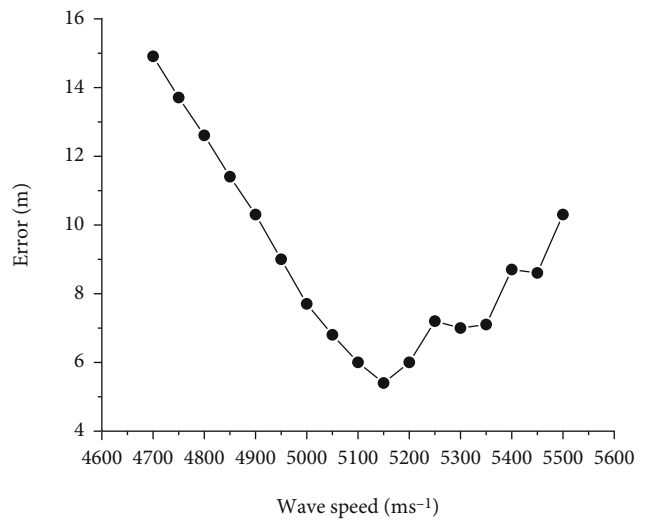
FIGURE 7: Relation curve between wave velocity and position error.

(a) Microseismic signal
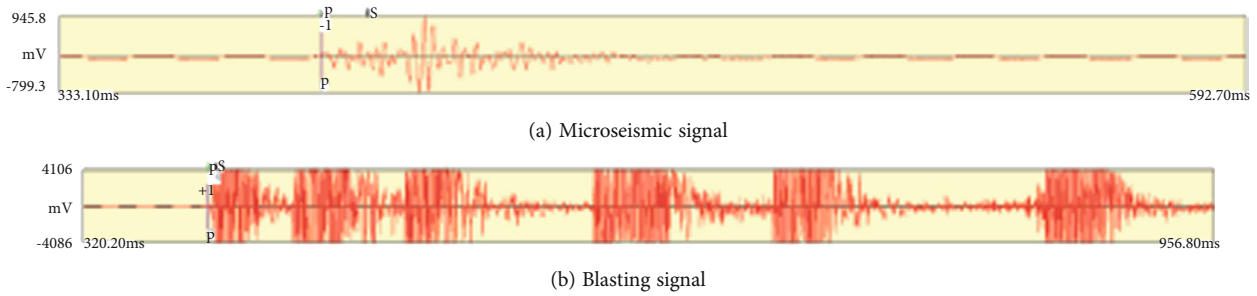
(b) Blasting signal

FIGURE 8: Typical microseismic and blasting event signal waveforms.
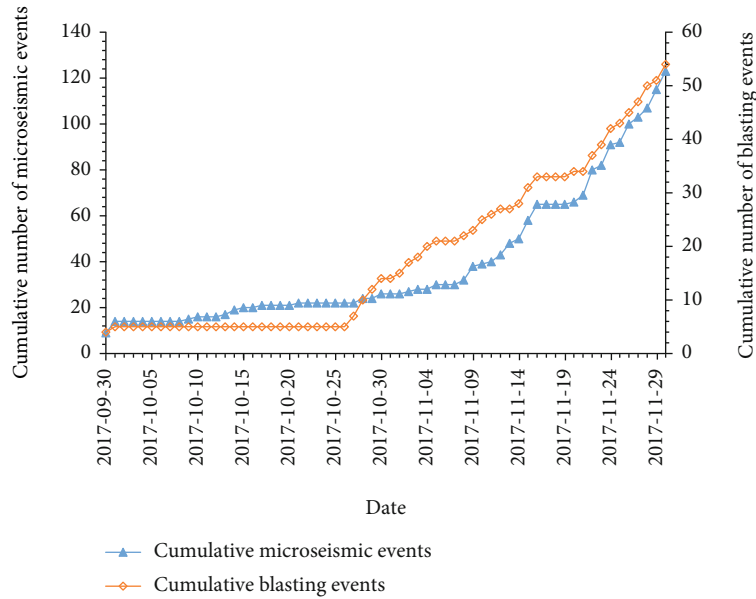
FIGURE 9: Evolution of accumulative microseismic events and blasting events over time.

4.1. Temporal Distribution of Microseismic Events. By analyzing the temporal distribution of microseismic events, it is possible to understand the temporal characteristics of the rock microcrack's initiation, development, and aggregation and find out the relationship between rock microcracks and construction disturbances such as underground cavern excavation [12]. Figure 9 shows the evolution of accumulated microseismic events and blasting events in the monitoring area of the underground powerhouse from September 30 to November 30, 2017. It can be seen from the figure that from September 30 to October 26, the evolution curve of cumulative microseismic events with time is gentle and the increment range is small, which indicates that there are few microfracture events in rock mass and the rockburst risk is low. There is no increase in cumulative blasting events. During this period of time, the construction was halted for some reason. The blasting operation was completely off at the site, the rock mass was almost not affected by the disturbance of external force, and the microseismic activity was not obvious After the construction was resumed, the cumulative microseismic events and blasting events showed an obvious increasing trend with time, and there was a positive correlation between the two types of

events. During this period, the microfracture events in rock mass were relatively active, and the rockburst risk was relatively high, which was obviously affected by the on-site excavation and blasting. It can be seen that external forces such as construction disturbance are the main factors inducing microseismic events.

4.2. Spatial Distribution of Microseismic Events. By means of the spatial distribution of microseismic events, the microfracture area of rock mass can be effectively identified, and then, the potential rockburst risk area of the underground powerhouse area can be predicted. The concentration area of microseismic events can be divided by analyzing the density and frequency of the spatial distribution of microseismic events. Figure 10 shows the spatial distribution of microseismic events in the monitoring area from September 30 to November 30, 2017. In this figure, a sphere represents a microseismic event, and its size represents energy, with a bigger sphere standing for greater energy and different colors representing different moment magnitudes. The microseismic events are mainly concentrated in the arch shoulder on the upstream side of the powerhouse with an elevation ranging from 150 m to 180 m (recorded as zone

(a) Axonometric view

(b) Front view
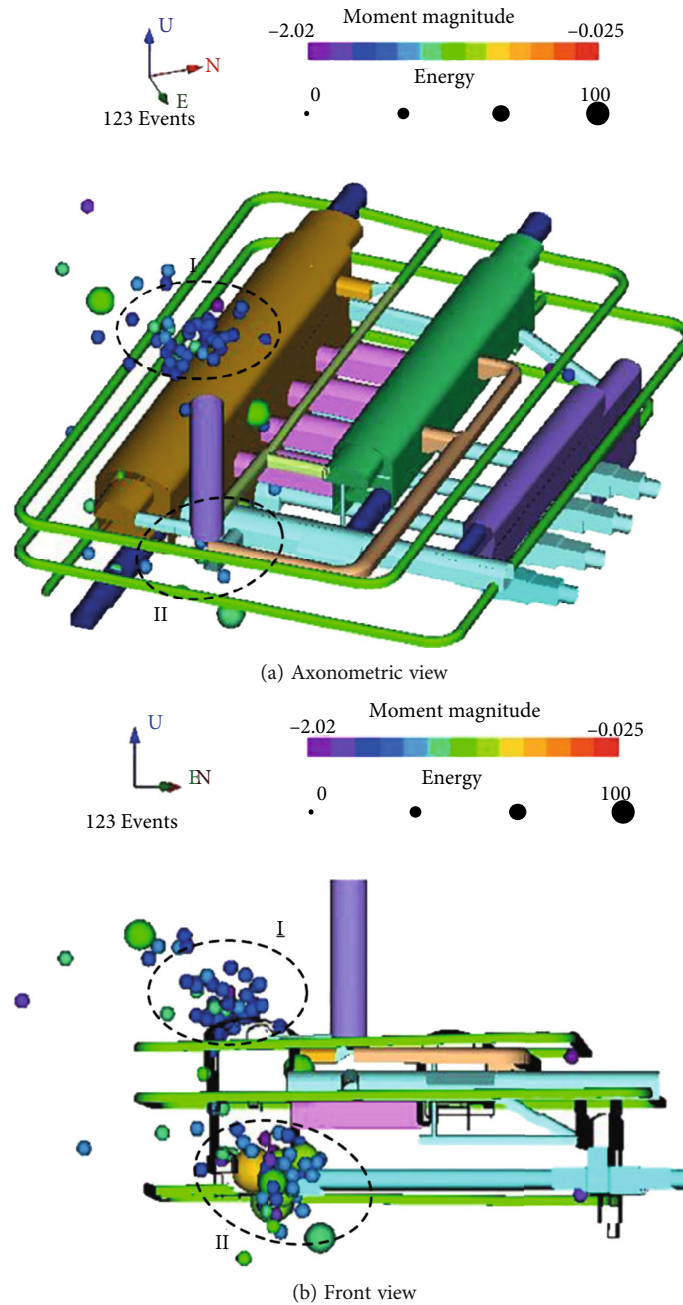
FIGURE 10: Spatial distribution of microseismic events.

I) and the intersection of the lower drainage corridor and the powerhouse installation room with an elevation ranging from 110 m to 140 m (recorded as zone II). Combined with the on-site construction of underground powerhouse and on-site survey analysis, microseismic events in these two zones are distributed along faults f_{31} and f_{34}. Microseismic events concentrate in the above zones because of dynamic disturbances such as mechanical vibration and blasting vibration during the excavation of the powerhouse. However, there is a main fault developed in the microseismic accumulation area of the surrounding rock, and the stress is likely to concentrate on the structural surface of the fault with lower strength, which induces microcracking of the rock.

4.3. Preliminary Analysis of Microseismic Events. After processing the microseismic data in two months and analyzing the construction of the underground powerhouse caverns, the concentration area of microseismic events is mainly caused by the dynamic disturbances brought about by the vibration of construction machineries and blasting operations. The magnitude, energy, and focal radius of microseismic events in zone I are small, while those in zone II are larger. At present, there is no large-scale rockburst in the monitoring area, but rock mass collapses occur occasionally in some parts of the microseismic event concentration area (see Figure 11). Microcracks constantly occur in rock mass, indicating the potentially dangerous places for rockburst,

(a) Located near the left 0 + 40 of the pile number factory on the inner side wall of the upstream side of the middle drainage corridor (elevation 155 m)

(b) Located near the left 0 + 35 of the pile number factory on the inner side wall (elevation 125 m) on the upstream side of the lower drainage corridor

FIGURE 11: Collapses of rock mass in microseismic accumulation area.

making it necessary to pay attention to microseismic activities in such places. All the microseismic events have been accurately captured by the monitoring system, which proves the reliability of this microseismic system in rockburst prediction and early warning as well as the evaluation of the stability of surrounding rocks.

The prevention of rockburst during the construction phase mainly includes optimizing the stress of the surrounding rock, optimizing the physical and mechanical characteristics of the surrounding rock, and comprehensively strengthening the surrounding rock. The existing microseismic monitoring results show that the rockburst risk in the underground powerhouse area is mainly a time-delay rockburst. The engineering prevention and control of rockburst mainly include the following. (1) During blasting, smooth blasting should be enhanced, and the excavation section should be smoothly treated to reduce stress concentration and effectively improve the quality of the excavation. (2) Cold water is often sprayed on the excavation surface or high-pressure water injection is drilled to improve the physical and mechanical properties of the surrounding rock. (3) Shorten the excavation footage, which generally does not exceed 2 m. After excavation, the initial anchor net shotcrete support will be used to reduce the exposure time and area of the rock mass. (4) Set up reasonable surrounding rock support and reinforcement measures. For example, strengthen the support of the surrounding rock in zone 1 and zone 2 and increase the length of bolts.

5. Conclusion

This paper takes the underground powerhouse area of the Huanggou Pumped Storage Hydropower Station as an example and uses a microseismic monitoring system to monitor and forecast rockbursts. Practices have proved that the microseismic system can effectively capture high-frequency blasting and low-frequency microseismic events. The monitoring results in two months show that the frequency of microseismic events in the underground powerhouse area is positively correlated with the construction frequency of blasting excavation. The microseismic events are mainly concentrated at the intersection of the arch shoulder on the upstream side of the powerhouse as well as at intersection between the lower drainage corridor and the powerhouse installation room and distributed in strips along the faults. At present, there are no large-scale rockbursts in the monitoring area, but close attention should be paid to the influence of construction intensity on the stability of surrounding rocks in the microseismic concentration area. Finally, targeted engineering prevention and control measures for rockbursts are proposed. This lays a foundation for the evaluation of the powerhouse's stability.

Data Availability

The data used to support the findings of this study are included within the article.

Conflicts of Interest

The authors declare no conflict of interest.

Acknowledgments

References

[1] M. F. Cai, D. Ji, and Q. F. Guo, "Study of rockburst prediction based on in-situ stress measurement and theory of tnergy accumulation caused by mining disturBance," *Chinese Journal of Rock Mechanics and Engineering*, vol. 32, no. 10, pp. 1973–1980, 2013.

[2] M. He, H. Xie, S. Peng, and Y. Jiang, "Study on rock mechanics in deep mining engineering," *Chinese Journal of Rock Mechanics and Engineering*, vol. 24, no. 16, pp. 2803–2813, 2005.

[3] G. S. Su, J. Q. Jiang, X. T. Feng, and C. Mo, "Experimental study of ejection process in rockburst," *Chinese Journal of Rock Mechanics and Engineering*, vol. 35, no. 10, pp. 1990–1999, 2016.

[4] Q. Yu, *Study on Rockburst Nucleation Process and Early Warning Method of Deep-Buried Tunnels*, The doctoral dissertation of Dalian University of Technology, 2016.

[5] C. S. ZHANG, N. LIU, and W. J. CHU, "Inducement mechanism and case analysis of tectonic rockburst in jinping II deep buried tunnel," *Chinese Journal of Rock Mechanics and Engineering.*, vol. 34, no. 11, pp. 2242–2250, 2015.

[6] F. Z. Jiang, X. D. Xiang, and D. S. Zhu, "The current status and developing tendency of rock blasting forecast at home and abroad," *Industrial Safety and Environmental Protection*, vol. 8, pp. 19–22, 2003.

[7] A. J. Mendecki, *Seismic Monitoring in Mines*, Chapman and Hall Press, London, 1996.

[8] Z. H. Lu and Z. Liancheng, "Evaluation of near-field monitoring efficiency of tremers in Mentougou mine," *Earthquake*, vol. 5, pp. 32–39, 1989.

[9] C. X. Yang, Z. Q. Luo, G. B. Hu, and X. M. Liu, "Application of a microseismic monitoring system in deep mining," *Journal of University of Science and Technology Beijing*, vol. 14, no. 1, pp. 6–8, 2007.

[10] S. L. Li, X. G. Yin, and W. D. ZHENG, "Cezar Trifu. Research of multi-channel microseismic monitoring system and its application to Fankou lead-zinc mine," *Chinese Journal of Rock Mechanics and Engineering*, vol. 24, no. 12, pp. 2048–2053, 2005.

[11] X. T. Feng, B. R. Chen, C. Q. Zhang, S. J. Li, and S. Y. Wu, *Mechanism, Warning and Dynamic Control of Rockburst Development Processes*, Science Press, Beijing, 2013.

[12] B. H. Zhang, J. H. Deng, and M. Z. Gao, "Safety evaluation research based on microseismic monitoring in underground powerhouse of hydropower station," *Chinese Journal of Rock Mechanics and Engineering*, vol. 31, no. 5, pp. 937–944, 2012.

[13] B. Li, F. Dai, N. W. Xu, Y. G. Zhu, C. X. I. A. O. Sha, and G. He, "Microseismic monitoring system and its engineering applications of deep-buried underground powerhouse," *Chinese Journal of Rock Mechanics and Engineering*, vol. 33, no. S1, pp. 3375–3383, 2014.

[14] B. H. Jie, Z. N. Zhao, B. R. Chen, Y. X. Xiao, and G. L. Feng, "Regularity of spatio-temporal distribution of rockburst in deep-buried long tunnels based on microseismic monitoring signals," *Journal of Yangtze River Scientific Research Institute*, vol. 29, no. 9, pp. 69–73, 2012.

[15] K. Ma, C. A. Tang, L. C. Li et al., "Reinforcement effects of anti-shear gallery of Dagangshan right bank slope based on microseismic monitoring and numerical simulations," *Chinese Journal of Rock Mechanics and Engineering*, vol. 32, no. 6, pp. 1239–1247, 2013.

[16] N. W. Xu, C. A. Tang, C. Sha, Z. Z. Liang, J. Y. Yang, and Y. Y. Zou, "Microseismic monitoring system establishment and its engineering applications to left bank slope of jinping I hydropower station," *Chinese Journal of Rock Mechanics and Engineering*, vol. 29, no. 5, pp. 915–925, 2010.

[17] N. W. Xu, C. A. Tang, Z. Zhou, C. Sha, and Z. Z. Liang, "Stability analysis of hydraulic rock slope based on three-dimensional numerical simulation and microseismic monitoring," *Chinese Journal of Rock Mechanics and Engineering*, vol. 29, no. 7, pp. 1373–1381, 2013.

[18] G. Z. Cai and C. Z. Yu, "Schedule and excavation of underground powerhouse for hydropower station," *Water Resources & Hydropower of Northeast*, vol. 34, no. 11, pp. 1-2, 2016.

[19] S. D. Bing and Y. S. Pan, "Microseismic orientation method for mine and its application," *Coal Mining Technology*, vol. 12, no. 5, pp. 1–4, 2007.

[20] Y. X. Xiao, X. T. Feng, J. A. Hudson, B. R. Chen, G. L. Feng, and J. P. Liu, "ISRM suggested method for in situ microseismic monitoring of the fracturing process in rock masses," *Rock Mechanics and Rock Engineering*, vol. 49, no. 1, pp. 343–369, 2016.

[21] H. Y. Wang, "Study of precise localization of microseismic events in a rock mass," *Engineering Blasting*, vol. 7, no. 3, pp. 5–8, 2001.

[22] L. L. Chen, H. Lian, Z. Liu, H. B. Chen, E. Atroshchenko, and S. P. A. Bordas, "Structural shape optimization of three dimensional acoustic problems with isogeometric boundary element methods," *Computer Methods in Applied Mechanics and Engineering*, vol. 355, pp. 926–951, 2019.

WILEY | Hindawi

Research Article

Study on the Fractal Characteristics of the Pomegranate Biotite Schist under Impact Loading

Jianguo Wang [ID],[1,2] **Ting Zuo** [ID],[1] **Xianglong Li** [ID],[1,2] **Zihao Tao** [ID],[1] **and Jun Ma** [ID][1]

[1]*Faculty of Land Resources Engineering, Kunming University of Science and Technology, Kunming, 650093 Yunnan, China*
[2]*Yunnan Key Laboratory of Sino-German Blue Mining and Utilisation of Special Underground Space, Kunming, 650093 Yunnan, China*

Correspondence should be addressed to Ting Zuo; ztkust@163.com and Xianglong Li; lxl00014002@163.com

In order to study the fractal characteristics of the pomegranate biotite schist under the effect of blasting loads, a one-dimensional SHPB impact test was carried out to test the dynamic compressive strength, damage morphology, fracture energy dissipation density, and other parameters of the rocks under different strain rates; besides, sieve tests were conducted to count the mass fractal characteristics of the crushed masses under different strain rates to calculate the fractal dimension of the crushed rock D. Finally, the relationships between fractal dimension and dynamic compressive strength, crushing characteristics, and energy dissipation characteristics were analysed. The results show that under different impact loads, the strain rate effect of the rock is significant and the dynamic compressive strength increases with the increasing strain rate, and they show a multiplicative power relationship. The higher the strain rate of the rock, the deeper the fragmentation and the higher the fractal dimension, and the fractal dimension and rock crushing energy density are multiplied by a power relationship. By performing the comparative analysis of the pomegranate biotite schist, a reasonable strain rate range of $78.75 \text{ s}^{-1} \sim 82.51 \text{ s}^{-1}$ and a reasonable crushing energy consumption density range of $0.78 \text{ J·cm}^{-3} \sim 0.92 \text{ J·cm}^{-3}$ were determined. This research provides a great reference for the analysis of dynamic crushing mechanism, crushing block size distribution, and crushing energy consumption of the roadway surrounding rock.

1. Introduction

The dynamic hazard is very frequent in the deep mining project [1, 2], and many scholars think that the fracture pattern is critical to studying the rock fractal in the mining, underground geotechnical engineering blasting, and other fields [3–5]. As one kind of typical rock in the deep mine roadway envelope, with fractal theory, the fractal evolution of crushed pomegranate biotite schist under impact loading was studied, and the relationship between its fractal dimension and the strain rate, dynamic compressive strength, average block size, and crushing energy dissipation density was also analysed, which is of great importance to blasting mining, hydraulic fracturing [6–8], and liquid CO_2 fracturing [9].

The SHPB technique has been widely used for testing the dynamic properties of materials under the condition of high strain rates, such as rock [10–15]. Based on the fractal theory,

Tyler developed a mass fractal model for modelling the distribution of rock fracture bulkiness. Weng et al. [16] used SHPB equipment to conduct impact experiments on sandstones treated at different temperatures and studied their fractal characteristics and energy dissipation characteristics, respectively. Li et al. [17] analysed the relationship between the fractal dimension of the fracture angle of coal sections and the intact degree of coal rock under impact loading. Following the SHPB experimental setup, Huang et al. [18] studied the fractal fragmentation characteristics of sandstones with different water contents and obtained the relationship between fractal dimension and water content and energy consumption. By subjecting cyclic loading to sandstone specimens and combining fractal theory with energy consumption principles, Hu et al. [19] studied the crushing bulk and energy dissipation. Deng et al. [20] conducted impact loading tests on granite and sandstone and analysed dissipation characteristics with
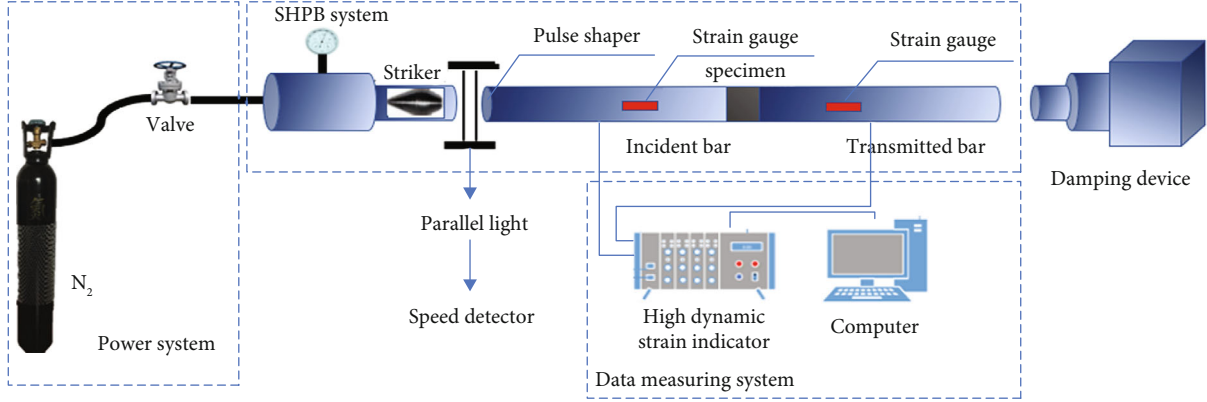
FIGURE 1: SHPB impact test system.

fractal theory. Zhao et al. [21] used the SHPB apparatus to test two types of rocks and analysed their relationships between the crushing characteristics and dynamic strength with fractal theory.

The present studies about the rock dynamics test mainly focus on the distribution of rock fragmentation bulk and energy dissipation; the relationships between fractal dimension and impact loading strain rate, average bulk, kinetic parameters, and energy density are rarely studied. Therefore, in this paper, SHPB kinetic tests and sieve tests were conducted on the pomegranate biotite schist, and the fractal dimension D was calculated using the G-G-S fractal model.

2. Test Preparation and Programme

2.1. Experimental Procedure and Principles. As shown in Figure 1, a $\Phi50$ mm variable section Hopkinson pressure bar (SHPB) in the Rock Mechanics Laboratory of the Kunming University of Science and Technology is chosen, which consists of a loading system, a bullet, an incident bar, a transmission bar, a test signal collection system, and an energy absorption device. The length of the bullet is 0.4 m, the length of the incident and the transmission bar is both 2.0 m, the elastic modulus of the bar is 210 GPa, the metal bar is made of alloy steel with a density of 7.8 g/cm^3, and the longitudinal wave speed is 5190 m/s. Besides, the bar is powered by nitrogen pressurisation, and the laser velocimeter is used to measure the speed of the bar while applying impact loading. In order to eliminate the end effect and tip effect of the rock specimen, petroleum jelly is applied between the rock specimen and the incident and transmission bars to ensure that both ends of the specimen and the bar contact surfaces are smooth.

The SHPB test is designed based on the theory of the stress wave propagating in an elastic compression bar [22, 23], in which there are 2 basic assumptions, including the one-dimensional elasticity and the uniform stress distribution. The cross section of the elastic compression bar is a plane during stress wave propagation, and the stress keeps constant. Because the two-wave method will cause errors while processing data, the three-wave method is usually adopted [24], by which the strain rate $\dot{\varepsilon}_s$, strain ε, and stress of the specimen σ_s can be expressed by

$$\dot{\varepsilon}_s = \frac{C_0}{L_s}[\varepsilon_I(t) - \varepsilon_R(t) - \varepsilon_T(t)],$$

$$\varepsilon = \frac{C_0}{L_s}\int_0^{t_0}[\varepsilon_I(t) - \varepsilon_R(t) - \varepsilon_T(t)]\,dt, \qquad (1)$$

$$\sigma_s = \frac{EA}{2A_s}[\varepsilon_I(t) - \varepsilon_R(t) - \varepsilon_T(t)],$$

where A_s, A is the cross section area of the specimen and the compressional bar (m^2); C_0 is the velocity of the elastic longitudinal wave of the compressional bar (m/s); E is the elastic modulus of the bar (GPa); L_s is the length of the specimen (m); ε_I, ε_R, and ε_T are the strains of the incident wave, reflected wave, and transmitted wave at a certain moment t; and t is the propagation time of the stress wave in the bar (s).

In the process of the rock crushing, the incident energy W_I, reflected energy W_R, and transmitted energy W_T of the compressional bar can be calculated by the following equations.

$$\begin{cases} W_I(t) = AEC_0\int_0^t \varepsilon_I^2(t)dt, \\[2mm] W_R(t) = AEC_0\int \varepsilon_R^2(t)dt, \\[2mm] W_T(t) = AEC_0\int \varepsilon_T^2(t)dt. \end{cases} \qquad (2)$$

After ignoring the energy loss in the propagation of the stress wave, the energy absorbed by the rock can be obtained as follows:

$$W_s = W_I - (W_R + W_T). \qquad (3)$$

If the crushing energy of the rock is supplied by the absorbed energy, the absorbed energy of the rock can be regarded as the crushing energy of the rock. To further reduce the influence of volumetric factors on the test results, the crushing energy density ω_{cp} is defined as follows for the crushing energy analysis.

TABLE 1: Average values of physical parameters of specimens.

Specimen type	Length (mm)	Diameter (mm)	Aspect ratio	Quality (g)	Density (kg·m^{-3})	Modulus of elasticity (GPa)	Poisson's ratio	Compressive strength (MPa)
Pomegranate biotite schist	49.36	48.50	1.01	266.64	2943.36	106.80	0.31	59.82

FIGURE 2: Pomegranate biotite schist.

$$\omega_{cp} = \frac{W_s}{V}. \tag{4}$$

2.2. Specimen Preparation. The rock samples were taken from the Yuxi Mining Dahongshan Copper Mine, and they have high integrity and uniformity. The surface of the specimen is dark grey and has few apparent cracks. According to the requirements of the rock mechanics test, the nonparallelism at both ends of the specimen should be in the range of -0.02 mm~+0.02 mm, and the central axis of the specimen must be perpendicular to both ends of the specimen with an axial deviation of -0.25°~+0.25°. In order to reduce the influence of the end effect and tip effect on the test result, the rock specimen was processed into a cylinder with the size of 50 mm ∗ 50 mm. The initial physical parameters of the specimens are shown in Table 1, in which specimens of pomegranate biotite schist are numbered as L-1#~L-15# as shown in Figure 2.

Before the test, the optimal impact pressure of 0.4 MPa to 0.6 MPa was determined with the test punches. For every impact pressure, more than 3 specimens were tested to guarantee the accuracy of the experimental results.

3. Test Analysis of the Test Results

3.1. Analysis of Fragmentation Patterns. After conducting impact tests on rock specimens under different impact pressures, seven sets of valid data were obtained, as shown in Table 2. The peak strain is defined as the strain value corresponding to the peak stress on the stress-strain curve.

Under the effect of impact loading, the crushing of rocks is actually a process of internal microscopic crack initiation, expansion, and accumulation, which finally leads to macroscopic fragmentation, and its damage pattern indicates the energy dissipation state and damage degree of rocks; besides, different impact velocities will induce the different fragmentation patterns of rocks, as shown in Figure 3.

It can be seen that the splitting damage occurred for the low strain rate, and the damage pattern gradually changed to edge spalling, core damage, block fragmentation, and crushing damage as the strain rate increased. From the perspective of fragmentation, as the impact velocity increased, the strain rate of the rock, the fine end of the fragmentation block, and the degree of fragmentation all increased, but the size of the fragmentation block decreased. This phenomenon can be explained as that when the rock specimen is subjected to impact loading at a low rate, the energy taken by the impact load is little, the internal microcracks will develop in an orderly direction, and a few cracks will develop and penetrate the rock specimen, inducing less broken pieces; with the increase in the impact loading rate, the energy subjected to the specimen increases, making the cracks within the specimen fully developed, which continuously expand and penetrate to form the apparent cracks, leading to more broken pieces, less size of the broken pieces, and high degree of fragmentation.

3.2. Analysis of Dynamic Strength Characteristics. The test results showed that the dynamic compressive strength of the pomegranate biotite schist was significantly affected by the strain rate. As shown in Figure 4, the dynamic compressive strength of the rock increased from 150.20 MPa to 209.06 MPa as the strain rate increased from approximately 46.89 s^{-1} to 93.84 s^{-1}; the relationship between them can be fitted by a multiplicative power function $\sigma_f = p\dot{\varepsilon}^q$ based on the research by Wang and Li [25, 26]. Under different strain rates, the significant change in dynamic compressive strength of rocks is known as the strain rate effect, which is a characteristic of the mechanical response of brittle materials due to change in the one-dimensional stress state. Moreover, as the strain rate increased, both the number of cracks within the rock and the required external energy increased; however, due to the extremely short duration of the impact loading, the required energy was not reached, so external energy can only be counteracted by increasing the stress. Therefore, the dynamic strength of the surrounding rock of the roadway should be taken into account to consider conditions such as roadway excavation blasting and mechanical dynamic loading, which will provide guidance for the optimisation of subsequent blasting parameters.

3.3. Study on Fractal Characteristics of Rocks

3.3.1. Calculation of Fragment Screening and Fractal Dimension. In order to quantitatively describe the fragmentation degree of the rock specimen, the distribution of the size of the broken pieces after the destruction was introduced to reflect the changing pattern of the destruction degree of the rock sample with the strain rate. The specimens were sieved using standard sieves of 0 mm~25 mm, and the fragments remaining

TABLE 2: Characteristic parameters of rock fragmentation at different strain rates.

Specimen number	Impact pressure (MPa)	Impact velocity (m·s⁻¹)	Strain rate (s⁻¹)	Dynamic compressive strength (MPa)	Peak strain	Absorbed energy (J)	Crushing energy density (J·cm⁻³)
L-5#	0.40	10.13	46.89	150.20	0.0108	51.53	0.57
L-4#	0.45	10.86	59.69	152.79	0.0096	57.09	0.63
L-3#	0.45	12.09	70.21	163.41	0.0101	66.95	0.74
L-7#	0.50	12.55	78.75	177.19	0.0112	71.21	0.78
L-8#	0.55	13.63	82.51	197.10	0.0126	81.23	0.89
L-10#	0.58	14.54	90.63	198.20	0.0115	83.31	0.92
L-14#	0.60	15.04	93.84	209.06	0.0142	89.16	0.98
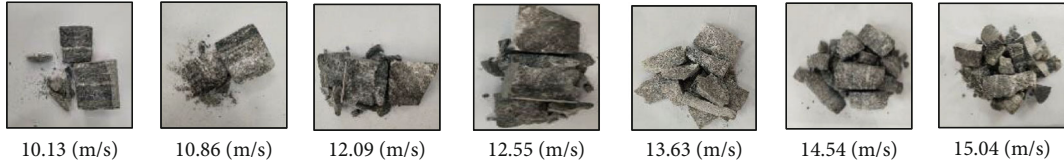
FIGURE 3: Damage pattern of pomegranate biotite schist at different impact velocities.
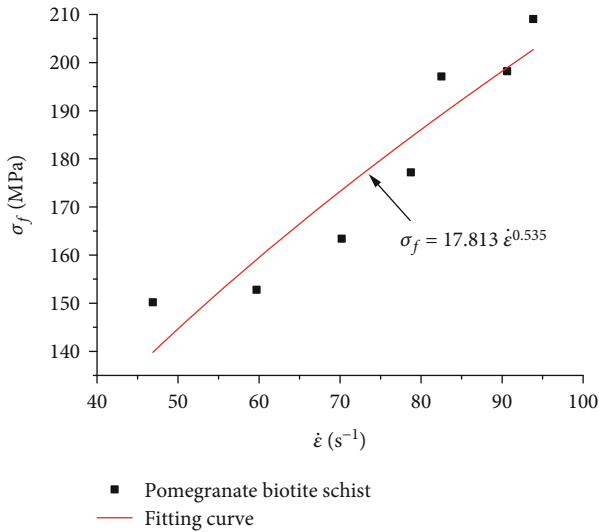
FIGURE 4: Dynamic compressive strength versus strain rate for pomegranate biotite schist.

above the sieve holes were weighed and converted into the percentage of fragments of rock (Table 3); thus, the fragmentation distribution curve of pomegranate biotite schist can be obtained and is shown in Figure 5.

According to Figure 5, after the pomegranate biotite schist specimen was subjected to conventional uniaxial impact loading, the percentage of fragments whose size was larger than 25 mm decreased from 66.78% to 31.28%, and the strain rate increased from 46.89 s⁻¹ to 93.84 s⁻¹. The change in the block size distribution of fragments whose size was less than 20 mm and below was relatively gentle.

Besides the particle size distribution, the fractal dimension is also an important indicator to characterise the fractal characteristics of the rock, and it increases with the degree of fragmentation of the specimen. The G-G-S model is now commonly used to describe the fractal bulkiness of fine-grained ends [27].

$$Y = \left(\frac{r}{r_m}\right)^b, \tag{5}$$

where b is the corresponding regression coefficient. Based on the relationship between mass and frequency, the fracture fragmentation distribution of the rock sample can be obtained:

$$Y = \frac{M_r}{M_t} = \left(\frac{r}{r_m}\right)^{3-D}, \tag{6}$$

where M_r is the mass of rock fragments with the particle size less than r, M_t is the total mass of rock fragments, r is the particle size of rock fragmentation, and r_m is the maximum particle size. By taking the logarithm of both sides in equation (6),

$$\lg Y = \lg \left[\frac{M_r}{M_t}\right] = (3-D) \lg \left(\frac{r}{r_m}\right). \tag{7}$$

In a new coordinate system of $\lg [M_r/M_t] - \lg r$, the slope of the line can be represented as $3 - D$. The $\lg [M_r/M_t] - \lg x$ curves describing the distribution of fragments of pomegranate biotite schist are shown in Figure 6.

It can be seen that the slope of the particle size characteristic curve decreased with the strain rate, indicating that the mass of the end of the fine of the crushed pomegranate nepheline gneiss gradually increased, and the crushing degree became higher. The average block size and fractal dimension of the fragmented pomegranate nepheline gneiss are shown in Table 4, and the large correlation coefficient R indicates that under impact loading, the distribution of block size is consistent with the fractal pattern.

3.3.2. Fractal Dimension versus Strain Rate and Mean Bulkiness. As shown in Figure 6, the double logarithmic function showed high linearity, indicating that the block distribution of the rock after fragmentation has a self-similarity or fractal character. This phenomenon can be explained as that the aggregation

TABLE 3: Table of impact test sieve sizes corresponding to weighing masses.

Sizes (mm) Mass (g) Strain rate (s^{-1})	0	0.3	0.5	1.0	2.5	5.0	10.0	15.0	20.0	25.0	Total mass
46.89	0.24	0.22	0.42	1.74	2.34	11.78	16.07	20.66	28.94	173.32	255.73
51.28	0.59	0.34	0.56	2.45	2.47	10.43	27.55	44.20	28.80	149.44	266.83
59.69	0.70	1.22	1.29	3.38	3.78	17.89	31.26	40.41	28.09	149.44	277.46
70.21	1.11	1.67	1.50	3.66	3.98	32.92	48.00	21.64	32.92	115.63	263.03
76.37	3.24	1.89	1.63	7.74	6.96	30.45	27.41	45.08	36.04	103.34	263.78
78.75	1.45	4.55	4.54	8.73	6.56	28.06	34.85	42.58	33.54	98.55	263.41
82.51	2.32	3.78	3.82	12.38	7.86	33.18	46.56	36.71	21.70	105.23	273.54
90.63	3.54	5.68	4.65	14.35	20.04	39.42	35.21	25.08	32.34	87.35	267.66
92.28	4.78	3.02	8.65	18.34	21.09	31.87	36.21	23.21	24.56	92.50	264.23
93.84	4.44	5.39	5.31	17.90	22.13	38.52	43.52	30.28	17.97	84.41	269.87
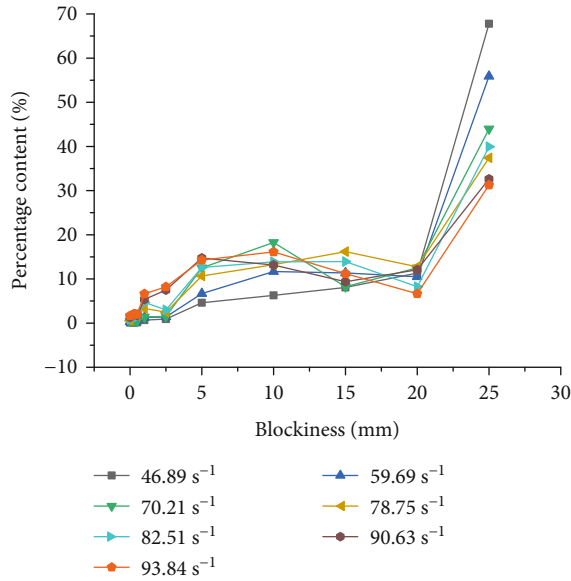
FIGURE 5: Distribution of fragmentation bulkiness of pomegranate biotite schist at different strain rates.

FIGURE 6: Curves for the distribution of fractional bulkiness of pomegranate biotite schist.

of small internal cracks lead to the macroscopic destruction of the rock, and the small fracture evolves from smaller micro-fractures. This self-similarity inevitably leads to the self-similar characteristics of the final block distribution. Therefore, the fractal dimension can be used to describe rock fragmentation quantitatively.

According to Figures 7 and 8, the fractal dimension D can be related to the strain rate and average block size, respectively. The average block size is defined as the block size whose cumulative percentage is less than 50%, as expressed in

$$d_s = \frac{\sum r_i d_i}{\sum r_i}, \tag{8}$$

where d_s is the average block size of rock fragments less than sieve diameters r_i and d_i is the mass percentage of rock fragments.

This parameter can quantify the distribution of bulkiness and the variation of fragmentation of the rock under different dynamic loads. Figures 7 and 8 show a strong correlation between the fractal dimension and strain rate $\dot{\varepsilon}$ and average block size d_s, in which the fractal dimension D increased from 1.80 to 2.51 and the average block size decreased from 23.78 mm to 15.60 mm, indicating that the fractal block size distribution of the pomegranate biotite schist is self-similar and has obvious fractal characteristics.

3.3.3. Fractal Dimension and Crushing Energy Consumption Density.
Based on the research of Hong et al. [28], the relationship between the fractal dimension of the rock D and the dissipation density of crushing energy ω_{cp} was fitted by a multiplicative power function in Figure 9.

As shown in Figure 9, the fractal dimension of the rock D exponentially increased with crushing energy density ω_{cp}, and the higher crushing energy density indicates that more

TABLE 4: Crushing bulkiness statistics of pomegranate biotite schist under impact loading.

Specimen number	L-5#	L-4#	L-3#	L-7#	L-8#	L-10#	L-14#
Average crushing size (mm)	23.78	21.76	19.65	18.61	18.16	16.48	15.60
Fractal dimension D	1.80	2.05	2.14	2.31	2.36	2.46	2.51
Correlation coefficient R	0.92	0.91	0.86	0.91	0.85	0.87	0.77
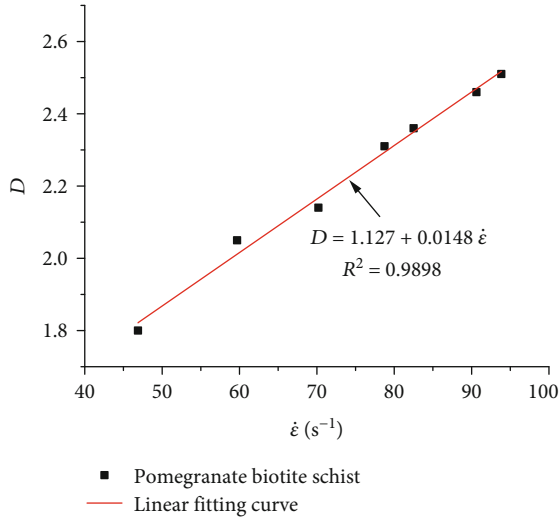
FIGURE 7: Fractal dimension versus strain rate for pomegranate biotite schist.

FIGURE 8: Relation between fractal dimension and average block size for pomegranate biotite schist.

FIGURE 9: Fractal dimension of pomegranate biotite schist versus crushing energy density.

FIGURE 10: Relationship diagram for determining the range of reasonable strain rates.

energy is required to crush the rock, and the more severe the rock crushing, the more fine-grained the fragments and the higher the fractal dimension D.

3.4. Study of Rock Crushing Effects and Energy Dissipation.
In summary, an increase in the strain rate makes the effective crushing bulk of the rock gradually migrate towards the fine-grain end, enhancing the crushing effect. However, an increase in the crushing effect means an increase in crushing energy density. Therefore, a reasonable range of the strain rate and crushing energy density is of great practical importance to enhance the crushing effect and reduce energy consumption.

In Figure 6, the particle size characteristic curve is characterised by the distribution of rock crushing bulk, and the slope of the curve is defined as the bulk distribution
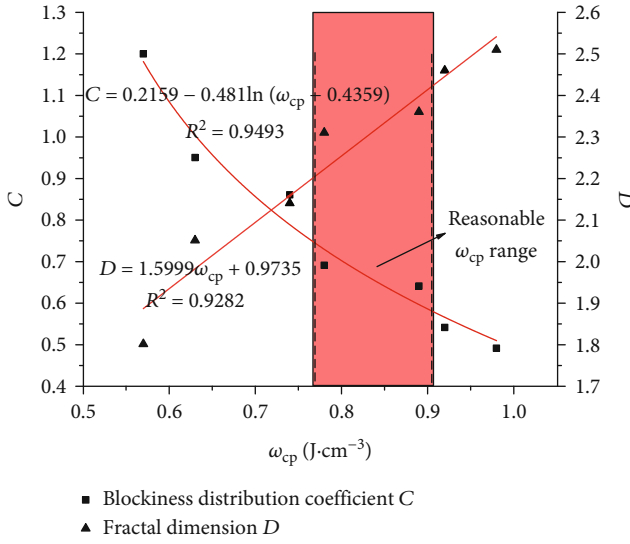
FIGURE 11: Relationship diagram for determining the range of reasonable crushing energy consumption densities.

coefficient C. Figures 10 and 11, respectively, show the relationship between the fractal dimension D and the strain rate and the relationship between the bulk distribution coefficient C and crushing energy consumption density.

It can be seen from Figure 10 that the slope of the curve changed fast and the decreasing rate started to increase when $\dot{\varepsilon}$ was close to $59.69\,\text{s}^{-1}$; after $\dot{\varepsilon}$ exceeds $82.51\,\text{s}^{-1}$, the decreasing rate of the curve decreased. Therefore, in order to achieve a better crushing effect, the $\dot{\varepsilon}$ should be controlled in the range of $59.69\,\text{s}^{-1}$~$82.51\,\text{s}^{-1}$, and the corresponding range of the fractal dimension curve was $70.21\,\text{s}^{-1}$~$90.63\,\text{s}^{-1}$. Similarly, in Figure 11, the dissipation density of crushing energy of two curves can be determined to be in the range of $0.74\,\text{J·cm}^{-3}$~$0.92\,\text{J·cm}^{-3}$ and $0.78\,\text{J·cm}^{-3}$~$0.98\,\text{J·cm}^{-3}$, respectively.

According to the relationship between the strain rate and crushing energy density in Table 2, it can be indicated that the reasonable strain rate range should be $78.75\,\text{s}^{-1}$~$82.51\,\text{s}^{-1}$ to achieve rock crushing and the reasonable crushing energy density range should be $0.78\,\text{J·cm}^{-3}$~$0.92\,\text{J·cm}^{-3}$ (the dashed line range in Figures 10 and 11).

4. Conclusion

In this paper, the typical tunnel envelope rock, pomegranate biotite schist, was selected to carry out SHPB rock dynamic mechanical tests, and rock fragmentation characteristics under different strain rates, strength indexes, and energy parameters were obtained to establish the relationship between fractal dimension and these parameters. This research provides a reference for further study of the dynamic mechanical properties of pomegranate biotite schist in deep mining and provides guidance for the optimisation design of blasting parameters for underground mine tunnelling. The main conclusions can be drawn as follows.

(1) The fragmentation distribution of pomegranate biotite schist is significantly affected by the strain rate under the effect of impact loading. As the strain rate increases, the degree of fragmentation decreases; the fine ends of the fragments increase with the fragmentation degree. Besides, the dynamic compressive strength increases with the strain rate, showing a power relationship

(2) The fractal dimension D can quantify the fracture characteristics of the rock, it increases as the strain rate increases, and when the strain rate ranges from $46.89\,\text{s}^{-1}$ to $93.84\,\text{s}^{-1}$, the fractal dimension D of pomegranate biotite schist is 1.80~2.51

(3) The fractal dimension D can quantify the fractal energy dissipation characteristics of a rock, and it increases with the fractal energy density ω_{cp} in a multiplicative power relationship

(4) The reasonable strain rate range to achieve good crushing effectiveness and reduce crushing energy consumption for pomegranate biotite schist is $78.75\,\text{s}^{-1}$~$82.51\,\text{s}^{-1}$, and the reasonable crushing energy consumption density range should be $0.78\,\text{J·cm}^{-3}$~$0.92\,\text{J·cm}^{-3}$

References

[1] J. Yang, T. J. Min, B. H. Liu, K. K. Chen, and L. Yang, "Research progress on disasters and prevention in deeping mining," *Science Technology and Engineering*, vol. 20, no. 36, pp. 14767–14776, 2020.

[2] H. P. Xie, "Research review of the state key research development program of China: deep rock mechanics and mining theory," *Journal of China Coal Society*, vol. 44, no. 5, pp. 1283–1305, 2019.

[3] R. S. Yang, P. Xu, C. Z. Jing, J. P. Fan, S. Z. Fang, and H. Zhang, "Experimental study on deformation failure and dynamic

tensile strength of layered sandstone under impact load," *Journal of China Coal Society*, vol. 44, no. 7, pp. 2039–2048, 2019.

[4] H. Wu, B. Dai, L. Cheng, R. Lu, G. Y. Zhao, and W. Z. Liang, "Experimental study of dynamic mechanical response and energy dissipation of rock having a circular opening under impact loading," *Mining, Metallurgy & Exploration*, vol. 38, no. 2, pp. 1111–1124, 2021.

[5] H. Wu and D. Ma, "Fracture response and mechanisms of brittle rock with different numbers of openings under uniaxial loading," *Geomechanics and Engineering*, vol. 25, no. 6, pp. 481–493, 2021.

[6] Z. Liu, J. Yang, L. Yang, X. Ren, X. Peng, and H. Lian, "Experimental study on the influencing factors of hydraulic fracture initiation from prefabricated crack tips," *Engineering Fracture Mechanics*, vol. 250, article 107790, 2021.

[7] L. Chen, Z. Wang, X. Peng, J. Yang, P. Wu, and H. Lian, "Modeling pressurized fracture propagation with the isogeometric BEM," *Geomechanics and Geophysics for Geo-Energy and Geo-Resources*, vol. 7, no. 3, 2021.

[8] Z. Liu, X. Ren, X. Lin, H. Lian, L. Yang, and J. Yang, "Effects of confining stresses, pre-crack inclination angles and injection rates: observations from large-scale true triaxial and hydraulic fracturing tests in laboratory," *Rock Mechanics and Rock Engineering.*, vol. 53, no. 4, pp. 1991–2000, 2020.

[9] J. Yang, H. Lian, and L. Li, "Fracturing in coals with different fluids: an experimental comparison between water, liquid CO_2, and supercritical CO_2," *Scientific Reports*, vol. 10, no. 1, 2020.

[10] M. M. He, Z. Q. Zhang, J. Zheng, F. F. Chen, and N. Li, "A new perspective on the constant mi of the Hoek-Brown failure criterion and a new model for determining the residual strength of rock," *Rock Mechanics and Rock Engineering*, vol. 53, no. 9, pp. 3953–3967, 2020.

[11] J. G. Wang, Y. Liu, and K. G. Li, "Dynamic characteristics of deep dolomite under one-dimensional static and dynamic loads," *Journal of The Institution of Engineers (India): Series A*, vol. 101, no. 1, pp. 49–56, 2020.

[12] M. M. He, Z. Q. Zhang, J. W. Zhu, N. Li, G. Li, and Y. S. Chen, "Correlation between the rockburst proneness and friction characteristics of rock materials and a new method for rockburst proneness prediction: field demonstration," *Journal of Petroleum Science and Engineering*, vol. 205, p. 108997, 2021.

[13] M. M. He, Z. Q. Zhang, and N. Li, "Deep convolutional neural network-based method for strength parameter prediction of jointed rock mass using drilling logging data," *International Journal of Geomechanics*, vol. 21, no. 7, 2021.

[14] Y. B. Wang, Y. Yang, Y. T. Zhang, and J. G. Wang, "Dynamic mechanical properties of coals subject to the low temperature-impact load coupling effect," *Scientific reports*, vol. 9, no. 1, 2019.

[15] R. S. Yang, S. Z. Fang, W. Y. Li, G. H. Wei, Q. Li, and S. F. Liang, "Temperature effects on dynamic compressive behavior of siliceous sandstone," *Arabian journal of geosciences*, vol. 13, no. 10, 2020.

[16] L. Weng, Z. J. Wu, Q. S. Liu, and Z. Y. Wang, "Energy dissipation and dynamic fragmentation of dry and water-saturated siltstones under sub-zero temperatures," *Engineering Fracture Mechanics*, vol. 220, article 106659, 2019.

[17] C. J. Li, Y. Xu, P. Y. Chen, H. L. Li, and P. J. Lou, "Dynamic mechanical properties and fragment fractal characteristics of fractured coal–rock-like combined bodies in split Hopkinson pressure bar tests," Natural Resources Research, 2020.

[18] M. Huang, J. Y. Qiu, J. W. Zhan, Y. Su, and X. D. Xie, "Fractal law of weak-weathered argillaceous siltstone with different water contents subjected to SHPB impact crushing," *Journal of Engineering Geology*, vol. 24, no. 4, pp. 597–603, 2016.

[19] H. Hu, Q. Q. Zheng, X. Gao et al., "Fracture characteristics and geometric fractal of damaged sandstone under impact load," *Shock and Vibration*, vol. 2020, Article ID 6617197, 2020.

[20] Y. Deng, M. Chen, Y. Jin, and D. W. Zou, "Theoretical analysis and experimental research on the energy dissipation of rock crushing based on fractal theory," *Journal of Natural Gas Science and Engineering*, vol. 33, pp. 231–239, 2016.

[21] H. H. Zhao, C. Liu, J. Zhang, and L. Ge, "Breakage behavior of gravel rock particles under impact force," Computational Particle Mechanics, 2021.

[22] K. W. Xia, S. Wang, Y. Xu, R. Chen, and B. B. Wu, "Advances in experimental studies for deep rock dynamics," *Chinese Journal of Rock Mechanics and Engineering*, vol. 40, no. 3, pp. 448–475, 2021.

[23] Z. L. Wang and Z. T. Lu, "Application of SHPB in experimental teaching of rock dynamics," *Research and Exploration in Laboratory*, vol. 33, no. 1, pp. 214–216, 2014.

[24] L. Song and S. S. Hu, "Two-wave and three-wave method in SHPB data processing," *Explosion and Shock Waves*, vol. 25, no. 4, pp. 368–373, 2005.

[25] J. J. Zhu, X. B. Li, F. Q. Gong, S. M. Wang, and W. He, "Experimental test and damage characteristics of sandstone under uniaxial impact compressive loads," *Journal of Centra South University (Science and Technology)*, vol. 43, no. 7, pp. 2701–2707, 2012.

[26] B. Wang and X. B. Li, "Mesomechanics analysis of static compressive strength and dynamic compressive strength of water-saturated rock under uniaxial load," *Explosion and Shock Waves*, vol. 32, no. 4, pp. 423–431, 2012.

[27] L. Xie, Q. H. Li, and S. L. Xu, "Experimental study on fractal of steam free reactive powder concrete under impact load," *Engineering Mechanics*, vol. 38, no. 3, pp. 169–180, 2021.

[28] L. Hong, X. B. Li, and C. D. Ma, "Study on size effect of rock dynamic strength and strain rate sensitivity," *Chinese Journal of Rock Mechanics and Engineering*, vol. 27, no. 3, pp. 526–533, 2008.

WILEY | Hindawi

Research Article

Influence of Hole Arrangement on the Section of Cavity Formed by Cutting Blast

Xianglong Li [ID],[1,2] Qiang Li [ID],[1] Jianguo Wang [ID],[1,2] Zichen Wang,[3] Hao Wang [ID],[4] and Zihao Tao [ID][1]

[1]*Faculty of Land Resources Engineering, Kunming University of Science and Technology, Kunming, Yunnan, China*
[2]*Yunnan Key Laboratory of Sino-German Blue Mining and Utilization of Special Underground Space, Kunming University of Science and Technology, Kunming, Yunnan, China*
[3]*Xi'an Research Institute of China Coal Technology Group Co., Ltd., Xi'an, Shanxi, China*
[4]*State Key Laboratory of Reservoir Geology and Development Engineering, Southwest Petroleum University, Chengdu, Sichuan, China*

Correspondence should be addressed to Jianguo Wang; wangjg0831@163.com

In order to optimize the arrangement of cutting holes in tunnel blast in Dahongshan Copper Mine, theoretical analysis and numerical simulation were combined to preliminarily determine the diameter of the hollow hole and the distance between the charge hole and the hollow hole during cut blast, which was verified through the field blast test. The research results show that with the increase of the hole diameter, the peak compressive stress of rock surrounding the empty hole gradually decreases, and the peak tensile stress gradually increases, which is consistent with the calculation results; when the hole diameter is 10 cm, the two first blast holes are arranged horizontally and 30 cm from the empty hole, two second blast holes are arranged vertically and 40 cm away from the empty hole, and the four third blast holes are arranged at a horizontal distance of 45 cm and a vertical distance of 45 cm from the empty hole; the contour area in numerical simulation is the maximum. The difference in contour area, contour width, and contour and contour height between the measured value and the simulation result is 5.3%, 3.3%, and 3.4%, respectively, indicating that the combination of theoretical calculation and numerical simulation is suitable for prediction of cavity section after blast in tunnel excavation.

1. Introduction

Cutting blast is a widely used technology for tunnel excavation, which creates a new free surface and more favorable blast conditions for other blast holes. Compared to other alternatives, for example, pulse fracturing [1] and hydraulic fracturing [2], cutting blast is more suitable for hard rocks and has low cost. During tunneling, there is only one free surface, and the surrounding rocks show great blast containment, inducing challenging blast conditions. By arranging large diameter holes in the cutting area, the stress concentration effect of the hollow holes, the free surface effect, and the unloading pressure effect can be used to improve the blast effect [3]. During the cutting blast, the hollow hole not only provides the initial compensation space for the rock swelling

of the groove cavity but also changes the stress distribution in the rock near the hollow hole and the blast effect of the adjacent slot hole. This phenomenon is called the empty hole effect of cutting blast. Because the hole effect plays an important role in promoting rock breaking, throwing, and cavity formation, it has been focused on by many scholars [4].

Mohanty [5] first proposed to set up empty holes between the blast holes to control the propagation direction of blast crack. Cho et al. [6] used a combination of numerical simulation and experiment to study the directional fracture effect of empty holes. Lai [7] established the calculation model of cutting blast effect on the basis of theoretical analysis. Under certain conditions, the quantitative relationship between the cutting efficiency and the hole diameter, the depth of the cut hole, and the hole distance between the

cut hole and the empty hole is obtained. Wu et al. [8] used ANSYS to simulate the distribution and variation trend of dynamic stress around blasting holes under different ground stress conditions. Tian et al. [9] based on the action mechanism of empty hole directional blasting, the influence of charge hole spacing on crack propagation is studied, deduced the calculation formula of charge hole spacing, and carried out numerical simulate of tunnel blasting excavation process. Li et al. [10] use ANSYS/LS-DYNA to simulate the process of rock fragmentation of double blast holes blasting with one empty hole at the center position. The rock fragmentation effect by blasting, the propagation of cracks between adjacent blast holes, and the pressure state of the element near the empty hole are analyzed. Zheng [11] used ANSYS simulation software to realize the visualization of the cavity formation and pressure propagation of cut blast and concluded that the blast effect is related to the distance between the charging hole to the empty hole. Zong et al. [12] used the cavity formation mechanism to explain the principle of adding holes in the deep hole vertical cutting. Zhu et al. [13] used numerical simulation methods to conduct comparative analysis of the single-hole cutting schemes under different diameter holes and found that the hole has the effect of reflecting stress waves and accumulating explosion energy, and its effect becomes more obvious as the increase of the hole diameter. Yue et al. [14] used the caustics test system to study the directional fracture failure under different hole shapes, and it was concluded that the diamond-shaped hole has the best effect on the directional propagation of the crack. By establishing the basic mechanical model of the straight hole cutting, Zhang Qi [15] quantitatively analyzed the influence of hole diameter on cutting effect of straight hole by numerical calculation; Li et al. [16] used explicit dynamic analysis software to simulate the crack penetration between the cut hole and empty holes with different diameters. The results show that as the hole diameter increased, the rock breaking extended failure area and compression failure area became more obvious; through numerical calculation, Wang et al. [17] found that the empty hole has the advantages of increasing the peak value of the stress wave and prolonging the action time. The stress wave in the rock mass around the empty hole was 2.2 times that of the traditional straight-hole cutting, which made the rock fragmentation more uniform and reduced the block rate. At the same time, the phenomenon of stress superposition and reflection of tensile explosion stress wave at the empty hole and the guiding role of the empty hole are intuitively displayed.

However, in terms of the cutting blast under the hollow hole arrangement, there is little research about the arrangement of the cutting holes. In this paper, the distance range was obtained through theoretical calculation, and the calculation result was simulated with LS-DYNA simulation software. Besides, different distances between the cutting holes and the hollow holes of the segmented detonation were simulated. Thus, the rock crushing range was determined to obtain the arrangement of the cutting hole and the distance between the empty holes until the hole network parameters of the cut holes are finally determined and used as a basis

for field tests. The test results show that the combination of theoretical calculations and numerical simulations can be used to predict the contour section after the blast of the cutting hole in tunnel excavation.

2. Theoretical Calculation of Vertical Cutting

2.1. Calculation of the Radius of the Rock Crushing Zone and the Fracture Zone under the Coupled Charge Condition. According to the roadway excavation requirements of Dahongshan Copper Mine of Yuxi Mining, the middle section of 330 m ~400 m was taken as a research subject, which is located in the third rock section of the Lower Proterozoic Manganghe Formation. This section is mainly composed of marble, and the overall rock quality is medium. The integrity of the rock mass is medium, and the surrounding rock of the chamber is stable during mining or roadway excavation. The geological type is the layered and quasilayered deposits dominated by hard and semihard rock groups and medium engineering geological conditions. There are locally wave-shaped undulating monoclinal structures and four groups of faults. The specific mechanical parameters [18, 19] are shown in Table 1:

The explosive used in blast is No. 1 rock emulsion explosive, and the parameters are shown in Table 2 below.

The radius of the rock crushing zone and the fracture zone of the coupled charge conditions are, respectively [20],

$$
\begin{cases}
R_c = \left(\dfrac{\rho_0 D_0^2 AB}{4\sqrt{2}\sigma_{cd}} \right)^{1/\alpha} r, \\[2mm]
A = \dfrac{2\rho_m C_p}{\rho_m C_p + \rho_0 D_0}, \\[2mm]
B = \left[(1+\lambda)^2 + (1+\lambda) - 2\mu_d(1-\mu_d)(1-\lambda)^2 \right]^{1/2}, \\[2mm]
R_t = \left(\dfrac{\sigma_{cd}}{\sigma_{td}} \right)^{1/\beta} \left(\dfrac{\rho_0 D_0^2 AB}{4\sqrt{2}\sigma_{cd}} \right)^{1/\alpha} r,
\end{cases}
\tag{1}
$$

where R_c is the radius of the crushing zone (m), ρ_e is the rock density (kg/m^3), C_p is the velocity of the longitudinal wave in the rock, ρ_0 is the explosive density, D_0 is the detonation velocity of explosive, σ_{cd} is the uniaxial dynamic compressive strength of the rock (MPa), $\sigma_{cd} = \sigma_c \dot{\varepsilon}^{1/3}$, σ_c is the uniaxial static compressive strength of rock, and $\dot{\varepsilon}$ is the strain loading rate (s^{-1}), which is between 10^0 and 105 s^{-1} in engineering blast. In the compression ring, the loading rate is higher, which can be taken as $\dot{\varepsilon} = 10^2 \sim 104$ s^{-1}; outside the compression ring, the loading rate is further reduced and can be taken as $\dot{\varepsilon} = 10^0 \sim 103$ s^{-1}; λ is the lateral stress coefficient, $\lambda = \mu_d/(1 - \mu_d)$; R_t is the radius of the crack zone (m); α is the attenuation index of shock wave propagation; μ_d is the dynamic Poisson's ratio of the rock,; r is the blast hole radius; μ is the static Poisson's ratio of the rock; σ_{td} is the dynamic tensile strength of the rock, due to the dynamic tensile strength of the rock changes little with loading strain rate. Within the range of strain loading rate of rock engineering blast, $\sigma_{td} = \sigma_t$; σ_t is the uniaxial static

Table 1: Statistics of physical and mechanical parameters of marble in Dahongshan Copper Mine.

| Rock type | Compressive strength/MPa | Tensile strength/MPa | Shear strength | | Elastic modulus/GPa | Poisson's ratio | Density/ kg·m^{-3} | Longitudinal wave speed/m·s^{-1} |
			Internal cohesion/MPa	Internal friction angle/°				
Marble	69.31	8.34	3.662	47.35	73.83	0.268	2908	3341

Table 2: Basic parameters of explosives.

Cartridge density/ g·cm^{-3}	Detonation transmission distance/cm	Detonation velocity/ m·s^{-1}	Function force/ml	Ferocity/ mm
0.95~1.30	≥4	≥4500	≥320	≥16.0

tensile strength of the rock, and β is the stress attenuation index, which is rewritten as $\bar{\beta}$ to distinguish from the crushing zone, $\bar{\beta} = 2 - \mu_d/(1 - \mu_d)$.

Thus, the radius of the crushing zone R_c and the radius of the crack zone R_t are determined to be 5.73 cm and 28.50 cm, respectively.

2.2. Diameter of Empty Hole. The surface of the empty hole is equivalent to the free surface, which has a directional effect on the broken rock. When the diameter of the empty hole is equal to or smaller than the diameter of the charge hole, the wave surface formed by the reflected stress wave is more convex than the incident wave surface, the degree of divergence is higher, so that the explosion energy is quickly attenuated, and the free surface of the empty hole has less effect. In order to improve the free effect of the empty holes and make full use of explosive energy to break the rocks, during the linear cutting, the diameter of the empty hole should be increased as much as possible or setting multiple small diameter holes. As the same time, the empty hole is also arranged to the location where stress is concentrated, and cracks are most likely to occur, because the empty hole provides expansion space for broken rocks. Cutting blast not only breaks the rock in the cavity but also pushes the broken rock out of the cavity so as to provide a new free surface for the rear blast hole [21]. Considering the construction efficiency, a single large diameter hole was selected and arranged in the middle of the cutting area.

According to the actual engineering situation, during rock drilling, the pore-forming velocity often decreases with the increase of the diameter of the empty hole. But in a certain range, the pore-forming velocity of blast holes does not need to decrease significantly with the increase of the hole diameter. The charge hole diameter in Dahongshan Copper Mine is 50 mm. When the diameter of the empty hole is larger than the aperture of the slot and the formula (2) is satisfied, not only the rock between the hole and the slot can be broken but also a crushing funnel can be formed [22]:

$$\frac{D}{d} \geq (1 + \sin \delta/2)/(1 - \sin \delta/2) = 1.7, \quad (2)$$
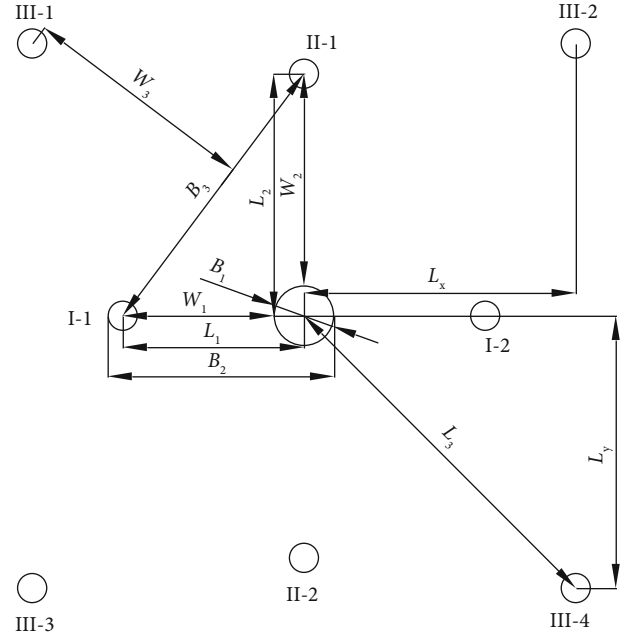
Figure 1: Schematic diagram of the layout position of the vertical cut of the empty hole.

where D is the diameter of the empty hole, d is the diameter of the charge hole, and δ is the rock blast fracture angle. When vertical cutting is used, $\delta > 30°$ is required.

Through theoretical analysis and calculation, the diameter of the hollow hole should be greater than the diameter of the charge hole, and their ratio needs to be greater than 1.7, that is, $D \geq 8.5$ cm. In order to form sufficient compensation space, a large diameter empty hole must be selected while cutting free surface and parallel to the blast hole.

2.3. Determination of Hole Distance. The layout of the blasting hole is shown in Figure 1. In the middle, there is an empty hole; the first blast hole is I-1 and I-2; the second blast hole is II-1 and II-2; the third blast hole is III-1, III-2, III-3, and III-4.

2.3.1. The Distance between the First Blast Hole and the Empty Hole. The distance between the first blast hole and the empty hole is mainly determined by the explosion energy, the volume of the blast hole, the explosion action index, and the blast hole deflection [23].

(1) The Influence of the Crushing Radius. Because the rock mass blasted by the first blast hole should be located in the fissure zone of the first blast hole, the center distance L_1

between the first blast hole and the empty hole should be less than the radius of the fissure zone, that is:

$$L_1 \le R_t + D/2, \tag{3}$$

where L_1 is the distance between the first blast hole and the hollow hole, and the diameter of the hollow hole is 10 cm according to the simulation result and $L_1 \le 33.50$ cm.

(2) The Influence of the Expansion Margin. The distance between the first blast hole and the empty hole should be greater than the radius of the crushing ring and smaller than the radius of the crack ring. When the hole spacing is less than the radius of the crushing, the groove may be "squeezed" due to excessive rock crushing or adjacent damage, which leads to the occurrence of rejection. When the blast hole spacing is greater than the radius of the fissure zone, it may cause insufficient rock fragmentation and fail to form a complete blast cavity. The volume of the empty hole should be close to the volume increment induced by the swelling of the rock under the impact of the first blast hole; therefore, this distance can be obtained:

$$L_1 \le \frac{\pi}{2(R+r)} \left[\frac{2(hr^2 + R^2)}{K-1} + R^2 + r^2 \right], \tag{4}$$

where R is the radius of the hole, r is the radius of the charge hole, h is the charge coefficient, and K is the breaking expansion coefficient of the rock, which was taken as $K = 1.5$ in this paper. The diameter of the charge hole is 5 cm, and the solution is $L_1 \le 31.68$ cm.

(3) The Influence of the Type of Crushing. When the crushed rock is completely thrown out, the distance between the first blast hole and the center of the hollow hole is

$$L_1 = \frac{2\pi}{\varepsilon} \left(\frac{R^2 + r^2}{R+r} \right) + R + r, \tag{5}$$

where ε is the coefficient relating to the rock type, lithology, and structure, and it is 2 in this research; after calculation, $L_1 = 21.28$ cm.

(4) The Influence of the Blast Hole Deflection. In order to prevent the penetration between the blast holes, formula (6) needs to be satisfied:

$$L_1 > \frac{D+d}{2} + 2H \sin a, \tag{6}$$

where H is the depth of the blast hole, and a is the deflection angle of the blast hole.

In Dahongshan Copper Mine, the rock drilling rig is a Kaishan brand KJ311 full hydraulic tunneling drill ring. The blast hole deflection angle can be controlled within 1°; so, it was calculated that $L_1 > 18.67$ cm.

TABLE 3: Explosive materials and state equation parameters.

ρ/(g/cm^3)	D_0/(m/s)	A/GPa	B/GPa	R_1	R_2	ω
1.3	4500	214.4	0.182	4.2	0.9	0.15

After comprehensively analyzing the influencing factors above, the distance range between the first blast hole and the empty hole is determined to be in the range 18.67 cm $< L_1 <$ 31.68 cm.

2.3.2. Distance from Blast Hole to the Empty Hole. The optimal resistance line and the free surface width of the charge can be determined according to the following empirical formula (7) [24]:

$$W = \left(d \frac{1.95e}{\sqrt{\rho_e}} + 2.3 - 0.0027B \right) (0.1B + 2.16), \tag{7}$$

where e is the correction coefficient of explosion force, which is 0.89 in this project, B is the width of the free surface, and W is the optimal resistance line of the segmented blast hole.

The hole layout diagram is shown in Figure 1. The distance between the first shot hole and the empty hole is $L_1 = 18.67$ cm ~ 31.68 cm, the free surface width is $B_2 = L_1 + D/_2 + d/_2$, $B_2 = 26.17$ cm ~ 39.18 cm, the optimal resistance line of the second shot hole is W_2 by formula (7), $W_2 = 31.92$ cm ~ 38.48 cm, and then the distance between the second shot hole and the empty hole is $L_2 = W_2 + D/_2$, $L_2 = 36.92$ cm ~ 43.48 cm. The free surface width of the third shot hole is $B_3 = \sqrt{L_1^2 + L_2^2} + D/2 + d/2$, $B_3 = 48.87$ cm ~ 61.29 cm. The optimal resistance line of the third shot hole is W_3 obtained by formula (7), $W_3 = 42.77$ cm ~ 47.53 cm, and then the distance between the third shot hole and the empty hole is $L_3 = W_3 + L_1 \cdot L_2 / \sqrt{L_1^2 + L_2^2}$, $L_3 = 59.43$ cm ~ 73.13 cm. The optimal resistance line of each charge hole is related to the width of the free surface, namely, the distance between the blast hole and the empty hole.

3. Numerical Simulation of Cut Hole Layout Parameters

3.1. Geometric Model. The ANSYS/LSDYNA was used to establish a two-dimensional finite element model with the size of 400 cm × 400 cm, in which the edge is defined as a nonreflective boundary, the blast hole diameter is 5 cm, the charge method is coupled charge, the charge diameter is 5 cm, and the holes with large diameter are located in the center of the model. The blast hole layout is shown in Figure 1.

Experimental scheme is as follows:

(1) After calculating the diameter of the hole, referring to the commonly used drill bits in the mine, the horizontal distance between the charging hole and the hole was set to 20 cm. The diameter of large holes used in China is 7.5 cm~ 10 cm [17]; so, D was selected as 7 cm, 7.5 cm, 8 cm, 9 cm, 10 cm, and

TABLE 4: Marble HJC constitutive model parameters.

ρ_0/kg·m^{-3}	f_c/MPa	A	B	C	S_{max}	G	T	D_1	D_2
2908	69.31	0.52	1.17	0.016 3	4	22.27	8.34	0.036	1
P_{crush}/MPa	μ_{crush}	P_{lock}/GPa	μ_{plock}	K_1	K_2	K_3	EF_{min}	N	FS
23.65	0.000 76	0.159	0.012	13	23	60	0.01	0.79	0.085

TABLE 5: Peak tensile stress of the hole wall with different hole diameters.

Empty hole diameter/cm	7	7.5	8	9	10	12.5
Simulated peak tensile stress/MPa	176	189	191	199	219	235
Calculate peak tensile stress/MPa	219	227	234	247	263	307

12.5 cm, respectively, and the two charge holes I-1 and I-2 detonate at the same time

(2) After the scheme (1), the hole diameter was determined to be 10 cm, the blast hole and the empty hole were arranged horizontally, the distance between the first blast hole and the empty hole L_1 was set as 20 cm, 25 cm, and 30 cm, respectively, and two blast holes I-1 and I-2 were set to detonate at the same time

(3) After determining the distance between the first blast hole and the empty hole, through the empirical formula, different hole spacings for the second blast hole were, respectively, set as 35 cm, 40 cm, and 45 cm for simulation, and the second blast hole was arranged along the longitudinal direction. The two first blast holes I-1 and I-2 were detonated at the same time. After the failure of the rock-free unit, the two second blast holes II-1 and II-2 were detonated again

(4) While calculating the distance $59.43\,\mathrm{cm} \leq L_3 \leq 73.13\,\mathrm{cm}$ between the third shot hole and the empty hole through the empirical formula, the blast holes were arranged symmetrically around the empty hole, and their horizontal and vertical distances were $42.02\,\mathrm{cm} \leq L_x \leq 51.71\,\mathrm{cm}$ and $42.02\,\mathrm{cm} \leq L_y \leq 51.71\,\mathrm{cm}$, respectively. In order to verify the accuracy of this parameter, set the horizontal distances L_x and vertical distances L_y spacing of the third blast hole was set to be 40 cm, 45 cm, 50 cm, and four third blast holes III-1, III-2, III-3, and III-4 detonated simultaneously after the first and second blast holes that were detonated, and the rock-free unit continued to fail

3.2. Material Model and Parameters.
The explosive used in the field is the No. 1 rock emulsion explosive [16], the model ∗MAT_HIGH_EXPLOSIVE_BURN is selected, and the state equation is defined by the keyword ∗EOS_JWL, which is used to describe the volume, pressure, and energy characteristics of the explosion. The equation parameters of explosive material and state used in this article are shown in Table 3. Many constitutive models have been proposed to describe

the effect of brittle materials under blast impact. According to the existing data of Dahongshan Copper Mine, various parameters of the marble material model can be obtained, as shown in Table 4 [25]. Using the ∗MAT_ADD_EROSION to define the tensile strength of the rock, when the effective stress of the element reaches the tensile strength, it will automatically disappear; thus, the dynamically displaying the broken process of the cut hole and the hollow hole can be realized [26, 27].

The rock fragmentation area is judged based on the failure of the rock element or the unfailed rock element that is separated from the surrounding rock mass, and the rock in the area is considered to be completely broken. If there is a slender area with a width of 1 unit, it is judged to be a crack, and the rock in this area is not included in the statistics.

3.3. Selection of Empty Hole Diameter.
After the explosion of the charge hole, the shock wave decays into a stress wave propagating in the rock, and when it reaches the wall of the hole, it will be reflected. The stress of the rock near the hole is larger than that of the condition without a hole. Because this is a hollow hole, the stress is concentrated, and the maximum tensile stress is generated at the connection line between the blast hole and the hollow hole. When this stress is greater than the dynamic tensile strength of the rock, radial cracks will appear at the hollow hole; as the structure is continuously charged, the initial maximum tensile stress around the blast hole can be expressed as follows [28–38]:

$$P = TC_p = \frac{2\rho_0 C_p}{\rho_0 C_p + \rho_0 D} \times \frac{\rho_e D^2}{\gamma + 1}, \tag{8}$$

$$\sigma_{\theta\theta\ max} = (3\lambda + 1)P\left(\frac{r_1}{L_1 - r_2}\right)^\alpha, \tag{9}$$

where $\sigma_{\theta\theta max}$ is the maximum peak value of tensile stress at the hole wall after blast (MPa), r_1 is the radius of the blast hole (m), and r_2 is the radius of the hole (m).

Under conditions of different hole diameters, the maximum tensile stress at the hole wall can be calculated, as shown in Table 5. According to Scheme 1, while simulating different hole diameters, the pressure history curves are shown in Figure 2, and the maximum tensile stress at the

min = A (0.00013, −1.76e+08)
max = A (9.96e-05, 9.67e+07)

(a) $D = 7\,\mathrm{cm}$

min = A (0.00013, −1.89e+08)
max = A (0.00011, 8.98e+07)

(b) $D = 7.5\,\mathrm{cm}$

min = A (0.00013, −1.91e+08)
max = A (9.96e-05, 8.22e+07)

(c) $D = 8\,\mathrm{cm}$

min = A (0.00013, −1.99e+08)
max = A (9.96e-05, 7.83e+07)

(d) $D = 9\,\mathrm{cm}$

min = A (0.000119, −2.19e+08)
max = A (9.96e-05, 8.14e+07)

(e) $D = 10\,\mathrm{cm}$

min = A (0.00011, −2.35e+08)
max = A (8.99e-05, 8.57e+07)

(f) $D = 12.5\,\mathrm{cm}$
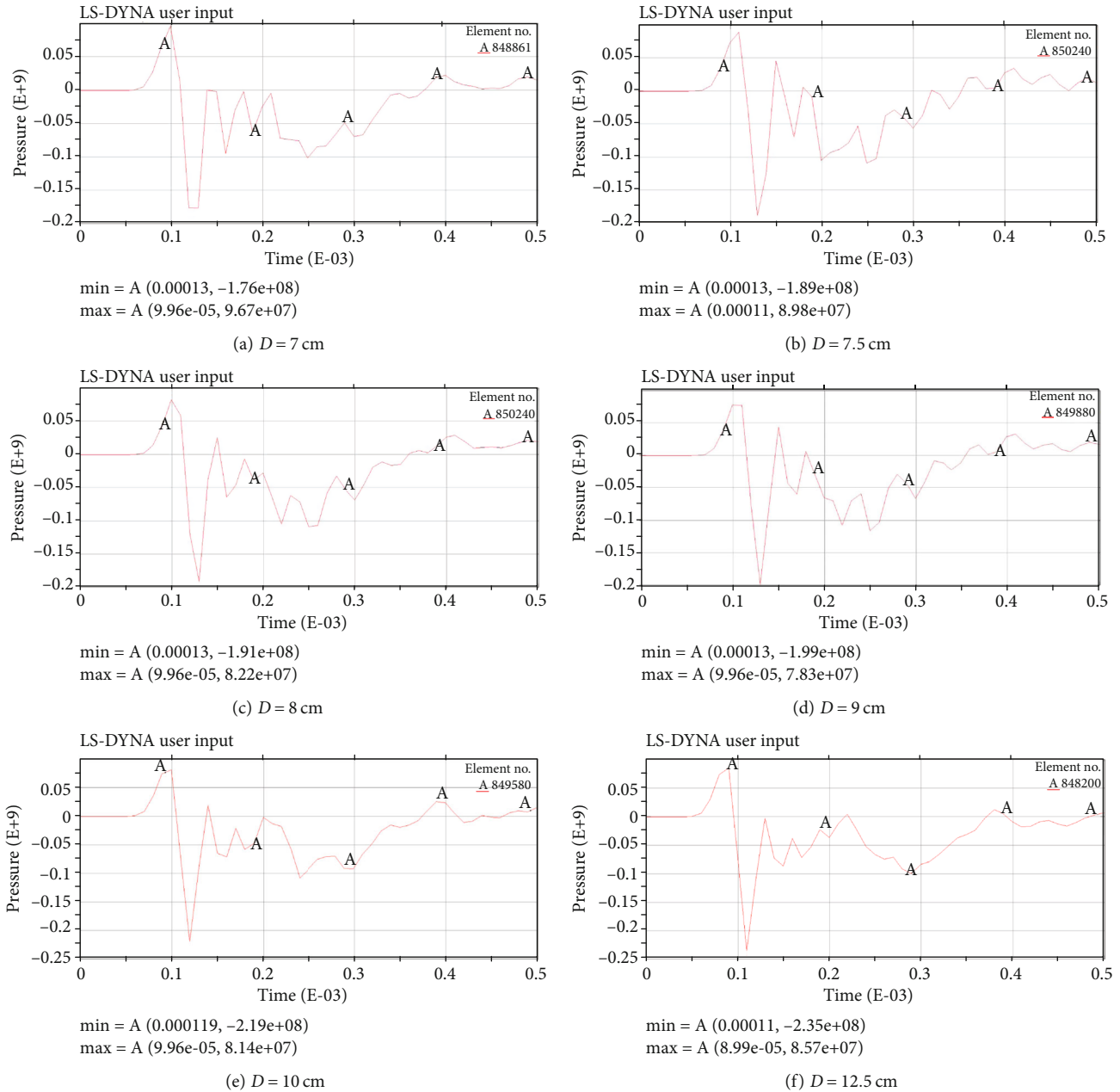
Figure 2: Pressure time history curve of hole wall under different hole diameters.

hole wall can be obtained. The calculation results and simulation results are plotted in Figure 3, and it can be seen that the calculation and simulation results are basically consistent with each other; they both increase with the increase of the hole diameter.

It can be seen from Figure 2 that with the hole diameter increases from 7 cm to 12.5 cm, the distance between the hole wall and the first blast hole gradually decreases; so, the time of reaching the peak compressive stress of the rock surrounding the hole wall decreases from 99.6 μs to 89.9 μs, and the peak compressive stress is reduced from 96.7 MPa to 85.7 MPa, indicating that when the shock wave is far away from the center of the blast hole, the shock wave continues to attenuate, and the stress value continues to drop. At the

same time, the time of reaching the peak tensile stress decreases from 130 μs to 110 μs, and the peak tensile stress increases from 176 MPa to 235 MPa, indicating when the compression wave propagates to the cavity, it will be reflected to form a tensile wave and has the same effect as the initial stress wave propagated to the free surface. It can also be known that the tensile stress of the rock around the wall of the cavity increases with the increase of the diameter of the cavity, and the larger the diameter of the cavity, the easier it is for the surrounding rock to be damaged by tension, which is helpful to the formation of the cavity. Considering the existing rock drilling equipment and rock drilling cost of Dahongshan Copper Mine, the diameter of the hole is selected as 10 cm.
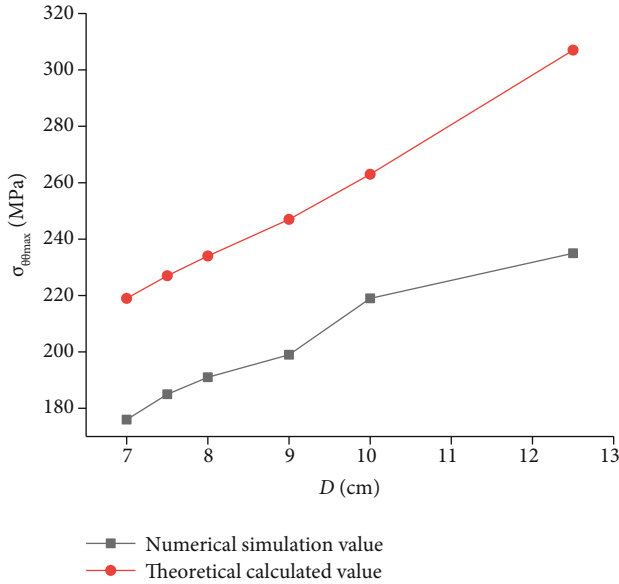
FIGURE 3: Comparison of maximum tensile stress between theoretical calculation and numerical simulation.

3.4. The Distance between the Empty Hole and the First Blast Hole. According to Scheme 2, after simulating different distances between the first blast hole and the empty hole, the damage range of the rock is shown in Table 6.

It can be seen that for the model of 20 cm hole spacing, after the blast, the width of the rock fragmentation zone is 70.21 cm, and its cross-sectional area is 1651.7 cm^2; when the hole spacing is 25 cm, the width and the cross-sectional area of the rock fragmentation zone is 76.61 cm and 2182.9 cm^2, respectively; for the 30 cm hole spacing, the rock fragmentation area is the largest, and the corresponding width and area is 83.1 cm and 2320.5 cm^2.

3.5. Spacing between the Empty Hole and the Second Blast Hole. The simulation is carried out according to Scheme 3, during which after the two first blast holes detonate for 25 ms, and the second blast hole detonates. The damage range of the rock is shown in Table 7. The pore wall pressure time history curve at the hole wall is shown in Figure 4.

It can be seen that before detonation, as the hole distance increases, the peak compressive stress of the blast hole wall is 221 MPa, 140 MPa, and 136 MPa, respectively, indicating that the smaller the distance between the second blast hole and the empty hole the greater the impact of the stress wave caused by the first blast hole. Besides, after the first blast hole is detonated, a large number of rock units around the second blast hole are destroyed, which is consistent with the actual situation. In the actual project, the explosives and detonators of the second hole may be "squeezed," which will affect the blast effect. When the spacing increases from 35 cm to 40 cm, the peak stress of the wall of the second blast hole is reduced by 36.6%, but when the spacing increases from 40 cm to 45 cm, the peak pressure is only reduced by 2.8%, indicating when the spacing is increased to a certain extent, the decreased amplitude of the pressure of the hole wall will

be reduced. When the distance between the second blast hole and the empty hole is 40 cm, the formed rock fragmentation zone is 88.7 cm in wide and 118.1 cm in high, and the cross-sectional area of the rock fragmentation zone is 6728 cm^2; the cross-sectional area of the rock crushing area formed is the largest. Therefore, the distance between the second blast hole and the empty hole is 40 cm.

3.6. Spacing between the Empty Hole and the Third Blast Hole. According to experimental Scheme 4, after the two first blast holes detonate, the second blast hole detonates for 25 ms and when the third blast hole detonates and lasts 25 ms. The rock damage range is shown in Table 8. The pore wall pressure time history curve at the hole wall is shown in Figure 5.

After the first and second blast holes are detonated, with the increase of the hole spacing, the peak compressive stress of rock units around the third blast hole reaches 190 MPa, 70.5 MPa, and 49.3 MPa, respectively. When the horizontal and vertical distance between the third blast hole and the empty hole changes from 40 cm to 45 cm, the peak compressive stress of the rock around the third blast hole drops by 62.8%, and the rock is broken. At the same time, the cross-sectional area of the rock fragmentation zone is increased by 16.8%. When the horizontal and vertical distance changes from 45 cm to 50 cm, the peak compressive stress of the rock drops by 30.1% after detonation, and the fissures around the holes are more fully developed; however, due to the larger blast hole spacing, the reflected tensile wave is weak, making the third segment of the blast hole unable to completely penetrate after the detonation, and the formation of the rock fragmentation area is not good. Therefore, the horizontal distance between the third blast hole and the empty hole is 45 cm, and the vertical distance is 45 cm.

4. Field Verification Test

4.1. Verification of Blast Hole Layout. The test site is in the middle section 285 of Dahongshan Copper Mine, level 370 m. According to the existing data, the primary rock is marble, and the rock mechanic parameters are close to those used in the numerical simulation. In the test, the charge hole diameter is 5 cm, the hollow hole diameter is 10 cm, and the blast hole depth is 320 cm. The section size of the blast test is 350 cm in wide and 330 cm in high. The cut area is located in the middle of the section, and the position is shown in Figure 1. The explosive used is the No. 1 rock emulsion explosive. According to the actual situation of the site, the charge coefficient is 0.8, and the coupled charge form is adopted. Moreover, the hollow cutting scheme requires three sets of detonators to be delayed at equal intervals of 25 ms. The sequence of initiation is as follows: the first blast holes I-1 and I-2 use two section detonators to detonate; the second blast holes II-1 and II-2 use four section detonators to detonate; the third blast holes III-1, III-2, III-3, and III-4 use six-section detonators to detonate. All the 25 ms equidistant delayed detonators are uniformly detonated by a magnetoelectric detonator.

TABLE 6: Rock failure range under the distance between the first blast hole and the empty hole.
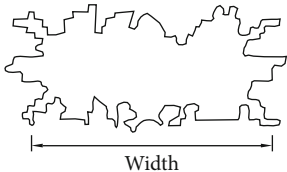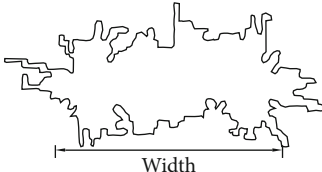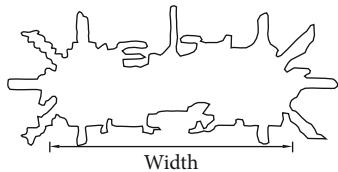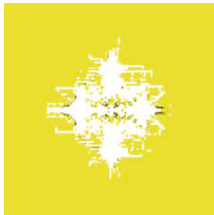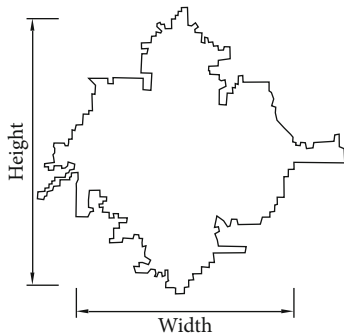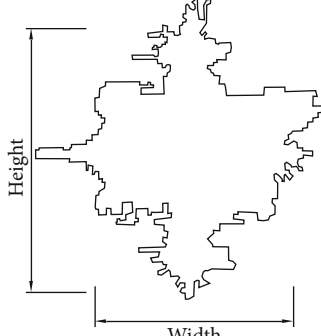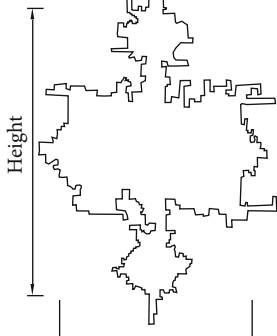
L_1/cm	20	25	30
Simulation result			
Fractured area outline			
Width/cm	70.21	76.61	83.10
Area/cm^2	1651.7	2182.9	2320.5

TABLE 7: Rock failure range at the distance between the second blast hole and the empty hole.

L_2/cm	35	40	45
Simulation result			
Fractured area outline			
Width/cm	87.9	88.7	85.9
Height/cm	107.4	118.1	127.1
Area/cm^2	6194	6728	6009

4.2. Effect and Analysis of Cavity Formation by Blast. After blast, the cavity is formed, as shown in Figure 6. The width and height of the cross-section of the cavity are measured and statistically calculated, as shown in Figure 7; In Figure 8, the area of the cavity is calculated and compared with the simulation results, and the statistics data are shown in Table 9.

The cross-sectional area of the cavity in the field test of the large-diameter hole vertical cutting scheme is 5.3% smaller than that of the simulation results, the width of the cavity in the field test is 3.3% larger than that of the simulation results, and the height of the cavity in the field test is 3.4% smaller than that of the simulation results. It can be seen that the difference between the cavity data obtained

(a) $L_2 = 30$ cm

(b) $L_2 = 40$ cm

(c) $L_2 = 50$ cm
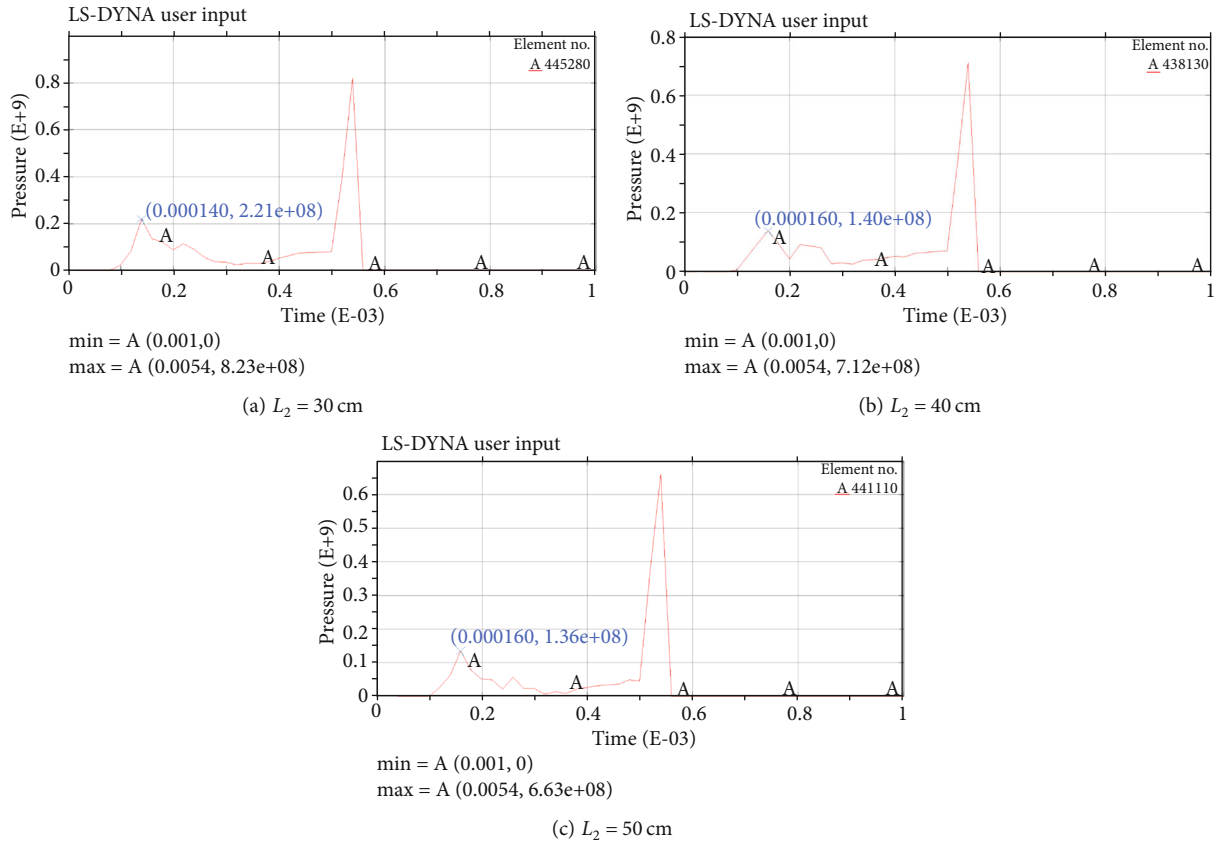
FIGURE 4: Pressure time history curve of hole wall.

TABLE 8: Rock failure range at the distance between the third blast hole and the empty hole.

L_x and L_y/cm	$L_x = L_y = 40$	$L_x = L_y = 45$	$L_x = L_y = 50$
Simulation result			
Fractured area outline			
Width/cm	108	117	125
Height/cm	106	116	129
Area/cm^2	11380	13282	12965
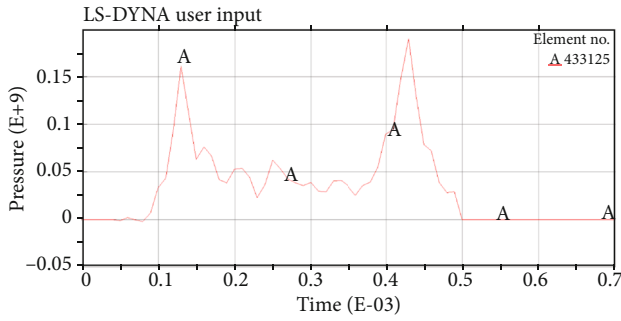
min = A (8e-05, −1.79e+06)
max = A (0.00043, 1.9e+08)

(a) $L_x = L_y = 40$ cm
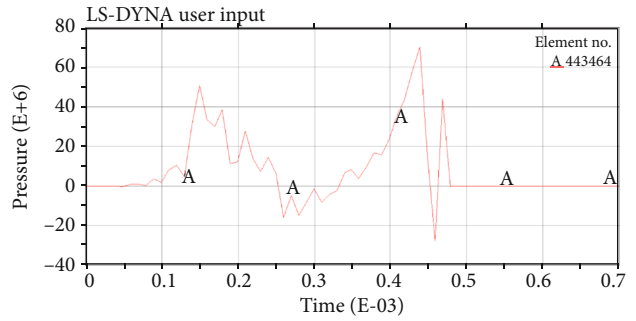
min = A(0.00046, −2.76e+07)
max = A(0.00044, 7.05e+07)

(b) $L_x = L_y = 45$ cm
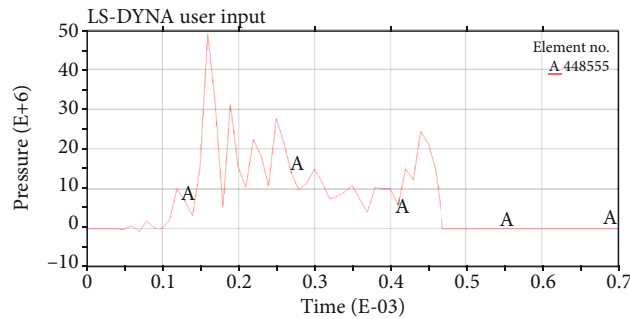
min = A(7e-05, −6.76e+05)
max = A(0.00016, 4.93e+07)

(c) $L_x = L_y = 50$ cm

Figure 5: Pressure time history curve of hole wall.

Figure 6: Blast effect diagram.
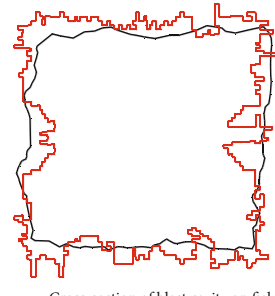
Figure 8: Effect comparison.
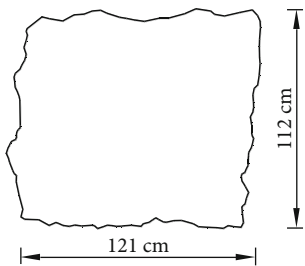
Figure 7: Contour of blast cavity.

Table 9: Blast effect statistic table.

Cutting method	Slot cavity width/cm	Slot cavity height/cm	Slot cavity cross-sectional area/cm^2
Test hollow cut	121	112	12500
Simulated hollow cut	117	116	13200

from the field test and the numerical simulation results is within 6%.

5. Discussion

In this paper, through combining theoretical calculation and numerical simulation, taking the rock fracture area as the evaluation basis, the diameter of the empty hole and the position of the cutting hole are gradually determined, and the reliability of the hole distribution parameters is verified by the field test. However, in this method, the rock is assumed to be completely homogeneous, without considering the influence of joints, cracks, and groundwater in the rock on the blasting effect. At the same time, only the marble lithology is selected to study, and the actual working condition is a composite rock mass dominated by marble; so, there must be some errors in the numerical calculation results. In addition, this study only analyzes the contour section after blasting by two-dimensional model and cannot obtain the influence of the hole depth on the cyclic footage in the cutting blasting. After the field test, only the section size of the cutting cavity is measured, and the cutting blasting effect is verified.

6. Conclusion

In this paper, through theoretical calculation and ANSYS/ LS-DYNA numerical simulation method, the influence of cutting hole arrangement on the size of cavity contour surface after blasting is studied, and the following conclusions are obtained:

(1) The maximum tensile stress will be generated at the wall of the empty hole closest to the center of the charge hole, and the tensile stress of the rock unit at the empty hole wall increases with the increase of the diameter of the empty hole diameter. According to the drilling cost and the actual mine equipment, the empty hole diameter is finally selected as 10 cm

(2) Taking the empty hole with a diameter of 10 cm as the center, two holes 30 cm away from the empty hole are arranged horizontally symmetrically as the first blast, two holes 40 cm away from the empty hole are arranged vertically symmetrically as the second blast, and four holes are arranged squarely as the third blast. The contour area of the cavity after blasting is the largest

(3) The field test shows the errors of the section area, width, and height and numerical simulation results of the cavity are within 6%, indicating that the combination of theoretical calculation and numerical simulation can be used to predict the contour section area after blast of cutting holes in roadway excavation. This numerical simulation method can be further expanded from two-dimensional to three-dimensional to study the cavity formation effect under different cutting modes and selectively carry out field test verification, so as to find a numerical method to predict the cavity formation effect of underground roadway cutting blasting

Data Availability

The data used to support the findings of this study are included in the article.

Conflicts of Interest

The authors declare that they have no conflicts of interest.

Authors' Contributions

Conceptualization, methodology, validation, data curation, visualization, writing—original draft preparation were contributed by J.W. and Z.T. Experimental guidance and data analysis were performed by Q.L. and Z.W. Theoretical analysis was contributed by X.L. and H.W. Formal analysis writing—review and editing was contributed by all authors. All authors have read and agreed to the published version of the manuscript. Qiang Li is the co-first author.

References

[1] P. Q. Lu, G. S. Li, Z. W. Huang, S. C. Tian, Z. H. Shen, and X. J. Li, "Numerical simulation for stress disturbance features of coal beds during pulsating hydro-fracturing," *Journal of Shock and Vibration*, vol. 34, no. 21, pp. 210–216, 2015.

[2] J. Yang, H. Lian, and L. Li, "Fracturing in coals with different fluids: an experimental comparison between water, liquid CO_2, and supercritical CO_2," *Scientific Reports*, vol. 10, no. 1, 2020.

[3] B. B. Zhong, H. Li, and Y. B. Zhang, "Numerical simulation of rock dynamic crack propagation under explosion load," *Explosion and Shock Wave*, vol. 36, no. 6, pp. 825–831, 2016.

[4] Z. R. Zhang, J. J. Zuo, and Y. X. Guo, "Study on the influence mechanism of empty holes and their defects on crack propagation under explosive load," *Journal of Vibration and Shock*, vol. 38, no. 18, pp. 115–121, 2019.

[5] B. Mohanty, "Explosion generated fractures in rock and rock-like materials," *Journal of China university of Mining & Technology*, vol. 35, no. 4-5, pp. 889–898, 1990.

[6] S. H. Cho, Y. Nakamura, B. Mohanty, H. S. Yang, and K. Kaneko, "Numerical study of fracture plane control in laboratory-scale blasting," *Engineering Fracture Mechanics*, vol. 75, no. 13, pp. 3966–3984, 2008.

[7] Z. Y. Lai, "Analysis on blasting effect of parallel cut with empty hole in tunnel construction," *IOP Conference Series: Earth and Environmental Science*, vol. 719, no. 3, p. 032002, 2021.

[8] Z. Y. Wu, D. Luo, F. Chen, and W. Huang, "Numerical simulation of empty-hole effect during parallel-hole cutting under different in situ stress conditions," *Advances in Civil Engineering*, vol. 2021, Article ID 8881491, 11 pages, 2021.

[9] G. B. Tian, J. Dai, Y. Wu, X. Xiong, and Z. Chen, "Influence of charge hole spacing on the crack propagation behavior under the effect of empty-hole directional blasting," *Advances in Civil Engineering*, vol. 2020, Article ID 8860816, 10 pages, 2020.

[10] H. C. Li, X. T. Zhang, D. Li et al., "Numerical simulation of the effect of empty hole between adjacent blast holes in the perforation process of blasting," *Journal of Intelligent & Fuzzy Systems*, vol. 37, no. 3, pp. 3137–3148, 2019.

[11] X. B. Zheng, S. J. Qu, L. H. Fan, and Y. Wang, "Numerical simulation study on the process of single spiral hollow straight-eye cutting into cavity," *Rock and Soil Mechanics*, vol. 153, no. 9, pp. 2589–2594, 2008.

[12] Q. Zong, L. P. Yan, and H. B. Wang, "Numerical simulation analysis on explosion stress field of different charge construction," *Advanced Materials Research*, vol. 1270, no. 13, pp. 2612–2616, 2011.

[13] B. Y. Zhu, Y. He, W. Y. Jiao, and Y. Kang, "Numerical simulation of hollow hole effect in straight hole cutting blast," *Mining Research and Development*, vol. 40, no. 2, pp. 58–61, 2020.

[14] Z. W. Yue, Y. Guo, X. Wang, H. B. Yang, and T. X. Han, "Study on the influence of hole shape on directional fracture blast of rock," *Rock and Soil Mechanics*, vol. 37, no. 2, pp. 376–382, 2016.

[15] Q. Zhang, Y. Q. Yang, Y. F. Yuan, X. L. Wang, and D. C. Lin, "Analysis of influencing factors of straight-hole cutting blast effect," *Rock and Soil Mechanics*, vol. 2001, no. 2, pp. 144–147, 2001.

[16] Q. Y. Li, M. Xu, Z. P. Fan, and W. H. Wang, "Rock breaking process simulation and hole effect analysis of straight hole cutting," *Blast*, vol. 28, no. 4, pp. 23–26, 2011.

[17] H. B. Wang, Q. Zong, and Y. C. Zhao, "Numerical simulation analysis and application of vertical shaft large diameter hollow hole straight hole blast stress field," *Chinese Journal of Rock Mechanics and Engineering*, vol. 34, Supplement 1, pp. 3223–3229, 2015.

[18] Z. Liu, X. Ren, X. Lin, H. Lian, L. Yang, and J. Yang, "Effects of confining stresses, pre-crack inclination angles and injection rates: observations from large-scale true triaxial and hydraulic fracturing tests in laboratory," *Rock Mechanics and Rock Engineering*, vol. 53, no. 4, pp. 1991–2000, 2020.

[19] Z. Liu, J. Yang, L. Yang, X. Ren, X. Peng, and H. Lian, "Experimental study on the influencing factors of hydraulic fracture initiation from prefabricated crack tips," *Engineering Fracture Mechanics*, vol. 250, p. 107790, 2021.

[20] S. Y. Xiao, Y. J. Jiang, Z. X. Liu, and L. J. Su, "Research on rock breaking characteristics and energy distribution of hard rock blast under high ground stress," *Journal of Vibration and Shock*, vol. 37, no. 15, pp. 143–149, 2018.

[21] Z. R. Li, X. L. Feng, H. W. Liu, M. Wu, X. D. Cui, and M. W. Liu, "Underground ore parallel center large hole blast trenching technology," *Metal Mine*, vol. 505, no. 7, pp. 78–81, 2018.

[22] J. Ma, X. Li, J. Wang et al., "Numerical simulation on selection of optimal delay time for precise delay blasting," *Shock and Vibration*, vol. 2021, Article ID 4593221, 9 pages, 2021.

[23] P. Li, Y. J. Wang, and B. Ke, "Theoretical calculation of hole spacing of progressive spiral cutting," *Blast*, vol. 28, no. 4, pp. 20–22, 2011.

[24] B. L. Huang, "Application of large diameter hollow straight hole cutting technology in tunnel rescue," *Blast*, vol. 35, no. 4, pp. 74–77, 2018.

[25] Y. J. Tian, G. L. Guo, J. G. Kang, and J. H. Gang, "Simulation of stone cutting process based on adaptive coupling method," *Journal of System Simulation*, vol. 30, no. 2, pp. 497–505, 2018.

[26] Q. D. Gao, W. B. Lu, Z. D. Leng, Z. W. Yang, P. Yan, and M. Chen, "Optimization of initiation position of cut hole during tunnel excavation," *Journal of Vibration and Shock*, vol. 37, no. 9, pp. 8–16, 2018.

[27] D. Y. Fan, X. S. Liu, Y. L. Tan, S. L. Song, J. G. Ning, and Q. Ma, "Numerical simulation research on response characteristics of surrounding rock for deep super-large section chamber under dynamic and static combined loading condition," *Journal of Central South University*, vol. 27, no. 12, pp. 3544–3566, 2020.

[28] S. Cui, S. Y. Liu, and J. Huang, "The experimental study of directional fracturing and rock breaking under the action of open hole," *Journal of Central South University (Natural Science Edition)*, vol. 52, no. 5, pp. 1570–1580, 2021.

[29] Y. Zhou, D. Zhao, B. Li, H. Y. Wang, Q. Q. Tang, and Z. Z. Zhang, "Fatigue damage mechanism and deformation behaviour of granite under ultrahigh-frequency cyclic loading conditions," *Rock Mechanics and Rock Engineering*, vol. 54, no. 9, pp. 4723–4739, 2021.

[30] Y. G. Zhang and L. Yang, "A novel dynamic predictive method of water inrush from coal floor based on gated recurrent unit model," *Natural Hazards*, vol. 105, no. 2, pp. 2027–2043, 2020.

[31] R. Kumar, P. K. Mandal, A. Narayan, and A. J. Das, "Evaluation of load transfer mechanism under axial loads in a novel coupler of dual height rock bolts," *International Journal of Mining Science and Technology*, vol. 31, no. 2, pp. 225–232, 2021.

[32] Y. G. Zhang, Y. L. Xie, Y. Zhang, J. B. Qiu, and S. X. Wu, "The adoption of deep neural network (DNN) to the prediction of soil liquefaction based on shear wave velocity," *Bulletin of Engineering Geology and the Environment*, vol. 80, no. 6, pp. 5053–5060.

[33] X. S. Liu, S. L. Song, Y. L. Tan et al., "Similar simulation study on the deformation and failure of surrounding rock of a large section chamber group under dynamic loading," *International Journal of Mining Science and Technology*, vol. 31, no. 3, pp. 495–505, 2021.

[34] X. S. Liu, D. Fan, Y. Tan et al., "New detecting method on the connecting fractured zone above the coal face and a case study," *Rock Mechanics and Rock Engineering*, vol. 54, no. 8, pp. 4379–4391, 2021.

[35] A. I. Lawal, S. Kwon, O. S. Hammed, and M. A. Idris, "Blast-induced ground vibration prediction in granite quarries: an application of gene expression programming, ANFIS, and sine cosine algorithm optimized ANN," *International Journal of Mining Science and Technology*, vol. 31, no. 2, pp. 265–277, 2021.

[36] X. S. Liu, D. Fan, Y. Tan et al., "Failure evolution and instability mechanism of surrounding rock for close-distance parallel chambers with super-large section in deep coal mines," *International Journal of Geomechanics*, vol. 21, no. 5, p. 04021049, 2021.

[37] Z. D. Leng, Y. Fan, Q. D. Gao, and Y. G. Hu, "Evaluation and optimization of blasting approaches to reducing oversize boulders and toes in open-pit mine," *International Journal of Mining Science and Technology*, vol. 30, no. 3, pp. 373–380, 2020.

[38] I. Vennes, H. Mitri, D. R. Chinnasane, and M. K. Yao, "Large-scale destress blasting for seismicity control in hard rock mines: a case study," *International Journal of Mining Science and Technology*, vol. 30, no. 2, pp. 141–149, 2020.

WILEY | Hindawi

Research Article

Earth Pressure on Retaining Wall with Surface-Inclined Cohesive Fill Based on Principal Stress Rotation

Hengli Wang [iD],[1,2,3] **Zhengsheng Zou** [iD],[1,2,3] **Jian Liu,**[4] **and Xinyu Wang**[1,2,3]

[1]*College of Civil Engineering, Henan Polytechnic University, Jiaozuo, Henan 454003, China*
[2]*International Joint Research Laboratory of Henan Province for Underground Space Development and Disaster Prevention, Jiaozuo, Henan 454003, China*
[3]*Henan Key Laboratory of Underground Engineering and Disaster Prevention, Jiaozuo, Henan 454003, China*
[4]*China Railway 16th Bureau Group Co., Ltd., Chaoyang District, Beijing 100018, China*

Correspondence should be addressed to Zhengsheng Zou; zouzs@hpu.edu.cn

When considering the friction and bonding force between the back of the retaining wall and the horizontal fill behind the wall, the principal stress of the soil element near the vertical back of the retaining wall is no longer vertical and horizontal but deflects to a certain extent. When the surface of the backfill becomes inclined, the principal stress of the soil behind the wall deflects in a more complicated way. In this paper, the cohesion of the soil element in the fill with an inclined surface is assumed, and the formulas for calculating the active and passive earth pressures of the retaining wall with inclined cohesive backfill are derived by rotating the principal stress of the soil element behind the wall. The proposed method is compared with the existing algorithm, and the influences of the inclination and the cohesion of the fill are analyzed. The results show that the proposed method is more universal. Both the active and passive earth pressures increase rapidly with the increase of the inclination of the fill. The active earth pressure and its horizontal component decrease with the increase of the cohesion of the fill, while the passive earth pressure and its horizontal component increase with the increase of the cohesion of the fill.

1. Introduction

The calculation of earth pressure is the precondition of designing a retaining wall, and the calculation results directly affect the rationality of design. Rankine's earth pressure theory and Coulomb's earth pressure theory are classical algorithms for calculating earth pressure, but there are some deviations between their assumptions and practical engineering. According to the actual engineering situation, researchers adopt different methods and ways to revise, supplement, or expand the classical earth pressure theories.

Based on Coulomb's earth pressure theory, Wang established a calculation method for earth pressure of cohesionless backfill retaining wall under uniform overloading by using the horizontal plate element method and through the force balance analysis on the soil element [1]. Later, many researchers established the calculation formula for active

earth pressure of a rigid retaining wall without cohesive backfill based on the assumption of a plane slip surface and considering the arching effect in the backfill of the wall with an improved horizontal plate element method [2–4]. In addition, some researchers adopted the pseudodynamic method and the horizontal plate element method to analyze the soil wedge behind the wall and established the seismic earth pressure calculation method for the rigid retaining wall with cohesionless backfill [5, 6]. Besides, Pain et al. [7] established a calculation method for calculating the passive earth pressure by using a pseudostatic method and considering the arching effect in the fill behind the wall and the friction of the wall-soil interface. In the study of seismic earth pressure, some researchers established the calculation formula of seismic earth pressure for cohesionless backfill considering the amplification effect of soil mass [8–10]. Based on the redistribution principle, Maskar and Madhekar [11] established

the calculation equation of seismic active earth pressure strength of cohesionless soil considering the earthquake action.

In practical engineering, the fill behind the wall is mostly cohesive soil, so some researchers have studied the calculation method of the earth pressure of cohesive fill. For example, Mazindrani and Ganjali [12] established active and passive earth pressure coefficient tables by analyzing the stress circle of inclined cohesive fill and gave an application example. In addition, Gnanapragasam [13] established the calculation formula of active earth pressure distribution of the retaining wall with cohesive fill by analyzing the stress of inclined cohesive fill. Based on the assumption of the plane sliding surface, Shukla et al. [14] established the calculation method of seismic earth pressure of retaining wall with cohesive fill through the force analysis of soil behind the wall. However, these methods ignored the interaction between the retaining wall and the cohesive backfill. Later, Shukla [15] gave the expression of active earth pressure under static and seismic loads, taking into account the interaction of the wall-soil bonding force, but did not consider the effect of the wall-soil friction. Besides, Peng and Zhu [16] took into account the effect of friction and bonding force on the wall-soil interface, analyzed the soil behind the wall by using the horizontal strip method, and derived the calculation formula of the active earth pressure distribution of the cohesive soil according to the mutual equality theorem of shear stress. Irdmoosa and Shahir [17, 18] established the calculation method of earth pressure for the retaining wall with cohesive backfill based on the assumption of principal stress rotation, taking into account the action of soil arch in the backfill and the interaction of friction and bonding force at the wall-soil interface. But these methods can only be used to calculate the earth pressure of the retaining wall with horizontal fill. Based on the limit equilibrium theory, some researchers analyzed the force of soil behind the wall and deduced the calculation method of earth pressure of inclined cohesive filling by considering the interaction of friction and bonding force at the wall-soil interface [19–21], and Vahedifard et al. [22] established the calculation method of active earth pressure of inclined cohesive soil under the condition of unsaturated steady flow based on the effective stress analysis of limit equilibrium. It should be noted that the above researchers assumed that the angle between the earth pressure acting on the wall back and the normal of the wall back is the angle of wall-soil friction. The results showed that the interaction between the retaining wall and the backfill behind the wall is not fully considered when the direction of earth pressure is limited [23].

The existence of the friction and bonding force between the back of the retaining wall and the backfill makes the principal stress in the soil near the vertical back of the retaining wall no longer in the vertical and horizontal directions, but in a certain degree of deflection. When the surface of the backfill becomes inclined, the deflection of principal stress is more complicated. In view of the deflection of the principal stress of the soil behind the wall, Lancellota [24] established the calculation method of active and passive

earth pressure of retaining wall with the horizontal surface of the cohesionless fill behind the wall based on the plastic lower bound theorem and considering the effect of the wall-soil friction by adopting the principal stress rotation method. Later, some researchers further considered the influence of inclined fill and adopted the principal stress rotation method to establish the calculation formula of seismic earth pressure of the retaining wall with cohesionless fill [25, 26]. Wang et al. [27] adopted the principal stress rotation method to derive the calculation method of active and passive earth pressures of the retaining wall with vertical back and horizontal surface of cohesive fill. However, the results of applying the principal stress rotation method to the inclined surface of cohesive fill have not been reported.

In this paper, the retaining wall of semi-infinite cohesive fill with an inclined surface is studied, and the effects of wall-soil friction and wall-soil bonding force are considered. Based on the principal stress rotation method, the calculation formulas of active and passive earth pressure of the retaining wall with inclined cohesive fill are derived, and the effects of the surface inclination of the fill and the cohesion of the fill on the earth pressure are analyzed.

2. Calculation of Passive Earth Pressure

For the infinite soil with an inclined surface, the vertical self-weight stress of the soil is the same at any same depth below the inclined surface of the fill. The angle between the inclined surface and the horizontal plane of the backfill is set as $\beta \, (\beta < \varphi)$, and the soil strip with unit width is taken for research (Figure 1); then, the earth pressure strength on the inclined plane bc is obtained [28]:

$$\sigma = \gamma z \cos \beta. \tag{1}$$

The normal and tangential strengths on the bc plane are as follows:

$$
\begin{aligned}
\sigma_{zz} &= \gamma z \cos^2 \beta, \\
\tau_{zz} &= \gamma z \cos \beta \sin \beta.
\end{aligned}
\tag{2}
$$

For the soil element on the back of the retaining wall, based on the bonding force and friction of the wall-soil interface, its shear strength can be obtained [28]:

$$\tau = c_w + \sigma_{xx} \tan \delta, \tag{3}$$

where c_w is the bonding force of the wall-soil interface, σ_{xx} is the normal stress of inclined backfill element, and δ is the angle of the wall-soil friction.

For the passive retaining wall, the soil behind the wall will be in two different stress states due to the influence of the friction and bonding force at the wall-soil interface and the inclined filling behind the wall, as shown in Figure 2. The soil element in region b far from the wall is affected by the gravity stress of the inclined fill, and the direction of the principal stress deflects relative to the vertical and horizontal directions. The principal stress of the soil element in
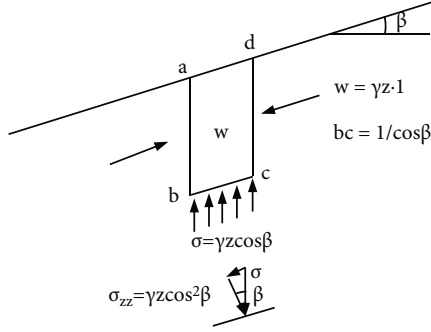
FIGURE 1: The stress vector on the plane parallel to the inclined surface.
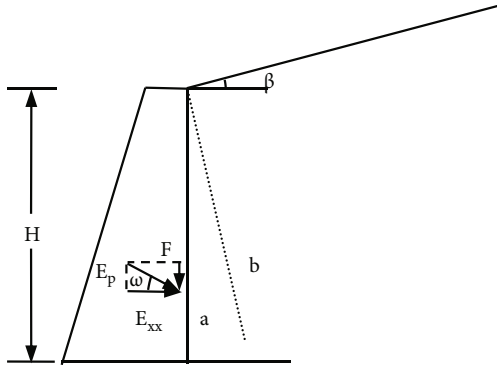
FIGURE 2: Retaining wall under passive limit state.

region a behind the wall deflects to a certain extent due to the friction and bonding force of the wall-soil interface. This results in a jump in the direction and magnitude of the principal stress at the interface between the two stress states of regions a and b. The variation of the stress magnitude and direction on the interface is analyzed, and the method of stress rotation is adopted.

The stress circles of soil in regions a and b behind the passive retaining wall are drawn in Figure 3. In order to facilitate analysis, the τ axis of the stress circle diagram of clay is shifted l ($l = c \cot \varphi$) to the left, which obtains a new coordinate system with the coordinate origin of (0, 0), as shown in Figure 3, where $s' = s + l, \sigma'_{xx} = \sigma_{xx} + l$. The abscissa of the center of stress circle 2 of the soil behind the wall is s'_2. The rotation of the principal stress direction is assumed to be a finite value θ, and stress circle 1 of the soil on the back of the wall is obtained, and the abscissa of the center of stress circle 1 is s'_1. The following relationship between the abscissa of the two stress centers is as follows:

$$\frac{s'_1}{s'_2} = e^{2\theta \tan \varphi}. \tag{4}$$

Terzaghi [28] studied the cohesive fill with an inclined surface and neglected the effect of cohesion on the soil element in the process of stress analysis of the soil element of inclined fill. In order to take into account the effect of the cohesion, the inclination of the fill behind the wall is β,

and it is assumed that the cohesion between soil elements is as follows:

$$c_m = c \cdot \frac{\tan \beta}{\tan \varphi}. \tag{5}$$

According to stress circle 2 after the deflection of the principal stress rotation caused by the filling with an inclined surface (Figure 3), the following geometric relations can be obtained:

$$O'H_2 = s'_2 \cos \beta,$$
$$H_2 M = \sqrt{r_2^2 - R_2 H_2^2} = s'_2 \sqrt{\sin^2 \varphi - \sin^2 \beta}, \tag{6}$$
$$O'M = O'H_2 - H_2 M.$$

The principal stress of the soil element of the cohesive fill due to an inclined surface is as follows:

$$OM = \gamma z \cos \beta,$$
$$\sigma'_{zz} = \gamma z \cos^2 \beta + c \cot \varphi. \tag{7}$$

The following equation can be obtained through geometric analysis:

$$O'M = \frac{\sigma'_{zz}}{\cos \beta} = s'_2 \left(\cos \beta - \sqrt{\sin^2 \varphi - \sin^2 \beta} \right). \tag{8}$$

According to stress circle 1 (Figure 3) after deflection of the principal stress direction caused by friction and bonding force between the wall and the backfill, the following geometric relations can be obtained:

$$O'C_1 = O'H_1 = s'_1 \cos \delta,$$
$$C_1 T = H_1 A = \sqrt{r_1^2 - H_1 R_1^2} = s'_1 \sqrt{\sin^2 \varphi - \sin^2 \delta},$$
$$O'T = O'C_1 + C_1 T = s'_1 \left(\cos \delta + \sqrt{\sin^2 \varphi - \sin^2 \delta} \right), \tag{9}$$
$$\sigma'_{xx} = O'T \cos \delta.$$

The following equation can be obtained through geometric analysis:

$$\sigma'_{xx} = s'_1 \cos \delta \left(\cos \delta + \sqrt{\sin^2 \varphi - \sin^2 \delta} \right), \tag{10}$$

where δ is the friction angle between the wall back and the fill.

(a)   (b)
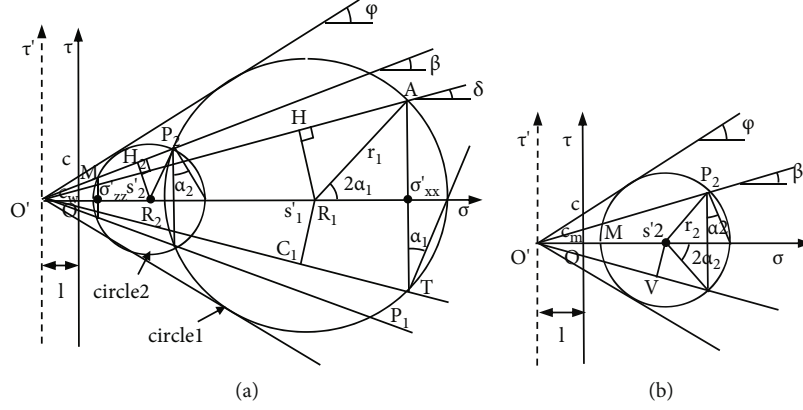
FIGURE 3: The passive earth pressure stress circle.

The formula is further deformed to

$$
\begin{aligned}
\sigma'_{xx} &= \frac{s'_1}{s'_2} \frac{\cos \delta \left(\cos \delta + \sqrt{\sin^2\varphi - \sin^2\delta} \right)}{\cos \beta - \sqrt{\sin^2\varphi - \sin^2\beta}} \cdot \frac{\left(\gamma z \cos^2\beta + c \cot \varphi \right)}{\cos \beta} \\
&= \frac{\cos \delta \left(\cos \delta + \sqrt{\sin^2\varphi - \sin^2\delta} \right)}{\cos \beta \left(\cos \beta - \sqrt{\sin^2\varphi - \sin^2\beta} \right)} e^{2\theta \tan \varphi} \cdot \left(\gamma z \cos^2\beta + c \cot \varphi \right).
\end{aligned}
\tag{11}
$$

The horizontal component of the passive earth pressure strength is as follows:

$$
\begin{aligned}
\sigma_{xx} &= \sigma'_{xx} - l = \frac{\cos \delta \left(\cos \delta + \sqrt{\sin^2\varphi - \sin^2\delta} \right)}{\cos \beta \left(\cos \beta - \sqrt{\sin^2\varphi - \sin^2\beta} \right)} e^{2\theta_p \tan \varphi} \\
&\quad \cdot \left(\gamma z \cos^2\beta + c \cot \varphi \right) - c \cot \varphi = K_{p1x} \gamma z \\
&\quad + K_{p2x} c \cot \varphi - c \cot \varphi,
\end{aligned}
\tag{12}
$$

where

$$
K_{p1x} = \frac{\cos \delta \cos \beta \left(\cos \delta + \sqrt{\sin^2\varphi - \sin^2\delta} \right)}{\cos \beta - \sqrt{\sin^2\varphi - \sin^2\beta}} e^{2\theta_p \tan \varphi},
$$

$$
K_{p2x} = \frac{\cos \delta \left(\cos \delta + \sqrt{\sin^2\varphi - \sin^2\delta} \right)}{\cos \beta \left(\cos \beta - \sqrt{\sin^2\varphi - \sin^2\beta} \right)} e^{2\theta_p \tan \varphi}.
\tag{13}
$$

The vertical component of the passive earth pressure strength is as follows:

$$
\begin{aligned}
\tau &= O'T \sin \delta = \frac{s'_1}{s'_2} \frac{\sin \delta \left(\cos \delta + \sqrt{\sin^2\varphi - \sin^2\delta} \right)}{\cos \beta \left(\cos \beta - \sqrt{\sin^2\varphi - \sin^2\beta} \right)} \cdot \left(\gamma z \cos^2\beta + c \cot \varphi \right) \\
&= \frac{\sin \delta \left(\cos \delta + \sqrt{\sin^2\varphi - \sin^2\delta} \right)}{\cos \beta \left(\cos \beta - \sqrt{\sin^2\varphi - \sin^2\beta} \right)} e^{2\theta_p \tan \varphi} \cdot \left(\gamma z \cos^2\beta + c \cot \varphi \right) \\
&= K_{p1y} \gamma z + K_{p2y} c \cot \varphi,
\end{aligned}
\tag{14}
$$

where

$$
K_{p1y} = \frac{\sin \delta \cos \beta \left(\cos \delta + \sqrt{\sin^2\varphi - \sin^2\delta} \right)}{\cos \beta - \sqrt{\sin^2\varphi - \sin^2\beta}} e^{2\theta_p \tan \varphi},
$$

$$
K_{p2y} = \frac{\sin \delta \left(\cos \delta + \sqrt{\sin^2\varphi - \sin^2\delta} \right)}{\cos \beta \left(\cos \beta - \sqrt{\sin^2\varphi - \sin^2\beta} \right)} e^{2\theta_p \tan \varphi}.
\tag{15}
$$

The passive earth pressure strength is as follows:

$$
\sigma_p = \sqrt{\sigma_{xx}^2 + \tau^2}.
\tag{16}
$$

The vertical component of passive earth pressure is as follows:

$$
F = \int_0^H \tau dz = \frac{1}{2} \gamma H^2 K_{p1y} + K_{p2y} c H \cot \varphi.
\tag{17}
$$

The horizontal component of passive earth pressure is as follows:

$$
E_{xx} = \int_0^H \sigma_{xx} dz = \frac{1}{2} \gamma H^2 K_{p1x} + K_{p2x} c H \cot \varphi - c H \cot \varphi.
\tag{18}
$$

The passive earth pressure is as follows:

$$
E_p = \sqrt{E_{xx}^2 + F^2}.
\tag{19}
$$

The included angle between the action direction of passive earth pressure and the normal of wall back is as follows:

$$
\omega_p = \arctan \frac{F}{E_{xx}}.
\tag{20}
$$

From circle 1 in Figure 3, the following equations are obtained:

$$H_1 R_1 = O'R_1 \sin \delta = \frac{r_1}{\sin \varphi} \sin \delta,$$

$$\sin (2\alpha_1 - \delta) = \frac{\sin \delta}{\sin \varphi}. \tag{21}$$

From circle 2 in Figure 3, the following equations are obtained:

$$H_2 R_2 = O'R_2 \sin \beta = \frac{r_2}{\sin \varphi} \sin \beta,$$

$$\sin (2\alpha_2 - \beta) = \frac{\sin \beta}{\sin \varphi}. \tag{22}$$

It can be seen from Figure 3 that

$$2\theta_p = 2(\alpha_1 + \alpha_2) = \arcsin \left(\frac{\sin \delta}{\sin \varphi} \right) + \arcsin \left(\frac{\sin \beta}{\sin \varphi} \right) + \delta + \beta, \tag{23}$$

where α_1 is the deflection angle of the principal stress of the cohesive soil element caused by the friction and bonding force between the retaining wall and the backfill and α_2 is the deflection angle of principal stress of the cohesive soil element caused by the inclined surface of the cohesive backfill behind the wall.

According to Figure 3, the relationship between the bonding force of the wall-soil interface (c_w), the friction angle of the wall-soil interface (δ), the cohesion of the fill (c), and the internal friction angle of the fill (φ) are as follows:

$$c_w = c \cdot \frac{\tan \delta}{\tan \varphi}. \tag{24}$$

If the fill behind the wall is cohesionless soil ($c = 0$), then Equation (12) degenerates into the following equation:

$$\sigma_{xx} = K_p \gamma z, \tag{25}$$

where

$$K_p = \frac{\cos \delta \cos \beta \left(\cos \delta + \sqrt{\sin^2 \varphi - \sin^2 \delta} \right)}{\cos \beta - \sqrt{\sin^2 \varphi - \sin^2 \beta}} e^{2\theta_p \tan \varphi}. \tag{26}$$

It is completely consistent with Lancellota's passive earth pressure formula for the retaining wall with inclined cohesionless fill [29].

If the back of the wall is smooth ($\delta = 0$) and the backfill level ($\beta = 0$), then $\theta_p = 0$, $c_w = 0$, and Equation (19) degenerates into the following equation:

$E_p = 1/2\gamma H^2 K_p + 2cH \sqrt{K_p}$,

where

$$K_p = \frac{1 + \sin \varphi}{1 - \sin \varphi} = \tan^2 \left(45° + \frac{\varphi}{2} \right). \tag{27}$$

This means that for the retaining wall with horizontal backfill, the calculation formula of passive earth pressure in this paper is the same as the formula of Rankine passive earth pressure if the friction and bonding force of the wall-soil interface are not considered.

3. Calculation of Active Earth Pressure

For the retaining wall in an active state (Figure 4), the stress state of the soil behind the wall also has a jump. Taking the soil element at the back of the wall and behind the wall for analysis, the molar stress circles of the soil at the back of the active retaining wall and behind the wall are shown in Figure 5. The τ axis is shifted l ($l = c \cot \varphi$) to the left by the same method, where the stress circle 1 is the stress circle of the soil element behind the wall, and the abscissa of the center of the stress circle is s_1', while the direction of principal stress is deflected due to the inclination of the fill. Stress circle 2 is the stress circle of the soil on the back of the wall, and the abscissa of the center of the stress circle is s'_2, while the direction of principal stress is deflected due to the friction and bonding force of the wall-soil interface.

Similarly, there is the following relationship between the abscissas of the two stress centers:

$$\frac{s_1'}{s_2'} = e^{2\theta \tan \varphi}. \tag{28}$$

When the inclination of the filling surface behind the wall is β, the cohesion between soil elements is assumed to be as follows:

$$c_m = c \cdot \frac{\tan \beta}{\tan \varphi}. \tag{29}$$

Stress circle 1 (Figure 5) after the deflection of the principal stress is caused by the filling with an inclined surface; the following geometric relations can be obtained:

$$O'M = O'H_1 + H_1 M,$$

$$O'H_1 = s_1' \cos \beta, \tag{30}$$

$$H_1 M = \sqrt{r_1^2 - H_1 R_1^2} = s_1' \sqrt{\sin^2 \varphi - \sin^2 \beta}.$$

The principal stress of soil element of the cohesive fill due to inclined surface is as follows:

$$OM = \gamma z \cos \beta,$$

$$\sigma'_{zz} = \gamma z \cos^2 \beta + c \cot \varphi. \tag{31}$$

The following equation can be obtained through geometric analysis

$$O'M = \frac{\sigma'_{zz}}{\cos \beta} = s_1' \left(\cos \beta + \sqrt{\sin^2 \varphi - \sin^2 \beta} \right). \tag{32}$$
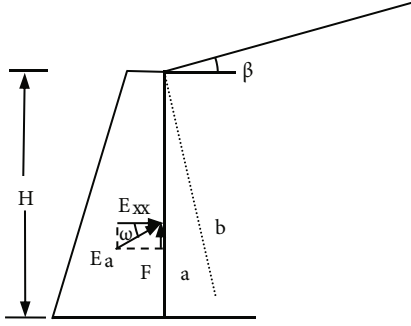
FIGURE 4: Retaining wall under active limit state.

According to stress circle 2 (Figure 5) after deflection of the principal stress direction caused by friction and bonding force between the wall and the fill, the following geometric relations can be obtained:

$$
\begin{aligned}
O'H_2 &= s_2' \cos \delta, \\
H_2 A &= \sqrt{r_2^2 - H_2 R_2^2} = s_2' \sqrt{\sin^2 \varphi - \sin^2 \delta}, \\
O'A &= O'H_2 - H_2 A = s_2' \left(\cos \delta - \sqrt{\sin^2 \varphi - \sin^2 \delta} \right), \\
\sigma_{xx}' &= O'A \cos \delta.
\end{aligned}
\tag{33}
$$

The following equation can be obtained through geometric analysis:

$$
\sigma_{xx}' = s_2' \cos \delta \left(\cos \delta - \sqrt{\sin^2 \varphi - \sin^2 \delta} \right). \tag{34}
$$

The formula is further deformed to

$$
\begin{aligned}
\sigma_{xx}' &= \frac{s_2'}{s_1'} \frac{\cos \delta \left(\cos \delta - \sqrt{\sin^2 \varphi - \sin^2 \delta} \right)}{\cos \beta + \sqrt{\sin^2 \varphi - \sin^2 \beta}} \cdot \frac{\left(\gamma z \cos^2 \beta + c \cot \varphi \right)}{\cos \beta} \\
&= \frac{\cos \delta \left(\cos \delta - \sqrt{\sin^2 \varphi - \sin^2 \delta} \right)}{\cos \beta \left(\cos \beta + \sqrt{\sin^2 \varphi - \sin^2 \beta} \right)} e^{-2\theta \tan \varphi} \cdot \left(\gamma z \cos^2 \beta + c \cot \varphi \right).
\end{aligned}
\tag{35}
$$

The horizontal component of the active earth pressure strength is as follows:

$$
\begin{aligned}
\sigma_{xx} &= \sigma_{xx}' - l = \frac{\cos \delta \left(\cos \delta - \sqrt{\sin^2 \varphi - \sin^2 \delta} \right)}{\cos \beta \left(\cos \beta + \sqrt{\sin^2 \varphi - \sin^2 \beta} \right)} e^{-2\theta_a \tan \varphi} \\
&\quad \cdot \left(\gamma z \cos^2 \beta + c \cot \varphi \right) - c \cot \varphi = K_{a1x} \gamma z \\
&\quad + K_{a2x} c \cot \varphi - c \cot \varphi,
\end{aligned}
\tag{36}
$$

where

$$
\begin{aligned}
K_{a1x} &= \frac{\cos \delta \cos \beta \left(\cos \delta - \sqrt{\sin^2 \varphi - \sin^2 \delta} \right)}{\cos \beta + \sqrt{\sin^2 \varphi - \sin^2 \beta}} e^{-2\theta_a \tan \varphi}, \\
K_{a1x} &= \frac{\cos \delta \left(\cos \delta - \sqrt{\sin^2 \varphi - \sin^2 \delta} \right)}{\cos \beta \left(\cos \beta + \sqrt{\sin^2 \varphi - \sin^2 \beta} \right)} e^{-2\theta_a \tan \varphi}.
\end{aligned}
\tag{37}
$$

The vertical component of the active earth pressure strength is as follows:

$$
\begin{aligned}
\tau &= O'A \sin \delta = \frac{s_2'}{s_1'} \frac{\sin \delta \left(\cos \delta - \sqrt{\sin^2 \varphi - \sin^2 \delta} \right)}{\cos \beta + \sqrt{\sin^2 \varphi - \sin^2 \beta}} \\
&\quad \cdot \frac{\left(\gamma z \cos^2 \beta + c \cot \varphi \right)}{\cos \beta} \\
&= \frac{\sin \delta \left(\cos \delta - \sqrt{\sin^2 \varphi - \sin^2 \delta} \right)}{\cos \beta \left(\cos \beta + \sqrt{\sin^2 \varphi - \sin^2 \beta} \right)} e^{-2\theta_a \tan \varphi} \\
&\quad \cdot \left(\gamma z \cos^2 \beta + c \cot \varphi \right) \\
&= K_{a1y} \gamma z + K_{a2y} c \cot \varphi,
\end{aligned}
\tag{38}
$$

where

$$
\begin{aligned}
K_{a1y} &= \frac{\sin \delta \cos \beta \left(\cos \delta - \sqrt{\sin^2 \varphi - \sin^2 \delta} \right)}{\cos \beta + \sqrt{\sin^2 \varphi - \sin^2 \beta}} e^{-2\theta_a \tan \varphi}, \\
K_{a2y} &= \frac{\sin \delta \left(\cos \delta - \sqrt{\sin^2 \varphi - \sin^2 \delta} \right)}{\cos \beta \left(\cos \beta + \sqrt{\sin^2 \varphi - \sin^2 \beta} \right)} e^{-2\theta_a \tan \varphi}.
\end{aligned}
\tag{39}
$$

The strength of the active earth pressure is as follows:

$$
\sigma_a = \sqrt{\sigma_{xx}^2 + \tau^2}. \tag{40}
$$

The depth of the tension crack on the surface of cohesive fill is as follows:

$$
\begin{aligned}
z_0 &= \frac{c \cot \varphi - K_{a2x} c \cot \varphi}{K_{a1x} \gamma}, \\
h &= H - z_0.
\end{aligned}
\tag{41}
$$

The soil within the depth of the cracked soil layer is equivalent to the uniformly distributed load

$$
q = \gamma z_0. \tag{42}
$$

The vertical component of the active earth pressure is as follows:
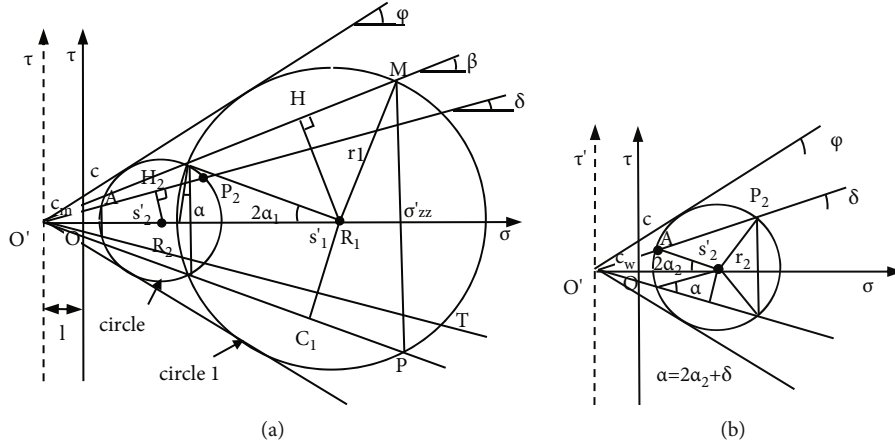
Figure 5: The active earth pressure stress circle.

$$F = \int_0^h \tau dz = K_{a1y} \left[\frac{1}{2} \gamma h^2 + qh \right] + K_{a2y} ch \cot \varphi. \qquad (43)$$

The horizontal component of the active earth pressure is as follows:

$$E_{xx} = \int_0^h \sigma_{xx} dz = K_{a1x} \left[\frac{1}{2} \gamma h^2 + qh \right] + K_{a2x} ch \cot \varphi - ch \cot \varphi. \qquad (44)$$

The active earth pressure is as follows:

$$E_a = \sqrt{E_{xx}^2 + F^2}. \qquad (45)$$

The included angle between the action direction of passive earth pressure and the normal of the wall back is as follows:

$$\omega_a = \arctan \frac{F}{E_{xx}}. \qquad (46)$$

From circle 1 in Figure 5, the following is obtained:

$$H_1 R_1 = O' R_1 \sin \beta = \frac{r_1}{\sin \varphi} \sin \beta ; \qquad (47)$$

therefore,

$$\sin (2\alpha_1 + \beta) = \frac{\sin \beta}{\sin \varphi}. \qquad (48)$$

From circle 2 in Figure 5, the following is obtained:

$$H_2 R_2 = O' R_2 \sin \delta = \frac{r_2}{\sin \varphi} \sin \delta,$$

$$\sin (2\alpha_2 + \delta) = \frac{\sin \delta}{\sin \varphi}. \qquad (49)$$

It can be seen from Figure 5 that

$$2\theta_a = 2(\alpha_2 - \alpha_1) = \arcsin \left(\frac{\sin \delta}{\sin \varphi} \right) - \arcsin \left(\frac{\sin \beta}{\sin \varphi} \right) - \delta + \beta, \qquad (50)$$

where α_1 is the deflection angle of principal stress of the cohesive soil element caused by the inclined surface of the cohesive backfill behind the wall and α_2 is the deflection angle of the principal stress of the cohesive soil element caused by the friction and bonding force between the retaining wall and the backfill.

According to Figure 5, the bonding force of the wall-soil interface can be expressed as

$$c_w = c \cdot \frac{\tan \delta}{\tan \varphi}. \qquad (51)$$

If the back of the wall is smooth ($\delta = 0$) and the backfill level ($\beta = 0$), then $\theta_a = 0$, $c_w = 0$, and Equation (45) degenerates into the following equation:

$$E_a = \frac{1}{2} \gamma H^2 K_a - 2cH \sqrt{K_a} + \frac{2c^2}{\gamma}, \qquad (52)$$

where

$$K_a = \frac{1 - \sin \varphi}{1 + \sin \varphi} = \tan^2 \left(45° - \frac{\varphi}{2} \right). \qquad (53)$$

This means that for the retaining wall with horizontal backfill, the calculation formula of the active earth pressure in this paper is equal to the formula of Rankine active earth pressure without considering the effect of friction and bonding force of the wall-soil interface.

4. Comparative Analysis Based on Examples

Example 1. The height of a retaining wall is 8 m, the back of the wall is vertical, the filling behind the wall is horizontal,
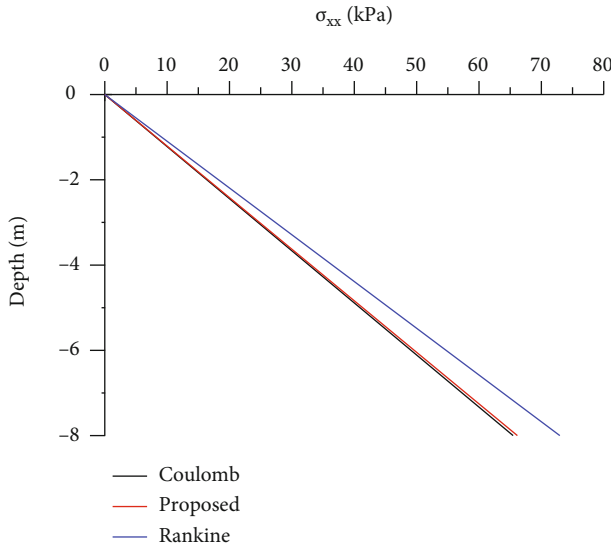
FIGURE 6: Comparison of horizontal components of the active earth pressure.

FIGURE 7: Comparison of horizontal components of the passive earth pressure.

and there is no overload on the surface of the filling behind the wall. The parameters of filling material are $\gamma = 18.6$ kN/m³, $c = 0$ kPa, $\varphi = 20°$, $\delta = 10°$. The calculation results are shown in Figures 6 and 7.

It can be seen from Figures 6 and 7 that the horizontal components of active and passive earth pressures obtained by the proposed method are between the calculation results of Rankine's theory and Coulomb's theory, which are similar to the calculation results of Coulomb's theory considering wall-soil friction. Both the proposed method in this paper and Coulomb's theory consider the effect of wall-soil friction, but these methods are different; thus, the calculation results are different, but the calculation results are in a reasonable range as a whole.

Example 2. The height of a retaining wall is 10 m, the wall back is vertical, and the gravity of filling is 18.6 kN/m³, $\varphi = 25°$, the inclination of the backfill material $\beta = 0°$, take $c = 0, 2, 5, 8, 10, 15, 18, 20, 25$ kPa, the angle of wall-soil friction $\delta = 0.5\varphi$.

Tables 1 and 2 show the earth pressure and its horizontal and vertical components obtained by the proposed method and Rankine's theory. The proposed method in this paper considers the friction and bonding force of the wall-soil interface, so there is also a vertical component along the back of the wall besides the horizontal force acting vertically on the back of the wall. The calculation method of Rankine's theory does not fully consider the interaction between the wall and backfill, and the calculated result is only a horizontal force, which is inconsistent with the actual force of the wall.

For the active earth pressure (Table 1), the results obtained by the proposed method are less than that obtained by Rankine's theory, and the results obtained by both methods decrease with the increase of the cohesion of the
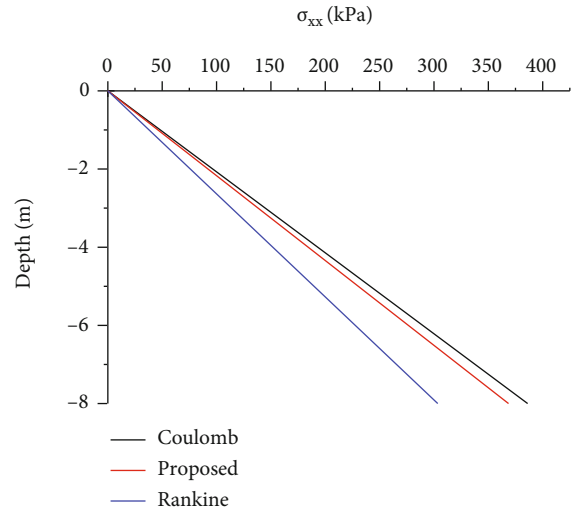
fill. When the cohesion of the fill is small, the horizontal component of the active earth pressure decreases with the increase of the cohesion of the fill, but the reduction speed is relatively slow. The value of the vertical component caused by the friction of the wall-soil interface changes little, while the bonding force of the wall-soil interface increases with the increase of the cohesion of the fill. The vertical component caused by the bonding force of the wall-soil interface increases obviously; the vertical component of active earth pressure increases as a whole. When the cohesion of the fill is large, the reduction rate of the horizontal component of the active earth pressure is accelerated, and the reduction of the vertical component caused by the friction of the wall-soil interface is also increased, while the bonding force of the wall-soil interface increases with the increase of the cohesion of the fill. The vertical component caused by the bonding force of the wall-soil interface is increasing, but the reduction of the vertical component caused by the friction of the wall-soil interface is more significant, while the vertical component of the active earth pressure decreases continuously as a whole. The proportion of the vertical component of the active earth pressure increases with the increase of the cohesion of the fill.

For the passive earth pressure (Table 2), the results obtained by the proposed method are greater than that obtained by Rankine's theory, and the results obtained by both methods increase with the increase of the cohesion of the fill. With the increase of cohesion of fill, the horizontal component of passive earth pressure increases, and the vertical component of earth pressure caused by wall soil interface friction also increases. The bonding force of the wall-soil interface increases with the increase of the cohesion of the fill, and the vertical component caused by the bonding force of the wall-soil interface is also increasing. The horizontal and vertical components of the passive earth pressure increase with the increase of the cohesion of the fill.

The earth pressure acting on the back of the wall is no longer horizontal because of the friction and bonding force

TABLE 1: The horizontal and vertical components of the active earth pressure (kPa).

c (kPa)	Proposed method			Rankine's theory		
	Horizontal component	Vertical component	Resultant force	Horizontal component	Vertical component	Resultant force
0	337.25	74.77	345.44	377.45	0	377.45
2	310.47	77.95	320.10	352.40	0	352.40
5	272.37	81.75	284.37	316.43	0	316.43
8	236.77	84.36	251.34	282.40	0	282.40
10	214.41	85.44	230.81	260.79	0	260.79
15	163.38	85.86	184.57	210.52	0	210.52
18	136.09	84.53	160.21	182.94	0	182.94
20	119.28	82.99	145.31	165.63	0	165.63
25	82.10	76.84	112.45	126.12	0	126.12

TABLE 2: The horizontal and vertical components of the passive earth pressure (kPa).

c (kPa)	Proposed method			Rankine's theory		
	Horizontal component	Vertical component	Resultant force	Horizontal component	Vertical component	Resultant force
0	2996.01	664.20	3068.75	2291.44	0	2291.44
2	3091.29	694.83	3168.42	2354.23	0	2354.23
5	3234.21	740.78	3317.96	2448.41	0	2448.41
8	3377.13	786.73	3467.56	2542.59	0	2542.59
10	3472.41	817.36	3567.31	2605.38	0	2605.38
15	3710.62	893.94	3816.78	2762.34	0	2762.34
18	3853.54	939.89	3966.50	2856.53	0	2856.53
20	3948.82	970.52	4066.33	2919.31	0	2919.31
25	4187.02	1047.10	4315.96	3076.28	0	3076.28

of the wall-soil interface, and the direction of the earth pressure is constantly changing under the influence of wall-soil parameters. The proposed method in this paper considers the interaction between the wall and the backfill. The action direction of the earth pressure is given, which is more consistent with the mechanical principle than Rankine's theory.

5. Influence of Fill Inclination and Cohesion on Earth Pressure

The height of the retaining wall is 10 m, the back of the wall is vertical, and the filling weight is $\gamma = 18.6 \, \text{kN/m}^3$, while the internal friction angle $\varphi = 20°$, $\delta = 0.5\varphi$, $\beta = 0°$, $5°$, $10°$, $15°$, and $c = 0, 5, 10, 15, 20, 25, 30 \, \text{kPa}$. These parameters are taken to analyze the influence of β and c on earth pressure. The results obtained by the proposed method in this paper are shown in Figures 8 and 9.

Figures 8 and 9, respectively, reflect the change of the active and passive earth pressures with c and β. It can be seen that the active earth pressure decreases with the increase of c, but the decreasing rate is gradually slowing down. In addition, the active earth pressure increases with the increase of β, and the increasing rate is gradually accelerated with the increase of β. The passive earth pressure increases with the increase of c and β.

6. Conclusions

Considering the influence of the backfill with inclined surface and the friction and bonding force at the wall-soil interface, the principal stress rotation method is used to deal with the principal stress deflection of the soil element behind the wall, and the calculation formulas of active and passive earth pressure of the retaining wall with cohesive fill are derived. Based on the comparison of the new formula with previous studies and parameter sensitivity analysis, the following conclusions are obtained:

(1) Lancellota's passive earth pressure formula for the retaining wall with inclined cohesionless fill and the formulas of Rankine's active and passive earth pressure are special cases of the proposed method, and the proposed method presented in this paper is more universal

(2) The earth pressure on the back of the wall obtained by the proposed method in this paper includes horizontal and vertical components, while Rankine's theory does not fully consider the interaction between the wall and the backfill, and the result is only the horizontal force. The horizontal components of active and passive earth pressure obtained by the proposed method in this paper are between the calculated results of Rankine's theory and Coulomb's
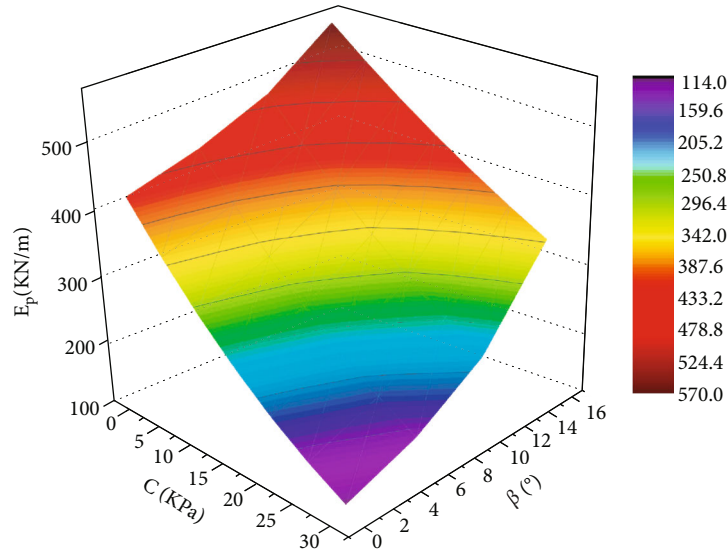
FIGURE 8: Change of active earth pressure with c and β.
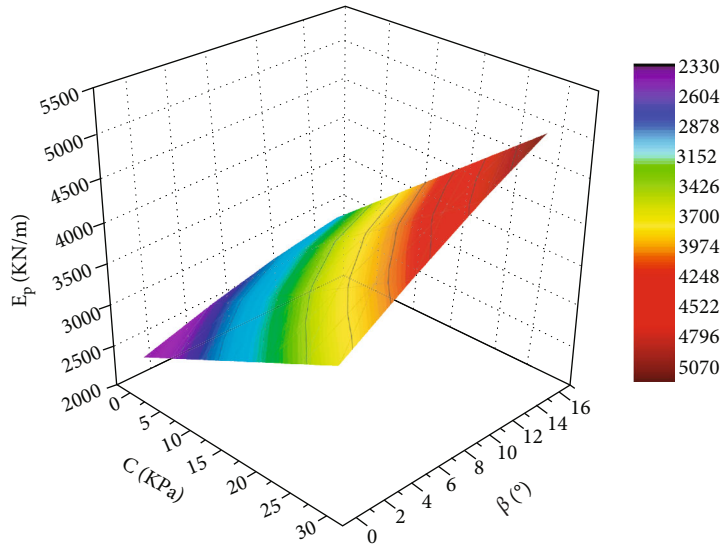
FIGURE 9: Change of passive earth pressure with c and β.

theory, which are similar to the results of Coulomb's theory considering wall-soil friction

(3) The active earth pressure and its horizontal component decrease with the increase of the cohesion of the fill, while the passive earth pressure and its horizontal component increase with the increase of the cohesion of the fill. Both the active and passive earth pressures increase with the increase of the inclination of the fill, and the increasing speed is gradually accelerated

Appendix

In order to study the geometric relationship between the stress centers of regions a and b, the deviation diagram of stress circle centers is drawn (Figure 10). There is a common point X in the two stress circles, and the direction of X acting on the ele-
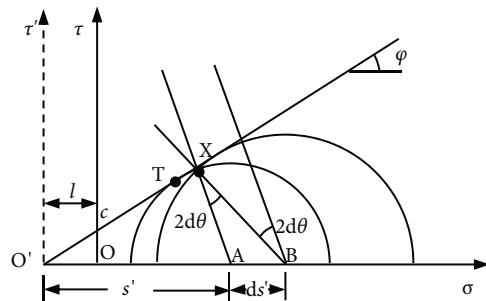
FIGURE 10: Deviation diagram of stress circle centers.

ments corresponding to the stress circles at center A and center B is inconsistent, and there is a deviation angle $d\theta$. In order to make them consistent, the latter is rotated $d\theta$, and the corresponding rotation angle on the stress circle is $2d\theta$.

For the triangle *ABX*, the sine theorem is applied:

$$\frac{BX}{\cos \varphi} = \frac{ds'}{\sin 2d\theta}. \tag{A.1}$$

When $ds' \longrightarrow 0$, the two circles tend to coincide, the common point $X \longrightarrow T$, and there is $\sin \theta \cong \theta$, $BX \cong AX$. The above formula becomes

$$\frac{s' \sin \varphi}{\cos \varphi} = \frac{ds'}{2d\theta}. \tag{A.2}$$

The formula is further deformed to

$$\frac{ds'}{s'} = 2d\theta \tan \varphi. \tag{A.3}$$

Integrating Equation (A.3) according to Figure 3, the following can be obtained:

$$\frac{s_1'}{s_2'} = e^{2\theta \tan \varphi}. \tag{A.4}$$

Equation (4) is proved.

Notations

c_w: Bonding force of wall-soil interface (kPa)
c: Cohesion of the fill (kPa)
φ: Internal friction angle of the fill (°)
δ: Angle of wall-soil friction (°)
β: Inclination of the fill (°)
σ: Earth pressure strength (kPa)
σ_{xx}:   Normal component of earth pressure strength (kPa)
c_m: Cohesion between soil elements of inclined fill (kPa)
σ_{zz}:   Normal stress of inclined fill element (kPa)
τ_{zz}:   Shear stress of inclined fill element (kPa)
E_a: Active earth pressure (kN/m)
E_p: Passive earth pressure (kN/m)
τ: Vertical component of passive earth pressure strength (kPa)
γ: Unit weight of the backfill material (kN/m³)
H: Depth of the backfill (m)
z: Depth of calculation (m)
z_0:   Thickness of upper zone (m)
θ: Rotation angle of principal stress direction (°)
θ_a: Rotation angle of principal stress under active state (°)
θ_p: Rotation angle of principal stress under passive state (°)
ω_a: Angle between the action direction of active earth pressure and the normal of wall back (°)
ω_p: Angle between the action direction of passive earth pressure and the normal of wall back (°).

Data Availability

The data used to support the findings of this study are available from the corresponding author upon request.

Conflicts of Interest

No potential conflict of interest was reported by the authors.

References

[1] Y. Z. Wang, "Distribution of earth pressure on a retaining wall," *Géotechnique*, vol. 50, no. 1, pp. 83–88, 2000.

[2] K. H. Paik and R. Salgado, "Estimation of active earth pressure against rigid retaining walls considering arching effects," *Géotechnique*, vol. 53, no. 7, pp. 643–653, 2003.

[3] M. H. Khosravi, T. Pipatpongsa, and J. Takemura, "Theoretical analysis of earth pressure against rigid retaining walls under translation mode," *Soils and Foundations*, vol. 56, no. 4, pp. 664–675, 2016.

[4] M. H. Khosravi, A. R. Kargar, and M. Amini, "Active earth pressures for non-planar to planar slip surfaces considering soil arching," *International Journal of Geotechnical Engineering*, vol. 14, no. 7, pp. 730–739, 2020.

[5] D. Choudhury and S. Nimbalkar, "Seismic passive resistance by pseudo-dynamic method," *Géotechnique*, vol. 55, no. 9, pp. 699–702, 2005.

[6] S. Ghosh and R. Prasad Sharma, "Seismic active earth pressure on the back of battered retaining wall supporting inclined backfill," *International Journal of Geomechanics*, vol. 12, no. 1, pp. 54–63, 2012.

[7] A. Pain, Q. S. Chen, S. Nimbalkar, and Y. T. Zhou, "Evaluation of seismic passive earth pressure of inclined rigid retaining wall considering soil arching effect," *Soil Dynamics and Earthquake Engineering*, vol. 100, pp. 286–295, 2017.

[8] A. Pain, D. Choudhury, and S. K. Bhattacharyya, "Seismic stability of retaining wall–soil sliding interaction using modified pseudo-dynamic method," *Géotechnique Letters*, vol. 5, no. 1, pp. 56–61, 2015.

[9] V. N. Khatri, "Determination of passive earth pressure with lower bound finite elements limit analysis and modified pseudo-dynamic method," *Geomechanics and Geoengineering*, vol. 14, no. 3, pp. 218–229, 2019.

[10] A. Gupta and V. A. Sawant, "Effect of soil amplification on seismic earth pressure using pseudo-dynamic approach," *International Journal of Geotechnical Engineering*, vol. 15, no. 1, pp. 40–51, 2021.

[11] A. Maskar and S. Madhekar, "Seismic earth pressure computation using modified Dubrova's model," *Journal of GeoEngineering*, vol. 14, no. 2, pp. 53–64, 2019.

[12] Z. H. Mazindrani and M. H. Ganjali, "Lateral earth pressure problem of cohesive backfill with inclined surface," *Journal of Geotechnical and Geoenvironmental Engineering*, vol. 123, no. 2, pp. 110–112, 1997.

[13] N. Gnanapragasam, "Active earth pressure in cohesive soils with an inclined ground surface," *Canadian Geotechnical Journal*, vol. 37, no. 1, pp. 171–177, 2000.

[14] S. K. Shukla, S. K. Gupta, and N. Sivakugan, "Active earth pressure on retaining wall for c-ϕ soil backfill under seismic

loading condition," *Journal of Geotechnical and Geoenvironmental Engineering*, vol. 135, no. 5, pp. 690–696, 2009.

[15] S. K. Shukla, "Dynamic active thrust from _c -ϕ_ soil backfills," *Soil Dynamics and Earthquake Engineering*, vol. 31, no. 3, pp. 526–529, 2011.

[16] J. G. Peng and Y. P. Zhu, "Simplified method for calculating active earth pressure against rigid retaining walls for cohesive backfill," *Soil Mechanics and Foundation Engineering*, vol. 55, no. 6, pp. 374–379, 2019.

[17] K. Ghaffari Irdmoosa and H. Shahir, "Analytical solution for active earth pressure of c-φ soil considering arching effect," *Geomechanics and Geoengineering*, vol. 14, no. 2, pp. 71–84, 2019.

[18] K. G. Irdmoosa and H. Shahir, "Analytical solution for passive earth pressure of c-φ soil using principal stress rotation assumption," *Journal of GeoEngineering*, vol. 14, no. 1, pp. 31–39, 2019.

[19] T. H. Lu, "A formula of active earth pressure including cohesion and adhesion," *Rock and Soil Mechanics*, vol. 23, no. 4, pp. 470–473, 2002.

[20] X. J. Hu, "Improvement on Coulumb accurate solution of active earth pressure to cohesive soil," *Chinese Journal of Geotechnical Engineering*, vol. 28, no. 8, pp. 1049–1052, 2006.

[21] M. X. Peng, "Coulumb's unified solution of active earth pressure on retaining wall," *Rock and Soil Mechanics*, vol. 30, no. 2, pp. 379–386, 2009.

[22] F. Vahedifard, B. A. Leshchinsky, K. Mortezaei, and N. Lu, "Active earth pressures for unsaturated retaining structures," *Journal of Geotechnical and Geoenvironmental Engineering*, vol. 141, article 04015048, no. 11, 2015.

[23] H. L. Wang, *Research on Calculation Method of Earth Pressure of Deep and Large Foundation Pit in Soft Ground*, Henan Polytechnic University, Henan, China, 2021.

[24] R. Lancellotta, "Analytical solution of passive earth pressure," *Géotechnique*, vol. 52, no. 8, pp. 617–619, 2002.

[25] R. Lancellotta, "Lower-bound approach for seismic passive earth resistance," *Géotechnique*, vol. 57, no. 3, pp. 319–321, 2007.

[26] G. Mylonakis, P. Kloukinas, and C. Papantonopoulos, "An alternative to the Mononobe-Okabe equations for seismic earth pressures," *Soil Dynamics and Earthquake Engineering*, vol. 27, no. 10, pp. 957–969, 2007.

[27] H. L. Wang, Z. S. Zou, J. M. Liu, and X. Y. Wang, "The earth pressure of retaining wall with cohesive fill based on principal stress rotation," *Hydrogeology & Engineering Geology*, vol. 48, no. 4, pp. 64–71, 2021.

[28] K. Terzaghi, *Theoretical Soil Mechanics*, John Wiley and Sons, New York, USA, 1943.

[29] R. Lancellotta, *Geotechnical Engineering*, Taylor and Francis, New York, USA, 2009.

WILEY | Hindawi

Research Article
Numerical Calculation of Fracture Seepage in Rough Rock and Analysis of Local Pressure Drop

Gang Chen [ID],[1] **Ling Ma** [ID],[2] **Hongsheng Gong** [ID],[1] **and Fengqiang Luo**[3]

[1]*City College, Kunming University of Science and Technology, Kunming 650051, China*
[2]*Faculty of Land Resources Engineering, Kunming University of Science and Technology, Kunming 650031, China*
[3]*Yunnan Kunrun Geological Exploration Technology Co., Ltd., Kunming 650051, China*

Correspondence should be addressed to Ling Ma; maling@kust.edu.cn

The seepage performance of a rock mass mainly depends on the rock fractures developed in it. Numerical calculation method is a common method to study the permeability properties of fractures. Seepage in rock fractures is affected by various factors such as fracture aperture, roughness, and filling, among which aperture and roughness are the two most widely influenced factors. The Navier-Stokes (NS) equation can be solved directly for the seepage flow in rock fractures with good accuracy, but there are problems of large computational volume and slow solution speed. In this paper, the fracture aperture space data is substituted into the local cubic law as an aperture function to form a numerical calculation method for seepage in rough rock fractures, namely, the aperture function method (AFM). Comparing with the physical seepage experiments of rock fractures, the calculation results of AFM will produce a small amount of error under the low Reynolds number condition, but it can greatly improve the calculation efficiency. The high efficiency of calculation makes it possible to apply AFM to the calculation of large-scale 3D rough fracture network models. The pressure drop of fluid in the fracture has viscous pressure drop (VPD) and local pressure drop (LPD). VPD can be calculated using the AFM. After analyzing the results of solving the NS equation for fracture seepage, it is concluded that the LPD includes the pressure drop caused by area crowding in the recirculation zone (RZ), kinetic energy loss in the RZ, kinetic energy loss in the vortices, and other reasons.

1. Introduction

Rock fractures are widely distributed in subsurface rock masses, and for fluid transport, the permeability of rock fractures is significantly greater than that of the rock matrix [1]. The hydraulic properties of rock fractures play an important role in assessing the performance of subsurface engineering, such as geothermal energy development, enhanced recovery, nuclear waste disposal, and groundwater pollution control [2–6]. Fluid flow in rock fractures can be calculated using the Navier-Stokes (NS) equation. The NS equation is used to solve the fracture flow with high accuracy, but the fracture aperture dimension is much smaller compared to the dimension in the extension direction, which makes the modeling difficult and the calculation workload is large. Zhou et al.

[7] used the NS equation to solve a real rock fracture seepage model with a size of $150 \text{ mm} \times 120 \text{ mm}$, and the number of model elements exceeded 10^6 to ensure the computational accuracy.

Due to the complexity of the NS equation solution, a concise fracture seepage equation, the cubic law, can be derived by neglecting the nonlinear terms in fluid flow. The same conclusion was obtained for the seepage experiments using two smooth flat plates [8]. The natural rock fracture surface is rough, which restricts the flow of fluid in the fracture, and using the cubic law to calculate the fracture flow would overestimate the permeability of the fracture [9, 10]. Through theoretical derivation and experimental research, some scholars proposed that under the condition of low Reynolds number (Re $\ll$ 1), the effect of inertial flow

of fluid can be neglected, and the local cubic law (Reynolds equation) can be used to calculate the fracture seepage flow, and its calculation results do not deviate much [11–14]. Zimmerman and Bodvarsson [12] found by single fracture seepage experiment that when Re is in the range of $1 \sim 10$, there is a weak inertia effect zone within the fluid in the fracture, and the fracture seepage flow gradually deviates from the linear relationship with the hydraulic gradient but becomes a nonlinear relationship. By correcting the geometric mean aperture, arithmetic mean aperture, surface roughness factor, and curvature factor, the local cubic law can still be used to evaluate the fluid flow in the fracture [11, 14, 15]. Zhu et al. [16] concluded by theoretical derivation and experimental study that the cubic law still has good applicability in the laminar flow range (Re ≤ 2300) when the flow of the fracture is long enough.

Javadi et al. [17] and Liu et al. [18] found that there is a deviation between the calculated results of linear and nonlinear flow in the fracture, but the difference is not too big at low Reynolds number conditions. Javadi et al. [17] considered that there are two types of pressure drop during fluid flow in the fracture: one is viscous pressure drop (VPD) due to fluid viscosity; the other is the local pressure drop (LPD) due to the sudden change of aperture. For laminar flow in a smooth flat plate, the VPD can be calculated using the cubic law. For rough fractures, corrections for fracture wall roughness and fracture curvature are required.

In this paper, the aperture function method (AFM) based on the local cubic law is introduced, which utilizes the fracture aperture function as the parameter of the numerical model, where one fracture wall surface is used as the geometric model, and the rough fracture seepage is calculated based on the local cubic law. The results of the AFM calculations are compared with the physical experiments and the results of the numerical model of rough fracture seepage based on the solution of the NS equation. Multiple pressure boundary conditions are applied to the inlet of the fracture models, and the rough fracture seepage flow is solved based on the NS equation, and the formation of the recirculation zone (RZ) in the fracture flow and the reasons for the influence on the seepage flow are analyzed in detail. The rotational motion of fluid flow is called vortex, and the presence of vortices has a significant effect on the motion of the fluid due to the vortices. This paper presents the mathematical definition and identification of vortices in fluids and identifies the vortices and their distribution in rough fracture flows. A comparative analysis of vortices in fracture flow and RZ is carried out, and the effect of vortices on fracture seepage flow is studied.

2. Methodology

2.1. Aperture Function Method (AFM)

2.1.1. Aperture Interpolation Method. Rough rock fracture surface morphology is complex and can be obtained by using high precision laser scanning technology [19–21], and the obtained data can well reflect the real fracture surface morphology. For the obtained fracture surface data, let the fracture surface undulation height be z and use x and y to represent the fracture plane coordinates; then, the fracture surface geometry can be represented by the function $z = g(x, y)$ in the Cartesian coordinate system. The 3D scanned fracture surface is processed to form a list of values that can be expressed by the function $z = g(x, y)$. For subsequent calculations, the x-direction is set to move in the shear direction. The upper fracture surface function is $g_U(x, y)$, and the lower fracture surface function is $g_L(x, y)$. To calculate the aperture between the two fracture walls, the following equation can be used [22–24].

$$e(x, y) = \begin{cases} g_U(x + u_s, y) - g_L(x, y) + u_v & (g_U(x + u_s, y) > g_L(x, y)) \\ 0 & (g_U(x + u_s, y) \leq g_L(x, y)) \end{cases},$$
(1)

where $e(x, y)$ is the upper and lower fracture wall aperture functions, u_s is the shear direction displacement, and u_v is the normal displacement.

When $e(x, y)$ does not correspond exactly to the spatial coordinates (x, y) of $g_U(x, y)$ (or $g_L(x, y)$), it is necessary to use the interpolation method to find the aperture value at the desired spatial location. In Figure 1(a), the $g_{i,j}$ point on the geometric slit surface corresponds to the $e'_{i,j}$ point in the aperture, but there is no aperture value at this point, so the interpolation method is used to obtain the aperture value at the $e'_{i,j}$ point.

The fracture aperture is a function of the spatial coordinates (x, y), so each of the four points can be expressed as $(x_1, y_1, e(x_1, y_1))$, $(x_1, y_2, e(x_2, y_1))$, $(x_2, y_1, e(x_2, y_1))$, and $(x_2, y_2, e(x_2, y_2))$ (Figure 1(b)). If we want to get the aperture value $e(x, y)$ at a certain position in the middle of the four points, we can use linear interpolation to estimate it:

First, interpolate x to find $e(x, y_1)$ and $e(x, y_2)$:

$$\begin{aligned} e(x, y_1) &= e(x_1, y_1) \cdot \frac{x_2 - x}{x_2 - x_1} + e(x_2, y_1) \cdot \frac{x - x_1}{x_2 - x_1}, \\ e(x, y_2) &= e(x_1, y_2) \cdot \frac{x_2 - x}{x_2 - x_1} + e(x_2, y_2) \cdot \frac{x - x_1}{x_2 - x_1}. \end{aligned}$$
(2)

Then, use the same idea to find $e(x, y)$:

$$e(x, y) = e(x_1, y_1) \cdot \frac{y_2 - y}{y_2 - y_1} + e(x, y_2) \cdot \frac{y - y_1}{y_2 - y_1}.$$
(3)

The above equation gives the value of the aperture at any position within the spatial distribution of the aperture. Each point $g_{i,j}(x, y)$ on the fracture wall grid can also be found corresponding to the desired aperture value.

When discretizing the fracture numerical model, each fracture wall grid point corresponds to a tiny geometric grid cell. Each grid cell can find the corresponding fracture aperture data, and within this cell, the aperture value is a given value; then, the geometric grid cell and the aperture value can form a tiny virtual flat flow model. For each tiny virtual flat plate model, the fracture flow calculation can be performed using the cubic law, and the overall view is an
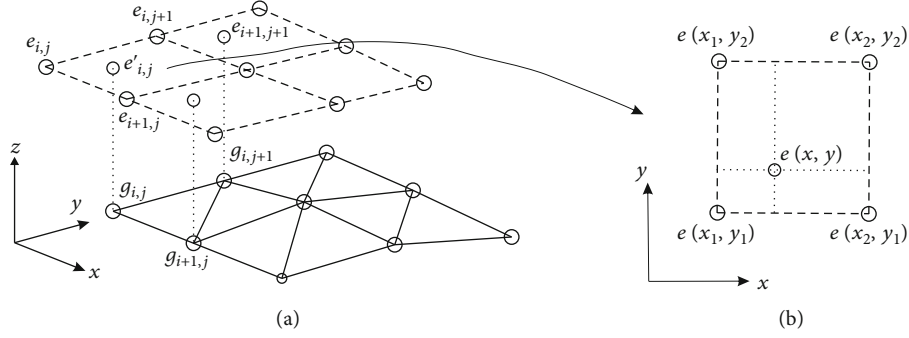
FIGURE 1: Schematic diagram of fracture aperture interpolation method: (a) schematic diagram of the relationship between the grid points of the fracture wall and the grid points of the aperture; (b) solve the value of the aperture at a certain position ($e(x, y)$).

application of the local cubic law. Since the fracture surface and fracture aperture values of each cell are a list of values that vary with space, a rough fracture model with two walls is formed. A triangular grid Figure 2(a) or a rectangular grid Figure 2(b) can be used when the fracture data are discrete.

2.1.2. From the NS to the Local Cubic Law Equations. The fluid flow in the fracture of the rock is very slow, and neglecting the effect of inertial forces, the Navier-Stokes (NS) equation can be derived from the [12, 25, 26] equation for the fracture flow in the laminar flow state, i.e., the Reynolds equation, also called the local cubic law.

The two-dimensional space is expressed as follows:

$$\frac{\partial}{\partial x}\left(\frac{\rho g e^3}{12\mu}\frac{\partial h}{\partial x}\right) + \frac{\partial}{\partial y}\left(\frac{\rho g e^3}{12\mu}\frac{\partial h}{\partial y}\right) = 0. \quad (4)$$

Substituting the aperture function $e(x, y)$ into Equation (4) yields a clearer expression of the equation [27].

$$\frac{\partial}{\partial x}\left(\frac{\rho g e^3(x, y)}{12\mu}\frac{\partial h}{\partial x}\right) + \frac{\partial}{\partial y}\left(\frac{\rho g e^3(x, y)}{12\mu}\frac{\partial h}{\partial y}\right) = 0, \quad (5)$$

where h is the hydraulic head, μ is the dynamic viscosity, ρ is the fluid density, and g is the gravitational acceleration, and $e(x, y)$ is the aperture function. Figure 2 shows the meaning of Equation (5) graphically by dividing the rough fracture surface into a series of connected small parallel plates.

In this paper, the calculation method of using the aperture function to characterize the aperture value and solving the rough fracture flow based on the local cubic law is referred to as the aperture function method (AFM).

2.2. Recirculation Zone in Fracture Seepage Flow. Lee et al. [25], Zhou et al. [28], and Zhou et al. [7] found through physical and numerical experiments that in the steady laminar flow state, the fluid in the fracture will generate a recirculation zone (RZ) when flowing through the abrupt change of aperture. The fluid in the RZ also consumes part of the flow energy, and because the fluid in the RZ occurs back on its own, it does not produce effective flow at the out-

let of the fracture. The size of the RZ is nonlinearly related to the fluid flow rate and the fracture roughness procedure, and its magnitude cannot be calculated using a simple equation. In addition, Lee et al. [29] found experimentally that under specific conditions, fluid can also produce slip phenomenon at the fracture wall, which also affects the overall seepage flow rate of the fracture.

In order to further verify whether a fluid RZ is generated in the fracture model in this paper and to analyze whether the RZ effect is a linear or nonlinear problem, with other geometric and aperture conditions unchanged, a variety of pressure boundary conditions are set, and two methods, NS solution and AFM solution, are used to calculate and compare, respectively, (Table 1). The JRC1 fracture model inlets were applied with pressures ranging from 10 Pa to 6000 Pa ($-dh/dl = 0.01 \sim 5.1$) for a total of 52 submodels. JRC3 fracture model inlets were applied with pressures ranging from 10 Pa to 890 Pa ($-dh/dl = 0.01 \sim 0.76$) for a total of 36 submodels. JRC6 fracture model inlets were applied 25 Pa~650 Pa pressure ($-dh/dl = 0.02 \sim 0.55$), respectively, for a total of 26 sub-models. JRC9 fracture model inlets were applied with 10 Pa~1000 Pa pressure ($-dh/dl = 0.01 \sim 0.85$), respectively, for a total of 34 submodels. The outlet pressure of all fracture models is 0 Pa. The fluid density in the model is 998.2 kg/m^3, and the dynamic viscosity coefficient is 0.0010093 Pa.s. The calculation software was carried out using COMSOL Multiphysics finite element method.

2.3. Identification of Vortices in Seepage Flow. The phenomenon of vortices is prevalent in the fluid flow process. Intuitively, vortices represent the rotational motion of the fluid; that is, where there is fluid rotation, there are vortices, and conversely, where there are vortices, there is fluid rotation [30]. In order to give a quantitative mathematical definition of vortex, a parameter Ω is introduced, representing the ratio of the size of the rotating part of the vortex to the size of the total vortex, calculated as [31]

$$\Omega = \frac{\|B\|_F^2}{\|A\|_F^2 + \|B\|_F^2 + \varepsilon}, \quad (6)$$

(a)   (b)
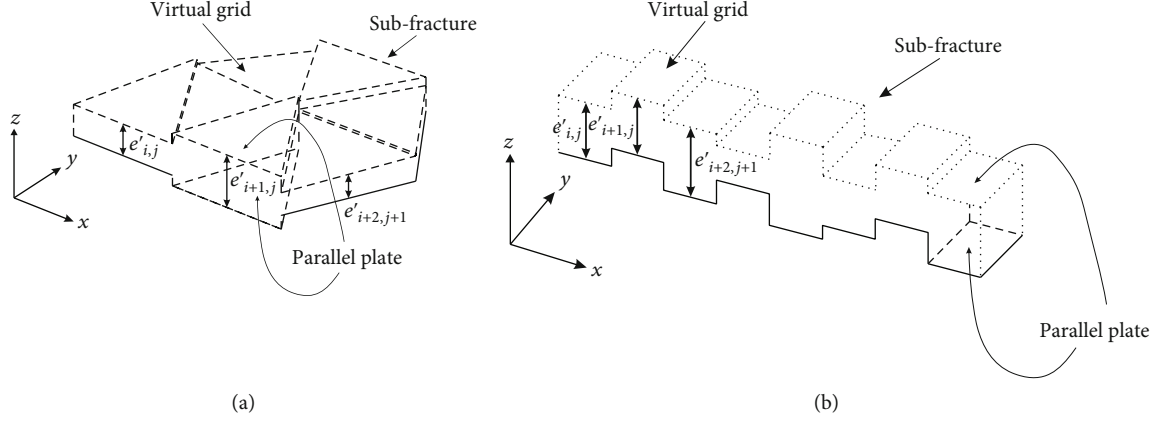
Figure 2: Discretizing the rock fracture to the volumetric elements: (a) triangular discrete grid; (b) quadrilateral discrete grid.

Table 1: Basic information of JRC1, JRC3, JRC6, and JRC9 numerical models.

	Solution	Number of elements	Element number ratio	Mesh size/m	Hydraulic gradients (-dh/dl)	Number of submodels
JRC1	NS	901791	8.76	$3.97 \times 10^{-8} \sim 1.33 \times 10^{-5}$	0.01~5.1	52
	AFM	102930		$3.36 \times 10^{-5} \sim 3.11 \times 10^{-4}$		34
JRC3	NS	743377	4.9	$3.58 \times 10^{-7} \sim 3.1 \times 10^{-5}$	0.01~0.76	36
	AFM	151790		$1.82 \times 10^{-5} \sim 2.78 \times 10^{-4}$		36
JRC6	NS	265772	3.41	$9.83 \times 10^{-7} \sim 8.52 \times 10^{-5}$	0.02~0.55	26
	AFM	77884		$2.54 \times 10^{-5} \sim 3.9 \times 10^{-4}$		26
JRC9	NS	178900	3.3	$1.80 \times 10^{-7} \sim 6.04 \times 10^{-5}$	0.01~0.85	34
	AFM	54202		$7.44 \times 10^{-5} \sim 6.88 \times 10^{-4}$		34

where

$$\|A\|_F^2 = \left(\frac{\partial u}{\partial x}\right)^2 + \left(\frac{\partial v}{\partial y}\right)^2 + \left(\frac{\partial w}{\partial z}\right)^2 + \frac{1}{2}\left(\frac{\partial u}{\partial y}\right)^2 + \frac{1}{2}\left(\frac{\partial u}{\partial z}\right)^2$$
$$+ \frac{1}{2}\left(\frac{\partial v}{\partial x}\right)^2 + \frac{1}{2}\left(\frac{\partial v}{\partial z}\right)^2 + \frac{1}{2}\left(\frac{\partial w}{\partial x}\right)^2 + \frac{1}{2}\left(\frac{\partial w}{\partial y}\right)^2$$
$$+ \frac{\partial u}{\partial y}\frac{\partial v}{\partial x} + \frac{\partial u}{\partial z}\frac{\partial w}{\partial x} + \frac{\partial v}{\partial z}\frac{\partial w}{\partial y},$$

$$\|B\|_F^2 = \frac{1}{2}\left(\frac{\partial u}{\partial y}\right)^2 + \frac{1}{2}\left(\frac{\partial u}{\partial z}\right)^2 + \frac{1}{2}\left(\frac{\partial v}{\partial x}\right)^2$$
$$+ \frac{1}{2}\left(\frac{\partial v}{\partial z}\right)^2 + + \frac{1}{2}\left(\frac{\partial w}{\partial x}\right)^2 + \frac{1}{2}\left(\frac{\partial w}{\partial y}\right)^2 \quad (7)$$
$$- \frac{\partial u}{\partial y}\frac{\partial v}{\partial x} - \frac{\partial u}{\partial z}\frac{\partial w}{\partial x} + \frac{\partial v}{\partial z}\frac{\partial w}{\partial y},$$

where $\| \, \|_F$ represents the Frobenius parametrization of the matrix, A is the symmetric part of the fluid velocity gradient tensor, and B is the antisymmetric tensor (vorticity).

According to its physical meaning, it is obvious that Ω takes values in the range $0 \leq \Omega \leq 1$, which can be interpreted as the concentration of vorticity, and more specifically, Ω represents the rigidity of fluid motion, and when $\Omega = 1$, it represents the fluid doing rigid body rotation. When $\Omega > 0.5$ represents that the antisymmetric tensor B dominates over the symmetric tensor A. Therefore, Ω slightly larger than 0.5 can be used as the criterion for vortex identification. Liu et al. [31] proposes to use $\Omega = 0.52$ to determine the boundary of vortex.

3. Results

3.1. Analysis of AFM Calculation Results. In order to verify the rationality of the AFM, this paper compares the physical experimental results of rough fracture fluid flow completed by Zhu et al. [16, 32]. The typical definition of rock fracture roughness curve (JRC) in rock mechanics was adopted for the experiment, and the 1st, 3rd, 6th, and 9th of these curves were selected and combined with a smooth flat plate to form four fracture models with different roughness, each with a fracture length of 100 mm and a minimum aperture value of 0.51 mm. The four models were numbered as JRC1, JRC3, JRC6, and JRC9, respectively. Multiple experiments were conducted for each artificial fracture sample, and the pressure gradient and flow rate were averaged.

Based on the AFM, the numerical model of the four fractures was completed and calculated using the finite element
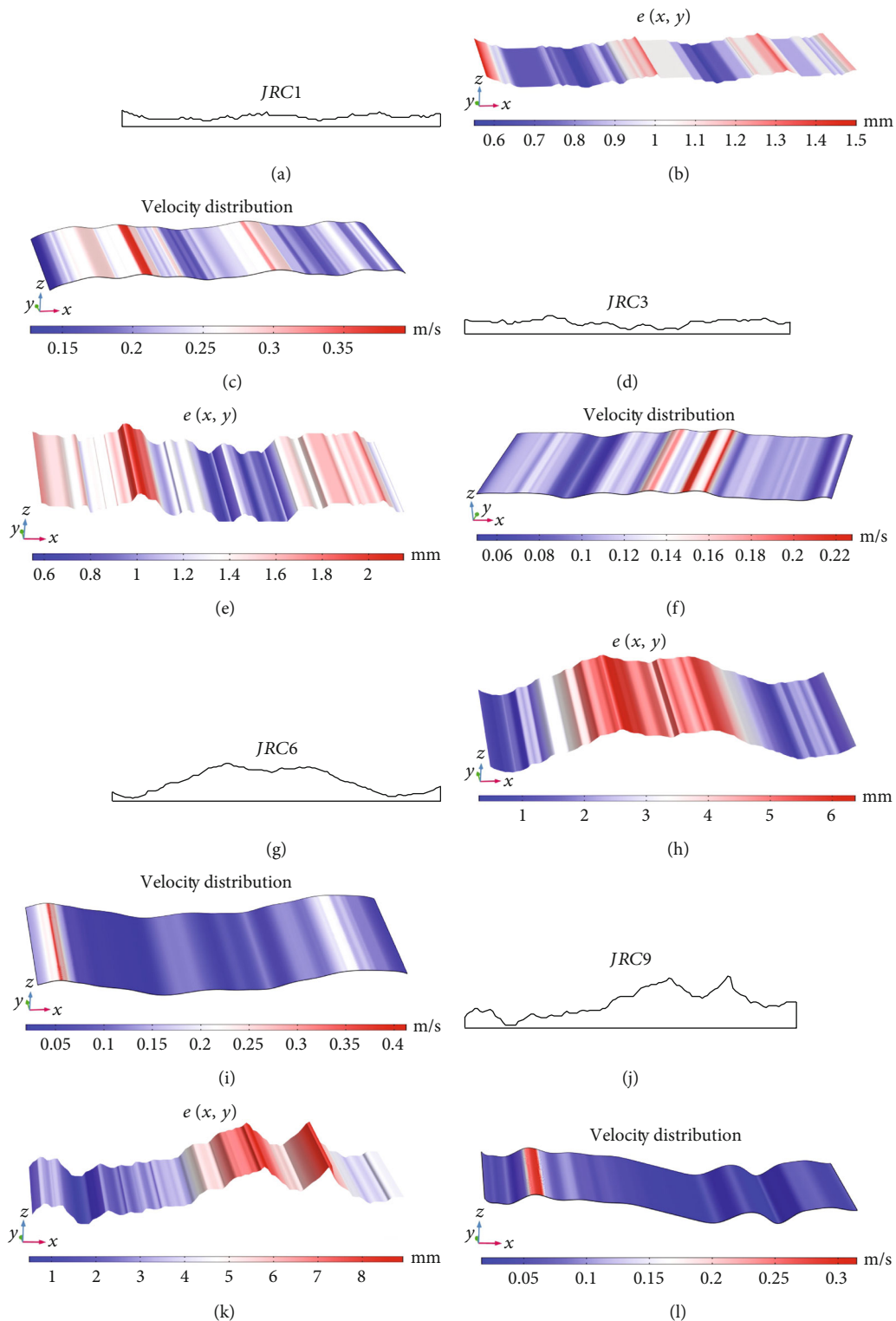
FIGURE 3: (a, d, g, j) 4 fracture curves (stretched properly for display). (b, e, h, k) Spatial distribution of fracture aperture. (c, f, i, l) Each numerical model fracture surface velocity distribution.

numerical calculation software COMSOL Multiphysics. For better display, all the 4 fracture curves are stretched along the direction perpendicular to the hydraulic gradient in the numerical model to form 4 fracture space surfaces.

Figure 3 shows the numerical model, the aperture spatial distribution, and the fracture seepage field. It can be observed from the figure that the seepage capacity of the fracture is very obviously affected by the minimum aperture.

TABLE 2: Comparative analysis of experiment results according to average aperture width and aperture interpolation function.

Specimen no.	P_s/Pa	$q_s/(10^{-3}\,\mathrm{m^2/_s})$	e_p (mm)	q_p (m²/ₛ)	$\varepsilon(q_p)$/%	$q_n/(10^{-3}\,\mathrm{m^2/_s})$	e_n (mm)	$\varepsilon(q_n)$/%
JRC1	486.50	0.165	0.91	0.268	62	0.185	0.773	12
	98.20	0.035	0.91	0.054	55	0.037	0.773	7
JRC3	147.50	0.097	1.35	0.265	174	0.106	0.956	9
	98.20	0.034	1.35	0.088	160	0.035	0.956	4
JRC6	290.20	0.187	3.30	7.623	3977	0.217	0.967	16
	149.00	0.106	3.30	3.914	3593	0.112	0.968	5
JRC9	49.80	0.120	4.37	3.038	2432	0.139	1.499	15
	29.90	0.081	4.37	1.824	2146	0.083	1.499	2

The subscript s represents the actual measurement result of the physical experiment; the subscript p represents the calculation result according to the average aperture and the cube law; the subscript n represents the calculation results of AFM. $\varepsilon(q_p)$ and $\varepsilon(q_n)$ represent the error calculated by the flow rate.

The error values in Table 2 are calculated as

$$\varepsilon = \frac{q_s - q_c}{q_s} \times 100\%, \tag{8}$$

where ε represents the flow error, q_s represents the experimentally measured flow rate per unit width of the fracture, and q_c represents q_p calculated according to the average aperture and the cube law or q_n calculated using the AFM.

Table 2 shows the comparison of different calculation methods with experimental results. It can be seen that the results calculated by the average aperture and the overall cubic law deviate very much from the experimental measured results. When the fracture roughness increases, the error of the overall cubic law calculation results is even larger. The results calculated by the numerical model using the AFM are in good agreement.

3.2. Comparison of the Results of AFM and NS Method.

The results of the flow calculated by the AFM are compared with the results of the NS equation solution. We plotted the flow rate variation curves with hydraulic gradient derived from the two calculation methods and plotted the error curves of the two calculation methods (Figure 4).

The error curve shows that the AFM calculation result overestimates the permeability of the fracture, causing its calculated flow rate to be large, which is consistent with the results of Yeo et al. [9] and Bauget and Fourar's study [10]. The errors of NS and AFM calculations are small at low hydraulic gradient and become larger as the hydraulic gradient gradually increases, which is consistent with the results of Oron and Berkowitz [11] and Zimmerman et al. [13]. The increase of fracture roughness also increases the flow error (the overall error of JRC9 model is the largest). The flow error variation also shows a nonlinear variation pattern, rather than a simple linear increase.

3.3. Recirculation Zone Analysis

3.3.1. Evolution of the Recirculation Zone.

The comparison of the flow results in Table 2 shows that the results calculated by the AFM under the low hydraulic gradient conditions are in good agreement, but there is still a certain degree of error. The theory of fracture seepage calculation used in the AFM is the local cubic law, which makes a linear relationship between flow and pressure drop (corresponding to the hydraulic gradient) because it ignores the effect of fluid inertia forces. In contrast, Javadi et al. [17] considers the pressure drop during the flow of fluid in a fracture as VPD and LPD. VPD is due to fluid viscosity and can be calculated using the cubic law.

LPD is the pressure drop (or energy loss) that occurs when the fluid flows through a part of the fracture where the aperture changes abruptly. When using the local cubic law-based AFM for seepage calculations, the full LPD cannot be calculated, which is the main reason for the deviation of the AFM calculation results. Zhu et al. [16] and Liu et al. [18] also found the phenomenon of LPD in their studies. The RZ in the fracture flow is one of the important reasons for the LPD. When using the NS solution method for fracture seepage calculations, the extent of the RZ can be determined in the fracture model using streamlines. In this paper, we take JRC3 and JRC6 models as examples to discuss the evolution of RZ and the influence of RZs on fracture seepage.

Figures 5(a) and 6(a) are discrete mesh of the JRC3 and JRC6 partial models, respectively. Figures 5(b) and 6(b) is a schematic outline of the two models. Figures 5(c)–5(h) and 6(c)–6(h) show the streamlines in the fracture under the typical hydraulic gradient conditions of JRC3 and JRC6, respectively, which can visualize whether there is a recirculation zone or not. Under the low hydraulic gradient (JRC3, −dh/dl = 0.13; JRC6, −dh/dl = 0.02) conditions, the fluid flow velocity in the fracture seepage field is slow, and the inertial force of the fluid has little influence, and no obvious RZ formation is observed (Figures 5(c) and 6(c)). With the increase of the applied hydraulic gradient, the influence of fluid inertial force gradually increases, and small RZs appear in the region of large changes in the fracture wall (Figures 5(f) and 6(f)), and the range of RZs is small and has little influence on the mainstream zone. The further increase of hydraulic gradient, the influence of fluid inertia force is further revealed, not only to expand the range of RZ but also the emergence of a number of RZs of different sizes, resulting in the narrowing of the mainstream zone, bending
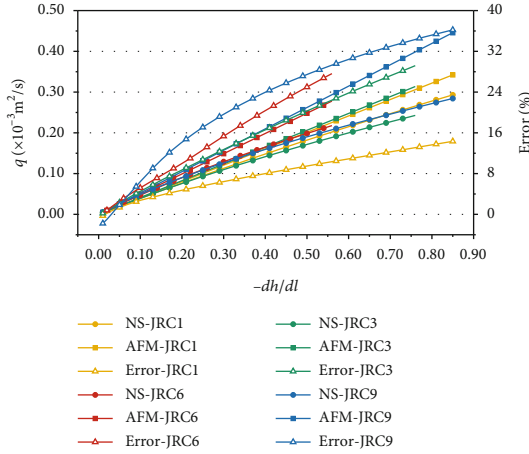
FIGURE 4: Flow per unit width (q) ~ hydraulic gradient (−dh/dl) curf. The solid circle indicates the NS calculation result curve, the solid square indicates the AFM calculation result curve, and the hollow triangle indicates the error in the calculation result of NS vs. AFM.

(Figures 5(g), 5(h), and 6(f)–6(h)). The RZ not only appears on the side of the rough fracture wall but also produces obvious RZ on the side of the smooth wall, which reflects the strong influence of fluid inertia force. Figures 5(i), 5(j), 6(i), and 6(j) are local streamlines enlargement diagrams; the arrows on the streamline show that the fluid in the RZ is obviously refluxed and does not enter the main flow zone. The fluid in the RZ consumes part of the energy of the fracture flow and generates LPD, but it cannot generate effective flow at the fracture outlet.

Figures 7 and 8 shows the variation of the fluid velocity profile with hydraulic gradients on a cut line in the JRC3 and JRC6 fractures. When the hydraulic gradient is small, the velocity distribution on the intercept line has a parabolic shape; when the hydraulic gradient continues to increase, the velocity profile has a bimodal shape due to the creation of the RZ, reflecting the formation of the RZ.

The most classical mathematical description of nonlinear flow of a fluid in a fracture is Forchheimer's law [13, 33]

$$-\nabla p = \frac{\mu}{k}v + \rho\beta v^2, \tag{9}$$

where ∇p is the hydraulic gradient $\nabla p = \rho g\,(dh/dl)$, v is the average flow velocity of the fluid under hydraulic gradient conditions $v = q/e_h$, and k is the intrinsic permeability of the fracture $k = e_h{}^2/12$. $\beta[m^{-1}]$ is the inertial resistance coefficient of the fluid, e_h is the equivalent hydraulic aperture of the fracture, μ is the viscosity coefficient of the fluid, and ρ is the fluid density. It should be noted that k is the permeability when the hydraulic gradient (−dh/dl) is tiny and the effect of fluid inertial forces can be neglected. When the hydraulic gradient increases, e_h changes when there is the creation of a RZ. The $k(e_h)$ and the coefficient β can be obtained from the applied hydraulic gradient and the flow fitting (Equation (9)). The fitted equations of the Forchheimer equation for the JRC3 and JRC6 models are labeled in Figure 9, respec-

tively, and the fitted curves are perfect, reflecting the phenomenon that the nonlinear flow in the fracture becomes progressively more pronounced with the increase of the hydraulic gradient.

Reynolds number is a quantified parameter to compare the proportional relationship between inertial and viscous forces in the fluid, and for the fluid passing through the fracture, the Reynolds number is calculated as [13]:

$$Re = \frac{\rho v D}{\mu} = \frac{\rho Q}{\mu w}, \tag{10}$$

where v is the average flow velocity of the fluid in the fracture, μ is the viscous coefficient of the fluid, ρ is the fluid density, and D is the characteristic length in the flow system; here, the average aperture of the fracture is taken. Q is the fracture flow rate, and w is the width of the fracutre sample perpendicular to the direction of the hydraulic gradient.

We calculated the Reynolds number for each hydraulic gradient condition in the JRC3 and JRC6 fracture NS seepage model, respectively, and the variation of the Reynolds number is represented as a curve (blue solid line in Figure 9). The obtained Reynolds number can only indicate the trend of increasing fluid inertia force with the hydraulic gradient, but it does not tell the kind of conditions in which significant nonlinear flow occurs.

In order to quantify the nonlinear flow, Javadi et al. [34] and Zhou et al. [33] proposed to use the critical Reynolds number (Re_c) to make a judgment. Re_c indicates the beginning of the transition from fluid flow to non-Darcy flow and can be defined as the Reynolds number when the percentage of nonlinear pressure drop ($\beta\rho v^2$) to total pressure drop ($\mu v/k + \beta\rho v^2$) reaches the critical point α. Re_c can be obtained from the following equation.

$$Re_c = \frac{\alpha e_h}{(1-\alpha)\beta k}, \tag{11}$$

where $\alpha = 5\%$ and e_h, β, and k are obtained from the Forchheimer's law fitting equations for the two models JRC3 and JRC6. Using Equation (11), we obtained that $Re_c = 109.27$ (Figure 9(a)) for JRC3, corresponding to a hydraulic gradient −dh/dl = 0.30 (Table 3) and $Re_c = 74.03$ (Figure 9(b)) for JRC6, corresponding to a hydraulic gradient −dh/dl = 0.16 (Table 3). Referring to the meaning of the critical Reynolds number, it can be considered that the hydraulic gradient corresponding to the critical Reynolds number, theoretically the fluid inertia force for the overall pressure drop is equal to 5%; combined with the Equation (10) to calculate the variation of Reynolds number, the smaller the hydraulic gradient, the smaller the Reynolds number, the impact of the inertia force is also smaller.

The critical Reynolds number (Re_c) indicates the critical point between linear and nonlinear flow in fracture flow. The formation of the RZ is again an important factor for the effect of nonlinearity in rough fracture flow. Therefore, when the Reynolds number of fracture flow is less than the critical Reynolds number (Re_c), it is not easy to form the
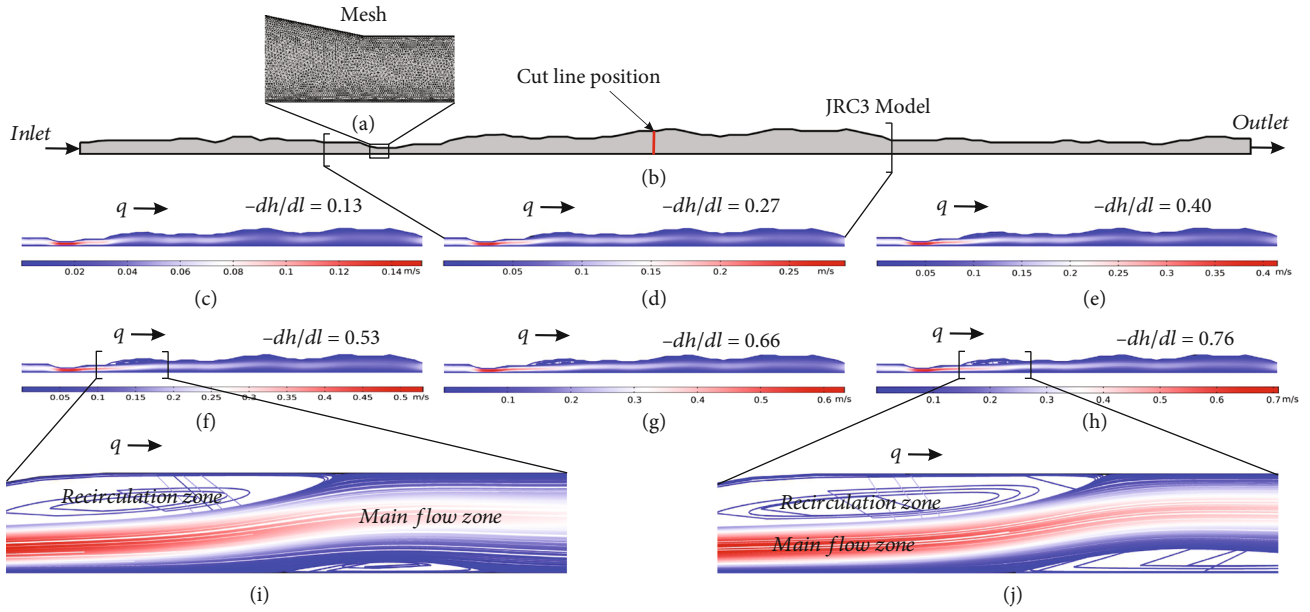
FIGURE 5: (a) Discrete mesh (partial). (b) JRC3 model. (c–h) The streamline with different hydraulic gradients (-dh/dl). (i, j) The streamlines in the local area are enlarged, and the recirculation zone and main flow zone are marked.
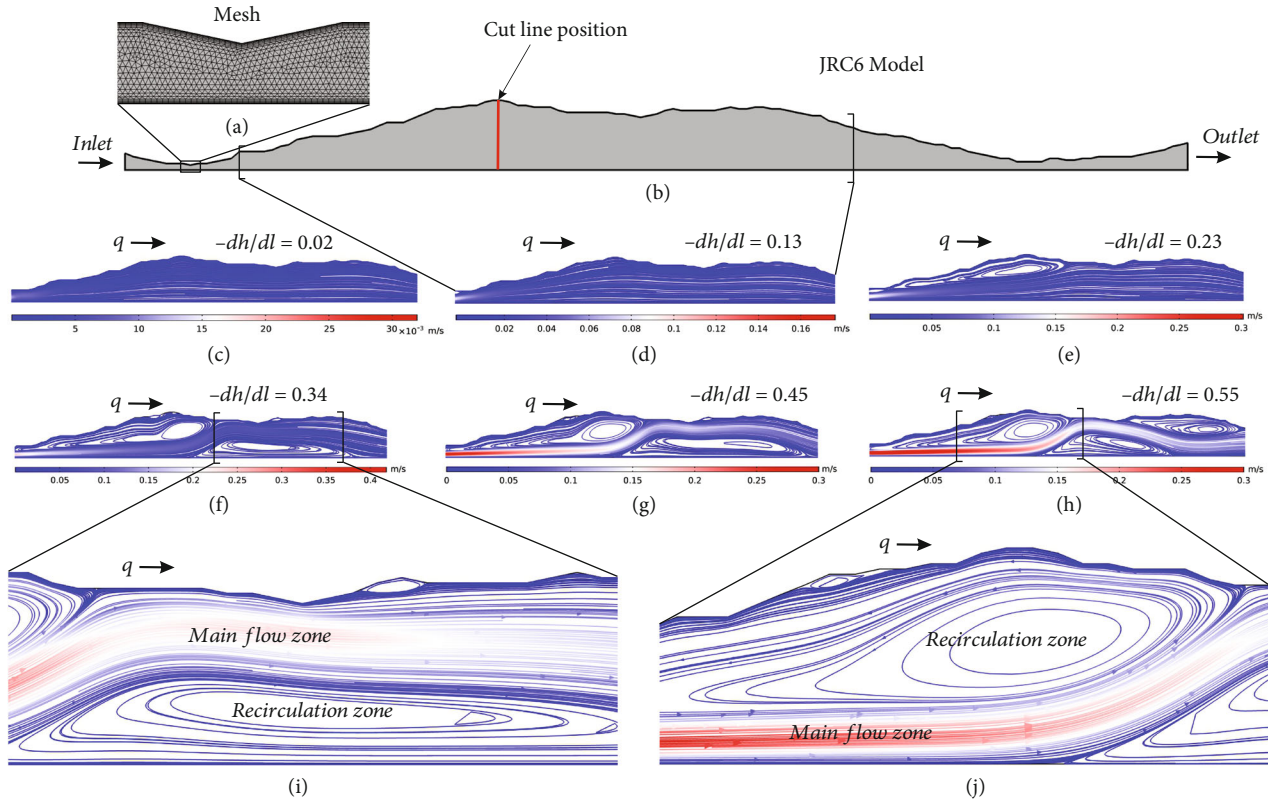
FIGURE 6: (a) Discrete mesh (partial). (b) JRC6 model. (c–h) The streamline with different hydraulic gradients (-dh/dl). (i, j) The streamlines in the local area are enlarged, and the recirculation zone and main flow zone are marked.

RZ or only a small RZ is formed, and the linear flow is dominant at this time. And when greater than the critical Reynolds number (Re_c), the formation of obvious RZ, and with the increase of hydraulic gradient and increase, the nonlinear flow in the fracture flow is more significant.

3.3.2. The Effect of Recirculation Zone. In order to further study the influence of RZ on fracture seepage, we analyze the area occupied by the RZ and the kinetic energy of fluid in the RZ, respectively. The extent of the RZ is difficult to be directly defined, but there must be a velocity vector in
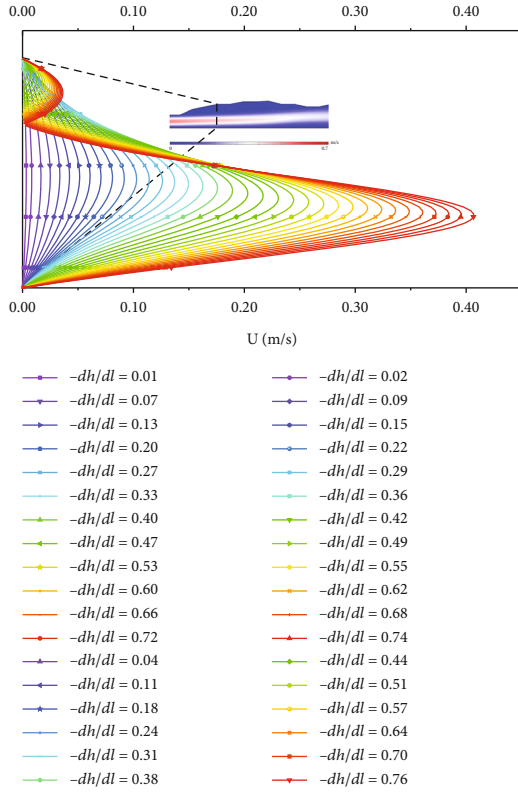
FIGURE 7: JRC3 model. The profiles of the velocity magnitude (U) on the cut line varying with different hydraulic gradients (-dh/dl), and the filled color represents the value of U.
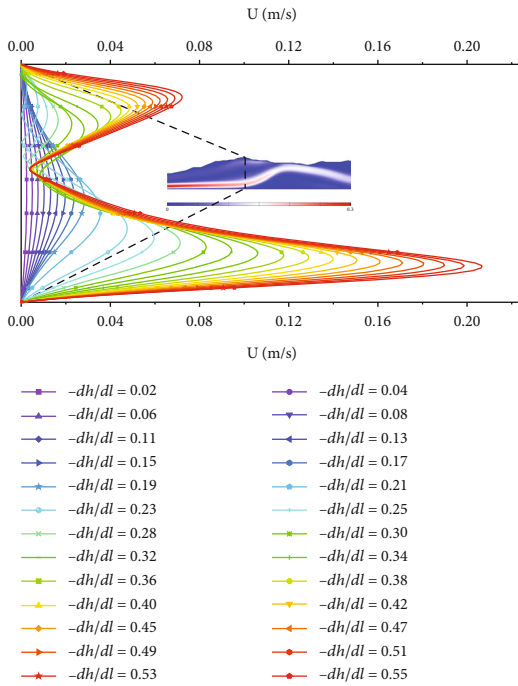
FIGURE 8: JRC6 model. The profiles of the velocity magnitude (U) on the cut line varying with different hydraulic gradients (-dh/dl), and the filled color represents the value of U.

the RZ that is opposite to the main seepage direction. The main seepage direction of all models in this paper is the x-direction, i.e., the range of velocity $u < 0$ in the x-direction is part of the RZ. According to the interrelationship between the velocity vector and the flow line in Figure 10, it is found that the range of $u < 0$ can be approximated to half of the area of the RZ. The area of $u < 0$ under a certain hydraulic gradient is calculated and taken as two times its size as the area of the RZ, although there is a certain deviation from the real RZ area, but it can reflect the RZ area change law.

The fluid in the RZ for circular flow, its internal fluid kinetic energy is calculated using a similar method. Calculate the kinetic energy of the fluid with velocity $u < 0$ in the x-direction and then multiply it by 2 as the total kinetic energy of the fluid in the RZ. Then, analyze the law of kinetic energy change in the RZ. The kinetic energy of the fluid is calculated as follows:

$$E_{\Omega} = \int_{\Omega} \frac{\rho \Delta V U^2}{2} dV, \tag{12}$$

where E is kinetic energy, Ω is the area of RZs, ρ is fluid density, U is fluid flow velocity (scalar), and ΔV is element volume.

The main purpose of this paper is to analyze the proportion of the RZ area to the total fracture area and the change of the proportion of the kinetic energy of the RZs to the total kinetic energy of the fluid. The influence of the RZs is analyzed according to the proportional change curve. The calculated results of solving the NS equation for four models, including JRC1, JRC3, JRC6, and JRC9, are counted to show the area of the RZs, the ratio of kinetic energy to total area, and total kinetic energy under each hydraulic gradient, and the change curves are plotted.

The JRC3 model is used as an example for illustration (Figure 11(a)). The hydraulic gradient of JRC3 fracture model ranges from 0.009 to 2.55, and the ratio of the RZ area to the total area is 0.06% to 12.02%. With the increase of the hydraulic gradient, the percentage change of the RZs area is very obvious. The proportion of the kinetic energy of the RZ area to the total kinetic energy is 0.0002% ~ 0.21%. The kinetic energy percentage is much lower compared to the area, and under the condition of small hydraulic gradient, the effect of kinetic energy in the RZs can even be ignored. The remaining three models JRC1, JRC6, and JRC9 have similar characteristics (Figures 11(b)–11(d)).

Therefore, it can be considered that the main effect of the RZs on the rough fracture seepage is that the fluid occurs back in the RZ by itself and does not produce an effective flow at the fracture outlet. The fluid flow in the RZs is slow, and the loss of kinetic energy of the fluid in the fracture is not significant. However, the RZs squeeze the seepage channel of the fracture, resulting in the reduction of the actual seepage capacity of the fracture. The area occupied by the RZ increases with the hydraulic gradient and shows a nonlinear variation.

In addition, the area of RZs and the proportion of kinetic energy do not increase infinitely with the increase of
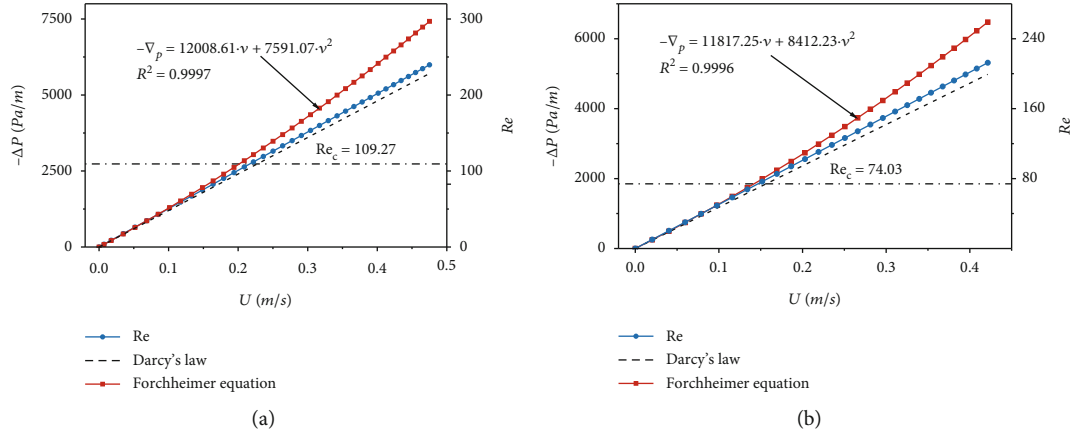
FIGURE 9: (a) JRC3 model. (b) JRC6 model. Solid lines refer to the fitting curves using the Forchheimer equation, while the dashed lines refer to that using Darcy's law.

TABLE 3: Main calculation results of JRC3 and JRC6 numerical models.

	Solution	Calculation duration/s	Calculate duration ratio	$\varepsilon(qn)/\%$	Critical Reynolds number Re_c	Hydraulic gradients corresponding to $Re_c/(-dh/dl)$
JRC1	NS	169415	8916.58	-0.26~ 14.34	143.06	0.39
	AFM	19			—	—
JRC3	NS	176712	6311.14	0.15~ 29.12	109.27	0.3
	AFM	28			—	—
JRC6	NS	58665	7333.13	0.73~ 32.47	74.03	0.16
	AFM	8			—	—
JRC9	NS	14772	1641.33	-1.78~ 36.21	39.6	0.0845
	AFM	9			—	—
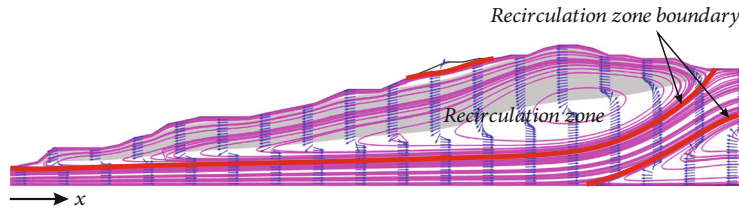
FIGURE 10: The magenta line represents the streamline; the blue arrow represents the velocity vector in the x-direction of the model; the gray shaded part represents the area where the velocity in the x-direction is less than 0.

hydraulic gradient, but gradually reach a peak, and then stabilize or slightly decrease. And the rougher the fracture is, the easier it is to reach the peak. In terms of the peak area share of the RZ, the four models JRC1, JRC3, JRC6, and JRC9 reach the peak at the hydraulic gradient of 5.1, 1.68, 0.76 (presumed), and 0.57, respectively.

3.4. Analysis of the Effect of Vortices. The RZ is circled according to the shape of the streamline, and its shape is influenced by the number of streamlines and the calculation method of the flow line. The RZ is intuitively seen as a back-flow or rotation of the fluid, which is similar to the physical concept of a vortex. However, the vortex determined according to a strict mathematical definition differs significantly

from the RZ (Figure 12). Vortices are generated near the fracture wall, inside the RZ, at the transition between the reflux and main flow zones, or even within the main flow zone. That is, when there is a velocity difference within the fluid, vortices may be generated. Figure 12 shows that the range of vortices also includes part of the mainstream zone; that is, there is also local fluid rotation within the mainstream zone. This part of the vortex is different from the RZ; it will lose part of the fluid energy but at the same time can produce effective flow.

To further analyze the effect of vortices on the seepage in the fracture, the value of the vortex parameter Ω in the fluid within the fracture is calculated using Equation (6), and the kinetic energy of the fluid in the range $\Omega \geq 0.52$ is calculated
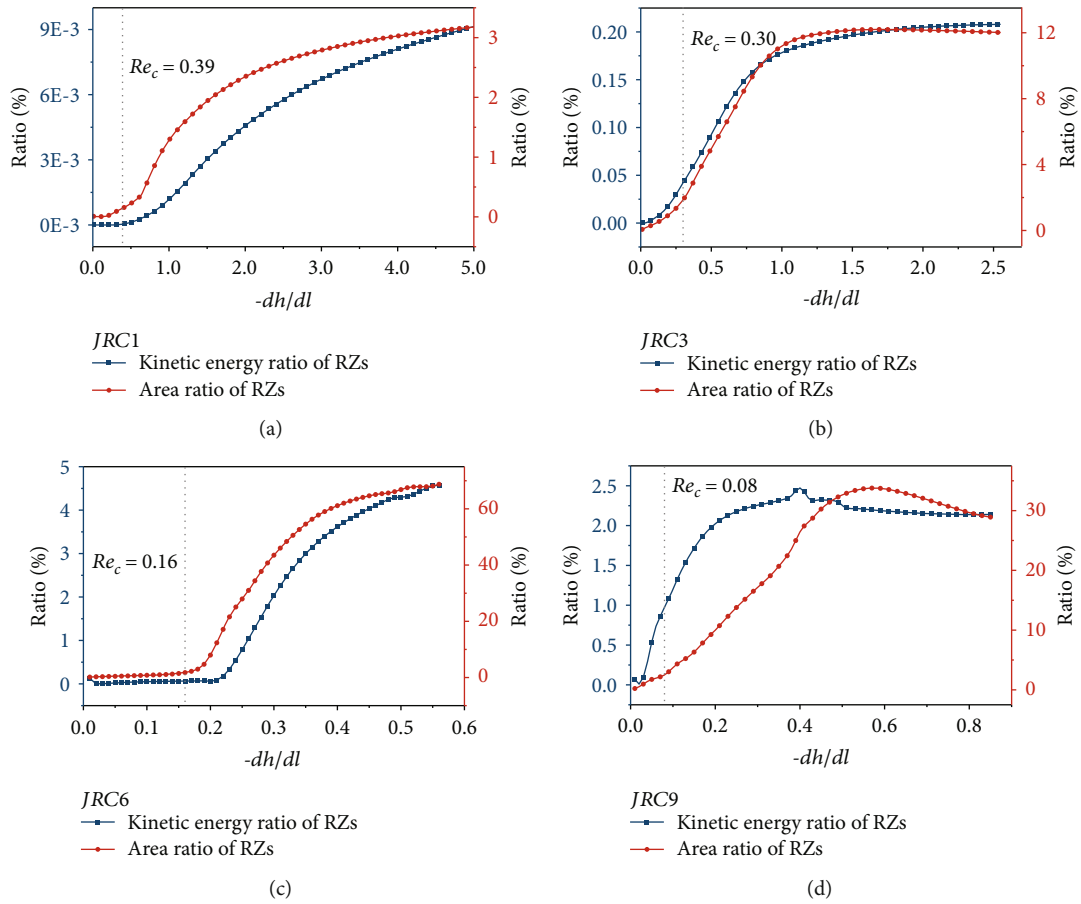
FIGURE 11: (a) JRC1 model; (b) JRC3 model; (a) JRC6 model; (b) JRC9 model. The solid red circle line represents the proportion of kinetic energy in the RZ to the total kinetic energy (%). The solid blue square line represents the ratio of the area of the RZ to the total area (%).
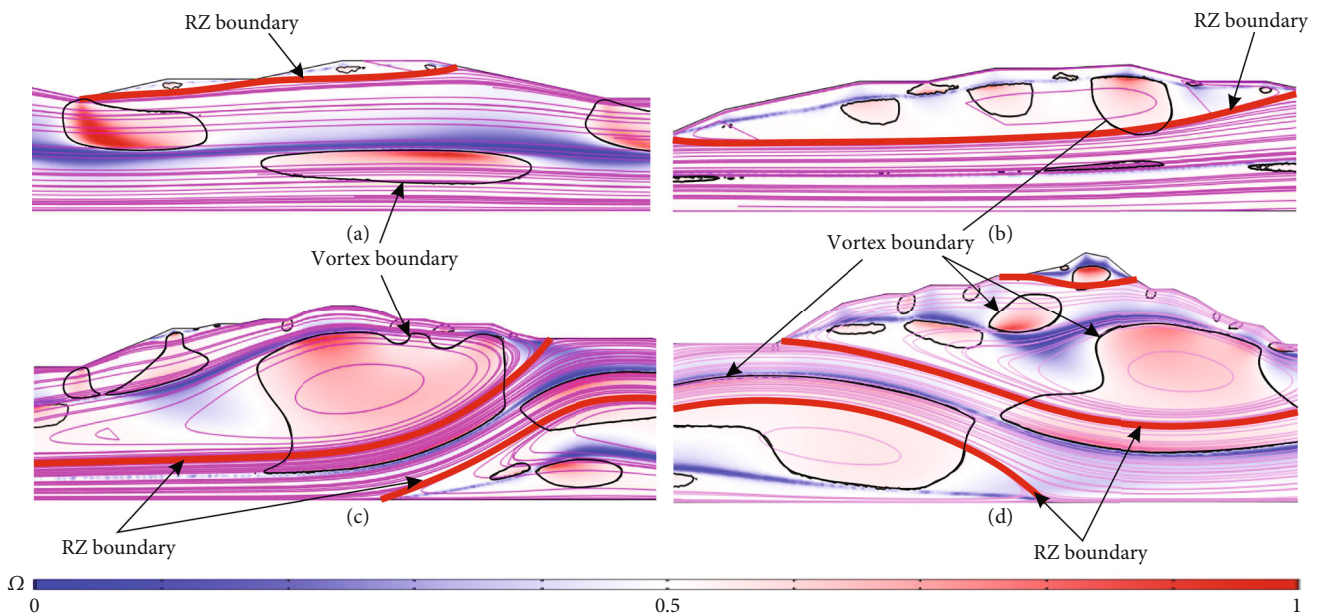
FIGURE 12: Comparison of the RZ and vortex for JRC1, JRC3, JRC6, and JRC9 models with large hydraulic gradients.

JRC1
- Kinetic energy in vortex
- Total kinetic energy
- The ratio of kinetic energy in vortex

(a)

JRC3
- Kinetic energy in vortex
- Total kinetic energy
- The ratio of kinetic energy in vortex

(b)

JRC6
- Kinetic energy in vortex
- Total kinetic energy
- The ratio of kinetic energy in vortex

(c)

JRC9
- Kinetic energy in vortex
- Total kinetic energy
- The ratio of kinetic energy in vortex

(d)
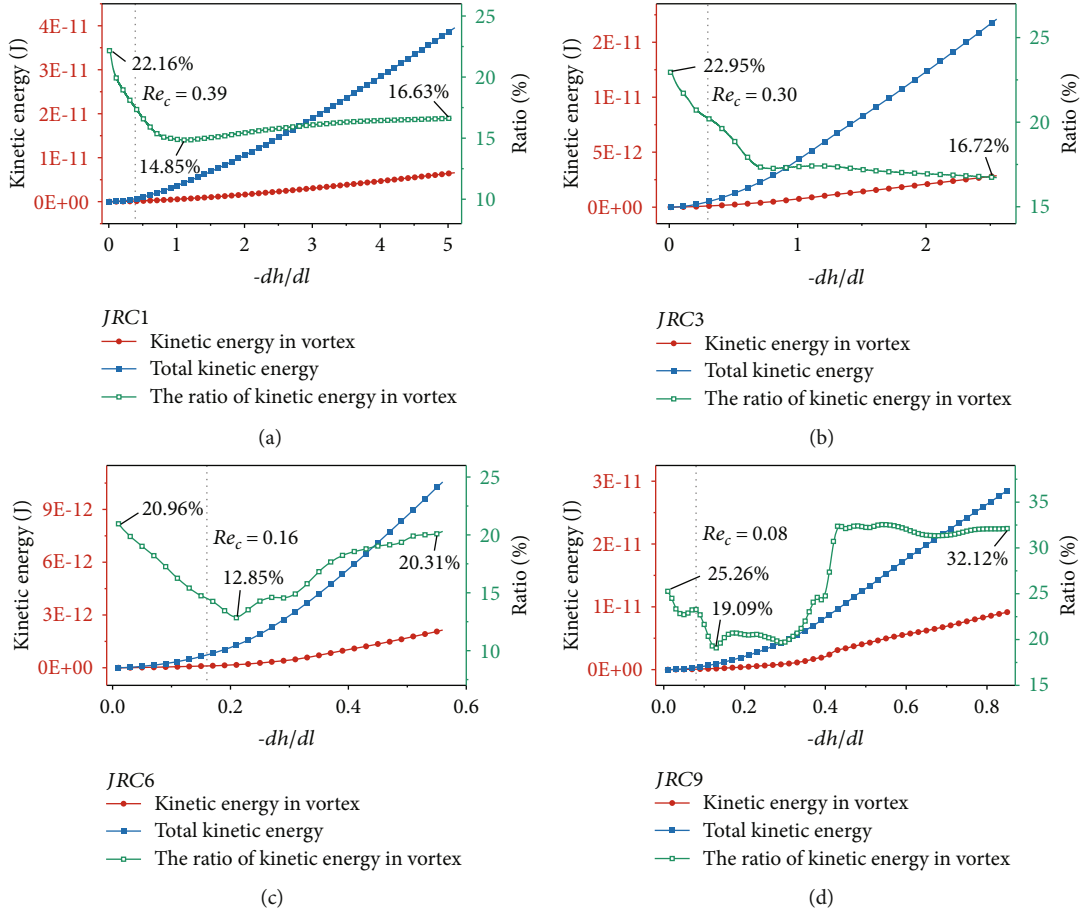
FIGURE 13: (a) JRC1 model; (b) JRC3 model; (a) JRC6 model; (b) JRC9 model. The solid blue squares represent the total kinetic energy in the fracture flow; the solid red circles represent the kinetic energy inside the vortex; the solid light blue hollow squares represent the percentage (%) of the kinetic energy inside the vortex to the total kinetic energy.

using Equation (12), along with its percentage of the total kinetic energy. Then, the variation of total kinetic energy, intravortex kinetic energy, and the proportion of intravortex kinetic energy of the fluid is shown as curves using the hydraulic gradient as the horizontal coordinate. Figure 13 shows the curves for the four fracture models. It can be seen that (a) the intravortex kinetic energy increases nonlinearly with the hydraulic gradient. (b) The variation of intravortex kinetic energy ratio is much more complicated. When the fluid Reynolds number is smaller than the critical Reynolds number (Re_c), the intravortex kinetic energy ratio shows a decreasing trend. (c) The proportion of kinetic energy in the vortex first decreases, then rises, and then the curve changes to a smooth, indicating that the kinetic energy in the vortex is not completely lost energy, and the fluid in the vortex both rotational motion, but also with the mainstream of the flat motion. (d) Compared with the proportion of kinetic energy in the RZ, the proportion of kinetic energy in the vortex is significantly larger. In the JRC1 model, for example, the highest is 22.16%, and the lowest is 14.85%, so it is obvious that the proportion of kinetic energy in the vortex is much larger and has a greater impact.

4. Discussion

For the rough fracture seepage model, it is obvious that solving the NS equation directly can reflect the nonlinear flow state in the fracture more accurately; for example, the fit of Forchheimer equation is very high, and the corresponding calculation results are more accurate. However, its disadvantage is also very obvious; that is, the computational effort is very large. In comparison, the computational efficiency of AFM is much higher than the former.

Comparing the four models, the number of discrete elements of the model is much larger than that of AFM when solving the NS equation directly (Table 1). This is because AFM only needs to discrete one fracture wall surface. The former has 8.76 times, 4.90 times, 3.41 times, and 3.3 times more than the latter (Table 1).

Numerical calculations were performed using the same computer (CPU: Intel(R) Xeon(R) CPU E5-1620 v3, RAM: 16G); the difference in computational efficiency between the two is huge. The JRC1, JRC3, JRC6, and JRC9 models took 169415 s, 176712 s, 58665 s, and 14772 s, respectively, to solve the NS equations (Table 3), while the computation time using AFM was 19 s, 28 s, 8 s, and 9 s, respectively (Table 3).

The huge computational efficiency advantage of AFM can complete more model computation work in a short time. Because the calculation time-consuming of a single rough fracture model is very short, the seepage calculation of a complex three-dimensional spatial rough fracture network (e.g., a fracture network composed of thousands of rough fractures) can be completed using only an ordinary computer, which is one of our future works. In addition, the geometric model of AFM requires only one fracture wall surface, and the modeling process of numerical model is simpler, while the aperture data can be produced more quickly with the help of third-party software or programming.

From this point of view, the huge numerical calculation efficiency of AFM can offset the impact of its calculation error, and the error is not significant at low Reynolds number conditions. This will help researchers to carry out seepage calculations and research work on large scale rock fracture networks.

5. Conclusions

From the above analysis and description, we can get several conclusions as follows.

(1) Under the low Reynolds number condition, the numerical calculation work of seepage flow in rough fractures can be done by using the AFM, but the calculation results will produce some small errors

(2) Due to the abrupt change of the fracture wall to produce recirculation zone (RZ), the main effect of RZ is that it crowds the main flow range, making the effective seepage channel of the fracture narrower. The area of the RZs is related to the hydraulic gradient and varies nonlinearly. In addition, the fluid motion inside the RZ is slow, and the loss of kinetic energy of the fluid is not large, accounting for a small proportion of the overall kinetic energy

(3) In addition to the RZ in the rough fracture, vortices are formed, i.e., local fluid rotation. Vortex and RZ area are very different, the fluid in the vortex loss of kinetic energy, but can produce effective flow, and its changes are more complex

(4) Using the local cubic law to solve the rough fracture seepage flow, the main source of error in the calculation results is the LPD. The LPD in fracture seepage includes the area crowding in the RZ, kinetic energy loss in the RZ, kinetic energy loss in the vortex, and pressure drop caused by other reasons

(5) The main advantage of AFM is the efficiency of its numerical calculation. Based on this advantage, AFM can quickly complete the numerical calculation of a huge number of 3D rough fracture networks

Strictly speaking, the fracture model in this paper is a single-wall rough fracture model, which has some shortcomings of its own; for example, the nonuniformity and anisotropy of the fracture are not sufficiently reflected. This is mainly due to the need to be consistent with the fracture physical model for comparative analysis. These will be improved gradually in our subsequent studies.

Data Availability

Previously reported physical experiment results of rough fracture fluid flow data were used to support this study and are available at http://rockmech.whrsm.ac.cn/CN/article/downloadArticleFile.do?attachType=PDF&id=28084 and https://kns.cnki.net/KCMS/detail/detail.aspx?dbcode=CDFD&dbname=CDFD2013&filename=1013132077.nh (pages 32-45). These prior studies (and datasets) are cited at relevant places within the text as references [16, 32].

Conflicts of Interest

The authors declare that they have no conflicts of interest.

Acknowledgments

References

[1] Y. T. Zhang, *Rock Hydraulics and Engineering*, China Water and Power Press, Beijing, China, 2005.

[2] K. Pruess, J. S. Y. Wang, and Y. W. Tsang, "On thermohydrologic conditions near high-level nuclear wastes emplaced in partially saturated fractured tuff: 1. Simulation studies with explicit consideration of fracture effects," *Water Resources Research*, vol. 26, no. 6, pp. 1235–1248, 1990.

[3] V. Cvetkovic, S. Painter, N. Outters, and J. O. Selroos, "Stochastic simulation of radionuclide migration in discretely fractured rock near the Äspö Hard Rock Laboratory," *Water Resources Research*, vol. 40, no. 2, article W02404, 2004.

[4] P. K. Kang, T. le Borgne, M. Dentz, O. Bour, and R. Juanes, "Impact of velocity correlation and distribution on transport in fractured media: field evidence and theoretical model," *Water Resource Research*, vol. 51, no. 2, pp. 940–959, 2015.

[5] Z. Yang, A. Niemi, F. Fagerlund, T. Illangasekare, and R. L. Detwiler, "Dissolution of dense non-aqueous phase liquids in vertical fractures: effect of finger residuals and dead-end pools," *Journal of Contaminant Hydrology*, vol. 149, no. 3, pp. 88–99, 2013.

[6] G. Chen, S. G. Xu, C. X. Liu, L. Lu, and L. Guo, "Groundwater flow simulation and its application in GaoSong ore field, China," *Journal of Water and Climate Change*, vol. 10, no. 2, pp. 276–284, 2019.

[7] J. Q. Zhou, L. C. Wang, C. D. Li, H. Tang, and L. Wang, "Effect of fluid slippage on eddy growth and non-Darcian flow in rock fractures," *Journal of Hydrology*, vol. 581, no. 9, pp. 124440–124449, 2020.

[8] P. A. Witherspoon, J. S. Y. Wang, K. Iwai, and J. E. Gale, "Validity of cubic law for fluid flow in a deformable rock fracture," *Water Resources Research*, vol. 16, no. 6, pp. 1016–1024, 1980.

[9] I. W. Yeo, M. H. De Freitas, and R. W. Zimmerman, "Effect of shear displacement on the aperture and permeability of a rock fracture," *International Journal of Rock Mechanics and Mining Sciences*, vol. 35, no. 8, article 1051e70, 1998.

[10] F. Bauget and M. Fourar, "Non-Fickian dispersion in a single fracture," *Journal of Contaminant Hydrology*, vol. 100, no. 3-4, article 137e48, pp. 137–148, 2008.

[11] A. P. Oron and B. Berkowitz, "Flow in rock fractures: the local cubic law assumption reexamined," *Water Resources Research*, vol. 34, no. 11, pp. 2811–2825, 1998.

[12] R. W. Zimmerman and G. S. Bodvarsson, "Hydraulic conductivity of rock fractures," *Transport in Porous Media*, vol. 23, no. 1, pp. 1–30, 1996.

[13] R. W. Zimmerman, A. al-Yaarubi, C. C. Pain, and C. A. Grattoni, "Non-linear regimes of fluid flow in rock fractures," *International Journal of Rock Mechanics and Mining Sciences*, vol. 41, Supplement 1, pp. 163–169, 2004.

[14] D. J. Brush and N. R. Thomson, "Fluid flow in synthetic rough-walled fractures: Navier–Stokes, Stokes, and local cubic law simulations," *Water Resources Research*, vol. 39, no. 4, p. 1085, 2003.

[15] S. Ge, "A governing equation for fluid flow in rough fractures," *Water Resources Research*, vol. 33, no. 1, pp. 53–61, 1997.

[16] H. G. Zhu, H. P. Xie, C. Yi et al., "Analysis of properties of fluid flow in rock fracutre," *Chinese Journal of Rock Mechanics and Engineering*, vol. 32, no. 4, pp. 657–663, 2013.

[17] M. Javadi, M. Sharifzadeh, and K. Shahriar, "A new geometrical model for non-linear fluid flow through rough fractures," *Journal of Hydrology*, vol. 389, no. 1-2, pp. 18–30, 2010.

[18] R. C. Liu, M. He, N. Huang, Y. Jiang, and L. Yu, "Three-dimensional double-rough-walled modeling of fluid flow through self-affine shear fractures," *Journal of Rock Mechanics and Geotechnical Engineering*, vol. 12, no. 1, pp. 41–49, 2020.

[19] Y. Li, Y. F. Chen, and C. B. Zhou, "Hydraulic properties of partially saturated rock fractures subjected to mechanical loading," *Engineering Geology*, vol. 179, pp. 24–31, 2014.

[20] J. Q. Zhou, S. H. Hu, Y. F. Chen, M. Wang, and C. B. Zhou, "The friction factor in the Forchheimer equation for rock fractures," *Rock Mechanics and Rock Engineering*, vol. 49, no. 8, pp. 3055–3068, 2016.

[21] B. Shu, R. J. Zhu, J. Q. Tan, S. Zhang, and M. Liang, "Evolution of permeability in a single granite fracture at high temperature," *Fuel*, vol. 242, no. 1, pp. 12–22, 2019.

[22] J. Q. Zhou, M. Wang, L. C. Wang, Y. F. Chen, and C. B. Zhou, "Emergence of nonlinear laminar flow in fractures during shear," *Rock Mechanics and Rock Engineering*, vol. 51, no. 11, pp. 3635–3643, 2018.

[23] X. G. Liu, W. C. Zhu, Q. L. Yu, S. Chen, and K. Guan, "Estimating the joint roughness coefficient of rock joints from translational overlapping statistical parameters," *Rock Mechanics and Rock Engineering*, vol. 52, no. 3, pp. 753–769, 2019.

[24] M. Wang, Y. F. Chen, G. W. Ma, J. Q. Zhou, and C. B. Zhou, "Influence of surface roughness on nonlinear flow behaviors in 3D self-affine rough fractures: Lattice Boltzmann simulations," *Advances in Water Resources*, vol. 96, no. 8, pp. 373–388, 2016.

[25] S. H. Lee, K. K. Lee, and I. W. Yeo, "Assessment of the validity of Stokes and Reynolds equations for fluid flow through a rough-walled fracture with flow imaging," *Geophysical Research Letters*, vol. 41, no. 13, pp. 4578–4585, 2014.

[26] N. Huang, R. C. Liu, and Y. Jiang, "Numerical study of the geometrical and hydraulic characteristics of 3D self-affine rough fractures during shear," *Journal of Natural Gas Science and Engineering*, vol. 45, pp. 127–142, 2017.

[27] N. Huang, R. Liu, and Y. Jiang, "Evaluating the effect of aperture variation on the hydraulic properties of the three-dimensional fractal-like tree network model," *Fractals*, vol. 28, no. 6, article 2050112, 2020.

[28] J. Q. Zhou, L. Wang, Y. F. Chen, and M. B. Cardenas, "Mass transfer between recirculation and main flow zones: is physically based parameterization possible?," *Water Resources Research*, vol. 55, no. 1, pp. 345–362, 2019.

[29] H. B. Lee, I. W. Yeo, and K. K. Lee, "Water flow and slip on NAPL-wetted surfaces of a parallel-walled fracture," *Geophysical Research Letters*, vol. 34, no. 19, pp. 1–5, 2007.

[30] C. Q. Liu, "Liutex-third generation of vortex definition and identification methods," *Acta Aerodynamica Sinica*, vol. 38, no. 6, pp. 413–431, 2020.

[31] C. Q. Liu, Y. Q. Wang, Y. Yang, and Z. W. Duan, "New omega vortex identification method," *Science China Physics, Mechanics & Astronomy*, vol. 59, no. 8, pp. 684–711, 2016.

[32] H. G. Zhu, *Flow Properties of Fluid in Fractured Rock, [Ph.D. thesis]*, China University of Mining and Technology, Beijing, China, 2012.

[33] J. Q. Zhou, S. H. Hu, S. Fang, Y. F. Chen, and C. B. Zhou, "Nonlinear flow behavior at low Reynolds numbers through rough-walled fractures subjected to normal compressive loading," *International Journal of Rock Mechanics and Mining Sciences*, vol. 80, no. 9, pp. 202–218, 2015.

[34] M. Javadi, M. Sharifzadeh, K. Shahriar, and Y. Mitani, "Critical Reynolds number for nonlinear flow through rough-walled fractures: the role of shear processes," *Water Resource Research*, vol. 50, no. 2, pp. 1789–1804, 2014.

WILEY | Hindawi

Research Article

Experimental Study on Vibration Reduction Technology of Hole-by-Hole Presplitting Blasting

Jun Ma [ID],[1] **Xianglong Li** [ID],[1,2] **Jianguo Wang** [ID],[1,2] **Zihao Tao** [ID],[1] **Ting Zuo** [ID],[1] **Qiang Li** [ID],[1] **and Xiaohua Zhang**[1]

[1]*Faculty of Land Resources Engineering, Kunming University of Science and Technology, Kunming, 650093 Yunnan, China*
[2]*Yunnan Key Laboratory of Sino-German Blue Mining and Utilization of Special Underground Space, Kunming University of Science and Technology, Kunming, 650093 Yunnan, China*

Correspondence should be addressed to Jianguo Wang; wangjg0831@163.com

In order to effectively reduce the disturbance of the precrack blasting vibration on slope rock mass, except paying attention to the damping effect of the precrack, it is also necessary to optimize the blasting parameters and initiation mode of the precrack itself. Based on the blasting theory and empirical formula, the parameters of presplitting blasting such as the hole diameter, hole spacing, charge decoupling coefficient, and line charge density were determined, and field tests of conventional pre-splitting blasting and presplitting blasting with precise delay and hole-by-hole initiation were carried out on the west slope of Buzhaoba. Regression analysis was carried out on the vibration monitoring data, and the blasting vibration attenuation regularity of slope particles was obtained. By comparing the monitored vibration velocity of the two presplitting blasting tests and the forecast results of theoretical calculation, the average reduction rate of the conventional same row blasting vibration is 26.40%, while that of the hole-by-hole blasting vibration can reach 41.45% with a half hole rate of 80.7% and an irregularity of about 130 mm. Results show that the effect of precise delay initiation between preholes based on the digital electronic detonator is better than that of the simultaneous initiation of preholes. Therefore, it is suggested that the hole-by-hole presplitting blasting technology should be applied in the excavation of boundary slope and the treatment of high and steep slope.

1. Introduction

Buzhaoba open-pit coal mine, which belongs to the Xiaolongtan Mining Bureau in Kaiyuan City of Yunnan Province, is the main operating mine crater. With the increase of mining depth, the tension cracks which formed on its western side are increasing in number and length [1]. The problem of the high-steep slope is becoming more and more serious, as the slope deformation is gradually accelerated. These hazards may cause damage of equipment, or even lives if no proper precautions are taken [2].

The upper portion in the west slope of the Buzhaoba is made up of a thin layer of argillaceous limestone with hard mudstone rocks and weak rock mass, with clear bedding and small fold, and there are $4 \sim 6$ jointed cracks per cubic

meter. The rocks are weak or moderately weathered rock mass, and the integrity of the rock mass is poor. Besides, many structural planes in rock mass are soft interlayers. Considering the combined effects of blasting, weathering, unloading, and water scouring, a lot of difficulties are brought in the maintenance of the permanent stability of the slope. In order to reduce negative effects induced by blasting operation in the final high wall and prevent landslide due to slope instability in the future, presplitting blasting technology is the first choice when conducting blasting operation on the Buzhaoba area [3–5]. On one hand, presplitting blasting can prevent the spread of explosion stress wave to the reserved rock mass by way of forming cracks with a certain width and depth between the main area and the reserved zone, so as to reduce or even cut off the blasting

vibration damage to the reserve rock mass [6]; on the other hand, the integrity of the reserve rock mass can be maintained because the cracks extending from the main area to the reserved zone is also cut off [7].

A lot of studies have been carried out on the precrack blasting. For example, Yang et al. [8] applied vertical and horizontal uniaxial pressures and blasting loads on gypsum by numerical simulation and studied the damage distribution characteristics of blasted specimens by using fractal theory, digital image method, and acoustic detection method. In addition, Raina [9] used historical data to establish the precracking response surface analysis model of explosion damage index and semimold coefficient. The above failure criteria are compared by the angles of blast hole relative to the main joint orientation, joint spacing, blast hole spacing, drill deviation, linear charge concentration, and compressive strength. Besides, Wang et al. [10] verified the synergistic antireflection technology of hydraulic fracturing and deep hole presplitting blasting in low permeability coal seam by field engineering test. Moreover, Yang et al. [11] obtained the deformation characteristics and failure mechanism of DHPB through numerical simulation and model test of specimens under horizontal compressive stress, compressive vertical stress, and noncompressive stress, as well as morphological analysis of presplitting cracks after presplitting blasting. What is more, Cheng et al. [12] put forward the pressure relief technology of advanced deep hole nonthrough directional presplitting blasting. The influence of nonpenetrating crack length on presplitting effect is studied by numerical simulation. Different from the above researches, Yuan et al. [13] studied the bearing characteristics and stress distribution characteristics of residual coal pillar by theoretical analysis and numerical simulation, analyzed the influence mechanism of presplitting blasting on residual coal pillar, revealed the disaster reduction mechanism of presplitting blasting on shallow buried residual coal pillar, and determined reasonable blasting parameters. Furthermore, Chen et al. [14] put forward the deep hole presplitting blasting, weakening THR to alleviate the strong pressure. LS-DYNA was used to establish the deep hole presplitting blasting model, and the crack evolution law and the attenuation characteristics of peak particle velocity of rock under the synergistic effect of blasting stress wave and detonation gas were analyzed to verify the rationality of blasting parameters. Besides, Shin et al. [15] studied the phenomenon that the blasting damage zone developed on the rock slope surface can be affected by the joint characteristics rather than the explosive force when the rock slope is presplitting excavated. However, more and more attention has been paid to the blasting seismic intensity produced by presplitting blasting itself [16–29].

It can be seen that parameter selection of the presplitting blasting and the initiation mode of presplit holes have great influence on the damage of surrounding rock. In view of the stability control requirements of west slope cutting and load reduction in the open-pit mine, it is urgent to optimize the conventional presplitting blasting control scheme to further reduce the harmful effect of vibration.

2. Selection of Presplitting Blasting Parameters

2.1. Blasting Diameter. Normally, the smaller the diameter of the presplit hole, the higher percentage of half hole and the easier controlling the roughness of slope surface, and also the less the damage ranges of surrounding rock mass. But at the same time, the drilling and charging will be more difficult to implement, and the decoupling charging becomes more difficult to control [30]. Combined with the existing construction machinery and equipment of Buzhaoba, hole diameter $d = 100$ mm is selected in this test [31].

2.2. Decoupling Coefficient of Charging. (1) According to the theory of explosive detonation, the initial average pressure p_0 of the exploding gas in hole can be determined by the following equation [32]

$$p_0 = \frac{1}{8} \rho_0 V^2, \tag{1}$$

where ρ_0 is the density of explosive in kg/m^3, and V is the explosive detonation velocity in m/s.

(2) The calculation method of decoupling coefficient is discussed theoretically by Zong et al. [33], and the following formula is used

$$\sigma_{r0} = p_a = K_d^{-8/3} K_l^{-4/3} p_k \left(\frac{p_0}{p_k} \right)^{4/9}. \tag{2}$$

In this formula, σ_{r0} represents the absolute value of the initial peak stress on the hole wall in MPa, p_a is the quasistatic pressure when blasting gas filled the holes, K_d is the radial decoupling coefficient, K_l is the axial decoupling coefficient, and p_k is the critical pressure, which is usually taken as 200 MPa.

In order to avoid the failure due to compression which might happen in the wall rock, it is required to ensure the peak value of the initial radial stress acting on the rock of hole wall lower than the compressive strength of the rock. According to the above formula, the following formula is obtained for calculating the axial decoupling coefficient:

$$K_l < \frac{1}{K_d^2} \left(\frac{p_k}{S_c} \right)^{3/4} \left(\frac{p_0}{p_k} \right)^{1/3}, \tag{3}$$

where S_c stands for the compressive strength of rock in MPa.

The above requirements must be satisfied when the axial charge decoupling coefficient of presplitting blasting determined. At the time of application, the axial decoupling coefficient is determined according to the formula (3). K_l is slightly greater than the required value to ensure that there is enough gas pressure in the blasting holes to form a long burst fracture.

The physical and mechanical rock indices are listed in Table 1. Considering these indices, theoretical research and engineering application results published by Zong et al. [33] and Wang et al. [34], it is found that the value of the decoupling coefficient is between 3.0 and 3.6. In this project,

TABLE 1: Rock physical and mechanical indexes.

Rock mass	Elasticity modulus (GPa)	Poisson ratio (μ)	Cohesion (MPa)	Internal friction angle (°)	Natural bulk density (kN.m^{-3})	Tensile strength (MPa)	Compressive strength (MPa)
Limestone	12.6	0.20	3.49	40.5	22.4	3.44	30.12

the presplit hole diameter is set 100 mm, and the cartridge diameter is set 32 mm, thus, the decoupling coefficient K_d is determined as 3.1.

2.3. Hole Spacing. (1) Since presplit hole spacing largely determines the blasting quality of the slope surface, the choose of the hole spacing should guarantee the explosive detonation formation of presplit cracks, while reserved rock mass is not damaged [35]. Only when the hole spacing is less than the length of the critical flaw can the cracks form between the blast holes [36], and the way forming such a crack can be approximated as

$$E = R_c + R_a, \tag{4}$$

where E is the hole spacing in mm; R_c and R_a are the length of cracks produced by the explosion stress wave and the blasting gas under the action of static pressure, respectively, which are calculated by:

$$R_c = r_b \left(\frac{\beta p_r}{S_t} \right)^{1/a}, \tag{5}$$

$$R_a = r_b \left(\frac{p_a}{S_t} \right)^{1/2}, \tag{6}$$

where S_t is the tensile strength of rock in MPa, r_b is the hole radius in mm, α is the stress wave attenuation index of rock in the equation $\alpha = 2 \pm \mu/(1 - \mu)$, β is the proportionality coefficient of tangential and radial stresses in the equation $\beta = \mu/(1 - \mu)$, μ is the rock's Poisson ratio, which takes "+" in shock wave action area and "-" in stress wave action area. As one of the main purpose for decoupling charging of the presplitting blasting is to eliminate shock wave action in rock, "-" is taken. p_r is the initial pressure produced on the hole wall of borehole when blasting gas expansion influence the hole wall, whose value is determined by Wang et al. [37]

$$p_r = \frac{n\rho_0 D^2 K_d^{-6}}{8K_l} = \frac{np_0 K_d^{-6}}{K_l}. \tag{7}$$

The following formula can be obtained:

$$E = r_b \left(\frac{n\beta p_0 K_d^{-6}}{S_t K_l} \right)^{1/a} + r_b \left(\frac{p_a}{S_t} \right)^{1/2}, \tag{8}$$

where n is the multiple pressure when blasting gas expansion affects the hole wall and is generally set to 8.

(2) In order to avoid compression damage around the hole wall, the sectional charging structure is adopted to reduce the charge, but the reasonable hole spacing should

be selected to ensure the penetration of cracks between holes. The presplit hole spacing can be calculated by the following empirical formula [33]

$$a = d_b \left(21D_e^{-1.4} + 47D_e^{-2.4} \right), \tag{9}$$

where a is the presplit hole spacing in mm, d_b is the hole diameter in mm, and its value is 100 mm, D_e is the decoupling coefficient, with the value of 3.1. Therefore, $a = 7.4d_b$ and the presplit hole spacing is taken as 0.8 m.

2.4. Linear Charge Density. Linear charge density is the ratio of charge quantity in a hole to charge length. It determines whether the cracks can run through between two adjacent holes, and the damage degree of rock on the hole wall. The empirical formula for calculating linear charge density can be referred to the following formula:

(1) Calculation formula by Changjiang Academy of Sciences:

$$q_l = 0.034 \left(\sigma_{cj} \right)^{0.63} a^{0.67}. \tag{10}$$

(2) Calculation formula by Gezhouba Engineering Bureau:

$$q_l = 0.367 \left(\sigma_{cj} \right)^{0.5} d^{0.36}. \tag{11}$$

(3) Calculation formula by Wuhan Institute of Water Resources and Hydropower:

$$q_l = 0.127 \left(\sigma_{cj} \right)^{0.5} a^{0.84} \left(\frac{d}{2} \right)^{0.24}, \tag{12}$$

where q_l is the linear charge density, and the unit is kg/m, σ_{cj} is the uniaxial compressive strength of rock, which takes as 30.12 MPa, a is the presplit hole spacing, which takes as 0.8 m, and d is the hole diameter, which takes as 0.1 m. Thus, the linear charge density is about 250~800 g/m.

2.5. Blast Hole Stemming. In presplitting blasting, the quality of hole stemming has a great influence on the energy utilization of explosive, the hole wall pressure, and the action duration, especially that completely depends on the blasting quasistatic pressure to destroy the rock mass. Therefore, it is necessary to ensure that the unloading time of the full lasting of the packing is greater than that of the gas pressure in the full lasting of the charge, so as to maximize the specific impulse transmitted to the rock.

Long stemming lasting can prolong the action time of the explosive gas, but it will cause no cracks or poor quality of cracks in the packing section. If the stemming is too

(a) Digital electronic detonator with 15 m wire   (b) A380 data collector detonator

FIGURE 1: Digital electronic detonator and priming equipment.

dense, it is easy to produce blasting funnel due to the lifting effect of the explosive gas. Therefore, the following empirical formula is used to determine the stemming length:

$$l_2 = (8 \sim 20)d, \tag{13}$$

where l_2 is stemming length, and the unit is m; d is the hole diameter, and the unit is mm. Therefore, according to the engineering experience, the stemming length is 1.0 m, and it can be compacted gently.

3. Field Tests of Presplitting Blasting

3.1. Selection of Explosives. The explosive used in the presplitting blasting should meet the basic performance indices of low detonation velocity, low brisance, low density, and good detonation transmission performance. According to the decoupling coefficient and the existing explosive in the mine, the 2# rock emulsion explosive with diameter of 32 mm is selected.

3.2. Selection of Detonator. The industrial electronic detonator uses electronic delay components to achieve delay function, and it can set and modify the delay time in the application site. It contains identity information and initiation password to control initiation. It can test its own integrity and conduct two-way communication. The detonator has high reliability, high stability, and strong anti-interference performance. The delay range is $0 \sim 10000$ ms, and the minimum time interval is 1 ms. The detonator and digital electronic detonator are shown in Figure 1 as below. In this test, the digital electronic detonator with 15 m wire is adopted, and the delay accuracy is 1 ms.

3.3. Charge Structure of Blast Hole. When charging of the presplit holes, the following principles should be complied with: strengthen the charge at the bottom, keep normal charge in the middle, and weaken the charge at the top.

TABLE 2: Charge increase of reinforced charge section at the bottom of hole in presplitting blasting.

Depth of the hole L/m	<3	$3 \sim 5$	$5 \sim 10$	$10 \sim 15$	$15 \sim 20$
L_1/m	$0.2 \sim 0.5$	$0.5 \sim 1.0$	$1.0 \sim 1.5$	$1.5 \sim 2.0$	$2.0 \sim 2.5$
q_{l1} / q_l	$1.0 \sim 2.0$	$2.0 \sim 3.0$	$3.0 \sim 4.0$	$4.0 \sim 5.0$	$5.0 \sim 6.0$

Note: L_1 is the length of bottom stiffening charge section in meters; q_{l1} is the linear charge density of the reinforcement section of the presplit hole, and the unit is g/m; q_l is the linear charge density of the normal section of the presplit hole, and the unit is g/m.

The length ratio of the three sites can be taken as the experience distribution of $2:5:3$. The empirical value of the added charge amount at the bottom of the hole can be selected by referring to Table 2.

Combined with the previous production experience of the mine, the lithology of the presplitting blasting produced in the nearest mine is the same as that in this test. The 2# rock emulsion explosive is used, and the average linear charge density of the whole hole is $q_l = 450$ g/m. The designed drilling depth in this project is $L = 9$ m, and the stemming length is 1.0 m. According to the actual conditions of the down-the-hole drill in the mine, vertical holes are made. The length of bottom stiffening charge section $L_1 = 0.2 L = 1.6$ m, $q_{l1} = 4.0 q_l = 1800$ g/m; the length of middle normal charge section $L_2 = 0.5 L = 4.0$ m, $q_{l2} = q_l = 450$ g/m; the length of top weaken charge section $L_3 = 0.3 L = 2.4$ m, $q_{l3} = (1/3)$, $q_l = 150$ g/m. Therefore, the explosive quantity of a single blast hole is 5.0 kg. The charge structure of blast hole is shown in Figure 2, and the drilling and charging are shown in Figures 3 and 4, respectively.

3.4. Delay Time. Optimal delay time can not only induce the seismic waves which produced by the adjacent holes interfered with each other to reduce the blasting vibration effect, at the same time, it can also add new free faces for the post-detonation blast hole and increase the rock collision and
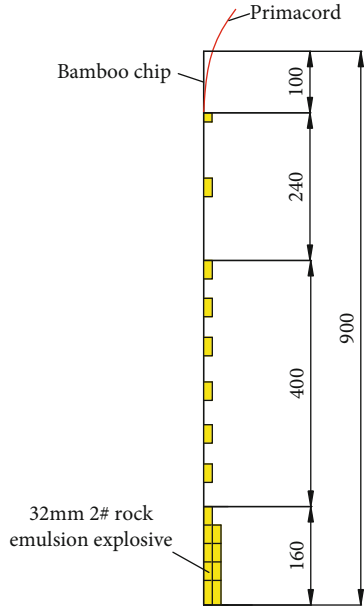
Figure 2: The charge structure of blast hole (unit: cm).

Figure 3: Down-the-hole drilling.

crushing to improve the rock blasting effect. Considering the stress wave and explosive gas energy [38], and correcting the semiempirical formula from previous study, a theoretical model of millisecond blasting delay time is obtained as follows:

$$\Delta t = t_1 + t_2 + t_3 = \frac{2W}{C_p} + \frac{2A}{V_t} + \frac{b}{V}, \quad (14)$$

$$C_p = \sqrt[2]{\frac{E(1 - \nu)}{\rho(1 + \nu)(1 - 2\nu)}}, \quad (15)$$

$$V_t = \frac{\pi r^2 C_0}{0.76Z}, \quad (16)$$

$$V = \frac{\pi r^2 a C_0}{2b\gamma Z} \left(\frac{Z}{C_0 t - H} \right)^{\gamma - a/\gamma}. \quad (17)$$

Figure 4: Air interval charging.

Table 3: Presplitting blasting parameters.

Bench height (m)	Hole depth (m)	Linear charge density (g·m^{-1})	Single hole charge (kg)	Delay time (ms)	Tilt angle (°)
9	9	450	5.0	12	90

When $r = \alpha$, the limit speed of crack propagation is as follows:

$$V_m = \frac{\pi r^2 C_0}{0.76Z}, \quad (18)$$

where Δt is the delay time, t_1 is the time of elastic stress wave propagation to free face and return, t_2 is crack formation time under explosion stress wave, t_3 is crack formation time under explosion gas pressure, W is line of least resistance, C_P is elastic longitudinal wave velocity, A is failure radius of explosion stress wave, V_t is crack propagation velocity affected by explosion stress wave, b is crack propagation width affected by explosive gas pressure, V is crack propagation velocity under explosive gas pressure, it takes $0.25V_m$, E is the elastic modulus, ν is the Poisson ratio, ρ is the density, α is the fracture length under explosive gas pressure, C_0 is the swelling pressure, which is usually taken as $1.5 \sim 2.0$ Pa, r is the blast hole radius, set as 50 mm, on the hole-by-hole detonated application, a takes 1.55, γ is the adiabatic exponent and it takes 1.4, L_b is the length of hole set as 9 m, $Z = 0.27L_b = 2.43$ m, $H = 0.83L_b = 7.6$ m. Therefore, in this test, the detonated delay time of presplit hole is taken as 12 ms.

3.5. Initiation Network. Only a row of 30 presplit holes was drilled and the hole spacing was 0.8 m, with the delay time between holes set to 12 ms. The presplitting blasting parameters of this test are shown in Table 3.

4. Blasting Effect and Analysis

4.1. Quality Evaluation of Presplitting Blasting. Half hole rate and plainness degree of slope are the main control items of

presplitting blasting quality acceptance index [39]. The acceptance quality standard of half cast factor is shown in Table 4, and the plainness degree of slope should be less than ±150 mm.

In this test, the total drilled borehole length is 277.9 m, and the total length of reminded half hole on slope is 224.3 m, while the half cast factor of the presplitting blasting is 80.7%, with the degree of flatness of 130 mm. Therefore, the comprehensive evaluation of this presplitting blasting quality is good. The local flatness of the slope surface after the blasting is shown in Figure 5.

4.2. Blasting Vibration Test. During the construction process, in order to grasp the vibration situation of the reserved slope, TC-4850 blasting vibration tester is used for vibration monitoring (as seen in Figure 6), which is produced by Chengdu Zhongke Measurement and Control Co. Ltd.

Due to the high-steep slope, the vibration velocity might demonstrate amplification effect along the elevation, which must be taken into account. According to the domestic and foreign research results, the following experience formula (19) based on the blasting vibration propagation and attenuation rule is adopted [40–43].

$$v = K \left(\frac{\sqrt[3]{Q}}{D} \right)^{\alpha} \left(\frac{\sqrt[3]{Q}}{H} \right)^{\beta}, \tag{19}$$

where Q is the maximum detonation dose per delay in kg corresponding to the peak vibration velocity; D is the horizontal distance in m between the explosion center and the measuring point; H is the altitude difference in m between the explosion center and the measuring point; K is a coefficient related to the geological conditions, blasting method, and other external causes; α is seismic wave attenuation coefficient related to the geological conditions; and β is elevation effect coefficient.

With 30 groups of blasting vibration data during 10 times construction in the final highwall of Buzhaoba west slope, binary regression analysis and calculation gives $\gamma = 0.86$, $K = 189.31$, $\alpha = 1.84$, and $\beta = 0.51$. Putting these data into the particle vibration velocity formula of west slope, the following formula can be achieved:

$$v = 189.31 \left(\frac{\sqrt[3]{Q}}{D} \right)^{1.84} \left(\frac{\sqrt[3]{Q}}{H} \right)^{0.51}. \tag{20}$$

4.3. Damping Effect. The vibration test is divided into two groups. The first group is the simultaneous detonated of presplit holes [44], and the second group is presplit holes detonated hole-by-hole [45]. Through blasting vibration monitoring, the damping effect of the two groups is evaluated.

4.3.1. Presplit Holes Simultaneous Detonated. Due to space limit, only five different groups of the maximum detonation dose per time are chosen to be used for analysis of presplitting blasting vibration reduction ratio, and the result is listed in Table 5. Here, Q is the maximum single dose of each

Table 4: Acceptance of presplitting blasting standard according to half cast factor.

Lithologic characters	Hard rock (I ~ II)	Medium-hard rock (III)	Weak rock (IV ~ V)
Half cast factor (η)	$\eta \geq 80$	$\eta \geq 60$	$\eta \geq 30$

Note: $\eta = \sum l_0 / \sum L_0$, l_0 is the total length of reminded half hole on slope, and L_0 is the total length of drilled borehole on the slope.
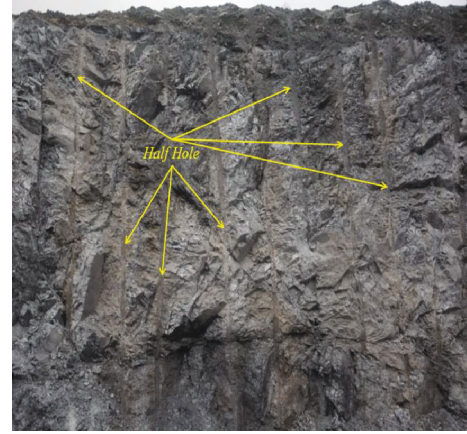
Figure 5: The slope surface smooth effect.

Figure 6: TC-4850 blasting vibration tester.

blasting, P_n is the number of measured points, D is the horizontal distance between the explosion center and the measuring point, H is the altitude difference between the explosion center and the measuring point, v_m is the measured velocity, v_t is the theoretical velocity, N is the vibration reduction rate, and N_{av} is the average damping rate.

In this site, the position is mainly located in the 1200 m level, and the measure points are, respectively, set in 1200 m, 1210 m, and 1220 m level, as shown in Figure 7.

From Table 5, it is shown that with the increase of the maximum single dose, the damping effect of the presplitting blasting is more and more significant when meeting design requirements, and the vibration reduction rate can even reach up to 40.14% with the average damping rate of 26.40%.

4.3.2. Presplit Holes Detonated Hole-by-Hole. From Table 6, it can be seen that the vibration reduction rate can even reach up to 55.38%, and the average damping rate is

TABLE 5: Comparative analysis of blasting vibration by presplit holes simultaneous detonated.

Q (kg)	P_n	D (m)	H (m)	v_m (cm/s)	v_t (cm/s)	N (%)	N_{av} (%)
	1#	70.0	1.5	2.97	4.42	32.79%	
510	2#	85.0	11.5	1.53	2.16	29.33%	31.42%
	3#	110.0	21.5	0.64	0.94	32.16%	
	1#	82.0	1.5	2.64	3.54	25.52%	
455	2#	100.0	11.5	1.30	1.47	11.44%	25.70%
	3#	123.0	21.5	0.44	0.74	40.14%	
	1#	80.0	1.0	2.75	3.47	20.78%	
443	2#	94.0	11.0	1.29	1.75	26.08%	23.30%
	3#	110.0	21.0	0.65	0.84	23.05%	
	1#	83.0	1.2	2.75	3.79	27.39%	
410	2#	110.0	11.2	0.91	1.14	19.84%	27.43%
	3#	135.0	21.2	0.44	0.68	35.05%	
	1#	85.0	0.5	2.96	3.64	18.78%	
345	2#	115.0	10.5	0.87	1.18	26.38%	24.16%
	3#	140.0	20.5	0.43	0.59	27.32%	
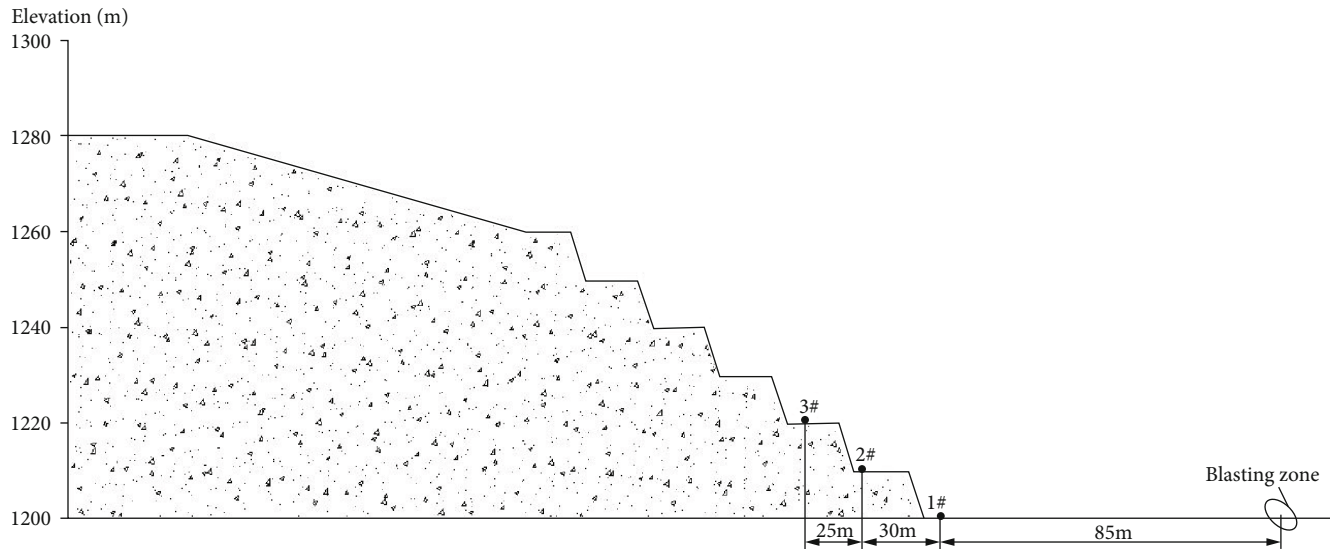
FIGURE 7: The schematic diagram of monitoring points arrangement.

TABLE 6: Comparative analysis of blasting vibration by presplit holes detonated hole-by-hole.

Q (kg)	P_n	D (m)	H (m)	v_m (cm/s)	v_t (cm/s)	N (%)	N_{av} (%)
	1#	70.0	1.0	1.78	3.98	55.25%	
446	2#	90.0	11.0	1.04	1.75	40.72%	47.36%
	3#	120.0	21.0	0.39	0.72	46.10%	
	1#	75.0	0.5	1.74	3.57	51.30%	
395	2#	100.0	10.5	0.90	1.31	31.50%	44.21%
	3#	120.0	20.5	0.33	0.66	49.84%	
	1#	90.0	1.0	1.65	2.35	29.77%	
355	2#	110.0	11.0	0.88	1.01	13.22%	32.79%
	3#	120.0	21.0	0.27	0.61	55.38%	

41.45%. When the presplit hole is detonated one by one, the vibration caused by the presplit hole blasting is reduced. Compared with the simultaneous detonated of presplit holes, the blasting vibration is reduced by 15.05%.

5. Conclusions

Based on the field test of high and steep slope mining in open-pit mine, this paper analyzed the difference between the traditional presplitting blasting and precracking hole-by-hole initiation blasting technology, and the following results are obtained:

(1) The calculation method for determining presplitting blasting parameters is summarized, and the parameters of presplitting blasting in the studied experiment site are determined as follows: hole diameter is 100 mm; cartridge diameter is 32 mm (decoupling coefficient $K_d = 3.125$); hole spacing is 0.8 m; charge density is 450 g/m; filling length is 1.0 m; and delay time between hole-by-hole is 12 ms

(2) The precise time-delay hole-by-hole initiation technology based on digital electronic detonator meets the requirements of presplitting blasting. The half-hole ratio of this test is 80.7%, and the irregularity is about 130 mm

(3) The comparison between the field measured vibration velocity value and the theoretical value under the two kinds of pre-splitting blasting schemes in the west slope shows that the average vibration reduction rate of the simultaneous presplitting blasting is 26.40%, and the vibration reduction rate of single-hole presplitting blasting can reach 41.45%. The vibration reduction effect is significant, and the wall smoothness can meet the requirements of relevant specifications

In total, it is shown that the precise delay blasting technology based on digital electronic detonator has a higher vibration reduction rate, which meets the requirements of slope wall smoothness, and has a very important significance for improving the excavation quality of open-pit to boundary slope and maintaining the long-term stability of slope.

Data Availability

The data used to support the findings of this study areincluded in the article.

Disclosure

Xianglong Li is the co-first author.

Conflicts of Interest

The authors declare that they have no conflicts of interest.

Authors' Contributions

Conceptualisation, methodology, validation, data curation, visualisation, and writing—original draft preparation were done by J.W. and J.M.; experimental guidance and data analysis were performed by X.L.; theoretical analysis was done by Q.L. and T.Z.; field test guidance was done by X.Z. and Z.T.; formal analysis writing—review and editing was done by all authors. All authors have read and agreed to the published version of the manuscript.

Acknowledgments

References

[1] J. G. Wang, L. F. Luan, Z. Y. Zhang, X. L. Li, and C. L. Fan, Eds., "Numerical simulation of blasting vibration effect on stability of high-steep slope," *Blasting*, vol. 29, no. 3, pp. 119–122, 2013.

[2] K. Zhang and P. Cao, "Slope seismic stability analysis on kinematical element method and its application," *Soil Dynamics and Earthquake Engineering. Volume*, vol. 50, pp. 62–71, 2013.

[3] X. L. Li, Q. W. Hu, X. B. Ma, K. G. Li, and J. Q. Xiao, "Experimental research on presplitting blasting of the final highwall of an opencast coal mine," *Journal of the balkan tribological association.*, vol. 22, no. 3, pp. 2857–2869, 2016.

[4] H. Tang, H. Li, Q. Zhou, X. Xia, B. Liu, and J. R. Li, "Experimental study of vibration effect of presplit blasting," *Chinese Journal of Rock Mechanics and Engineering*, vol. 29, no. 11, pp. 2277–2284, 2010.

[5] J. Hu, T. Lei, K. Zhou, and Q. F. Chen, "Effect of blasting vibration on pre-splitting crack in filling-environment," *Journal of Central South University (Science and Technology)*, vol. 42, no. 6, pp. 1704–1709, 2011.

[6] W. D. Wang, Y. Zhang, H. T. Jiang, and L. Wang, "Low cost quasi presplit blasting technology in side slope rock excavation," *Chinese Journal of Scientific Instruments*, vol. 34, no. 6, pp. 293–296, 2012.

[7] L. Wang, X. X. Li, and Y. X. Zhao, "The practice about deep hole pre-split blasting in mining faces of low permeability extra-thick seam," *Advanced Materials Research. Volume*, vol. 1792, pp. 781–785, 2012.

[8] L. Y. Yang, S. Y. Chen, A. Y. Yang, C. Huang, and H. Xie, "Numerical and experimental study of the presplit blasting failure characteristics under compressive stress," *Soil Dynamics and Earthquake Engineering*, vol. 149, p. 106873, 2021.

[9] A. K. Raina, "Influence of joint conditions and blast design on pre-split blasting using response surface analysis," *Rock Mechanics and Rock Engineering*, vol. 52, no. 10, pp. 4057–4070, 2019.

[10] W. Wang, Y. Z. Wei, M. G. Guo, and Y. Li, "Coupling technology of deep-hole presplitting blasting and hydraulic fracturing enhance permeability technology in low-permeability and gas outburst coal seam: a case study in the no. 8 mine of Pingdingshan, China," *Advances in Civil Engineering*, vol. 2021, 12 pages, 2021.

[11] L. Y. Yang, A. Y. Yang, S. Y. Chen, S. Fang, C. Huang, and H. Xie, "Model experimental study on the effects of in situ stresses on pre-splitting blasting damage and strain development," *International Journal of Rock Mechanics and Mining Sciences*, vol. 138, p. 104587, 2021.

[12] S. X. Cheng, Z. G. Ma, P. Gong, K. Li, N. Li, and T. Wang, "Controlling the deformation of a small coal pillar retaining roadway by non-penetrating directional pre-splitting blasting with a deep hole: a case study in Wangzhuang Coal Mine," *Energies*, vol. 3084, 2020.

[13] Y. Yuan, C. F. Yuan, C. Zhu, H. X. Liu, and S. Z. Wang, "Study on the disaster reduction mechanism of presplitting blasting and reasonable blasting parameters for shallowly buried remnant pillars," *Energy Science & Engineering*, vol. 7, no. 6, pp. 2884–2894, 2019.

[14] B. B. Chen, C. Y. Liu, and C. Bedon, "Analysis and application on controlling thick hard roof caving with deep-hole position presplitting blasting," *Advances in Civil Engineering*, vol. 1, 15 pages, 2018.

[15] K. Shin, L. S. Joong, and O. Choi Sung, "A study on applicability of pre-splitting blasting method according to joint frequency characteristics in rock slope," *Explosives and Blasting*, vol. 28, no. 2, 2010.

[16] Z. H. Liu, J. Yang, L. S. Yang, X. K. Ren, X. Peng, and H. Lian, "Experimental study on the influencing factors of hydraulic fracture initiation from prefabricated crack tips," *Engineering Fracture Mechanics*, vol. 250, p. 107790, 2021.

[17] K. Deng, M. Chen, W. B. Lu, P. Yan, and Z. D. Leng, "Investigation of influence of in-situ stress on presplitting induced fracture in abutment slot," *Rock and Soil Mechanics*, vol. 40, no. 3, pp. 1121–1128, 2019.

[18] Z. Zhou, R. Cheng, X. Cai, J. Jia, and W. Wang, "Comparison of presplit and smooth blasting methods for excavation of rock wells," *Shock and Vibration*, vol. 2019, Article ID 3743028, 12 pages, 2019.

[19] H. W. Ye, J. Y. Wang, and R. Tibor G, "Effect of decreasing blasting vibration by presplitting blasting and its application in open pit mines," *International Symposium on Mining Science and Safety Technology,Jiaozuo, PEOPLES R CHINA*, vol. 1, pp. 77–781, 2007.

[20] J. H. Chen, J. S. Zhang, and X. P. Li, "Study of presplitting blasting parameters and its application based on rock blasting-induced damage theory," *Rock and Soil Mechanics*, vol. 37, no. 5, pp. 1441–1450, 2016.

[21] Y. Hu, W. Lu, M. Chen, P. Yan, and J. Yang, "Comparison of blast-induced damage between presplit and smooth blasting of high rock slope," *Rock Mechanics and Rock Engineering*, vol. 47, no. 4, pp. 1307–1320, 2014.

[22] S. Xiao, H. Wang, and G. Dong, "A preliminary study on the design method for large-diameter deep-hole presplit blasting and its vibration-isolation effect," *Shock and Vibration*, vol. 2019, no. 11, Article ID 2038578, 2019.

[23] D. Shaunik and M. Singh, "Bearing capacity of foundations on rock slopes intersected by non-persistent discontinuity," *International Journal of Mining Science and Technology*, vol. 30, no. 5, pp. 669–674, 2020.

[24] Z. Tao, S. Yu, X. Yang, Y. Peng, Q. Chen, and H. Zhang, "Physical model test study on shear strength characteristics of slope sliding surface in Nanfen open-pit mine," *International Journal of Mining Science and Technology*, vol. 30, no. 3, pp. 421–429, 2020.

[25] Y. G. Zhang, Y. L. Xie, Y. Zhang, J. B. Qiu, and S. X. Wu, "The adoption of deep neural network (DNN) to the prediction of soil liquefaction based on shear wave velocity," *Bulletin of Engineering Geology and the Environment*, vol. 80, no. 6, pp. 5053–5060, 2021.

[26] A. McQuillan, I. Canbulat, and O. Joung, "Methods applied in Australian industry to evaluate coal mine slope stability," *International Journal of Mining Science and Technology*, vol. 30, no. 2, pp. 151–155, 2020.

[27] Z. Leng, Y. Fan, Q. Gao, and H. Yingguo, "Evaluation and optimization of blasting approaches to reducing oversize boulders and toes in open-pit mine," *International Journal of Mining Science and Technology*, vol. 30, no. 3, pp. 373–380, 2020.

[28] Y. G. Zhang and L. N. Yang, "A novel dynamic predictive method of water inrush from coal floor based on gated recurrent unit model," *Natural Hazards*, vol. 105, no. 2, pp. 2027–2043, 2021.

[29] I. Vennes, H. Mitri, D. R. Chinnasane, and M. Yao, "Large-scale destress blasting for seismicity control in hard rock mines: a case study," *International Journal of Mining Science and Technology*, vol. 30, no. 2, pp. 141–149, 2020.

[30] M. B. Xu and D. H. Peng, "Parameter optimization of the slope pre-splitting blasting," *Explosion and shock waves.*, vol. 28, no. 4, pp. 355–359, 2008.

[31] L. He, J. Wang, J. Xiao, L. Tang, and Y. Lin, "Pre-splitting blasting vibration reduction effect research on weak rock mass," *Disaster Advances.*, vol. 6, no. 3, pp. 338–343, 2013.

[32] X. L. Yang and M. S. Wang, "Mechanism of rock crack growth under detonation gas loading," *Explosion and Shock Waves*, vol. 21, no. 2, pp. 111–116, 2001.

[33] Q. Zong, P. J. Lu, and Q. Luo, "Theoretical study on axial decoupling coefficients of smooth blasting with air cushion charging construction[J]," *Chinese Journal of Rock Mechanics and Engineering*, vol. 24, no. 6, pp. 1047–1051, 2005.

[34] F. Wang, S. Tu, Y. Yuan, Y. Feng, F. Chen, and H. Tu, "Deep-hole pre-split blasting mechanism and its application for controlled roof caving in shallow depth seams," *International Journal of Rock Mechanics and Mining Sciences*, vol. 64, no. 4, pp. 112–121, 2013.

[35] M. Monjezi, H. A. Khoshalan, and A. Y. Varjani, "Optimization of open pit blast parameters using genetic algorithm," *International Journal of Rock Mechanics and Mining Sciences*, vol. 48, no. 5, pp. 864–869, 2011.

[36] X. M. Feng, J. Z. Zhuang, J. S. Ju, X. Jiang, and J. Yuan, "Smooth blasting hole spacing and smooth surface layer depth optimization," *Advanced Science Letters*, vol. 4, no. 8, pp. 2703–2707, 2011.

[37] W. Wang and X. C. Li, "Experimental study of propagation law of explosive stress wave under condition of decouple charge," *Rock and Soil Mechanics*, vol. 31, no. 6, pp. 1723–1728, 2010.

[38] E. Ghasemi, M. Sari, and M. Ataei, "Development of an empirical model for predicting the effects of controllable blasting parameters on flyrock distance in surface mines," *International Journal of Rock Mechanics and Mining Sciences*, vol. 52, pp. 163–170, 2012.

[39] W. H. Zhou and W. B. Jian, "Millisecond blasting optimal time delay control based on rock breaking mechanism," *Journalof Harbin Instituteof Technology*, vol. 49, no. 2, pp. 158–163, 2017.

[40] Ministry of Railways of the PRC, *Code for Smooth (Pre-Splitting) Blasting on Cutting of Railway. (TB10122-2008)*, pp. 7–9, 2008.

[41] X. H. An, K. M. Li, S. S. Xiao, and W. M. Hu, "Analysis of key technologies and development of integrated digital processing system for cast blasting design," *Journal of Central South University*, vol. 22, no. 3, pp. 1037–1044, 2015.

[42] H. F. Deng, G. D. Zhang, L. H. Wang, C. J. Deng, J. Guo, and T. Lu, "Monitoring and analysis of blasting vibration in diversion tunnel excavation," *Rock and Soil Mechanics*, vol. 32, no. 3, pp. 855–860, 2011.

[43] Y. Zhou, D. Zhao, B. Li, H. Wang, Q. Tang, and Z. Zhang, "Fatigue damage mechanism and deformation behaviour of granite under ultrahigh-frequency cyclic loading conditions," *Rock Mechanics and Rock Engineering*, vol. 54, no. 9, pp. 4723–4739, 2021.

[44] X. Z. Shi and S. R. Chen, "Delay time optimization in blasting operations for mitigating the vibration- effects on final pit walls' stability," *Soil Dynamics and Earthquake Engineering*, vol. 31, no. 8, pp. 1154–1158, 2011.

[45] Z. Y. Wang, C. Fang, Y. L. Chen, and W. Cheng, "A comparative study of delay time identification by vibration energy analysis in millisecond blasting," *International Journal of Rock Mechanics and Mining Sciences*, vol. 60, pp. 389–400, 2013.

WILEY | Hindawi

Research Article

Study on the Impact of Hydraulic Fracturing on Surrounding Ancillary Buildings considering SSI

Shishan Cheng [ID],[1] **Dewen Liu** [ID],[1] **Sitong Fang** [ID],[2] **Qianqian Wu,**[1] **Lin Liu,**[1] **Tianming Li,**[1] **Tong Shu,**[1] **and Ming Lei**[3]

[1]*College of Civil Engineering, Southwest Forestry University, Kunming 650000, China*
[2]*College of Civil Engineering, Dalian University of technology, Dalian, 116024, China*
[3]*College of Civil Engineering, Southwest Jiaotong University, Chengdu 610031, China*

Correspondence should be addressed to Dewen Liu; civil_liudewen@sina.com and Sitong Fang; 1048084186@qq.com

Hydraulic fracturing is a key technology in the development of unconventional oil and gas reservoirs. With the continuous industrialization and large-scale development of shale gas production in China, the workload of hydraulic fracturing is also increasing rapidly, and the induced seismic events are also increasing gradually, resulting in different degrees of damage to the surrounding ancillary buildings. In order to study the impact of hydraulic fracturing on ancillary buildings, the finite element software ABAQUS was used to establish a three-dimensional model of middle and high-rise isolated structures to simulate the earthquake triggered by hydraulic fracturing. Then, considering the SSI (soil-structure interaction) effect of soil-based structure, the nonlinear dynamic response of the structure under the action of ground motion was analyzed. Through the adoption of different types of soil and the foundation depth, the influence of various parameters is discussed. The study found that in the case of not considering SSI, basal shear force, and displacement between floors of the seismic-isolation structure significantly greater than considering SSI, using hard soil layer, base shear displacement is greater than the soft soil layer and interlayer, shows that due to the effect of hydraulic fracturing, making fluid diffusion in soil, the seismic energy dissipation effect. It is also found that the period, base shear, peak displacement, and interlayer displacement of deep foundation pit are increased compared with shallow foundation pit considering SSI effect.

1. Introduction

Hydraulic fracturing is a technology to improve productivity by increasing the number and degree of fractures in the fluid channel between the formation and the well. The principle is to inject fluid to low permeability rock under high-pressure state, usually water, so that rock ruptures or stimulates the existing fault or crack slip. In addition to fluid, the proppant is also injected, for example, sandstone sand, stone ceramics, to maintain the newly formed crack open, and finally releases oil and gas. The purpose of hydraulic fracturing is to make fractures without fractures, change small fractures into large ones, from less fractures to more fractures, and connect multiple fractures into mesh fractures. The cracks

of new or existing cracks get reactivated and will induce a large number of microseismic activity in the process of fracturing. And small disturbances affecting fault stability can activate the slip of nearby faults and induce higher intensity of natural seismic activity when these microseismic activities occur within tectonic areas such as plate boundaries or distributed deformation zones. The principle of hydraulic fracturing and seismic relationship is shown in Figure 1.

In recent years, with the wide application of horizontal well multistage fracturing technology in shale gas development, the increase in pore fluid pressure caused by hydraulic fracturing causes reactivation of existing tomography or cracks and induces higher strength earthquake activity has also increased significantly [1, 2]. Since 2008, Sichuan Basin
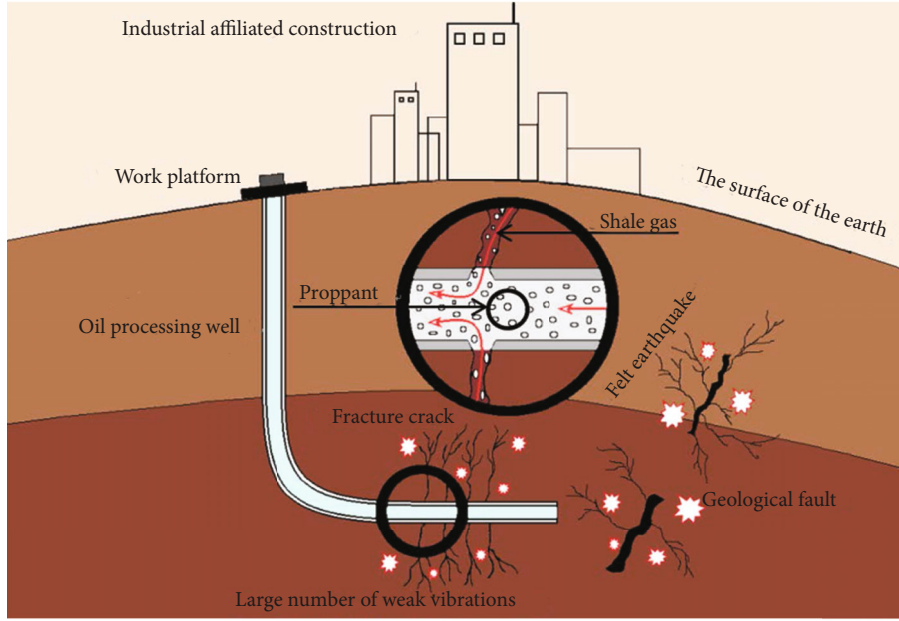
FIGURE 1: Schematic diagram of the relationship between hydraulic fracturing principle and seismic.
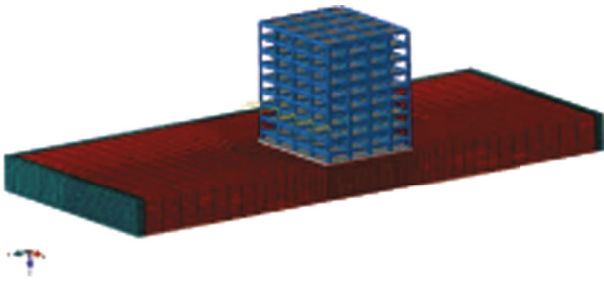
FIGURE 2: The three-dimensional numerical model of midstory isolated structure.

TABLE 1: Parameters of different foundation soil.

Number	Young's modulus (Pa)	Poisson's ratio	Cohesive forces (Pa)	Friction angle (°)	Density (kg/m^3)
1	4.8E7	0.4	22552	13.5	1835
2	2.73E8	0.35	15345	22.2	2040

TABLE 2: Boundary viscous element.

Damping ratio	Density (kg/m^3)	Young's modulus (Pa)	Poisson's ratio
$\alpha = 0.076$ $\beta = 0.053$	1E-009	0.0674	0.3

FIGURE 3: Seismic response spectrum diagram.

TABLE 3: The first six order modal periods of the structure with different soil properties.

Mode	Considering SSI effect (hard soil) (s)	Considering SSI effect (soft soil) (s)	Regardless of the SSI effect (s)
1	1.643	1.704	1.302
2	1.524	1.649	1.101
3	1.355	1.564	0.713
4	1.311	1.422	0.609
5	1.265	1.349	0.611
6	1.182	1.286	0.588

in Southwest China has exploited shale gas. Two shale gas highly enriched areas, Changning and Fuling, have been found on the eastern edge of the southern edge of the basin. On the basis of these two blocks, demonstration area construction and expansion of mining scope have been carried

(a) Seismic wave i

(b) Seismic wave ii

——— Considering SSI effects (soft soil)

——— Considering SSI effects (hardsoil)

——— Regardless SSI effects

(c) Seismic wave iii

Figure 4: Comparison of base shear with different soil properties under the effect of ground motion.

out. At the same time, the seismic frequency in this area has also increased sharply [3–5]. For example [6–9], the Junlian earthquake with magnitude 4.9, Xingwen Earthquake with magnitude 5.7, Weiyuan earthquake with magnitude 5.4 occurring in Sichuan Basin, and Red Dee earthquake with magnitude 4.2 occurring in Western Canada Basin have been proved to have a time and space correlation with the fracturing operation in the nearby horizontal well. Based on the above, it is particularly important to take necessary seismic isolation measures for industrial ancillary buildings. Since hydraulic fracturing causes vibration in the depth of the formation to cause seismic, the energy of the earthquake is transmitted to the building through the soil, so the seismic structure system considering the soil-structural interaction is more in line with the actual situation. ATC-40 [10]estab-

lished a soil spring model and defined the damping model to consider the SSI effect. Bi et al. [11] studied the comprehensive effects of spatial variation of ground motion, local site amplification, and SSI on bridge response and estimated the required separation distance that modular expansion joints must provide to avoid seismic impact. The minimum total clearance between two adjacent decks or between deck and adjacent abutment to prevent seismic shock was estimated by using the standard random vibration method to estimate the peak structural response. Numerical results show that SSI had significant influence on structural response and cannot be ignored. In [12], considering soil-structure interaction, pushover method, natural frequency, vertex limit displacement, and plastic hinge expansion were used to analyze the frame structure of a 6-story office
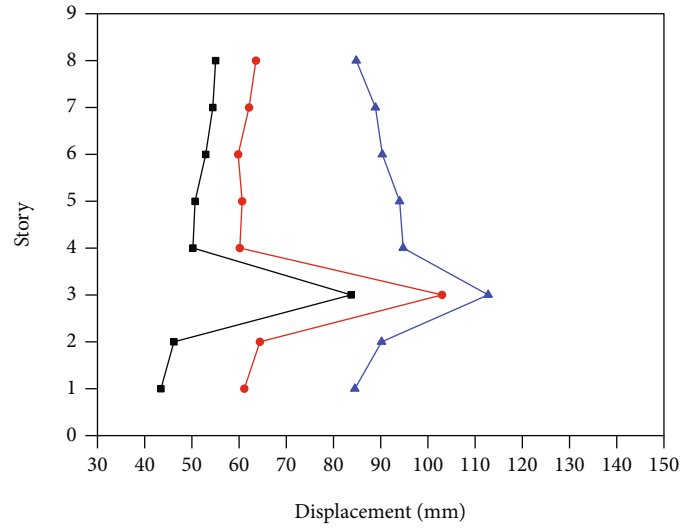
(a) Seismic wave i
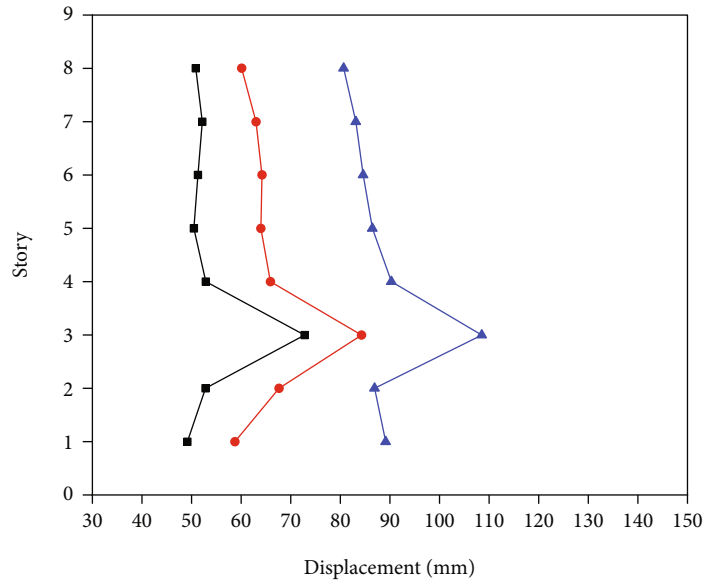
(b) Seismic wave ii

Figure 5: Continued.

(c) Seismic wave iii
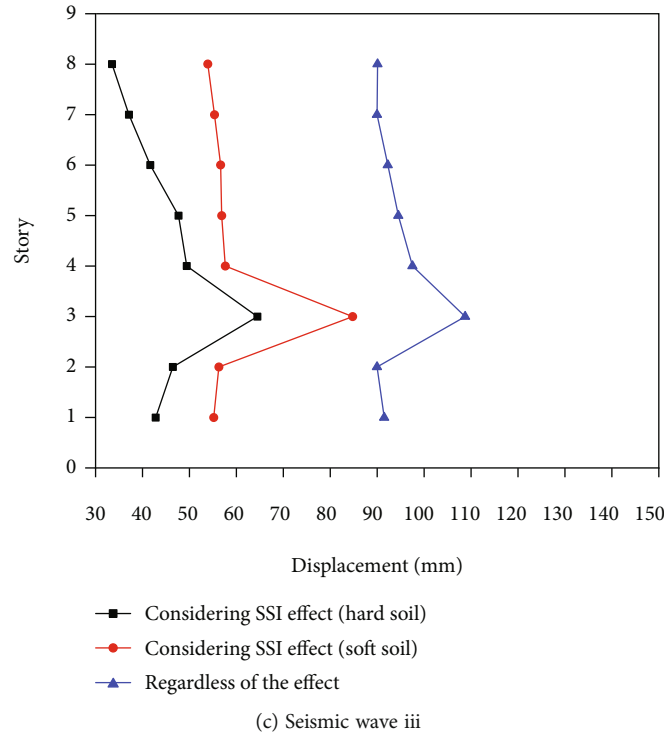
FIGURE 5: Comparison of story displacement with different soil properties under the effect of ground motion.

building under the assumption of rigid foundation. The results show that considering soil-structure interaction, the natural vibration period of RC frame structure became longer, and more hinges appeared at the bottom of column with the increase of vertex displacement. In [13, 14], a simple three-dimensional model was presented for the linear interaction analysis of fully coupled soil-pile-structure system under harmonic shear seismic waves. By comparing the amplification of coupling system with the amplitude amplification of free site surface response to bedrock vibration, it was proved that the dynamic interaction of coupling system cannot be neglected in the dynamic analysis and design of stacking structure. This was the basis for detailed numerical analysis and experimental study of soil-pile-structure dynamic interaction. Grange et al. [15] proposed a numerical strategy to simulate a three-hole viaduct made of prestressed concrete, showing the influence of soil-structure interaction (SSI). The research results show that SSI was a complex phenomenon and caused the structure of the displacement and internal force, and it was difficult to predict the displacement and internal force and linear method. At the same time, the influence of near-fault vertical ground motion on building seismic response had also become an important consideration [16]. Liu et al. [17] used isolators with quasizero stiffness and vertical dampers to control vertical earthquakes near faults. The results show that increasing the vertical period and damping ratio could make the vertical isolated structure perform well in reducing the swaying response of the structure.

The above research focuses on the seismic and isolation system of the damage effect of hydraulic fracturing on underground rock strata and the structural seismic effect, while the research on the soil structure seismic effect caused by hydraulic fracturing is very limited. Therefore, a seismic isolation structure model considering the SSI effect is established in this paper to reveal the seismic response of the isolated structure in the case of earthquakes caused by hydraulic fracturing.

2. The Finite Element Model

2.1. Project Overview. An 8-story seismic isolation frame structure model is established. The site fortification intensity is 8 degrees, the site category is second class, and the design earthquake group is second group. In the frame structure system, the seismic isolation layer is on top of the second story. The column concrete strength model is C40, the beam concrete strength model is C30, the longitudinal reinforcement model is HRB400 with a design value of tensile strength and compressive strength is $360 \, \text{N/mm}^2$, and the stirrup model is HRB335 with a design value of $270 \, \text{N/mm}^2$ for tensile and compressive strength. The raft foundation was adopted, the upper structure damping ratio is 0.05, the soil damping ratio of the foundation is 0.1 [18], and Rayleigh damping is adopted. Because even the shear waves are assumed to propagate vertically in the soil, kinematic interactions will occur in structures with embedded foundations, and this paper used two different soil layers of the raft foundation to simulate the seismic response of the structure encountering the earthquake. Figure 2 shows the three-dimensional finite element model of the structure. Table 1 shows the parameters of soil below the foundation, number 1 represents the soft soil layer, and number 2 represents the hard soil layer. Considering the unconfined

S, Mises
Multiple section points
(avg: 75%)

+2.492e−01
+9.000e−04
+8.250e−04
+7.500e−04
+6.750e−04
+6.000e−04
+5.250e−04
+4.500e−04
+3.750e−04
+3.000e−04
+2.250e−04
+1.500e−04
+7.500e−04
+0.000e+00

(a) Considering SSI effect (hard soil)

S, Mises
Multiple section points
(avg: 75%)

+2.492e−01
+9.000e−04
+8.250e−04
+7.500e−04
+6.750e−04
+6.000e−04
+5.250e−04
+4.500e−04
+3.750e−04
+3.000e−04
+2.250e−04
+1.500e−04
+7.500e−04
+0.000e+00
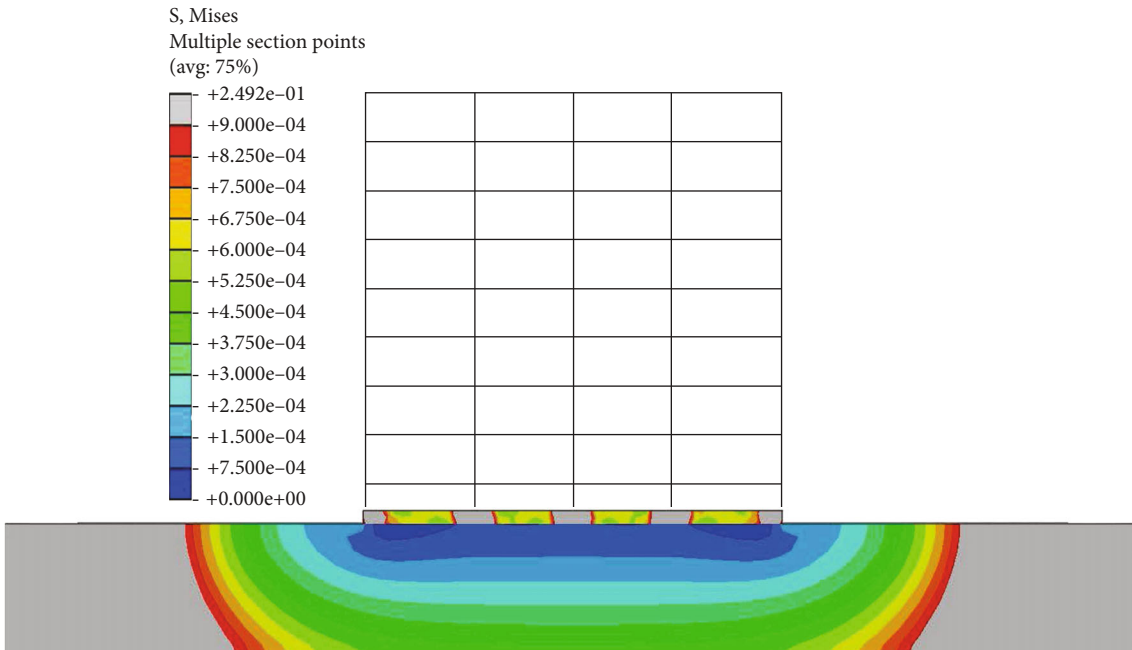
(b) Considering SSI effect (soft soil)

FIGURE 6: Stress of soil with different soil properties under ground motion.

condition of soil, Young's modulus was adopted. Table 2 lists the cohesive boundary parameters.

During the simulation, the beams and columns of the model adopt beam units, the floor slab adopts shell units, the foundation adopts solid units, they are bound by the tie, and coacting nodes adopt a coupling connection. The simulated soil is filled in a rectangle about 16 times the square plan, 400 m in length, 300 m in width, and 30 m in depth. The viscoelastic boundary was used to absorb the seismic wave at the boundary of the soil [19]. Seismic waves are applied at the bottom of the bedrock to produce seismic effects on the structure and soil. Nonlinear springs were used to simulate seismic isolation bearings [20].

2.2. Ground Motion Data Sets. The maximum fortification acceleration of the site is 0.2 g, and the impact coefficient of fortification is 0.45. The acoustic emission recorder could collect the acoustic emission parameters in the process of

(a) Considering SSI effect (hard soil)

(b) Considering SSI effect (soft soil)
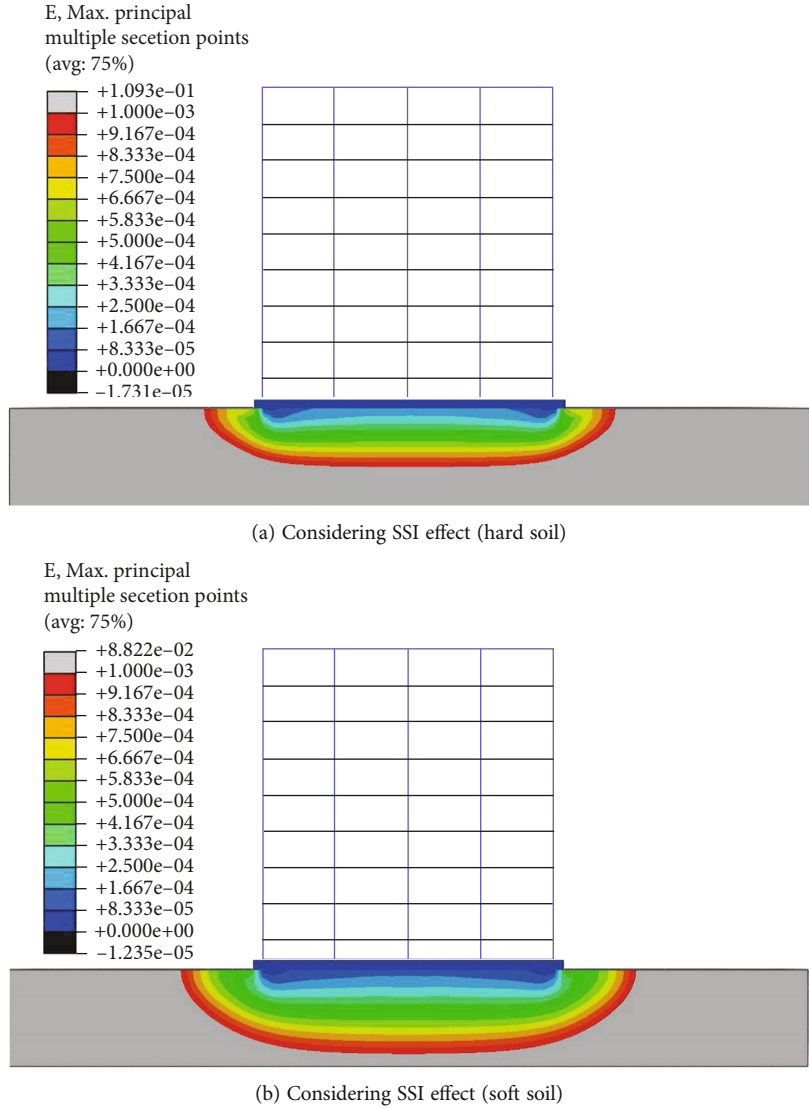
Figure 7: Strain of soil with different soil properties under the effect of ground motion.

Table 4: The first six order modal periods of the structure with different soil properties with different foundation buried depths.

Mode	Shallow-buried foundation (s)	Deep-buried foundation (s)	Regardless of the SSI effect (s)
1	3.631	3.503	3.225
2	3.013	2.822	2.737
3	2.571	2.419	2.333
4	2.402	2.404	2.171
5	1.833	1.835	1.524
6	1.721	1.721	1.325

reservoir rock fracture. By simplifying the waveform of parameters such as energy, amplitude, duration, and rise time, it could simulate the amplitude, frequency, phase, and other parameters of seismic wave generated by different lithology, summarize the characteristics of fracture signal, and establish the template of seismic signal generated by dif-ferent types of rock sample fracture. For example, Zhou et al. [21] measured the full-field deformation data of granite samples under different loading amplitudes, obtained the threshold value of rock breakage under ultrasonic vibration, and reproduced the process of crack initiation and propagation through numerical simulation. In the process of hydraulic fracturing, the small fracture of soil and rock will gradually become larger fracture [22]. Compared with the natural seismic wave, the vibration wave generated by hydraulic fracturing would migrate to the low-frequency part with the aggregation of microfracture and the expansion of crack, and the larger the crack, the lower the frequency. Therefore, the frequency of source signal decreased exponentially with the increase of radius [23]. In this study, according to the hydraulic fracturing sites monitored by acoustic emission recorder, three relatively stable vibration energy waves were selected to simulate the energy release of seismic waves, which were denoted as seismic waves i, seismic wave ii, and seismic wave iii, respectively. At the

(a) Seismic wave i

(b) Seismic wave ii

———— Shallow-buried foundation
———— Deep-buried foundation
———— Regardless of the SSI effects

(c) Seismic wave iii
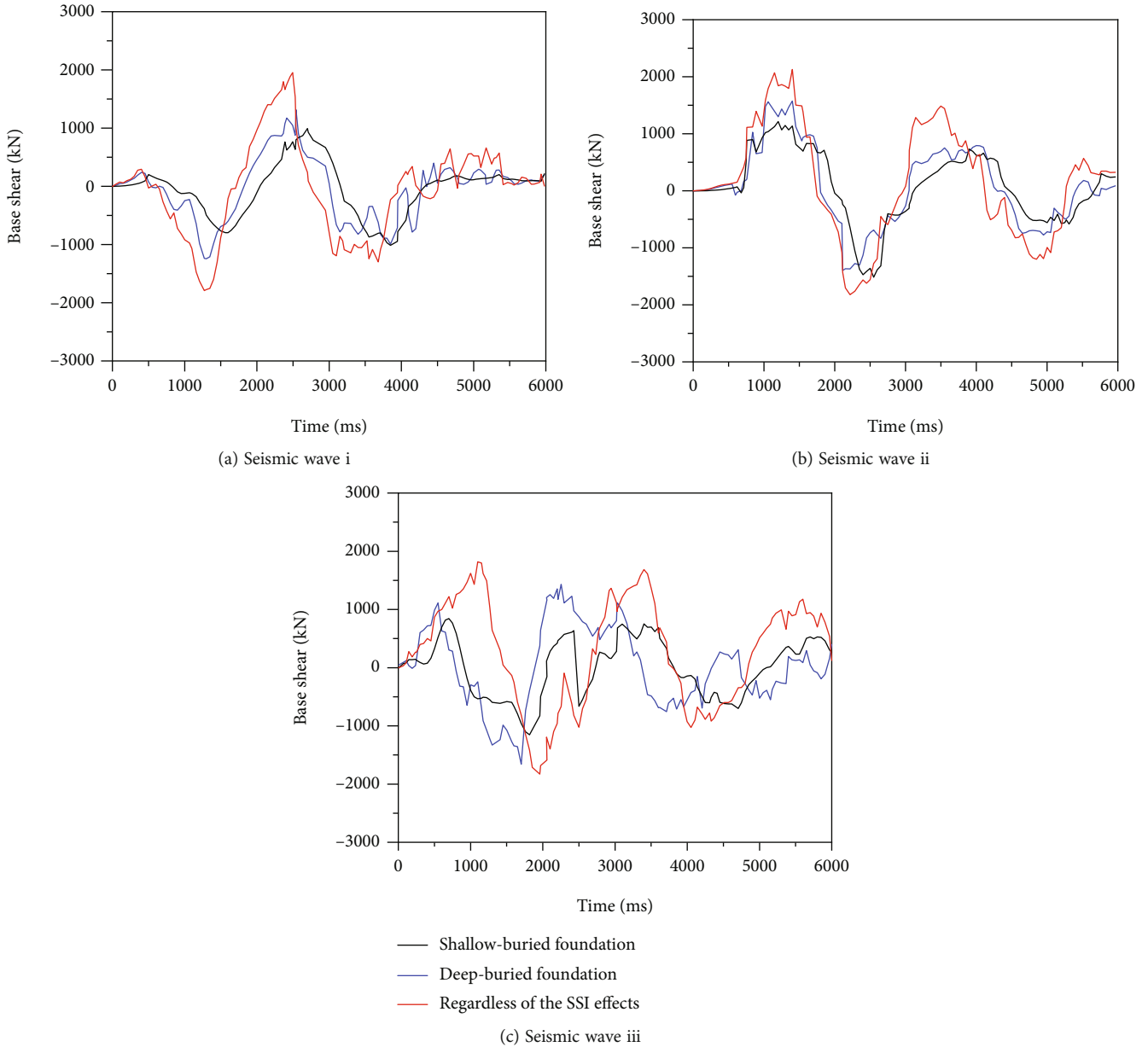
FIGURE 8: Comparison of base shear with the different buried depth of foundation under the effect of ground motion.

same time, soil liquefaction had been recognized as one of the factors causing natural disasters and engineering damage in earthquake disasters [24–27], so the seepage effect of rock bottom fluid on hydraulic fracturing fractures was also considered. Figure 3 shows the response spectra of the three seismic waves.

3. Seismic Response of the Isolated Structure

3.1. Seismic Response of the Isolated Structure with Different Soils.
The modal periods of the isolated structure when the basement adopted different properties of soil are shown in Table 3.

It can be seen from Table 3 that for the soft soil basement, the natural period of the isolated building was greater

than that of the hard soil basement. The period of the overall system was the smallest without considering the SSI effect. When considering the SSI effect, the harder the soil is, and the larger the shear wave speed of the soil is. By setting different soil shear wave speeds, the soil with different hard degrees was simulated, and the corresponding different periods were obtained. It was found that the effect of softness on the period value became more and more obvious, indicating that the soil has the effect of seismic isolation. The elastoplastic time history analysis of the structure under three kinds of rare earthquakes was carried out, and the corresponding base shear force of the structure with different properties of soil is shown in Figure 4.

It can be seen that without considering the SSI effect, the base shear force was significantly greater than that
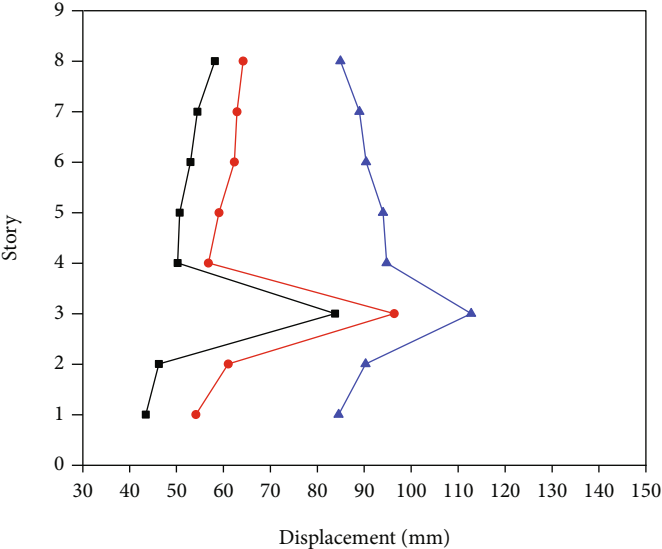
(a) Seismic wave i
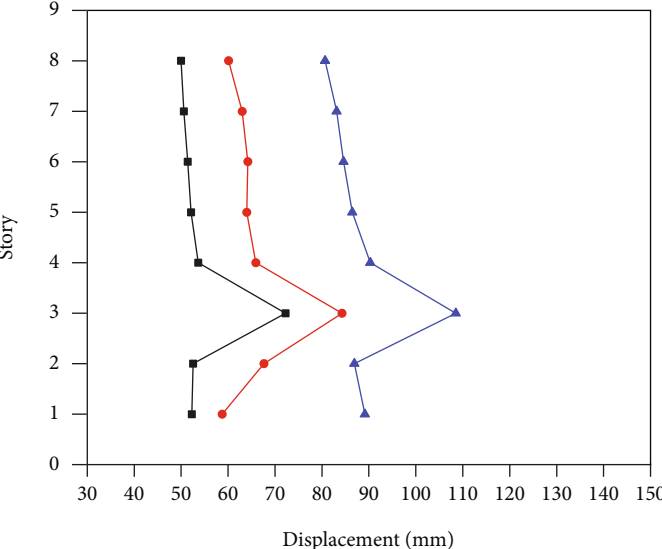
(b) Seismic wave ii

Figure 9: Continued.

(c) Seismic wave iii
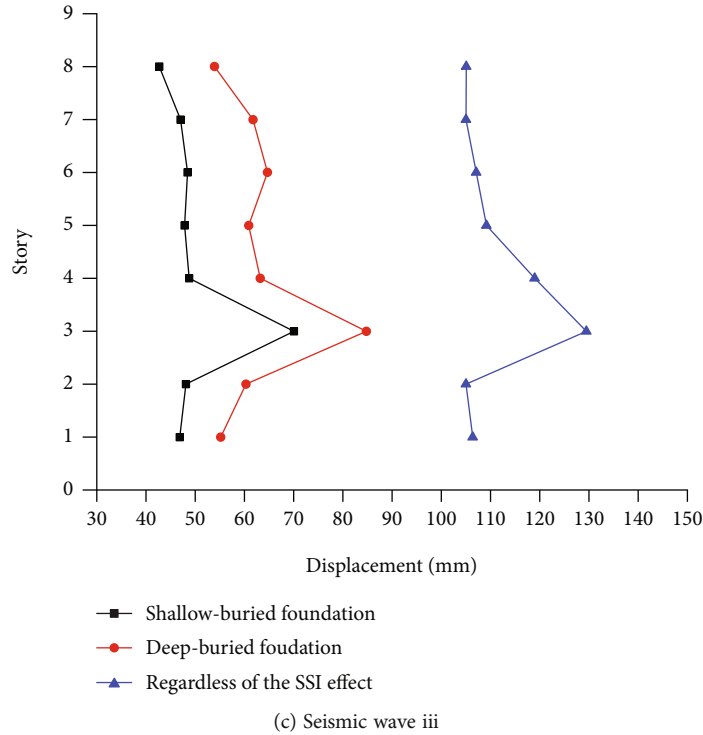
FIGURE 9: Comparison of story displacement with the different buried depth of foundation under the effect of ground motion.

(a) Shallow-buried foundation

(b) Deep-buried foundation
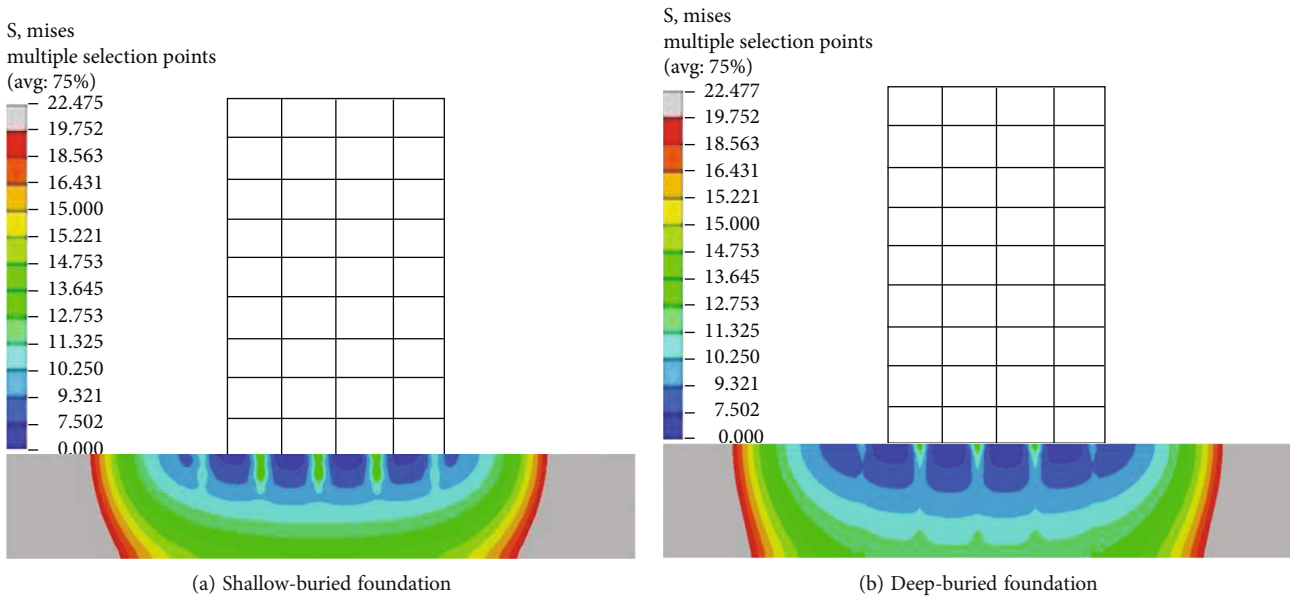
FIGURE 10: Stress of soil with the different buried depth of foundation under the effect of ground motion.

considering SSI, and when the base was made of hard soil, the shear force was greater than that of soft soil. The story displacement under the condition of three kinds of seismic waves is shown in Figure 5.

As shown in Figure 5, under conditions of three kinds of seismic waves, the seismic response analysis of the midstory isolated structure considering the SSI effect was conducted; the results showed that the displacement of the layer 3 increased dramatically under different ground motion effects, which is because the isolation layer in the structural

model is located at the third story, and the seismic isolation bearing used to simulate the seismic isolation layer deformed greatly. Without considering the SSI effect, the story displacement was obviously greater than considering the SSI, indicating that the isolation structure considering the SSI effect has a better shock absorption effect. However, under the seismic wave, the different softness of the foundation soil made the filtering effect of the midstory isolated structure considering the SSI effect obviously different. When hard soil was used as the base, the interlayer displacement of the

(a) Shallow-buried foundation   (b) Deep-buried foundation
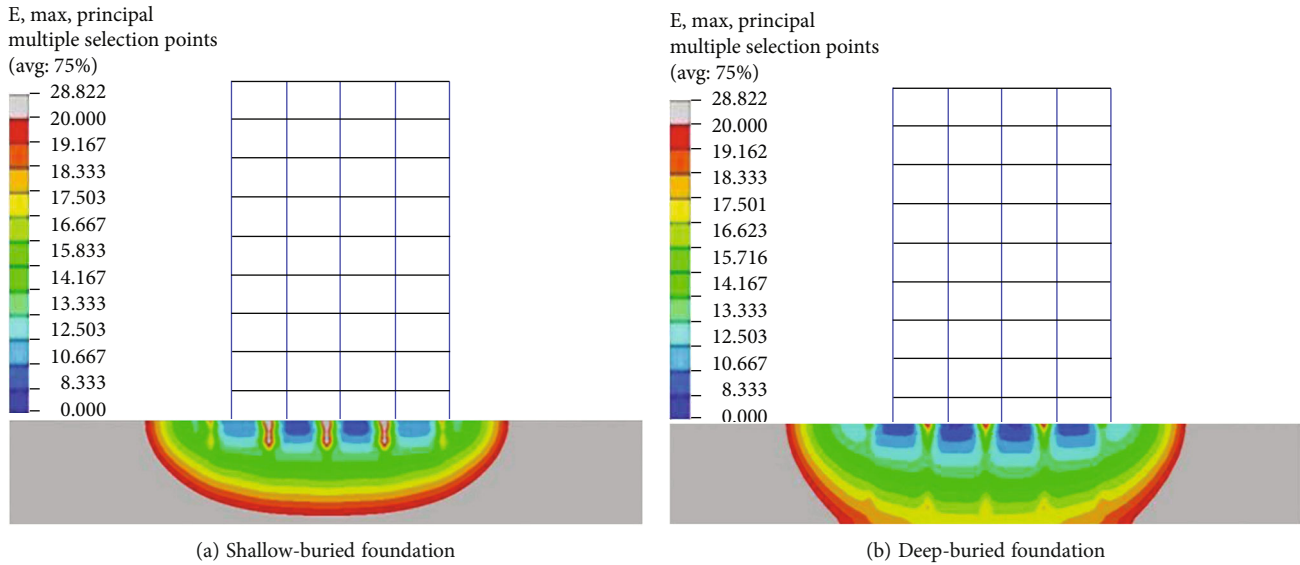
FIGURE 11: Strain of soil with different buried depth of foundation under ground motion.

structure was larger than that of soft soil, which indicates that the filtering effect of soft soil is obviously better than that of hard soil. Under the effect of ground motion, the stress and strain of soils with different properties are shown in Figures 6 and 7.

As shown in Figures 6 and 7, when soils with different properties were used as the basement, the stress and strain of the soil were different. As the stiffness of the soil increased, the stress and strain of the soil layer in the basement became greater.

3.2. Seismic Response of the Isolated Structure with Different Foundation Burial Depths.
Considering the SSI effect, the modal period of the isolated structure with different foundation buried depths is shown in Table 4, in which the buried depth of the top surface of the shallow buried foundation is 50 cm, and that of the deep buried foundation is 150 cm.

According to Table 4, considering the SSI effect, the period of the first two order modes of the deep-buried foundation was smaller than that of the shallow-buried foundation, and the period value of the higher-order structure was similar. The seismic responses of foundations with different buried depths under three seismic waves are shown in Figure 8.

Figures 6 and 7 show that without considering the SSI effect, the seismic response was significantly greater than that considering the SSI effect, and the base shear value of the structure with the shallow buried foundation was lower than that of the deeply buried foundation, this is because that the deep-buried foundation provided more constraints around the foundation on the structure, strengthening the constraint effect on the structure, reducing the rotation of the foundation and increasing the acceleration transmitted. Under three seismic waves, displacement responses of structures with different foundation burial depths are shown in Figure 9.

Figures 8 and 9 show that without considering SSI, the structural displacement response was significantly larger than that considering SSI, and for the deeply buried foundation, the displacement of each layer of the structure was larger than that shallow buried foundation. For the different buried depths of the foundation, the stress of the structure and stress and strain of soil under the effect of ground motion are shown in Figures 10 and 11.

As Figures 10 and 11 show, under the action of raft foundation, there was little difference in stress between the structure of deeply buried and shallow buried foundations, while compared with the shallow buried foundation, the soil stress and strain of deep-buried foundation were greater, and the action range was wider, which means that the stress field and strain field were different for different foundation.

4. Conclusion

In this paper, the vibration generated by hydraulic fracturing is used to simulate the earthquake, the isolation structure model considering SSI effect is established, the nonlinear response and seismic response law of the lower isolation structure are studied and analyzed, and the following conclusions are drawn:

(1) The fluid in the hydraulic fracturing effect spread to the soil, and make the role of soft soil has absorption dissipation of earthquake energy

(2) Considering the SSI effect, when hard soil was used as the basement, the structural base shear force and story displacements were larger than that of soft soil

(3) Under different seismic waves, the seismic response considering the SSI effect is smaller than that without considering the SSI

(4) Considering the SSI effect, for the deeply buried foundation, the structural base shear force and story displacements were larger than the shallow buried foundation

Data Availability

All data included in this study are available upon request by contact with the corresponding author.

Conflicts of Interest

The authors declare that there is no conflict of interests regarding the publication of this paper.

Acknowledgments

References

[1] G. M. Atkinson, D. W. Eaton, H. Ghofrani et al., "Hydraulic fracturing and seismicity in the western Canada sedimentary basin," *Seismological Research Letters*, vol. 87, no. 3, pp. 631–647, 2016.

[2] R. Schultz, R. Wang, Y. J. Gu, K. Haug, and G. Atkinson, "A seismological overview of the induced earthquakes in the Duvernay play near Fox Creek, Alberta," *Journal of Geophysical Research Solid Earth*, vol. 122, no. 1, pp. 492–505, 2017.

[3] Y. Tan, J. Hu, H. Zhang et al., "Hydraulic fracturing induced seismicity in the southern Sichuan Basin due to fluid diffusion inferred from seismic and injection data analysis," *Geophysical Research Letters*, vol. 47, no. 4, 2020.

[4] M. Wang, H. Yang, L. Fang et al., "Shallow faults reactivated by hydraulic fracturing: the 2019 Weiyuan earthquake sequences in Sichuan, China," *Seismological Research Letters*, vol. 91, no. 6, pp. 3171–3181, 2020.

[5] H. Yang, P. Zhou, N. Fang et al., "A shallow shock: the 25 February 2019 ML 4.9 earthquake in the Weiyuan shale gas field in Sichuan, China," *Seismological Research Letters*, vol. 91, no. 6, pp. 3182–3194, 2020.

[6] X. Lei, D. Huang, J. Su et al., "Fault reactivation and earthquakes with magnitudes of up to Mw4.7 induced by shale-gas hydraulic fracturing in Sichuan Basin, China," *Scientific Reports*, vol. 7, no. 1, p. 7971, 2017.

[7] X. Lei, Z. Wang, and J. Su, "The December 2018 ML 5.7 and January 2019 ML 5.3 earthquakes in south Sichuan Basin induced by shale gas hydraulic fracturing," *Seismological Research Letters*, vol. 90, no. 3, pp. 1099–1110, 2019.

[8] X. Lei, J. Su, and Z. Wang, "Growing seismicity in the Sichuan Basin and its association with industrial activities," *Science China Earth Sciences*, vol. 63, no. 11, pp. 1633–1660, 2020.

[9] R. Schultz and R. Wang, "Newly emerging cases of hydraulic fracturing induced seismicity in the Duvernay East Shale Basin," *Tectonophysics*, vol. 779, article 228393, 2020.

[10] C. D. Comartin, R. W. Niewiarowski, S. A. Freeman, and F. M. Turner, "Seismic evaluation and retrofit of concrete buildings: a practical overview of theATC 40document," *Earthquake Spectra*, vol. 16, no. 1, pp. 241–261, 2000.

[11] K. Bi, H. Hong, and N. Chouw, "Influence of ground motion spatial variation, site condition and SSI on the required separation distances of bridge structures to avoid seismic pounding," *Earthquake Engineering & Structural Dynamics*, vol. 40, no. 9, pp. 1027–1043, 2011.

[12] Z. Wangxi, L. Rui, C. Yadong et al., "Study on aseismic performance of reinforced concrete frame structures considering the soil-footing-structure interaction," *Earthquake Engineering and Engineering Vibration*, vol. 39, no. 4, pp. 86–97, 2019.

[13] S. Shang, X. Zou, and W. Cao, "Experimental investigation on soil-structure interaction of steel frame-raft foundation," *Journal of Building Structures*, vol. 33, no. 9, pp. 74–80, 2012.

[14] H. Ren, S.-P. Shang, G. Li, and J. Yu, "Simplified analysis on dynamic linear soil-pile-structure interaction," *Journal of Hunan University*, vol. 34, no. 11, pp. 6–11, 2007.

[15] S. Grange, L. Botrugno, P. Kotronis, and C. Tamagnini, "The effects of soil–structure interaction on a reinforced concrete viaduct," *Earthquake Engineering & Structural Dynamics*, vol. 40, no. 1, pp. 93–105, 2011.

[16] D. Liu, Y. Liu, D. Sheng, and W. Liao, "Seismic response analysis of an isolated structure with QZS under near-fault vertical earthquakes," *Shock and Vibration*, vol. 2018, Article ID 9149721, 12 pages, 2018.

[17] D. Liu, Y. Zhang, S. Fang, and Y. Liu, "Horizontal-vertical-rocking coupled response analysis of vertical seismic isolated structure under near-fault earthquakes," *Shock and Vibration*, vol. 2020, Article ID 6519808, 10 pages, 2020.

[18] W. Chen, L. W. Kong, and J. Q. Zhu, "A simple method to approximately determine the damping ratio of soils," *Rock and Soil Mechanics*, vol. 28, pp. 789–791, 2007.

[19] J.-T He, H. Ma, B.-Y. Zhang, and H.-Q. Chen, "Method and realization of seismic motion input of viscous-spring boundary," *Journal of Hydraulic Engineering*, vol. 41, no. 8, pp. 960–969, 2010.

[20] R. Lin, W. Liu, S. Wang, and D. Du, "Numerical simulation of nonlinear characteristics of isolation bearing," *World Earthquake Engineering*, vol. 30, no. 3, pp. 240–246, 2014.

[21] Y. Zhou, D. Zhao, B. Li, H. Wang, Q. Tang, and Z. Zhang, "Fatigue damage mechanism and deformation behaviour of granite under ultrahigh-frequency cyclic loading conditions," *Rock Mechanics and Rock Engineering*, vol. 54, no. 9, pp. 4723–4739, 2021.

[22] G. Nolet, *Quantitative Seismology, Theory and Methods*, Elsevier, 1980.

[23] E. J. Kaiser, *A Study of Acoustic Phenomena in Tensile Test [Ph.D. thesis]*, Technische Hochschule München, Munich, Germany, 1959.

[24] Y. Zhang, Y. Xie, Y. Zhang, J. Qiu, and S. Wu, "The adoption of deep neural network (DNN) to the prediction of soil liquefaction based on shear wave velocity," *Bulletin of Engineering Geology and the Environment*, vol. 80, no. 6, pp. 5053–5060, 2021.

[25] X. Liu, D. Fan, Y. Tan et al., "Failure evolution and instability mechanism of surrounding rock for close-distance parallel chambers with super-large section in deep coal mines," *International Journal of Geomechanics*, vol. 21, no. 5, p. 04021049, 2021.

[26] X. Liu, D. Fan, Y. Tan et al., "New detecting method on the connecting fractured zone above the coal face and a case study," *Rock Mechanics and Rock Engineering*, vol. 54, no. 8, pp. 4379–4391, 2021.

[27] X. Liu, S. Song, Y. Tan et al., "Similar simulation study on the deformation and failure of surrounding rock of a large section chamber group under dynamic loading," *International Journal of Mining Science and Technology*, vol. 31, no. 3, pp. 495–505, 2021.

Research Article

Experimental Study on Optimization of Polymer Preslug Viscosity of ASP Flooding in Interlayer Heterogeneous Well Group Artificial Sandstone Core

Qiji Sun [1,2] **Kesen Yang,**[1,2] **Guomin Xu** [3] **Shunde Yin** [4] **and Chunsheng Wang** [1,2]

[1]*School of Petroleum Engineering, Northeast Petroleum University, Daqing 163318, China*
[2]*Key Laboratory of Enhanced Oil Recovery(Northeast Petroleum University), Ministry of Education, Daqing 163318, China*
[3]*PetroChina Daqing Oilfield Co. Ltd., Daqing 163318, China*
[4]*Department of Civil and Environmental Engineering, University of Waterloo, Waterloo, ON, Canada N2L 3G1*

Correspondence should be addressed to Qiji Sun; sunqiji@nepu.edu.cn, Guomin Xu; xuguomin@petrochina.com.cn, Shunde Yin; shunde.yin@uwaterloo.ca, and Chunsheng Wang; wangchunsheng@nepu.edu.cn

An artificial sandstone core model of large well group of positive rhythmic heterogeneous reservoir was designed and made for the simulation of ASP flooding experiment in the moderate heterogeneous reservoir. The well layout of one injection and one production was employed for the core model, to simulate the influence of polymer preslugs with different viscosity on ASP flooding effect. The experimental results show that the injectability of the polymer preslug and the effect of relieving the conflict of remaining oil production in each layer are related to the viscosity of the system. In the heterogeneous core model with the coefficient of variation of 0.65, under the constraint of the same amount of polymer agent, the ASP flooding effect of the 0.075 PV, 60 mPa·s polymer preslug was better than that of the 0.093 PV, 40 mPa·s and 0.064 PV, 80 mPa·s polymer preslugs. The change in the viscosity of the polymer preslug did not enable the ASP system to effectively exploit the low-permeability layer though. As the viscosity increased, the pressure difference between injection and production increased; the remaining oil could be exploited effectively at the bottom of the high-permeability layer and the medium-permeability layer as well as the injection end of the medium-permeability layer. If the viscosity is too small, the high-permeability area cannot be effectively blocked by the injected chemical agent, and if the viscosity is too large, the injected chemical agent cannot produce good elastic displacement relationship, which will lead to ineffective chemical agent flow. Therefore, the polymer preslug viscosity of the ASP flooding system should be moderate, and cores with different heterogeneity should have a reasonable viscosity matching range.

1. Introduction

As a major oilfield in China, Daqing Oilfield has entered the stage of tertiary oil recovery with high water cut after 62 years of exploitation [1–3]. The development of conventional homogeneous high-permeability reservoirs using alkali/surfactant/polymer (hereinafter referred to as ASP) ternary compound chemical flooding system can enhance oil recovery by more than 20% for water flooding [4–6]. In recent years, due to the increasing cost of chemical agents and the application of ASP flooding in heterogeneous reservoirs, the

injection mode of multislug chemical agent combination or the multislug alternate injection of chemical agents of different viscosity systems is adopted in the field test area to save costs [7, 8].

In low-permeability reservoirs with fractured development, Algharaib et al. [9] reduced the loss of alkali agents and the loss of surfactant adsorption in the ASP system by the injection of polymer preslugs and also proved that the polymer preslug can adjust the displacement profile, so that the ASP system can further enter areas that are not affected in the water flooding stage. For highly saline reservoirs, a

large number of preflush slugs are required prior to chemical flooding to reduce the loss of chemical agents by highly saline water in the reservoir. Therefore, the use of various types of slugs before main agent injection can provide protection of chemical main agent [10–12]. Khan et al. carried out the alternate injection scheme of high-viscosity slug and low-viscosity slug [13]. The study shows that the alternate multislug injection enhanced oil recovery by more than 2% over single-slug injection and reduced polymer consumption by about 15%. That is, multislug injection is conducive to enhancing oil recovery and saving the use of chemical agents. For areas with severely developed reservoir heterogeneity (medium heterogeneity: 0.5-0.7, strong heterogeneity: >0.7), the cost input of chemical flooding is more risky [14–16]. Therefore, polymer protection slugs are added before and after ASP main and secondary slugs, to ensure that the ASP slugs enter the remaining oil-rich area and avoid the dominant channel after water flooding [17, 18]. Hou et al. defined the critical displacement viscosity ratio (ratio of displacement fluid viscosity to crude oil viscosity) through a large number of laboratory experiments and studied the viscosity matching between heterogeneous reservoir and ASP system [19]. Shedid optimized the concentration and length of each ASP slug in low-permeability carbonate reservoirs and demonstrated the effectiveness of ASP flooding system in low-permeability carbonate reservoirs [20]. The results show that the higher the degree of reservoir heterogeneity, the higher the viscosity ratio of the optimal displacement fluid to reservoir fluid required for profile adjustment [21–23]. When the viscosity ratio of polymer system to underground crude oil reaches 3.0 or more, the polymer system has a stronger ability to expand the swept volume and improve the oil displacement efficiency [24–26].

In this paper, by taking the polymer preslug in the ASP multislug flooding system as the main research objective, the effect of preslugs with different polymer concentrations on chemical flooding recovery was mainly considered under the same agent cost (that is, the same amount of polymer). In this paper, the effect of polymer preslugs with different viscosity on the recovery factor of ASP flooding was investigated, with a particular focus on multislug ASP flooding in a three-layer heterogeneous large-scale well group made of artificial sandstone cores of different permeabilities. The optimal polymer preslug injection viscosity of the heterogeneous reservoir rich in remaining oil in Daqing Oilfield was investigated and demonstrated. At the same time, this paper discusses in detail the preparation of the artificial sandstone core model of large well group and the parts, component proportion, and manufacturing technology needed in the preparation process, which improves the quality of core processing and makes the core preparation process and details more scientific. With the development of oil fields, several projects have proposed the method of fracturing to tap more potential after ASP flooding [27, 28]. The simulation of the artificial sandstone core displacement experiment has gradually changed from the simple displacement method to the study of displacement method considering complex stress conditions and fracture conditions [29–31].

2. Preparation of the Artificial Sandstone Core Model of Large Well Group

The artificial sandstone core model of large well group was a cemented curing model, which was mainly composed of quartz sand and epoxy resin mixed in proportion and solidified after compaction by hydraulic press. The finished model is shown in Figure 1. The vertical heterogeneity of each layer in the core model was mainly controlled by the particle size of quartz sand and the amount of epoxy resin. The permeability variation range of cores with the same composition can be controlled within 20~50 mD only by the size and duration of compaction pressure.

The purpose of establishing reservoir physical model is to make the oil saturation distribution in the model conform to the real underground situation, which is complicated and affected by many factors. In general, the physical model should be as close to the actual oilfield as possible in geometric conditions, physical conditions, boundary conditions, and initial conditions. Some of these conditions, such as model length, production pressure difference, and oil-water viscosity ratio, can be directly controlled and selected. However, it is relatively difficult to control the gas permeability of the artificial sandstone core model, and the core permeability should be consistent with the field permeability in the physical experiment. The main factors affecting the permeability of artificial cores are the particle size of sand, the intergranular porosity, and the amount of cementing agent. Therefore, before the physical experiment, a large number of artificial sandstone core models should be made for permeability testing so as to find the appropriate sand diameter ratio, compaction pressure and time, and the dosage of cementing agent. The results of a large number of artificial sandstone core production show that under the same compaction pressure and sand dosage, increasing the particle size of sands and reducing the dosage of cementing agent can keep the porosity unchanged and improve the gas permeability of the core. The artificial sandstone core model (shown in Figure 1) used the same porosity as the oilfield prototype, the same polymer solution, alkali, surfactant, and the same crude oil and remained geometrically similar in size. Model parameters for physical simulation calculated based on oilfield prototype parameters are shown in Table 1.

3. Artificial Sandstone Core Making Method

The artificial sandstone core model of large well group was 500 mm long, 500 mm wide, and 45 mm high. The vertical three layers had heterogeneous arrangement, with the high-permeability layer at the lower layer of the model, the medium-permeability layer at the middle layer, and the low-permeability layer at the upper layer. Electrode monitoring points, aluminum pressure monitoring points, and injection/production holes were arranged on the upper surface of the core, to monitor the change in internal resistivity of the core (the resistance values in cores are different with different water cut), the change in internal pressure of the core, and the saturation during the core flooding
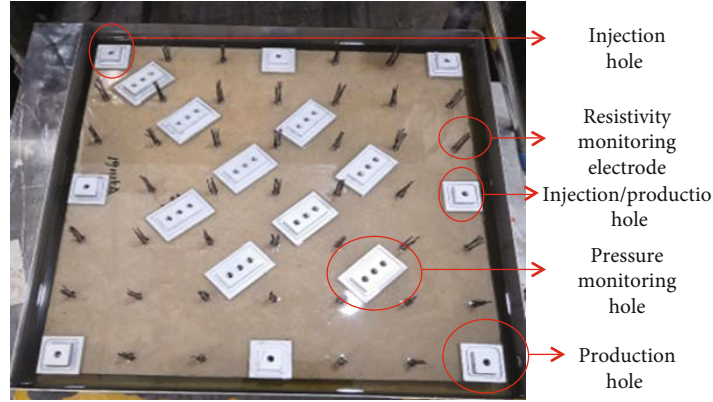
FIGURE 1: Artificial sandstone core model of large well group and main accessories.

TABLE 1: Comparison of prototype and model parameters.

Similarity criteria	Attribute similarity	Purpose	Physical model values	Field values
$\left(\dfrac{kz}{q_I\mu_w}\rho_o gh\right)_m = \left(\dfrac{kz}{q_I\mu_w}\rho_o gh\right)_n$	Ratio of gravity to driving force	Determine the amount of model injection	0.3 mL/min	30 m³/d
$x_D = \dfrac{x_m}{x_n}$	Geometric similarity	Determine the model size	70.7 cm	50 m
$z_D = \dfrac{z_m}{z_n}$	Geometric similarity	Determine the model thickness	42 cm	30 m
$\left(\dfrac{kz\Delta P}{q_I\mu_w}\right)_m = \left(\dfrac{kz\Delta P}{q_I\mu_w}\right)_n$	Dynamic similarity	Determine the injection-production pressure difference of the model	0.2 MPa	15 MPa
$\Phi_m = \Phi_n$	Consistent porosity	Determine the model porosity	22%	22%
$\mu_m = \mu_n$	Consistent crude oil viscosity	Determine the crude oil viscosity	10 mPa·s	10 mPa·s
$k_m = k_n$	Consistent gas log permeability	Determine the model average permeability	500 mD	500 mD

Subscript m: model; subscript n: oilfield prototype; z: reservoir thickness, m; h: reservoir depth, m; ρ_o: oil-phase density, kg/m³; k: gas permeability, mD; μ_w: water-phase viscosity, mPa·s; q_I: the volume of water injected into the reservoir by the injection well per unit time, m³/s; x_D: the similarity ratio of characteristic length; x_m: the model length, m; x_n: the field prototype length, m; Φ: porosity, %; ΔP: pressure difference between production and injection, MPa; %; μ: oil-phase viscosity, mD; g: acceleration of gravity, m/s².
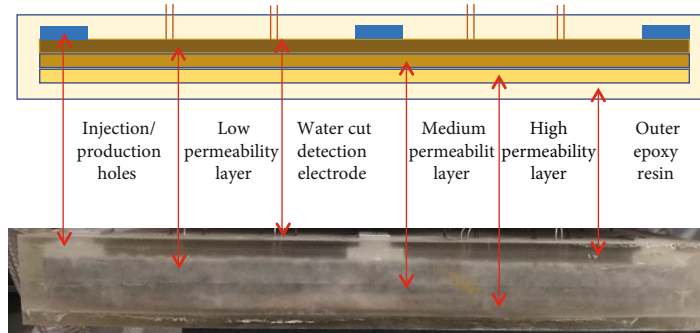
FIGURE 2: Side structure of the artificial sandstone core model of large well group.

experiment, respectively, as shown in Figure 2. A variety of injection and production methods can be simulated by the layout of injection and production holes. The well pattern in this paper was the diagonal layout, simulating the development mode of one injection and one production well. The vertical coefficient of variation of the model was 0.65, and the gas permeability and making process of each layer are shown in Table 2.

TABLE 2: Compaction method of each vertical layer of the core.

Gas permeability mD	Porosity %	Particle size of quartz sand μm	Quartz sand ratio %	Epoxy resin ratio %	Curing agent %	Compaction pressure MPa	Compaction time h
150	18	120~180	85	13.5	6.4	60	4
417	22.5	150~250	86	7.6	6.4	45	3
933	22.6	160~325	88	5.6	6.4	30	2

4. Design and Making of Pressing Plate Mold and Related Accessories

The pressing plate mold is a key technology to make the core physical model of well group with electrode and pressure holes. The pressing plate is mainly to distribute the downward pressure of the hydraulic press and acts directly on the cemented sand body to compact the sand body. In the previous model making process, the core is first compacted with a flat pressing plate without any reserved holes, then cemented, and drilled with monitoring holes of various functions. On the improved pressing plate, the orifice locations are drilled first for the monitoring resistor, pressure collecting hole, and production/injection fluid, and a cylindrical tube is inserted into the core to reserve holes before the core is pressed and cemented. Thus, the well location, electrode monitoring point and pressure probe hole can be made synchronously in the process of core compaction and cementing, so as to avoid the link of drilling and extending with drill tools after core compaction and cementing, reduce the damage to sand body after compaction and cementing, and keep physical properties such as porosity and permeability in the core unchanged. Compared with the model of postprocessed orifice, the one-step forming core physical model can withstand greater chemical displacement pressure.

The pressing plate was designed as 510 mm long, 510 mm wide, and 30 mm thick. A total of 8 injection/production holes were designed on the plate, each of which allows for the collection of injected and produced fluids as well as simulating water inflow, water retreat, and core oil saturation processes during the initial stage of the experiment. There were 41 groups of electrode monitoring points. Each group of electrode monitoring points included 3 pairs of 6 electrodes, with a spacing of 6 mm between each pair, which were, respectively, used to monitor the resistance change caused by the change of water cut in the high-permeability layer, medium-permeability layer, and low-permeability layer. There were 9 groups of pressure monitoring points. Each group of pressure monitoring points included 3 pressure holes with a diameter of 4 mm and a spacing of 15 mm between each hole, which were, respectively, used to monitor the pressure changes in the high-permeability layer, medium-permeability layer, and low-permeability layer. The details are shown in Figures 3 and 4.

Pressure probe hole mould is shown in Figure 5. It is composed of upper and lower parts. The lower thin part is inserted into the core to prefabricate the orifice, while the upper thick end bears the downward pressure. The upper bearing cylinder had a diameter of 15 mm and a height of 30 mm, while the lower insertion cylinder had a diameter of 3 mm, and lengths of 37.5 mm, 52.5 mm, and 67.5 mm, respectively. The different length of the lower thin part of the pressure measuring point is mainly to cooperate with the pressing plate mold, so that it can be accurately inserted into different layers at different longitudinal depths of the core to accurately measure the fluid pressure of each layer.

The injection/production wellbore mould consists of upper and lower parts (as shown in Figure 6). It is mainly
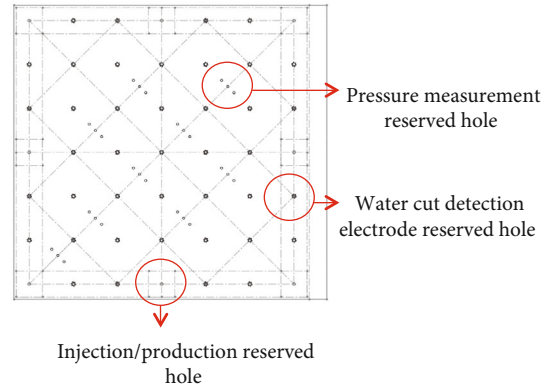
FIGURE 3: Design drawing of pressing plate mold.

Pressure measurement reserved hole

Water cut detection electrode reserved hole

Injection/production reserved hole

used to form a cylindrical longitudinal flow channel in the core. The upper bearing cylinder had a diameter of 45 mm and a height of 30 mm. The lower thin insertion end had a diameter of 3 mm and a length of 70 mm. The wellbore mould and the pressure probe hole mould had the same upper cylinder part of 30 mm, so that the pressure end is in the same horizontal plane once they are put in the pressing plate to keep the core pressing surface level.

Monitoring electrode wires were made of copper wires coated with insulating paint, and the exposed copper wire of the monitoring end monitored the resistance change caused by the change of water cut inside the core. Each electrode monitoring point had 3 pairs of electrodes, each of which was used to test water cut changes in a layer. If a single electrode is inserted directly into the core, the wire will bend, resulting in large error in the measured data [11, 16]. Therefore, an integrated accessory for the electrode wire was designed and processed. Thus, 6 electrodes can be inserted simultaneously at different depths before the core is pressed and cemented. The electrode integrated accessory was designed as 6 mm in diameter and 10 mm in height. 6 semicircular grooves with a diameter of 1.5 mm were uniformly distributed on the circumferential surface (as shown in Figure 7(a)).

The grooves were used to place electrodes, and the electrodes were fastened with rubber rings to ensure flush tops. Then, electrodes of different lengths of 10 cm, 8.5 cm, and 7 cm can be inserted into the specified depth, with the 10 cm electrode pair for monitoring the high-permeability layer, the 8.5 cm electrode pair for the medium-permeability layer, and the 7 cm electrode pair for the low-permeability layer. The assembled electrode wires are shown in Figure 7(b).

Quartz sand and epoxy resin corresponding to different permeability were mixed evenly and spread into the mold successively from low-permeability to high permeability. Then, the electrode assembly, wellbore mould, and pressure probe hole mould were inserted (as shown in Figure 8(a)). The flat plate was used to press the low-permeability layer, then the medium-permeability layer, and finally, the high-permeability layer, to ensure that the sand body is 1.5 cm thick after each layer is compacted. After compaction, the

Figure 4: Picture of pressing plate mold.
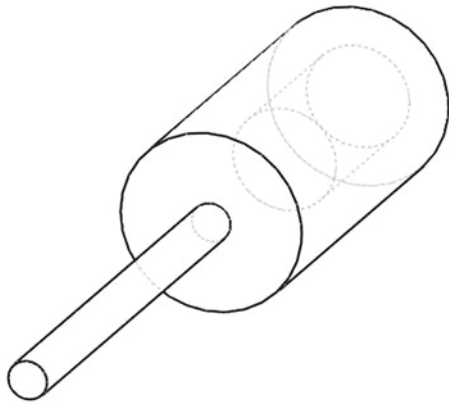
Figure 5: Schematic diagram of pressure probe hole mould.

Figure 6: Wellbore mould.

accessories were removed to dry the core and obtain a core model not coated with epoxy resin (as shown in Figure 8(b)).

5. Experiment Scheme

The flooding scheme in this experiment: water flooding (water cut at the outlet stable at 98%) + polymer preslug (fixed polymer dosage) + 0.3 PV ASP main slug + 0.2 PV ASP secondary slug + 0.2 PV subsequent polymer slug + 0.2 PV subsequent water flooding. With the purpose to save

the chemical flooding costs in moderately heterogeneous reservoirs, oil recovery factors were investigated under polymer preslugs with different viscosities, subsequent displacement scheme being the same. A particular viscosity of the polymer preslug is implemented by changing the concentration of the polymer preslug while ensuring that the total amount of polymer used in the polymer preslug stage is the same. The viscosity of the polymer preslug was set at 40 mPa·s, 60 mPa·s, and 80 mPa·s according to the maximum operating conditions of the field injection pump system. The injection amount of each slug in the three experiment schemes was designed by maintaining the same amount of polymer in the polymer preslug in all schemes (as shown in Table 3).

The polymer preslug has a great influence on the function of ASP system. Its main function is to adjust the inner plane and longitudinal direction of the core using the viscoelasticity of polymer, reduce the heterogeneity in the reservoir, and protect the ASP main slug [32]. This helps the ASP main slug enter the oil enrichment area not affected by water flooding and reduce the adsorption loss of expensive chemical agents. The ASP main and secondary slugs can reduce the water cut of the produced fluid and increase the oil production. The concentration of chemical agents in the ASP secondary slug was lower than that in the ASP main slug [33]. At the oilfield site, it is believed that the affected area after the injection of the main slug is close to the adsorption saturation state, and the secondary slug supplements the main slug. The injection stage of ASP slug is the same as the field operation of the oilfield. The alkali, surfactant, and polymer were mixed in proportion and injected into the core. The injected chemical agent has high viscosity and can form ultralow interfacial tension with crude oil, which can extend swept volume, enhance oil displacement efficiency, and improve oil washing ratio [34]. In the ASP system, the polymer is to increase the viscosity of the system and control the fluidity, the surfactant is to reduce the oil-water interfacial tension and improve the oil washing ratio, and the alkali is to react with the acidic components of crude oil to produce surfactants in situ [35]. The subsequent polymer slug is to prevent the breakthrough of injected water in the subsequent water flooding stage from affecting the oil displacement efficiency of ASP slug and also protect the ASP slug [1, 2]. The subsequent water flooding is to maintain the displacement pressure and reduce the agent use and cost [3, 5, 7] [2].

There is no clear standard and regulation for oil displacement experiment of large plate artificial core. The experiment refers to the Chinese small natural cylindrical core test standard GB/T 28912-2012 Test method for two-phase relative permeability in rock, and the advance velocity of the displacement front is recommended as the criterion to investigate the recovery efficiency, pressure, and other parameters. According to the daily injection volume of injection wells, the spacing between production wells and production wells, and the output of production wells, the calculated thrust velocity of the mainline of the water flooding front is 1 m/d. The purpose of the experiment is to select the optimal viscosity of polymer preslug by comparison.

(a) (b)
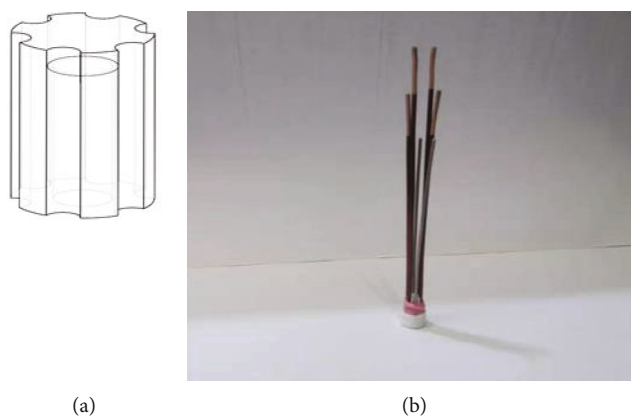
FIGURE 7: (a) Design drawing of electrode accessory; (b) electrode space diagram.

(a) (b)
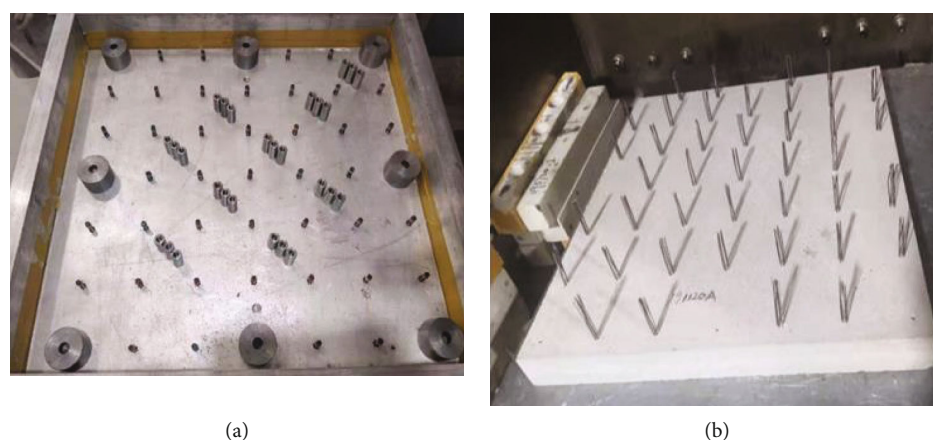
FIGURE 8: (a) Assembly of accessories; (b) the artificial sandstone core model not coated with epoxy resin.

TABLE 3: Experiment scheme for viscosity optimization of polymer preslug.

Name of chemical slug	Slug size PV	Polymer concentration mg/L	System viscosity mPa·s	Alkali concentration wt%	Surfactant concentration wt%
Polymer preslug					
1	0.093	1900	40	——	——
2	0.075	2360	60	——	——
3	0.064	2775	80	——	——
ASP main slug	0.3	2450	30	1.2	0.3
ASP secondary slug	0.2	2300	30	1.0	0.1
Subsequent polymer slug	0.2	1635	30	——	——

TABLE 4: Simulated water ion salinity.

No.	Agents	Mass concentration g/L
1	NaCl	3.977
2	$CaCl_2$	0.028
3	$MgCl_2 \cdot 6H_2O$	0.046
4	Na_2SO_4	0.093
5	$NaHCO_3$	2.634
	Total salinity	6.778

Therefore, the experiment mainly focuses on the changing trend of injection pressure and recovery degree and does not carry out error comparison analysis with field or other artificial cores. The experimental data in this paper are arithmetic average values of parallel experiments.

The specific steps are implemented as below: (1) the core physical model of large well group is vacuumed and saturated with simulated water; (2) the core physical model is saturated with oil with oil saturation of over 65%; (3) water flooding is carried out with simulated water at a rate of 0.3 mL/min until the water cut at the outlet stabilizes at more
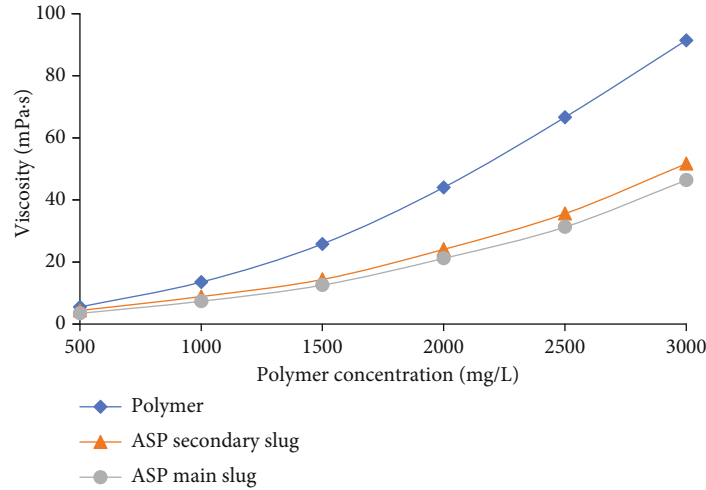
FIGURE 9: Concentration-viscosity curve of polymer.

FIGURE 10: Microelectrode core model of different permeability.

than 98%. It is injected into the polymer preslug, ASP main slug, ASP secondary slug, and polymer postslug; (4) subsequent water flooding is carried out until the water cut at the outlet stabilizes at more than 98%; (5) electrodes and pressure monitoring devices are used to monitor the pressure of each layer and the distribution of remaining oil.

6. Determination of Experimental Oil, Water, Chemical Agent, and Rock Electricity Relationship

The oil used in the experiments was D4-1-22 wellhead crude oil from Daqing Oilfield, and the viscosity of crude oil was 10 mPa·s at 45°C. According to the ion salinity provided in the oilfield site, the simulated water was used for the preparation of saturated water, water flooding, polymer preslug, ASP main slug, ASP secondary slug, postslug, and subsequent water flooding stage of the core model of well group. The specific salinity is shown in Table 4.

In the chemical flooding agent used in the experiment, the molecular weight of the polymer was 12×10^4 ~16×10^4 g/mol, the surfactant was petroleum sulfonate, and the alkali was analytical pure Na_2CO_3.

6.1. Determination of Polymer Viscosity-Concentration Relationship. Determination of the viscosity-concentration relationship of the polymer preslug, the ASP main slug, the ASP secondary slug, and the polymer postslug is of great significance for the precise preparation of the system viscosity in the experiment program. Polymer preslug and polymer postslug have the same composition and are collectively referred to as polymer slug in the test.

The polymer slug, ASP main slug, and ASP secondary slug with different concentrations of 500 mg/L~3000 mg/L were prepared from the polymer mother liquid with simulated water. The viscosity of different concentrations was determined at 45°C, and the corresponding concentration relationship curves of viscosity systems of 40 mPa·s, 60 mPa·s, and 80 mPa·s were finally determined. The determined results are shown in Figure 9.

6.2. Establishment of the Relationship between Oil Saturation and Resistivity of Rock. There are two phases of oil and water in the pore medium of the core model. Anion and cation can be ionized from the salt substance in the water phase, ions will move directionally under the action of the electric field and generate current, and the current intensity is related to the content of ions in the water phase. It is assumed that other physical properties remain unchanged in the core model and that resistivity is only a function of the amount of oil and water in the pores; a standard curve of resistance values and oil saturation (water cut) can be established. The theoretical method of the relationship between Archie saturation and lithology was applied to calibrate the saturation. Since other components in the core are nonconductive, oil saturation in the core can be directly reflected by different resistance values:

$$I = \frac{R_t}{R_o}, \tag{1}$$

where R_t is the resistivity of rock containing oil, Ωm; R_o is the resistivity of rock completely containing water, Ωm.
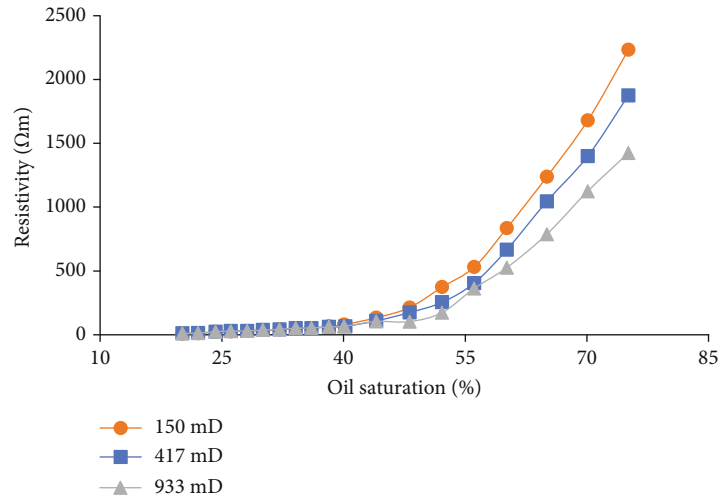
FIGURE 11: Test results of resistivity and oil saturation curves of different permeability layers.

TABLE 5: Recovery degree of different polymer preslug viscosity.

Scheme	Preslug viscosity mPa·s	Recovery degree by water flooding %	Enhancement by chemical flooding %	Total recovery degree %
1	40	35.12	18.02	53.14
2	60	35.44	19.35	54.79
3	80	35.5	18.74	54.24
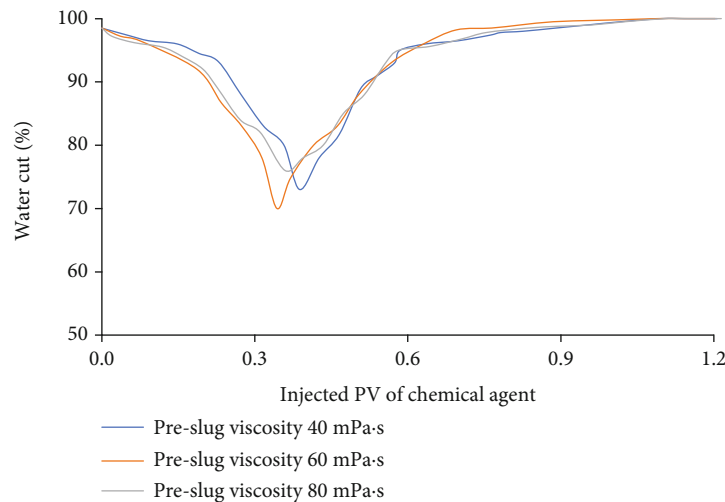
FIGURE 12: Water cut trend during chemical flooding with different polymer preslug viscosity.

The microelectrode core model with a width of 15 mm, a height of 15 mm, and a length of 100 mm, as shown in Figure 10, was used to carry out the physical simulation experiment of water flooding. The microelectrode core model was used to determine the resistance values of cores with different permeability under different oil saturation, and then, the standard curve of the relationship between oil saturation and resistivity of rock was established (as shown in Figure 11). In the flooding experiment of the core model, the resistance values at different test points were monitored by a resistance recording system, and the oil saturation value of each test point can be calculated reversely according to the standard curve. Thus, the distribution of oil saturation of the whole heterogeneous well core model at any time was plotted.

7. Experimental Results

Table 5 shows the recovery degree of the water flooding stage and the total recovery degree of the final chemical
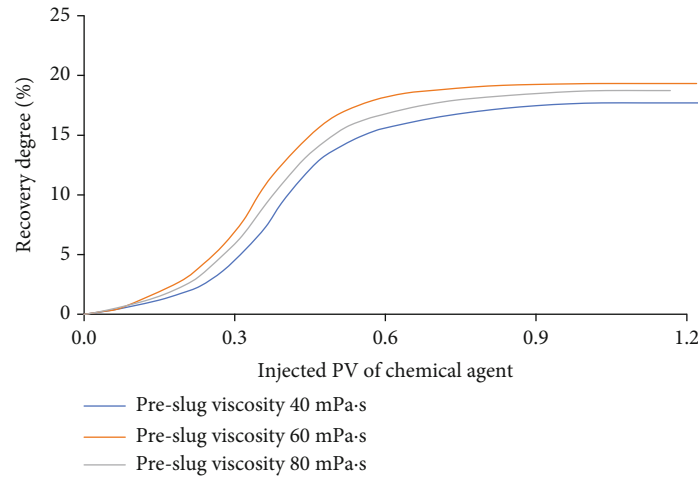
FIGURE 13: Recovery degree during chemical flooding with different polymer preslug viscosity.
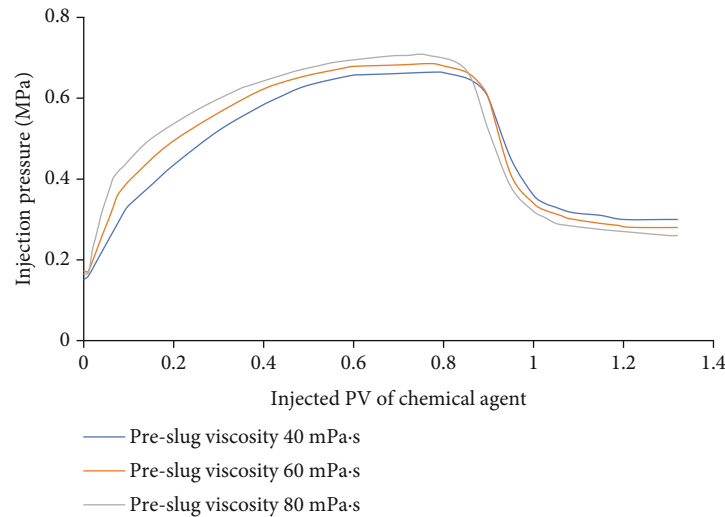
FIGURE 14: Injection pressure of different polymer preslug viscosity.

flooding in the ASP preslug experimental scheme. It is concluded that the 60 mPa·s polymer preslug scheme had the best displacement effect, while the worst displacement effect was found in the 40 mPa·s polymer preslug scheme. Increasing the polymer preslug viscosity can effectively improve the recovery degree during chemical flooding, which does not mean that the higher the viscosity the better, for example, the 80 mPa·s polymer preslug scheme had a weaker oil displacement effect than the 60 mPa·s polymer preslug scheme.

Taking the end of water flooding as the monitoring starting point, the relationship curve between the injected PV of chemical agent and the water cut at the core outlet was plotted (as shown in Figure 12). At the initial stage of chemical flooding (0-0.31 PV), the water cut of the 60 mPa·s polymer preslug system decreased rapidly, proving that the 60 mPa·s system has more prominent advantages in profile control by chemical flooding, which allows for earlier water injection effect of the ASP main slug. In the middle stage of chemical flooding (0.31-0.51 PV), the water cut recovered slowly,

which proved the full water injection effect of main and secondary slugs. Under the experimental conditions, the improvement by chemical flooding in the 60 mPa·s system was 1.33% and 0.6% higher than the 40 mPa·s and 80 mPa·s systems, respectively.

The polymer preslug chemical flooding scheme of three viscosity systems had a stable oil production time (as shown in Figure 13). The 60 mPa·s system showed good oil recovery effect from the initial stage of chemical flooding, indicating that the 60 mPa·s system has a good match with the reservoir with a coefficient of variation of 0.65.

7.1. Pressure Change. Increasing the viscosity of the polymer preslug can increase the injection-production pressure difference. However, the high viscosity of the system will result in pressure concentration near the injection well, and the area near the well has large pressure loss, short pressure propagation distance, and small spreading range. Pressure
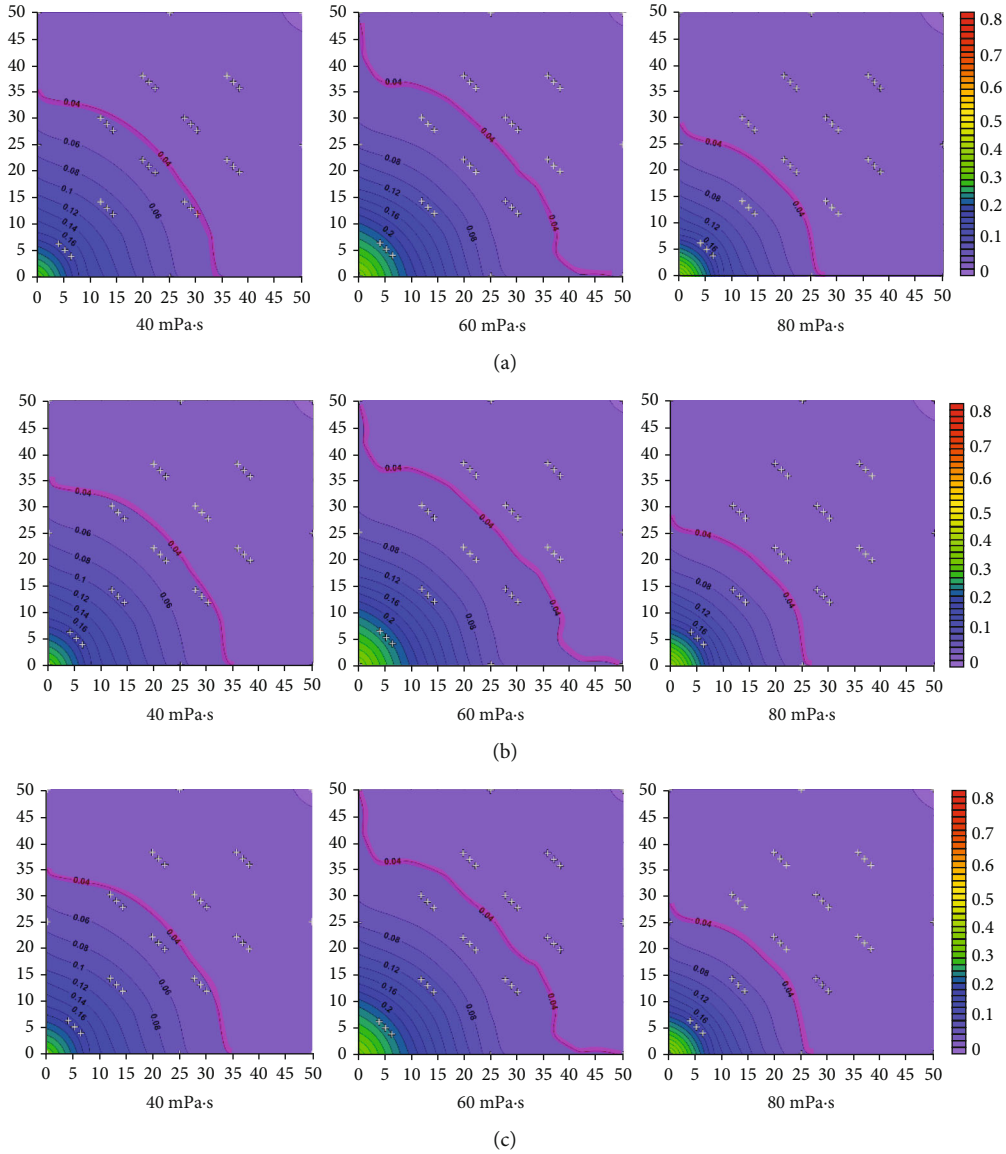
FIGURE 15: Pressure field distribution at the end of the ASP main slug stage under different polymer preslug viscosity; (a) pressure field distribution in low-permeability layer; (b) pressure field distribution in medium-permeability layer; (c) pressure field distribution in high-permeability layer.

changes during the chemical flooding are shown in Figure 14.

High-viscosity polymer will lead to increased injection pressure, the polymer accumulates at the injection end, and the viscosity decreases due to severe shear, resulting in serious displacement pressure loss, which exhibits a small pressure sweep area in the core. According to the pressure monitoring data, the pressure field diagram of each layer at the end of the ASP main slug stage was plotted (as shown in Figure 15). There was no obvious difference in the pressure sweep range of displacement fluid in reservoirs with different permeability, and the pressure and sweep range of each layer were close [36, 37]. However, the stress condition in the core matrix was obviously different according to poroelasticity or thermo-poroelasticity theory [38, 39]. It is planned in the next phase of the project, with additional

experimental modules to be added, it will be possible to monitor the changes of stress in the matrix.

7.2. Remaining Oil Distribution. At the end of the ASP main slug stage, the remaining oil distribution of each permeability layer in the core physical model of well group is shown in Figure 16. Increasing the viscosity of the polymer preslug is beneficial for the ASP system to expand along the diagonal main stream line to the sides rich in remaining oil in the high-permeability layer, the producing degree of the medium-permeability layer significantly increases, and significant producing effect appears near the injection well in the low-permeability layer. If the polymer preslug system has very high viscosity, the profile control system will have similar longitudinal and lateral advance effect as the low-viscosity system, and the difference of remaining oil
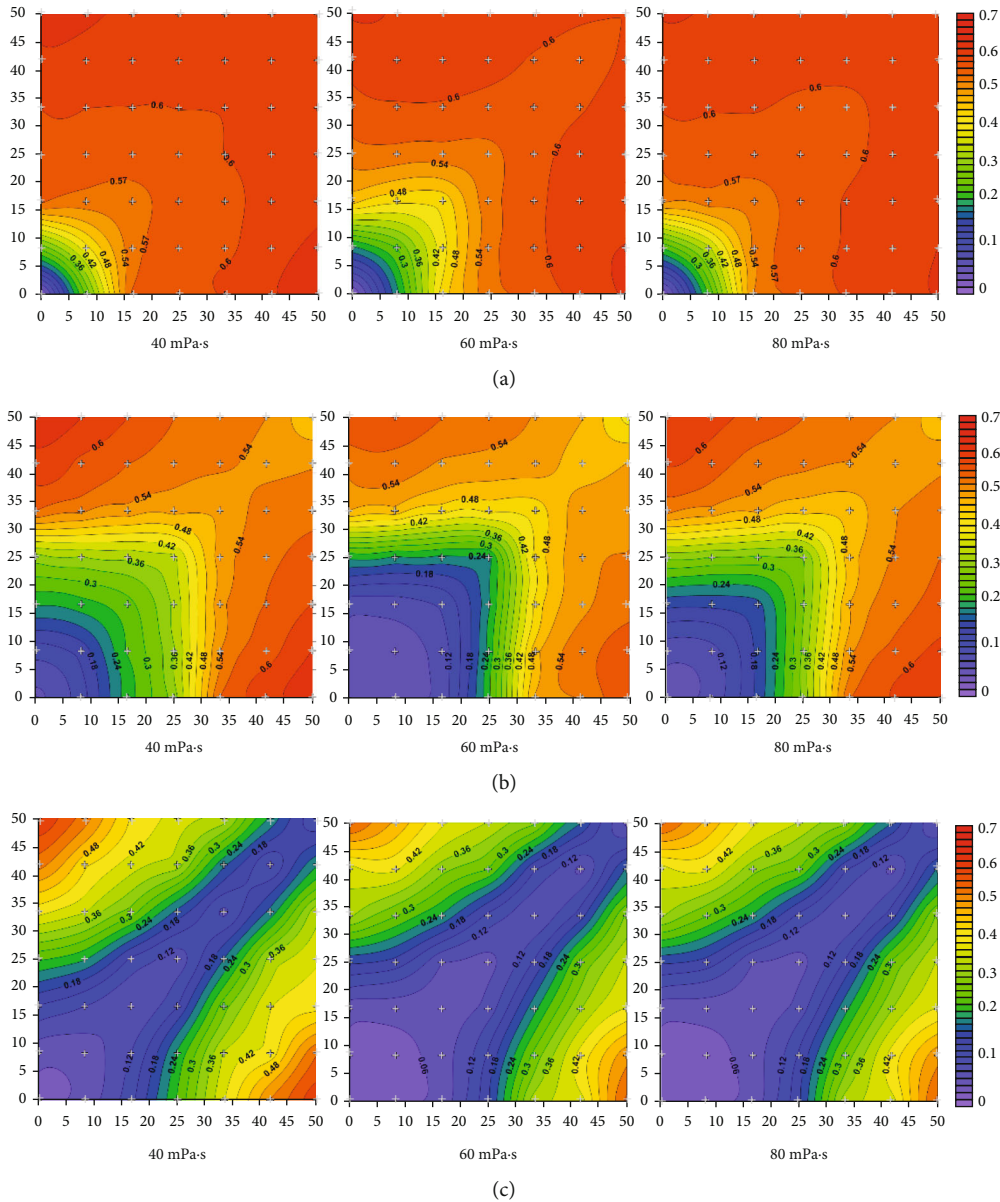
FIGURE 16: Remaining oil distribution at the end of the ASP main slug stage under different polymer preslug viscosity; (a) remaining oil distribution in low-permeability layer; (b) remaining oil distribution in medium-permeability layer; (c) remaining oil distribution in high-permeability layer.

production between layers is quite significant after the ASP main slug flooding.

According to the electrode test resistance, the oil saturation distribution of the longitudinal profile along the diagonal direction of the core, namely, the direction of the main stream line, was plotted (as shown in Figure 17). The 40 mPa·s polymer preslug chemical flooding system did not improve the displacement profile vertically. Due to the low viscosity and small displacement differential pressure increment, the displacement fluid only improved the displacement channel after water flooding in the high-permeability layer. Due to the large injection pressure difference of 80 mPa·s polymer preslug chemical flooding system, the displacement fluid did not exhibit a good elastic displacement

relationship with the reservoir. In the middle area of the injection well and the production well, the displacement fluid did not diffuse in the upper medium-permeability layer and low-permeability layer, but flew to the bottom of production well along the bottom of high-permeability layer. This also shows that the high-viscosity polymer preslug has a better profile-control effect for wells close to each other. With high injection pressure, the polymer will suffer severe shear and high viscosity loss in the reservoir, and the chemical flooding system cannot maintain effective viscosity.

Different from the pressure distribution field, the distribution of oil saturation field is quite different in different permeability layers, which can effectively determine the production degree of ASP chemical flooding. The remaining oil
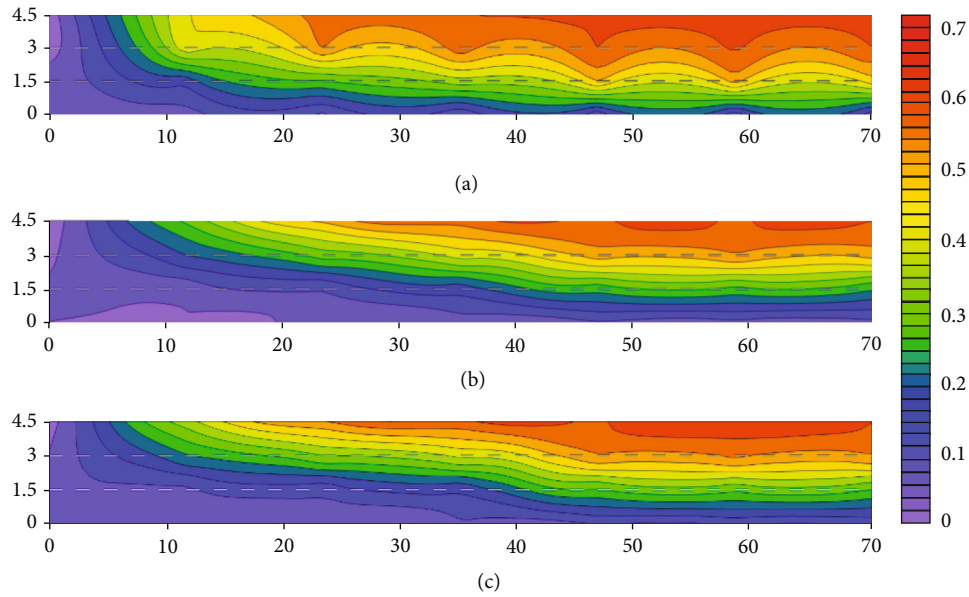
FIGURE 17: Distribution profile of residual oil along main stream line at the end of the ASP main slug stage under different polymer preslug viscosity, (a) the polymer preslug viscosity is 40 mPa·s; (b) the polymer preslug viscosity is 60 mPa·s; (c) the polymer preslug viscosity is 80 mPa·s.

in the high-permeability layer was more thoroughly exploited, with oil saturation as low as 12% in the main stream line and an average oil saturation of about 27%. At the bottom of the medium-permeability layer, the main stream line runs through injection and production wells, while no obvious main producing area running through injection and production wells was found in the low-permeability layer. This indicates that the main increased oil production area of the ASP system comes from the lateral profile control in the high-permeability layer, and a small part comes from the near-wellbore area of the injection well and the main stream line area at the bottom of the medium-permeability layer. The low-permeability reservoir had a very limited producing effect, and the change in the viscosity of the polymer preslug had an obvious effect on the profile-control of medium- and high-permeability layers for moderately developed heterogeneous reservoirs. Therefore, the injectability of polymer preslug and the effect of alleviating interlayer conflicts are related to the viscosity of chemical flooding system, so the viscosity of polymer preslug shall not be too high, and cores with different heterogeneity should have a reasonable viscosity matching range.

8. Conclusions

In this paper, economical use of the ASP is investigated. Preslug is beneficial, and the viscosity of polymer preslug shall not be too high. Higher viscosity will lead to increased injection pressure, ineffective elastic displacement of polymer and ASP chemical flooding systems, and fast viscosity loss of the injected displacement fluid, resulting in the waste of chemical agents. The reasonable polymer preslug viscosity is 60 mPa·s in a heterogeneous reservoir with a coefficient of variation of 0.65.

Under the same pressure field, remaining oil distribution, recovery degree, and chemical agent dosage, the polymer preslug with viscosity of 60 mPa·s and slug size of 0.075 PV are more beneficial for the pressure to extend to the nonmain stream line area on both sides and tend to increase the sweep area of the plane. Longitudinally near the injection well, the production conflict between medium- and high-permeability layers can be alleviated, which effectively improves the degree of production at the bottom of the high-permeability and the medium-permeability layers, as well as the injection end of the medium-permeability layer.

The remaining oil in the low-permeability layer cannot be effectively displaced by changing the viscosity of the polymer preslug in the ASP chemical flooding system. The major areas of increased oil production at the ASP flooding stage are the high-permeability layer and the bottom of medium-permeability layer.

The making process of core physical model of large well group was explored and improved, the pressing mold and accessories were designed, and the arrangement of water cut monitoring electrode was optimized. Moreover, the process of drilling pressure holes and injection/production holes after core cementation was avoided, which ensures that the physical parameters of core after cementation were not affected by the installation of accessories. It can satisfy the high-pressure requirements of chemical flooding experiments and accurately detect water cut and pressure changes in the core.

After ASP flooding, thick reservoirs are mostly exploited by subsequent water flooding to maintain formation pressure, but the subsequent development effect is staggeringly inefficient. At present, both laboratory and field experiments show that the recovery degree of low- and medium-

permeability reservoirs after ASP flooding is low, and it has great potential for further tapping the remaining oil of low- and medium-permeability reservoirs by fracturing technology [40]. In laboratory experiments, the large size of the core can be complete debonding or no water cut, can capture area of low- and medium-permeability core samples for triaxial fracturing experiment, which can be used to investigate the enhanced oil recovery range of the ternary system after fracturing, and can also be compared with the triaxial fracturing of the core sample of the low- and medium-permeability reservoir after water flooding to investigate the fracturing effect of the ternary system after flooding [41, 42].

Data Availability

All data used can be found in our manuscript.

Conflicts of Interest

The authors declare no conflicts of interest.

Acknowledgments

References

[1] G. Shutang and G. Qiang, "Recent progress and evaluation of ASP flooding for EOR in Daqing oil field," in *SPE EOR Conference at Oil & Gas West Asia*, pp. 1–7, Muscat, Oman, 2010.

[2] J. Cheng, G. Liao, Z. Yang, L. I. Qun, Y. Yao, and X. U. Dian, "Pilot test of asp flooding in Daqing oilfield," in *Petroleum Geology & Oilfield Deuelopment*, vol. 20no. 2, pp. 46–49, Daqing, 2001.

[3] M. Ajay, "Chemical flood enhanced oil recovery: a review," *International Journal of Oil Gas & Coal Technology*, vol. 9, no. 3, p. 241, 2015.

[4] B. Dehdari, R. Parsaei, M. Riazi, N. Rezaei, and S. Zendehboudi, "New insight into foam stability enhancement mechanism, using polyvinyl alcohol (PVA) and nanoparticles," *Journal of Molecular Liquids*, vol. 307, article 112755, 2020.

[5] A. A. Adasani and B. Bai, "Analysis of EOR projects and updated screening criteria," *Journal of Petroleum Science & Engineering*, vol. 79, no. 1-2, pp. 10–24, 2011.

[6] P. J. Liyanage, S. Solairaj, G. W. Arachchilage et al., "Alkaline surfactant polymer flooding using a novel class of large hydrophobe surfactants," in *SPE Improved Oil Recovery Symposium*, pp. 14–18, Tulsa Oklahoma USA, April 2012.

[7] O. Mohammadzadeh, M. H. Sedaghat, S. Kord, S. Zendehboudi, and J. P. Giesy, "Pore-level visual analysis of heavy oil recovery using chemical-assisted waterflooding process - use of a new chemical agent," *Fuel*, vol. 239, pp. 202–218, 2019.

[8] H. Guo, Y. Li, F. Wang et al., "ASP flooding: theory and practice progress in China," *Journal of Chemistry*, vol. 2017, Article ID 8509563, 18 pages, 2017.

[9] M. Algharaib, A. Alajmi, and R. Gharbi, "Improving polymer flood performance in high salinity reservoirs," *Journal of Petroleum Science and Engineering*, vol. 115, pp. 17–23, 2014.

[10] W. Demin, Z. Zhenhua, C. Jiecheng, Y. Jingchun, G. Shutang, and L. Li, "Pilot test of alkaline surfactant polymer flooding in Daqing oil field," *SPE Reservoir Engineering*, vol. 12, no. 4, pp. 229–233, 1997.

[11] B. Huang, W. Zhang, H. Liu, C. Fu, P. Feng, and Y. Wang, "A study on the optimization of surfactants in the main and vice slug in weak base ASP flooding," *Energies*, vol. 10, no. 3, p. 304, 2017.

[12] J. Hu, A. Li, and A. Memon, "Experimental investigation of polymer enhanced oil recovery under different injection modes," *ACS Omega*, vol. 5, no. 48, pp. 31069–31075, 2020.

[13] M. Y. Khan, A. Samanta, K. Ojha, and A. Mandal, "Design of alkaline/surfactant/polymer (ASP) slug and its use in enhanced oil recovery," *Petroleum Science and Technology*, vol. 27, no. 17, pp. 1926–1942, 2009.

[14] J. B. Lawson and J. Reisberg, "Alternate slugs of gas and dilute surfactant for mobility control during chemical flooding SPE/-DOE enhanced oil recovery symposium," *Society of Petroleum Engineers*, vol. 4, pp. 289–295, 1980.

[15] S. S. Riswati, W. Bae, C. Park, A. K. Permadi, I. Efriza, and B. Min, "Experimental analysis to design optimum phase type and salinity gradient of alkaline surfactant polymer flooding at low saline reservoir," *Journal of Petroleum Science and Engineering*, vol. 173, pp. 1005–1019, 2019.

[16] D. Yin, S. Song, Q. Xu, and K. Liu, "Experimental research on the optimization and evaluation of the polymer/chromium-ion deep profile control system for the fractured low-permeability reservoirs," *Processes*, vol. 8, no. 9, article 1021, 2020.

[17] X. Nie, J. Chen, Y. Cao et al., "Investigation on plugging and profile control of polymer microspheres as a displacement fluid in enhanced oil recovery," *Polymers*, vol. 11, no. 12, p. 1993, 2019.

[18] J. J. Sheng, "A comprehensive review of alkaline-surfactant-polymer (ASP) flooding," *Journal of Chemical Engineering*, vol. 9, no. 4, pp. 471–489, 2014.

[19] J. Hou, S. Zhang, M. Dong, X. Yue, and J. Yang, "Effect of viscosity of alkaline/surfactant/polymer (ASP) solution on enhanced oil recovery in heterogeneous reservoirs," in *Canadian International Petroleum Conference*, vol. 45, pp. 27–33, Calgary, Alberta, 2006.

[20] S. A. Shedid, "Experimental investigation of alkaline/surfactant/polymer (ASP) flooding in low permeability heterogeneous carbonate reservoirs," in *SPE North Africa Technical Conference and Exhibition*, Cairo, Egypt, 2015.

[21] B. Huang, X. Hu, C. Fu, and L. Wang, "Experimental evaluation of ASP flooding to improve oil recovery in heterogeneous reservoirs by layered injection approach," *Energy Science & Engineering*, vol. 8, no. 9, pp. 3148–3164, 2020.

[22] X. Sui, Z. Chen, I. Kurnia, X. Han, J. Yu, and G. Zhang, "Alkaline-surfactant-polymer flooding of active oil under reservoir conditions," *Fuel*, vol. 262, article 116647, 2020.

[23] Y. Li, M. Long, L. Zuo, W. Li, and W. Zhao, "Brittleness evaluation of coal based on statistical damage and energy evolution theory," *Journal of Petroleum Science and Engineering*, vol. 172, pp. 753–763, 2019.

[24] J. J. Li, H. Q. Jiang, J. R. Hou, X. Wang, and L. Su, "The effects of oil displacement efficiency and conformance efficiency on viscosity of asp flooding in a heterogeneous reservoir," *Journal of Natural Gas Science and Engineering*, vol. 32, no. 7, pp. 830–839, 2014.

[25] Q. Sun, C. Wang, X. Wang, and B. Dong, "Development of a new high-temperature-resistant plugging agent for heavy oil recovery by steam flooding of resevoirs," *Chemistry and Technology of Fuels and Oils*, vol. 52, no. 4, pp. 462–468, 2016.

[26] Z. Liu, S. Wang, H. Ye et al., "Experimental study on the effects of pre-cracks fracturing fluid and rock mechanical characteristics on directional hydraulic fracturing with axial pre-cracks," *Geomechanics and Geophysics for Geo-Energy and Geo-Resources*, vol. 7, no. 2, p. 29, 2021.

[27] A. A. Olajire, "Review of ASP EOR (alkaline surfactant polymer enhanced oil recovery) technology in the petroleum industry: prospects and challenges," *Energy*, vol. 77, pp. 963–982, 2014.

[28] Z. Fengshou, A. Mengke, Z. Lianyang, F. Yi, and E. Derek, "Effect of mineralogy on friction-dilation relationships for simulated faults: implications for permeability evolution in caprock faults," *Geoscience Frontiers*, vol. 11, no. 2, pp. 439–450, 2020.

[29] L. Zhenghe, R. Xiaokai, L. Xiao, L. Haojie, Y. Lusheng, and Y. Jianfeng, "Effects of confining stresses pre-crack inclination angles and injection rates: observations from large-scale true triaxial and hydraulic fracturing tests in laboratory," *Rock Mechanics and Rock Engineering*, vol. 53, no. 4, pp. 1991–2000, 2020.

[30] K. Panthi, H. Sharma, and K. K. Mohanty, "ASP flood of a viscous oil in a carbonate rock," *Fuel*, vol. 164, pp. 18–27, 2016.

[31] L. Yuwei, L. Min, T. Jizhou, C. Mian, and F. Xiaofei, "A hydraulic fracture height mathematical model considering the influence of plastic region at fracture tip," *Petroleum Exploration and Development*, vol. 47, no. 1, pp. 184–195, 2020.

[32] A. Kumar and A. Mandal, "Core-scale modelling and numerical simulation of zwitterionic surfactant flooding: designing of chemical slug for enhanced oil recovery," *Journal of Petroleum Science and Engineering*, vol. 192, article 107333, 2020.

[33] L. Daoshan, L. Shouliang, L. Yi, and W. Demin, "The effect of biosurfactant on the interfacial tension and adsorption loss of surfactant in ASP flooding," *Colloids and Surfaces A: Physicochemical and Engineering Aspects*, vol. 244, no. 1-3, pp. 53–60, 2004.

[34] J. J. Sheng, "Investigation of alkaline-crude oil reaction," *Petroleum*, vol. 1, no. 1, pp. 31–39, 2015.

[35] S. Gao, Y. He, Y. Zhu, P. Han, S. Peng, and X. Liu, "Associated polymer ASP flooding scheme optimization design and field test after polymer flooding in Daqing oilfield," in *SPE Improved Oil Recovery Conference*, Virtual, 2020.

[36] Q. Sun, H. Li, Y. Xu, and X. Zhao, "The research of vapor phase front migration rules in steam assisted gravity drainage," *The International Journal of Multiphysics*, vol. 14, no. 4, pp. 359–371, 2020.

[37] S. Yin, M. B. Dusseault, and L. Rothenburg, "Thermal reservoir modeling in petroleum geomechanics," *International Journal for Numerical and Analytical Methods in Geomechanics*, vol. 33, no. 4, pp. 449–485, 2009.

[38] S. Yin, "Numerical analysis of thermal fracturing in subsurface cold water injection by finite element methods," *International Journal for Numerical and Analytical Methods in Geomechanics*, vol. 37, no. 15, pp. 2523–2538, 2013.

[39] S. Yin, "A fully coupled finite element framework for thermal fracturing simulation in subsurface cold CO_2 injection," *Petroleum*, vol. 4, no. 1, pp. 65–74, 2018.

[40] Z. Cong, Y. Li, Y. Pan et al., "Study on CO_2 foam fracturing model and fracture propagation simulation," *Energy*, vol. 238, p. 121778, 2021.

[41] N. Y. Erik and A. Faruk, "Use of petrological and organic geochemical data in determining hydrocarbon generation potential of coals: Miocene coals of Malatya Basin (Eastern Anatolia-Turkey)," *International Journal of Coal Science & Technology*, 2021.

[42] L. Yuwei, J. Dan, R. Zhenhua, P. Jiyong, F. Chunkai, and Z. Jun, "Evaluation method of rock brittleness based on statistical constitutive relations for rock damage," *Journal of Petroleum Science and Engineering*, vol. 153, pp. 123–132, 2017.

WILEY | Hindawi

Research Article

A Study of Acoustic Emission and Damage Evolution of Limestone under Different Stress Paths and Confining Pressures

Jianjun Zhao [ID],[1] **Xun Wan** [ID],[1] **Lan Ji,**[1] **Jinshi Zhu,**[2] **Xinran Dai,**[1] **and Jun Wang**[1]

[1]*State Key Laboratory of Geohazard Prevention and Geoenvironment Protection (Chengdu University of Technology),*
610059 Chengdu, China
[2]*Three Gorges Geotechnical Consultants Co., Ltd., 430074 Wuhan, China*

Correspondence should be addressed to Jianjun Zhao; j.j.zhao@qq.com

Buried depth is an important factor affecting the deformation and failure of gob surrounding rock. Basing on triaxial compression unloading test and acoustic emission (AE) of limestone under three different initial confining pressures (5 MPa, 10 MPa, and 20 MPa) and three different stress paths, we analyzed the deformation and failure characteristics and energy releasing process of the virgin rock, the gob overburden rock, and the gob sidewall rock with different buried depths (within 1000 m). The results showed that, with the increase of buried depth, the shear fracture mainly propagated and the failure mode of the gob sidewall rock changed from brittleness to plasticity; however, the gob overburden rock was all brittle failure. Compared with shallow buried depths, the energy releasing triggered by confining pressure reduction in deep buried depths was more concentrated and intense. Under the background of deep buried depths, the peak strength and residual strength of the gob sidewall rock were the lowest, and the damage variable was the largest. We proposed that the first "acute phase" of AE can be wielded as the precursor information of the gob sidewall rock failure and crack propagation of hydraulic fracturing. The findings of the study are beneficial for the disaster prevention and control of deep mining in mountainous area, as well as fracturing evaluation.

1. Introduction

With the consumption and utilization of coal resources, deep mining gradually tends to be normalized, and the coal mines with mining depth close to 1000 m are increasing yearly [1, 2]. Under the influence of deep in situ stress and mining disturbance, the gob surrounding rock shows nonlinear mechanical characteristics [3], which further lead to large-scale geohazards. In mountainous areas of Guizhou, China, the stress redistribution of gob surrounding rock after mining further induces deformation of overburden rock and coal pillar failure and even the whole instability of slope [4–6]. We investigated the mining forms and slope structure conditions of some mines in mountainous areas of Guizhou (Table 1), which have the following common characteristics: (a) large buried depth span of coal seam (160~1100 m); (b) small dip angle of coal seam (8~12°); (c) medium-thick coal seam (1.59~3.6 m); (d) limestone, sand-

stone, siltstone, and other hard rocks exist in the roof; and (e) longwall mining method adopted. Among them, the buried depth of coal seam determines the initial in situ stress conditions of gob surrounding rock, affecting the deformation of gob overburden rock and gob sidewall rock [7]. However, the deformation and failure characteristics and instability prediction of gob surrounding rock affected by buried depth were rarely studied by scholars.

In shallow underground mining, the failure of gob surrounding rock limited in a small area usually occurs after a period of accelerated deformation. However, in deep mining, the destruction of gob surrounding rock is often large scale [8]. It is an important prerequisite to understand the deformation and failure characteristics of gob sidewall rock and overburden rock under the influence of mining-induced stress redistribution. Many scholars have studied the laboratory mechanical tests of different rocks under various stress paths [9–11]. Furthermore, the use of AE brings more precursory

TABLE 1: Mining forms and slope structure conditions of some mines in mountainous areas of Guizhou.

	Faer mine	Lvtang mine	Yongsheng mine	Qingshan mine	Zuojiaying mine	Daqing mine	Guobao mine
Location	Liupanshui city	Bijie city	Bijie city	Duyun city	Bijie city	Bijie city	Xingren county
Depth of coal seams (m)	300~1020	220~1000	200~1000	160~900	280~1100	400~1050	600~1000
Coal seam plunge (°)	10	10	8	10	12	12	8
Average thickness of coal seams (m)	2.8	1.99	2.65	3.6	1.7	2.35	1.59
Direct roof lithology	Mudstone	Siltstone	Limestone	Sandstone	Limestone	Pelitic siltstone	Limestone, marlstone
Indirect roof lithology	Pelitic siltstone	Packsand, limestone	Limestone	Macker	Limestone	Limestone	Limestone
Coal mining method				Longwall mining method			

information of rock deformation and failure and can even be used as a reliable method to identify fracture propagation during hydraulic fracturing [12, 13]. The process energy releasing law based on AE characteristic parameters has been studied a lot [14], and a series of damage constitutive relations have been proposed [15]. Under specific geological background, the deformation and failure characteristics of rock under different stress paths and confining pressures have been proved to be able to reflect the deformation properties of gob surrounding rock [16]. Hence, it is necessary to study the deformation and failure characteristics of gob surrounding rock based on the stress-strain relations and energy releasing law.

The background of this study is the growing deep mining operations in mountainous areas of Guizhou Province. Basing on triaxial compression unloading experiment and AE test, we studied the deformation and failure characteristics of gob sidewall rock and overburden rock under different buried depths. The findings of the study would be useful for strength characteristics and failure predicting of gob surrounding rock under different buried depths and also provide some inspiration for the evaluation of deep hydraulic fracturing.

2. Experimental Material, System, and Procedures

2.1. Test Specimens and Apparatus. In this study, as the overburden and sidewall rock of the gob, the thick limestone of Feixianguan Formation of the Lower Triassic, which is exposed from the mining slope of Daqing Coal Mine in Nayong County, Guizhou Province, was selected as the experimental object. According to the rock test standards of the International Society for Rock Mechanics (ISRM) [17], cylindrical samples with a diameter of 50 mm and a length of 100 mm were prepared. In order to avoid the discretization of experimental results, all samples are prepared from the same rock mass, the cutting direction is perpendicular to the rock layer, and the samples do not contain the layers and primary joints [18].

The MTS815 Flex Test GT triaxial rock mechanics test system was used for the test (Figure 1), which can provide normal load capacity up to 4600 kN and maximum allowable
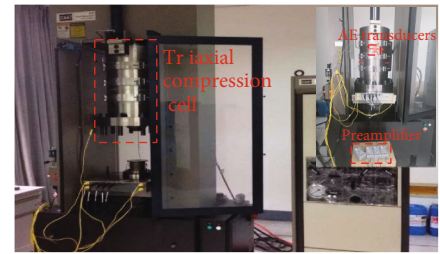
FIGURE 1: MTS815 Flex Test GT triaxial rock mechanics test system and Micro-II Digital AE System.

confining pressure 140 MPa. Linear variable differential transformer (LVDT) was used to obtain the full stress-strain curve of the rock. The Micro-II Digital AE System was used to monitor the acoustic signal of material fracture. Before the test, four AE sensors were symmetrically fixed on the pressure chamber (Figure 1), and the adhesive was Vaseline. In the test, the threshold of acoustic emission amplitude was set at 40 dB to eliminate the influence of environmental noise. The elastic wave generated by rock fracture is received by the sensors after passing through the cold shrinkable tube on the sample surface, hydraulic oil, and the outer wall of the pressure chamber, which will weaken the intensity of the AE signal, which is inevitable. However, this measurement method has little influence on the determination of characteristic AE signals such as yield, macroscopic fracture, and friction sliding between fracture surfaces [16].

2.2. Testing Scheme. Deep mining is often met with huge gob surrounding rock stress. We collected the original stress data at different buried depths and calculated the equivalent confining pressure at different buried depths. According to the statistical results in Table 2, in the range of buried depth less than 1000 m, excluding data noise, the confining pressure fluctuates within 5~20 MPa [19–21]. In this study, the confining pressures of 5 MPa, 10 MPa, and 20 MPa were selected to simulate the original rock stress under different buried depths.

Under the same confining pressure (that is, the same buried depth), three different stress paths were considered to represent the stress environment of the virgin rock

TABLE 2: Statistic results of original rock stress in some underground engineering in China (with the downdip angle as positive) [19–21].

Number	Project	Buried depth	Maximum principal stress			Intermediate principal stress			Minimum principal stress			Equivalent confining pressure
			Value (MPa)	Azimuth (°)	Plunge (°)	Value (MPa)	Azimuth (°)	Plunge (°)	Value (MPa)	Azimuth (°)	Plunge (°)	Value (MPa)
1	Hebi Six Mine	447.66	32.50	258.07	12.35	22.16	101.54	75.56	4.07	349.21	5.19	5.47
2	Jiaozuo Jiulishan Mine	318.70	8.85	357.59	74.80	5.70	192.08	14.53	1.06	101.12	8.9	5.60
3	Lianshao Niumasi Mine	556.57	21.78	87.99	18.56	17.43	282.23	70.89	1.86	170.46	4.38	5.31
4	Beipiao Guanshan Mine	989.05	52.96	34.79	11.25	30.85	148.24	63.45	13.23	299.77	23.71	6.57
5	Xinwen Suncun Mine	870	38.13	100.1	24.2	28.35	79.2	61.5	1.61	14.8	14.1	14.27
6	Jinping II Hydropower Station Tunnel	169	10.9	157	-3	7.2	70	50	6.5	64	-40	9.59
7		169	12.5	139	-18	11.1	39	-29	7.9	77	55	13.57
8		259	16.79	106	-11.04	10.9	23	-27.6	8.9	35.5	59.9	14.05
9		317	11.11	126	-24	7.7	1	-52	5.17	50	27	8.51
10		616	19.11	148	58	9.97	326	31	7.19	56	1	11.17
11		1079	40.69	146	49	18.81	75	-16	12.82	177	-36	18.88

(Scheme 1), gob overburden rock (Scheme 2), and gob sidewall rock (Scheme 3) (Figure 2). In a short time after the formation of the gob, the gob overburden hard strata still bear the gravity of the strata below the ground surface. Furthermore, the lateral constraints of the gob boundary gradually disappear, leading to the development of tensile fractures extending upward from the gob boundary, resulting in a small confining pressure reduction of the gob overburden rock [22]. Without the support of the coal seam, the gravity of the rock above the extracted panel will be completely borne by the gob sidewall rock, leading to the rapid concentration of axial stress on the sidewall rock. The decrease of confining pressure makes the sidewall rock exposed to adverse stress environment.

Different stress path schemes were designed as follows (Figure 3). In order to ensure the representativeness of results, each experimental condition was repeated for 3 times, and AE counting was carried out throughout the whole process.

For each experimental scheme, the confining pressure was first increased to the preset value (5 MPa, 10 MPa, and 20 MPa) at a constant rate of 0.5 MPa/s. Considering that the change of confining pressure of overburden rock lags behind the sidewall rock, the unloading rate of confining pressure of Scheme 2 was set in this paper to be less than that of Scheme 3.

Scheme 1. Axial load is applied to sample at a constant rate of 0.1 MPa/s until the specimen fails.

Scheme 2. Increase the axial load at a rate of 0.1 MPa/s to 0.8 q_u (q_u is the peak compressive strength of the rock in Scheme 1). With the axial load unchanged, the confining pressure is reduced at a rate of 0.1 MPa/s until the specimen fails.

Scheme 3. Increase the axial load at a rate of 0.1 MPa/s to 0.6 q_u, and then, decrease the confining pressure at a constant rate of 0.2 MPa/s and continue to increase the axial load at a constant rate of 0.1 MPa/s until the specimen fails.

In each experiment scheme, the confining pressure was kept unchanged, and the residual strength was obtained by continuous axial compression.

3. Results

In this part, the stress and strain characteristics and process energy releasing of rock deformation and failure under different experimental settings are analyzed. In the process of compression deformation of rock specimens, the initiation, expansion, and coalescence of microcracks often result in energy releasing, and the magnitude of which can be directly characterized by AE counting. The damage variable defined by AE counting is used to characterize the whole process of energy releasing. Considering that the rock still retains different degrees of residual strength after failure under different loading conditions [14], the damage variable D' is defined as
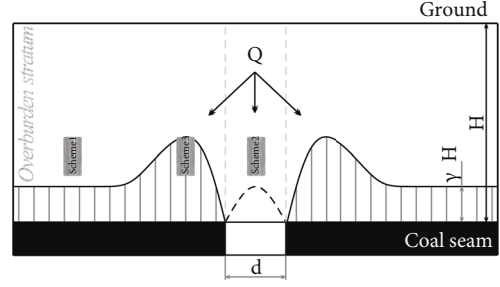
Figure 2: The stress environment of gob surrounding rock (d: the width of open-off cut; γ: unit weight of rock; H: thickness of rock; Q: weight of gob overburden rock).

$$D' = \left(1 - \frac{\sigma_c}{\sigma_d}\right) \times \frac{C_d}{C_0}, \tag{1}$$

where σ_c is the residual strength, σ_d is the peak compressive strength, C_d is the cumulative ringing count at any time, and C_0 is the cumulative ringing count in the whole process.

According to the ringing count and the characteristics of damage variables, the deformation and failure of rock under different test conditions can be divided into three periods, namely, A—the quiet phase, B—the transition phase, and C—the acute phase.

3.1. The Virgin Rock. The confining pressure was kept constant throughout the test process for studying the mechanical properties of the virgin rock at different buried depths. Figures 4 and 5 show the whole process of stress-strain relations under three different confining pressures and the fracture sketch after failure. It is obvious that with the increase of confining pressure, the peak compressive strength increases significantly, and the elastic modulus increases slightly. We determined the primary and secondary fractures by observing the sequence and the width of fractures, the fracture sketch shows that the failure mode of rock changes from brittleness to ductility, and the increase of confining pressure leads to more secondary fractures in the failure process, which intersect with the main fractures to form several groups of "shear joints." See in Figure 6, under the confining pressure of 5 MPa, the rock deformation and failure experience "A-C-A," which is manifested as the energy short-term releasing, and brittle failure occurs after the completion of the releasing of high-level energy. Under 10 MPa, the rock deformation and failure experience "B-C-A," and part of the energy releasing occurs in the elastic deformation stage. The "acute phase" starts almost at the same time as the plastic deformation, and the residual strength appears after the end of the "acute phase," and then, it enters the "quiet phase." Under 20 MPa, the rock deformation and failure experience "A-B-C-A." Compared with the condition of low confining pressure, the energy releasing is less in elastic deformation stage, and the "acute phase" starts only after the partial plastic deformation of the rock. It can be seen that the increase of confining pressure brings the hysteresis of energy releasing.
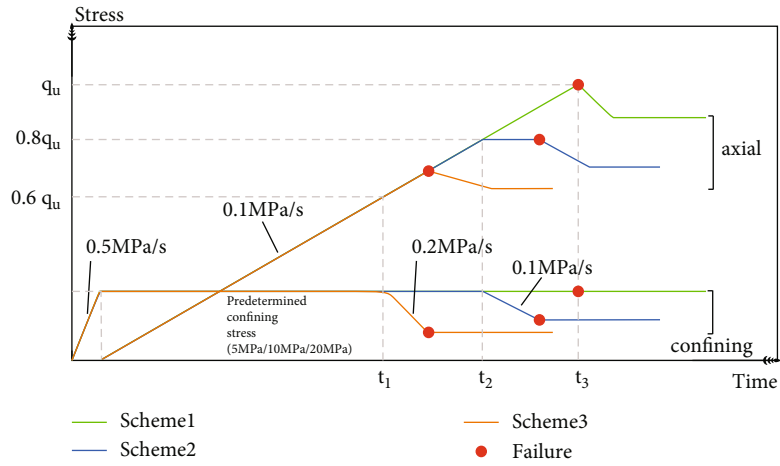
FIGURE 3: The experimental design of three stress paths (q_u is the peak compressive strength under different confining pressures in Scheme 1; t_1 and t_2 represent the moment when the confining pressure in Schemes 3 and 2 begins to change, and t_3 represents the moment when the sample in Scheme 1 is in peak stress).
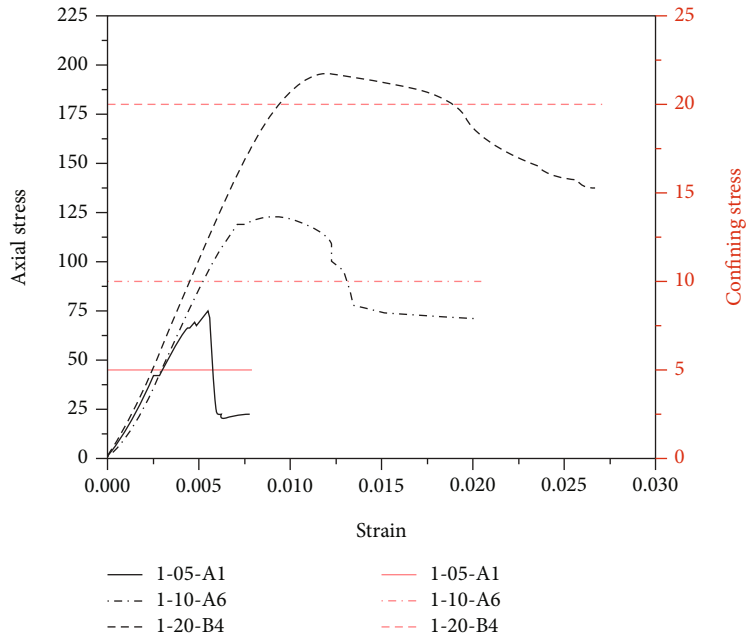
FIGURE 4: Axial stress/confining pressure-strain relations of Scheme 1 under different confining pressures.
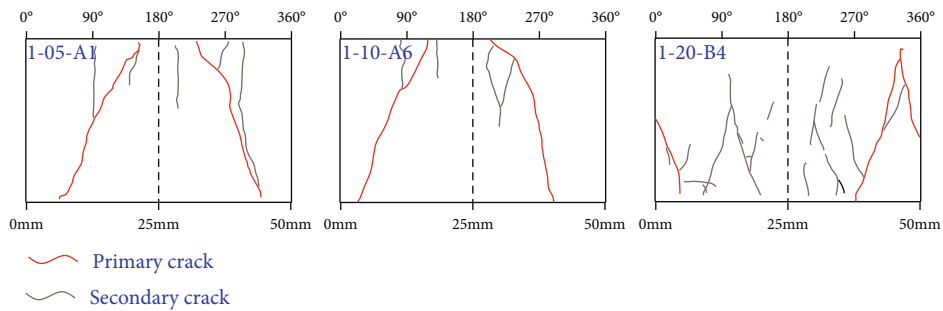
FIGURE 5: Sketch of fractures after failure of Scheme 1 under different confining pressures.

(a)

(b)

(c)
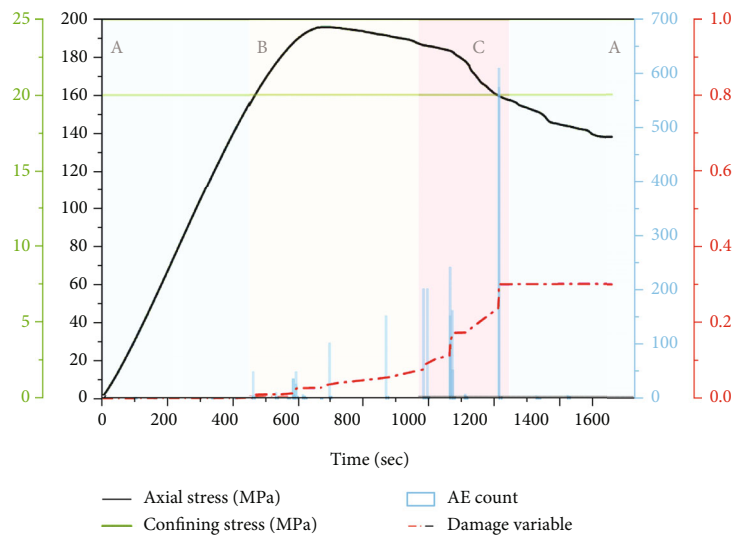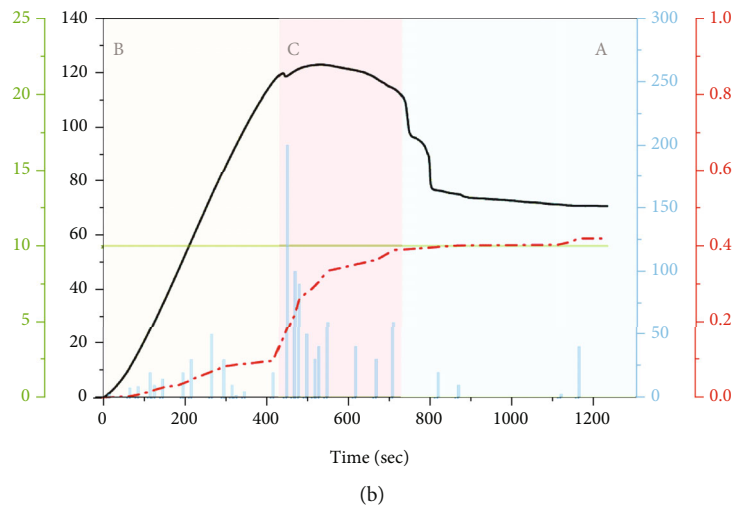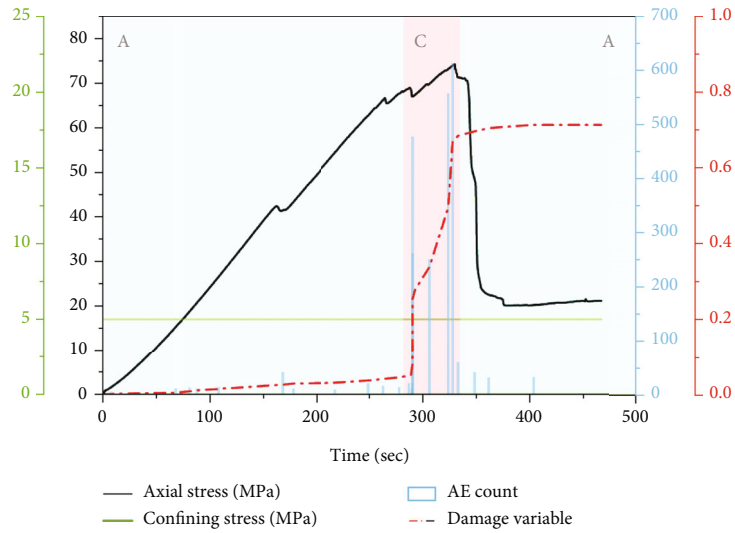
Figure 6: AE ringing count/damage variable-time relations of Scheme 1 under different confining pressures (confining pressure setting: (a) 5 MPa, (b) 10 MPa, and (c) 20 MPa).
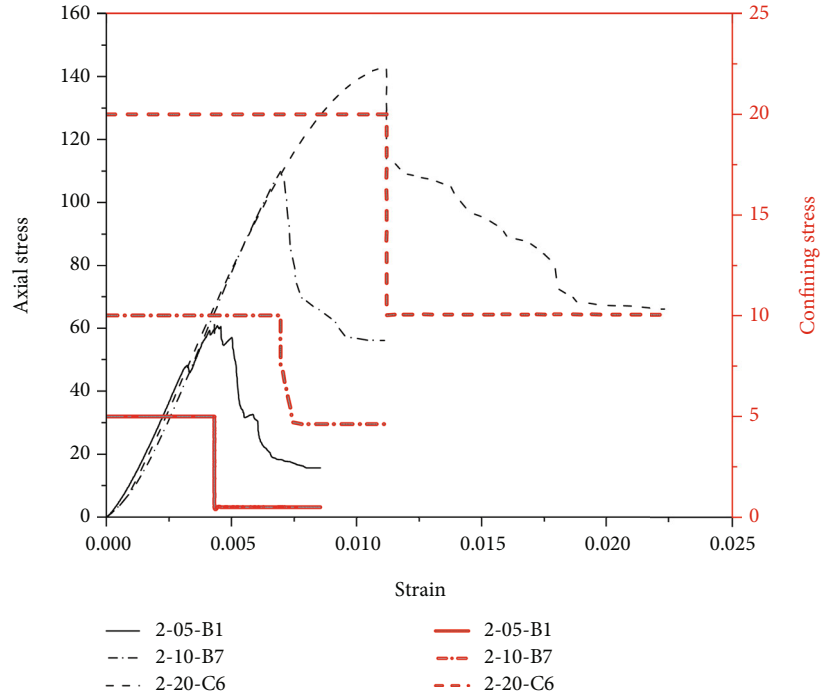
FIGURE 7: Axial stress/confining pressure-strain relations of Scheme 2 under different confining pressures.
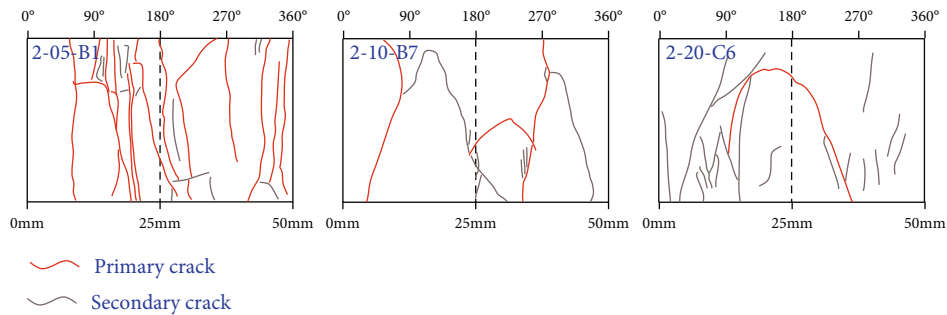
FIGURE 8: Sketch of fractures after failure of Scheme 2 under different confining pressures.

3.2. The Gob Overburden Rock. Under different confining pressure conditions, the rock presents brittle failure, and the axial stress drop almost appears when the confining pressure decreases (Figure 7). Under 20 MPa, the postpeak residual deformation is larger. Under low confining pressure, the deformation and failure are controlled by tensile crack, while under high confining pressure they are controlled by shear crack (Figure 8). See in Figure 9, under 5 MPa, the rock deformation and failure experience "A-C-A." Obviously, confining pressure unloading causes a longer "acute phase," in which "the acute phase" mainly contains two major energy releasing events, the first one occurs before the unloading stage of confining pressure and the second one in the postpeak stress adjustment stage. The energy releasing at the second one may be caused by further dislocations of the coarse joints inside the rock [16]. Under

10 MPa, the rock deformation and failure experience "A-B-C-A," and the unloading of confining pressure, plastic deformation, and the beginning of the "acute phase" appear almost at the same time. Under 20 MPa, the rock deformation and failure experience "A-B-C-A," which is different from the energy releasing of the virgin rock. The plastic deformation starts almost at the same time as the "acute phase," and sustain time is slightly longer.

3.3. The Gob Sidewall Rock. With the increase of confining pressure, the failure form changes from brittleness failure to plasticity failure. However, different from the virgin rock, the threshold value of confining pressure required by the transition from brittleness to plasticity becomes higher in this case (Figure 10). The deformation and failure are controlled by the "tension-shear" composite crack, and the failure tends to

(a)

(b)

(c)
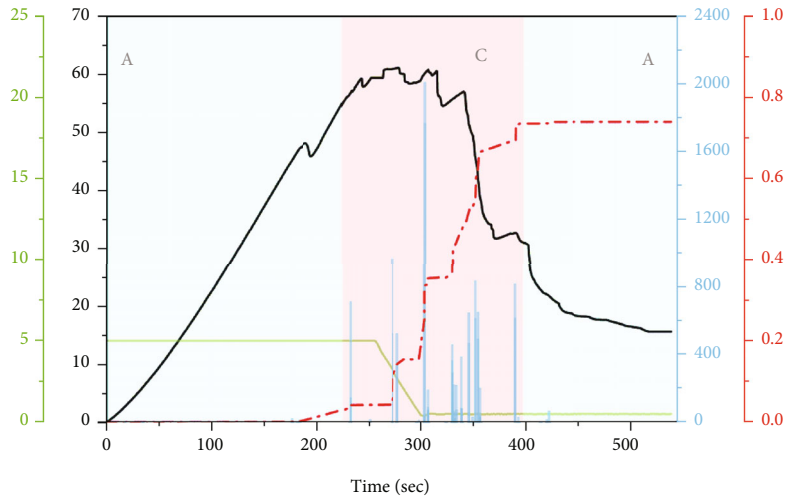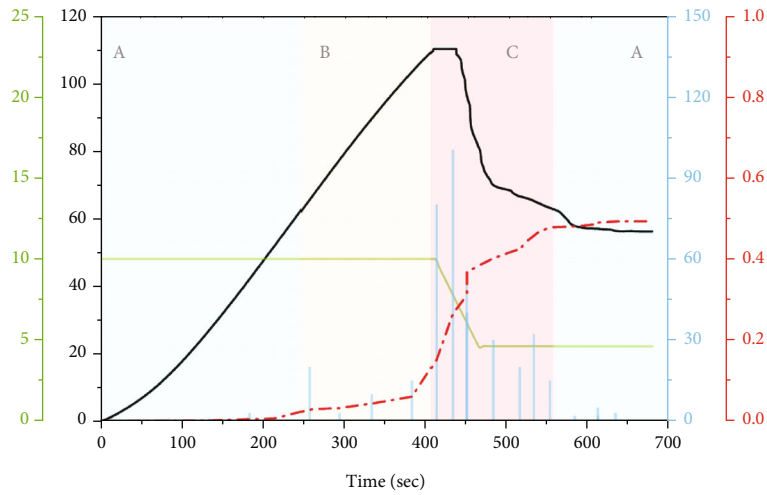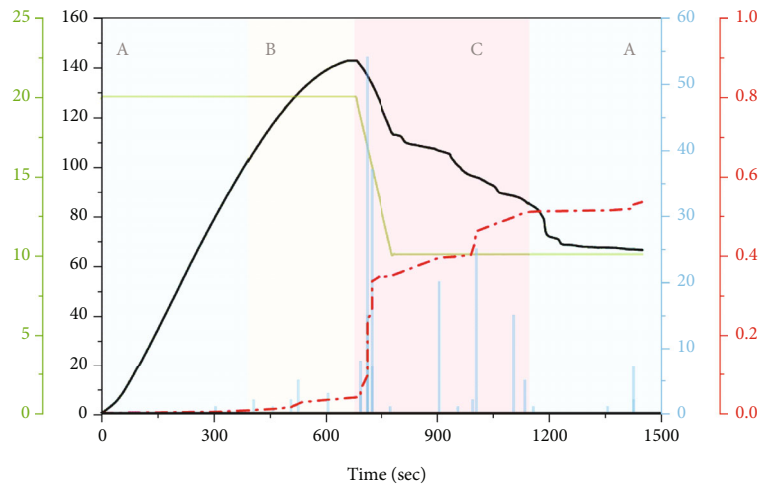
Figure 9: AE ringing count/damage variable-time relations of Scheme 2 under different confining pressures (confining pressure setting: (a) 5 MPa, (b) 10 MPa, and (c) 20 MPa).
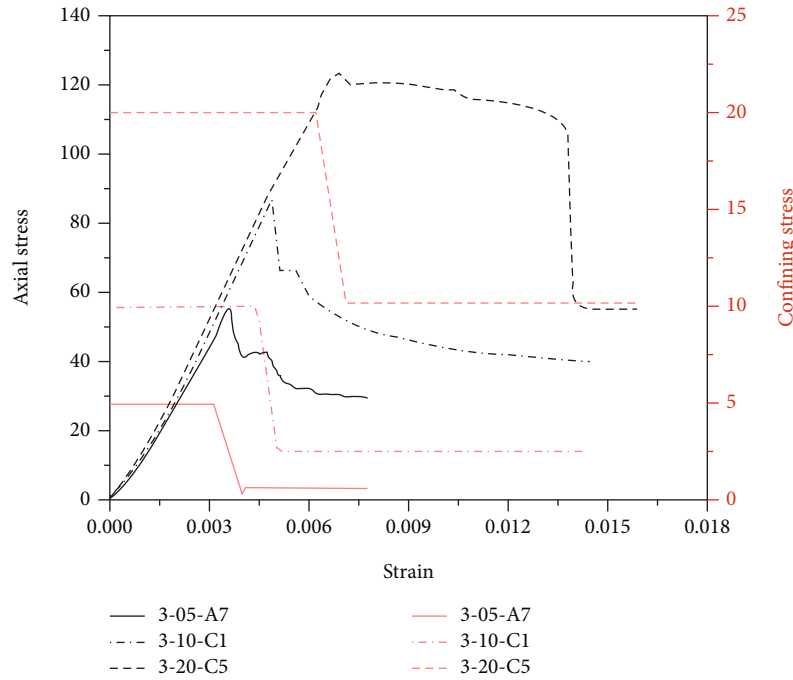
FIGURE 10: Axial stress/confining pressure-strain relations of Scheme 3 under different confining pressures.
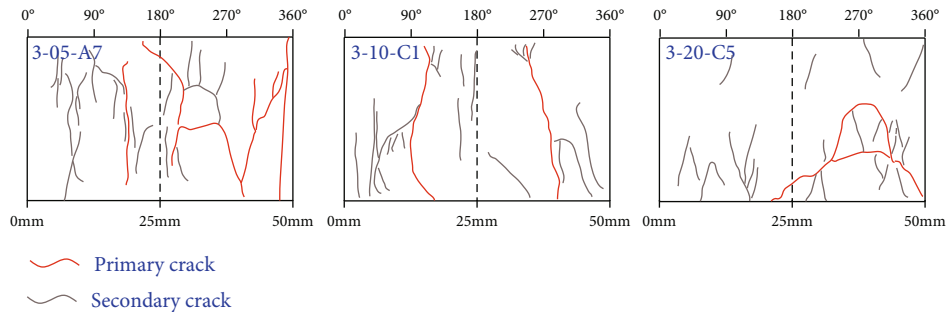
FIGURE 11: Sketch of fractures after failure of Scheme 3 under different confining pressures.

integrate from fragmentation with the increase of confining pressure (Figure 11). See in Figure 12, under 5 MPa, the rock deformation and failure experienced "A-C-A," and the unloading of confining pressure triggered the energy releasing in the "acute phase." The first postpeak stress drop event did not release too much energy, and after the stress adjustment in the later period, there appeared an energy release event with the largest ring count. Under 10 MPa, the rock deformation and failure experience "A-C-B-A." Similarly, the unloading of confining pressure almost happens at the same time as the energy releasing in the "acute phase." A large amount of energy is released near the peak compressive strength, and a small amount of energy is released in the residual deformation stage. Under 20 MPa, rock deformation and failure experience "A-C-B-C-A," the unloading of confining pressure causes the energy releasing of the first "acute phase," and as the rock strain softening phenomenon, a small number of AE signal is received. After the accumulation of deformation, the second

"acute phase" occurs, the axial stress drops rapidly, and then, the residual deformation occurs. Obviously, under low confining pressure, the advance reduction of confining pressure makes the energy releasing in the "acute phase" more dispersed and the duration longer. With the increase of the initial confining pressure (buried depth), the failure mode of the rock changes from brittleness to plasticity and causes several "acute phases."

4. Discussion

Table 3 statistics the peak compressive strength, residual strength, and damage variables of the virgin rock, the gob overburden rock, and the gob sidewall rock under different confining pressures (buried depths).

For peak compressive strength and residual strength: compared with the virgin rock and the gob overburden rock, the gob sidewall rock always has the lowest peak compressive

(a)

(b)

(c)
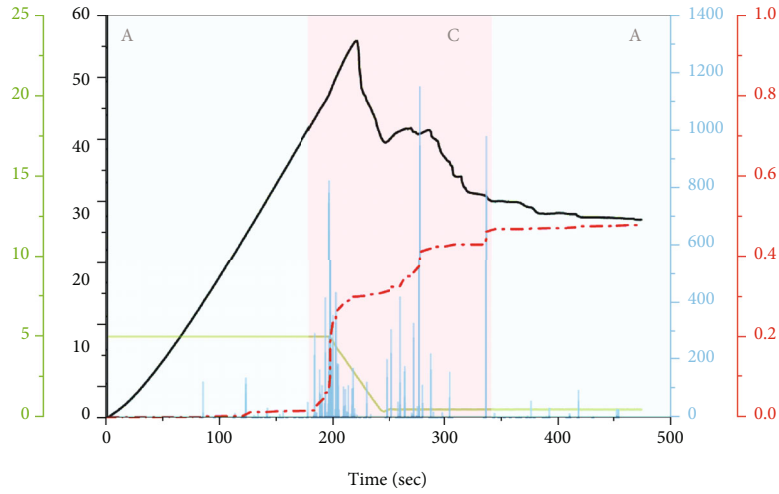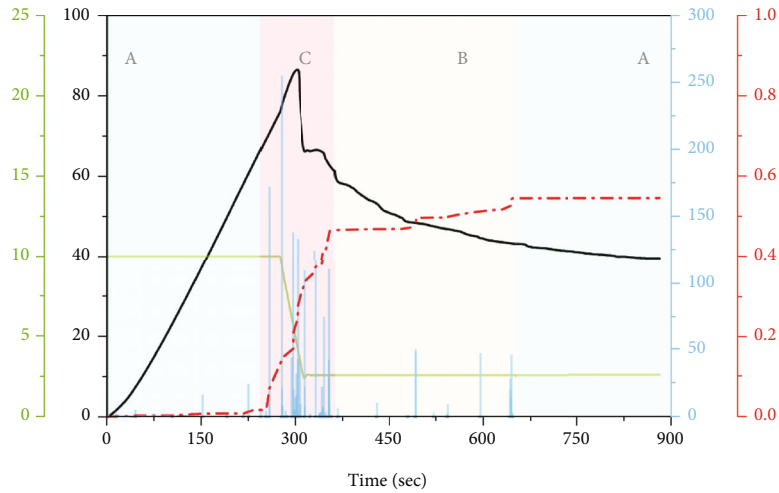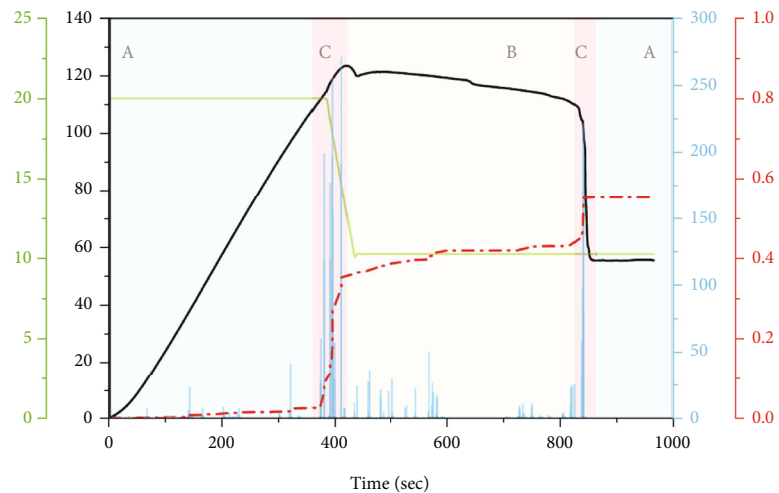
FIGURE 12: AE ringing count/damage variable-time relations of Scheme 3 under different confining pressures (confining pressure setting: (a) 5 MPa, (b) 10 MPa, and (c) 20 MPa).

TABLE 3: The mechanics and damage characteristic values of each scheme.

	Specimen number	Confining stress (MPa)	Peak strength (MPa)	Residual strength (MPa)	Damage variable
	A1	5	74.63	21.11	0.712
Scheme 1	A6	10	123.29	70.55	0.419
	B4	20	196.38	137.66	0.298
	B1	5	60.10	15.64	0.740
Scheme 2	B7	10	110.46	56.08	0.492
	C6	20	143.01	66.63	0.534
	A7	5	56.54	29.55	0.477
Scheme 3	C1	10	87.59	39.46	0.545
	C5	20	123.92	55.24	0.552
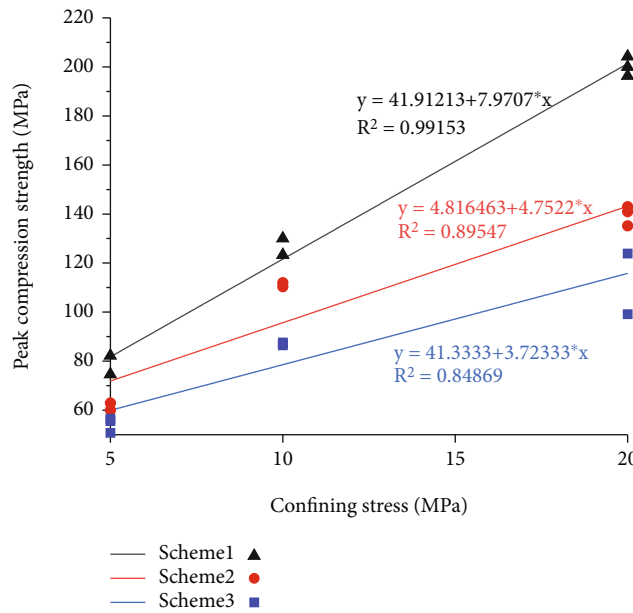
FIGURE 13: The peak compressive strength of each scheme.

strength under different confining pressures (Figure 13). After the stress redistribution, the probability of instability failure is great. Cai et al. [23] and Liang et al. [16] proposed that the gob surrounding rock with higher residual strength tends to have a smaller yield range, and the residual strength is of great significance to underground construction and support design. By comparing the experimental results in this paper, it is found that the increase of confining pressure can effectively improve the residual strength of the gob overburden rock and sidewall rock. In addition, the residual strength of the gob overburden rock is the minimum when the confining pressure is 5 MPa, while the residual strength of the gob sidewall rock is the minimum when the confining pressure is 10 MPa or 20 MPa.

For damage variables: with the increase of confining pressure, the damage variables of the virgin rock, the gob overburden rock, and the gob sidewall rock show the characteristics of gradually decreasing, decreasing first and then increasing, and gradually increasing, respectively. Under 5 MPa, the damage variable of the gob overburden rock is the largest (value is up to 0.740). Under 10 MPa and 20 MPa, the damage variable of the gob sidewall rock is the largest (value is 0.545 and 0.552, respectively).

According to the above analysis of peak compressive strength, residual strength, and damage variables, it is shown that with the increase of confining pressure (buried depth), the gob sidewall rock is the most vulnerable to damage and the degree of damage is the largest. Therefore, the gob sidewall rock is the key point of disaster prevention during deep mining in mountainous area. Furthermore, horizontal wells are more stable than vertical ones during deep hydraulic fracturing. As can be seen from Figure 12, with the increase of confining pressure, the failure mode of the gob sidewall rock changes from brittleness to plasticity. Under high confining pressure (20 MPa), rock failure occurs after two "acute phases." Therefore, the "acute phase" of AE for the first time can be used as the precursor information of the failure of the gob sidewall rock under high confining pressure. The precursor information of surrounding rock failure under high
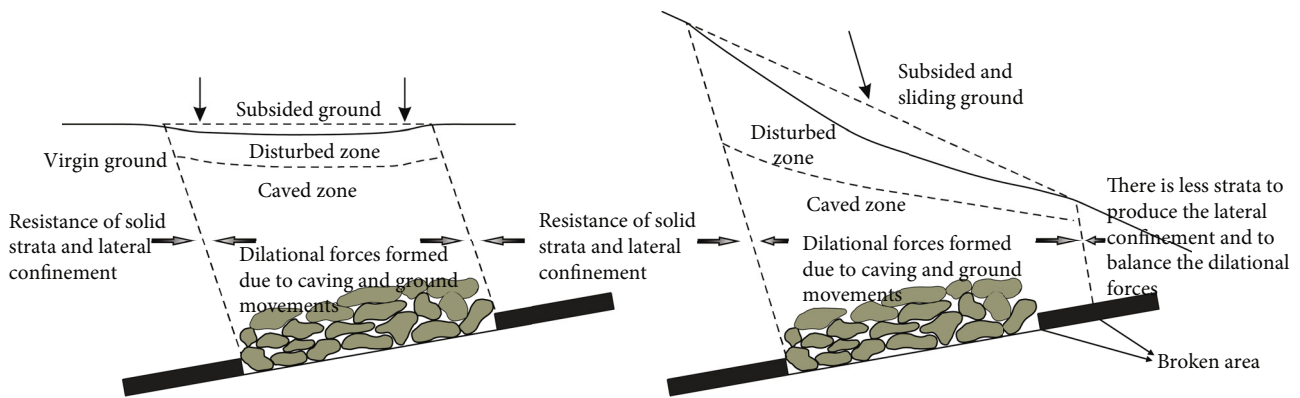
FIGURE 14: The gob overburden rock stress state of flat/sloping terrain in mountainous areas ((a) flat terrain and (b) sloping terrain, adapted from [6]).

pressure determined by the "acute phase" of AE can also be used to predict the formation of fracture network during hydraulic fracturing.

It should be noted that, under the background of mining in mountainous areas, the change of stress environment of the gob overlying rock is extremely complex in a long time after mining (Figure 14). In order to quantify the deformation and failure properties of the gob surrounding rock more accurately, the authors will consider the influence of complex stress paths on the gob overburden rock in the further study.

5. Conclusion

Three different initial confining pressures were set, and triaxial compression unloading tests were carried out on limestone under different stress paths. The deformation and failure characteristics of the virgin rock, the gob overburden rock, and the gob sidewall rock under different confining pressures (buried depths) were studied. Meanwhile, the damage variables were obtained through the whole-process AE monitoring. Based on the analysis of the experimental results, the failure precursors of the gob sidewall rock in deep mining (within 1000 m) are proposed.

The main conclusions are as follows:

(1) The gob sidewall rock has higher confining pressure threshold of brittle-plastic transformation than the virgin rock, while the gob overburden rock has brittle failure at different confining pressures (buried depths).

(2) Under 10 MPa and 20 MPa, the unloading of confining pressure triggers the immediate energy releasing of the gob overburden rock and sidewall rock. However, under 5 MPa, the unloading of the confining pressure causes the energy releasing of the gob overburden rock and sidewall rock to be more dispersed, and part of the energy can only be released in the postpeak stress adjustment stage. In addition, the increase of confining pressure (buried depths) will cause a lag in the energy releasing of the virgin rock.

(3) With the increase of confining pressure (buried depth), the part with the greatest damage degree changes from the gob overburden rock to the sidewall rock, and the peak compressive strength and residual strength of the sidewall rock are the lowest under the background of deep mining.

(4) Under the background of deep mining in mountainous areas, the gob sidewall rock mainly appears plastic failure, and the "acute phase" of AE for the first time can be used as the precursor information for the failure of the gob sidewall rock and crack propagation of hydraulic fracturing.

Data Availability

The AE and triaxial compression unloading data used to support the findings of this study are available from the corresponding author upon request.

Conflicts of Interest

The authors declare that they have no conflicts of interest.

Acknowledgments

References

[1] L. Driad-Lebeau, F. Lahaie, M. Al Heib, J. P. Josien, P. Bigarré, and J. F. Noirel, "Seismic and geotechnical investigations following a rockburst in a complex French mining district,"

International Journal of Coal Geology, vol. 64, no. 1-2, pp. 66–78, 2005.

[2] A. G. Yardimci and M. Karakus, "A new protective destressing technique in underground hard coal mining," *International Journal of Rock Mechanics and Mining Sciences*, vol. 130, article 104327, 2020.

[3] Z. L. Li, X. Q. He, L. M. Dou, D. Z. Song, and G. F. Wang, "Numerical investigation of load shedding and rockburst reduction effects of top-coal caving mining in thick coal seams," *International Journal of Rock Mechanics and Mining Sciences*, vol. 110, pp. 266–278, 2018.

[4] E. Fathi Salmi, M. Nazem, and M. Karakus, "Numerical analysis of a large landslide induced by coal mining subsidence," *Engineering Geology*, vol. 217, pp. 141–152, 2017.

[5] C. Yu, C. Han, R. Xie, and L. Wang, "Mechanical behavior analysis of buried pipeline under stratum settlement caused by underground mining," *International Journal of Pressure Vessels and Piping*, vol. 188, article 104212, 2020.

[6] Z. Jianjun, W. Xun, S. Yanbing, W. Jiangbo, and M. L. Lee, "Deformation behavior of mining beneath flat and sloping terrains in mountainous areas," *Geofluids*, vol. 2021, Article ID 6689966, 16 pages, 2021.

[7] J. L. Yu, J. J. Zhao, H. Y. Yan et al., "Deformation and failure of a high-steep slope induced by multi-layer coal mining," *Journal of Mountain Science*, vol. 17, no. 12, pp. 2942–2960, 2020.

[8] J. G. Zhang, W. Yang, B. Lin, J. J. Zhang, and M. Wang, "Strata movement and stress evolution when mining two overlapping panels affected by hard stratum," *International Journal of Mining Science and Technology*, vol. 29, no. 5, pp. 691–699, 2019.

[9] Q. Sun, F. Ma, J. Guo et al., "Excavation-induced deformation and damage evolution of deep tunnels based on a realistic stress path," *Computers and Geotechnics*, vol. 129, article 103843, 2021.

[10] Y. Wang, D. Liu, J. Han, C. Li, and H. Liu, "Effect of fatigue loading-confining stress unloading rate on marble mechanical behaviors: an insight into fracture evolution analyses," *Journal of Rock Mechanics and Geotechnical Engineering*, vol. 12, no. 6, pp. 1249–1262, 2020.

[11] Z. Zhang, M. Deng, J. Bai, X. Yu, Q. Wu, and L. Jiang, "Strain energy evolution and conversion under triaxial unloading confining pressure tests due to gob-side entry retained," *International Journal of Rock Mechanics and Mining Sciences*, vol. 126, article 104184, 2020.

[12] Z. Jiang, Q. Li, Q. Hu et al., "Acoustic emission characteristics in hydraulic fracturing of stratified rocks: a laboratory study," *Powder Technology*, vol. 371, pp. 267–276, 2020.

[13] B. Q. Li, B. Gonçalves da Silva, and H. Einstein, "Laboratory hydraulic fracturing of granite: acoustic emission observations and interpretation," *Engineering Fracture Mechanics*, vol. 209, pp. 200–220, 2019.

[14] P. Jin, E. Wang, X. Liu, N. Huang, and S. Wang, "Damage evolution law of coal-rock under uniaxial compression based on the electromagnetic radiation characteristics," *International Journal of Mining Science and Technology*, vol. 23, no. 2, pp. 213–219, 2013.

[15] A. Cao, G. Jing, Y. L. Ding, and S. Liu, "Mining-induced static and dynamic loading rate effect on rock damage and acoustic emission characteristic under uniaxial compression," *Safety Science*, vol. 116, pp. 86–96, 2019.

[16] Y. Liang, Q. Li, Y. Gu, and Q. Zou, "Mechanical and acoustic emission characteristics of rock: effect of loading and unloading confining pressure at the postpeak stage," *Journal of Natural Gas Science and Engineering*, vol. 44, pp. 54–64, 2017.

[17] C. E. Fairhurst and J. A. Hudson, "Draft ISRM suggested method for the complete stress-strain curve for intact rock in uniaxial compression," *International Journal of Rock Mechanics and Mining Sciences*, vol. 36, pp. 281–289, 1999.

[18] G. Gao, M. A. Meguid, and L. E. Chouinard, "On the role of pre-existing discontinuities on the micromechanical behavior of confined rock samples: a numerical study," *Acta Geotechnica*, vol. 15, no. 12, pp. 3483–3510, 2020.

[19] H. Kang, L. Wu, F. Gao, H. Lv, and J. Li, "Field study on the load transfer mechanics associated with longwall coal retreat mining," *International Journal of Rock Mechanics and Mining Sciences*, vol. 124, article 104141, 2019.

[20] A. Saeidi, S. Heidarzadeh, S. Lalancette, and A. Rouleau, "The effects of in situ stress uncertainties on the assessment of open stope stability: case study at the Niobec Mine, Quebec (Canada)," *Geomechanics for Energy and the Environment*, vol. 25, p. 100194, 2021.

[21] C. Zhang, X. T. Feng, and H. Zhou, "Estimation of in situ stress along deep tunnels buried in complex geological conditions," *International Journal of Rock Mechanics and Mining Sciences*, vol. 52, pp. 139–162, 2012.

[22] G. Feng and P. Wang, "Simulation of recovery of upper remnant coal pillar while mining the ultra- close lower panel using longwall top coal caving," *International Journal of Mining Science and Technology*, vol. 30, no. 1, pp. 55–61, 2020.

[23] M. Cai, P. K. Kaiser, Y. Tasaka, and M. Minami, "Determination of residual strength parameters of jointed rock masses using the GSI system," *International Journal of Rock Mechanics and Mining Sciences*, vol. 44, no. 2, pp. 247–265, 2007.

Research Article

Numerical Simulation of Fracturing in Coals Using Water and Supercritical Carbon Dioxide with Potential-Based Cohesive Zone Models

Jianfeng Yang, Yuqing Ren, Dingding Zhang🆔, Yongliang Liu🆔, and Zhe Ma

Key Laboratory of Western Mine Exploitation and Hazard Prevention, Ministry of Education, Xi'an University of Science and Technology, Xi'an, Shaanxi 710054, China

Correspondence should be addressed to Dingding Zhang; zhangdd@xust.edu.cn

The Park-Paulino-Roesler (PPR) cohesive zone model (CZM) for coal was established for analyzing mixed-mode I/II fractures using semicircular specimens under punch-through shear (PTS) and three-point bending (SCB) tests. In these methods, the main parameters of the fracture were obtained through SCB tests and PTS tests. And according to the experimental results, the coal specimens show obvious characteristics of ductile fracture under mode I and II loading. Moreover, hydraulic and supercritical carbon dioxide (ScCO$_2$) fracture tests were conducted, and accordingly, it was found that the crack initiation pressure of coal specimens for hydraulic fracturing is 17.76 MPa, about 1.59 times that driven by ScCO$_2$. And the crack initiation time of coal with ScCO$_2$ fracturing is 123.73 s, which is 1.58 times that for hydraulic fracturing. A macrocrack eventually formed in the coal specimen due to the hydraulic drive, which penetrated through the entire specimen. Yet, there was no crack penetrating the whole fracture specimen and several widely distributed secondary cracks in the fractured coal specimens by ScCO$_2$. Furthermore, zero-thickness pore pressure cohesive elements were utilized to investigate multicrack propagation in coals undergoing hydraulic and ScCO$_2$ fracturing. The constitutive relationships of the established PPR CZM were introduced into the cohesive elements. The obtained results are consistent with the hydraulic and ScCO$_2$ fracturing experiment results for the coal specimens. This indicates that the established PPR CZMs can accurately represent the crack propagation behavior in coals for hydraulic and ScCO$_2$ fracturing.

1. Introduction

As an essential type of clean energy, the exploitation of coalbed methane (CBM) is of significant importance to increase the supply of clean energy, thereby decreasing concerns about greenhouse gases and realizing safe coal mining [1, 2]. Studies show that the low permeability of coal seams is one of the main challenges for the efficient exploitation of CBM. Generally, coal permeability in Chinese mines is less than 1 mD [3], which is much lower than that in the United States, Australia, and other countries. In this regard, hydraulic fracturing is a widely adopted technology to improve the CBM permeability and, therefore, production by injecting a large volume of water-based fluid to create and extend fracture networks [4, 5]. Hence, in the process of

hydraulic fracturing, the crack propagation behavior in coals will have a direct influence on the effect of CBM exploitation. However, there are some drawbacks to the hydraulic fracturing technology; for example, it will cause a lot of waste and pollution of water resources, and the fracturing fluid will cause "water sensitive" and "water lock" influence on coalbed methane reservoir [6]. In order to resolve these shortcomings, numerous nonaqueous fracturing technologies have been proposed [7, 8], among which the supercritical carbon dioxide (ScCO$_2$) fracturing technology has attracted much attention [9]. ScCO$_2$ refers to a special state of CO$_2$ when its temperature and pressure exceed 31.1°C and 7.38 MPa, respectively, which has unique physical and chemical characteristics, including low viscosity, high diffusion coefficient, and high density [10]. Some researchers have conducted

experiments on rocks with $ScCO_2$ fracturing, and the results show that $ScCO_2$ fracturing can produce more widely distributed and complex fracture networks in rocks than hydraulic fracturing, which can significantly increase reservoir permeability [11–13]. In addition, $ScCO_2$ also has a good displacement effect on methane adsorbed in the coal seam, which will be beneficial to improve the yield of coalbed methane [14]. Therefore, $ScCO_2$ fracturing technology can promote the efficient exploitation of coalbed methane, and the most important thing is the research on the crack propagation law of coal driven by $ScCO_2$.

Since the groundbreaking work of Irwin [15] and Griffith [16], linear elastic fracture mechanics (LEFM) was established, becoming a highly effective theory framework for analyzing crack propagation in brittle solid materials. Bieniawski [17, 18] systematically introduced the LEFM into the research of crack propagation behavior in rocks, and since then, rock fracture mechanics has been widely used in rock materials. Generally, the fracture toughness (K_c) is applied as an indicator, reflecting the crack propagation in natural materials [19–21]. Nevertheless, LEFM is mostly limited to investigating crack propagation in brittle rocks. Yet, some soft rocks, such as coal, exhibit generally ductile failure behaviors, represented by an obvious strain-softening stage after the peak stress when the crack initiates [22, 23]. It is because of the fracture process zone (FPZ) [24] of these soft rocks, i.e., the particular region in front of the crack tip, where a series of nonlinear softening behaviors including microcrack initiation, and plastic strain and mineral crystal friction occurrence, are sizable. It is also nonnegligible relative to the size of the rock specimen and the size of the crack. In comparison to brittle rocks, abundant primary pores and microfissures exist in the coal body [25], causing the ductile fracture characteristics of coals to be more prominent. Thus, the theory of LEFM does not apply to the study of the fracture behavior of coals.

The CZM inspired by the studies of Barenblatt [26], Dugdale [27], and Hillerborg et al. [28] has been used with success to represent the crack propagation behavior in nonlinear FPZ of ductile materials. In this theory, the FPZ is simplified hypothetically to a discrete line or plane corresponding to either a two-dimensional or three-dimensional case, respectively, in which the hypothetical cohesive stress causes the virtual crack to close (see Figure 1). The constitutive relation of CZM is represented by the relationship between the cohesive stress and relative displacement across this line or plane. The above constitutive relation is usually nonlinear and depends on the form of stress and the evolution characteristics of damage variables. When the material in this region is completely damaged, the cohesive stress will be lost, which means that a new macrocrack surface is generated. The energy consumed in this damaging process is the fracture energy of the material. Accordingly, it is concluded that the cohesive crack model can effectively characterize the ductile fracture behavior of coal.

Based on CZM, the numerical crack propagation model for hydraulic fracturing in a rock is established by the finite element method [29], extended finite element method [30], etc. However, the constitutive relationship of the softening
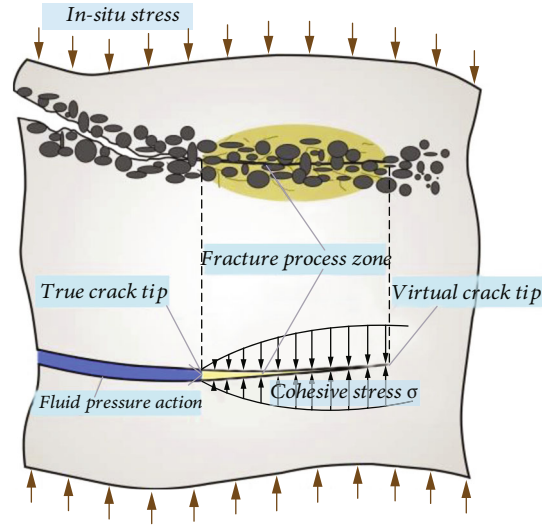
FIGURE 1: Schematic of CZM.

curve has a huge impact on fracture behaviors [31, 32], and the linear or bilinear constitutive relationships of CZMs have been adopted in previous numerical models. Hence, it is necessary to establish the CZM of coals to provide an accurate numerical model to predict crack propagation. Mixed-mode I/II crack propagation is prone to occurrence in coals under engineering conditions, especially in supercritical carbon dioxide fracturing [33]. Reviewing the literature indicates that since the LEFM method does not reflect ductile fractures, it is the most widely used scheme to investigate the crack propagation in coal [34, 35]. On the other hand, cohesive interactions between fractured surfaces are the main failure mechanisms in the mixed-mode I/II CZM. It should be indicated that these interactions can be expressed through stress-strain equations in fractured surfaces. Nonpotential-based models [36–38] were established to characterize the ductile fracture behavior of materials. Considering symmetric systems in cohesive interactions, these models can be simply developed.

Nevertheless, the main drawback of the nonpotential-based model is that one model cannot explain all possible separations in ductile materials. Furthermore, asymmetric tangential stiffness of material increases the computational expenses. An effective solution for this problem is to apply potential-based models to utilize the initial derivative of the fracture potential energy function [39]. This scheme is based on the cohesive stress over the fractured surfaces, while the second derivative reflects the constitutive association. Based on potential-based models, Park et al. [40] proposed the Park-Paulino-Roesler (PPR) model to simulate the cohesive fracture [41, 42]. In this model, fracture energy (including modes I and II) and different initial slopes and cohesive strengths are considered. Meanwhile, corrective variables are defined to cover a wide range of failures in different ductile materials. This model resolves the disadvantages of traditional potential-based models.

In this work, we performed semicircular specimens under PTS and SCB tests to calculate the fracture parameters

and establish a model of PPR for describing the mixed-mode I/II crack propagation in coals. Then, the established model is applied to perform the crack propagation simulation in hydraulic fracturing and $ScCO_2$ fracturing in coals. Hydraulic fracturing and $ScCO_2$ fracturing experiments were then performed for the coals. Finally, comparisons between the test results of hydraulic fracturing and $ScCO_2$ fracturing in coals and the obtained results were utilized to evaluate the performance of the proposed model.

2. Experimental Methods and Process

2.1. Semicircular Specimen under SCB Test. The coal sample in this study is long-flame coal, which is taken from the Huojitu well of Daliuta Coal Mine in Shaanxi Province and buried at a depth of 97 meters. In this experiment, the semicircular specimen under the SCB experiment was used to study the mode I crack propagation behavior of coal samples and to measure the fracture parameters. As shown in Figure 2, coal samples were prepared into semidisk-like specimens, and an artificial crack was prefabricated along the symmetric center starting from the center of the bottom edge of the specimen, and vertical loads were applied on the top of the arc to cause mode I fracture of the specimen. The diameter ($2R$) and thickness (B) of the coal rock SCB specimen were set as 70 mm and 25 mm, respectively. The ratio (α/R) of the preset crack length to the specimen radius was set as 0.35, and the ratio (S/R) of the base supporting roller span to the specimen diameter was 0.5. The loading mode is displacement control, and the loading speed is 0.02 mm/min. In addition, the crack tip opening displacement (CTOD) of the specimen was measured by the fiber grating (FBG) technique (with an accuracy of 0.5 microstrains) throughout the experiment. In this study, three groups of effective SCB tests were conducted on the coal specimens. In this regard, Figure 3 illustrates the load-CTOD curve of coal SCB specimens during the whole experiment, and according to the various characteristics of the experimental curve, the experimental process is generally divided into four steps, including the compaction, elastic deformation, peak load stage, and postpeak damage stages. When crack initiation occurs in coal specimens, the accumulated energy is not released instantaneously, and there is a nonlinear damage process in the postpeak loading stage. The CTOD of the three coal SCB specimens increased by 0.1192 mm, 0.1153 mm, and 0.0895 mm, respectively, with an average value of 0.108 mm, from the beginning of the specimen subjected to the force to the formation of a new crack surface, that is, from the intact specimen to the fracture of the specimen.

2.2. PTS Test. This method was first proposed by Backers et al. [43] to investigate the fracture of materials in mode II loading conditions. The PTS test was used here to simulate mode II fracture experiments in coal, as it is easy to process, and the experimental results are reliable. As shown in Figure 4, the specimen was a circular cylinder with a diameter D and had circular notches with a diameter ID drilled into the upper and lower end faces along the central axis
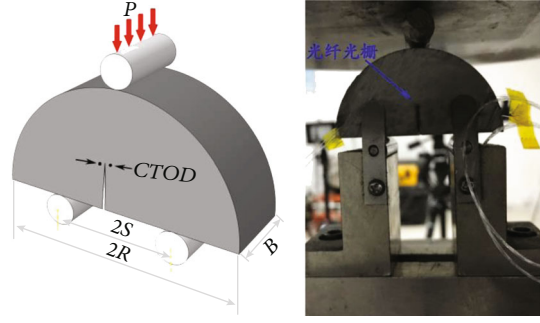
FIGURE 2: Coal SCB specimen [20].
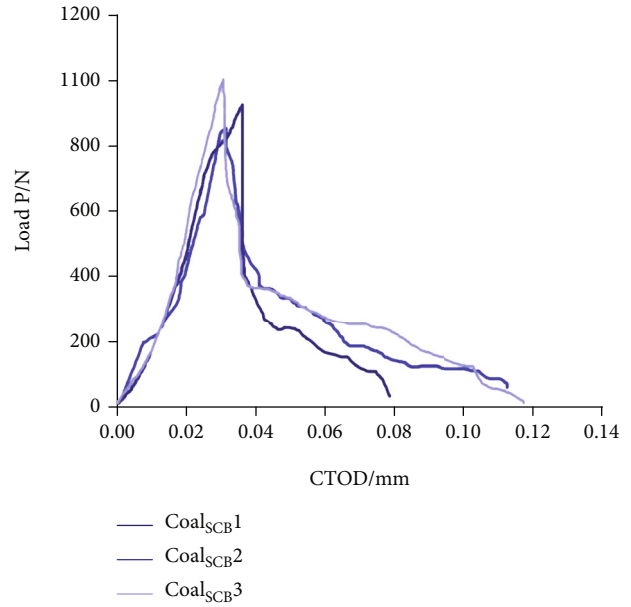
FIGURE 3: Loading-CTOD curve of coal SCB specimens.

of the cylinder. Circular cylinders with diameter D and height L were prepared. Moreover, two circular notches were prepared with depths a and b near the upper end and lower end of the specimen, respectively. The width of notches was set to t, and the effective shear length was $IP = L\text{-}a\text{-}b$. The experiment was performed using a loading cylinder to apply a vertical shear force (P). It is found that as the applied shear stress increases, the crack propagates along the notches parallel to the axis of the cylinder, as well as mode II fracture characteristics which were then able to be acquired from the experimental results. The diameter D and height L of the specimens was set to 50 mm, and the coals were cut into the PTS specimens using diamond wire cutting under the CNC machine tools. This can limit the micromechanical damage to the coal specimens and improves machining accuracy. In addition, notches with a diameter of $ID = 35$ mm were prefabricated along the same central axis utilizing a 0.5-millimeter-thick diamond bit with the CNC machine tools. Parameters a and b of these notches were set to 10 mm and 30 mm, respectively. Moreover, the
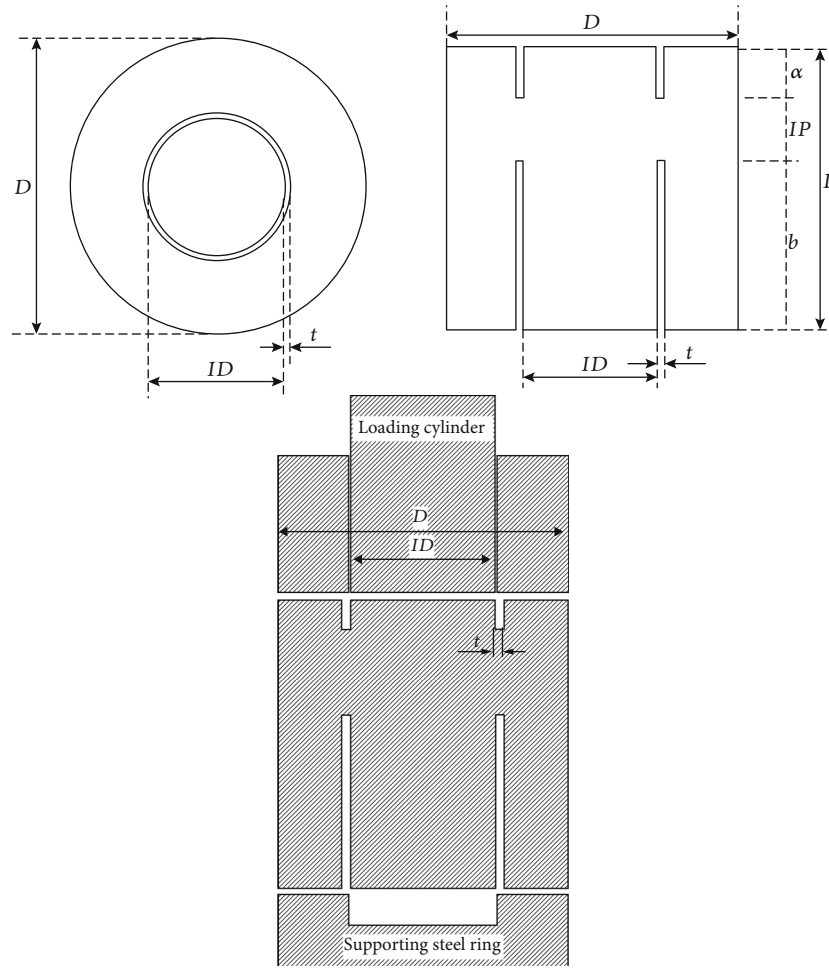
FIGURE 4: Layout of PTS specimen [43].

length of IP was set to 10 mm. Over the experiment, the specimen of coal PTS was located in advance on the bottom support, which possesses cylindrical grooves with a diameter of 35 mm and a depth of 15 mm. A shear load was employed to the specimen of coal using a loading cylinder with a diameter of 35 mm. Finally, the test was in the mode of displacement control with a constant rate of 0.02 mm/min to ensure stable crack propagation. Three experiments were executed each for the coal. The stress-strain curves were recorded. Figure 5 shows the experimental curve of coal shear load and tangential displacement, which represents the typical coal type II fracture characteristics. In the initial stage, the shear load has a linear correlation with the shear displacement. When the critical value was obtained for the shear displacement, mode II cracks begin to occur in the FPZ of the coal sample and local damage occurs. Within the postpeak stage, the shear load progressively reduces with the enhancement of shear displacement, and the coal sample presents the characteristics of ductile fracture. The average maximum tangential displacement of the PTS coal specimen is 0.055 mm, and the nonlinear damage softening stage appears in the postpeak stage of the shear process of the PTS coal specimen. In addition, by calculating the ratio of
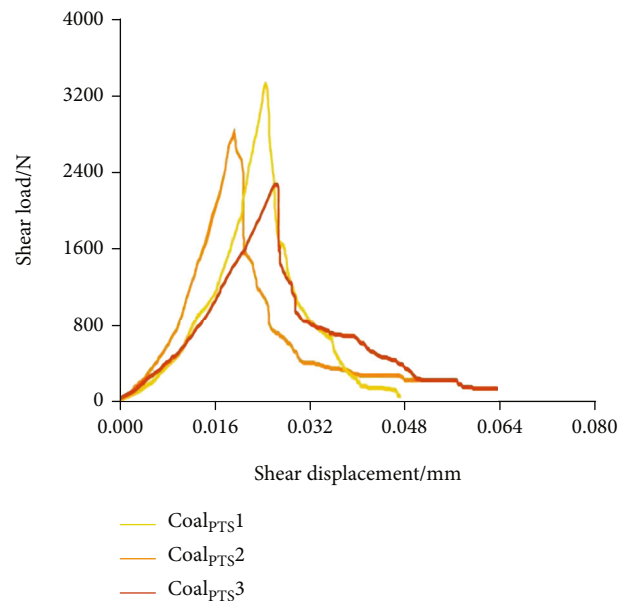
FIGURE 5: Curves of shear load displacement for specimens of coal PTS.

the peak shear load to the effective shear area, the shear strength (τ_t) of coal can be obtained directly. The calculation formula is as follows:

$$\tau_t = \frac{P_{\mathrm{scr}}}{IP \cdot ID \cdot \pi}, \tag{1}$$

where P_{scr} is the peak shear load. According to the above formula, the shear strength of the coal sample is 2.36 MPa.

3. PPR CZM for Coals

In the PPR model, the normal and tangential cohesive interactions (T_n, T_t) are functions of the normal or tangential separation (Δ_n, Δ_t), respectively. It should be indicated that T_n approaches zero when Δ_t reaches the tangential conjugate final crack opening displacement ($\bar{\delta}_t$) or Δ_n reaches the maximum normal crack opening width (δ_n). This represents complete normal failure. Similarly, when Δ_t reaches its maximum displacement of tangential crack opening (δ_t) or Δ_n attains the normal conjugate final crack opening width ($\bar{\delta}_n$), full tangential failure takes place. The expressions are as follows:

$$T_n(\delta_n, \Delta_t) = 0 \quad T_n(\Delta_n, \bar{\delta}_t) = 0, \tag{2}$$

$$T_t(\bar{\delta}_n, \Delta_t) = 0 \quad T_t(\Delta_n, \delta_t) = 0. \tag{3}$$

When Δ_n (Δ_t) reaches the critical opening width δ_{nc} (δ_{tc}), the value of T_n (T_t) is the maximum normal cohesive strength ($\sigma_{\max}$). This is shown as follows:

$$\left.\frac{\partial T_n}{\partial \Delta_n}\right|_{\Delta_n = \delta_{nc}} = 0 \quad T_n(\delta_{nc}, 0) = \sigma_{\max}, \tag{4}$$

$$\left.\frac{\partial T_t}{\partial \Delta_t}\right|_{\Delta_t = \delta_{tc}} = 0 \quad T_t(0, \delta_{tc}) = \tau_{\max}. \tag{5}$$

The mode I and mode II fracture energy (Φ_n, Φ_t) can be calculated by the area underneath the cohesive interactions, as follows:

$$\Phi_n = \int_0^{\delta_n} T_n(\Delta_n, 0) d\Delta_n \quad \Phi_t = \int_0^{\delta_t} T_n(0, \Delta_t) d\Delta_t. \tag{6}$$

In this study, the mode I and II fracture energies of coal samples were calculated, respectively, by the unit integral area under the load-relative opening displacement curves in Figures 3 and 5 of the above two kinds of tests. The specific shape of the softening response, i.e., the constitutive relationship of the softening process, remarkably affects the crack propagation. Therefore, nondimensional shape parameter indices (α, β) are introduced into the PPR model. When the shape parameter indices are equal to 2, the gradient of the softening process represents a nearly linear relationship. If the shape criteria are lower than 2, the cohesive interactions have concave softening trends. Conversely, if the shape indi-

ces are higher than 2, the gradient of the softening procedure demonstrates a convex shape.

Considering the foregoing macroscopic fracture criteria and boundary conditions, the potential energy function can then be mathematically expressed in the form below:

$$\begin{aligned} \Psi(\Delta_n, \Delta_t) = {}& \min\left(\phi_n, \phi_t\right) \\ & + \left[\Gamma_n\left(1 - \frac{\Delta_n}{\delta_n}\right)^{\alpha}\left(\frac{m}{\alpha} + \frac{\Delta_n}{\delta_n}\right)^m + \langle\phi_n - \phi_t\rangle\right] \\ & \times \left[\Gamma_t\left(1 - \frac{|\Delta_t|}{\delta_t}\right)^{\beta}\left(\frac{n}{\beta} + \frac{|\Delta_t|}{\delta_t}\right)^n + \langle\phi_t - \phi_n\rangle\right]. \end{aligned} \tag{7}$$

The cohesive interactions T_n and T_t are obtained by taking the first derivative of the PPR model along with the normal vector and tangential vector, respectively, as follows:

$$\begin{aligned} T_n(\Delta_n, \Delta_t) = {}& \frac{\Gamma_n}{\delta_n}\left[m\left(1 - \frac{\Delta_n}{\delta_n}\right)^{\alpha}\left(\frac{m}{\alpha} + \frac{\Delta_n}{\delta_n}\right)^{m-1}\right. \\ & \left. - \alpha\left(1 - \frac{\Delta_n}{\delta_n}\right)^{\alpha-1}\left(\frac{m}{\alpha} + \frac{\Delta_n}{\delta_n}\right)^m\right] \\ & \times \left[\Gamma_t\left(1 - \frac{|\Delta_t|}{\delta_t}\right)^{\beta}\left(\frac{n}{\beta} + \frac{|\Delta_t|}{\delta_t}\right)^n + \langle\phi_t - \phi_n\rangle\right], \end{aligned} \tag{8}$$

$$\begin{aligned} T_t(\Delta_n, \Delta_t) = {}& \frac{\Gamma_t}{\delta_t}\left[n\left(1 - \frac{\Delta_n}{\delta_n}\right)^{\beta}\left(\frac{n}{\beta} + \frac{|\Delta_t|}{\delta_t}\right)^{n-1}\right. \\ & \left. - \beta\left(1 - \frac{|\Delta_t|}{\delta_t}\right)^{\beta-1}\left(\frac{n}{\beta} + \frac{|\Delta_t|}{\delta_t}\right)^n\right] \\ & \times \left[\Gamma_n\left(1 - \frac{\Delta_n}{\delta_n}\right)^{\alpha}\left(\frac{m}{\alpha} + \frac{\Delta_n}{\delta_n}\right)^m + \langle\phi_n - \phi_t\rangle\right]\frac{\Delta_t}{|\Delta_t|}, \end{aligned} \tag{9}$$

where $\langle \cdot \rangle$ is the Macaulay bracket function, whose calculation is as follows:

$$\langle x \rangle = \begin{cases} 0 & (x < 0), \\ x & (x \geq 0), \end{cases} \tag{10}$$

where m and n are the nondimensional exponents, which are determined by the shape parameter indices (α, β) and the boundary conditions of the critical separations (Equations (4) and (5)). m and n are determined by

$$\begin{aligned} m &= \frac{\alpha(\alpha - 1)\lambda_n^2}{(1 - \alpha\lambda_n^2)}, \\ n &= \frac{\beta(\beta - 1)\lambda_t^2}{(1 - \beta\lambda_t^2)}, \end{aligned} \tag{11}$$

TABLE 1: Fracture criteria of the PPR CZMs for the coal.

λ_n	λ_t	Φ_n (J/m^2)	Φ_t (J/m^2)	Γ_n	Γ_t	$\bar{\delta}_t$ (mm)	$\bar{\delta}_n$ (mm)	α	β
0.386	0.317	22.16	51.62	3.678	-186.677	0.009	0.108	4.15	3.26

where λ_n and λ_t are the initial slope indicators, i.e., the ratio of the critical crack opening displacement to the maximum crack separation displacement, as determined by

$$\lambda_n = \frac{\delta_{nc}}{\delta_n},$$
$$\lambda_t = \frac{\delta_{tc}}{\delta_t}, \qquad (12)$$

where Γ_n and Γ_t are considered energy constants, which are functions of mode I and II fracture energy (Φ_n, Φ_t). When Φ_n is different from Φ_t, the formulas of the energy constants are as follows:

$$\Gamma_n = \left(-\phi_n\right)^{\langle\phi_n-\phi_t\rangle/(\phi_n-\phi_t)}\left(\frac{\alpha}{m}\right)^m,$$
$$\Gamma_t = \left(-\phi_t\right)^{\langle\phi_t-\phi_n\rangle/(\phi_t-\phi_n)}\left(\frac{\beta}{n}\right)^n. \qquad (13)$$

When the values between Φ_n and Φ_t are equal, the simplification of energy constants to the following expression is possible:

$$\Gamma_n = -\phi_n\left(\frac{\alpha}{m}\right)^m,$$
$$\Gamma_t = \left(\frac{\beta}{n}\right)^n. \qquad (14)$$

The unknown parameters of the PPR model needed to establish the PPR CZMs for the coals can be calculated based upon data acquired from the SCB tests and PTS tests. The maximum normal and tangential crack opening width can be determined by considering the boundary conditions of the cohesive strength (4) and (5) and fracture energy (6). The equations are as follows:

$$\delta_n = \frac{\Phi_n}{\sigma_{max}}\alpha\lambda_n(1-\lambda_n)^{\alpha-1}\left(\frac{\alpha}{m}+1\right)\left(\frac{\alpha}{m}\lambda_n+1\right)^{m-1}, \qquad (15)$$

$$\delta_t = \frac{\Phi_t}{\tau_{max}}\beta\lambda_t(1-\lambda_t)^{\beta-1}\left(\frac{\beta}{n}+1\right)\left(\frac{\beta}{n}\lambda_t+1\right)^{n-1}, \qquad (16)$$

where the parameters of $\delta_n, \delta_t, \Phi_n, \Phi_t, \sigma_{max}$, and τ_{max} have already been determined. The initial slope indicators λ_n and λ_t can be calculated by Equation (12). The calculation results of the different coals are listed in Table 1. Finally, substituting Equation (11) into Equations (15) and (16), the nondimensional shape parameter indices (α, β) could be ascertained by solving the above equations. The values
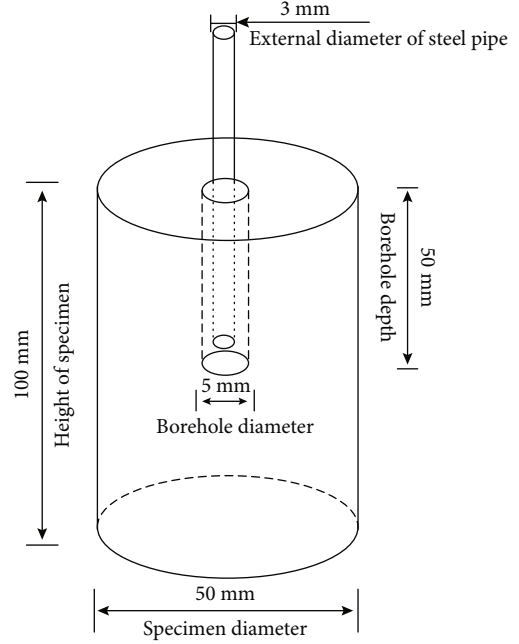
FIGURE 6: Configuration of the prepared specimens.

of $\alpha(\beta)$ for the three different coals are shown in Table 1 as well.

Based on the experimental results, Φ_n is different from Φ_t for the coals; hence, the energy constants Γ_n and Γ_t were calculated using Equation (12). The results are listed in Table 1. In addition, in order to determine the cohesive interaction region, the last displacements of conjugate crack opening $\bar{\delta}_t$ and $\bar{\delta}_n$ can be calculated by Equations (14) and (15). The cohesive interaction region of mode I is (0.108, 0.009), and the cohesive interaction region of mode II is (0.108, 0.055). When the normal or tangential separation displacement (Δ_n, Δ_t) exceeded the region, the cohesive stresses of mode I and mode II were set to zero.

4. Crack Propagation Experiment of Coals for Hydraulic and ScCO$_2$ Fracturing

4.1. Experimental Preparation and Process. In this section, trimmed samples with a diameter of 50 mm and a length of 100 mm were used in the experiment. Figure 6 illustrates the configuration of samples, indicating that there is a central borehole in the upper surface of the specimen. Then, a 3 mm steel pipe was inserted into the borehole to inject the fluid to simulate the fracturing well. The schematic diagram of the hydraulic and ScCO$_2$ fracturing experimental device is shown in Figure 7. In order to perform the fracturing tests,
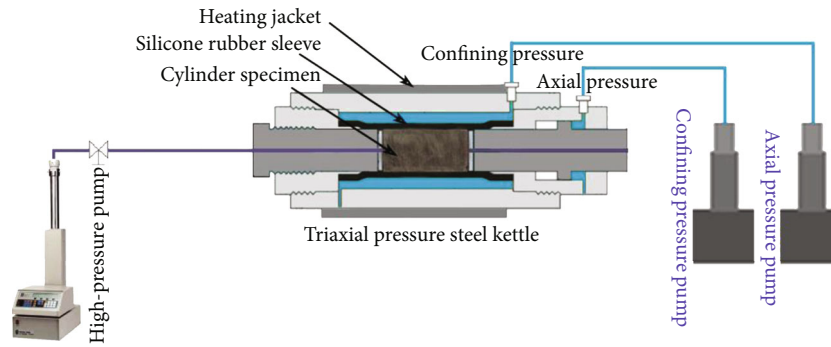
FIGURE 7: Schematic diagram of the hydraulic fracturing experimental device.
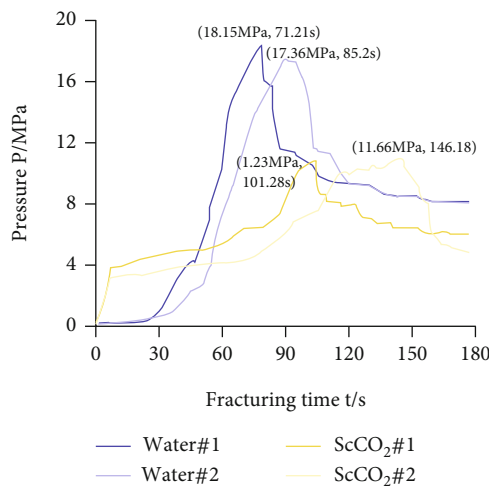
FIGURE 8: Fracturing pressure versus time curves of the coals for hydraulic and ScCO$_2$ fracturing.

the prepared specimens were placed in a pressurized kettle. In order to prevent damage to the specimens, the pressure increment rate was set to 1 MPa min^{-1}. Meanwhile, σ_a and σ_c were set to 10 MPa and 8 MPa, respectively. In addition, the temperature of the triaxial pressure kettle was set at 40°C and maintained for 3 hours prior to the fracturing test to ensure that the coal sample was fully heated, and the injection flow of the fracturing fluid was set to 20 mL min^{-1}. When ScCO$_2$ fracturing is performed, the steel injection pipe was heated to 40°C in advance so that the temperature of carbon dioxide is above its critical temperature (31.1°C). Sample breakdown was identified to have occurred once the fracturing fluid pressure reduces suddenly and simultaneously; the confining pressure increases abruptly.

4.2. Hydraulic and ScCO$_2$ Fracturing Experimental Results. Two samples were run for each experimental condition. Figure 8 shows the four fluid pressure-time curves of coal specimens by the two kinds of fluid fracturing. The fracturing process of all coal specimens can be divided into three stages. The first stage consists of fluid pressure rising. Fracturing fluid is continuously injected into the fracture specimen by a high-pressure pump to resist the strength of

the specimen under confining pressure. At the beginning of this stage, the growth rate of the fluid pressure in each coal specimen is very low, especially for ScCO$_2$ fracturing, because it takes time to fill the anhydrite section of the coal specimen after the fracturing fluid injection. In addition, fracturing fluid injection into the coal body immerses and infiltrates the specimen. In this early stage, the slow increase in fluid pressure becomes significant for ScCO$_2$ fracturing; this is attributed to the relatively developed fracture structure in the center hole of the coal body, and the infiltration effect of ScCO$_2$ is noticeable than water. The second stage consists of crack initiations. When the injected fluid pressure reaches a specific critical value, the critical condition for the crack propagation of the coal specimen is reached, and the coal specimen ruptures. The critical pressure is called the crack initiation pressure of fracturing, and the critical fracturing time it takes to reach the crack initiation pressure is called the crack initiation time. The two kinds of fluid fracturing results of the coal specimens are shown in Table 2. The average crack initiation pressure of coal specimens for hydraulic fracturing is 17.76 MPa, about 1.59 times that driven by ScCO$_2$ fracturing. The third stage is the pressure drop stage; when fracturing occurs in the coal sample, the water pressure accordingly decreases. For hydraulic fracturing in coals, the fluid pressure obviously decreases after fracturing. And there is a significant fluctuation in the fluid pressure after ScCO$_2$ fracturing. This is because the crack in the coal sample does not completely penetrate the sample. Due to the surrounding rock and axial pressure, the crack closes once again in the coals, and the continuously injected ScCO$_2$ will drive crack propagation in the specimen repeatedly until the specimen is completely broken.

Figure 9 shows the final crack propagation morphology in the cylindrical coal specimens. The coal specimen eventually formed a macrocrack under the hydraulic drive, which penetrated through the whole cylindrical specimen. Yet, there was no crack penetrating the whole fracture specimen and several widely distributed secondary cracks in the fractured coal specimens by ScCO$_2$. This is because water has greater viscosity and density, which is easy to produce tensile failure in coal specimens, and eventually forms a single penetrating crack. On the other hand, because of the large diffusion coefficient and strong permeability of ScCO$_2$, the influence range in the coal is large, so it is easy to form a

TABLE 2: Hydraulic and ScCO$_2$ fracturing test results of the coal specimens.

Sample number	Fracturing fluid	σ_a (MPa)	σ_c (MPa)	Initiation pressure (MPa)		Initiation time t (s)	
				Test value	Average value	Test value	Average value
Water#1	Water	10	8	18.15	17.76	71.21	78.24
Water#2	Water	10	8	17.36		85.26	
ScCO$_2$#1	ScCO$_2$	10	8	11.23	11.15	101.28	123.73
ScCO$_2$#2	ScCO$_2$	10	8	11.66		146.18	

FIGURE 9: Crack propagation paths for the coal samples fractured by (1) water and (2) ScCO$_2$.
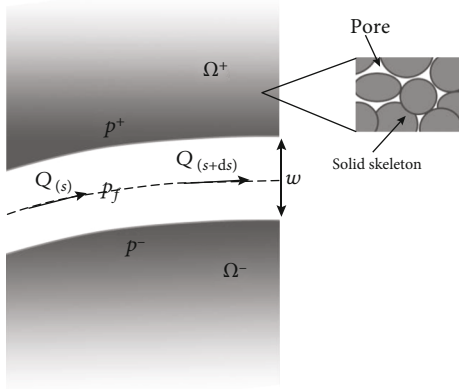
FIGURE 10: Physical model of fluid fracturing in coals.

wide range of tensile and shear mixed-mode cracks in the coal specimens.

5. Numerical Simulation of Fracturing in Coals Based on the PPR Model

5.1. Governing Equations. Hydraulic and ScCO$_2$ fracturing of coal is a complex, multifield coupling process. Compared with the multiphysical coupling problems in rock mechanic engineering, this crack propagation process in a solid is coupled with fracturing, causing it to be more challenging to model and calculate. The physical model of the fracturing process in coals is shown in Figure 10. Ω represents the entire range of the hydraulic fracturing models, and the fracture width w is located in the center of the model. The two sides of the fracture consist of coal materials. The coal is a porous medium, containing the solid skeleton and pores.
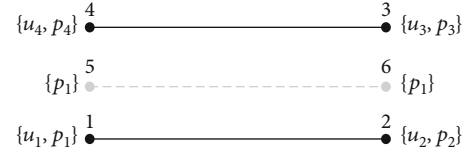
FIGURE 11: The pore pressure cohesive element.

In the fracture, Q represents the flow rate of the injected fracturing fluid. Some of the fluid will be filtered along the upper and lower crack surfaces and permeate into the coal through the pores. The pressure generated by the injected fracturing fluid in the fracture is defined as P_f. When the fluid pressure reaches a critical value, the crack in the coal body will expand.

The coal fracturing numerical simulation was performed through the pore pressure cohesive element. Figure 11 shows the pore pressure cohesive element with the fluid pressure node. When the cohesive element is affected by the external force, the upper node (1, 2) and the lower node (3, 4) in the element are relatively displaced, which damages the cohesive element. Once the critical condition is reached, the cohesive element is destroyed, fracturing the material. During this process, the normal cohesion of the element also changes with the change in normal opening displacement. Also, the tangential cohesion of the element changes with the change of the tangential displacement. The relationship between the two cohesive forces and the displacement of the element nodes is the constitutive relationship of the cohesive crack. As shown in Figure 11, the pore pressure cohesive element consists of adding a group of pore pressure injection nodes (5, 6) in the center of the original cohesive element. The injected fluid pressure is already included in the cell calculation model through this pressure node, and the injected fluid pressure causes the relative displacement on the lower and upper surfaces of the cohesive element, resulting in continuous damage to the cohesive element until it is destroyed. This represents crack growth in the fracturing model. In this multifield coupled numerical model, there are four governing equations, including the deformation equation of porous media in coal, the pore seepage equation of porous media in coal, the fracture flow equation in coal, and the constitutive equation of a cohesive crack in coal.

(1) In this model, if the pores in the coal body are filled with a single liquid (water or ScCO$_2$), the deformation of the coal body includes deformation of the

solid skeleton and deformation of the liquid in the pores. According to the momentum conservation equation, the following formula can be obtained:

$$\nabla\sigma + \rho b = 0, \tag{17}$$

where σ is the total stress tensor of the porous media, b is the physical force of the porous medium, and ρ is the density of the coal. The coal density has the following formula:

$$\rho = (1 - n)\rho_s + n\rho_f, \tag{18}$$

where n is the porosity of the coal, ρ_s is the solid skeleton density of coal, and ρ_f is the fluid density in the coal pore. According to the Biot porous elasticity theory [44] and the Terzaghi theory [45], the effective stress in coal can be calculated as follows:

$$\sigma'_{ij} = \sigma_{ij} + \alpha p_w \delta_{ij}, \tag{19}$$

where δ_{ij} is the Kronecker-delta symbol, p_w is the pore pressure in the coal, and α is the Biot coefficient. The Biot coefficient is defined as follows:

$$\alpha = 1 - \frac{K_b}{K_S}, \tag{20}$$

where K_b is the total volume modulus of the porous coal media and K_S is the modulus of the solid skeleton in the coal. For the incompressible solid material, $K_s = \infty, \quad \alpha = 1$. If the Biot coefficient (α) is equal to 0, the porous media material will degenerate into a dense linear elastic solid material.

Based on the hypothesis of small deformation, the formula is as follows:

$$\varepsilon_{ij} = \frac{1}{2}\left(u_{i,j} + u_{j,i}\right), \tag{21}$$

where $\varepsilon_{i,j}$ is the strain tensor, u_i is the displacement vector, and $u_{i,j}$ and $u_{j,i}$ are the partial derivatives of displacement. The constitutive relation between the stress and strain of coal can be expressed as follows:

$$\sigma_{ij} = D_{ijkl}\varepsilon_{kl}, \tag{22}$$

where D_{ijkl} is the elastic tensor of coal.

(2) Pore seepage in the coal body should satisfy the following mass conservation equation:

$$\frac{1}{Q}p_w + \alpha\nabla\dot{u} + \nabla\dot{w}_w = 0, \tag{23}$$

where $1/Q$ is the compressibility coefficient of the fluid, p_w is the pore pressure of coal, and $\dot{w}_w$ is the velocity vector of

Darcy flow. The compressibility coefficient $1/Q$ can be calculated as follows:

$$\frac{1}{Q} = \frac{\alpha - n}{K_s} + \frac{n}{K_w}, \tag{24}$$

where n is the porosity of coal and K_w is the modulus of the fluid. In Equation (16), the flow rate and fluid pressure gradient in porous media satisfy Darcy's law, and the expression is as follows:

$$\dot{w}_w = k_w(-\nabla p_w + \rho_w(b - \ddot{u})), \tag{25}$$

where ρ_w is the density of the fracturing fluid and k_w is the permeability coefficient of the fracturing fluid, which can be calculated as

$$k_w = \frac{k}{\mu_w}, \tag{26}$$

where μ_w is the viscosity of the fracturing fluid and k is the permeation matrix.

The effect of the inertia term of the fracturing fluid and the roughness of the crack surface are not considered. The fracturing fluid in the fracture itself can be divided into the tangential flow and normal flow. According to the mass conservation theorem, the fluid in the fracture should satisfy the following equation:

$$\frac{1}{W_f}\dot{p}_f + \alpha_f\dot{w} + \frac{\partial q}{\partial s} + (q_t + q_b) = Q(t)\delta(x, y), \tag{27}$$

where $1/W_f$ is the compressibility of the fluid in the fracture, p_f is the fluid pressure of the fracturing fluid in the fracture, w is the crack opening, s is the coordinate of the tangential direction along the fracture surface, q_t is the flow rate of the fracturing fluid filtered from the upper surface of the fracture into the porous media, q_b is the flow rate of the fracturing fluid infiltrating from the lower surface of the fracture into the porous media, $Q(t)$ is the flow rate of the source term of the fluid, and $\delta(x, y)$ is the Dirac-delta function. If the fracturing fluid is incompressible, the first fluid compression term in the above equation can be ignored.

The tangential flow and pressure gradient of the fracture fluid in the fracture satisfy the cubic seepage model [46, 47]. They can be related by the following expression:

$$q = -\frac{w^3}{12\mu_f}\frac{\partial p_f}{\partial s}, \tag{28}$$

where μ_f is the viscosity of the fracture fluid. Some of the fracturing fluid in the fracture infiltrates into the coal body through the fractures. In this numerical model, the fluid flow rate is related to the gradient between the pore pressure in

the coal and the pressure of the fracturing fluid in the fracture, calculated as follows:

$$q_t = k_t \left(p_f - p_t \right),$$ (29)

$$q_b = k_b \left(p_f - p_b \right),$$ (30)

where p_t and p_b are the pore pressures on the upper and lower surfaces of the crack, respectively, and k_t and k_b are the fluid filtration coefficients on the upper and lower surfaces of the crack, respectively. The equation of the tangential fluid flow in the fracture and the equation of normal fluid flow are taken into the mass conservation equation and expressed as follows:

$$\dot{w} - \nabla \cdot \left(\frac{w^3}{12\mu_w} \nabla p_f \right) + c_1 \left(p_f + p_t \right) + c_b \left(p_f - p_b \right) = Q(t)\delta(x, y).$$ (31)

(3) The constitutive relationship of the cohesive element in the numerical simulation of hydraulic fracturing is derived from the mixed-mode I/II PPR potential energy function. In Section 3, the fracture parameter values in the PPR CZMs of the coal were determined through the SCB tests and the PTS tests. The constitutive equations of mixed-mode I/II for a cohesive crack of the different coals were established. The normal and tangential cohesions were obtained by taking the first derivative of the normal displacement and tangential displacement, respectively, by the PPR potential function, and the stiffness matrix of the cohesive element is as follows:

$$D(\Delta_n, \Delta_t) = \begin{bmatrix} D_{nn} & D_{nt} \\ D_{tn} & D_{tt} \end{bmatrix} = \begin{bmatrix} \dfrac{\partial^2 \Psi}{\partial \Delta_n{}^2} & \dfrac{\partial^2 \Psi}{\partial \Delta_n \partial \Delta_t} \\ \dfrac{\partial^2 \Psi}{\partial \Delta_t \partial \Delta_n} & \dfrac{\partial^2 \Psi}{\partial \Delta_t{}^2} \end{bmatrix}.$$ (32)

The stiffness components of the PPR cohesive constitutive equation are as follows:

$$\begin{aligned} D_{nn} = \frac{\Gamma_n}{\delta_n{}^2} &\left[(m^2 - m) \left(1 - \frac{\Delta_n}{\delta_n} \right)^\alpha \left(\frac{m}{\alpha} + \frac{\Delta_n}{\delta_n} \right)^{m-2} \right. \\ &+ (\alpha^2 - \alpha) \left(1 - \frac{\Delta_n}{\delta_n} \right)^{\alpha-2} \left(\frac{m}{\alpha} + \frac{\Delta_n}{\delta_n} \right)^m \\ &\left. -2\alpha m \left(1 - \frac{\Delta_n}{\delta_n} \right)^{\alpha-1} \left(\frac{m}{\alpha} + \frac{\Delta_n}{\delta_n} \right)^{m-1} \right] \\ &\cdot \left[\Gamma_t \left(1 - \frac{\Delta_t}{\delta_t} \right)^\beta \left(\frac{n}{\beta} + \frac{\Delta_t}{\delta_t} \right)^n + \langle \phi_t - \phi_n \rangle \right], \end{aligned}$$ (33)

$$\begin{aligned} D_{tt} = \frac{\Gamma_t}{\delta_t{}^2} &\left[(n^2 - n) \left(1 - \frac{\Delta_t}{\delta_t} \right)^\beta \left(\frac{n}{\beta} + \frac{\Delta_t}{\delta_t} \right)^{n-2} \right. \\ &+ (\beta^2 - \beta) \left(1 - \frac{\Delta_t}{\delta_t} \right)^{\beta-2} \left(\frac{n}{\beta} + \frac{\Delta_t}{\delta_t} \right)^n \\ &\left. -2\beta n \left(1 - \frac{\Delta_t}{\delta_t} \right)^{\beta-1} \left(\frac{n}{\beta} + \frac{\Delta_t}{\delta_t} \right)^{n-1} \right] \\ &\cdot \left[\Gamma_n \left(1 - \frac{\Delta_n}{\delta_n} \right)^\alpha \left(\frac{m}{\alpha} + \frac{\Delta_n}{\delta_n} \right)^m + \langle \phi_n - \phi_t \rangle \right], \end{aligned}$$ (34)

$$\begin{aligned} D_{nt} = \frac{\Gamma_n \Gamma_t}{\delta_n \delta_t} &\left[m \left(1 - \frac{\Delta_n}{\delta_n} \right)^\alpha \left(\frac{m}{\alpha} + \frac{\Delta_n}{\delta_n} \right)^{m-1} \right. \\ &\left. - \alpha \left(1 - \frac{\Delta_n}{\delta_n} \right)^{\alpha-1} \left(\frac{m}{\alpha} + \frac{\Delta_n}{\delta_n} \right)^m \right] \\ &\cdot \left[n \left(1 - \frac{\Delta_t}{\delta_t} \right)^\beta \left(\frac{n}{\beta} + \frac{\Delta_t}{\delta_t} \right)^{n-1} - \beta \left(1 - \frac{\Delta_t}{\delta_t} \right)^{\beta-1} \left(\frac{n}{\beta} + \frac{\Delta_t}{\delta_t} \right)^n \right]. \end{aligned}$$ (35)

5.2. Numerical Models of Hydraulic Fracturing for the Coals. In order to compare the experimental fracturing results of the coals, the coal material parameters and boundary conditions of the coals in the fracturing numerical models were set to be the same as those in the experiments. Figure 12 shows the boundary conditions on the coal fracturing numerical geometric model with a size of $50\,\text{mm} \times 50\,\text{mm}$, as well as the meshing conditions for a section of the model. In the fracturing numerical model, the coal materials were characterized by triangular solid elements, and the pore pressure cohesive elements were inserted between the triangular solid elements to simulate multiple crack propagation driven by hydraulic or $ScCO_2$ fracturing. To avoid the influence of the overall stiffness of the model after a large number of cohesive elements were inserted between the solid elements (see Figure 12), the corresponding upper and lower nodes in the cohesive element and their intermediate fluid pressure nodes were defined at the same position in the local coordinate system. This numerical simulation method is called the zero-thickness element method [48]. And the fluid injection point was set at the center of the numerical model, and the fluid injection rate was set to 20 mL/min. The involved numerical simulation parameters are given in Table 3, and the PPR model parameters of the three types of coals are listed in Table 1 for the numerical simulation for the hydraulic and $ScCO_2$ fracturing of the coal specimens. In addition, the contrast numerical simulation of the fracturing in coals was also carried out in which the constitutive relationship of the pore pressure cohesive elements was represented by the common linear elastic fracture mechanics (LEFM).

Figure 13 shows the numerical simulation results of hydraulic and $ScCO_2$ fracturing of the coals. The fracture initiation pressure of the coal with water or $ScCO_2$ is 18.45 MPa and 11.75 MPa, respectively. These numerical simulation outcomes are in agreement with the experiment's achievements. Compared with the established PPR model, the numerical simulation results of fracturing and $ScCO_2$
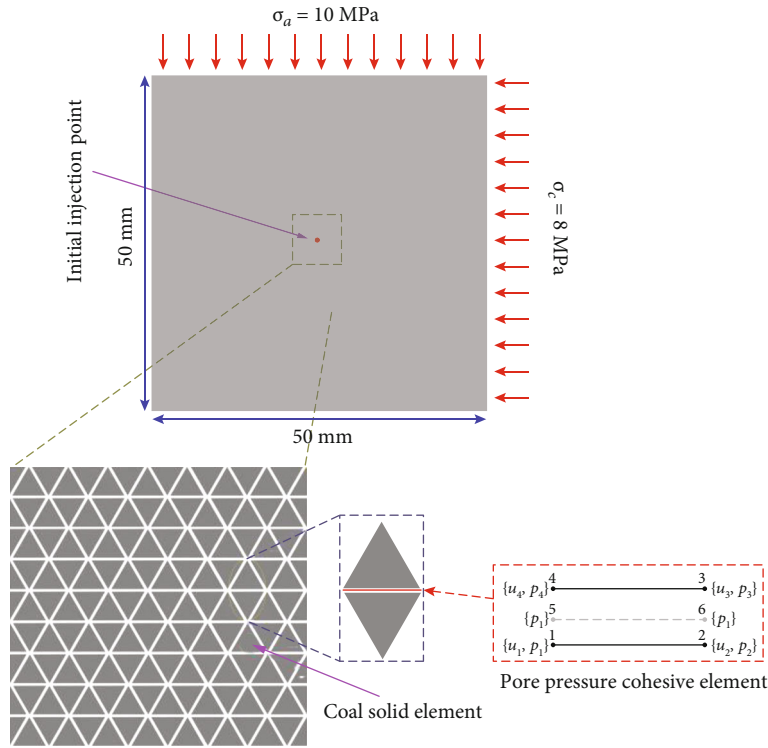
FIGURE 12: The numerical model for fracturing in coals.

TABLE 3: Numerical simulation parameters of the different fluid fracturing in coals.

Fracturing fluid	Water	ScCO$_2$
Permeability K (m^2)	0.2×10^{-15}	0.6×10^{-14}
Initial pore pressure P_0 (MPa)	0.1	0.1
Injection velocity Q (mL/min)	20	20
Dynamic viscosity coefficient of fracturing fluid (Pa·s)	0.79×10^{-3}	0.31×10^{-3}
Fracturing fluid density ρ (kg/m^3)	1000	770
Filtration coefficient C_t (m^3/MPa s)	1.0×10^{-6}	3.5×10^{-6}
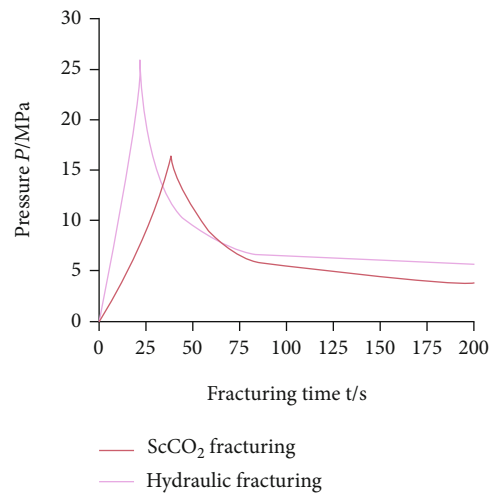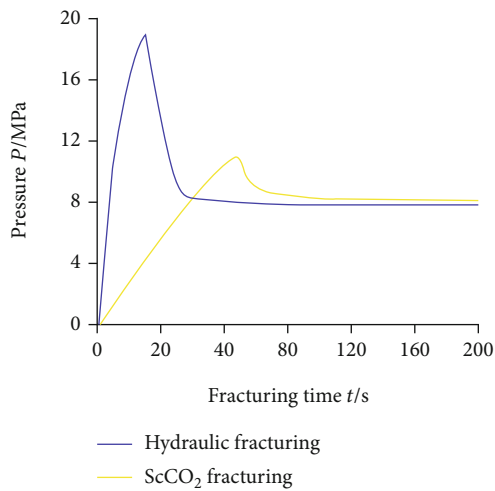
FIGURE 13: Fracturing pressure over time for hydraulic and ScCO$_2$ fracturing numerical simulation of coals based on the PPR model.

FIGURE 14: Fracturing pressure over time for hydraulic and ScCO$_2$ fracturing numerical simulation of coals based on LFEM.
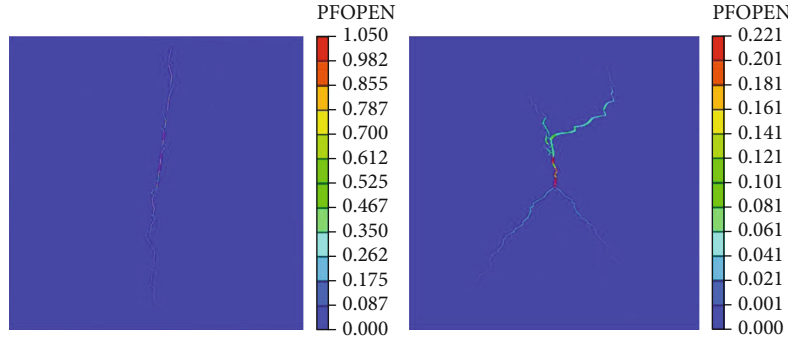
FIGURE 15: Crack propagation numerical simulation of coals caused by (1) hydraulic fracturing and (2) ScCO$_2$ fracturing.

in the coals are shown in Figure 14 based on the LFEM, and there are obvious deviations between the simulation results and the test results. Figure 15 shows the simulation results of crack growth for hydraulic and ScCO$_2$ fracturing in the coal samples. The crack induced by hydraulic fracturing expands along the direction of the maximum principal stress, and at the same time, secondary crack propagation occurs near the main crack. And the multiple crack propagation appears in the coal model with ScCO$_2$ fracturing. This is also consistent with the experimental results of crack propagation in coal specimens caused by hydraulic and ScCO$_2$ fracturing. Therefore, this demonstrates that the established PPR CZMs can accurately describe crack propagation behavior in varying coal types for hydraulic and ScCO$_2$ fracturing.

6. Conclusion

In this research, the mixed-mode I/II PPR cohesive zone model (CZM) of coals was determined using PTS and SCB tests. The constitutive relationships of the established PPR CZMs were introduced into the pore pressure cohesive elements to simulate crack growth in coals caused by hydraulic and ScCO$_2$ fracturing. In addition, hydraulic and ScCO$_2$ fracturing experiments on the coal specimens were performed, and the numerical simulation outcomes were compared with the corresponding experimental results. The following conclusions can be drawn:

(1) Several key fracture parameters, including the maximum normal open displacement (δ_n), the maximum tangential open displacement (δ_t), mode I fracture energy (Φ_n), and mode II fracture energy (Φ_t), were obtained through SCB tests and PTS tests. According to the experimental results, there are visible nonlinear damage processes in the stage of postpeak loading, and the coal specimens show obvious characteristics of ductile fracture under mode I and II loading. In addition, the mode II fracture energy of coal type II is 51.62 J/m^2, which is considerably greater compared with fracture energy of mode I for coal (22.16 J/m^2); this shows that the mode II crack propagation in coals will use remarkable energy in coals

(2) In the hydraulic and ScCO$_2$ fracturing experiments of coals, the crack initiation pressure of coal specimens for hydraulic fracturing is 17.76 MPa, about 1.59 times that driven by ScCO$_2$ fracturing. And the crack initiation time of coal with ScCO$_2$ fracturing is 123.73 s, which is 1.58 times that for hydraulic fracturing. A macrocrack eventually formed in the coal specimen due to the hydraulic drive, which penetrated through the entire specimen, whereas there was no crack penetrating the whole fracture specimen and several widely distributed secondary cracks in the fractured coal specimens by ScCO$_2$. This is because water has greater viscosity and density, which is easy to produce tensile failure in coal specimens, and eventually forms a single penetrating crack. On the other hand, because of the large diffusion coefficient and strong permeability of ScCO$_2$, the influence range in the coal is large, so it is easy to form a wide range of tensile and shear mixed-mode cracks in the coal specimens

(3) The PPR CZMs of the coal were established using PTS and SCB tests for analyzing the mixed-mode I/II crack propagation. Zero-thickness pore pressure cohesive elements were used to simulate multicrack propagation in coals caused by hydraulic and ScCO$_2$ fracturing. The constitutive relationships of the established PPR CZM were introduced into the cohesive elements. Overall, the numerical simulation results are consistent with the hydraulic and ScCO$_2$ fracturing experimental results for the coal specimens. This indicates that the established PPR CZMs can accurately represent crack propagation behavior in coals caused by hydraulic and ScCO$_2$ fracturing

Data Availability

The underlying data and figures can be found in the manuscript.

Conflicts of Interest

The authors declare that they have no conflicts of interest.

Acknowledgments

References

[1] C. Fan, S. Li, D. Elsworth, J. Han, and Z. Yang, "Experimental investigation on dynamic strength and energy dissipation characteristics of gas outburst-prone coal," *Energy Science & Engineering*, vol. 8, no. 4, pp. 1015–1028, 2020.

[2] J. Zhang, L. Si, J. Chen, M. Kizil, and Z. Chen, "Stimulation techniques of coalbed methane reservoirs," *Geofluids*, vol. 2020, 23 pages, 2020.

[3] C. Fan, D. Elsworth, S. Li, L. Zhou, Z. Yang, and Y. Song, "Thermo-hydro-mechanical-chemical couplings controlling CH_4 production and CO_2 sequestration in enhanced coalbed methane recovery," *Energy*, vol. 173, pp. 1054–1077, 2019.

[4] X. Wang, Q. Hu, and Q. Li, "Investigation of the stress evolution under the effect of hydraulic fracturing in the application of coalbed methane recovery," *Fuel*, vol. 300, p. 120930, 2021.

[5] S. Chen, D. Tang, S. Tao, P. Liu, and J. P. Mathews, "Implications of the in situ stress distribution for coalbed methane zonation and hydraulic fracturing in multiple seams, western Guizhou, China," *Journal of Petroleum Science and Engineering*, vol. 204, p. 108755, 2021.

[6] Y. Meng, D. Tangm, H. Xu, Y. Li, and L. Gao, "Coalbed methane produced water in China: status and environmental issues," *Environmental Science and Pollution Research*, vol. 21, no. 11, pp. 6964–6974, 2014.

[7] R. Middleton, H. Viswanathan, R. Currier, and R. Gupta, "CO_2 as a fracturing fluid: potential for commercial- scale shale gas production and CO_2 sequestration," *Energy Procedia*, vol. 63, pp. 7780–7784, 2014.

[8] H. Yan, J. Zhang, N. Zhou, B. Li, and Y. Wang, "Crack initiation pressure prediction for SC-CO_2 fracturing by integrated meta-heuristics and machine learning algorithms," *Engineering Fracture Mechanics*, vol. 249, p. 107750, 2021.

[9] H. Yan, J. Zhang, B. Li, and C. Zhu, "Crack propagation patterns and factors controlling complex crack network formation in coal bodies during tri-axial supercritical carbon dioxide fracturing," *Fuel*, vol. 286, p. 119381, 2021.

[10] M. Meng and Z. Qiu, "Experiment study of mechanical properties and microstructures of bituminous coals influenced by supercritical carbon dioxide," *Fuel*, vol. 219, pp. 223–238, 2018.

[11] T. Ishida, K. Aoyagi, T. Niwa et al., "Acoustic emission monitoring of hydraulic fracturing laboratory experiment with supercritical and liquid CO_2," *Geophysical Research Letters*, vol. 39, no. 16, pp. 1–6, 2012.

[12] X. Zhang, Y. Lu, J. Tang, Z. Zhou, and Y. Liao, "Experimental study on fracture initiation and propagation in shale using supercritical carbon dioxide fracturing," *Fuel*, vol. 190, pp. 370–378, 2017.

[13] D. Zhou, G. Zhang, Y. Wang, and Y. Xing, "Experimental investigation on fracture propagation modes in supercritical carbon dioxide fracturing using acoustic emission monitoring," *International Journal of Rock Mechanics and Mining Sciences*, vol. 110, pp. 111–119, 2018.

[14] D. Wu, X. Liu, B. Liang, K. Sun, and X. Xiao, "Experiments on displacing methane in coal by injecting supercritical carbon dioxide," *Energy & Fuels*, vol. 32, no. 12, pp. 12766–12771, 2018.

[15] G. R. Irwin, "Analysis of stresses and strains near the end of a crack traversing a plate," *J Appl Mech*, vol. 24, no. 3, pp. 361–364, 1957.

[16] A. A. Griffith, "VI. The phenomena of rupture and flow in solids," *Philosophical transactions of the royal society of london. Series A, containing papers of a mathematical or physical character*, vol. 221, no. 582-593, pp. 163–198, 1921.

[17] Z. T. Bieniawski, "Mechanism of brittle fracture of rock: part I–theory of the fracture process," *Int J Rock Mech Min Sci (1997)*, vol. 4, no. 4, pp. 395–406, 1967.

[18] Z. T. Bieniawski, "Mechanism of brittle fracture of rock: part II–experimental studies," *Int J Rock Mech Min Sci (1997)*, vol. 4, no. 4, pp. 407–423, 1967.

[19] F. Dai, Y. Xu, T. Zhao, N. W. Xu, and Y. Liu, "Loading-rate-dependent progressive fracturing of cracked chevron-notched Brazilian disc specimens in split Hopkinson pressure bar tests," *Int J Rock Mech Min Sci (1997)*, vol. 88, pp. 49–60, 2016.

[20] M. D. Kuruppu, Y. Obara, M. R. Ayatollahi, K. P. Chong, and T. Funatsu, "ISRM-suggested method for determining the mode I static fracture toughness using semi-circular bend specimen," *Rock Mechanics and Rock Engineering*, vol. 47, no. 1, pp. 267–274, 2014.

[21] G. Feng, Y. Kang, X. Wang, Y. Hu, and X. Li, "Investigation on the failure characteristics and fracture classification of shale under Brazilian test conditions," *Rock Mechanics and Rock Engineering*, vol. 53, no. 7, pp. 3325–3340, 2020.

[22] C. Yang, J. J. K. Daemen, and J. H. Yin, "Experimental investigation of creep behavior of salt rock," *Int J Rock Mech Min Sci (1997)*, vol. 36, no. 2, pp. 233–242, 1999.

[23] B. Du, H. Bai, and G. Wu, *Dynamic Compression Properties and Deterioration of Red-Sandstone Subject to Cyclic Wet-Dry Treatment*, Advances in Civil Engineering, 2019.

[24] Z. P. Bažant and M. T. Kazemi, "Determination of fracture energy, process zone length and brittleness number from size effect, with application to rock and conerete," *International Journal of Fracture*, vol. 44, no. 2, pp. 111–131, 1990.

[25] B. Nie, X. Liu, L. Yang, J. Meng, and X. Li, "Pore structure characterization of different rank coals using gas adsorption and scanning electron microscopy," *Fuel*, vol. 158, pp. 908–917, 2015.

[26] G. I. Barenblatt, "The mathematical theory of equilibrium cracks in brittle fracture," *Advances in Applied Mechanics*, vol. 7, no. C, pp. 55–129, 1962.

[27] D. S. Dugdale, "Yielding of steel sheets containing slits," *Journal of the Mechanics and Physics of Solids*, vol. 8, no. 2, pp. 100–104, 1960.

[28] A. Hillerborg, M. E. Modéeer, and P. E. Petersson, "Analysis of crack formation and crack growth in concrete by means of fracture mechanics and finite elements," *Cement and Concrete Research*, vol. 6, no. 6, pp. 773–781, 1976.

[29] Z. Chen, A. P. Bunger, X. Zhang, and R. G. Jeffrey, "Cohesive zone finite element-based modeling of hydraulic fractures," *Acta Mechanica Solida Sinica*, vol. 22, no. 5, pp. 443–452, 2009.

[30] H. Wang, "Numerical modeling of non-planar hydraulic fracture propagation in brittle and ductile rocks using XFEM with

cohesive zone method," *Journal of Petroleum Science and Engineering*, vol. 135, pp. 127–140, 2015.

[31] J. Planas and M. Elices, "Asymptotic analysis of a cohesive crack: 2. Influence of the softening curve," *International Journal of Fracture*, vol. 64, no. 3, pp. 221–237, 1993.

[32] Y. Gong, Y. Hou, L. Zhao, W. Li, J. Zhang, and N. Hu, "A modified mode I cohesive zone model for the delamination growth in DCB laminates with the effect of fiber bridging," *International Journal of Mechanical Sciences*, vol. 176, p. 105514, 2020.

[33] Z. Bennour, T. Ishida, Y. Nagaya et al., "Crack extension in hydraulic fracturing of shale cores using viscous oil, water, and liquid carbon dioxide," *Rock Mechanics and Rock Engineering*, vol. 48, no. 4, pp. 1463–1473, 2015.

[34] J. R. K. Zipf and Z. T. Bieniawski, "Mixed-mode fracture toughness testing of coal," *International Journal of Rock Mechanics and Mining Science & Geomechanics Abstracts*, vol. 27, no. 6, pp. 479–493, 1990.

[35] Y. Zhao, S. Gong, X. Hao, Y. Peng, and Y. Jiang, "Effects of loading rate and bedding on the dynamic fracture toughness of coal: laboratory experiments," *Engineering Fracture Mechanics*, vol. 178, pp. 375–391, 2017.

[36] M. J. Lee, T. M. Cho, W. S. Kim, B. C. Lee, and J. J. Lee, "Determination of cohesive parameters for a mixed-mode cohesive zone model," *International Journal of Adhesion and Adhesives*, vol. 30, no. 5, pp. 322–328, 2010.

[37] R. D. S. G. Campilho, M. F. S. F. De Moura, A. M. G. Pinto, J. J. L. Morais, and J. J. M. S. Domingues, "Modelling the tensile fracture behaviour of CFRP scarf repairs," *Composites Part B: Engineering*, vol. 40, no. 2, pp. 149–157, 2009.

[38] S. H. Song, G. H. Paulino, and W. G. Buttlar, "A bilinear cohesive zone model tailored for fracture of asphalt concrete considering viscoelastic bulk material," *Engineering Fracture Mechanics*, vol. 73, no. 18, pp. 2829–2848, 2006.

[39] K. Park and G. H. Paulino, "Cohesive zone models: a critical review of traction-separation relationships across fracture surfaces," *Applied Mechanics Reviews*, vol. 64, no. 6, pp. 60–80, 2011.

[40] K. Park, G. H. Paulino, and J. R. Roesler, "A unified potential-based cohesive model of mixed-mode fracture," *Journal of the Mechanics and Physics of Solids*, vol. 57, no. 6, pp. 891–908, 2009.

[41] A. Needleman, "A continuum model for void nucleation by inclusion debonding," *Journal of Applied Mechanics*, vol. 54, no. 3, pp. 525–531, 1987.

[42] X. P. Xu and A. Needleman, "Void nucleation by inclusion debonding in a crystal matrix," *Modelling and Simulation in Materials Science and Engineering*, vol. 1, no. 2, pp. 111–132, 1993.

[43] T. Backers, O. Stephansson, and E. Rybacki, "Rock fracture toughness testing in mode II–punch-through shear test," *Journal of Rock Mechanics and Mining Sciences*, vol. 39, no. 6, pp. 755–769, 2002.

[44] M. A. Biot, "General theory of three-dimensional consolidation," *Journal of Applied Physics*, vol. 12, no. 2, pp. 155–164, 1941.

[45] K. Terzaghi, *Theoretical Soil Mechanics*, Chapman and Hall, Limited, London, 1951.

[46] Y. Chen, A. P. S. Selvadurai, and W. Liang, "Computational modelling of groundwater inflow during a longwall coal mining advance: a case study from the Shanxi province, China," *Rock Mechanics and Rock Engineering*, vol. 52, pp. 917–934, 2019.

[47] Y. Chen, A. P. S. Selvadurai, and Z. Zhao, "Modeling of flow characteristics in 3D rough rock fracture with geometry changes under confining stresses," *Computers and Geotechnics*, vol. 130, p. 103910, 2021.

[48] V. P. Nguyen, "An open source program to generate zero-thickness cohesive interface elements," *Advances in Engineering Software*, vol. 74, pp. 27–39, 2014.

WILEY | Hindawi

Research Article

Study on Supporting Protection of Tunnel Opening near a Rock Layer under Elastic Deformation of Surrounding Rock

Zhigang Jia [iD] and Yongsong Li [iD]

School of Architecture Engineering, Huanghuai University, Zhumadian, China

Correspondence should be addressed to Zhigang Jia; jiazhigang@huanghuai.edu.cn and Yongsong Li; liys@huanghuai.edu.cn

Due to the limitation of geological conditions and route alignment, tunnel engineering will inevitably pass through special sections such as shallow buried section, broken rock layer, and loss and weak rock stratum. Tunnel construction in these special sections will easily lead to tunnel collapse, landslide of portal slope, excessive deformation of supporting structure, and even deformation and damage accidents, which are high-incidence areas of engineering safety accidents. In this paper, a 3D numerical model is established based on a practical engineering to analyze the deformation and stress variation of surrounding rock of the tunnel with the in-advance support technology. According to the monitoring results of the actual project, the deformation law of the soft rock section at the tunnel entrance is mastered. The deformation of surrounding rock of the tunnel under the support condition of changing the three main parameters, such as ring spacing, pipe diameter, and pipe length, is analyzed, and the effect of controlling the deformation of surrounding rock with different parameters is studied. The deformation, stress characteristics, and plastic zone distribution of surrounding rock by a single side wall guide method and ring excavation and retaining core soil method in advance support are numerically simulated and studied.

1. Introduction

When the tunnel passes through the mountain, it will be inclined to cross with the mountain with an asymmetrical terrain and inclined angle, resulting in asymmetrical load of rock mass on the tunnel. In this case, it is a biased tunnel. The tunnel is very prone to collapse due to the uneven stress of surrounding rock [1–3]. Therefore, in the tunnel construction in these sections with poor geological conditions, in order to ensure the smooth completion of the project, in-advance support technologies such as shed pipe, small duct, and the horizontal rotary jet grouting piles should be adopted to control the deformation of surrounding rock [4]. In order to improve the support effect, different advanced support technologies are often used together.

(1) The construction of a tunnel opening section is the beginning of the tunnel engineering and the key section connecting the tunnel body. The successful completion of the tunneling project has a great impact on the progress and cost of the later project and is closely related to the safety of the whole tunnel. It is very necessary for each mountain tunnel to ensure that the deformation of surrounding rock is controlled within the allowable range during construction. Therefore, it is of great value to study the deformation control of surrounding rock at the entrance [5–7]

(2) At present, the supporting measures of the tunnel portal section have been very comprehensive, among which the advanced support is necessary for each tunnel with poor geological conditions. However, the terrain, geological conditions, surrounding rock characteristics, and design parameters of each tunnel portal section are different. The deformation of surrounding rock under the advanced support is not the same, and the support effect is also different.

Therefore, the design plan of advanced support is not universal for each tunnel. Selecting the most suitable advanced support plan and excavation method can improve the construction quality and production efficiency of the tunnel engineering, ensure the construction safety, save the construction period, reduce the cost, and increase the production capacity. Therefore, it is of great construction promotion value to compare and select plans [8].

In this paper, based on a coal mine tunnel under construction as the background, the tunnel exit portal section buried depth is shallow, geological conditions are not ideal, the field construction process found that the tunnel portal section of multiple surrounding rock settlement is too large, and deformation is large, prone to collapse and roof fall accidents [9–12]. The buried depth of this section is 3.5 m to 16 m, and the slope is 31.3%. The measured spacing for the exit is 16.1 m, and the general spacing for the hole body is 25-35 m. Compared with other positions of the tunnel, the shallow hole section of the tunnel is more vulnerable to weathering, which will reduce the mechanical parameters of surrounding rock and make it difficult for the shallow hole to form arch effect, further affecting the stability of the shallow hole. When the new Austrian tunneling method is adopted, the shallow buried hole section of the tunnel can effectively alleviate the complicated geological conditions, rock fragmentation, and serious weathering of the tunnel opening by adopting the way of advance support. Therefore, the advance support is of great significance to the reinforcement of shallow buried tunnel openings.

2. Theoretical Analysis and Supporting Principles of the Short-Range Coal Seam Roadway

2.1. Supporting Theory of the Short-Range Coal Seam Roadway

(1) The core content of the suspension theory is as follows: if there is a weak rock layer on the roof of the roadway, the weak rock layer needs to be connected with the stable rock layer at the bottom, and the anchor acts as a suspension [12]. When the roof of the roadway is a hard rock layer and a soft broken rock layer, respectively, the effect diagram of suspension action is shown in Figure 1, respectively

(2) Composite beam theory

The theory is analyzed in view of multiple layers of the roadway roof. At this time, the application of bolt support can, on the one hand, increase the friction between layers and effectively prevent the occurrence of sliding and separation in each layer. On the other hand, the shear strength of the rock layer is increased, and the thin layers are fixed to each other, equivalent to a thick coal seam. The theoretical effect diagram is shown in Figure 2.
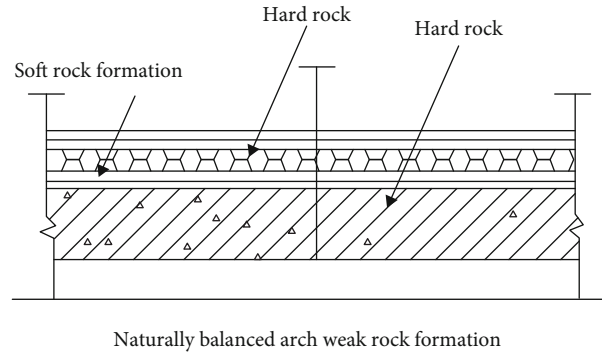
Figure 1: Suspension action of bolt support.

(3) Combination arch theory

In this theory, in order to prevent the continuous expansion of the crushing area of surrounding rock, a prestressed bolt is installed to achieve the supporting effect. A pressure stress zone with conical distribution will be formed from both ends of the supporting bolt to the center of the bolt. Moreover, when the bolt spacing is small, a uniform composite compression arch will be formed to increase the strength of surrounding rock, which is commonly used in circular or arch tunnels.

2.2. Support Optimization of Surrounding Rock of the Near Coal Seam Mining Roadway.
Taking the coal mine as an example, the main coal seams are no. 4 and no. 5 coal. Among them, the average thickness of no. 4 coal seam is 4.2 m, most of which can be mined; the average thickness of no. 5 coal seam is 4.5 m, all of which can be mined. The average interval between the two coal seams is 6.0 m, which belongs to the typical close distance coal seam. The downward mining method is adopted; that is, the no. 4 coal seam is first mined, the roadway section is 4.2 × 4.7 m, and the 20 m protective coal pillar is reserved, and then, the no. 5 coal seam is mined. After the no. 4 coal seam is mined out, the no. 5 coal working face's transportation gateway is arranged under the no. 4 coal goaf and 8.3 m away from the protection coal pillar of the no. 4 coal section. The roadway section is 4.5 × 4.7 m, and the combined symmetrical support plan of "bolt (cable)+metal mesh" is adopted. Due to the neglect of the asymmetry of the stress and deformation of the roadway side, although the no. 5 coal seam transport gateway is arranged in the stress-reducing area, there are still serious side heave and roof subsidence deformation, the convergence rate of the two sides is as high as 40~45 mm/d, the roadway side still has serious asymmetric deformation, and the side bolt (cable) turns over in different degrees, which seriously affects the normal mining of the no. 5 coal seam. In this section, the limit equilibrium zone width, fracture zone width, and safe staggered distance of upper and lower coal seams will be determined according to the above theoretical equation, and the bolt support design plan will be optimized. The original support plan of the upper and lower coal seam roadway is shown in Figure 3.
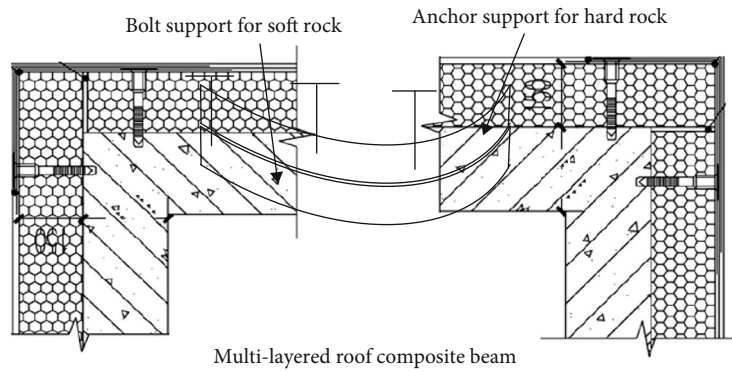
Figure 2: Composite beams with a multilayered roof.
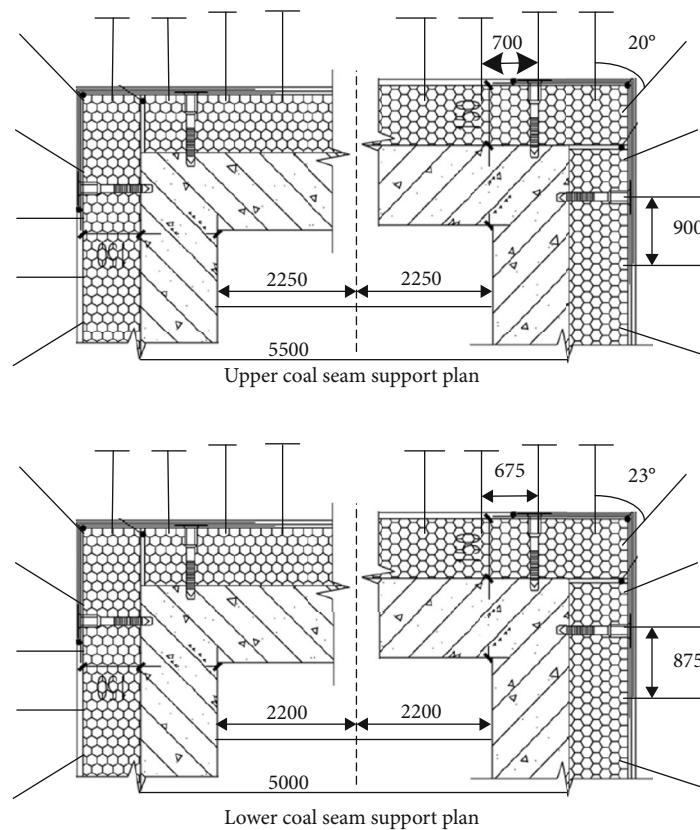
Figure 3: Original supporting plan of the face transportation channel.

2.2.1. Original Supporting Plan of the Roadway in the Upper Coal Seam

(1) Roadway Roof Support. The roof bolt adopts a $\Phi18 \times 2200$ mm left screw rigid resin bolt, with 4 bolts in each row, and the spacing between rows is 1400×1000 mm. The bolt adopts two z2360 medium resin anchoring agents, adopts a high-strength arch tray with the specification of $150 \times 150 \times 8$ mm, and is equipped with a high-strength spherical washer. The installation angle of the bolt at both ends near the roof is offset by 20° to the inner side of the roadway; the roof anchor cable adopts $\Phi18 \times 7000$ mm high-strength prestressing. There are 3 anchor cables in total, which are symmetrically arranged along the center line of the roadway, with a spacing of 1400×2100 mm, and three Z2360 medium resin anchoring agents are used; the metal mesh is a square metal mesh woven with a 10# iron wire, with a mesh size of 100×100 mm, which shall be cut reasonably according to the size of the roadway roof, and the metal mesh shall be flattened and tightened during laying.

(2) Parameters of the Sidewall Bolt. A sidewall bolt adopts a $\Phi18 \times 2200$ mm left screw rigid resin anchor rod, with 5

bolts in each row, with row spacing of 900×900 mm. The bolt adopts two branches of the Z2360 medium resin anchoring agent, adopts a high-strength arch tray with specification of $150 \times 150 \times 8$ mm, and is equipped with a high-strength spherical washer. The installation angle of the anchor rod near the top plate and bottom plate end is, respectively, $20°$ to the top plate and bottom plate; the metal mesh is woven with a 10# iron wire square metal mesh with a mesh size of 50×50 mm which shall be cut reasonably according to the size of roadway side, and the metal mesh shall be flattened and tightened during laying [12].

2.2.2. Original Supporting Plan of the Lower Coal Seam Roadway

(1) *Roadway Roof Support.* The roof bolt adopts a $\Phi 18 \times 2200$ mm left screw rigid resin bolt, with 4 bolts in each row, and the spacing between rows is 1400×1000 mm. The bolt adopts two Z2360 medium resin anchoring agents, adopts a high-strength arch tray with the specification of $150 \times 150 \times 8$ mm, and is equipped with a high-strength spherical washer. The installation angle of the bolt at both ends near the roof is offset by $23°$ to the inner side of the roadway; the roof anchor cable adopts $\Phi 18 \times 5500$ mm high-strength prestressing. There are 3 anchor cables in total, which are symmetrically arranged along the center line of the roadway, with a spacing of 1400×2100 mm, and three Z2360 medium resin anchoring agents are used; the metal mesh is a square metal mesh woven with a 10# iron wire, with a mesh size of 100×100 mm, which shall be cut reasonably according to the size of the roadway roof, and the metal mesh shall be flattened and tightened during laying [13].

(2) *Parameters of the Sidewall Bolt.* The sidewall bolt adopts a $\Phi 18 \times 2200$ mm left screw rigid resin bolt, with 5 bolts in each row and 875×875 mm spacing between rows. The bolt adopts two Z2360 medium resin anchoring agents, adopts a high-strength arch tray with specification of $150 \times 150 \times 8$ mm, and is equipped with a high-strength spherical washer. The installation angle of the bolt near the end of the top plate and bottom plate is, respectively, $23°$ to the direction of the roof and bottom plate; the metal mesh is made of a 10# iron wire The mesh size of a square metal mesh is 50×50 mm, which is cut reasonably according to the size of the roadway side, and the metal mesh shall be flattened and tightened during laying [14].

2.3. Optimization Calculation of Bolt Support Parameters

(1) When the bolt length supports the surrounding rock of the roadway, the length of all anchors in the supporting structure of the roadway is the same and no less than L_0 [15]. In combination with the actual engineering situation, it is found that the support effect of the roof of the mining roadway is realized through the formation of "combined arch of anchoring layer" by anchor rods, so the "combined arch theory" is adopted for analysis and calculation [16].

Therefore, the roof length can be calculated by the following equation:

$$L_p \geq L_1 + L_2 + L_3. \tag{1}$$

In equation (1), L_1 is the exposed length of the bolt, L_1 = the thickness of backing plate + the thickness of nut + ($0.02 \sim 0.03$) m, and $L_1 = 0.10$ m; L_2 is the effective length of the bolt; and L_3 is the anchorage length of the bolt and $L_3 = 0.3 \sim 0.4$ m.

Calculation of effective length L_2 of the roof bolt

(i) Roof bolt for the upper seam

In combination with the geological data of the roadway, the values of relevant parameters are determined as follows: $a = 2.30$ m and width $L_s = 2.42$ m of the side fracture zone, and the value of the Platt coefficient is 2.5, so that

$$a_1 = 2.3 + 2.42 = 4.72, \tag{2}$$

$$L_2' = \frac{4.72}{2.5} = 1.89 \text{ m}. \tag{3}$$

(ii) Lower seam roof bolt

In combination with the geological data of the roadway, the relevant parameters are determined as follows: half width $a = 2.30$ m and width $L_s' = 2.93$ m of the fracture zone at the side, and the value of the Platt coefficient is 2.7, so that

$$a_1 = 2.3 + 2.93 = 5.23 \text{ m}, \tag{4}$$

$$L_2' = \frac{5.23}{2.7} = 1.94 \text{ m}. \tag{5}$$

The roof length of the upper coal seam is calculated as follows: $L_n \geq 2.29 \sim 2.39$ m. In combination with the actual situation and engineering analogy, the length of the anchor rod is 2.4 m. The roof length of the lower coal seam is obtained as follows: $L_0' \geq 2.34 \sim 2.44$ m. By combining the actual situation and engineering analogy, the bolt length is 2.4 m [17].

(2) Calculation of effective length L_2 of the floor anchor rod

According to the results of mining roadway floor analysis and considered according to the most unfavorable combination, the effective length of roadway roof rock when it reaches the failure depth is the effective length of the roadway roof bolt, that is, the effective length of the roof bolt in the upper coal seam floor $L_2 = 3.0$ m and the effective length of the roof bolt in the lower coal seam floor $L_2 = 3.39$ m [18].

The length of the upper coal seam floor is calculated as follows: $L_0 \geq 3.40 \sim 3.50$ m. In combination with the actual situation on the site and engineering analogy, the length of

the anchor rod is 3.4 m. The roof length of the lower coal seam is obtained as follows: $L_0' \geq 3.79 \sim 3.89$ m. In combination with the actual situation and engineering analogy, the length of the anchor rod is 3.8 m [19].

(3) Calculation of effective length L_2 of the sidewall bolt

(i) Upper seam sidewall bolt

The width of the coal sidewall crushing zone of the coal seam is $L_s = 2.42$ m; then, the effective length of the bolt L_2 is

$$L_2 \geq L_r = 2.42 \text{ m.} \tag{6}$$

(ii) Lower seam sidewall bolt

The width of the coal sidewall crushing zone of the coal seam is $L_s = 2.93 m$; then, the effective length of the bolt L_2 is

$$L_2 \geq L_s = 2.93 \text{ m.} \tag{7}$$

The roof length of the upper coal seam is calculated as follows: $L_0 \geq 2.82 \sim 2.92$ m. In combination with the actual situation and engineering analogy, the length of the anchor rod is 2.9 m. The roof length of the lower coal seam is obtained as follows: $L_0' \geq 3.33 \sim 3.43$ m. In combination with the actual situation and engineering analogy, the bolt length is 3.4 m.

(4) For the use of bolt support in stoping the roadway, it is generally considered to take equal bolt spacing in construction technology to deal with; then, the bolt spacing a can be calculated according to the following equation:

$$a \leq 0.5 L_0. \tag{8}$$

(i) Upper coal seam spacing roof bolt spacing from equation (8):

$$a \leq 0.5 \times 2.4 = 1.2 \text{ m.} \tag{9}$$

In combination with the engineering practice and construction experience, considering the roadway cross section size, the row spacing between the roof and anchor is 1200 × 1200 mm.

(ii) The row spacing between floor bolts is shown in equation (8) as follows:

$$a \leq 0.5 \times 3.4 = 1.7 \text{ m.} \tag{10}$$

In combination with the engineering practice and construction experience, considering the roadway section size, the row spacing between bottom anchors is 830 × 830 mm.

(iii) The row spacing of sidewall bolts is shown in equation (8) as follows:

$$a \leq 0.5 \times 2.9 = 1.45 \text{ m.} \tag{11}$$

In combination with the engineering practice and construction experience, considering the roadway cross section size, the row spacing between the sidewalls is 900 × 900 mm.

(5) The row spacing of bolts in the lower coal seam

(i) The row spacing of roof bolts is shown in equation (8) as follows:

$$a \leq 0.5 \times 2.4 = 1.2 \text{ m.} \tag{12}$$

In combination with the engineering practice and construction experience, considering the roadway cross section size, the row spacing between the roof and anchor is 1200 × 1200 mm.

(ii) The row spacing between the bottom bolts is shown in equation (8) as follows:

$$a \leq 0.5 \times 3.8 = 1.9 \text{ m.} \tag{13}$$

In combination with the engineering practice and construction experience, considering the roadway section size, the row spacing between bottom anchors is 850 × 850 mm.

(iii) The row spacing between the side bolts is shown in equation (9) as follows:

$$a \leq 0.5 \times 3.4 = 1.7 \text{ m.} \tag{14}$$

In combination with the engineering practice and construction experience, considering the roadway cross section size, the row spacing between the sides is 1000 × 1000 mm.

(iv) The diameter of the anchor rod is determined by the relationship between the anchoring force and the tensile strength of the bolt body materials:

$$Q \leq \frac{\pi d^2 \sigma}{4}. \tag{15}$$

Then, the calculation equation of the bolt diameter shall

meet the following equation:

$$d \geq 1.13\sqrt{\frac{Q}{\sigma_t}}, \tag{16}$$

where d is the diameter of the anchor rod; σ_t is the tensile strength of the bolt rod material, which is 360 MPa according to the actual measurement; and Q is the anchoring force of the anchor rod (not less than 70 kN), taking 90 kN.

Substituting the relevant data into equation (16) shows that

$$d \geq 1.13\sqrt{\frac{90 \times 10^3}{360 \times 10^7}} = 17.9 \text{ mm}. \tag{17}$$

In order to meet the requirement of support strength, the bolt diameter is 20 mm.

3. Optimization Design of the Bolt Support Plan

3.1. Support Plan after Optimization of the Upper Coal Seam Roadway

3.1.1. Roadway Roof Support. The roof bolt adopts a left screw rigid resin bolt, 4 in each row, with $\Phi 20 \times 2400$ mm spacing between rows. The roof bolt adopts 2 Z2360-type resin anchorage agents, adopts a high-strength arch tray, with the specification of 1200×1200 mm, and is matched with a high-strength spherical washer. The installation angle of the bolt near the two ends of the roof is offset by 20° to the inside of the roadway. The roof anchor cable is made of a high-strength prestressed steel strand, with a total of three anchor cables arranged symmetrically along the center line of the roadway. The spacing between the cables is $\Phi 18 \times 7000$ mm. Three Z2360-type resin anchor agents are adopted. The metal mesh is a square metal mesh woven with a 10# iron wire, and the mesh size is 100×100 mm. The mesh should be cut reasonably according to the size of the roadway roof, and the metal mesh should be paved and tensioned [20].

3.1.2. Roadway Floor Bolt Support. The floor bolt adopts a $\Phi 20 \times 3400$ mm left screw rigid resin bolt, 5 pieces in each row, and the spacing between rows is 830×830 mm. The bolt adopts two Z2360 medium resin anchoring agent, adopts a high-strength arch tray with specification of $150 \times 150 \times 8$ mm, and is equipped with a high-strength spherical washer; the metal mesh adopts a square metal mesh woven with a 10# iron wire, with mesh size of 100×100 mm, which is cut reasonably according to the side size of the roadway, and the metal mesh shall be laid smooth and tightened [21].

3.1.3. Bolt Support of the Roadway Sidewall. The sidewall bolt is a $\Phi 20 \times 2900$ mm left screw rigid resin bolt, 5 pieces in each row, and the spacing between rows is 900×900 mm. The bolt adopts two Z2360 medium resin anchoring agents, adopts a high-strength arched tray with the specification of $150 \times 150 \times 8$ mm, and is equipped with a high-strength spherical washer. The installation angle of the bolt near the end of the roof and bottom plate is, respectively, 20° to the direction of the roof and bottom plate; the metal mesh is a square metal mesh woven with a 10# iron wire. The mesh size is 50×50 mm, which should be cut reasonably according to the size of the roadway side, and the metal mesh should be flattened and tightened during laying [22].

The optimized support plan of the upper coal seam roadway is shown in Figure 4.

3.2. Support Plan after Optimization of the Lower Coal Seam Roadway

3.2.1. Roadway Roof Support. The roof bolt adopts a $\Phi 20 \times 2400$ mm left screw resin bolt with 4 bolts in each row and 1200×1200 mm row spacing. The bolt adopts two Z2360-type resin anchorage agents, adopts a high-strength arch tray with $150 \times 150 \times 8$ mm specification, and is matched with a high-strength spherical gasket. The installation angle of the bolt near the two ends of the roof is offset by 20° to the inside of the tunnel. The roof anchor cable is made of a high-strength prestressed steel strand, with a total of three anchor cables arranged symmetrically along the center line of the roadway. The spacing between the cables is 1400×2100. Three Z2360-type resin anchor agents are adopted. The metal mesh is a square metal mesh woven with an iron wire 10#, and the mesh size is 100×100 mm. The mesh is cut reasonably according to the size of the roadway roof, and the metal mesh should be paved and tensioned [23].

3.2.2. Roadway Floor Bolt Support. The bottom bolt adopts a $\Phi 20 \times 3800$ mm left screw resin bolt with 5 bolts in each row and 850×850 mm spacing between rows. The bolt adopts 2 Z2360 medium resin anchorage agents, adopts a high-strength arch tray with $150 \times 150 \times 8$ mm specification, and is matched with a high-strength spherical washer. The metal mesh is a square metal mesh woven with an iron wire $10^\#$, and the mesh size is 100×100 mm. The mesh should be cut reasonably according to the size of the roadway side, and the metal mesh should be paved and tensioned [24].

3.2.3. Roadway Sidewall Bolt Support. The left screw rigid resin bolt of $\Phi 20 \times 3400$ mm is used for the sidewall bolt, with 5 bolts in each row and the spacing 1000×1000 mm between rows. The bolt adopts two Z2360 medium resin anchoring agents, adopts a high-strength arched tray, and is equipped with a high-strength spherical washer. The installation angle of the bolt near the top plate and bottom plate end is, respectively, 20° to the top plate and bottom plate; the metal mesh adopts a square metal mesh woven with a 10# iron wire, and the mesh is 50×50 mm in size. It should be cut reasonably according to the size of the side of the roadway. When laying, the metal mesh should be flattened and tightened [25].
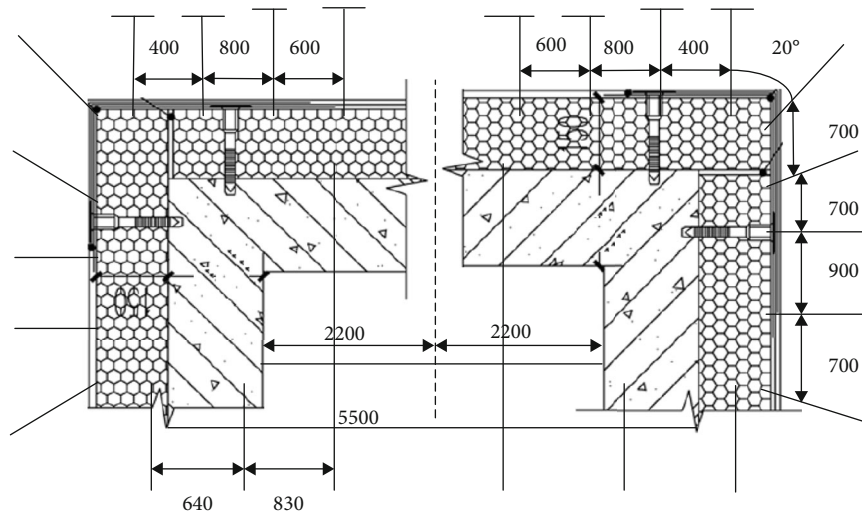
FIGURE 4: Support plan after optimization of the upper seam roadway.
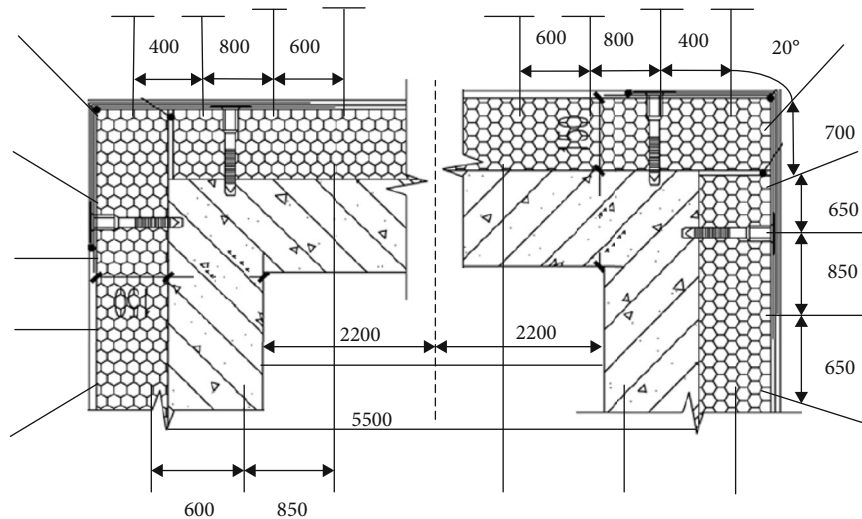
FIGURE 5: Support plan after optimization of the lower coal seam roadway.

The optimized support plan of the lower coal seam roadway is shown in Figure 5.

3.3. On-Site Monitoring

3.3.1. Monitoring Purpose. Due to the complex and diverse geological conditions of coal mine projects, it is difficult to accurately grasp the surrounding rock deformation and support structure deformation caused by excavation in the construction process, which brings great safety risks to the coal mine construction [26]. Therefore, coal mine monitoring is an essential work in coal mine construction and an important measure to ensure construction safety. In the process of coal mine construction, it is necessary to strengthen the monitoring and measurement of surrounding rock deformation, real-time feedback of monitoring information, and timely processing and analysis of monitoring results, so as to ensure the smooth progress of coal mine work and ensure the safety of construction operation and on-site personnel [27].

The purpose of this engineering monitoring is shown as follows:

(1) Timely grasp the deformation law of surrounding rock and support structure during coal mine excavation, and provide data support for field operations, which can quickly and effectively deal with the occurrence of abnormal surrounding rock in the tunnel during excavation and ensure the safety of construction [28, 29]

(2) The monitoring of the support structure can enable the construction personnel to deeply understand the role and effect of the support structure, so as to determine a more reasonable and effective support plan

TABLE 1: Contents of required test items.

Serial number	Work content	Measuring instrument	Measurement accuracy
1	Observation inside and outside the cave	Field observation	
2	Vault sinking measurement	Electronic level, steel hanging ruler, indium steel ruler, total station	0.01 mm
3	Peripheral displacement measurement	Convergence meter, total station	0.01 mm
4	Ground settlement measurement	Electronic level, indium steel ruler, total station	0.01 mm

(3) By analyzing the daily monitoring data, the field personnel can find the problems as soon as possible, communicate with the designer, and make design changes in time, so that the design plan is more in line with the actual situation of the site

3.3.2. Monitoring Content and Plan

(1) Required Items of Monitoring Measurement Are Shown in Table 1.

(2) Layout of Monitoring Points. The deformation and stress change of surrounding rock of coal mine can be grasped in time by arch settlement monitoring, and the stability of coal mine can be determined effectively. Measuring point layout: an anchor pile is set at the measuring point of the mining wool hole. The depth of the measuring point is 30 mm, and the diameter of the drilling hole is 22 mm. It is fixed with fast setting cement or early-strength anchoring agent, and an angle iron is fixed at the measuring pile head.

The remote measurement of the settlement of the vault and the surrounding measurement and monitoring section is shown in Table 2.

In addition, the reading of initial deformation value should be completed before the next cycle of excavation.

(3) Measuring Frequency. According to the observation frequency of arch settlement and peripheral convergence, it is determined according to the deformation rate and the distance from the dug surface, as shown in Tables 3 and Table 4, respectively.

The measurement frequency determined by the rate of convergence and the distance from the excavation face is in principle high frequency.

(4) Measurement Method. The arch vault subsidence measurement method uses the total station plus reflector to measure the coordinates of the measurement points, and the measured elevation difference value is the settlement amount [30–38].

In the peripheral convergence measurement method, the total station and reflector are used for measurement. The coordinates of the measuring points are measured by

TABLE 2: Principles for selecting monitoring surfaces.

Surrounding rock level	Section spacing
II	According to the specific situation
III	30~50 m
IV	10~30 m
V	5~10 m

TABLE 3: Measuring frequency of dome subsidence and peripheral convergence displacement (displacement according to velocity).

Displacement speed (mm/d)	Measuring frequency
≥5	2~3 times/d
1~5	1 time/d
0.5~1.0	1 time/2~3 d
0.2~0.5	1 time/3 d
<0.2	1 time/3~7 d

TABLE 4: Measurement frequency of dome subsidence and peripheral convergence displacement (according to the distance from the excavation surface).

Distance between measuring section and working surface (m)	Measuring frequency
(0~1) B	2 times/d
(1~2) B	1 time/d
(2~5) B	1 time/2~3 d
>5 B	1 time/3~7 d

cross-sectional measurement at the rear of the total station, and the distance between the measuring points is calculated according to the coordinates. The distance difference between the two measurements is the convergence.

3.3.3. Analysis of Monitoring Results.

Three sections of the right line opening section are selected to carry out monitoring measurement and data analysis for the settlement of the arch roof and horizontal convergence of the side wall. The data curves of the three sections within 70 observation days are shown in Figure 6.

As shown in Figures 6, 10 days before coal mine excavation, the settlement and horizontal convergence of the section arch roof increase rapidly. With the increase in
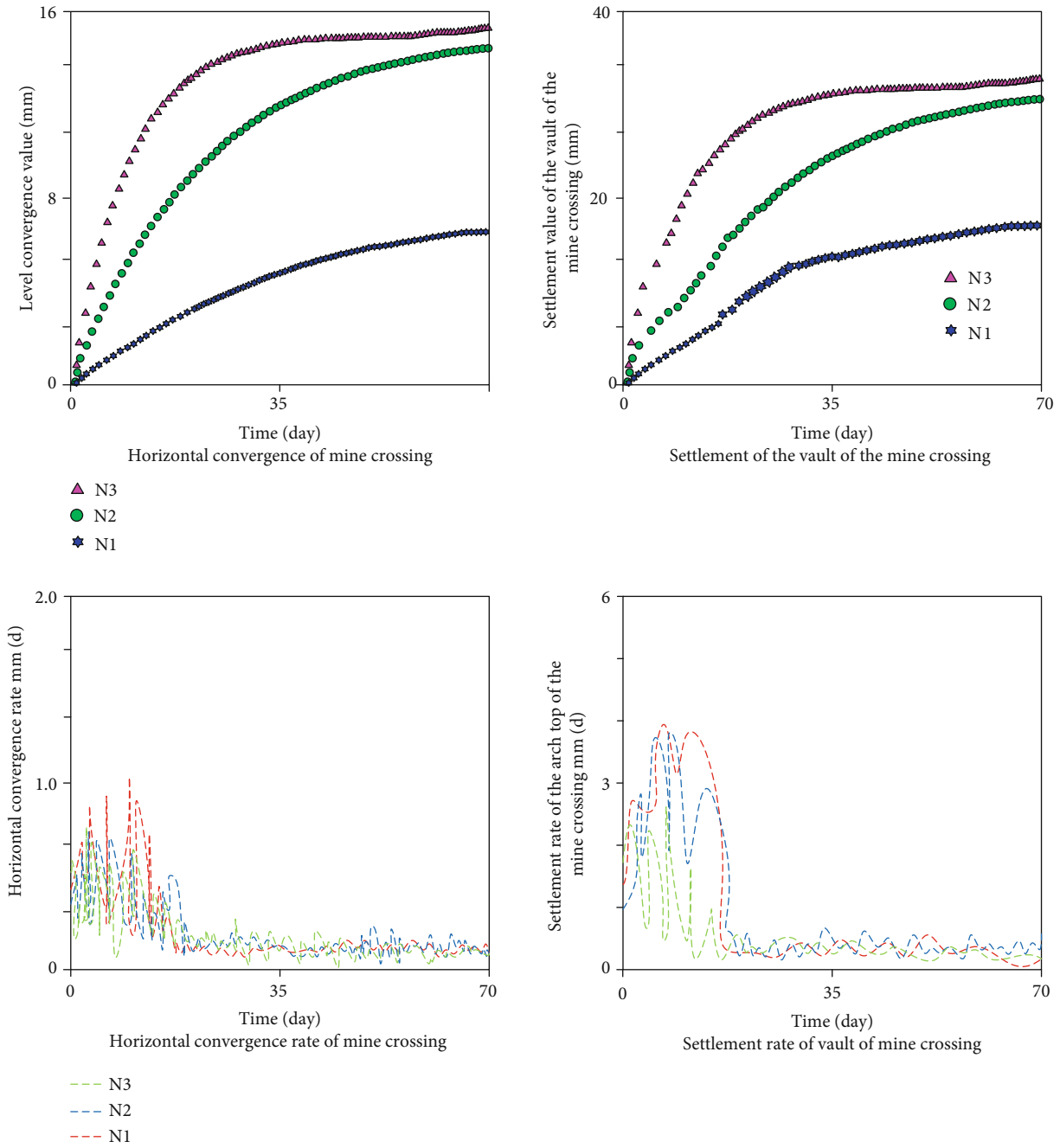
FIGURE 6: Data curve of the coal mine opening section.

excavation time, the settlement and horizontal convergence of the section arch roof continue to increase, but the growth rate gradually decreases. After about 60 days, the settlement of the vault tends to be stable; after about 60 days, the horizontal convergence of N1 and N2 tends to be stable; and after about 50 days, the horizontal convergence of N3 tends to be stable. With the increase in excavation depth and section burial depth, the cumulative settlement value and horizontal convergence value of the arch roof gradually decrease, the surrounding rock stability is high, and the support structure plays a role. It can be seen that coal mine surrounding rock deformation can be divided into three stages on the whole:

(1) The initial surrounding rock deformation is rapid, and the deformation rate is very high. In just 10 days, the maximum settlement rate of the N1 section reaches 4.7 mm/d, the settlement of vault reaches 24.9 mm, accounting for 65.4% of the total settlement, and the horizontal convergence reaches 10.92 mm, accounting for 71.4% of the total convergence. The maximum settlement rate of the N2 section reaches 5.6 mm/d, the settlement amount of vault reaches 26.43 mm, accounting for 74.1% of the total settlement amount, and the horizontal convergence amount reaches 10.03 mm, accounting for 67.3% of the total settlement amount. Within 15

days of excavation, the maximum settlement rate of section N3 reaches 2.7 mm/d, the settlement amount of vault reaches 15.79 mm, accounting for 64.2% of the total settlement amount, and the horizontal convergence amount reaches 6.53 mm, accounting for 62.0% of the total convergence amount. This is because the surrounding rock of the entrance of the coal mine is not stable enough, the construction has great disturbance to it, and the supporting structure has not played an effective supporting role

(2) After 10 to 15 days of excavation, the deformation rate of surrounding rock decreases and the amount of deformation increases slowly. Within about 45 days, the maximum settlement rate of section N1 is 0.41 mm/d, the increase in settlement is 13.2 mm, accounting for 35.0% of the total settlement, and the increase in horizontal convergence is 5.03 mm, accounting for about 32.9%. The maximum settlement rate of section N2 is 0.55 mm/d, the increase in settlement is 9.27 mm, accounting for about 26.0%, and the increase in horizontal convergence is 4.87 mm, accounting for about 32.7%. The maximum settlement rate of section N3 is 0.52 mm/d, the increase in settlement is 8.81 mm, accounting for about 35.8%, and the increase in horizontal convergence is 4.01 mm, accounting for about 38.1%. It can be seen that the surrounding rock is still in deformation at this stage, but the speed is slow and the increment is small. This is because the supporting structure in the cave plays its own role at this time, and the surrounding rock stress is redistributed

(3) After the deformation relaxation period, the deformation rate tends to be zero, the settlement of the N1 arch crown reaches 38.1 mm, and the horizontal convergence amount reaches 15.3 mm; the settlement of section N2 vault reaches 35.7 mm, and the horizontal convergence amount reaches 14.9 mm; the settlement of section N3 vault reaches 24.6 mm, and the horizontal convergence amount reaches 10.54 mm. At this stage, the deformation of the three sections is basically unchanged, and the surrounding rock is in a stable state on the whole

According to the above analysis, the deformation of surrounding rock of coal mine changes dynamically with the excavation time, which can be divided into three deformation stages: (1) the early rapid deformation stage, (2) the middle slow deformation stage, and (3) the late basic stability stage.

3.4. Comparison between Numerical Simulation Results and Monitoring Results. In order to verify the rationality of the numerical simulation, this paper compares the finite element simulation results of vault settlement and horizontal convergence with the field measured values. The comparison results are shown in Table 5.

It can be seen from Table 5 that the numerical simulation results of vault subsidence and horizontal convergence

TABLE 5: Comparison of calculated and measured values (unit: mm).

Fault plane	Comparison item	Vault settlement	Horizontal convergence
N1	Calculated	44.16	11.45
	Monitoring value	37.72	10.05
	Relative error	14.58%	12.23%
N2	Calculated	45.19	12.89
	Monitoring value	42.65	11.64
	Relative error	5.62%	9.70%
N3	Calculated	46.69	13.49
	Monitoring value	40.67	13.01
	Relative error	12.89%	3.56%

of the three monitored sections are close to the field monitoring values, and the error is less than 15%, which indicates that the numerical simulation results are reasonable. Due to field construction and measurement methods, the simulated calculated value is larger than the measured value, and the deformation of surrounding rock is mainly generated after excavation, so part of the deformation at the initial excavation stage cannot be measured.

4. Conclusion

In order to solve the engineering problems caused by the deformation of the upper and lower roadways in the process of mining and driving near the mine mouth, based on the elastic theory, this paper establishes the mechanical analysis model of the upper coal seam roadway under the action of the abutment pressure. By calculating the stress of any unit rock mass in the roadway side and based on the stress diffusion principle of soil mechanics theory, the surrounding rock deformation of the roadway in the lower coal seam is carried out. Through the establishment of the stress diffusion model under the abutment pressure of the coal pillar of the inner staggered upper coal seam roadway in the close distance coal seam, the lower coal seam is determined to be outside the stress influence range of the upper coal seam left coal pillar floor, and the calculation equation of the upper and lower roadway safety offset is given, which greatly reduces the difficulty of roadway maintenance in the later stage.

Data Availability

The data used to support the findings of this study are included within the article.

Conflicts of Interest

The authors declare no conflict of interest.

Acknowledgments

References

[1] D. R. H. Jones and M. F. Ashby, "Creep and creep fracture," *Engineering Materials 1*, vol. 1, 2019.

[2] H. Altenbach, "Fundamentals of continuum mechanics – classical approaches and new trends," *J Phys: Conf Ser*, vol. 991, article 012003, 2018.

[3] S. Aziznejad, K. Esmaieli, and J. Hadjigeorgiou, "Responses of jointed rock masses subjected to impact loading," *Journal of Rock Mechanics and Geotechnical Engineering*, vol. 10, no. 4, pp. 624–634, 2018.

[4] Nguyen and H. T. Tai, "Modelling the mechanical behaviour of asphalt concrete using the Perzyna viscoplastic theory and Drucker–Prager yield surface," *Speculum vitae humanae*, vol. 18, no. sup2, pp. 264–280, 2017.

[5] B. Wassermann, S. Kollmannsberger, and S. Yin, "Integrating CAD and numerical analysis: 'dirty geometry' handling using the finite cell method," *Computer Methods in Applied Mechanics and Engineering*, vol. 351, pp. 808–835, 2019.

[6] L. W. Liu and H. K. Hong, "Clifford algebra valued boundary integral equations for three-dimensional elasticity," *Applied Mathematical Modelling*, vol. 54, pp. 246–267, 2018.

[7] D. Lukáš, O. F. Gunther, and J. Zapletal, "A boundary element method for homogenization of periodic structures," *Mathematical Methods in the Applied Sciences*, vol. 43, no. 3, pp. 1035–1052, 2020.

[8] J. C. Lachat and J. O. Watson, "Effective numerical treatment of boundary integral equations: a formulation for three-dimensional elastostatics," *International Journal for Numerical Methods in Engineering*, vol. 10, no. 5, pp. 991–1005, 2010.

[9] C. N. Van, "Numerical investigation of circle defining curve for two-dimensional problem with general boundaries using the scaled boundary finite element method," *Frontiers of Structural and Civil Engineering*, vol. 92, 102 pages, 2019.

[10] A. Lisjak, Q. Liu, and Q. Zhao, "Numerical simulation of acoustic emission in brittle rocks by two-dimensional finite-discrete element analysis," *Geophysical Journal International*, vol. 195, no. 1, pp. 423–443, 2013.

[11] H. S. Kazemi and S. M. Tavakkoli, "ON the performance of isogeometric analysis for elasto-plastic plane stress problems," *Asian Journal of Civil Engineering*, vol. 19, no. 1, pp. 55–65, 2018.

[12] Q. Xu, P. Cheng, P. Su, J. Dong, and G. Chen, "Study on the mechanical characteristics of shallow-buried unsymmetrical pressure tunnel entry construction," *Chinese Journal of Underground Space and Engineering*, vol. 13, no. 5, pp. 1311–1318, 2017.

[13] Y. Liang, "Study on the construction mechanics characteristics and control technology of the opening section of shallow-buried unsymmetrical pressure tunnel," *China Highway*, vol. 21, pp. 116-117, 2017.

[14] Z. Xu, "The application of the combined support technology of pile foundation guide wall and long pipe roof in the construction of soft surrounding rock tunnel," *Construction Technology*, vol. 46, no. S 1, pp. 729–732, 2017.

[15] Z. Song, T. Wang, J. Zhou, and W. Yu, "Construction optimization and stress characteristics analysis of shallow buried large cross-section tunnels," *Chinese Journal of Underground Space and Engineering*, vol. 13, no. 2, pp. 459–468, 2017.

[16] H. Dong, "Research on the layout of coal mining roadways at very close distances," *Coal Technology*, vol. 35, no. 4, pp. 50–52, 2016.

[17] Y. Yang, "Research on the reasonable location of the short-distance coal mining roadway under the coal pillar," *Modernization of Coal Mines*, vol. 3, pp. 19–22+25, 2018.

[18] W. Wang, "Layout optimization of short-distance coal seams under the goaf," *Modernization of Coal Mines*, vol. 6, pp. 1–3, 2018.

[19] F. Yong, "Research on the reasonable layout of dynamic pressure mining roadway under the short-distance coal seam goaf," *Coal Technology*, vol. 39, no. 4, pp. 6–9, 2020.

[20] X. Qu, F. Jiang, H. Wang et al., "Research on the mechanism of coal seam impact induced by coal pillar instability in goaf," *Journal of Mining and Safety Engineering*, vol. 34, no. 6, pp. 1134–1140, 2017.

[21] Z. Hua, C. Zhiwei, and Z. Xue, "Numerical analysis and support design of surrounding rock deformation of low-level coal seam roadway at close range," *Shenhua Science and Technology*, vol. 16, no. 11, pp. 42–46, 2018.

[22] F. Xiaofei, "Research on the deformation and failure law of coal roadway surrounding rock under the influence of fully mechanized caving mining," *Shanxi Coking Coal Science and Technology*, vol. 43, no. 9, pp. 49–52, 2019.

[23] Z. Li, D. Liu, X. Liu, D. Yuan, L. Du, and X. Xiao, "Research on the surrounding rock control of the mining roadway near the coal seam in a mine," *Modern Mining*, vol. 35, no. 3, pp. 78–80+92, 2019.

[24] Z. Buyuan, "Research and application of surrounding rock control technology for mining roadways in short distance coal seam goaf," *Modernization of Coal Mines*, vol. 5, pp. 1–3, 2019.

[25] M. Guo, G. Peilin, and L. Peng, "Research on reinforcement and support parameters of roadway under goaf in extremely close coal seams," *Coal Engineering*, vol. 52, no. 1, pp. 54–58, 2020.

[26] J. Liu, Z. Yu, S. Liu, G. Jing, and H. Liu, "Study on the stability and reasonable offset of surrounding rock in combined mining of thin coal seams at close range," *Coal Technology*, vol. 36, no. 3, pp. 49–51, 2017.

[27] S. Hao and C. Wenhua, "Research on reasonable distance between coal mining faces in extremely short distance coal seams," *China Work Safety Science and Technology*, vol. 14, no. 4, pp. 51–56, 2018.

[28] L. Jianguang, "Research on the safety staggered distance of joint mining in close coal seam face," *Contemporary Research in Chemical Industry*, vol. 14, pp. 37-38, 2019.

[29] Y. Dong, "Asymmetric deformation and failure characteristics and control technology of the surrounding rock of the tunnel under the short-distance mined-out area," *Coal Engineering*, vol. 51, no. 4, pp. 26–29, 2019.

[30] M. Qingni, "Research on roadway support of lower working face in short-distance coal seam goaf," *Coal Engineering*, vol. 52, no. 5, pp. 63–66, 2020.

[31] Y. G. Zhang, J. Tang, R. P. Liao et al., "Application of an enhanced BP neural network model with water cycle algorithm on landslide prediction," *Stochastic Environmental*

Research and Risk Assessment, vol. 35, no. 6, pp. 1273–1291, 2021.

[32] Y. G. Zhang, J. Tang, Z. Y. He, J. K. Tan, and C. Li, "A novel displacement prediction method using gated recurrent unit model with time series analysis in the Erdaohe landslide," *Natural Hazards*, vol. 105, no. 1, pp. 783–813, 2021.

[33] Y. G. Zhang and L. N. Yang, "A novel dynamic predictive method of water inrush from coal floor based on gated recurrent unit model," *Natural Hazards*, vol. 105, no. 2, pp. 2027–2043, 2021.

[34] Y. G. Zhang, Z. Zhang, and S. Xue, "Stability analysis of a typical landslide mass in the Three Gorges Reservoir under varying reservoir water levels," *Environmental Earth Sciences*, vol. 79, no. 1, 2020.

[35] Y. G. Zhang, S. Y. Zhu, J. K. Tan, L. D. Li, and X. J. Yin, "The influence of water level fluctuation on the stability of landslide in the Three Gorges Reservoir," *Arabian Journal of Geosciences*, vol. 13, no. 17, p. 845, 2020.

[36] Y. G. Zhang, Y. Zhu, W. Q. Zhang, and H. Liu, "Analysis of deformation characteristics and stability mechanisms of typical landslide mass based on the field monitoring in the Three Gorges Reservoir, China," *Journal of Earth System Science*, vol. 1, 2019.

[37] B. Gong, Y. J. Jiang, P. Yan, and S. Zhang, "Discrete element numerical simulation of mechanical properties of methane hydrate-bearing specimen considering deposit angles," *Journal of Natural Gas Science and Engineering*, vol. 76, p. 103182, 2020.

[38] B. Gong, Y. J. Jiang, and L. J. Chen, "Feasibility investigation of the mechanical behavior of methane hydrate- bearing specimens using the multiple failure method," *Journal of Natural Gas Science and Engineering*, vol. 69, p. 102915, 2019.

WILEY | Hindawi

Research Article

Stochastic Fracture Analysis Using Scaled Boundary Finite Element Methods Accelerated by Proper Orthogonal Decomposition and Radial Basis Functions

Xiaowei Shen [ID],[1] **Haowen Hu** [ID],[2,3] **Zhongwang Wang,**[2,3] **Xiuyun Chen,**[3]
and Chengbin Du [ID][1]

[1]*Department of Engineering Mechanics, Hohai University, Nanjing 211100, China*
[2]*College of Architecture and Civil Engineering, Xinyang Normal University, Xinyang 464000, China*
[3]*School of Architectural and Civil Engineering, Huanghuai University, Zhumadian 463000, China*

Correspondence should be addressed to Haowen Hu; hhwxynu@163.com and Chengbin Du; cbdu@hhu.edu.cn

This paper presents a stochastic analysis method for linear elastic fracture mechanics using the Monte Carlo simulations (MCs) and the scaled boundary finite element method (SBFEM) based on proper orthogonal decomposition (POD) and radial basis functions (RBF). The semianalytical solutions obtained by the SBFEM enable us to capture the stress intensity factors (SIFs) easily and accurately. The adoption of POD and RBF significantly reduces the model order and increases computation efficiency, while maintaining the versatility and accuracy of MCs. Numerical examples of cracks in homogeneous and bimaterial plates are provided to demonstrate the effectiveness and reliability of the proposed method, where the crack inclination angles are set as uncertain variables. It is also found that the larger the scale of the problem, the more advantageous the proposed method is.

1. Introduction

Fracture mechanics is central to many engineering applications, but the simulation of fractures poses great challenges to finite element analysis. To address this problem, a number of numerical algorithms were developed, such as meshfree methods [1, 2], extended finite element methods [3–5], phase field methods [6], boundary element methods [7] and peridynamics methods [8]. Song and Wolf proposed a new semianalytical numerical method, the so-called scaled boundary finite element method (SBFEM) [9, 10], which combines the advantages of the finite element method (FEM) and boundary element method (BEM). For the elasticity with simple geometries in which the entire boundary of the geometry can be seen from a scaling center, only the boundary needs to be discretized like BEM. For more complex problems, the interior domain can be divided into subdomains straightforwardly to meet the scaling center requirement. With SBFEM, the singularity of crack tips can be characterized with high accuracy, and the fracture parameters such as stress intensity factors can be directly obtained according to their definitions. In the past two decades, SBFEM has developed rapidly. Song and Wolf [11, 12] studied the singular stress field at cracks in anisotropic composite materials. The crack propagation is simulated in [13–17] based on SBFEM. Zhang et al. [18] used SBFEM to solve the crack face contact problem and verified the effectiveness of the method. Tian et al. [19] employ SBFEM to calculate dynamic stress intensity factor and T-stress based on the improved continued fraction formula. Jiang et al. [20] proposed a method of using SBFEM to simulate strong and weak discontinuities by incorporating enrichment methods. Because of the advantages of isogeometric analysis in integrating computer-aided design and numerical analysis [21–25], Natarajan et al. [26] introduced isogeometric analysis to SBFEM for linear fracture mechanics where the physical fields are discretized with the spline basis functions of computer-aided design.

Uncertain problems are ubiquitous in practical engineering applications, and it is of paramount importance to evaluate the responses of the uncertain factors to ensure a

reliable analysis result. Since deterministic analysis cannot characterize random fields, stochastic analysis has been extensively studied in recent years [27]. Stochastic analysis techniques can be divided into three categories: Karhunen-Loeve (KL) expanded stochastic spectrum methods [28], perturbation methods (PM) [29, 30], and Monte Carlo simulation (MCs) [31–33]. As a direct sampling technique, MCs is considered to be a versatile method for uncertainty qualification with the merit of easy implementation [34, 35]. Chowdhury et al. employ MCs and SBFEM to investigate the influence of crack geometric uncertainty [36, 37] by taking crack lengths and angles as uncertain variables. On the other hand, MCs requires a large number of data samples to achieve high accuracy, leading to a huge computational cost. Alleviating the computational burden is critical for improving the performance of MCs. The model order reduction method based on the combination of proper orthogonal decomposition (POD) and radial basis functions (RBFs) provides an effective way to accelerate MCs [38–41]. POD can obtain the bases for the initial problems after they are projected to reduced spaces, thereby reducing the degrees of freedom of the governing equations. Ding et al. [42–44] coupled POD and MCs to conduct multidimensional uncertainty analysis and verified the effectiveness and efficiency of the method. RBF is used for continuous approximation of the system response that enables fast evaluation of the coefficients of the interpolation in the reduced space [45].

This paper proposes a novel procedure for stochastic analysis of linear fracture mechanics. With this method, SBFEM is used for linear elastic fracture analysis and MCs for uncertainty qualification, which is accelerated by the combination of POD and RBF. The remainder of this paper is structured as follows. Section 2 outlines the MCs in stochastic analysis. Section 3 introduces POD and RBF and how to integrate them with MCs. Section 4 outlines the SBFEM formula in linear elasticity fracture mechanics and the evaluation of stress intensity factors with SBFEM. Section 5 gives numerical examples to test the reliability and accuracy of the proposed method, followed by the conclusions in Section 6.

2. Monte Carlo Model

Monte Carlo simulation (MCs) is considered to be the simplest, more direct, and the main general-purpose tool in the study of uncertain problems. It is an experiment-based method to study the uncertain output caused by uncertainty of input parameters. Normally, expectations and standard deviations are used to describe this uncertainty. Due to the nature of expectation and variance, it is an integral problem. The Monte Carlo integral can be expressed as

$$q = \int_{\Omega} g(\mathbf{x}) dx, \tag{1}$$

where $g(\mathbf{x})$ is any integrable function and $\Omega \subseteq R^d$ is the integration area. $\mathbf{x}$ is the d-dimensional random variable in the integration area Ω, which can be expressed as $\mathbf{x} = [x_1, x_2, \cdots x_d]$. Suppose a set of uniformly distributed

and independent random variables $\{\mathbf{x}_i\}$ in interval $[a, b]$ with the density function $f_X(\mathbf{x})$. Similarly, $g^*(\mathbf{x})$ is also a random variable with the same distribution and independent of each other, for any $g^*(\mathbf{x})$ that has $g^*(\mathbf{x}) = g^*(\mathbf{x})/f_X(\mathbf{x})$. So, the expectation of $g^*(\mathbf{x})$ can be expressed as

$$E[g * (\mathbf{x})] = \int_a^b g * (\mathbf{x}) f_X(\mathbf{x}) d\mathbf{x} = \int_a^b g(\mathbf{x}) d\mathbf{x} = I. \tag{2}$$

According to the theorem of large numbers, when $n \longrightarrow \infty$, the mean value of the mutually independent and identically distributed random variable sequence $\{\mathbf{x}_i\}$ converges to the mean value of the probability distribution 1, i.e.,

$$P_r \left(\lim_{n \longrightarrow \infty} \frac{1}{n} \sum_{i=1}^{n} g^*(\mathbf{x}_i) = I \right) = 1. \tag{3}$$

We define the average value $\bar{I}$ as follows:

$$\bar{I} = \frac{1}{n} \sum_{i=1}^{n} g^*(\mathbf{x}_i). \tag{4}$$

By (3) and (4), it can be known that $\bar{I}$ converges to probability 1 of I, while $\bar{I}$ can provide an approximation of the expectation of solving I.

For more general problems, supposing that the problem domain is controlled by the single variable element $\boldsymbol{\alpha}_i$ and that the probability density function of each individual random variable is $P(\boldsymbol{\alpha}_i)$, then their joint probability density $P(\boldsymbol{\alpha})$ can be expressed as

$$P(\boldsymbol{\alpha}) = P(\boldsymbol{\alpha}_1) P(\boldsymbol{\alpha}_2) \cdots P(\boldsymbol{\alpha}_n) = \prod_{i=1}^{n} P(\boldsymbol{\alpha}_i). \tag{5}$$

$\lambda(\boldsymbol{\alpha})$ stands for the structural response of random variable $\boldsymbol{\alpha}$, and the mathematical expectation of any function f related to $\lambda(\boldsymbol{\alpha})$ can be represented as

$$E[f(\lambda(\boldsymbol{\alpha}))] = \int_{\Omega} f(\lambda(\boldsymbol{\alpha})) p(\boldsymbol{\alpha}) dV, \tag{6}$$

where $dV = d\boldsymbol{\alpha}_1 \cdot d\boldsymbol{\alpha}_2 \cdots d\boldsymbol{\alpha}_n$ is an infinite small volume element; the expectation of function $f(\lambda(\boldsymbol{\alpha}))$ can be obtained by Equation (4), i.e.,

$$E[f(\lambda(\boldsymbol{\alpha}))] \approx \frac{1}{M} \sum_{i=1}^{M} f(\lambda(\boldsymbol{\alpha}_i)), \tag{7}$$

where M is the number of sampling points; formula (7) can know that the prediction accuracy of Monte Carlo simulation depends on the number of sampling points. The more sampling points, the higher the prediction accuracy, but as the number of sample points increases, it will result in a large amount of computation. In order to solve this problem, consider using singular value decomposition (SVD) and

radial base function (RBF) method to accelerate the stochastic analysis of MCs.

3. Proper Orthogonal Decomposition and Radial Basis Functions

It can be seen from the analysis above that direct Monte Carlo simulations require the consideration of computational efficiency. In order to improve computational efficiency, MCs has to be combined with other discrete algorithms. The proper orthogonal decomposition (POD) is usually used to improve computational efficiency. Following the idea of POD, the first step is to introduce design variable $\boldsymbol{\alpha}_i$ and its response $\lambda(\boldsymbol{\alpha}_i)$ as a matrix, which can obtain a solution space $\boldsymbol{\Lambda}$ after a series of high-fidelity calculations; the solution space $\boldsymbol{\Lambda}$ can be represented as follows:

$$\boldsymbol{\Lambda} = [\lambda(\boldsymbol{\alpha}_1), \lambda(\boldsymbol{\alpha}_2), \cdots, \lambda(\boldsymbol{\alpha}_m)] = \begin{bmatrix} \lambda_{11} & \lambda_{12} \cdots. & \lambda_{1m} \\ \lambda_{21} & \lambda_{22} \cdots. & \lambda_{2m} \\ \cdots & & \\ \lambda_{n1} & \lambda_{n2} \cdots. & \lambda_{nm} \end{bmatrix}, \tag{8}$$

where $\boldsymbol{\Lambda} \in \mathbf{R}^{n \times m}$, n is the number of response functions under any random input variable, and m is the number of design variables; that is, the number of sample points. In Equation (8) matrix, the m and n subscript in $\lambda_{n,m}$ represents the nth response of the structure under the mth design variable, respectively. By the singular value decomposition method (SVD), the solution spaces $\boldsymbol{\Lambda}$ matrix can be decomposed into

$$\boldsymbol{\Lambda} = \mathbf{U}\boldsymbol{\Sigma}\mathbf{V}^{\mathbf{T}} = \sum_{j=1}^{r} \mathbf{u}_j \sigma_j \mathbf{v}_j^T, \tag{9}$$

where $r = \min(m, n)$; $\mathbf{U} \in \mathbf{R}^{n \times n}$ and $\mathbf{V} \in \mathbf{R}^{n \times n}$ are all orthogonal matrices; u_{ij} and v_{ij} are the elements in the corresponding orthogonal matrices, respectively. In addition, $\mathbf{u}_j$ and $\mathbf{v}_j$ are the eigenvectors of $\boldsymbol{\Lambda}\boldsymbol{\Lambda}^{\mathrm{T}}$ and $\boldsymbol{\Lambda}^{\mathrm{T}}\boldsymbol{\Lambda}$, respectively, which can also be called the left and right singular eigenvectors of matrix $\boldsymbol{\Lambda}$; $\boldsymbol{\Sigma} \in \mathbf{R}^{n \times m}$ is a diagonal matrix in which the diagonal element σ_j is arranged in a descending order from the largest to the smallest. By defining $\boldsymbol{\varphi}_j = \mathbf{u}_j$ and $A_j(\alpha_i)$, we obtain

$$\boldsymbol{\lambda}(\alpha_i) = \sum_{j=1}^{r} \boldsymbol{\varphi}_j A_j(\alpha_i), \tag{10}$$

where $\boldsymbol{\varphi}_j$ and $A_j(\alpha_i)$ are the orthogonal basis and the corresponding amplitude, respectively. According to Equation (10), the system response can be simplified and expressed by the linear combination of $\boldsymbol{\varphi}_j$ and $A_j(\alpha_i)$, and the degree of freedom of the simplified model is much smaller than that of the initial model. In addition, we use radial basis function

(RBF) to interpole the subspace $A_j(\alpha_i)$. And we can get an approximation of the system response under any parameter. The approximate expression is as follows:

$$A(\alpha) \approx \tilde{A}(\alpha) = \sum_{i=1}^{m} \eta_i \phi_i(\alpha), \tag{11}$$

where ϕ is the base function, $\varphi_i(\alpha)$ is taken as the Gauss kernel function, η is the coefficient corresponding to the base function, and m is the number of design variables. The $\varphi_i(\alpha)$ expression is as follows:

$$\varphi_i(\alpha) = e^{-\left(1/\gamma_i^2\right)\|\alpha - \alpha_i\|}, \tag{12}$$

in which the symbol $\|\cdot\|$ represents the Euclidean norm and the coefficient γ_i is the width parameter of the function. Let $A(\alpha) \approx \tilde{A}(\alpha)$; Equation (11) can be rewritten as the following linear equations:

$$\begin{bmatrix} \phi_1(\alpha_1) & \phi_2(\alpha_1) & \cdots & \phi_m(\alpha_1) \\ \phi_1(\alpha_2) & \phi_2(\alpha_2) & \cdots & \phi_m(\alpha_2) \\ \cdots & \cdots & \cdots & \cdots \\ \phi_1(\alpha_m) & \phi_1(\alpha_m) & \cdots & \phi_m(\alpha_m) \end{bmatrix} \begin{bmatrix} \eta_1 \\ \eta_2 \\ \cdots \\ \eta_m \end{bmatrix} = \begin{bmatrix} A(\alpha_1) \\ A(\alpha_2) \\ \cdots \\ A(\alpha_m) \end{bmatrix}. \tag{13}$$

According to the above linear equation system, we can get the coefficient η, and by substituting Equation (11) into Equation (10), we obtain

$$\lambda(\boldsymbol{\alpha}) = \sum_{j=1}^{r} \boldsymbol{\varphi}_j \tilde{A}_j(\alpha). \tag{14}$$

In summary, the system response under any stochastic variable can be approximated by solving the above linear equation system without the need to use a full model to calculate. Using this feature, we can use a small part of the sample data to form a matrix that approximates the full-order system response. It avoids the iteration of complex physical algorithms and quickly obtains the response of variables based on MCs.

4. The Scaled Boundary Finite Element Method (SBFEM)

The scaled boundary finite element method (SBFEM) is a new semianalytical numerical calculation method. When performing numerical analysis, SBFEM is similar to FEM. Their basic idea is to discretize the calculation area into one or more subdomains and then follow a certain order. Assemble the subdomains to form an overall solution equation to solve the unknown parameters. As shown in Figure 1(a), an ordinary SBFEM arbitrary polygon unit is described. A so-called scaling center O is chosen in a region from which the total boundary S is visible. As shown in Figure 1(b), in the unit containing cracks, in addition to
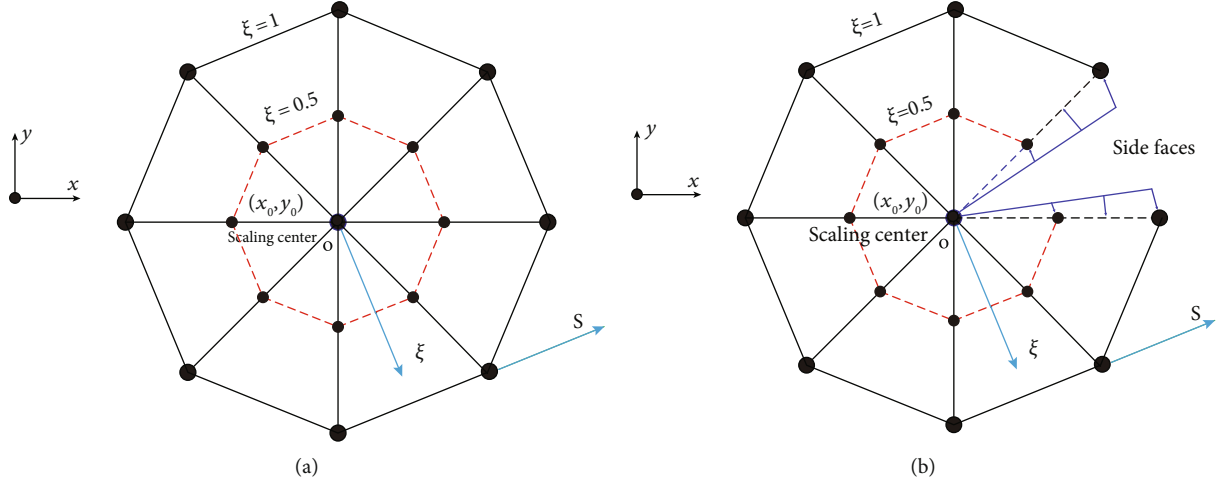
FIGURE 1: Polygon representation of SBFEM: (a) polygon S-domain; (b) polygon S-domain with cracks.

satisfying the condition of being visible to all boundaries, the scaling center must be placed at the crack tip, and the crack surface is described by two "side faces."

4.1. Scaled Boundary Finite Element Formulation. During the derivation of the SBFEM equilibrium equation, the local coordinate system (ξ, s) should be established at the scaling center of the element, which is located at the crack tip O (x_0, y_0). The local coordinate system for a 2-D problem is defined in the local circumferential direction (s axis) and radial direction (ξ axis). The radial coordinate ξ is selected as $\xi = 0$ at the scaling center and $\xi = 1$ on the boundary. The coordinates ξ and s are called the scaled boundary coordinates. As shown in Figure 1, the coordinates of any point about Cartesian system on the boundary of the element can be obtained by interpolation using the local coordinates of the element:

$$x(s) = [\mathbf{N}(s)]x_h,$$
$$y(s) = [\mathbf{N}(s)]y_h, \tag{15}$$

where x_h and y_h are the node coordinates of the element and $[\mathbf{N}(s)]$ is the shape function matrix, that is, $[\mathbf{N}(s)] = [N_1(s)\ N_2(s) \cdots N_n(s)]$.

The coordinates of any point inside the element can be obtained by scaling the corresponding coordinates on the boundary in the radial direction ξ. Therefore, the coordinates of any point inside the element can be represented by the local coordinate system (ξ, s) as

$$x(\xi, s) = x_0 + \xi x(s) = x_0 + \xi[\mathbf{N}(s)]x_h,$$
$$y(\xi, s) = y_0 + \xi y(s) = y_0 + \xi[\mathbf{N}(s)]y_h, \tag{16}$$

where (x_0, y_0) is the coordinate of the scaling center O. Similarly, if the polar coordinate system (r, θ) is established at the scaling center, then the polar coordinate r and θ can be, respectively, expressed as

$$r(\xi, s) = \xi r(s) = \xi\sqrt{x^2(s) + y^2(s)},$$
$$\theta(s) = \arctan \frac{y(s)}{x(s)}. \tag{17}$$

In SBFEM, the displacement field of S element is expressed in a semianalytical way. Then, in the Cartesian coordinate system, the displacement of point (ξ, s) in the S element can be expressed as

$$\{\mathbf{u}\} = \{\mathbf{u}(\xi, s)\} = [\mathbf{N}(s)]\{\mathbf{u}(\xi)\}. \tag{18}$$

As can be seen from Equation (18), when the displacement of any point in the region is expressed, SBFEM only adopts interpolation function in the circumferential direction and is analytical in the radial direction. This is different from FEM which adopts interpolation function in both directions. Therefore, SBFEM is a semianalytical numerical method. The strain field and stress field under linear elastic conditions can be expressed as

$$\{\boldsymbol{\varepsilon}\} = [\mathbf{B}^1(s)]\{\mathbf{u}(\xi)\}_{,\xi} + \frac{1}{\xi}[\mathbf{B}^2(s)]\{\mathbf{u}(\xi)\},$$
$$\boldsymbol{\sigma}(\xi, s) = [\mathbf{D}]\left([\mathbf{B}^1(s)]\{\mathbf{u}(\xi)\}_{,\xi} + \frac{1}{\xi}[\mathbf{B}^2(s)]\{\mathbf{u}(\xi)\}\right), \tag{19}$$

where $[\mathbf{D}]$ is the elasticity matrix and $[\mathbf{B}^1(s)]$ and $[\mathbf{B}^2(s)]$ describe the strain-displacement relationship [10, 46].

At present, three different theories can be used to derive the governing equation of SBFEM, which are, respectively, Galerkin's weighted residual method [46], similarity principle [47], and virtual work principle [48]. The SBFEM static equilibrium equation is derived by using Galerkin's weighted residual method. The static equilibrium equation of SBFEM in two dimensions can be expressed as

$$\left[\mathbf{E}^0\right]\xi^2\{\mathbf{u}(\xi)\}_{,\xi\xi} + \left(\left[\mathbf{E}^0\right] - \left[\mathbf{E}^1\right] + \left[\mathbf{E}^1\right]^T\right)\xi\{\mathbf{u}(\xi)\}_{,\xi} \\ - \left[\mathbf{E}^2\right]\{\mathbf{u}(\xi)\} = 0, \tag{20}$$

where $[\mathbf{E}^0]$, $[\mathbf{E}^1]$, and $[\mathbf{E}^2]$ are coefficient matrices. It can be proved that $[\mathbf{E}^0]$ is a positive definite matrix, $[\mathbf{E}^1]$ is a positive semidefinite matrix, and $[\mathbf{E}^2]$ is an asymmetric matrix. The internal node forces along radial lines can be expressed as [49]

$$\{\mathbf{q}(\xi)\} = \left[\mathbf{E}^0\right]\xi\{\mathbf{u}(\xi)\}_{,\xi} + \left[\mathbf{E}^1\right]^T\{\mathbf{u}(\xi)\}. \tag{21}$$

By solving the static equation of scaled boundary finite element, the displacement field and stress field in each subdomain are, respectively, expressed as

$$\{\mathbf{u}(\xi, s)\} = [\mathbf{N}(s)][\mathbf{V}_{11}]\xi^{-[\mathbf{S}_{11}]}\{\mathbf{c}\}, \tag{22}$$

$$\{\boldsymbol{\sigma}(\xi, s)\} = -[\mathbf{D}]\left[\mathbf{B}^1(s)\right][\mathbf{V}_{11}][\mathbf{S}_{11}]\xi^{-[\mathbf{S}_{11}]-[\mathbf{I}]}\{\mathbf{c}\} \\ + [\mathbf{D}]\left[\mathbf{B}^2(s)\right][\mathbf{V}_{11}]\xi^{-[\mathbf{S}_{11}]-[\mathbf{I}]}\{\mathbf{c}\}, \tag{23}$$

where and $[\mathbf{V}_{11}]$ are eigenvalue matrices and eigenvector matrices obtained by block diagonal Schur decomposition in the process of solving equations. Meanwhile, $[\mathbf{S}_{11}]$ contains all nonpositive eigenvalues, $[\mathbf{V}_{11}]$ is the corresponding eigenvector, and $\{\mathbf{c}\}$ are integration constants.

4.2. Computation of Generalized Stress Intensity Factors Using SBFEM.

The definition of generalized stress intensity factors (SIFs) is not only to eliminate the stress singularity in the asymptotic solution of the crack tip but also to characterize the strength of the stress field near the crack tip. Therefore, generalized stress intensity factor is a very important physical quantity, which is often used as one of the important conditions for judging whether the crack is propagating. Otherwise, even the smallest external load can make its value tend to infinity, which is obviously not suitable for the criteria and basis of structural design. Generally speaking, the asymptotic solution is obtained from the eigenvalue problem. The eigenvalue and eigenfunction, respectively, correspond to the singular order and angle change of the stress field. Whether they are real or complex numbers is determined by the material properties and geometric characteristics. Because the mathematical functions of singular real numbers and complex numbers are different, the traditional definitions of generalized stress intensity factor in these two forms are independent of each other. In SBFEM, a polygon element as shown in Figure 1 can be used to simulate the crack, and only the boundary and crack surface need not be discretized.

In order to explain that the stress field obtained by SBFEM can explicitly characterize the singularity of the crack tip, eigenvalue matrix $[\mathbf{S}_{11}]$ and eigenvalue vector matrix $[\mathbf{V}_{11}]$ in Equation (23) are further divided into blocks as [50]

$$[\mathbf{S}_{11}] = \text{diag}\left(\left[\mathbf{S}_{n1}\right], -[\mathbf{I}], \left[\mathbf{S}^{(s)}\right], 0\right), \\ [\mathbf{V}_{11}] = \left[\left[\boldsymbol{\psi}_{n1}\right], \left[\boldsymbol{\psi}^{(T)}\right], \left[\boldsymbol{\psi}^{(s)}\right], \left[\boldsymbol{\psi}^{(r)}\right]\right], \tag{24}$$

where the eigenvalues of $[\mathbf{S}^{(s)}]$ (superscript (s) for singular) and $[\mathbf{S}_{n1}]$ need to satisfy $-1 < \lambda([\mathbf{S}^{(s)}]) < 0$ and $\lambda([\mathbf{S}_{n1}]) < -1$, respectively. If $-1 < \lambda([\mathbf{S}_{11}]) < 0$ and ξ tends to 0, the value of matrix function $\xi^{-[\mathbf{S}_{11}]-[\mathbf{I}]}$ in Equation (23) tends to infinity; then, singularity exists. Therefore, $[\mathbf{S}^{(s)}]$ and its corresponding eigenvector $[\boldsymbol{\psi}^{(s)}]$ can be directly used to express the stress singularity of the crack tip [51]. Therefore, according to the partition of eigenvalue matrix in Equation (24), Equation (23) can be rewritten as

$$\{\boldsymbol{\sigma}(\xi, s)\} = \left[\boldsymbol{\psi}_\sigma^{(s)}(s)\right]\xi^{-[\mathbf{S}^{(s)}]-[\mathbf{I}]}\left\{\mathbf{c}^{(s)}\right\} + \left[\boldsymbol{\psi}_\sigma^{(T)}(s)\right]\left\{\mathbf{c}^{(T)}\right\} + o(1), \tag{25}$$

where

$$\left[\boldsymbol{\psi}_\sigma^{(s)}(s)\right] = [\mathbf{D}]\left(-\left[\mathbf{B}^1(s)\right]\left[\boldsymbol{\psi}^{(s)}\right]\left[\mathbf{S}^{(s)}\right] + \left[\mathbf{B}^2(s)\right]\left[\boldsymbol{\psi}^{(s)}\right]\right), \\ \left[\boldsymbol{\psi}_\sigma^{(T)}(s)\right] = [\mathbf{D}]\left(\left[\mathbf{B}^1(s)\right]\left[\boldsymbol{\psi}^{(T)}\right]\left[\mathbf{S}^{(s)}\right] + \left[\mathbf{B}^2(s)\right]\left[\boldsymbol{\psi}^{(T)}\right]\right), \tag{26}$$

where $[\boldsymbol{\psi}_\sigma^{(s)}(s)]$ is stress singular term, $[\boldsymbol{\psi}_\sigma^{(T)}(s)]$ is T stress term, and $\{\mathbf{c}^{(s)}\}$ and $\{\mathbf{c}^{(T)}\}$ are integration constants.

For convenience in fracture analysis, the stress modes are transformed to polar coordinates (r, θ). By introducing the polar coordinate system (r, θ) at the crack tip as shown in Figure 2, the definition of the generalized stress intensity factor is further proposed. The original scale boundary coordinate ξ can be expressed as [50]

$$\xi = \frac{r\wedge}{r(\theta)} = \left(\frac{L}{r(\theta)}\right) \times \left(\frac{r\wedge}{L}\right), \tag{27}$$

where $r(\theta)$ is the distance from the center of the scale to the boundary along the radial coordinate at the angle θ. The purpose of introducing the characteristic length L is to put forward the definition of the stress intensity factor independent of the unit. In Equation (25), the matrix power function of ξ is rewritten in the polar coordinates as [49]

$$\xi^{-[\mathbf{S}^{(s)}]-[\mathbf{I}]} = \left(\frac{L}{r(\theta)}\right)^{-[\mathbf{S}^{(s)}]-[\mathbf{I}]}\left(\frac{r\wedge}{L}\right)^{-[\mathbf{S}^{(s)}]-[\mathbf{I}]}. \tag{28}$$

By substituting Equation (28) into Equation (26), we obtain

$$\left\{\boldsymbol{\sigma}^{(s)}(r\wedge, \theta)\right\} = \left[\boldsymbol{\psi}_{\sigma L}^{(s)}(\theta)\right]\left(\left(\frac{r\wedge}{L}\right)^{-[\mathbf{S}^{(s)}]-[\mathbf{I}]}\right)\left\{\mathbf{c}^{(s)}\right\}, \tag{29}$$
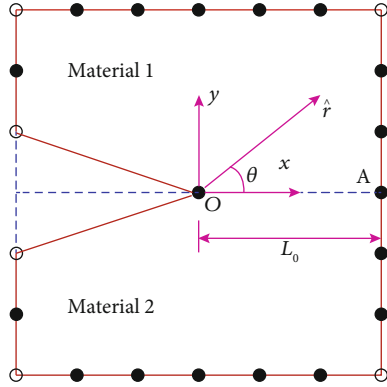
FIGURE 2: Polygon representation of SBFEM [17].

$$\left[\mathbf{\psi}_{\sigma L}^{(s)}(\theta)\right] = \left[\mathbf{\psi}_{\sigma}^{(s)}(s)\right]\left(\frac{L}{r(\theta)}\right)^{-\left[\mathbf{S}^{(s)}\right]-\left[\mathbf{I}\right]}, \tag{30}$$

where $\{\mathbf{\sigma}^{(s)}(r\wedge, \theta)\}$ and $[\mathbf{\psi}_{\sigma L}^{(s)}(\theta)]$ are singular stress in polar coordinates and stress modes at the characteristic length L, respectively. At present, there are two definitions of stress intensity factor commonly used.

When materials 1 and 2 are the same homogeneous material as shown in Figure 2, the stress intensity factor of crack can be defined as

$$\left\{\begin{array}{c} \sigma_{\theta\theta}^{(s)}(r, 0) \\ \tau_{r\theta}^{(s)}(r, 0) \end{array}\right\} = \frac{1}{\sqrt{2\pi r}}\left\{\begin{array}{c} K_I \\ K_{II} \end{array}\right\}, \tag{31}$$

where K_I and K_{II} are stress intensity factors and $\sigma_{\theta\theta}^{(s)}(r, 0)$ and $\sigma_{r\theta}^{(s)}(r, 0)$ are two stress components in the front of the crack tip $\theta = 0$. In two different isotropic materials, the cracks are distributed at the interface of the two materials; the stress intensity factor can be defined as

$$\left\{\begin{array}{c} \sigma_{\theta\theta}^{(s)}(r\wedge, 0) \\ \tau_{r\theta}^{(s)}(r\wedge, 0) \end{array}\right\} = \frac{1}{\sqrt{2\pi r\wedge}}\left[\begin{array}{cc} c(r\wedge) & -s(r\wedge) \\ s(r\wedge) & c(r\wedge) \end{array}\right]\left\{\begin{array}{c} K_I \\ K_{II} \end{array}\right\}, \tag{32}$$

$$c(r\wedge) = \cos\left(\varepsilon \ln\left(\frac{r\wedge}{L}\right)\right),$$
$$s(r\wedge) = \sin\left(\varepsilon \ln\left(\frac{r\wedge}{L}\right)\right), \tag{33}$$

where L is the characteristic length. In this definition, the characteristic length L can be taken to any value, and the amplitude of the stress intensity factor does not change with the change of L. In general, L is the length of the crack. ε is the oscillation coefficient of the bimaterials, whose magnitude is only determined by the material parameters of the two materials. According to Equations (31) and (32), Equation (29) can be written as

$$\left\{\mathbf{\sigma}^{(s)}(r\wedge, \theta)\right\} = \frac{1}{\sqrt{2\pi L}}\left[\mathbf{\psi}_{\sigma L}^{(s)}(\theta)\right]\left(\left(\frac{r\wedge}{L}\right)^{-\left[\mathbf{S}^{(s)}\right]-\left[\mathbf{I}\right]}\right)\left[\mathbf{\psi}_{\sigma L}^{(s)}(\theta)\right]^{-1}\{\mathbf{K}(\theta)\}, \tag{34}$$

$$\{\mathbf{K}(\theta)\} = \sqrt{2\pi L}\left[\mathbf{\psi}_{\sigma L}^{(s)}(\theta)\right]\left\{\mathbf{c}^{(s)}\right\}, \tag{35}$$

where $\{\mathbf{K}(\theta)\}$ is the definition of generalized stress intensity factor. In the process of solving the stress intensity factor and simulating the crack growth, the stress value of the intersection points along the crack surface and the boundary is generally used to calculate the stress intensity factor, where $\theta = 0$. In order to explain the relationship between the generalized stress intensity factor and the traditional stress intensity factor, auxiliary variables are introduced:

$$\left[\tilde{\mathbf{S}}^{(S)}(\theta)\right] = \left[\mathbf{\psi}_{\sigma L}^{(s)}(\theta)\right]\left(\left[\mathbf{S}^{(s)}\right] + \left[\mathbf{I}\right]\right)\left[\mathbf{\psi}_{\sigma L}^{(s)}(\theta)\right]^{-1}. \tag{36}$$

Considering Equation (36), Equation (34) can be rewritten as

$$\left\{\mathbf{\sigma}^{(s)}(r\wedge, \theta)\right\} = \frac{1}{\sqrt{2\pi L}}\left(\frac{r\wedge}{L}\right)^{-\left[\tilde{\mathbf{S}}^{(S)}(\theta)\right]}\{\mathbf{K}(\theta)\}. \tag{37}$$

In the homogeneous material plate with cracks, the singularity order obtained by SBFEM is $[\tilde{\mathbf{S}}^{(S)}] = 0.5[\mathbf{I}]$, and $[\mathbf{I}]$ is the identity matrix. By substituting singularity order into Equation (37), take point A as an example, we obtain the classical definition:

$$\left\{\begin{array}{c} K_I \\ K_{II} \end{array}\right\} = \sqrt{2\pi r}\left\{\begin{array}{c} \sigma_{\theta\theta}^{(s)}(r, 0) \\ \tau_{r\theta}^{(s)}(r, 0) \end{array}\right\}. \tag{38}$$

Note that the characteristic length L vanishes from the definition.

In an isotropic bimaterial plate with interface cracks, the singular order obtained by SBFEM is

$$\left[\tilde{S}^{(S)}\right] = \left[\begin{array}{cc} 0.5 & +\varepsilon \\ -\varepsilon & 0.5 \end{array}\right]. \tag{39}$$

According to the matrix change, we can obtain

$$\left(\frac{r\wedge}{L}\right)^{-\left[\tilde{s}^{(s)}\right]} = \left(\frac{r\wedge}{L}\right)^{-0.5[I]-\left[\begin{array}{cc} 0 & +\varepsilon \\ -\varepsilon & 0 \end{array}\right]} = \left(\frac{r\wedge}{L}\right)^{-0.5}\left[\begin{array}{cc} c(r\wedge) & -s(r\wedge) \\ s(r\wedge) & c(r\wedge) \end{array}\right]. \tag{40}$$

Substituting Equation (40) into Equation (37), take point A as an example, we can obtain

$$\left\{ \begin{array}{c} K_I \\ K_{II} \end{array} \right\} = \sqrt{2\pi r \wedge} \begin{bmatrix} c(r\wedge) & -s(r\wedge) \\ s(r\wedge) & c(r\wedge) \end{bmatrix}^{-1} \left\{ \begin{array}{c} \sigma_{\theta\theta}^{(s)}(r\wedge, 0) \\ \tau_{r\theta}^{(s)}(r\wedge, 0) \end{array} \right\}.$$

(41)

In an anisotropic bimaterial plate with interface cracks, the singular order obtained by SBFEM is $0.5 \pm i\varepsilon$ [50]. Cho et al. [52] gave the formula for calculating the generalized stress intensity factor. However, there was an error in the original formula, which was corrected by Song et al. [49]. The specific formula is as follows:

$$\left\{ \begin{array}{c} \sigma_{\theta\theta}^{(s)}(r\wedge, 0) \\ \tau_{r\theta}^{(s)}(r\wedge, 0) \end{array} \right\} = \frac{1}{\sqrt{2\pi r\wedge}} \begin{bmatrix} W_1 & W_2 \\ 0 & 1 \end{bmatrix} \begin{bmatrix} c(r\wedge) & -s(r\wedge) \\ s(r\wedge) & c(r\wedge) \end{bmatrix} \left\{ \begin{array}{c} K_I \\ K_{II} \end{array} \right\},$$

(42)

where W_1 and W_2 can be determined by the material constant of the anisotropic plate. Considering Equation (34), Equation (42) can be rewritten as

$$\left\{ \begin{array}{c} \sigma_{\theta\theta}^{(s)}(r\wedge, 0) \\ \tau_{r\theta}^{(s)}(r\wedge, 0) \end{array} \right\} = \frac{1}{\sqrt{2\pi L}} \begin{bmatrix} W_1 & W_2 \\ 0 & 1 \end{bmatrix} \left(\frac{r\wedge}{L}\right)^{\begin{bmatrix} 0.5 & +\varepsilon \\ -\varepsilon & 0.5 \end{bmatrix}}$$
$$\cdot \begin{bmatrix} W_1 & W_2 \\ 0 & 1 \end{bmatrix}^{-1} \left\{ \begin{array}{c} K_I \\ K_{II} \end{array} \right\}.$$

(43)

Therefore, the generalized stress intensity factor is unified with the traditional stress intensity factor, and there is no requirement for special modification when used, and when dealing with these three types of singular problems, a unified expression can be used for calculation, making the solution process more concise and clear.

5. Numerical Examples

5.1. Angled Crack in Rectangular Orthotropic Body. A homogeneous plate with an angled crack is considered in this section, as shown in Figure 3(a). The homogeneous plate is represented by rectangular orthotropic body with the same material properties. The dimensions are chosen as $b/h = 1$ and $a/h = 0.5$. Length of crack is $2a = 2$; edge length is $2b = 2h = 4$. $P = 1$ is uniformly applied in the vertical direction. The elastic properties of the material are as follows: $E_{11} = E_{22} = E_{33} = 15.4 \times 10^6$ psi, $G_{11} = G_{22} = G_{33} = 15.7 \times 10^6$ psi, and $\nu_{12} = \nu_{23} = \nu_{13} = 0.4009$. Here, the structure is considered as a plane strain model. The plate is divided into two subdomains, each of which contains a crack tip, as shown in Figure 3(b). Each side of the subdomain is divided into 14 high-order (linear) elements with Gauss-Lobatto-Legendre shape functions, and the overall DOFs is 280. Herein, take the crack angle $\alpha \in [0, \pi/2]$ as the uncertain parameter.

The numerical solution of this paper the SIFs is compared with the reference solution obtained by Banks-Sills et al. [53] using M-integral and displacement extrapolations, as shown in Figure 4, where they are normalized with $P\sqrt{\pi a}$. It can be seen from Figure 4 that the numerical solution based on SBFEM has a good agreement with that of Banks-Sills et al. [53], which verifies the correctness and effectiveness of solving SIFs in fracture problem based on SBFEM. Meanwhile, the relationship between SIFs and crack angle with different order elements is also considered, as shown in Figure 5. It can be seen that with the increase of crack angle, the value of normalized K_1 gradually decreases, and that of K_2 increases and then gradually decreases. However, when the crack angle is the same, the values of SIFs under different order elements are very close to almost the same, indicating that the order element has little effect on SIFs.

Since the mesh generation of SBFEM is more convenient and flexible than that of the FEM, only the position of the scaling center at the crack tip needs to be changed in this example without needing remeshing procedure.

We randomly selected 40 samples as the total number of input variables. In addition, we, respectively, construct several of small-scale response matrices containing 10, 20, and 30 samples from the total number of samples to form a low-order sample space vector. Then, perform SVD decomposition and RBF interpolation approximate calculation on the low-order matrix Λ formed by the three sets of small sample data. Figure 6 shows the normalized values of SIFs, which consist of original solution calculated using SBFEM and approximate solution using POD and RBF.

From Figure 6, it can be seen that when the sample numbers of a reduced model are 20, 30, and 40, the results of the reduced model are very close to the original solution, but when the sample number is 10, the result fluctuates slightly. It indicates that the combination of POD and RBF can accurately predict the response results of any input variable.

In order to further illustrate the reliability and accuracy of the algorithm. We introduce R^2 to evaluate the accuracy of the interpolation result and the formula is as follows:

$$R^2 = 1 - \frac{\sum_{i=1}^{n}(y_i - y\wedge_i)^2}{\sum_{i=1}^{n}(y_i - \bar{y}_i)^2},$$

(44)

where n is the number of predictor variables when using RBF interpolation approximation and y_i is the predicted value under the ith input variable; $y\wedge_i$ is the analytical solution, which is approximated by the numerical solution; $\bar{y}_i$ is the average value of the analytical solution. The evaluation coefficient R^2 represents the relative error between the numerical solution and the approximate solution, and its value range is (0-1). The closer R^2 is to 1, the higher the interpolation accuracy.

Table 1 shows the comparison of the accuracy results of normalized K_1 and K_2 under four different schemes. In Table 1, the number of prediction points is 40, which means that the original 40 samples are selected as the prediction points. The number of prediction points is not equal to 40

(a)

(b)
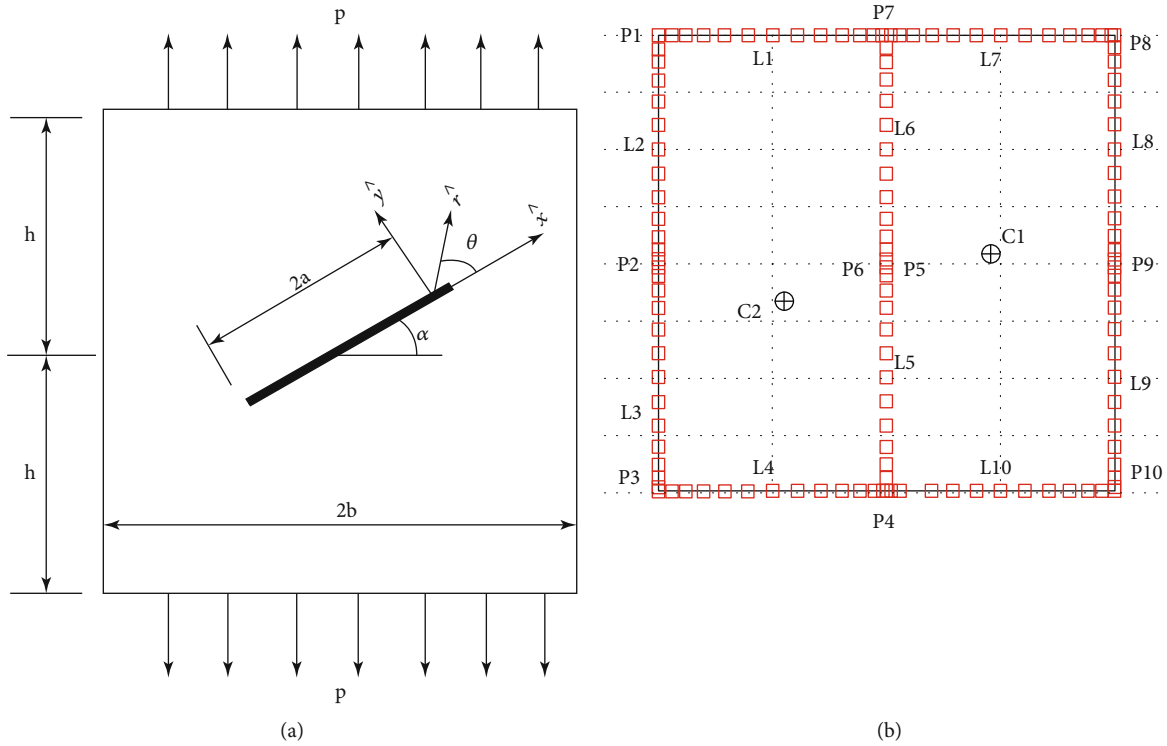
FIGURE 3: A rectangular plate with an angled crack [50]: (a) geometry; (b) mesh of 14th-order elements.

(a)

(b)
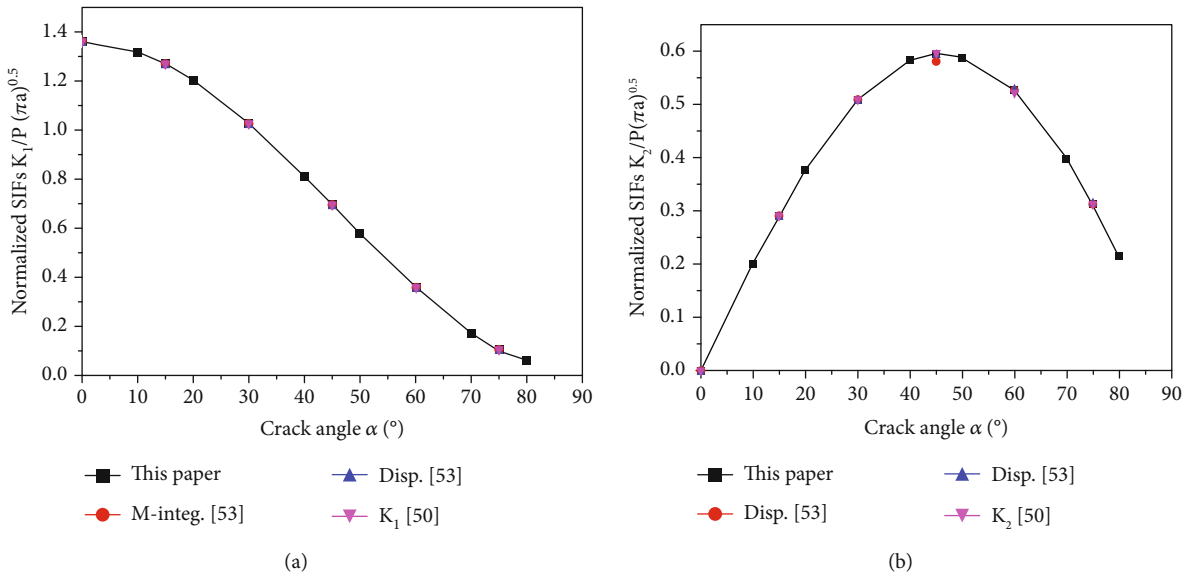
FIGURE 4: Normalized SIFs of angled crack in a homogeneous rectangular plate: (a) normalized SIFs $K_1/P(\pi a)^{0.5}$ at different crack angles; (b) normalized SIFs $K_2/P(\pi a)^{0.5}$ at different crack angles.

in the table, which means that some sample points are uniformly selected from the original 40 samples as new sample points, while the rest of the sample points are the number of predicted points. When the number of prediction points is 40, the accuracy evaluation coefficient R^2 is 1, which indicates that the approximate result of the RBF interpolation is consistent with the given numerical solution. As the number of samples decreases, the number of prediction points

increases, and the value of the evaluation coefficient is gradually decreasing, which indicates that the interpolation accuracy of RBF is decreasing. However, when the number of samples is 10, the evaluation coefficient values of normalized K_1 and K_2 are both above 0.987, which can indicate that RBF can obtain high-precision numerical results by using small sample interpolation and verifies the reliability of the combination of POD and RBF to predict the response
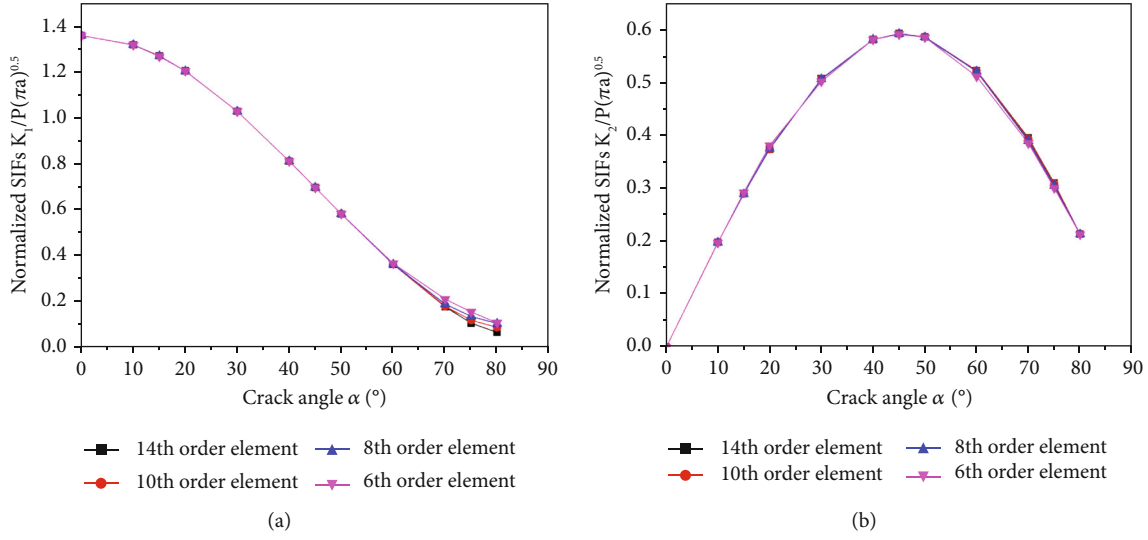
FIGURE 5: The relationship between SIF and crack angle under different element orders. (a) The normalized SIFs $K_1/P(\pi a)^{0.5}$ varies with the crack angle under different element orders. (b) The normalized SIFs $K_2/P(\pi a)^{0.5}$ varies with the crack angle under different element orders.
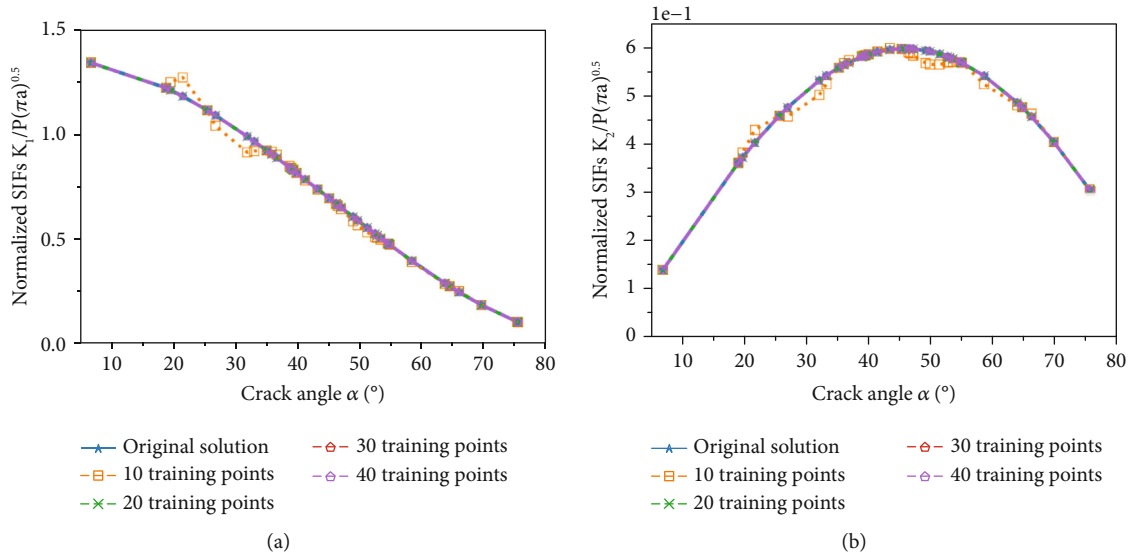
FIGURE 6: Curve graph of normalized SIFs and numerical solution under different training points. (a) The normalized SIFs $K_1/P(\pi a)^{0.5}$ varies with the crack angle under different training points. (b) The normalized SIFs $K_2/P(\pi a)^{0.5}$ varies with the crack angle under different training points.

TABLE 1: Comparison of the accuracy results of four different schemes.

Number of samples	Number of prediction points	R^2 for normalized $K_1/P(\pi a)^{0.5}$	R^2 for normalized $K_2/P(\pi a)^{0.5}$
40	40	1	1
30	10	1	1
20	20	1	1
10	30	0.9946	0.9875

results. Although the calculation accuracy will increase as the number of sample points increases, as the complexity of the problem increases, the calculation cost will also increase greatly. Therefore, it is necessary to select an appropriate number of sample points.

Next, we will use POD and RBF to accelerate MCs to obtain the expectations and standard deviation of SIFs. Adopt the above physical model and take the crack angles $\alpha\,(\epsilon\,(0, \pi/2)$ as the uncertain parameter which satisfies the Gaussian distribution ($\mu = 0.785, \sigma = 0.262$). The value of SIFs and the displacement values at 140 points are selected to form the response vector. Using 10, 20, 30, and 40 training data, respectively, we get 40 samples for random analysis
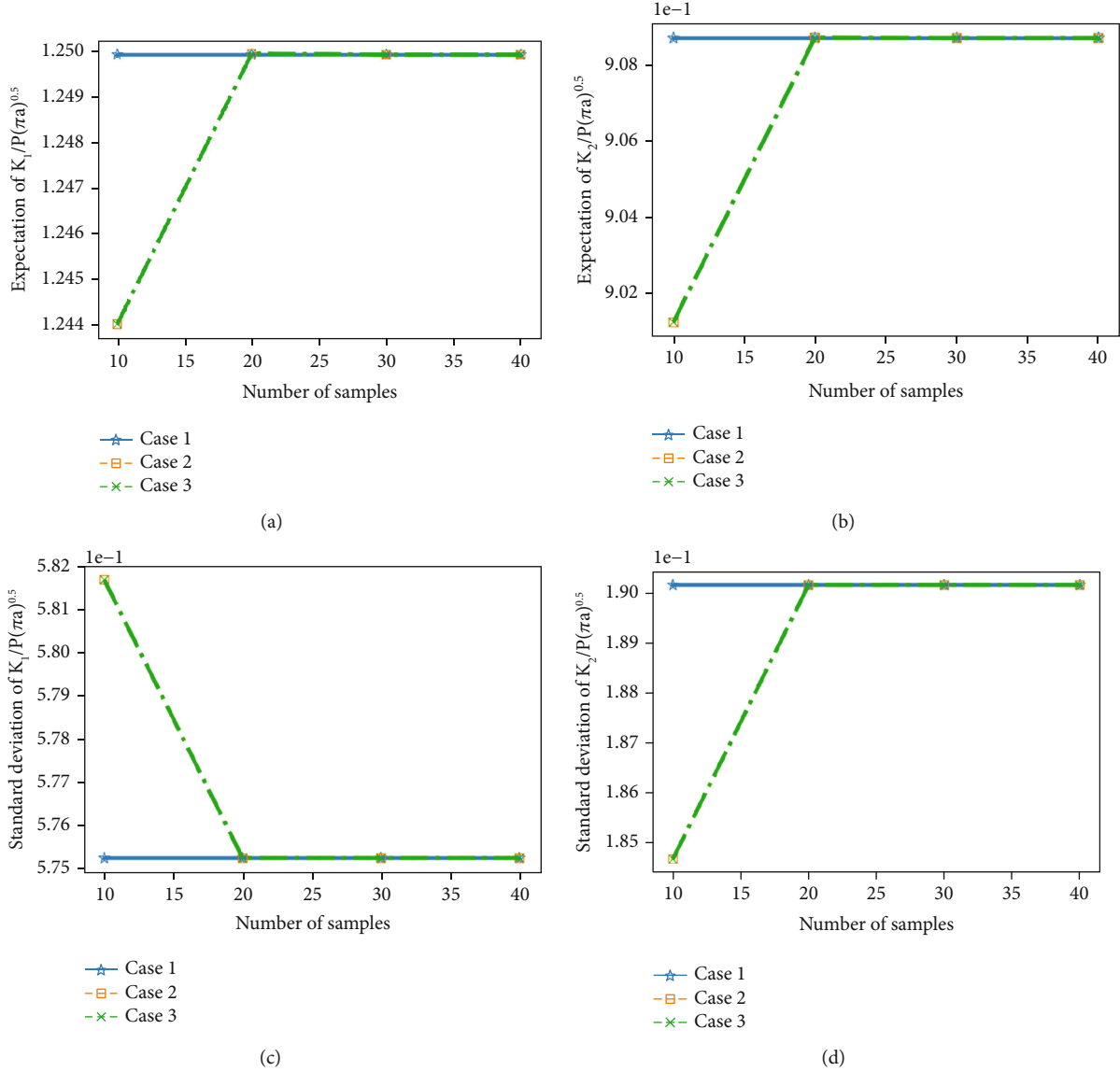
FIGURE 7: Expectations and standard deviation of different degrees of reduction: (a) expectations of the normalized SIFs $K_1/P(\pi a)^{0.5}$; (b) expectations of the normalized SIFs $K_2/P(\pi a)^{0.5}$; (c) standard deviation of the normalized SIFs $K_1/P(\pi a)^{0.5}$; (d) standard deviation of the normalized SIFs $K_2/P(\pi a)^{0.5}$.

through the reduced-order fast algorithm and RBF interpolation. The dimensions of the different sample snapshot matrix are 142×10, 142×20, 142×30, and 142×40, which can be reduced by the SVD method in POD. Then, the full-order 142×40 matrix is obtained by using RBF interpolation. In addition, before the RBF interpolation, we also truncated the decomposition matrix of SVD to varying degrees according to the size of the singular value. Different schemes are used as follows: case 1: direct Monte Carlo simulation is used to perform full-order simulation calculations using SBFEM; case 2: using SVD decomposition without truncating the singular value matrix after decomposition; and case 3: using SVD decomposition, the singular value matrix after decomposition is truncated according to the smallest row and column dimension. We compare the accuracy of statistical characteristics after different operations in Figure 7.

From Figure 7, we can see that the accuracy of the reduced-order fast algorithm increases with the increase of training samples which indicates that the accuracy of POD and RBF is directly related to the number of samples. Case 1 has 40 training samples, which can realize a full-level Monte Carlo simulation. But the number of samples is small, the deviation of cases 2, 3, and 1 are large. It is because the data space of cases 2 and 3 are smaller than that of case 1, where the degree of reduction of case 3 is the largest. When the number of samples is less than 20, cases 2 and 3 have the same calculation effect, but the dimension of case 3 is much smaller than that of case 2, so the prediction accuracy is higher. It indicates that this method can not only reduce the dimensionality of the data but also obtain the response results accurately and quickly. Besides, it is particularly important to select an appropriate number of samples for order reduction operations.
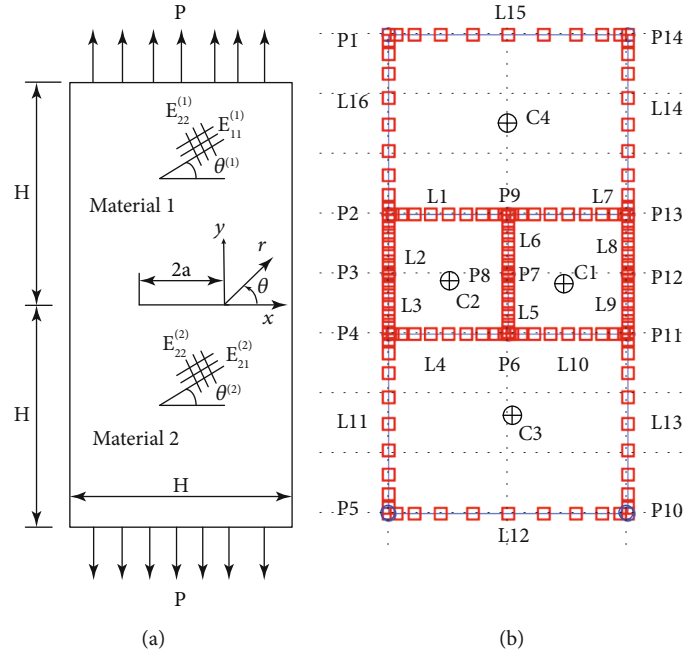
FIGURE 8: Rectangular bimaterial plate with an interfacial central crack [50]: (a) geometry; (b) mesh of 10th-order elements.
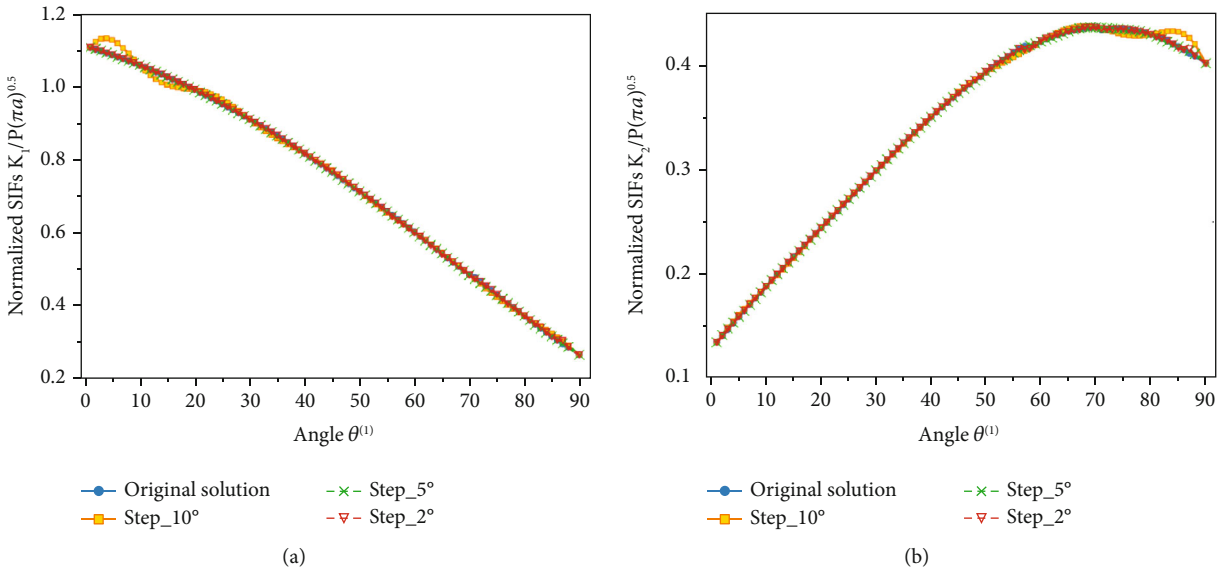
FIGURE 9: Different length interpolation results: (a) normalized SIFs $K_1/P(\pi a)^{0.5}$ under different angles $\theta^{(1)}$; (b) normalized SIFs $K_2/P(\pi a)^{0.5}$ under different angles $\theta^{(1)}$.

5.2. Interfacial Central Crack between Isotropic-Orthotropic Materials. The rectangular bimaterial plate composed of isotropic-orthotropic materials is considered in this section, as shown in Figure 8(a). The height and the width of the rectangular plate are $2H$ and H, respectively. The length of the central crack is $2a$. Uniform tension P is applied in the vertical direction. The elastic properties are $E_{11} = 100$ GPa, $E_{22} = 30$ GPa, $G_{12} = 23.5212$ GPa, and $\nu_{12} = 0.3$ for orthotropic material 1 and $E = 100$ GPa and $\nu = 0.3$ for isotropic

material 2. Plane stress conditions are assumed. The characteristic length is chosen as $L = 2a$.

The plate is divided into four subdomains, as shown in Figure 8(b). The scaling center of the subdomains is indicated by the marker "⊕." The crack tips are at the scaling center of subdomains 1 and 2. Each side of the subdomain is divided into 10. We consider the main material angle $\theta^{(1)} \in [0, \pi/2]$ to be the only uncertain parameter. The principal material axis 1 of material 1 is rotated from the

TABLE 2: Relative error table of approximate value and numerical solution under different interpolation steps.

Angle $\theta^{(1)}$	|RBF-exact|/exact					
	Normalized SIFs $K_1/P(\pi a)^{0.5}$			Normalized SIFs $K_2/P(\pi a)^{0.5}$		
	Step = 2	Step = 5	Step = 10	Step = 2	Step = 5	Step = 10
7°	0.006%	0.040%	2.753%	0.035%	0.251%	0.800%
13°	0.004%	0.025%	1.931%	0.044%	0.166%	0.492%
27°	0.002%	0.004%	0.945%	0.004%	0.005%	0.287%
37°	0.001%	0.004%	0.604%	0.024%	0.039%	0.212%
53°	0.004%	0.004%	0.360%	0.057%	0.057%	0.668%
67°	0.054%	0.066%	0.379%	0.067%	0.131%	0.555%
73°	0.129%	0.377%	1.217%	0.064%	0.101%	0.601%
87°	0.051%	0.604%	2.601%	0.071%	0.518%	3.570%

(a)

(b)
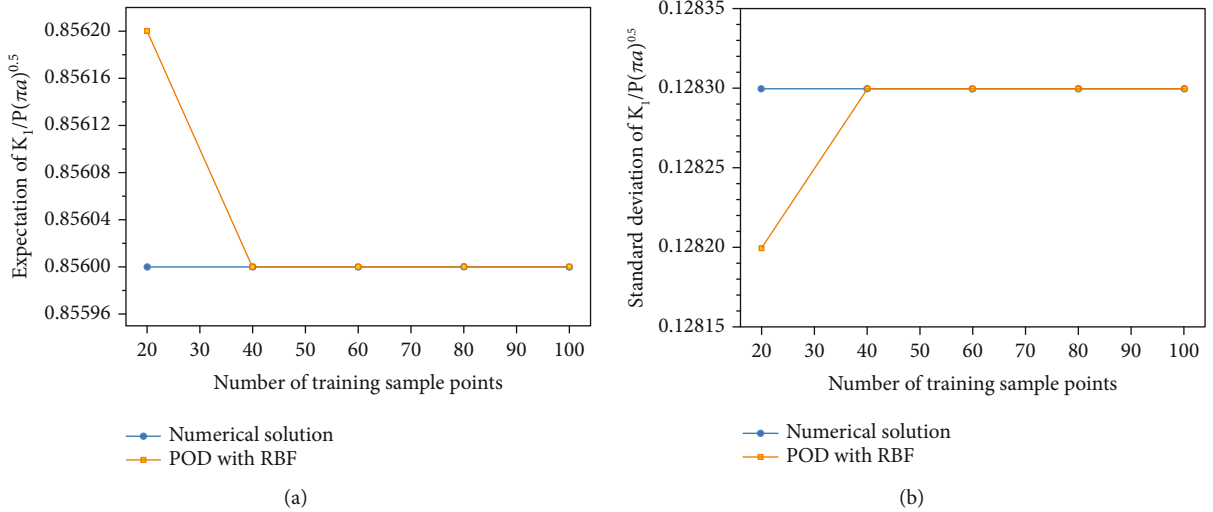
FIGURE 10: Expectations and standard deviation of different degrees of reduction: (a) expectations of the normalized SIFs $K_1/P(\pi a)^{0.5}$ under different sample points; (b) standard deviation of the normalized SIFs $K_1/P(\pi a)^{0.5}$ under different sample points.

horizontal x-axis by an angle $\theta^{(1)}$ to simulate anisotropic material behavior with reference to the crack. The step size of the design variable is set as 1, so we can get 90 samples. The two component values of SIFs and 158 nodal displacements values are taken as the response vector. The approximate effect of POD combined with RBF was tested here. Sampling points are selected according to step sizes 2, 5, and 10, respectively, to form 160×45, 160×18, and 160×9 matrices in sequence, and 160×90 matrix is obtained by SVD and RBF approximate interpolation. The comparison between interpolation result and numerical solution is shown in Figure 9.

From Figure 9, it can be seen that the results under different interpolation steps are in good agreement with the numerical solution, which indicates that the POD combined with the RBF method has a good approximation and prediction effect on the system response. Different steps correspond to different amounts of data, through interpolation computation, which can fit the full-order 160×90 matrix, which indicates that this method has a certain potential in accelerating computation. Table 2 shows the relative error

between the approximate value and the numerical solution after POD order reduction and RBF interpolation under different steps. By comparison, it is found that the finer the interpolation steps, the closer the predicted value to the numerical solution, but the more interpolation points are needed. In general, the prediction accuracy is positively correlated with the number of interpolation points.

Next, we consider that when the input variable $\theta^{(1)}$ obeys the Gaussian distribution, the normalized K_1 expectation and standard deviation can be obtained after accelerating MCs through POD and RBF reduction. The mean value of Gaussian distribution function is $\mu = 45°$, the standard deviation is $\sigma = 15°$, and the other parameters remain unchanged. The specific computation process is to stochastically select 100 sample points (satisfy the Gaussian distribution), obtain the numerical solution of K_1 based on SBFEM, and then directly use MCs to get expectations and standard deviation as a comparison. In addition, it can be seen from the previous example that the accuracy of the fast algorithm is positively correlated with the number of training samples. Therefore, in this example, we select 20, 40, 60, and 80

samples from the original samples as the training samples and then combine POD and RBF to get the expectations and standard deviations of these 100 sample points. It is worth noting that in this example, we all take case 3 reduced-order operation. The expectations and standard deviations of the full-order numerical solution and the reduced-order are shown in Figure 10. From Figure 10, it can be seen that the reliability of the reduced-order fast algorithm improves with the increase in the number of sample points. When the number of samples is close to 40% of the total number of samples, the results of the order reduction is consistent with the numerical solution. It shows that it is necessary to select the appropriate sample points for order reduction computation. Besides, it is also shown that the combination of POD and RBF is effective in model reduction and accelerating MCs computation, which achieves the goal of reducing computing cost and improving computing efficiency.

6. Conclusions

This paper presents an efficient stochastic analysis method for linear elastic fracture problems. The MCs is used to capture the statistical characteristics of the structural responses under the impact of uncertain variables. SBFEM is applied for fracture analysis which is able to evaluate the stress intensity factors directly with high accuracy. The model order reduction method based on proper orthogonal decomposition (POD) and radial basis function (RBF) is employed to accelerate Monte Carlo simulation (MCs). Numerical examples analyze the angled cracks in the orthotropic body and the interface crack structure between orthotropic-isotropic materials. The results show that the full-order simulation computation results based on SBFEM are in good agreement with the results based on the POD and RBF model order reduction method, which verifies the effectiveness and efficiency of the proposed method. In the future, we will incorporate cohesive crack models for simulating fracture behaviors of quasibrittle materials that are commonly found in rock mechanics [54]. Additionally, the present method can also be used for accelerating structural optimization with large-scale design variables [55, 56].

Data Availability

All date used to support the findings of this study are included within the article.

Conflicts of Interest

The authors declare that there are no conflicts of interest regarding the publication of this paper.

Acknowledgments

References

[1] Y. Gu and H. G. Sun, "A meshless method for solving three-dimensional time fractional diffusion equation with variable-order derivatives," *Applied Mathematical Modelling*, vol. 78, pp. 539–549, 2020.

[2] S. Han, D.-S. Jeng, and C. C. Tsai, "Meshfree model for earthquake-induced transient response in a porous seabed," *Soil Dynamics and Earthquake Engineering*, vol. 145, p. 106713, 2021.

[3] S. Y. Jiang and C. B. Du, "Study on dynamic interaction between crack and inclusion or void by using XFEM," *Structural Engineering and Mechanics*, vol. 63, no. 3, pp. 329–345, 2017.

[4] W. H. Zhao, C. B. Du, and S. Y. Jiang, "An adaptive multiscale approach for identifying multiple flaws based on XFEM and a discrete artificial fish swarm algorithm," *Computer Methods Applied Mechanics Engineering*, vol. 339, pp. 341–357, 2018.

[5] C. B. Du, W. H. Zhao, S. Y. Jiang, and X. Deng, "Dynamic XFEM-based detection of multiple flaws using an improved artificial bee colony algorithm," *Computer Methods in Applied Mechanics and Engineering*, vol. 365, article 112995, 2020.

[6] C. Miehe, F. Welschinger, and M. Hofacker, "Thermodynamically consistent phase-field models of fracture: Variational principles and multi-field FE implementations," *International Journal for Numerical Methods in Engineering*, vol. 83, no. 10, pp. 1273–1311, 2010.

[7] L. L. Chen, Z. W. Wang, X. Peng, J. Yang, P. Wu, and H. Lian, "Modeling pressurized fracture propagation with the isogeometric BEM," *Geomechanics and Geophysics for Geo-Energy and Geo-Resources*, vol. 7, no. 3, 2021.

[8] D. F. Han, Y. H. Zhang, Q. Wang, W. Lu, and B. Jia, "The review of the bond-based peridynamics modeling," *Journal of Micromechanics and Molecular Physics*, vol. 4, no. 1, p. 1830001, 2019.

[9] C. M. Song and J. P. Wolf, "The scaled boundary finite-element method–alias consistent infinitesimal finite-element cell method–for elastodynamics," *Computer Methods in Applied Mechanics and Engineering*, vol. 147, no. 3–4, pp. 329–355, 1997.

[10] C. M. Song and J. P. Wolf, "The scaled boundary finite-element method: analytical solution in frequency domain," *Computer Methods in Applied Mechanics and Engineering*, vol. 164, no. 1–2, pp. 249–264, 1998.

[11] C. M. Song and J. P. Wolf, "Semi-analytical representation of stress singularities as occurring in cracks in anisotropic multi-materials with the scaled boundary finite-element method," *Computers & Structures*, vol. 80, no. 2, pp. 183–197, 2002.

[12] C. M. Song, *The Scaled Boundary Finite Element Method: Introduction to Theory and Implementation*, John Wiley, 2018.

[13] Z. J. Yang, "Fully automatic modelling of mixed-mode crack propagation using scaled boundary finite element method," *Engineering Fracture Mechanics*, vol. 73, no. 12, pp. 1711–1731, 2006.

[14] E. T. Ooi and Z. J. Yang, "A hybrid finite element-scaled boundary finite element method for crack propagation

modelling," *Computer Methods in Applied Mechanics and Engineering*, vol. 199, no. 17–20, pp. 1178–1192, 2010.

[15] P. Zhang, C. B. Du, C. Birk, and W. H. Zhao, "A scaled boundary finite element method for modelling wing crack propagation problems," *Engineering Fracture Mechanics*, vol. 216, article 106466, 2019.

[16] E. T. Ooi and Z. J. Yang, "Modelling dynamic crack propagation using the scaled boundary finite element method," *International Journal for Numerical Methods in Engineering*, vol. 88, no. 4, pp. 329–349, 2011.

[17] S. Q. Dai, C. Augarde, C. B. Du, and D. Chen, "A fully automatic polygon scaled boundary finite element method for modelling crack propagation," *Engineering Fracture Mechanics*, vol. 133, pp. 163–178, 2015.

[18] P. Zhang, C. B. Du, X. R. Tian, and S. Jiang, "A scaled boundary finite element method for modelling crack face contact problems," *Computer Methods in Applied Mechanics and Engineering*, vol. 328, pp. 431–451, 2018.

[19] X. Tian, C. B. Du, S. Dai, and D. Chen, "Calculation of dynamic stress intensity factors and T-stress using an improved SBFEM," *Structural Engineering and Mechanics*, vol. 66, no. 5, pp. 649–663, 2018.

[20] S. Y. Jiang, C. B. Du, and E. T. Ooi, "Modelling strong and weak discontinuities with the scaled boundary finite element method through enrichment," *Engineering Fracture Mechanics*, vol. 222, 2019.

[21] L. L. Chen, C. Liu, W. C. Zhao, and L. Liu, "An isogeometric approach of two dimensional acoustic design sensitivity analysis and topology optimization analysis for absorbing material distribution," *Computer Methods in Applied Mechanics and Engineering*, vol. 336, pp. 507–532, 2018.

[22] L. L. Chen, C. Lu, H. Lian et al., "Acoustic topology optimization of sound absorbing materials directly from subdivision surfaces with isogeometric boundary element methods," *Computer Methods in Applied Mechanics and Engineering*, vol. 362, p. 112806, 2020.

[23] L. L. Chen, H. Lian, Z. W. Liu, H. B. Chen, E. Atroshchenko, and S. P. A. Bordas, "Structural shape optimization of three dimensional acoustic problems with isogeometric boundary element methods," *Computer Methods in Applied Mechanics and Engineering*, vol. 355, pp. 926–951, 2019.

[24] L. L. Chen, Y. Zhang, H. Lian, E. Atroshchenko, C. Ding, and S. P. A. Bordas, "Seamless integration of computer-aided geometric modeling and acoustic simulation: isogeometric boundary element methods based on Catmull-Clark subdivision surfaces," *Advances in Engineering Software*, vol. 149, p. 102879, 2020.

[25] L. L. Chen, L. Lu, W. C. Zhao, H. Chen, and C. Zheng, "Subdivision surfaces — boundary element accelerated by fast multipole for the structural acoustic problem," *Journal of Theoretical and Computational Acoustics*, vol. 28, no. 2, p. 2050011, 2020.

[26] S. Natarajan, J. C. Wang, C. M. Song, and C. Birk, "Isogeometric analysis enhanced by the scaled boundary finite element method," *Computer Methods in Applied Mechanics and Engineering*, vol. 283, pp. 733–762, 2015.

[27] G. Stefanou, "The stochastic finite element method: past, present and future," *Computer Methods in Applied Mechanics Engineering*, vol. 198, no. 9-12, pp. 1031–1051, 2009.

[28] R. G. Ghanem and P. D. Spanos, *Stochastic Finite Elements: A Spectral Approach*, Springer verlag, 1991.

[29] N. Z. Chen and C. Guedes Soares, "Spectral stochastic finite element analysis for laminated composite plates," *Computer Methods in Applied Mechanics Engineering*, vol. 197, no. 51–52, pp. 4830–4839, 2008.

[30] K. Marcin, "Generalized perturbation-based stochastic finite element method in elastostatics," *Computers and Structures*, vol. 85, no. 10, pp. 586–594, 2007.

[31] J. E. Hurtado and A. H. Barbat, "Monte Carlo techniques in computational stochastic mechanics," *Archives of Computational Methods in Engineering*, vol. 5, no. 1, pp. 3–29, 1998.

[32] P. D. Spanos and B. A. Zeldin, "Monte Carlo treatment of random fields: a broad perspective," *Applied Mechanics Reviews*, vol. 51, no. 3, pp. 219–237, 1998.

[33] Y. T. Feng, C. F. Li, and D. R. J. Owen, "A directed Monte Carlo solution of linear stochastic algebraic system of equations," *Finite Elements in Analysis Design*, vol. 46, no. 6, pp. 462–473, 2010.

[34] J. M. Hammersley, "Monte Carlo methods for solving multivariable problems," *Annals of the New York Academy of Sciences*, vol. 86, pp. 844–874, 2010.

[35] F. J. Ma, S. W. Zhang, and H. Krakauer, "Excited state calculations in solids by auxiliary-field quantum Monte Carlo," *New Journal of Physics*, vol. 15, no. 9, 2013.

[36] M. S. Chowdhury, C. M. Song, and W. Gao, "Probabilistic fracture mechanics by using Monte Carlo simulation and the scaled boundary finite element method," *Engineering Fracture Mechanics*, vol. 78, no. 12, pp. 2369–2389, 2011.

[37] M. S. Chowdhury, C. M. Song, and W. Gao, "Probabilistic fracture mechanics with uncertainty in crack size and orientation using the scaled boundary finite element method," *Computers & Structures*, vol. 137, pp. 93–103, 2014.

[38] D. S. Broomhead and D. Lowe, "Radial basis functions, multivariable functional interpolation and adaptive networks," *Royal Signals and Radar Establishment Malvern (United Kingdom)*, vol. 26, no. 3, pp. 801–849, 1998.

[39] V. Buljak and G. Maier, "Proper orthogonal decomposition and radial basis functions in material characterization based on instrumented indentation," *Engineering Structures*, vol. 33, no. 2, pp. 492–501, 2011.

[40] V. Buljak, "Proper orthogonal decomposition and radial basis functions for fast simulations," in *In Inverse Analyses with Model Reduction*, pp. 85–139, Springer, 2012.

[41] C. A. Rogers, A. Kassab, E. Divo, Z. Ostrowski, and R. A. Bialecki, "An inverse POD-RBF network approach to parameter estimation in mechanics," *Inverse Problems in Science and Engineering*, vol. 20, no. 5, pp. 749–767, 2012.

[42] C. S. Ding, R. R. Deokar, X. Cui, G. Li, Y. Cai, and K. K. Tamma, "Proper orthogonal decomposition and Monte Carlo based isogeometric stochastic method for material, geometric and force multi-dimensional uncertainties," *Computational Mechanics*, vol. 13, no. 3, pp. 521–533, 2019.

[43] C. S. Ding, R. R. Deokar, Y. J. Ding et al., "Model order reduction accelerated Monte Carlo stochastic isogeometric method for the analysis of structures with high-dimensional and independent material uncertainties," *Computer Methods in Applied Mechanics and Engineering*, vol. 349, pp. 266–284, 2019.

[44] C. S. Ding, K. K. Tamma, H. J. Lian, Y. Ding, T. J. Dodwell, and S. P. A. Bordas, "Uncertainty quantification of spatially uncorrelated loads with a reduced-order stochastic isogeometric method," *Computational Mechanics*, vol. 67, no. 5, pp. 1255–1271, 2021.

[45] S. Li, J. Trevelyan, Z. Wu, H. Lian, D. Wang, and W. Zhang, "An adaptive SVD-Krylov reduced order model for surrogate based structural shape optimization through isogeometric boundary element method," *Computer Methods in Applied Mechanics and Engineering*, vol. 349, pp. 312–338, 2019.

[46] C. M. Song, "Evaluation of power-logarithmic singularities, _T_ -stresses and higher order terms of in-plane singular stress fields at cracks and multi-material corners," *Engineering Fracture Mechanics*, vol. 72, no. 10, pp. 1498–1530, 2005.

[47] J. P. Wolf and C. M. Song, "The scaled boundary finite-element method - a primer: derivations," *Computers & Structures*, vol. 78, no. 1–3, pp. 191–210, 2000.

[48] A. J. Deeks and J. P. Wolf, "A virtual work derivation of the scaled boundary finite-element method for elastostatics," *Computation Mechanics*, vol. 28, no. 6, pp. 489–3504, 2002.

[49] C. M. Song, F. Tin-Loi, and W. Gao, "Transient dynamic analysis of interface cracks in anisotropic bimaterials by the scaled boundary finite-element method," *International Journal Solids and Structures*, vol. 47, no. 7–8, pp. 978–989, 2010.

[50] C. M. Song, F. Tin-Loi, and W. Gao, "A definition and evaluation procedure of generalized stress intensity factors at cracks and multi-material wedges," *Engineering Fracture Mechanics*, vol. 77, no. 12, pp. 2316–2336, 2010.

[51] J. P. Wolf and C. M. Song, "Consistent infinitesimal finite-element cell method: in-plane motion," *Computer Methods in Applied Mechanics and Engineering*, vol. 123, no. 1–4, pp. 355–370, 1995.

[52] S. B. Cho, K. R. Lee, Y. S. Choy, and Y. Ryoji, "Determination of stress intensity factors and boundary element analysis for interface cracks in dissimilar anisotropic materials," *Engineering Fracture Mechanics*, vol. 43, no. 4, pp. 603–614, 1992.

[53] L. Banks-Sills, I. Hershkovitz, P. A. Wawrzynek, R. Eliasi, and A. R. Ingraffea, "Methods for calculating stress intensity factors in anisotropic materials: part I– _z_ = 0 is a symmetric plane," *Engineering Fracture Mechanics*, vol. 72, no. 15, pp. 2328–2358, 2005.

[54] J. F. Yang, H. J. Lian, and V. P. Nguyen, "Study of mixed mode I/II cohesive zone models of different rank coals," *Engineering Fracture Mechanics*, vol. 246, p. 107611, 2020.

[55] H. J. Lian, P. Kerfriden, and S. P. A. Bordas, "Shape optimization directly from CAD: an isogeometric boundary element approach using T-splines," *Computer Methods in Applied Mechanics and Engineering*, vol. 317, pp. 1–41, 2017.

[56] H. J. Lian, A. N. Christiansen, D. A. Tortorelli, O. Sigmund, and N. Aage, "Combined shape and topology optimization for minimization of maximal von Mises stress," *Computer Methods in Applied Mechanics and Engineering*, vol. 55, no. 5, pp. 1541–1557, 2017.

WILEY | Hindawi

Research Article
Uncertainty Quantification for a Hydraulic Fracture Geometry: Application to Woodford Shale Data

Batoul M. Gisler [ID]

The University of Neuchâtel, Centre for Hydrogeology and Geothermics (CHYN), 2000 Neuchâtel, Switzerland

Correspondence should be addressed to Batoul M. Gisler; batoul.gisler@unine.ch

Hydraulic fracturing enhances hydrocarbon production from low permeability reservoirs. Laboratory tests and direct field measurements do a decent job of predicting the response of the system but are expensive and not easily accessible, thus increasing the need for robust deterministic and numerical solutions. The reliability of these mathematical models hinges on the uncertainties in the input parameters because uncertainty propagates to the output solution resulting in incorrect interpretations. Here, I build a framework for uncertainty quantification for a 1D fracture geometry using Woodford shale data. The proposed framework uses Monte-Carlo-based statistical methods and is comprised of two parts: sensitivity analysis and the probability density functions. Results reveal the transient nature of the sensitivity analysis, showing that Young's modulus controls the initial pore pressure, which after 1 hour depends on the hydraulic conductivity. Results also show that the leak-off is most sensitive to permeability and thermal expansion coefficient of the rock and that temperature evolution primarily depends on thermal conductivity and the overall heat capacity. Furthermore, the model shows that Young's modulus controls the initial fracture width, which after 1 hour of injection depends on the thermal expansion coefficient. Finally, the probability density curve of the transient fracture width displays the range of possible fracture aperture and adequate proppant size. The good agreement between the statistical model and field observations shows that the probability density curve can provide a reliable insight into the optimal proppant size.

1. Introduction

Hydraulic fracturing (HF) improves the flow rate of recoverable reserves from low permeability geological formations [1, 2]. The process induces rock failure by simply injecting fluid into the reservoir to counteract the in situ stresses and its tensile strength. Such newly created fractures are maintained using proppants often mixed with the fracturing fluid. HF is an expensive practice that requires careful design and good numerical modelling, and a principal problem with these mathematical models is that they are based on ideal systems with physical simplifications, thus neglecting either fracture initiation from wellbore, or near-tip effects, or fracture aperture evolution of preexisting fractures [3]. Although these simplifications facilitate the problem-solving process, they introduce sources of error that reduce the degree of confidence in the output solution [4]. Furthermore, uncertainty is embedded in the initial conditions, boundary conditions,

geometry, and input parameters [4]. Some uncertainties create a large variance of the output solution and contribute most to the prediction of the degree of confidence while others have smaller effects [5]. Here, I address the uncertainties in shale formation properties generally calculated in a laboratory/field setting. Shale is a sensitive material, easily disturbed by normal drilling techniques, and specimens are difficult to sample, core, characterize, and test [6]. Furthermore, well logs measure formation properties such as Young's modulus, Poisson's ratio, and permeability, but well log interpretation is a subjective practice, where the tools have a margin of error and the measured properties are spatially limited. In this study, I investigate Woodford shale, a major source rock located in the Midwestern U.S. Its low permeability makes it difficult to fully profit from its potential, making it a perfect case study for HF. Field observations for Woodford shale [7] show that its natural fractures have a vertical dip and strike West-East with an average distance

between fractures of 1.2-1.5 (m) (Figure 1). Hydraulic fracturing reactivates these preexisting fractures, thus creating multibranch fractures (Figure 2).

Quantifying the effects of spatial variability in formation properties [8, 9] on the reliability of hydraulic fracture simulations has been studied [6, 10–13] but is restricted by simplified deterministic solutions or computational timescales of numerical solutions. The uncertainty quantification for the simple linear elastic model given by [12] calculates the range of possible fracture apertures using Monte-Carlo simulations where Young's modulus and the confining stress are random parameters, and they consequently reformulate the governing equations as stochastic partial differential equations (SPDEs). They adopt a stochastic collocation method to solve these SPDEs and replace the classic Monte-Carlo methods with two different methodologies: (1) the input parameters respect a log-normal distribution function, where only the mean and the dispersion values are used to calibrate the model, and (2) the input parameters fall within 96% of the log-normal distribution (a method called maximum entropy). They show that the probability distribution function of Young's modulus and the confining stress greatly impact that of the fracture aperture. Furthermore, [12] were inspired by [8] who developed the stochastic framework to efficiently perform uncertainty quantification for fluid transport in porous media in the presence of both stochastic permeability and multiple scales and present the solution as a polynomial approximation. In a recent publication, [13] address variability in discrete fracture network geometry using the very robust multilevel Monte-Carlo methods, rather than the stochastic methodology claiming that the classic stochastic collocation fails to provide reliable estimates of first-order moments of the output solution due to the lack of smoothness. In another recent publication, [14] proposes the (MLMC) methods in conjunction with a well-assessed underlying solver to perform DFN flow simulations using Darcy flow and prove that the method is robust enough to tackle complex geometrical configurations, even with very coarse meshes. [15] address the heterogeneities in fractured reservoirs and assume that the fracture intensity, orientation, and conductivity of different fracture sets are the uncertain parameters. They confer each parameter with a probability distribution and create an integrated history matching workflow for fractured reservoirs assuming numerical methods for multiphase flow simulation, while updating the fracture properties via dynamic flow responses, such as continuous rate and pressure measurements. They generate initial realizations using Monte-Carlo simulations and based on observed fractures at the well locations. The automated history matching approach results in multiple equally probable discrete fracture network models, where upscaled flow simulation models honour both the geological information and the dynamic production history. Furthermore, [16] use uncertainty quantification for coupled subsurface flow and deformation processes. They circumvent the slow convergence of the traditional Monte-Carlo methods using an intrusive polynomial chaos expansion method for Biot's poroelasticity equations based on Galerkin projection with uniform and log-normally distributed material parame-
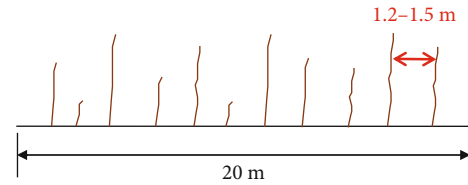
Figure 1: Simplified drawing of the natural fractures in Woodford shale.
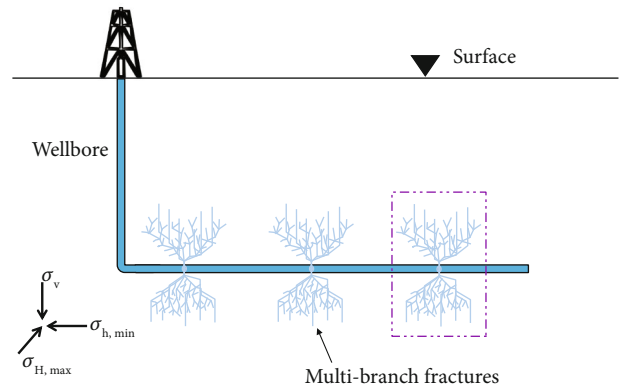
Figure 2: Conceptual model for hydraulic fracturing in shale reservoir with preexisting natural fractures. Horizontal well injection initiates multibranch fractures. I delimit the study to one multibranch fracture highlighted with a purple dashed box.

ters. Results show good agreement with the Monte-Carlo and ANOVA-based probabilistic collocation methods.

Although significant studies have been presented on uncertainty quantification in hydraulic fracturing, they are restricted to finite element schemes with defined mesh size and number of random values. Furthermore, they focus on geometric properties or are limited to elastic formation parameters, rather than rank all formation properties including the thermal properties, which is covered in this paper. The purpose here is to address formation inhomogeneity and spatial variability in low permeability shale reservoirs and their impact on fracture response using a unique but simple framework for uncertainty quantification comprising of sensitivity ranking and probability density curves. Then, I test the validity of the framework on the 1D porothermoelastic analytical solution for pressure, temperature, leak-off, and width given by [3], with application to Woodford shale data. A series of simulations demonstrate uncertainty propagation in the deterministic solution and describe the probability density function (PDF) for the fracture width to explain why some proppants have higher success rates than others.

2. Materials and Methods

2.1. Conceptual Model.
Analytical solutions for pressure, temperature, strain, and displacement are derived in detail by [3] following the 1D consolidation theory.

Figure 3 zooms in to a multibranch fracture and shows how the fracture apertures are perpendicular to the
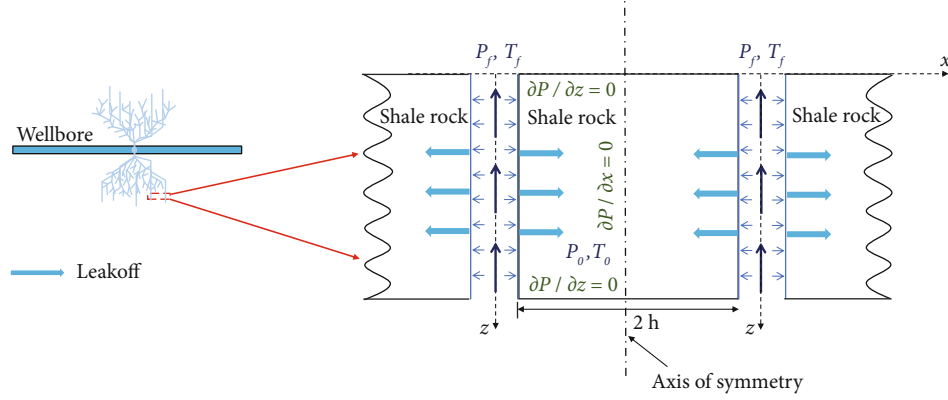
FIGURE 3: The red dashed box zooms in to two consecutive fractures and shows the fracture geometry with the initial and boundary conditions: P_f and T_f are the fluid pressure and temperature, respectively. P_0 and T_0 are the initial pressure and temperature, respectively. The 1D solution is limited to h because of the symmetry.
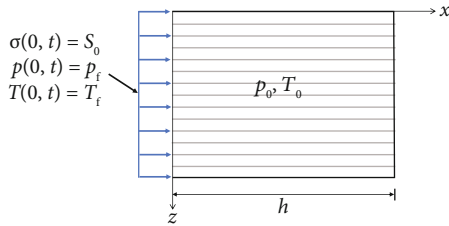
FIGURE 4: One-dimensional consolidation setup showing the initial and top boundary conditions, where the plane (xy) is the isotropic plane, where the x axis has a subscript of 1, and the z axis is the axis of rotational symmetry with a subscript of 3. The top, bottom, and right boundaries (in bold) are assumed impermeable, adiabatic, and frictionless.

minimum horizontal stress $\sigma_{h,\min}$ and intersect a porous medium characterized with an initial pore pressure p_0 and an original temperature T_0 and subject to fracturing fluid with pressure p_f and temperature T_f at its faces (Figure 3). Figure 3 also shows that the distance between two consecutive fracture apertures is $2h$, but because of the mirror symmetry, the one-dimensional solution is constrained to the length h. Furthermore, the pore pressure gradient induces fluid leak-off from the fracture into the formation at each fracture face, and impermeable, adiabatic, and frictionless boundary conditions prevail at the axis of symmetry.

2.2. Governing Equations.

The one-dimensional consolidation for transversely isotropic material is described in detail by [3], but a brief summary of the equations is presented here for the sake of completeness. Assuming the (xy) plane is the isotropic plane and the z axis is the axis of rotational symmetry (Figure 4), the coupled equations for pressure, temperature, and displacement represent the response of the hydraulic fracture system.

First, the analytical pressure solution is derived as

$$p(x,t) = \frac{2}{h}\sum_{m=0}^{\infty}\frac{1}{\xi}\left(c_1 e^{-\gamma_1\xi^2 t} + c_2 e^{-\gamma_2\xi^2 t}\right)\sin\xi x + \Delta P, \quad (1)$$

then, the temperature is given by

$$T(x,t) = \frac{2}{h}\sum_{m=0}^{\infty}\frac{1}{\xi}\left(c_3 e^{-\gamma_1\xi^2 t} + c_4 e^{-\gamma_2\xi^2 t}\right)\sin\xi x + \Delta T, \quad (2)$$

finally, the displacement is given by

$$u(x,t) = \frac{S_0 - \alpha_1\Delta P - \beta_1^s\Delta T}{M_{11}}(x-h)$$
$$+ \frac{2\alpha_1}{M_{11}h}\sum_{m=0}^{\infty}\frac{1}{\xi^2}\left(c_1 e^{-\gamma_1\xi^2 t} + c_2 e^{-\gamma_2\xi^2 t}\right)\cos\xi x \quad (3)$$
$$+ \frac{2\beta_1^s}{M_{11}h}\sum_{m=0}^{\infty}\frac{1}{\xi^2}\left(c_3 e^{-\gamma_1\xi^2 t} + c_4 e^{-\gamma_2\xi^2 t}\right)\cos\xi x,$$

where h is the half distance (m), ξ is $(2m+1)\pi/2h$ (m^{-1}), S_0 is the stress boundary condition that is the difference between the fracturing fluid pressure P_f (MPa) and the minimum horizontal stress $S_{h\ \min}$ (MPa), M_{11} is the stiffness coefficient (MPa) calculated from Young's modulus and Poisson's ratio, β_1^s is a thermal parameter calculated from the stiffness coefficients and the solid thermal expansion coefficient (MPa°C^{-1}) and α_1 is Biot's coefficient [1], and c_1, c_2, c_3, c_4, γ_1, and γ_2 are lumped parameters defined as

$$c_1 = \frac{\gamma_1\gamma_2[g_{11}(p_0 - \Delta P) - g_{12}\Delta T] - (p_0 - \Delta P)\gamma_1}{(-\gamma_1 + \gamma_2)};$$
$$c_2 = p_0 - \Delta P - c_1;$$
$$c_3 = \frac{c_1(1 - \gamma_1 g_{11})}{\gamma_1 g_{12}};$$
$$c_4 = -\Delta T - c_3; \quad (4)$$
$$\gamma_1 = \frac{g_{11} + g_{22} + \sqrt{(g_{11} + g_{22})^2 - 4g^*}}{2g^*};$$
$$\gamma_2 = \frac{g_{11} + g_{22} - \sqrt{(g_{11} + g_{22})^2 - 4g^*}}{2g^*};$$

and $g_{11}, g_{12}, g_{21}, g_{22}$, and $g*$ are defined as

$$g_{11} = \frac{\mu}{k_1}\left(\frac{1}{M} + \frac{{\alpha_1}^2}{M_{11}}\right);$$

$$g_{12} = \frac{\mu}{k_1}\left(\frac{\alpha_1\beta_1^s}{M_{11}} - \beta^{sf}\right);$$

$$g_{21} = \frac{\alpha_1\beta_1^s T_0}{\lambda_1 M_{11}}; \tag{5}$$

$$g_{22} = \frac{1}{\lambda_1}\left(\rho C_v + \frac{(\beta_1^s)^2 T_0}{M_{11}}\right);$$

$$g^* = g_{22}g_{11} - g_{12}g_{21},$$

where μ is the fluid viscosity (Pa s), k_1 is the permeability (m^2), M is a poroelastic parameter in (MPa), λ_1 is the thermal conductivity (J m^{-1}s$^{-1\circ}$C^{-1}), and ρC_v is the overall thermal capacity (J/(m$^{3\circ}$C)). Note that subscripts 1 and 3 represent the x direction and the z direction, respectively.

The initial and boundary conditions associated with Equations (1)–(3) are given as follows:

$$p(x, 0) = p_0;$$

$$p(0, t) = p_f;$$

$$T(x, 0) = T_0;$$

$$T(0, t) = T_f;$$

$$\left.\frac{\partial p}{\partial x}\right|_{(h,t)} = 0; \tag{6}$$

$$\left.\frac{\partial T}{\partial x}\right|_{(h,t)} = 0;$$

$$u(h, t) = 0.$$

Despite the complexity of the porothermoelastic solution, one can easily identify the contributing formation properties. The theory of linear elasticity assumes the rock as a dry solid material characterized by E, Young's modulus (GPa), and ν Poisson's ratio [1]. However, pore fluid alters the mechanical behaviour of the porous rock, thus introducing three additional poroelastic parameters: α Biot's coefficient [1], M Biot's modulus (GPa), and κ the mobility ratio (ratio between permeability of the formation and viscosity of the pore fluid: k/μ) (m^{2}Pa^{-1}s^{-1}). In addition, the one-dimensional anisotropic solution couples the poroelastic solution with the effects of the thermal gradient (between the fracturing fluid and the rock formation), thus introducing thermal parameters to the solution: the solid skeleton linear thermal expansion coefficient α_i^s($^\circ$C^{-1}) in the ith direction, the volumetric thermal expansion coefficient of the pore fluid α^f($^\circ$C^{-1}), the thermal conductivity of the porous medium λ_1 (in the x direction) (J m^{-1}s$^{-1\circ}$C^{-1}), and the overall thermal capacity ρC_v(J m$^{-3\circ}$C^{-1}). Finally, the anisotropic nature of shale has a significant impact on its

TABLE 1: Formation properties used to model the uncertainty in the hydraulic fracture responses.

E_i	Young's modulus in the ith direction
ν_i	Poisson's ratio
α_i^s	Solid skeleton linear thermal expansion coefficient in the ith direction
κ_1	Mobility ratio in the x direction
λ_1	Thermal conductivity in the x direction
ρC_v	Overall thermal capacity

mechanical responses [3] and is included in this study. Table 1 enumerates the formation properties contributing to the uncertainty study for the 1D anisotropic porothermoelastic solution.

In the following, I detail the proposed uncertainty quantification (UQ) framework comprised of two parts: (1) sensitivity ranking to rank the input parameters by order of degree of influence on the output solution and (2) probability density function of the output solution that depicts all possible HF responses and their corresponding likelihood.

2.3. Part I: Sensitivity Analysis. To analyse the propagation of uncertainties, one must study how the output solution varies when the input variable takes on different values [5]. Using the popular Monte-Carlo methods, one generates a set of realizations of the input data $\{d_1, d_2, d_3, \cdots\}$, each characterized by a known probability distribution law, and calculates the correspondent solution s of the model $\{s_1, s_2, s_3, \cdots\}$, then measures its statistics [4]. The Monte-Carlo methods have the advantage of being robust; that is, there are no constraints on the variances of the input data and the output. These methods are independent from the dimensionality of the random values (RVs) but require the deterministic solution and are characterized with a slow convergence rate. Although there are methods to increase the convergence rate such as variance reduction methods, a convergence rate of $M^{-1/2}$ governs all Monte-Carlo methods, thus requiring a large population size M [4, 5]. As a result, these methods are impeded by high computational cost and time.

Sensitivity analysis addresses the first part of the framework, where I rank input parameters by their order of influence on the variance of the solution. One of the simplest and most practical methods to perform sensitivity analysis is the one at a time method (OAT). In this method, one studies each parameter individually to minimize the chances of computer crashes. Typically, one random input parameter is assumed, while maintaining all others to their originally assigned values. The sensitivity analysis is driven by this random parameter that produces a host of possible output solutions. The steps for the OAT approach are listed in the following text for a deterministic solution, $y = f(x_{i=1}, x_{i=2}, \cdots.x_{i=m})$ with m input parameters.

(1) Consider x_1 a random input parameter that fits a defined distribution function, e.g., normal
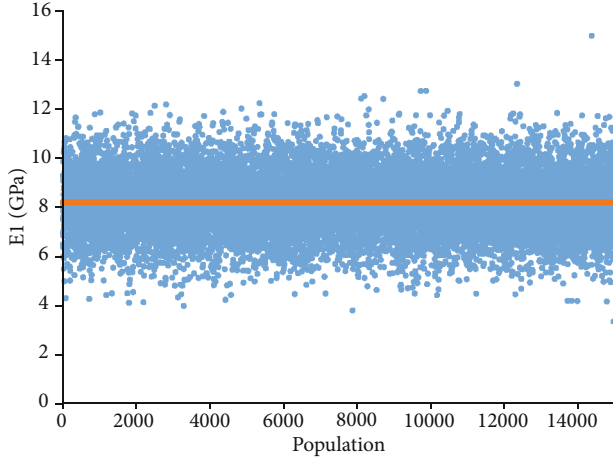
FIGURE 5: Monte-Carlo population simulation for Young's modulus with $N_{\text{population}} = 15,000$ with an average of 8.21 (GPa) and a standard deviation of 1.2 (GPa) assuming a normal distribution.

TABLE 2: Woodford shale data used to test the sensitivity of the model to the input uncertainties.

Mobility ratio κ_1, m^2/(Pa s)	45
Solid skeleton linear thermal expansion coefficient α^s, /°C	2×10^{-5}
Overall heat capacity ρC_v, J/$\left(m^{3\circ}C\right)$	2.75
Thermal conductivity λ_1, J/(m s°C)	1.4
Original pore pressure p_o, MPa	27.6
Original temperature T_o, °C	90
Minimum horizontal stress $\sigma_{h,\text{min}}$, MPa	52
Stress boundary condition S_0, MPa	12
Fracturing fluid pressure p_f, MPa	64
Fracturing fluid temperature T_f, °C	30
Young's modulus E_1, E_3, GPa	5.6, 4.6
Poisson's ratios ν_1, ν_3	0.3
Distance between vertical apertures $2h$, m	1.2

distribution, with an assigned mean and standard deviation, and generate $N_{\text{population}}$ of x_1. Figure 5 shows the population distribution for Young's modulus E_1 (GPa) converging for $N_{\text{population}} = 15,000$

(2) Calculate the deterministic solution for each value of x_1

(3) Calculate the variance of the $N_{\text{population}}$ values of output solution and note it as y_1

(4) Repeat procedure for each of the other input parameters $i = [2 : m]$

(5) Calculate the sum of the output solution y_i for m values of variance. $\sum_{i=0}^{m} y_i$

TABLE 3: Variability of some Woodford shale formation properties from field measurements.

Mobility ratio κ_1, nD/cP	20-60
Solid skeleton linear thermal expansion coefficient α^s, /°C	$(0.9 - 4.8) \times 10^{-5}$
Overall thermal capacity ρC_v, J/$\left(m^{3\circ}C\right)$	2.57-2.94
Thermal conductivity λ_1, J/(m s°C)	0.7-1.4
Young's modulus E_1, E_3,GPa	6.8-9.8; 3.85-5.6
Poisson's ratio ν_1, ν_3	0.1-0.15; 0.23-0.3
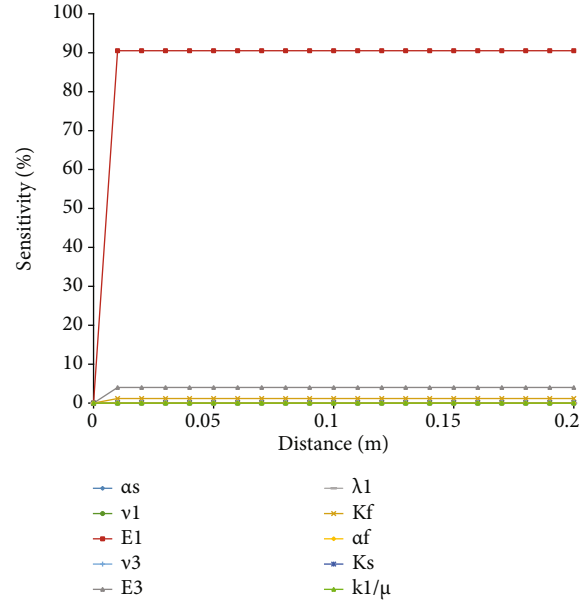
FIGURE 6: Sensitivity ranking for pressure in the fracture at time $t = 0 +$. The instantaneous pore pressure jump is 90% governed by Young's modulus E_1.

(6) Calculate the coefficient of variation $y_1 / \sum_{i=1}^{m} y_i$ for each input parameter. This coefficient represents the degree of influence of each input parameter on the output solution

2.4. Part II: Probability Density Curves. Proposed methods for uncertainty quantification include the probability density function (PDF), where its value is always positive and its integral over the entire range of possible values equals to one. To generate the PDF, one simultaneously introduces the high-ranking random input variables (from the first part of the framework) in the deterministic solution and fits the range of output results to a probabilistic distribution type (normal, triangular, Gumbel, lognormal, etc.). The procedure for a deterministic solution $y = f(x_{i=1}, x_{i=2}, \cdots x_{i=m})$ with m input parameters is as follows:

(1) Select the input parameters with a high sensitivity ranking (from sensitivity analysis) as random variables and keep the formation parameters with a negligible effect to their original value

(a)

(b)

(c)
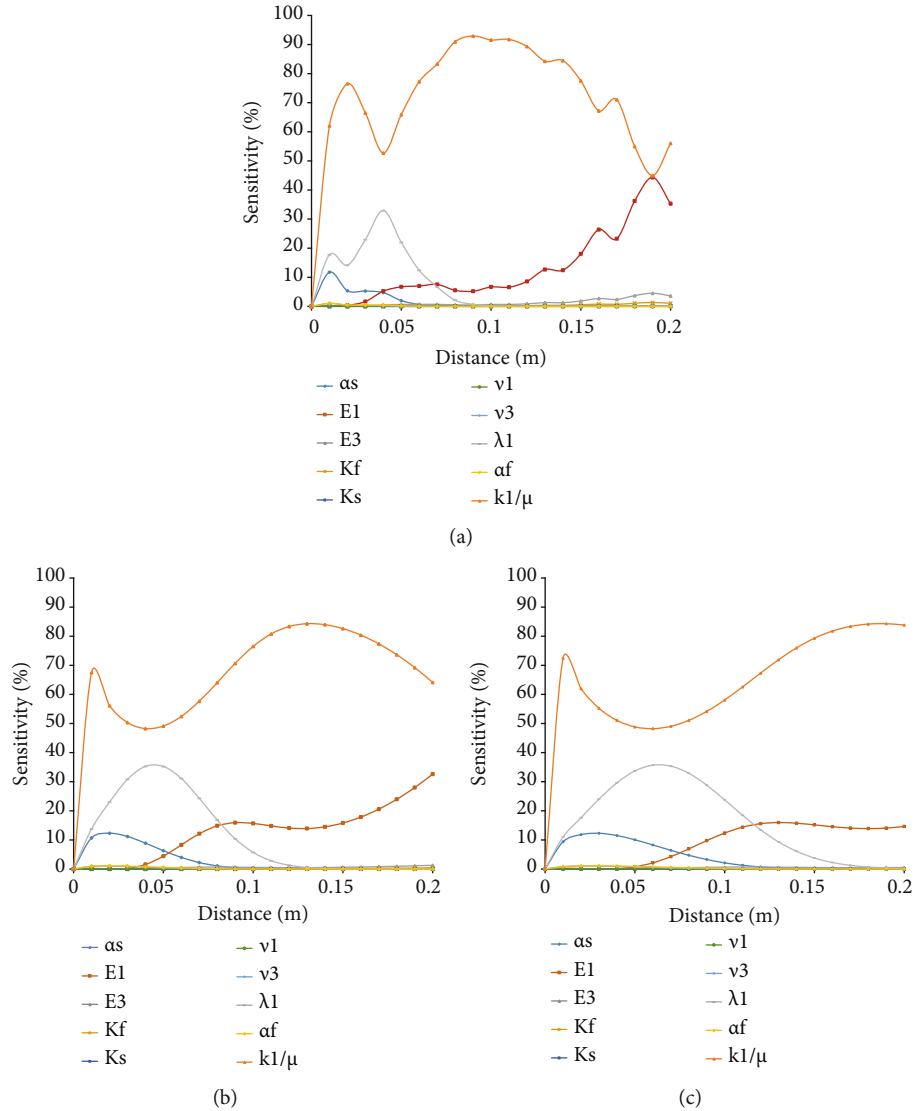
FIGURE 7: Sensitivity ranking for pressure in the fracture at time (a) $t = 15$ (min), (b) $t = 30$ (min), and (c) $t = 60$ (min).

(2) Generate a population of n values for each of the selected random variables and calculate the output solution

(3) Plot the histogram of all the n output values y

(4) Fit the histogram to a distribution function and calculate the PDF function

3. Results

3.1. Woodford Shale Data. I test the proposed framework on the 1D solution with typical Woodford Shale data presented in Table 2 [17–20]. The transversely isotropic nature of this low permeability shale signifies that its properties depend on the direction, where x has a subscript of 1 and z a subscript of 3 (Figure 3), except for the linear thermal expansion coefficient that is independent of the direction and is replaced with one value α^s. The model considers thermal effects because of the significant temperature difference ($\Delta T = 60°$

C) between the fracturing fluid temperature ($T_f = 30°$C) and the formation temperature ($T_0 = 90°$C).

However, literature review [17, 19, 20] confirms a large variability in some of those properties, summarized in Table 3.

3.2. Sensitivity Analysis: Application to Woodford Shale. The saturated porous medium in Figure 4 is subjected to an instantaneous compression due to injection, and as a result experiences a pore pressure jump, also known as Skempton's effect. The pressure at the shale-fracture interface is the constant injection pressure P_f, and consequently, the sensitivity score for all parameters is zero at $x = 0$ (m) (Figure 6). Figure 6 shows that the dominant control on the initial pore pressure (Equation (1)) is the elastic Young's modulus E_1 with a sensitivity score of 90%. As pressure distribution stabilizes inside the half-space, the sensitivity of the pore pressure to E_1 decreases and other formation properties come into play, as shown in Figure 7. Figures 7(a)–7(c) show that

(a)

(b)

(c)
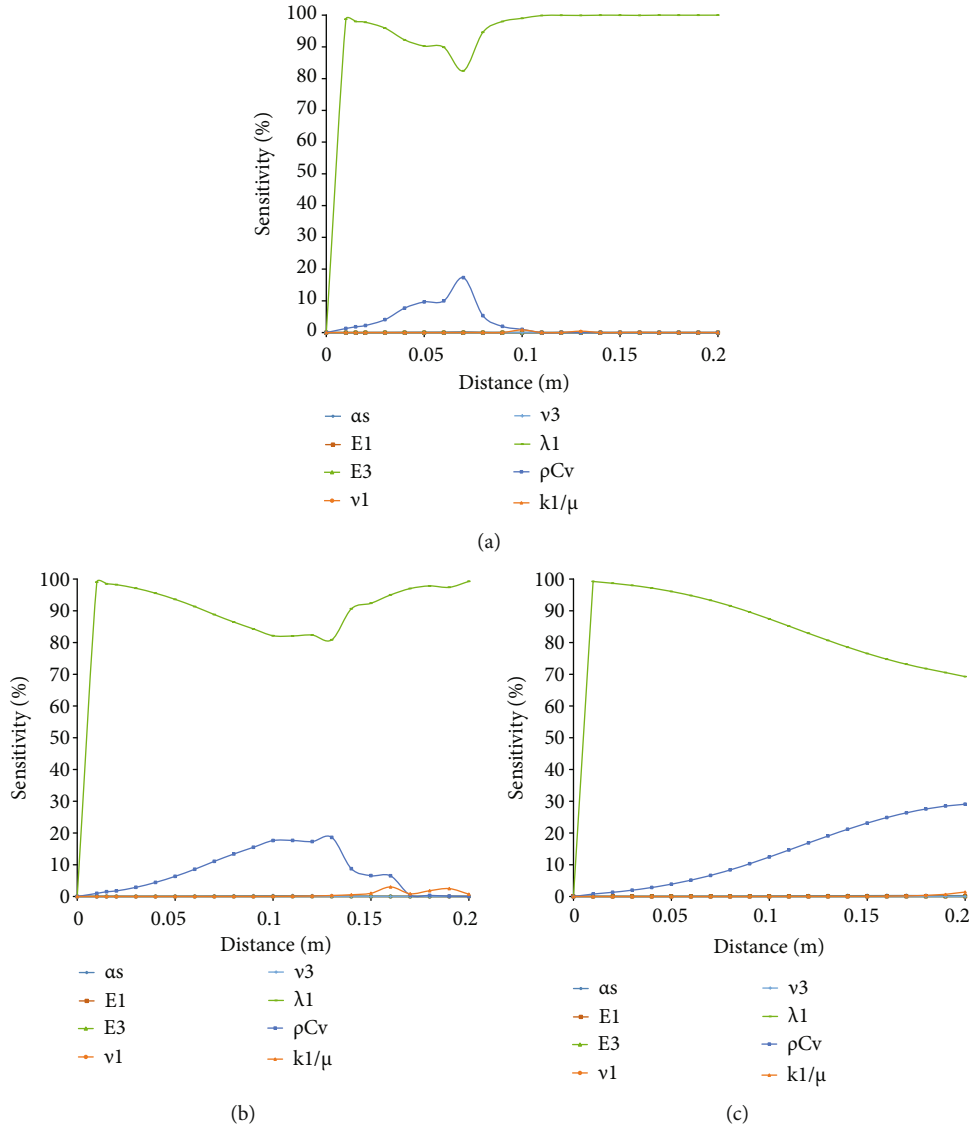
FIGURE 8: Sensitivity ranking for temperature in the fracture at time (a) $t = 15$ (min), (b) $t = 30$ (min), and (c) $t = 60$ (min).

as the pore pressure front diffuses inside the formation, the sensitivity of pressure to E_1 significantly decreases and the pore pressure becomes more sensitive to the mobility ratio κ_1, the thermal conductivity λ_1, and the skeleton linear thermal expansion coefficient α^s, respectively. The reason why thermal properties influence the pore pressure response is that the temperature gradient forces the fluid and rock to contract as the cooling front penetrates further inside the half-space.

λ_1 is the second most dominant parameter, where its influence reaches 0.09 (m) at $t = 15$ (min) (Figure 7(a)), 0.12 (m) at $t = 30$ (min) (Figure 7(b)), and 0.18 (m) at $t = 60$ (min) (Figure 7(c)), and α^s is the third most dominant parameter, where its influence reaches 0.06 (m) at $t = 15$ (min) (Figure 7(a)), 0.09 (m) at $t = 30$ (min) (Figure 7(b)), and 0.12 (m) at $t = 60$ (min) (Figure 7(c)). The thermal conductivity λ_1 sensitivity curve presents a peak that coincides with the dip in the mobility ratio sensitivity curve for $x =$

0.04 (m) at $t = 15$ (min) (Figure 7(a)), $x = 0.05$ (m) at $t = 30$ (min) (Figure 7(b)), and $x = 0.06$ [m] at $t = 60$ (min) (Figure 7(c)), highlighting a lower pressure zone, as seen in [3]. After 30 (min) of injection, the dip of the mobility ratio κ_1 stabilizes at 48% and the peak in the thermal conductivity λ_1 stabilizes at 38%. Figures 7(a)–7(c) also show that beyond the pore pressure front lies a zone where pore pressure is only sensitive to E_1 and κ_1, such as $x > 0.1$ (m) at $t = 15$ (min) (Figure 7(a)), $x > 0.12$ (m) at $t = 30$ (min) (Figure 7(b)), and $x > 0.18$ (m at $t = 60$ (min) (Figure 7(c)).

I proceed to perform sensitivity ranking for the temperature (Equation (2)), where contrary to the pore pressure, temperature is independent of any formation parameter at time $t = 0 +$, because the temperature front takes finite time to diffuse inside the formation.

Figure 8(a) shows that at $t = 15$ (min), the cooling front reaches 0.11 (m) and depends on the thermal conductivity λ_1 and the overall thermal capacity ρC_v. Figures 8(b) and

FIGURE 9: Sensitivity ranking for the transient leak-off velocity (m/s) for time interval $t = [0, 60]$ (min).

FIGURE 10: Sensitivity ranking for the fracture width (mm) for time interval $t = [0, 60]$ (min).

TABLE 4: Sensitivity analysis summary showing which input parameters influence the solution. Y is for yes and N is for No.

Output	Parameters							
	α^s	E_1	E_3	ν_1	ν_3	λ_1	ρC_ν	κ_1
Pressure	Y	Y	N	N	N	Y	N	Y
Temperature	N	N	N	N	N	Y	Y	N
Leak-off	N	N	N	N	N	N	N	Y
Fracture width	Y	Y	N	N	N	Y	N	Y

Next, the 1D solution provides an expression for the fluid flow based on Darcy's law, where the leak-off velocity is the flow at the shale-fracture interface ($x = 0$ (m)).

Figure 9 shows that the leak-off velocity is most sensitive to the mobility ratio κ_1 and the thermal conductivity λ_1, with a sensitivity score of 90% and 10%, respectively.

Finally, the fracture width is the displacement at the shale-fracture interface, $x = 0$ (m) (Equation (3)).

Similar to the pressure (Figure 6(a)), fracture width is initially ($t = 0 +$) most sensitive to the elastic Young's modulus E_1 (Figure 10), but because thermal effects are factored in the rock deformation process, the influence of E_1 decreases with time, while the linear thermal expansion coefficient α^s, the mobility ratio κ_1, and the thermal conductivity λ_1 start to play a larger role in the displacement solution. Figure 10 shows that after 60 (min), the fracture width becomes most sensitive to α^s (75%), followed by κ_1 (12%), λ_1 (9%), and E_1 (3%).

Table 4 summarizes the formation properties with a high sensitivity ranking. I consider the parameters with Y attribute for this second part and generate the probability density functions to quantify uncertainty in the output solution.

3.3. Probability Density Functions: Application to Woodford Shale. Figures 11(a)–11(c) show the probability density functions (PDFs) of the pore pressure response (considering the simultaneous variability of the four parameters indicated with Y in Table 4), at times $t = 15$ (min), $t = 30$ (min), and $t = 60$ (min), respectively. The pore pressure variability fits a normal distribution function, where the pressure is fixed at 64 (MPa) at the shale-fracture interface, $x = 0$ (m). That is, PDF at this boundary is 100% and is not included in the plots.

Figure 11(a) shows that the transient pore pressure front diffuses from the boundary and reaches a depth of $x = 0.1$ (m) at $t = 15$ (min), to stabilize at a pressure range of 30-35 (MPa), for $x > 0.1$ (m), which corresponds to the pore pressure jump felt in the porous medium at $t = 0^+$. Figure 11(b) shows that the pressure diffusion reaches 0.15 (m), and Figure 11(c) shows diffusion reaches 0.2 (m). Also, it is important to talk about the standard deviation because it indicates the amount of dispersion or variation observed in the population [21]. The pressure PDF follows a normal distribution function and has the highest standard deviation at $t = 15$ (min), which decreases with time, where the PDF curve becomes sharper at 30 (min) and 60 (min).

Figures 12(a)–12(c) show the probability density functions (PDF) of the thermal diffusion, assuming a random

8(c) show that the sensitivity of the temperature to ρC_ν increases while the influence of λ_1 continues to decrease but remains dominant, with a sensitivity score of 70% for λ_1 and for of 30% for ρC_ν at $t = 60$ (min) and for $x = 0.2$ (m). This is particularly interesting because while pressure depends on thermal properties, temperature only depends on two temperature properties, where the temperature at the shale-fracture interface ($x = 0$ (m)) only depends on the thermal conductivity λ_1. Note that the Monte-Carlo simulation for temperature becomes smoother as the system stabilizes and reaches a steady condition.

(a)

(b)

(c)

FIGURE 11: Probability density functions for pressure at times (a) $t = 15$ (min), (b) $t = 30$ (min), and (c) $t = 60$ (min).

thermal conductivity λ_1 and a random overall heat capacity ρC_v, calculated at times $t = 15$ (min), $t = 30$ (min), and $t = 60$ (min), respectively. Like pressure, PDF of the temperature at the shale-fracture boundary is 100% (constant injection temperature of 30 (°C)) and is not included in the plots. The thermal diffusion front fits a normal distribution func-

tion and shows that the temperature of the porous medium decreases as a cooling front progresses deeper inside the medium to reach a depth of about 0.13 (m) at $t = 60$ (min) (Figure 12(c)). The temperature also follows a normal distribution PDF, where its standard deviation, contrary to the pore pressure, does not seem to decrease with time.
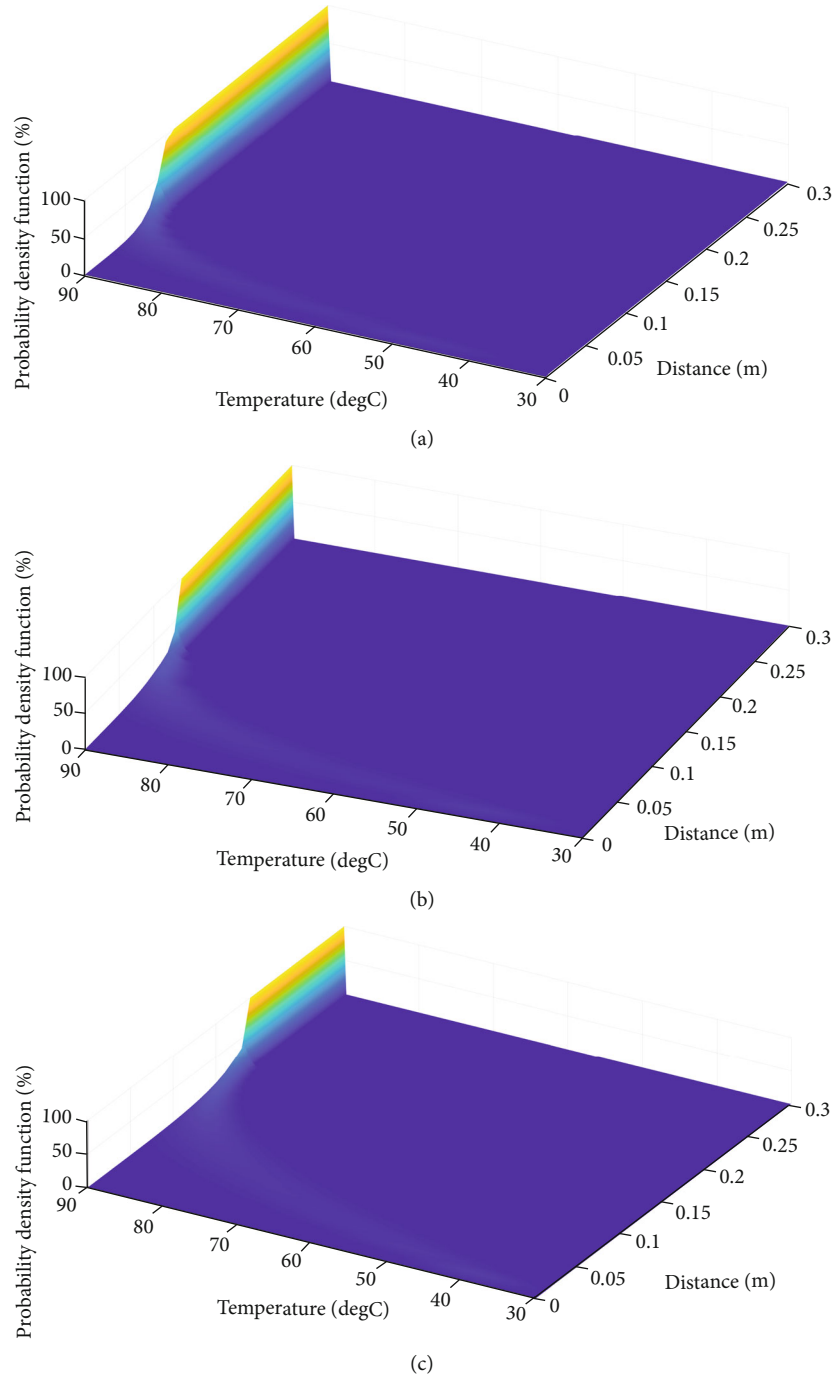
FIGURE 12: Probability density functions for temperature at times (a) $t = 15$ (min), (b) $t = 30$ (min), and (c) $t = 60$ (min).

Figure 13 shows the transient PDF of the leak-off velocity characterized by a normal distribution function. The leak-off velocity is the Darcy flow at the shale-fracture interface, which depends on the pore pressure gradient and is highest in the beginning of the injection 1.5×10^{-3} (m s^{-1}) and slows down to 0.3×10^{-3} (m s^{-1}) after 30 (min) of injection, as the pressure gradient nears zero.

Finally, Figure 14 shows the PDF of the transient fracture width, assuming the variability of the four input parameters (Table 4) for time interval [0,60] (min).

The mean fracture width is 0.72 (mm) at $t = 0^+$ and 0.84 (mm) at $t = 60$ (min). All possible values of fracture width fit a normal distribution and fall within a narrow range with a standard deviation of $\sigma = 0.04$ (mm) at $t = 0^+$, then the range of variation widens, and the standard deviation is $\sigma = 0.15$ (mm) at $t = 60$ (min). The reason for this is that, at early times, the fracture width evolution is an elastic problem, depending primarily on one parameter Young's modulus E_1, and with time, becomes a porothermoelastic problem that depends on both the thermal and hydraulic properties,
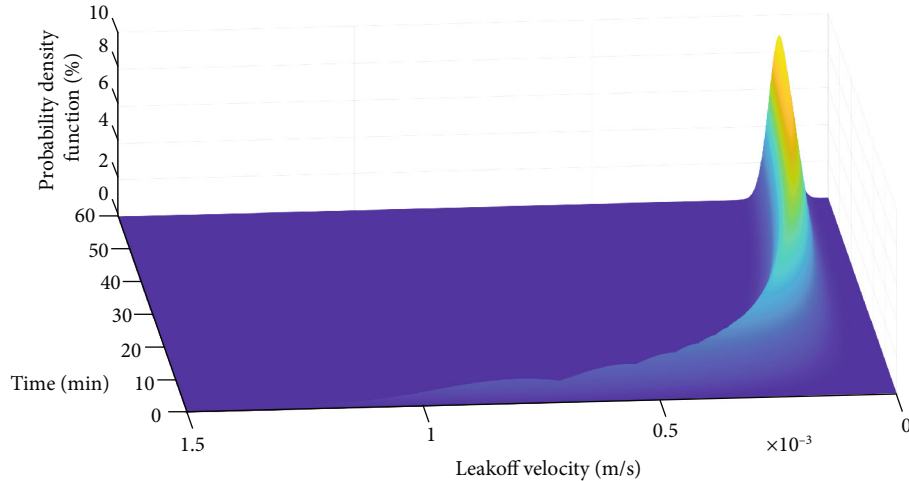
FIGURE 13: Probability density function of the leak-off velocity for time interval $t = [0, 60]$ (min).
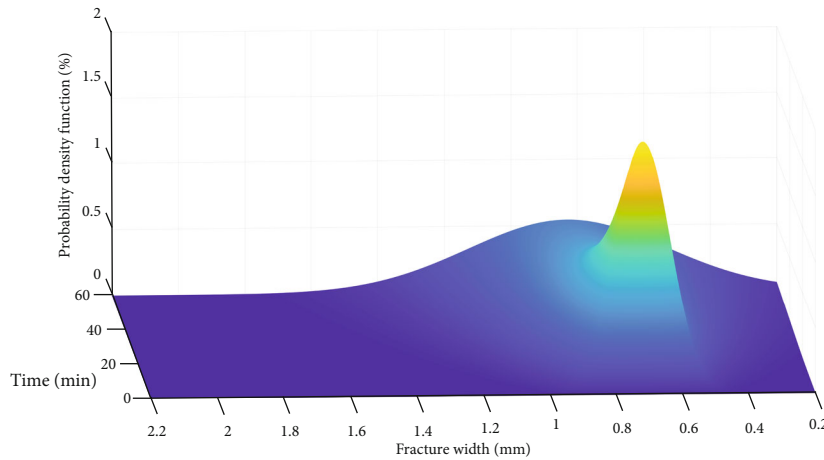
FIGURE 14: Probability density function for fracture width for time interval $t = [0, 60]$ (min).

therefore simultaneously considering random parameters (Young's modulus E_1, linear thermal expansion coefficient α^s, the mobility ratio κ_1, and the thermal conductivity λ_1).

4. Discussion of Findings

When ranking the parameters by order of influence on the solution, one must pay attention to the parameters with high variability as this may affect the sensitivity score. In this problem, the mobility ratio, thermal conductivity, and thermal expansion coefficient are high variability parameters (Table 3) and are also the dominating parameters for the pressure solution (Figure 7). Although high variability affects the sensitivity score, it does not eliminate the reliability of the method, because its main purpose is to rank the contributing parameters, as can be seen in Figure 8 where ρC_v does not have a large variability but is the second most important parameter in the temperature solution. Results also show that temperature takes longer than pressure to stabilize in the system, clearly depicted in the resonance of the sensitivity curves in Figure 8. While at 30 (min), the pressure sensitivity ranking curves stabilize, and the temperature ones

stabilize only at 60 (min). Figure 9 shows that the sensitivity ranking for the leak-off velocity, that is, Darcy flow at the shale-fracture interface, depends primarily on the mobility ratio, where its sensitivity score remains constant after 5 (min), thus indicating that the pressure gradient tends to zero and consequently generates a slow leak-off. Figure 10 shows that the fracture width evolution depends initially only on the elastic parameter E_1 and, with time, becomes mainly driven by thermal effects and depends primarily on the thermal expansion coefficient α^s of the rock. Figure 11 shows that the applied excess pore pressure at the shale-fracture interface leads to an instantaneous pore pressure jump in the medium with a variability of [30-35] (MPa), and then, as time progresses, pressure diffuses further and deeper into the formation. We can also note that the normal distribution of the PDF of the pressure becomes narrower with time, meaning that as time progresses, the effects of the variability in formation properties decrease. Figure 12 clearly shows the temperature diffusion, where the cooling front reaches $x < 0.08$ (m) after 15 (min) and $x < 0.12$ (m) at 30 (min) and $x < 0.175$ (m) at 60 (min). Results also show that the standard deviation of the temperature PDF is
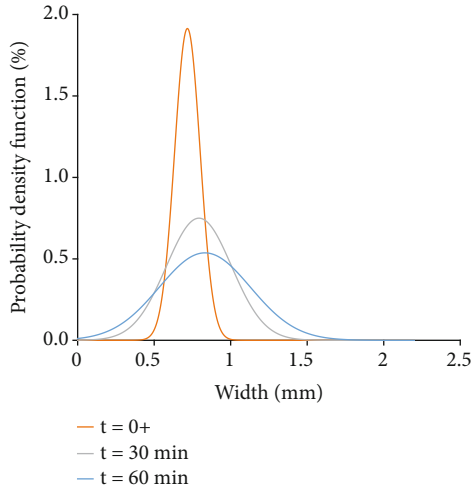
FIGURE 15: Probability density function of the fracture width at different time steps.

independent of time. Further, Darcy flow at the shale-fracture interface (the leak-off) stabilizes after 20 (min) (Figure 13), thus meaning that pressure at the boundary is reaching a constant value. Finally, the PDF of the fracture width provides its range of possible values and corresponding likelihood, which in turn determines if proppants will fit inside the created fracture. Figure 15 shows the "most likely" fracture width for three different time steps, $t = 0^+$, $t = 30 (\text{min})$, and $t = 60 (\text{min})$. Because of the thermal gradient at the shale-fracture interface, fracture width is continuously widening to reach a range of 0-1.5 (mm) after 60 (min) of injection, which means that one must wait before pumping proppants to profit from this mechanism. [3] found that fracture aperture can be as much as 70% larger when the temperature gradient at the interface is 60 (°C), contrary to when the rock and the injected fluid have the same temperature, in which case the fracture width starts to decrease shortly after pumping.

A proper combination of fracturing fluid and proppant kind/mesh size is paramount for a successful fracture job. The industry designs proppants to migrate far enough, thus maintaining a sufficient length/width of the fracture, and to keep the induced hydraulic fracture open, thus providing good fracture conductivity. According to API standards, two types of proppant mesh/size are primarily used in the field: $D_{20/40}$ with a diameter of 0.69 (mm) and $D_{40/70}$ with a diameter of 0.33 (mm). I test the agreement between the width PDF and the industry preferred proppant mixture of D_{100} (0.152 (mm)) (60%) and $D_{40/70}$ (40%) and find that the probability that the proppants $D_{20/40}$ and $D_{40/70}$ will fit inside the fracture at $t = 0^+$ is 63% and 100%, respectively (Figure 16). Consequently, the mixture of 60% D_{100} and 40% $D_{40/70}$ has a probability success rate of 100%, which is observed in the field.

Figure 17 shows the PDF for the fracture aperture at $t = 60$ (min), where the probability that the proppants $D_{20/40}$ and $D_{40/70}$ will fit the fracture is 68% and 96%, respectively. This explains the success rate of the 60% D_{100} and 40% $D_{40/70}$ mixture even at larger times.

(a)

(b)
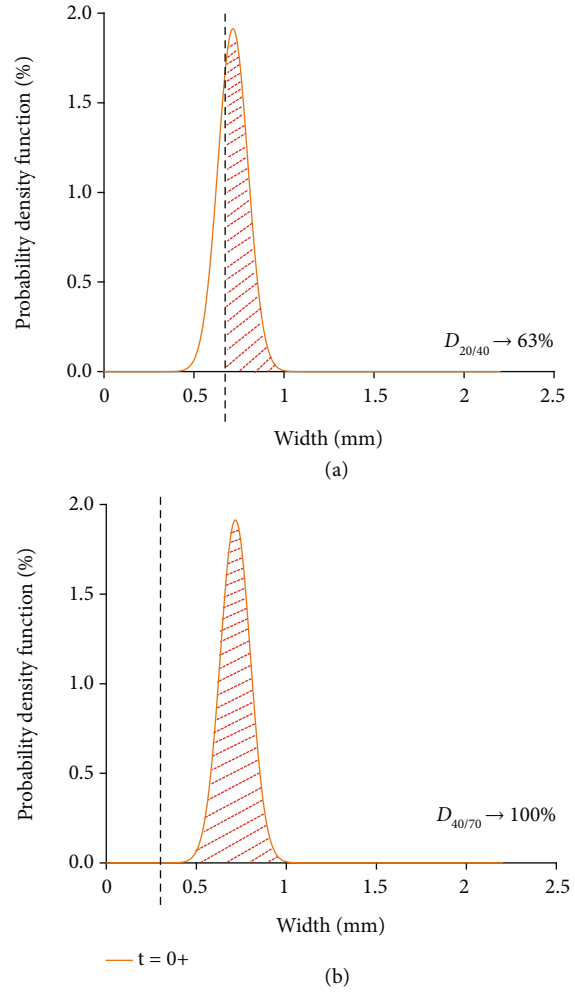
FIGURE 16: PDF of the fracture width at $t = 0 +$. The probability of the proppant to fit inside the created fracture width is represented by the hashed area. The success rate of 63% for $D_{20/40}$ and of 100% for $D_{40/70}$.

5. Conclusions

I investigate here two important parts of uncertainty quantification in hydraulic fracture responses: sensitivity analysis and probability density functions. The study examines the impact of the uncertainty in the formation properties on the one-dimensional problem output solution. The analysis indicates that a large variability in the formation properties propagates a large uncertainty in the fracture responses, most importantly the fracture width. The result is consistent with field observations of successful proppant size, thus proving that uncertainty quantification for fracture width can be a powerful decision-making tool to seek critical proppant mesh/size.

Nevertheless, the investigated problem has some limitations. First, the one-dimensional solution is limited to model the flow of a Newtonian fluid with a constant viscosity, independent from both pressure and temperature. Further, we assume the fracturing fluid pressure and temperature inside the apertures to be constant throughout the stimulation

(a)

— t = 60 min

(b)
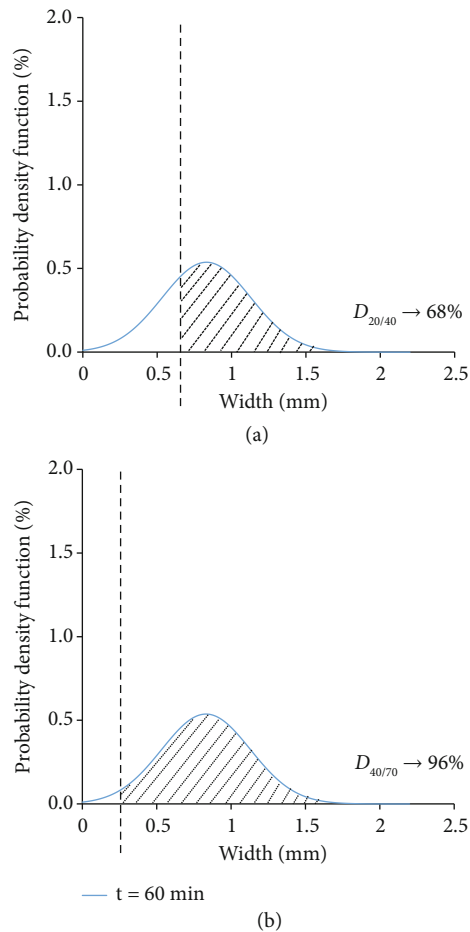
FIGURE 17: Probability density function of the fracture width at $t = 60$ (min). The probability of the proppant to fit inside the created fracture width is represented by the hashed area. The success rate of 68% for $D_{20/40}$ and 96% for $D_{40/70}$.

period and only address the leak-off and heat transfer from the fracture into the formation.

Secondly, despite the simplicity of the Monte-Carlo methods and their robustness, they have the disadvantage of a slow convergence rate and consequently require a large sampling of the stochastic (or random) input parameters. To determine the variability induced on the solution, one must repeatedly calculate the solution with the generated population of random input parameters. Furthermore, these methods are limited to the local variability of the solution because the impact of the input uncertainties is not simultaneously considered (one at a time) to avoid long computation times and computer crashes.

In conclusion, uncertainty quantification (UQ) is a large field of study where some methods may be more effective than others depending on the complexity of the problem. The choice of the optimum statistical method is usually achieved through trial and error and past literature review. Other statistical methods characterized by lower computational time and population size include the spectral methods and dimensional analysis and are worth further developing with application to hydraulic fracturing.

References

[1] M. J. Economides, *Petroleum Production Systems*, Pearson Education, 2013.

[2] P. Valkó and M. J. Economides, *Hydraulic Fracture Mechanics*, Wiley, Chichester, 1995.

[3] Y. N. Abousleiman, S. K. Hoang, and C. Liu, "Anisotropic porothermoelastic solution and hydro-thermal effects on fracture width in hydraulic fracturing," *International Journal for Numerical and Analytical Methods in Geomechanics*, vol. 38, no. 5, pp. 493–517, 2014.

[4] O. Le Maître and O. M. Knio, *Spectral Methods for Uncertainty Quantification: With Applications to Computational Fluid Dynamics*, Springer Science & Business Media, 2010.

[5] Q. Wang, "Uncertainty quantification for unsteady fluid flow using adjoint-based approaches," Citeseer, 2009.

[6] G. R. Lashkaripour, "Predicting mechanical properties of mudrock from index parameters," *Bulletin of Engineering Geology and the Environment*, vol. 61, no. 1, pp. 73–77, 2002.

[7] R. M. Portas Arroyal, "Characterization and origin of fracture patterns in the Woodford shale in southeastern Oklahoma for application to exploration and development," MSc. thesis University of Oklahoma, 2009.

[8] X. Ma and N. Zabaras, "A stochastic mixed finite element heterogeneous multiscale method for flow in porous media," *Journal of Computational Physics*, vol. 230, no. 12, pp. 4696–4722, 2011.

[9] T. Miranda, A. Gomes Correia, and L. Ribeiro e Sousa, "Bayesian methodology for updating geomechanical parameters and uncertainty quantification," *International Journal of Rock Mechanics and Mining Sciences*, vol. 46, no. 7, pp. 1144–1153, 2009.

[10] H. Amanipoor, M. Ghafoori, and G. R. Lashkaripour, "The use of statistical techniques in studying petrophysical properties of hydrocarbon reservoirs: a case study of SW Iran," *Petroleum Science and Technology*, vol. 30, no. 10, pp. 1040–1052, 2012.

[11] G. R. Lashkaripour and M. B. Dusseault, "A statistical study on shale properties: relationships among principal shale properties," in *Probabilistic Methods in Geotechnical Engineering*, pp. 195–200, CRC Press, 2020.

[12] S. Zio and F. A. Rochinha, "A stochastic collocation approach for uncertainty quantification in hydraulic fracture numerical simulation," *International Journal for Uncertainty Quantification*, vol. 2, no. 2, pp. 145–160, 2012.

[13] S. Berrone, C. Canuto, S. Pieraccini, and S. Scialò, "Uncertainty quantification in discrete fracture network models: stochastic

geometry," *Water Resources Research*, vol. 54, no. 2, pp. 1338–1352, 2018.

[14] S. Pieraccini, "Uncertainty quantification analysis in discrete fracture network flow simulations," *GEM-International Journal on Geomathematics*, vol. 11, no. 1, pp. 1–21, 2020.

[15] S. Nejadi, J. Y. Leung, J. J. Trivedi, and C. Virues, "Integrated characterization of hydraulically fractured shale-gas reservoirs—production history matching," *SPE Reservoir Evaluation & Engineering*, vol. 18, no. 4, pp. 481–494, 2015.

[16] P. Delgado and V. Kumar, "A stochastic Galerkin approach to uncertainty quantification in poroelastic media," Fluids Engineering Division Summer Meeting, American Society of Mechanical Engineers, 2014.

[17] Y. N. Abousleiman, M. H. Tran, S. Hoang, C. P. Bobko, A. Ortega, and F.-J. Ulm, "Geomechanics field and laboratory characterization of the Woodford shale: the next gas play," in *SPE Annual Technical Conference and Exhibition, Society of Petroleum Engineers*, Anaheim, California, USA, 2007.

[18] K. Aoudia, "Analysis of rock mechanical properties by mineralogy and their potential effects on hydraulic fracturing in the Woodford shale, West Texas, [Ph.D. thesis]," Colorado School of Mines, 2009.

[19] T. Gilliam and I. Morgan, "Shale: measurement of thermal properties," Oak Ridge National Lab, TN, USA, 1987.

[20] R. Sierra et al., "Woodford shale mechanical properties and the impacts of lithofacies," in *44th US Rock Mechanics Symposium and 5th US-Canada Rock Mechanics Symposium*, American Rock Mechanics Association, 2010.

[21] M. Kanj, Y. Abousleiman, and R. Ghanem, "Poromechanics of anisotropic hollow cylinders," *Journal of Engineering Mechanics*, vol. 129, no. 11, pp. 1277–1287, 2003.

Research Article

Experimental and Numerical Simulation Study of Hydraulic Fracture Propagation during Coalbed Methane Development

Qingshan Ren [iD],[1] **Yaodong Jiang,**[2,3] **Pengpeng Wang** [iD],[1] **Guangjie Wu** [iD],[2] **and Nima Noraei Danesh** [iD][1]

[1]*School of Energy and Mining Engineering, China University of Mining and Technology (Beijing), Beijing, China*
[2]*School of Mechanics and Civil Engineering, China University of Mining and Technology (Beijing), Beijing, China*
[3]*State Key Laboratory of Coal Resources and Safe Mining, China University of Mining and Technology (Beijing), Beijing, China*

Correspondence should be addressed to Qingshan Ren; bqt1900101024@student.cumtb.edu.cn

The extraction of low-permeability coalbed methane (CBM) has the dual significance of energy utilization and safe mining. Understanding hydraulic fracturing mechanism is vital to successful development of CBM. Therefore, it is important to improve the law of hydraulic fracture propagation in coal and rigorously study the influencing factors. In this paper, laboratory experiments and numerical simulation methods were used to investigate the hydraulic fracture propagation law of coal in coalbed methane reservoir with natural fractures. The results show that the maximum and minimum horizontal in situ stress and the difference in stress significantly affect the direction of crack propagation. The elastic modulus of coal, the mechanical properties of natural fractures, and the injection rate can affect the fracture length, fracture width, and the amount of fracturing fluid injected. To ensure the effectiveness of hydraulic fracturing, a reservoir environment with a certain horizontal stress difference under specific reservoir conditions can ensure the increase of fractured reservoir and the controllability of fracture expansion direction. In order to increase the volume of fractured reservoir and fracture length, the pumping speed of fracturing fluid should not be too high. The existence of stress shadow effect causes the hydraulic fracture to propagate along the main fracture track, where the branch fracture cannot extend too far. Complex fractures are the main hydraulic fracture typology in coalbed methane reservoir with natural fractures. The results can provide a benchmark for optimal design of hydraulic fracturing in coalbed methane reservoirs.

1. Introduction

Coalbed methane (CBM) is a valuable resource, and meanwhile, it can affect the safe production of coal. China's CBM reserves are very large, and the amount of such resources at the depth of 0-2000 meters has reached $3.68 \times 10^{12} \, \text{m}^3$. However, one of the key issues restricting the development of CBM in China is that the permeability is generally very low. The coal reservoir fracture system is the main channel for gas flow that controls the permeability characteristics of the coal reservoir [1]. Through hydraulic fracturing to increase permeability, hydraulic fracture can conduct the original natural fractures in coal to a certain extent, which can greatly increase the production of coalbed methane. The mutual coupling relationship between hydraulic frac-

tures and natural fractures has become a research hotspot in recent years [2, 3].

Scholars have conducted extensive research on the relationship between natural fractures and hydraulic fractures in shale and tight sandstone reservoirs [4–7]. The fine description of natural fractures in coalbed methane reservoirs and the quantitative analysis of fractures are particularly important for describing the growth of hydraulic fractures in coal. At present, microseismic and geoelectric methods are widely used in industrial field to monitor the fracture propagation. These methods enable monitoring the range of stress and fluid propagation. The monitoring results are much longer than the real effective support fracture section and cannot distinguish the specific fracture shape. In addition, the experimental method is an effective way to

(a)

(b)
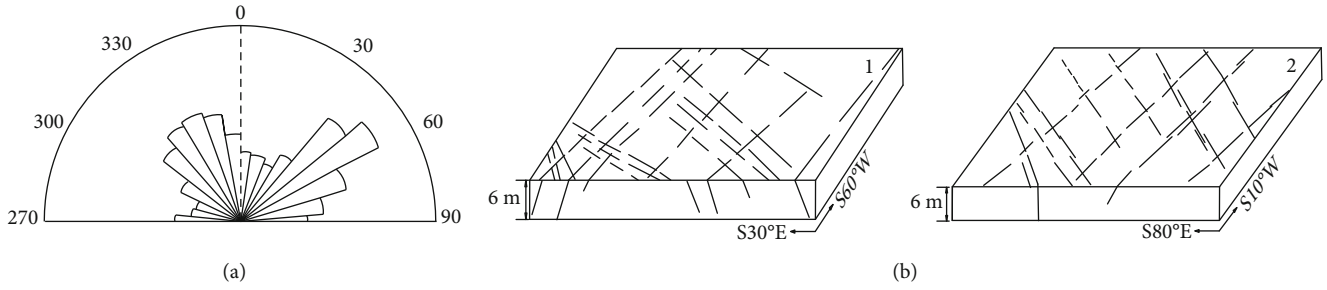
FIGURE 1: Macroscopic fracture development characteristics of Qinshui Basin [24, 25]: (a) rose diagram of the macroscopic fracture spreading orientation of the Qinshui Basin stratigraphy; (b) 1—macroscopic fracture map of coal seam #15 in Si-he coal mine; 2—macroscopic fracture map of coal seam #15 in Cheng-zhuang coal mine.

study the problem, but the size of the laboratory test blocks is very small. In addition, the hydraulic fracture in the experiment starts and expands inside the closed test block, where we cannot directly observe the fracture initiation and propagation process. The monitoring methods of the hydraulic fracturing experiment in a laboratory include computer tomography and acoustic emission monitoring, However, these technologies do not allow visual observation of the dynamic propagation process of the fractures [8–10].

With the development of numerical simulation technology, many scholars have adopted the method to study the change in morphology and expansion of hydraulic fractures in different reservoirs. The numerical simulation methods include finite element method (FEM) [11–13], two-dimensional particle flow code (PFC) [14–17], continuous-discontinuous coupling method [18–20], and discrete element method (DEM) [21–23], which can visualize and quantify the fracture morphology and fracturing process. Among these methods, the finite element method is the most widely used one. The cohesive unit method model based on the ABAQUS platform is the most commonly used model for analyzing hydraulic fracturing of reservoirs.

However, the cohesive element method based on the ABAQUS platform cannot simulate the random propagation of hydraulic fractures in fractured reservoirs. Therefore, a new method of random propagation of hydraulic fracture based on a zero thickness cohesive element embedded in finite element mesh is established by using a grid node splitting method. This has been carried out based on the characteristics of natural fracture growth in coalbed methane reservoir and the topological data structure of element nodes.

This method identifies the random expansion process of hydraulic fractures through secondary development, which can make up for the insufficiency of the built-in cohesion unit of the ABAQUS platform to effectively simulate the random propagation of hydraulic fractures. Numerical examples are used to study the influence of horizontal stress difference and natural fractures in the reservoir on the propagation process of hydraulic fractures, which can accurately describe the random propagation behavior of complex hydraulic fractures and provide references for numerical simulation of fractured reservoirs.

In this paper, the effects of stress and fluid injection rate on the hydraulic fracture propagation in the similar material block with fractures were experimentally studied. Also, a

TABLE 1: Mechanical parameters of similar material test blocks and coal #15.

	Elastic Modulus (GPa)	Poisson's ratio	Compressive strength (MPa)
Coal #15	1.59-4.67	0.21-0.35	9.49-13.5
Specimen 1	2.94	0.23	11.36
Specimen 2	2.41	0.27	12.75

global cohesive zone model was established to simulate the interaction between hydraulic fractures and natural fractures, and the effects of four factors on hydraulic fracture propagation were discussed. Furthermore, a comprehensive discussion on the properties and causes and control factors of hydraulic fractures in the coal containing natural fractures was carried out.

2. Experiments

2.1. Specimen Preparation. Coal strata often contain fractures of different scales that are usually produced by geological tectonic movement. Under the same tectonic background, the development law of surface rock joints can predict the direction and density of coal reservoir fractures. Coal mining often causes fracture development, where these fractures extend from the surface to the deep part of the stratum (Figure 1(b)). As shown in Figure 1(a), a statistical analysis of the fracture development of gas reservoirs in the Qinshui Basin is concentrated in two directions; the dominant joint development direction is in 40°~80° and 320°~350° [24].

In order to simulate the fracture growth morphology of hydraulic fractures in the coal reservoir of interest, containing natural fractures. The material of cement : gypsum : coal dust : water = 3 : 1 : 1 : 3 was mixed together by experimental measurements, and the mechanical parameters (Table 1) were similar to those of coal seam #15 in Qinshui Basin after it was solidified and maintained for one month. As shown in Figure 2(a), the mentioned proportion of the materials was mixed evenly. First, pour it to half the height of the 100 mm × 100 mm × 100 mm cubic mold. A thin cardboard of 25 mm in length and width (as shown in Figure 2(b)) was inserted into the middle of the test block on the bottom surface. After the material in the mold lost fluidity, fill the mold slowly and vibrate evenly to eliminate the weak contact surface of twice pouring slurry. After the test
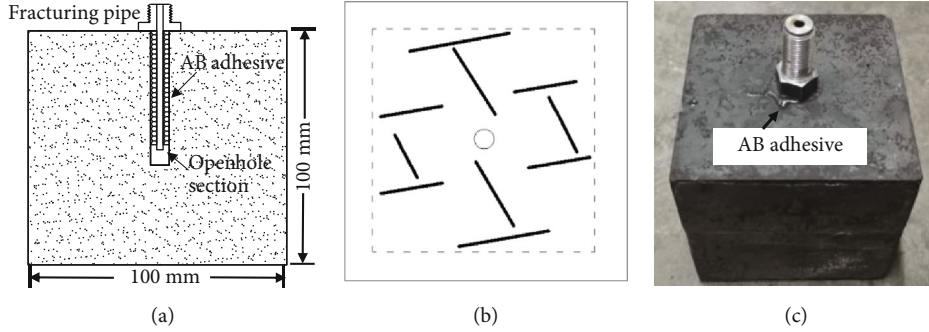
FIGURE 2: Production process of similar material specimen with fractures.
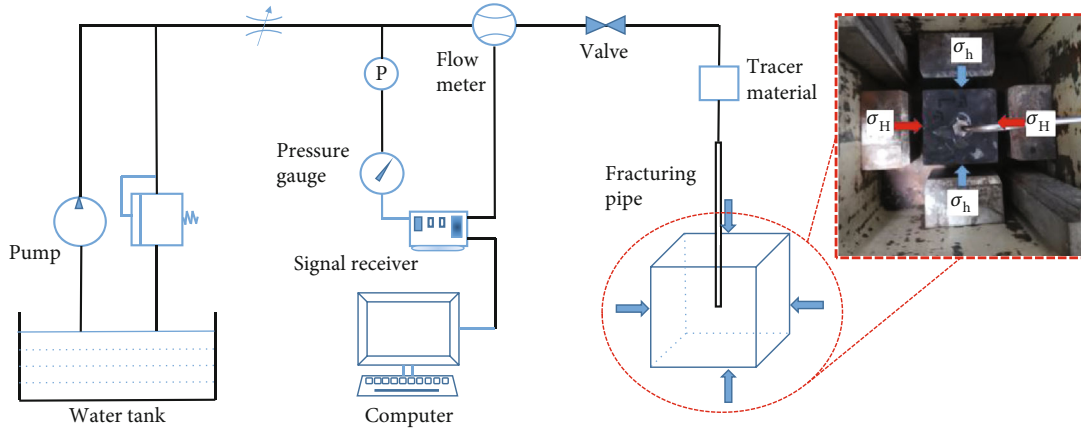
FIGURE 3: True triaxial hydraulic fracturing physical simulation test system.

TABLE 2: Fracturing test parameters.

Sample numbering	Triaxial loading stress parameters (MPa)			$\sigma_H - \sigma_h$	K	Inject rate (ml·min^{-1})
	σ_v	σ_H	σ_h			
1	18	9	8	1	0.125	10
2	18	11	8	3	0.25	10
3	18	13	8	5	0.625	10
4	18	15	8	7	0.875	10
5	18	17	8	9	1.125	10
6	18	17	8	9	1.125	30

blocks were demolded and maintained at constant temperature and humidity for 28 days, a hole with a diameter of 8 mm and a depth of 55 mm was drilled at the top center of each cube, and the wellbore were glued with high-strength epoxy resin AB adhesive as shown in Figure 2(c) and left to stand for 24 hours before conducting the experiment.

2.2. Experimental Setup and Method

2.2.1. Experimental Setup.
Figure 3 shows a true triaxial hydraulic fracturing experimental system. The experimental system consists of a high-pressure water pump system, a true three-axis servo loading system, and a monitoring and control system. The triaxial servo loading system applies the true triaxial stress by hydraulic jacks in three directions on the cubic test block to simulate the suit stress. A high-pressure pumping system injects high-pressure water into the test block. The monitoring and control system is used to accurately control the pressure and flow rate of high-pressure water.

2.2.2. Experimental Method.
As shown in Table 2, the fracturing parameters designed for the experiment are used to simulate the fracture propagation law in coal #15 with natural fractures in Qinshui Basin. $K = (\sigma_H - \sigma_h)/\sigma_h$, where K is the in situ stress difference coefficient. The experiment simulates hydraulic fracturing of vertical wells, and water was chosen as the fracturing fluid, while an appropriate amount of fluorescent agent was added to the water to observe the propagation of the fracture. When triaxial stresses were applied, a
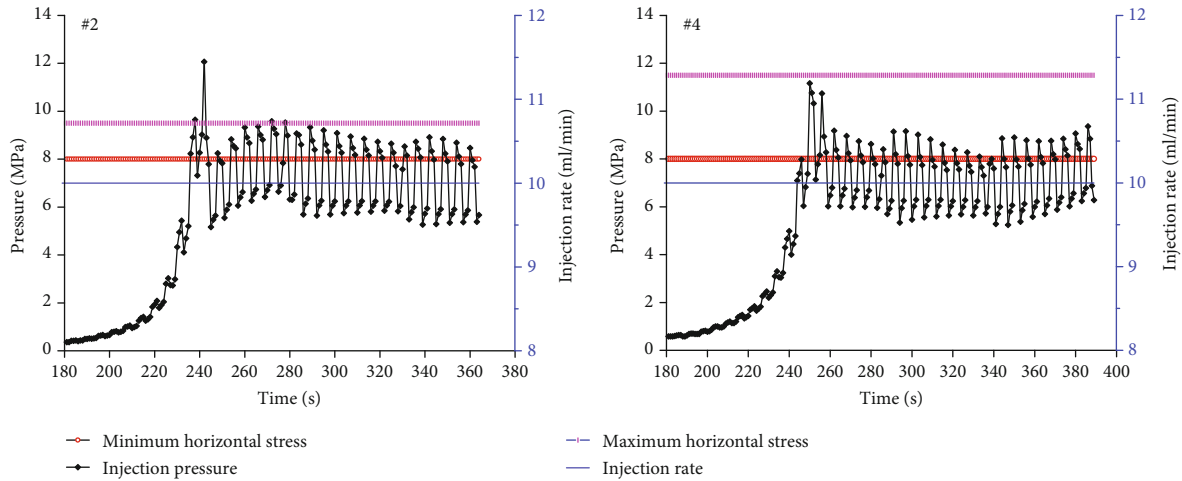
FIGURE 4: Injection pressure process of samples #2 and #4.
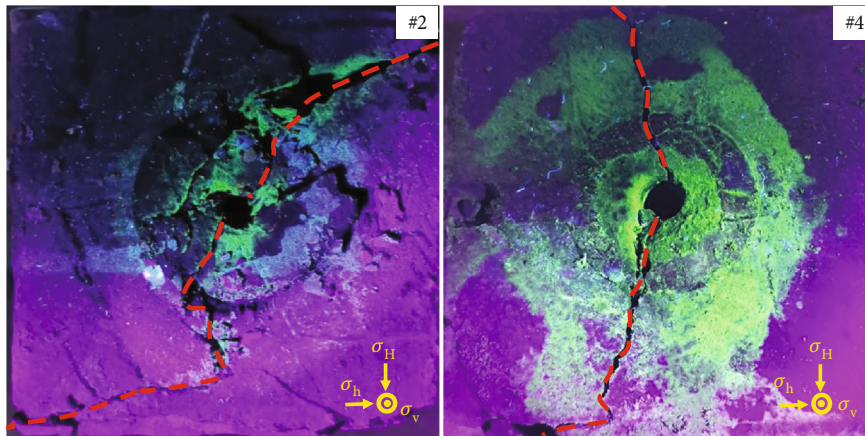
FIGURE 5: Fracture morphology with horizontal stress difference.

multistep loading mode was used to avoid sample shear damage caused by unbalanced loading of three-dimensional stresses. First, the three-dimensional stress was applied at the value of the minimum horizontal principal stress at the same time and remains stable. Then, the vertical stress and the maximum horizontal stress slowly increased to the value of the maximum horizontal principal stress. Finally, the vertical stress was slowly increased to the design value, and after the triaxial stress loading was completed and kept stable for 30 minutes, the high-pressure hydraulic fracturing operation can be carried out. The fracturing pump was controlled by a constant displacement mode, while the computer collects real-time information on the high-pressure pump pressure, piston displacement, and three-way stress.

2.3. Experimental Results and Analysis

2.3.1. Injection Pressure Characteristics. Figure 4 shows the detailed pump pressure curves for samples #2 and #4. Along with the gradual increase of injection pressure, both samples can reach the maximum pump pressure at the initial fracture of the specimens, which corresponded to the opening of the

hydraulic fracture, and the subsequent rapid decrease in injection pressure means that the fracturing fluid entered into the hydraulically induced fractures. Subsequently, the injection pressure fluctuated frequently, which means that the hydraulic fractures propagated during the fracturing process, forming more secondary fractures, and the fracturing fluid filled these new fractures. As fluid seeped into the new fractures, the pressure in the old fractures decreased rapidly, which also resulted in a rapid decrease in pump pressure. In this experiment, a constant injection rate was applied, and the fluid buildup in the new fracture space rapidly increased the injection pressure until the opening of the next fractures. This process was repeated until the experiment was completed, and the increase and decrease of injection pressure fluctuation indicate the continuous creation of fractures [26, 27].

2.3.2. Propagation Characteristics. As shown in Figure 5, the experimental results show that fracture propagation is more complicated for the case of small horizontal deviatoric stress and accompanied by the generation of branch cracks. The major fracture growth direction has a large intersection angle
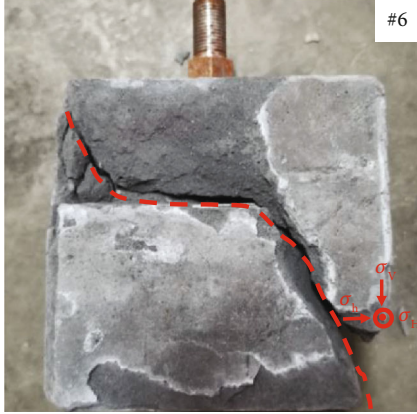
FIGURE 6: Fracture morphology under the injection rate of 30 ml/min.

with the maximum horizontal stress (#2). When horizontal stress difference (HSD) is small, the direction of cracks tends to the direction of the maximum horizontal stress (#4).

In the hydraulic fracturing process, a small injection flow rate (10 ml/min) formed a more obvious major fracture. Also, the fracture direction was controlled by the stress. However, when the injection rate was increased to 30 ml/min, the fracture plane did not extend along the maximum principal stress direction. It first extended perpendicular to the wellbore axis with a portion deflected and extended toward the maximum stress direction and then through the sample (Figure 6). This shows that the high rate of injection can cause the sample to not expand along the direction of maximum horizontal stress at the fracture initiation. This is consistent with the findings in the literature [28, 29].

3. Numerical Simulation

The reservoir hydraulic fractures extend far away, and the fracture extension morphology is often derived indirectly by means of microseismic monitoring or geodetic electrical methods. The small size of experimental samples for indoor experiments also makes it difficult to accurately simulate the real hydraulic fracture extension morphology. Numerical simulation can clearly show the hydraulic fracture propagation under the influence of various factors such as ground stress and natural cracks, which are an effective means to invest in the hydraulic fracture propagation. In this paper, ABAQUS software was used to establish a global cohesive zone model which can simulate the hydraulic fracture extension process in reservoirs containing conjugate fractures. Taking Qinshui coalfield as the background, a two-dimensional numerical model was established.

3.1. Coupling Equations. In this simulation, the tensile-separation criterion with degraded cell stiffness in ABAQUS was used to simulate the fracture initiation and propagation. As the stress on the cohesive unit became larger, the unit stiffness degraded gradually; and when the unit stiffness dropped to 0, the cohesive unit started to fracture and expand. This simulation used the maximum positive stress criterion that

is when the unit in either direction reaches its critical stress, the unit begins to fracture.

$$\max \left\{ \frac{\sigma_n}{\sigma_n^{\max}}, \frac{\tau_s}{\tau_s^{\max}}, \frac{\tau_t}{\tau_t^{\max}} \right\} = 1, \tag{1}$$

where $\sigma_n^{\max}$ refers to the most tensile stress that the unit can withstand in the vertical direction and $\tau_s^{\max}$ and $\tau_t^{\max}$ refer to the maximum shear stress that the unit can withstand in both directions.

A dimensionless damage factor (D) is introduced, taking a value range between 0 and 1. When $D = 0$, no damage occurs to the material; when $D = 1$, the material is completely damaged, and fractures form and continue to propagate; and when $0 < D < 1$, the material is undergoing damage; the following equations are applicable:

$$
\begin{aligned}
\sigma_n &= \begin{cases} (1\text{-}D)\sigma_n', \sigma_n' \geq 0, \\ \sigma_n', \sigma_n', 0, \end{cases} \\
\sigma_s &= (1\text{-}D)\sigma_s', \\
\sigma_t &= (1\text{-}D)\sigma_t',
\end{aligned}
\tag{2}
$$

where $\sigma_n' \geq 0$ represents a cohesive unit subjected to tensile stress and $\sigma_n' < 0$ represents the cohesive unit subjected to compressive stress. σ_n, σ_s, and σ_t represent the normal stress component and the two tangential stress components of the cell under linear elastic condition before the material is damaged.

The fluid flow direction in the cohesive unit is divided into a tangential flow along the cohesive unit and a normal flow perpendicular to the cohesive unit. The tangential flow follows the Newtonian flow formula:

$$q = -\frac{d^2}{12\mu} \nabla P, \tag{3}$$

where q denotes the fracturing fluid discharge volume, m³/min; d denotes the fracture opening width, m; μ denotes the dynamic viscosity of fracturing fluid, mPa·s; and p is the flow pressure, MPa.

The fluid in the fracture is mainly tangential flow, and a small amount of fluid will pass through the normal flow of the fracture to the formation on the upper and lower surface of the cohesive unit. The normal seepage formula of fracturing fluid in the cohesive unit is as follows:

$$
\begin{cases} q_t = c_t(p_i - p_t), \\ q_b = c_b(p_i - p_b), \end{cases}
\tag{4}
$$

where q_t and q_b are the velocity of normal fluid flowing into the upper and lower surfaces of the cohesive unit, m³/s; c_t and c_b are the filtration coefficient of the upper and lower surfaces of the cohesive unit, m/s$^{1/2}$; p_i is the fluid pressure in the plane of cohesive unit; and p_t and p_b are the fluid pressure of the upper and lower surfaces of the cohesive unit, MPa.

3.2. Numerical Simulation Model. Figure 7 shows the 2D reservoir model, which is a square with a side length of 50 meters and two sets of natural fractures. The minimum horizontal stress direction was assumed to be 30° and 150° with respect to the two natural fracture sets in this model. The center of the simulation model is the injection point, and the injection hole is oriented in the same direction as that of maximum horizontal stress. X is the direction of minimum horizontal principal stress, and the Y-axis is the direction of maximum horizontal principal stress. The boundary condition with full displacement constraints was used around the model to limit its horizontal displacement or deformation. Table 3 lists the parameters used in the model.

3.3. Simulation Results

3.3.1. Changes in Stress Field during Fracture Propagation. As the hydraulic fracture opens and expands, the stress field around the hydraulic fracture changes. The hydraulic pressure in the hydraulic fracture will mainly produce induced compressive stress on both sides of the crack, called stress shadow effect. The process of propagation of the dominant hydraulic fracture also forms several small branches of hydraulic fracture, but only one branch can become the main hydraulic fracture. The other fractures close immediately, which is caused by the stress shadow effect. We also observed the change of stress during hydraulic fracture generation and expansion by simulating hydraulic fracturing with horizontal stress difference HSD = 9 MPa.

(1) Variation of the σ_H and Shear Stress τ. From Figure 8(a), the effect of Hydraulic fracture expansion on σ_H was reflected in a significant increase in a small area of the fracture tip region and a smaller increase in other regions. σ_H decreased slightly on both sides of hydraulic fracture. From Figure 8(b), it can be seen that the variation of the shear stress τ is almost 0 at the fracture tip along the fracture length and in the regions on both sides of the fracture. There were obvious changes in shear stress on both tips of the fracture, and the shear stress on both sides of the fracture end point increased on one side and decreased on the other side, which made the fracture end more susceptible to shear damage.

(2) Variation of the Minimum Horizontal Principal Stress σ_h. From Figure 8(c), it can be seen that σ_h increased to various degrees in the whole model area after the creation of hydraulic fracture, especially on both sides perpendicular to the fracture extension direction. The increase in σ_h increased the breaking pressure required to form other hydraulic fractures around the initial fracture and narrowed the width of the generated fractures, which was not conducive to the development of other branch fractures in the same direction.

3.3.2. Main Fracture Morphology and Controlling Factors. Figure 9 shows the morphology of hydraulic fracture when five stress differences HSD = 1 MPa, 3 MPa, 5 MPa, 7 MPa, and 9Mpa were used in the numerical simulation in this paper. Figures 9(a) and 9(b) show that HDS is small, the expansion of hydraulic fractures was obviously affected by
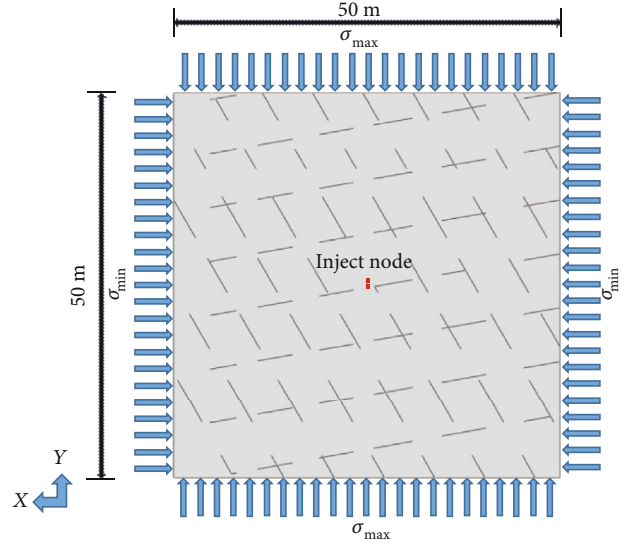
FIGURE 7: Simulation setup for reservoirs with two preexisting natural fracture sets.

TABLE 3: Input parameters for simulating hydraulic fracture propagates in naturally fractured reservoirs.

Parameters	Value
Young's modulus	2.6 GPa
Poisson's ratio	0.25
Formation effective permeability	$2.6E^{-4}$ D
Porosity	8%
Pressure dependent leak-off coefficient	$1E^{-14}$
Specific weight of injection fluid	9800
Fluid viscosity	1 cp
Tensile strength of intact coal	2 MPa
Shear strength of intact coal	6 MPa
Tensile strength of natural fracture	0.55 MPa
Shear strength of natural fracture	1.75 MPa
Fracture displacement	0.001 m
Injection rate	0.01 m³/s
Initial pore pressure	3.14 MPa

natural fractures, and the expansion path was relatively curved. The length of hydraulic fractures on one wing was obviously greater than that of the other wing. The length of the fracture has obvious characteristics of asymmetric expansion. Figures 9(c)–9(e) show the expansion path of the hydraulic fracture under the condition of increasing HSD which was straighter than that of Figures 9(a) and 9(b), and the expansion of the hydraulic fracture was more balanced in both wings.

The stress shadow effect of hydraulic fractures directly affects fracture width, morphology, extension direction, and fracture initiation pressure, which in turn affects the production, recovery, and economic efficiency of horizontal well fracturing design. Wang [12] pointed out that the stress shadow effect and resistance-related fluid distribution were
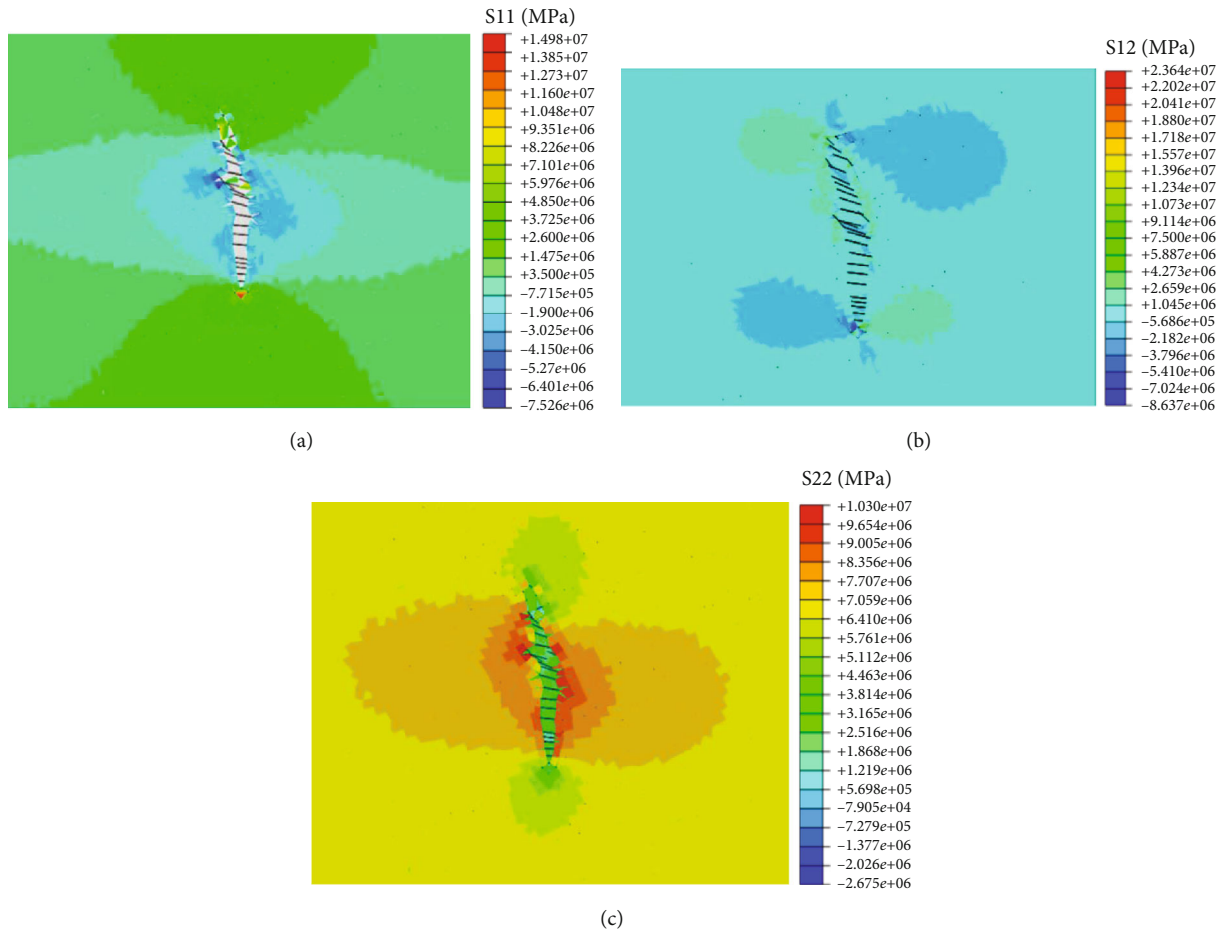
FIGURE 8: Change of hydraulic fracturing on stress field (unit/MPa) (HSD = 9 MPa, step time = 42.55 s): (a) cloud diagram of σ_H; (b) cloud diagram of shear stress τ; (c) cloud diagram of σ_h.
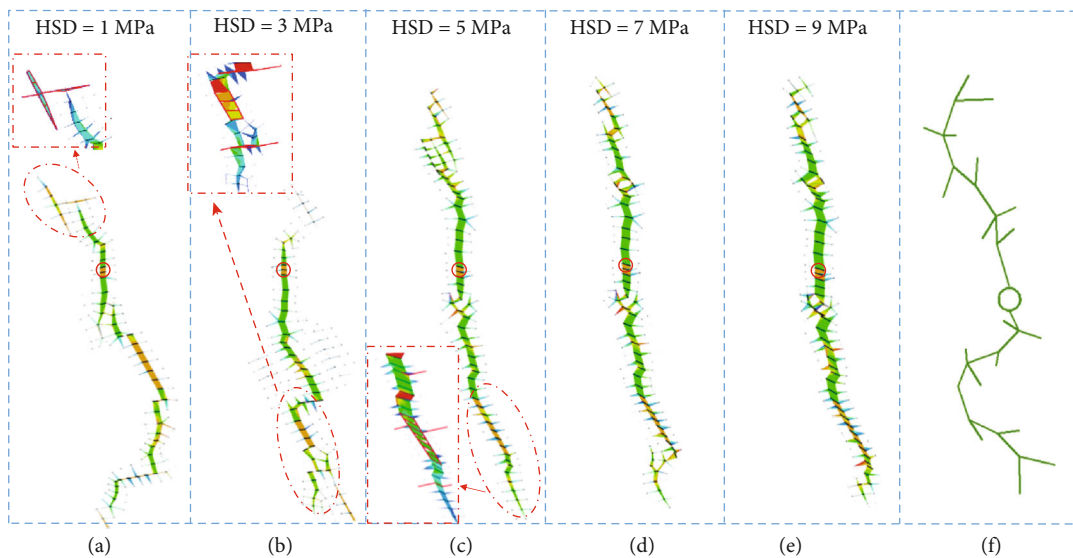
FIGURE 9: Hydraulic fracture morphology with different stress differences.

the main reasons why the hydraulic fractures do not form the expected "tree-like" hydraulic fracture network. Four possible fracture morphologies in the reservoir were predicted.

As shown in Figure 9(f), the hydraulic fracture morphology of this simulation was in good agreement with the complex fracture morphology pointed out by Wang, and the hydraulic
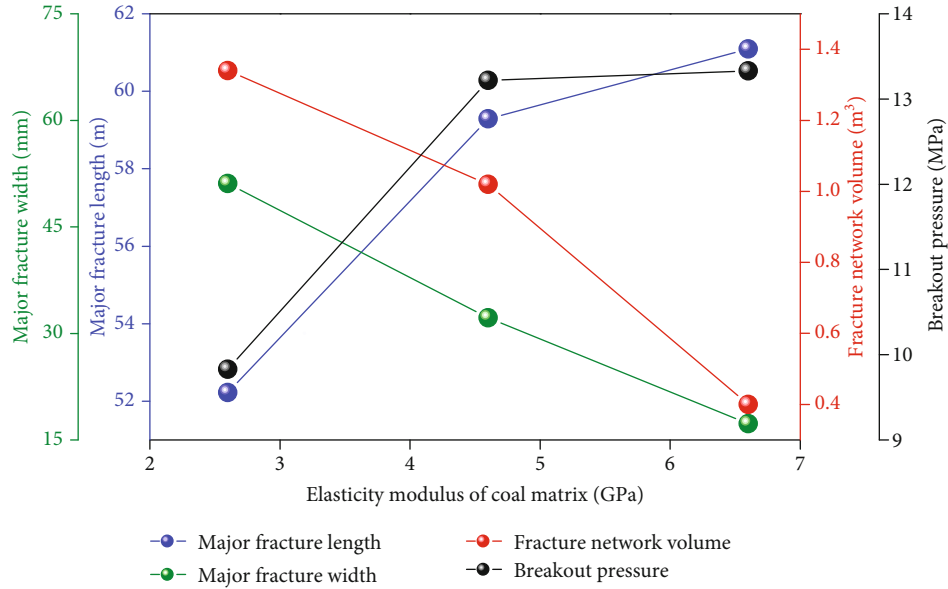
FIGURE 10: Influence of elastic modulus of coal matrix on hydraulic fracture propagation.

fracture consisted of a main fracture and a large number of component branch fractures, with the tip of the main fracture expanding in the opposite direction and the branch fractures not fully developed.

Comparing the experimental results (Figure 5 (#2)) and numerical simulation results (Figure 9(b)), when the HSD = 3 MPa, there is a more obvious angle deviation between the fracture and σ_H. By comparing Figure 5 (#4) and Figure 9(d), when HSD is 7 MPa, the fracture expansion direction tends to the direction of σ_H. The experimental and simulation results verify that the in situ stress has an obvious control effect on the horizontal principal stress. In this simulation, when the local stress difference HSD > 5 MPa, that is, when $K > 0.625$, the fracture direction and σ_H were relatively uniform. The results shown in Figure 9 also demonstrate that the propagation of fractures in fractured coal is obviously controlled by the in situ stress. Even when a large number of natural fractures exist, the main propagation path has not completely changed. Especially when HSD is large, the fractures tend to be single-plane fractures. In the case of high stress difference, the control effect of fracture propagation along the main stress direction is very strong, while in the case of small stress difference, the extension direction of the main fracture is more obviously affected by natural fractures.

3.3.3. Expansion Pattern of Hydraulic Fractures Encountering Natural Fractures.
The numerical simulation shows that there are three forms of expansion when hydraulic fractures encounter natural fractures: (1) stagnation of hydraulic fractures after propagation along natural fractures; (2) the hydraulic fracture extends in the natural fracture for a certain distance, then extends out of the natural fracture and continues to expand; and (3) hydraulic fractures propagate directly through natural fractures. Figure 9(a) shows the fracture extension process when HSD = 1 MPa, the hydraulic

fracture in the upper part stagnates at the fracture along the natural fracture surface while the hydraulic fracture in the lower part continues to extend forward; Figure 9(b) shows the fracture extension process for the case of HSD = 3 MPa. The hydraulic fracture in the upper part first extends within the fracture and then continues to extend forward from the right boundary of the natural fracture. As shown in Figure 9(c), the hydraulic fracture directly passes through the natural fracture and expanded forward when the HSD = 5 MPa, where the shear effect of the hydraulic fracture is obvious. The HSD determines the form of hydraulic fracture through the natural fracture when the approach angle is large. Similarly, Figures 9(d) and 9(e) similarly show the shearing effect of hydraulic fractures on natural fractures under high stress conditions. The higher shearing effect caused friction particles at the interface to plug some of the fractures and thereby decrease the fracture permeability. This situation is not conducive to the development of coalbed methane.

3.3.4. Parametric Analysis on Fracture Propagation

(1) Effect of Elasticity Modulus. To investigate the effect of elastic modulus on hydraulic fracturing, the elastic modulus of coal was set to 2.6, 4.6, and 6.6 GPa, while the elastic moduli of natural fracture were taken as 0.80 GPa, and the model with HSD = 5 MPa was selected; the numerical results are shown in Figure 10. As elastic modulus of coal increases, the fracture fluid injection volume and maximum fracture width of the main fracture decreased, and the length and fracture pressure of the main fracture increased. The analysis shows that the maximum fracture width of the main crack is strongly correlated with the variation of the elastic modulus. When the elastic modulus increased from 2.6 GPa to 4.6 GPa, the maximum fracture width of the main fracture decreased by about 37.0%, the fracturing fluid injection volume
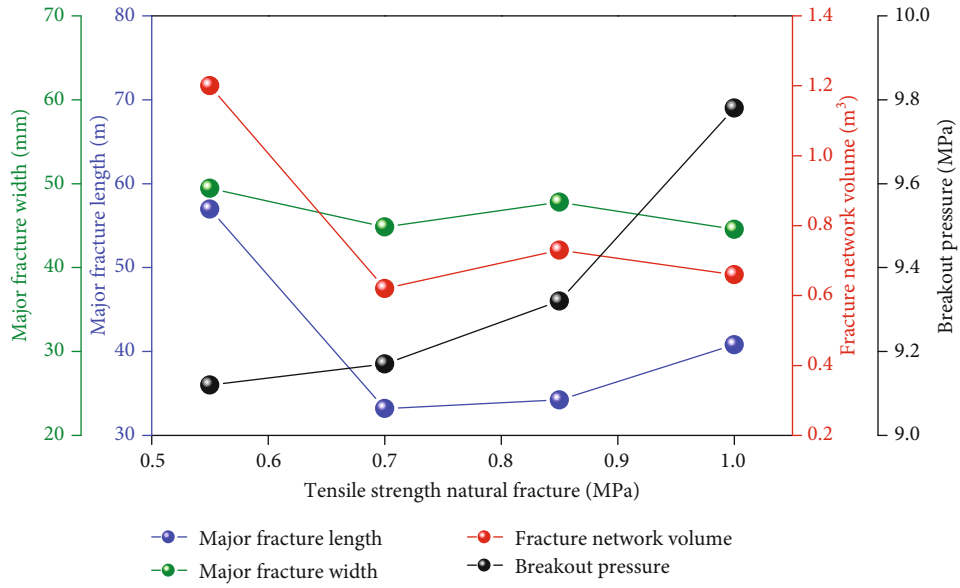
FIGURE 11: Effect of tensile strength of natural fractures on the expansion of hydraulic fractures.
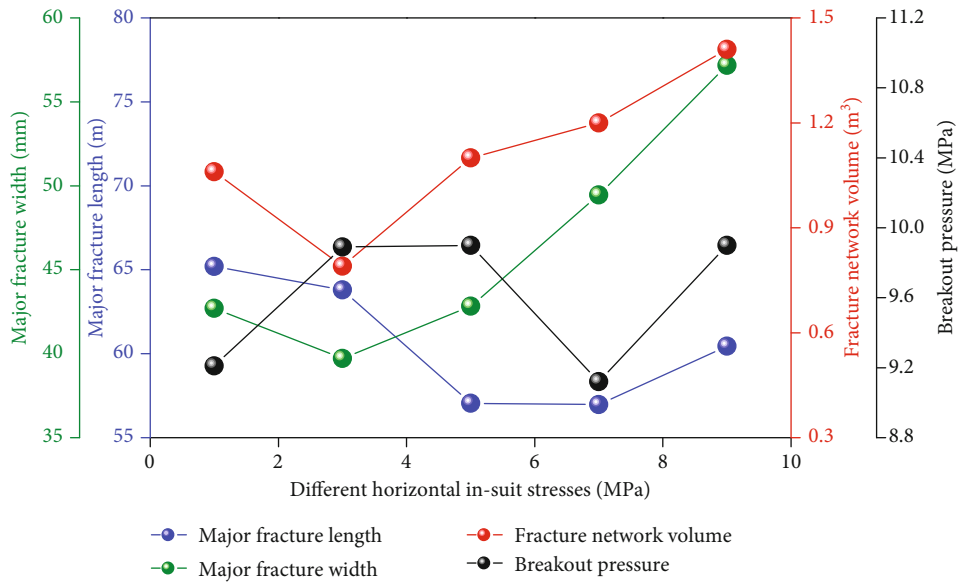
FIGURE 12: Effect of HSD on hydraulic fracture extension.

decreased by about 23.9%, the main fracture length increased by 13.5%, and the fracture pressure increased by 34.5%. This is because the increase of the elastic modulus of the matrix makes the fluid carry more energy into the fracture [30].

(2) Effect of Fracture Toughness on Fracture Propagation. In order to study the effect of tensile strength of natural fractures on hydraulic fracture extension, the tensile strength values of simulated natural fractures were set to 0.55, 0.70, 0.85, and 1 MPa, and the shear strength value was set to be 5 times the tensile strength value, and the fracture strength value of coal matrix was kept constant. Set HSD = 7 MPa, and the values of other parameters were chosen as shown in Table 3. The calculated results (Figure 11) show that the

breaking pressure tends to increase with the increase of natural fracture tensile strength. The length and maximum width of the primary fracture show a decreasing trend, while the fracture volume also shows a decreasing trend. The total volume of hydraulic fractures decreased with increasing tensile strength of natural fractures, because the volume of fractures within the coal matrix produced per unit energy is smaller than that of hydraulic fractures extending within the natural fractures [31–35].

(3) Effect of HSD on Fracture Propagation. To study the effect of in situ stress difference on fracture extension, the HSD were set to 1, 3, 5, 7, and 9 MPa, while keeping the other parameters constant. The results of simulation are shown in
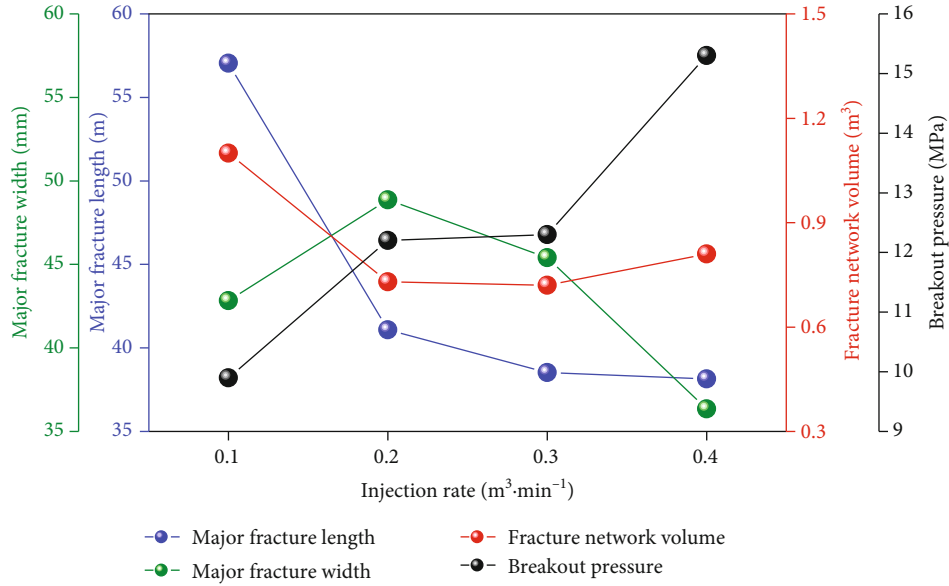
FIGURE 13: Effect of fracturing fluid injection rate on hydraulic fracture propagation.

Figure 12. With the increase of HSD, the length of the main fracture tends to decrease, the width of the main fracture and the volume of fracturing fluid injection increase, and the change in the fracture pressure was not evident. The length of the fracture tends to decrease as the stress difference increases, which is caused by the flatter extension of the fracture when the in situ stress difference increases. When the HSD was large, especially greater than 5 MPa, the hydraulic fracture became more flat and the complexity of the fracture was reduced. The increase of the HSD has a great effect on the fracture fluid injection volume and maximum fracture width of the fracture, while other factors have little influence. When the HSD increases from 1 MPa to 9 MPa, the injection volume of fracturing fluid increases by 33.02%, the maximum fracture width increases by 34.31%, and the fracture length of the main fracture decreases by 7.27%. This shows that HSD controls the geometry of the fractures, and when HSD is small, the angle between the fractures' morphological expansion and the maximum principal stress will increase significantly. This is because the higher HSD increases the initial shear stress in the coal seam, especially in locations with natural fractures, where hydraulic fractures are more likely to expand [36–38].

(4) Effect of Injection Rate on Fracture Propagation. In order to explore the influence of injection rate of fracturing fluid on hydraulic fracture propagation, the injection rate was set to 0.1, 0.2, 0.3, and 0.4 m^3/min. Figure 13 shows the main geometric parameters of hydraulic fractures in different injection rates when the HSD was 5 MPa. The other parameters are presented in Table 3. According to the data in Table 3, the fracture pressure of the fracture has a tendency to increase with the increase of the fracturing fluid injection rate. The fracture volume and length have an obvious tendency to decrease. Meanwhile, from the fracture morphology, the hydraulic fracture is more developed in both wings when the pumping rate is 0.1 m^3/min. Also, the phenomenon that

one wing is fully expanded and the other is not exists when the pumping rate was 0.2, 0.3, and 0.4 m^3/min. Therefore, the pumping speed of hydraulic fracturing was not conducive to the formation of complex fracture network and the high production of CBM when the pumping speed was too large, which is consistent with the findings by the references in the literature [39, 40].

In order to obtain better fracturing effect in industrial field, appropriate stress difference should be utilized during the fracturing process to ensure a larger volume of hydraulic fracture. The stress difference should not be too low in order to make the hydraulic fracture extend farther, pass through more natural fractures, and obtain more complex fractures. The injection rate should also not to be too high in order to ensure that the volume of the hydraulic fracture is larger and the hydraulic fracture extends farther [41, 42].

4. Conclusions

Understanding the law of hydraulic fracture propagation in low-permeability CBM reservoirs with natural fractures is essential for evaluating the complexity of hydraulic fractures and improving the efficiency of CBM development. This study uses a combination of experiments and numerical simulations to study the expansion pattern of hydraulic fractures in fracture-bearing coal reservoirs. The following conclusions can be drawn:

(1) The existence of stress shadow effect makes the hydraulic fractures expand along the main fracture trace, and the branch fractures close quickly without extending too far. Complex fractures are the main fracture morphology in naturally fractured CBM reservoirs. It is difficult for hydraulic fractures to form a complex tree-like seam network in coal reservoirs. The stress shadow effect is caused by the increase of

the minimum principal stress in the surrounding coal of the hydraulic fracture

(2) The horizontal stress difference and natural fractures jointly determine the overall shape of the hydraulic fracture network. When HSD is small, the hydraulic fractures are more complex and the morphology of the hydraulic fractures is significantly influenced by the natural fractures

(3) To ensure the efficiency of hydraulic fracturing, a reservoir environment with a certain horizontal stress difference under specific reservoir conditions can ensure the increase of fractured reservoir volume and the controllability of fracture expansion direction. In order to increase the fractured reservoir volume and fracture length, the pumping rate of fracturing fluid should not be too large

Data Availability

The data that support the findings of this study are available from the corresponding author upon reasonable request.

Conflicts of Interest

No potential conflicts of interest were reported by the authors.

Acknowledgments

References

[1] X. Zhang, C. Wu, Z. Wang, and D. Xu, "Postfracturing permeability prediction for CBM well with the analysis of fracturing pressure decline," *Energy Science & Engineering*, vol. 7, no. 6, pp. 3111–3123, 2019.

[2] T. Jiang, H. Ye, G. Ren et al., "Crack initiation and propagation in coalbed gas reservoir during hydraulic fracturing," *Sādhanā*, vol. 44, no. 2, 2019.

[3] T. Wang, W. Hu, D. Elsworth et al., "The effect of natural fractures on hydraulic fracturing propagation in coal seams," *Journal of Petroleum Science and Engineering*, vol. 150, pp. 180–190, 2017.

[4] Z. Liu, S. Wang, H. Zhao et al., "Effect of random natural fractures on hydraulic fracture propagation geometry in fractured carbonate rocks," *Rock Mechanics and Rock Engineering*, vol. 51, no. 2, pp. 491–511, 2018.

[5] J. Rueda, C. Mejia, R. Quevedo, and D. Roehl, "Impacts of natural fractures on hydraulic fracturing treatment in all asymptotic propagation regimes," *Computer Methods in Applied Mechanics and Engineering*, vol. 371, article 113296, 2020.

[6] J. Zhou, M. Chen, Y. Jin, and G. Q. Zhang, "Analysis of fracture propagation behavior and fracture geometry using a triaxial fracturing system in naturally fractured reservoirs," *International Journal of Rock Mechanics and Mining Sciences*, vol. 45, no. 7, pp. 1143–1152, 2008.

[7] A. Dahi-Taleghani and J. E. Olson, "Numerical modeling of multistranded- hydraulic-fracture propagation: accounting for the interaction between induced and natural fractures," *SPE Journal*, vol. 16, no. 3, pp. 575–581, 2011.

[8] C. Ai, X. X. Li, J. Zhang, D. Jia, and W. J. Tan, "Experimental investigation of propagation mechanisms and fracture morphology for coalbed methane reservoirs," *Petroleum Science*, vol. 15, no. 4, pp. 815–829, 2018.

[9] T. Jiang, J. Zhang, and H. Wu, "Experimental and numerical study on hydraulic fracture propagation in coalbed methane reservoir," *Journal of Natural Gas Science and Engineering*, vol. 35, pp. 455–467, 2016.

[10] B. Huang and J. Liu, "Experimental investigation of the effect of bedding planes on hydraulic fracturing under true triaxial stress," *Rock Mechanics and Rock Engineering*, vol. 50, no. 10, pp. 2627–2643, 2017.

[11] Z. Chen, R. G. Jeffrey, X. Zhang, and J. Kear, "Finite-element simulation of a hydraulic fracture interacting with a natural fracture," *SPE Journal*, vol. 22, no. 1, pp. 219–234, 2017.

[12] H. Y. Wang, "Hydraulic fracture propagation in naturally fractured reservoirs: complex fracture or fracture networks," *Journal of Natural Gas Science and Engineering*, vol. 68, p. 102911, 2019.

[13] B. Carrier and S. Granet, "Numerical modeling of hydraulic fracture problem in permeable medium using cohesive zone model," *Engineering Fracture Mechanics*, vol. 79, pp. 312–328, 2012.

[14] Z. Chong, S. Karekal, X. Li, P. Hou, G. Yang, and S. Liang, "Numerical investigation of hydraulic fracturing in transversely isotropic shale reservoirs based on the discrete element method," *Journal of Natural Gas Science and Engineering*, vol. 46, pp. 398–420, 2017.

[15] J. Zhou, L. Zhang, A. Braun, and Z. Han, "Numerical modeling and investigation of fluid-driven fracture propagation in reservoirs based on a modified fluid-mechanically coupled model in two-dimensional particle flow code," *Energies*, vol. 9, no. 9, p. 699, 2016.

[16] J. S. Yoon, G. Zimmermann, and A. Zang, "Numerical investigation on stress shadowing in fluid injection-induced fracture propagation in naturally fractured geothermal reservoirs," *Rock Mechanics and Rock Engineering*, vol. 48, no. 4, pp. 1439–1454, 2015.

[17] T. Wang, W. Zhou, J. Chen, X. Xiao, Y. Li, and X. Zhao, "Simulation of hydraulic fracturing using particle flow method and application in a coal mine," *International Journal of Coal Geology*, vol. 121, pp. 1–13, 2014.

[18] W. Peng, M. Xian-biao, L. Jin-bin, and D. Chun-zhi, "Study of the borehole hydraulic fracturing and the principle of gas seepage in the coal seam," *Earth & Planetary Science*, vol. 1, no. 1, pp. 1561–1573, 2009.

[19] Y. Ju, Y. Wang, H. Dong, and Y. Yang, "Numerical analysis of the hydrofracturing behaviour of heterogeneous glutenite considering hydro-mechanical coupling effects based on bonded particle models," *International Journal for Numerical and Analytical Methods in Geomechanics*, vol. 42, no. 13, pp. 1493–1515, 2018.

[20] Y. Ju, P. Liu, J. Chen, Y. Yang, and P. G. Ranjith, "CDEM-based analysis of the 3D initiation and propagation of hydro-fracturing cracks in heterogeneous glutenites," *Journal of Natural Gas Science and Engineering*, vol. 35, pp. 614–623, 2016.

[21] F. Zhang and M. Mack, "Integrating fully coupled geomechanical modeling with microsesmicity for the analysis of refracturing treatment," *Journal of Natural Gas Science and Engineering*, vol. 46, pp. 16–25, 2017.

[22] H. Kang, H. Lv, F. Gao, X. Meng, and Y. Feng, "Understanding mechanisms of destressing mining-induced stresses using hydraulic fracturing," *International Journal of Coal Geology*, vol. 196, pp. 19–28, 2018.

[23] M. M. Rahman, "Constrained hydraulic fracture optimization improves recovery from low permeable oil reservoirs," *Energy Sources, Part A: Recovery, Utilization, and Environmental Effects*, vol. 30, no. 6, pp. 536–551, 2008.

[24] S. Lyu, S. Wang, X. Chen et al., "Natural fractures in soft coal seams and their effect on hydraulic fracture propagation: a field study," *Journal of Petroleum Science and Engineering*, vol. 192, p. 107255, 2020.

[25] X. Hou, Y. Zhu, S. Chen, and Y. Wang, "Gas flow mechanisms under the effects of pore structures and permeability characteristics in source rocks of coal measures in Qinshui Basin, China," *Energy Exploration & Exploitation*, vol. 35, no. 3, pp. 338–355, 2017.

[26] A. N. Dehghan, K. Goshtasbi, K. Ahangari, Y. Jin, and A. Bahmani, "3D numerical modeling of the propagation of hydraulic fracture at its intersection with natural (pre-existing) fracture," *Rock Mechanics and Rock Engineering*, vol. 50, no. 2, pp. 367–386, 2017.

[27] S. J. Lee and K. S. Lee, "Performance of shale gas reservoirs with nonuniform multiple hydraulic fractures," *Energy Sources, Part A: Recovery, Utilization, and Environmental Effects*, vol. 37, no. 13, pp. 1455–1463, 2015.

[28] T. Guo, S. Zhang, Z. Qu, T. Zhou, Y. Xiao, and J. Gao, "Experimental study of hydraulic fracturing for shale by stimulated reservoir volume," *Fuel*, vol. 128, pp. 373–380, 2014.

[29] A. Pak and D. H. Chan, "Effects of permeability and cementation on the pattern of hydraulically induced fractures in oil sands," *Energy Sources, Part A: Recovery, Utilization, and Environmental Effects*, vol. 31, no. 2, pp. 149–162, 2009.

[30] S. Yaobin, L. Weiyong, H. Changchun, and B. Erhu, "Numerical simulation of the influence of natural fractures on hydraulic fracture propagation," *Geofluids*, vol. 2020, Article ID 8878548, 12 pages, 2020.

[31] Z. Chong, Q. Yao, and X. Li, "Effect of joint geometrical parameters on hydraulic fracture network propagation in naturally jointed shale reservoirs," *Geofluids*, vol. 2018, Article ID 1852604, 23 pages, 2018.

[32] Y. Zheng, J. Liu, and Y. Lei, "The propagation behavior of hydraulic fracture in rock mass with cemented joints," *Geofluids*, vol. 2019, Article ID 5406870, 15 pages, 2019.

[33] F. Dou, J. G. Wang, H. Wang, B. Hu, and C. Li, "Discrete element analysis for hydraulic fracture propagations in laminated reservoirs with complex initial joint properties," *Geofluids*, vol. 2019, Article ID 3958583, 23 pages, 2019.

[34] J. Zhang, Y. W. Li, W. Li et al., "Study on propagation behaviors of hydraulic fracture network in tight sandstone formation with closed cemented natural fractures," *Geofluids*, vol. 2020, Article ID 8833324, 22 pages, 2020.

[35] K. Zhao, P. Jiang, Y. Feng, X. Sun, L. Cheng, and J. Zheng, "Numerical investigation of hydraulic fracture propagation in naturally fractured reservoirs based on lattice spring model," *Geofluids*, vol. 2020, Article ID 8845990, 18 pages, 2020.

[36] Z. Zhao, Y. Zheng, Y. Kang, B. Zeng, and Y. Song, "Investigation on nonuniform extension of hydraulic fracture in shale gas formation," *Geofluids*, vol. 2021, Article ID 5516040, 11 pages, 2021.

[37] Z. Q. Li, X. L. Li, J. B. Yu et al., "Influence of existing natural fractures and beddings on the formation of fracture network during hydraulic fracturing based on the extended finite element method," *Geomechanics and Geophysics for Geo-Energy and Geo-Resources*, vol. 6, no. 4, 2020.

[38] O. Kresse, X. Weng, H. Gu, and R. Wu, "Numerical modeling of hydraulic fractures interaction in complex naturally fractured formations," *Rock Mechanics and Rock Engineering*, vol. 46, no. 3, pp. 555–568, 2013.

[39] V. P. Nguyen, H. Lian, T. Rabczuk, and S. Bordas, "Modelling hydraulic fractures in porous media using flow cohesive interface elements," *Engineering Geology*, vol. 225, pp. 68–82, 2017.

[40] Q. Bai, Z. Liu, C. Zhang, and F. Wang, "Geometry nature of hydraulic fracture propagation from oriented perforations and implications for directional hydraulic fracturing," *Computers and Geotechnics*, vol. 125, p. 103682, 2020.

[41] Z. Liu, J. Yang, L. Yang, X. Ren, X. Peng, and H. Lian, "Experimental study on the influencing factors of hydraulic fracture initiation from prefabricated crack tips," *Engineering Fracture Mechanics*, vol. 250, p. 107790, 2021.

[42] Y. Jiang, H. Lian, V. P. Nguyen, and W. Liang, "Propagation behavior of hydraulic fracture across the coal-rock interface under different interfacial friction coefficients and a new prediction model," *Journal of Natural Gas Science and Engineering*, vol. 68, p. 102894, 2019.

WILEY | Hindawi

Research Article

Study on the Relationship between Fracture Morphology and Splitting Strength of Granite Based on Fabric Distribution

GuangSheng Du [ID],[1] ShiJiang Chen [ID],[1] Xiaoyi Chen [ID],[1] Yunfeng Gao,[2] and Hailong Wu[2]

[1]*College of Mining and Coal, Inner Mongolia University of Science and Technology, Baotou, 014010 Inner Mongolia, China*
[2]*Wulat Front Banner Yuanda Business Company with Limited Liability, China*

Correspondence should be addressed to ShiJiang Chen; chenshijiang_2003@163.com

Because of the requirement of the mechanical properties of the damaged surrounding granite rock and the existence of the fracture water in hydraulic fracturing engineering, the strength of granite is related to the fabric, and the roughness of the section is also related to the liquid flow rate, a method of roughly determining the strength of the specimen by observing the failure mode of rock is needed. Considering that the physical and mechanical properties of granite are obviously affected by the fabric, the discrete element numerical simulation method was used to reconstruct the granite fabric based on the spatial correlation function to simulate the splitting experiment to investigate the failure mode of the specimen. The relationship between strength, the fractal value of cross-section, and the fabric was analyzed, which was verified through experiment. The results show that (1) the Voronoi GBM model with spatial correlation function of the discrete element can effectively simulate the controllable granite fabric and carry out micromechanical analysis. (2) The strength of the granite specimen and the fractal value of the cross-section have an obvious linear relationship with the fabric; besides, there is also a certain linear relationship between the strength of the specimen and the fractal value, which is influenced by granite fabric. (3) The predicted strength of the specimen according to the fractal value of the section is in good agreement with the actual strength with the error rate of 30%. In a word, this method can predict the strength of the specimen through the failure section and analyze the hydraulic fracture section and water pressure.

1. Introduction

During the hot dry rock mining, because surrounding rocks are mainly composed of granite, the main construction method is hydraulic fracturing; the hydraulic pressure strength and the shape of water fracture are the most important aspects to be focused [1–3]. For multicomponent crystalline rocks such as granite, the strength characteristic and fracture distribution are related to the internal crystal fabric. Therefore, an interactive relationship can be established to evaluate the hydraulic fracturing effect and water fracture development under different water pressures. Moreover, the strength characteristics are required by hydraulic fracturing [4–11], but it is difficult to carry out the test on-site; therefore, there is a certain engineering significance to establish a

model for predicting the strength of the rock through the preliminary detection of the failure morphology of the rock so as to delimit the range of water pressure.

Previous research found that the root cause of the macrofailure of rock is the development and expansion of internal microcracks. Therefore, it is more suitable to analyze the failure mechanism of granite rock from the microperspective, and it is found that the mineral content and distribution have a great impact on its strength to some extent [12–16]. As shown in Figure 1, there are three kinds of microcracks formed in the process of failure, including intergranular cracks between different components, intergranular cracks between the same component, and cracks through the crystal. Obviously, they are greatly related to the mineral content, distribution pattern, and crystal interface. Some researchers

(a)   (b)
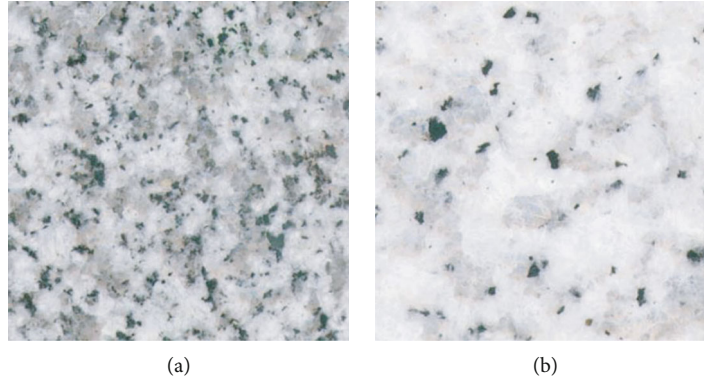
FIGURE 1: Comparison of granites with different fabrics with length and width of 30 mm [16].

found that the mineral content and distribution also had a significant impact on its morphology after failure [17–21], as shown in Figure 2.

According to the study mentioned above, it can be found that the characteristics of granite structure have a certain influence on the strength and failure form of the specimen. On the one hand, it is necessary to define a parameter that can effectively represent the shape of granite after failure. In fact, rock failure generally presents tensile shear failure, which is the most important failure form. Xie and Wang [22] put forward a fractal theory to describe rock fractures, and it can effectively quantify the damage of rock. Scholars have done much research on rock structure and fracture [23–26]; Chen et al. [27] described the rock surface roughness using the fractal method. On the other hand, for granite with different mineral contents and distributions, it is generally difficult to control its structure characteristic. So, the numerical simulation method is used in the study [28–33]. Some scholars have adopted the finite element method to construct the model, but there are some defects in reflecting the rock failure form. The discrete element numerical model method is used to reconstruct the mesoscopic rock structure [34–37]. Considering the distribution of minerals and anisotropy in granite, some scholars have considered homogenization, Weibull strength distribution, digital image restoration, and spatial correlation distribution [38–45]; it is difficult to control the randomness of homogeneous material modelling and Weibull function distribution modelling accurately. The digital image reconstruction method has high accuracy in modelling, but the workload is huge and still affected by the original rock distribution. The construction method of the digital function model represented by the spatial correlation function has the advantage of a highly quantitative model. In addition, the GBM model and structure model with Voronoi were proposed to take the crystal distribution into account [46–49]; they can effectively construct the crystal structure inside granite and make the failure effect consistent with the actual situation.

In this study, the spatial correlation function image Voronoi GBM modelling method is used to build the numerical model of granite rock with different mineral distributions and different component contents. Because the rock failure is mostly tensile shear failure, and the complete section is easy
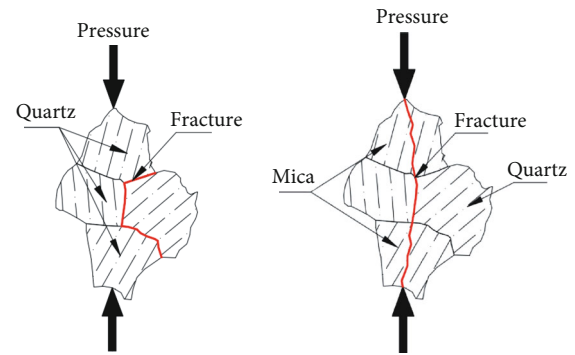
FIGURE 2: Development of granite fractures under different fabric conditions [19].

to be formed by splitting, the Brazilian splitting test is carried out on the numerical model, and the microcracks of the section are obtained, and then, the fractal calculation is carried out on this section. The correlation analysis of the results is carried out to establish a model for estimating the strength of the specimen with the section shape of the specimen.

2. Construction of Granite Model

In this study, particle flow code element numerical simulation software (PFC) is used for model construction and research; it is necessary to calibrate the corresponding parameter. Firstly, the vector models of different fabrics in granite are constructed by digital image technology. Then, the crystal structure is constructed through the Voronoi GBM model. Finally, the actual physical tests are carried out to match the strength.

2.1. Vectorization of Different Fabric Distributions

(1) The same parameters of a digital camera are set to obtain the information of granite surface and adjust it

(2) The recorded image is processed in MATLAB software. Firstly, the grey level processing is carried out to make the image into 0-255 different grey levels. Then, the grey value of 0-96 is used for mica, 96-195 is used for quartz, and 196-255 is for feldspar.

Finally, the images with three textures are obtained by median denoising

(3) After median denoising, the edge image is imported into R2V for vectorization to form the recognized vector boundary model

The numerical image processing and components are shown in Figure 3.

2.2. Numerical Model of the Internal Structure of Granite. According to many experimental results, it can be known that different minerals in granite will form their own crystallization during diagenesis; in order to ensure the accuracy of the model, Potyondy [50] proposed the GBM equivalent crystal model, which is used to construct the internal crystal structure of granite. At the same time, in order to improve the controllability of the crystal, the Voronoi polygon is used to construct the crystal grid, whose strength is set to be 40% of its mineral strength. The process is shown in Figure 4.

(1) Import the vector structure into Rhinoceros software and adjust the orientation

(2) The total number of crystals generated in different mineral areas is determined by crystal size

(3) The generated crystal structure network is imported into PFC, and different models and parameters are set

2.3. Parameter Calibration of Numerical Model. In the PFC model, the parallel bond model was adopted, which can define the bond component and transfer the force between particles. When the ultimate strength of the bond component is reached, it will fail, and the model changes into a linear contact model. Then, the vector boundary of the image of the granite specimen is imported into PFC software to construct the model reflecting the original rock fabric characteristics. Referring to the previous calibration of the microparameter of granite [51–59], combined with some physical and mechanical parameters measured in this test, the parameters of this model were determined. After repeated calibration, the stress curve of the numerical test is almost consistent with the indoor test, as shown in Figure 5. The calibration results of mesoscopic parameters are shown in Tables 1 and 2.

3. The Numerical Simulation of Granite with Different Fabrics

It is difficult to obtain the samples with the controllable component distribution and mineral content in the actual test, but the granite surface with different component distributions and mineral contents controlled by parameters can be effectively reconstructed by using the spatial correlation coefficient. Furthermore, the splitting test, which is easy to obtain the section morphology, was carried out.

3.1. Construction of Granite Surface with Different Fabrics. In the process of diagenesis, the components of each mineral are
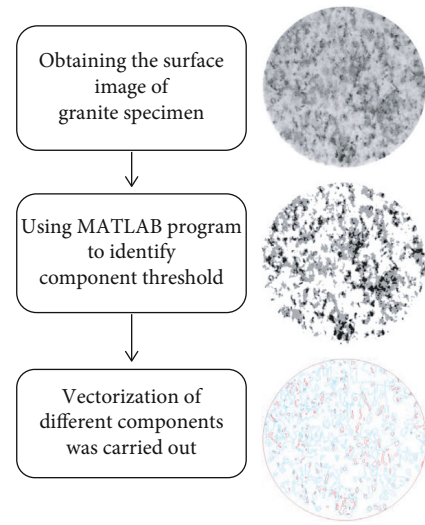
Figure 3: Acquisition process of the component position structure of the test piece.
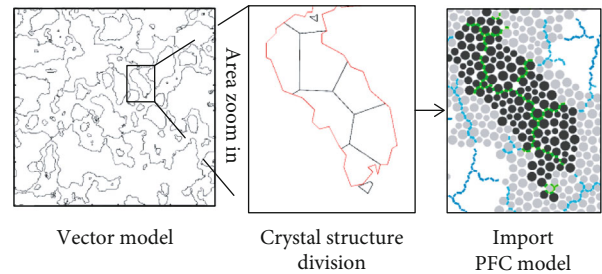
Figure 4: GBM-Voronoi crystal structure construction process.
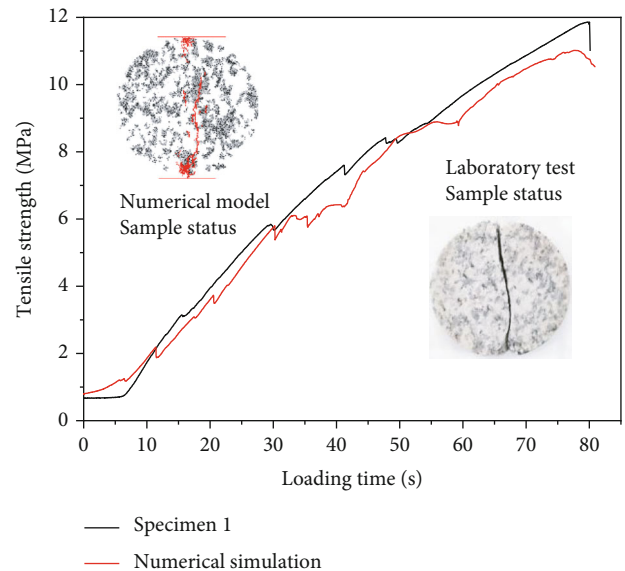
Figure 5: Matching curve of the numerical model and indoor test parameters.

TABLE 1: Particle mesoscopic parameters.

Component parameters	Mineral		
	Feldspar	Quartz	Mica
Minimum particle size (mm)	0.15	0.15	0.15
Particle size ratio	1.60	1.60	1.60
Density (kg/m^3)	2750	3100	2650
Particle modulus (GPa)	20	40	10
Normal/tangential stiffness ratio	2.5	2	4
Friction coefficient	0.75	0.80	0.25
Porosity (%)		0.954	

not random but have certain correlation characteristics; the mineral distribution in a certain area has specific aggregation, and different minerals maintain certain differentiation. Because of the different mechanical properties of minerals, it has an important influence on the fracture development of rock. In this paper, the spatial correlation function is introduced to generate rock images with different fabric characteristics by changing the correlation parameters.

(1) A two-dimensional random array A is established in MATLAB; the values of "$a_{i,j}$" in the array are evenly distributed in (0-1). In order to calculate the aggregation superposition, the elements in matrix A are binarized. When $0 < a_{i,j} < 0.5$, $a_{i,j} = -1$; when $0.5 < a_{i,j} < 1$, $a_{i,j} = +1$

(2) In order to generate the rock image with obvious characteristics of mineral fabric aggregation, it is necessary to process the random image of array A by introducing the spatial correlation function to transform it. The spatial correlation function is shown in formula (1), and the superposition method is shown in formula (2). Then, array B is obtained, and rock images with obvious mineral fabric aggregation characteristics are generated. In Equation (1), parameter L controls the degree of fabric accumulation of rocks and minerals. Array B is the rock image at $L = 6$

$$f(d) = e^{-d/L}, \tag{1}$$

where L is the spatial correlation length and D is the effective distance between two element points.

$$bi, j = \sum_{p=-n}^{n} \sum_{q=-n}^{n} ai + p, j + qf(d(p,q)) \tag{2}$$

(3) The solved array B is converted into a matrix with a numerical range of 0-255. At this time, the numerical range of the matrix is consistent with the grey value of the image. Different thresholds are selected for different component contents using the grey value component partition method. Figure 6 is the distribution map of three different components after greyscale division

3.2. Model Characteristics of Granite with Different Fabrics. During the formation of rock crystallization, if the spatial correlation of different components (i.e., mineral accumulation) is only considered, the spatial correlation length segment should be selected as $L = 2, 4, 6, 8, 10$ and mica content $x = 0.1$. At this time, the calculation results of different spatial correlation lengths are shown in Figure 7. Given the content of mica in low-strength minerals, which has an obvious influence on the mechanical properties of the specimen, the mesostructure characterization of its spatial correlation is considered when the content of the component is different. Taking the space-related length $L = 6$ as an example, the mica content $x = 0.1, 0.15, 0.2, 0.25,$ and 0.3 are obtained. The calculation results of different mineral composition contents are shown in Figure 7.

3.3. Numerical Model Results. The images of different structures generated above were imported into the PFC to build the corresponding numerical model. The Brazilian splitting test method was used to load the model, and the peak strength of the final specimen is shown in Table 3.

4. Fractal Calculation of Granite with Different Fabric Sections

Through the processing above, the splitting strength of different fabric granite and the fracture distribution can be observed and recorded. In actual engineering, the information of the section is relatively easy to obtain, and it is a key to conduct a deeper study of granite. In recent years, fractal dimension has been widely used to describe rough surface because of its quantitative advantage and accuracy in describing fracture structure. In this study, the fractal dimension is selected to quantitatively describe the failure section.

4.1. Fractal Principle and Process. Fractal dimension is a method that can describe the complexity of the surface. In this experiment, a simple and classic box algorithm in a fractal is used, in which the image is divided into $2n$ ($n = 1, 2, 3 \cdots$) different scales and the lattice of the pixels is counted. Equation (3) is used for calculation and fitting to obtain the final fractal dimension D. Figure 8 shows the fractal calculation results of $L = 6, x = 0.1$ fracture.

$$D = -\lim \frac{\lg N(L)}{\lg L}, \tag{3}$$

where D is the box-counting dimension, $N(L)$ is the number of grids of the fractal body covered when the grid-scale is L, and L is the grid scale.

The fractal process is as follows:

(1) At the end of the test, the image of the fracture point of the numerical specimen is derived

(2) The image is adjusted to 2^n pixels so as to facilitate the next fractal calculation

(3) The processed image is imported into MATLAB for further image contour extraction and grey denoising

TABLE 2: Contact micromechanical parameters.

Parameter	Mineral composition					
	Feldspar	Quartz	Mica	Feldspar texture	Quartz texture	Mica texture
Normal/tangential stiffness ratio	1.5	1.5	2.5	1.5	1.5	2.5
Bond modulus (GPa)	45	61	20	36	48.8	16
Tensile force (MPa)	46.2	58.2	23.1	18.4	23.3	9.24
Cohesion (MPa)	83.0	90.1	45.1	33.2	36.1	18.0
Friction angle (°)	23	25	27	23	25	27
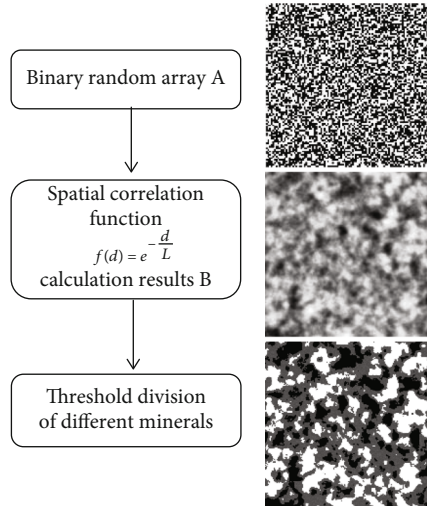
FIGURE 6: Numerical realization of rock fabric image.

(4) Finally, the box dimension algorithm programmed by MATLAB is used to divide the recognition domain of the image and fit the final fractal result D

4.2. Fractal Calculation Test Results. After the experiment, the image of the fracture is extracted, as shown in Figure 5, the fracture profile of the specimen. Considering the randomness of the model and fracture, specimens with the different number of fractures is tested. The purpose of this experiment is to investigate the variation of the fracture with the composition changing and to unify the treatment of fractures, which is done by counting the fractal results of 1000 fractures. The specific method calculates the fractal of the total fracture image and then brings the $D_c = D_{initial} \times (N/1000)$ value, where n is the total number of counted fractures. The stable fractal results of 1000 fractures can be obtained, which can represent the relative complexity of the fracture section, as shown in Table. 4.

5. Numerical Experiments and Fractal Analysis

5.1. Analysis of Numerical Test Results. In this experiment, the samples with different mineral aggregations, i.e., spatial correlation coefficient $L = 2, 4, 6, 8, 10$, were constructed; besides, each mineral aggregation was also constructed with different mica content, i.e., $x = 10\%, 15\%, 20\%, 25\%, 30\%$. In order to improve the accuracy and generality of the test, five groups of tests were carried out for every specimen, and the

test results were averaged. According to the numerical test results, it can be indicated that there is a certain relationship between the distribution of different fabrics and its strength, which is fitted by the Pearson correlation coefficient, as shown in Formula (4).

$$\text{Correl}(X, Y) = \frac{\sum (x - \bar{x})(y - \bar{y})}{\sqrt{\sum (x - \bar{x})^2 (y - \bar{y})^2}}. \quad (4)$$

While considering the influence of the component content, the correlation coefficients of strength and mica content are set as -0.9843, -0.98295, -0.8239, -0.7052, and -0.8049 when $L = 2, 4, 6, 8$, and 10, respectively. It can be seen that there is a strong negative correlation between the strength and mica content regardless of the component distribution; at the same time, as the L value increases, the correlation between strength and mica content decreases. It is observed that as the degree of polymerization of components increases, the homogeneity of the specimens decreases, making the strength fluctuate. According to the linear fitting analysis based on the strong correlation, the linear relationship between the strength of five groups of specimens and the mica content can be obtained, as shown in Figure 9(a). It can be seen that except for $L = 8$, the R^2 of the fitting curve for other L values is relatively high and maintain a high value, suggesting that there is a very strong linear relationship between the component content and the strength of the granite samples.

While considering the effect of component distribution, the correlation coefficients between L and strength are -0.9365, -0.9755, -0.9093, -0.9190, and -0.9557 when the mica content is 10%, 15%, 20%, 25%, and 30%, respectively. The results show that there is a strong negative correlation between the strength of the specimen and the polymerization of its components; the strength of the specimen decreases with the increase of the aggregation degree of the components. At the same time, based on the strong correlation, the linear fitting between the strength of the specimen and its polymerization is carried out, and the results are shown in Figure 9(b). The results show that there is an obvious linear relationship between the strength of the specimen and the degree of polymerization.

5.2. Fracture Fractal Analysis Results. In this experiment, the fractal of the crack image is calculated after the stress dropping; then, the crack is processed to show the state of its section. In order to explore the relationship between the
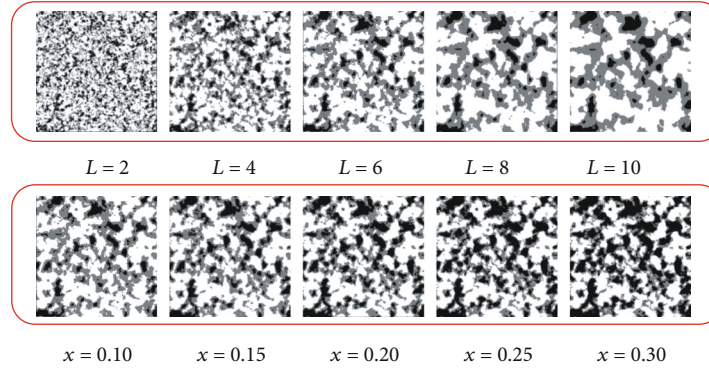
FIGURE 7: Image of different fabric granite specimens.

TABLE 3: Results of splitting strength of specimens with different fabrics.

| Components distribution | Tensile strength (MPa) | | | | |
Mica content	$L = 2$	$L = 4$	$L = 6$	$L = 8$	$L = 10$
$x = 0.10$	17.07	15.28	13.67	12.71	11.94
$x = 0.15$	13.45	12.15	10.74	10.25	9.46
$x = 0.20$	10.39	11.28	9.73	9.78	8.39
$x = 0.25$	9.61	9.76	9.93	9.51	7.77
$x = 0.35$	9.13	8.37	8.51	8.59	6.97

- ■ Data point
- —— Fit line $y = 1.341x + 3.7713$ $R^2 = 0.9988$
- $D = 1.341$
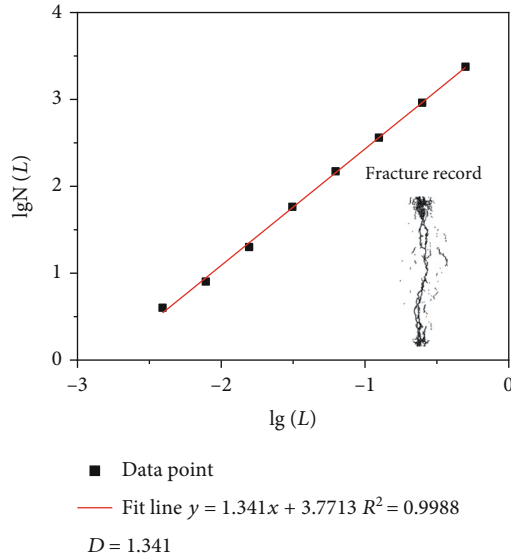
FIGURE 8: Calculation results of fractal dimension of $L = 6$ specimen.

complexity of the section and the internal fabric of the rock, the same correlation algorithm is used for the correlation test.

While considering the effect of the component content, under the condition of different polymerization degrees, The correlation coefficients of mineral aggregation degree and fractal dimension of fracture surface are -0.9674, - 0.9326, - 0.8295, -0.9477, -0.9962, and -0.9346 for $L = 2$, 4, 6, 8, and 10, respectively. The results show that the fractal

dimension of the fracture is strongly correlated with the mica content under conditions of different mineral polymerizations, and the correlation is as high as -0.9962 for $L = 8$, as shown in Figure 10(a). Obviously, there is a strong positive linear relationship between the fractal value of cross-section and the mica content of the specimen.

While considering the effect of component distribution, the correlation coefficients are 0.6819, 0.6452, 0.8536, 0.9621, and 0.8773 when the mica content $x = 10\%$, 15%, 20%, 25%, and 30%, respectively. It can be seen that the mineral polymerization has a certain correlation with the cross-section of the specimen, as shown in Figure 10(b). When the mica content is low, this correlation is low, which can be explained as that when the mica content is low, the specimen with a high degree of polymerization presents obvious anisotropy, affecting the fractal value of the specimen section. For a certain degree of correlation, the fractal distribution of different components in the section is fitted in Figure 10(b). Similarly, when the mica content is low, the correlation between the component distribution and the fracture section is poor, which can not be fitted by an obvious linear relationship. However, according to the observation, it can be seen that with the increase of mineral aggregation, the fracture fractal also presents an increasing trend.

5.3. Fractal Analysis of Specimen Strength and Fracture Section. It is analyzed that there is a very obvious linear relationship between the strength of the specimen and its fabric, as well as the fractal of the section and the fabric of the specimen. So, accordingly, the correlation between the strength of the specimen and the fractal of the section can be established, which is 0.45574. The correlation between the two groups of data is low, which is corresponding to the phenomenon of poor regularity found before. In fact, the influence of component polymerization degree and mica content on fracture fractal should also be considered. When $L = 2, 4, 6, 8$, and 10, the correlation between fractal dimension and strength is 0.9595, 0.97725, 0.4452, 0.5345, and 0.8211, and the average value is 0.7475, which is obviously higher than the simply calculated fractal value. It can be seen that there is a high correlation between the section fractal and the strength of the specimen of different component contents under the condition of different degrees of polymerization, as shown in

TABLE 4: Fractal results of fracture numerical test section of specimens with different fabrics.

| Components distribution | Section fractal dimension D | | | | |
Mica content	$L = 2$	$L = 4$	$L = 6$	$L = 8$	$L = 10$
$x = 0.10$	0.912315	0.992276	0.992943	1.060564	0.991415
$x = 0.15$	0.890919	0.894577	0.844273	0.930608	0.96675
$x = 0.20$	0.846622	0.838361	0.835241	0.906288	0.942929
$x = 0.25$	0.781603	0.819526	0.835196	0.857879	0.929199
$x = 0.35$	0.782504	0.803829	0.79966	0.826024	0.90456

(a) Relationship between mica content and specimen strength

- $L = 2$ —— $y = -25.70x + 19.28$ $R^2 = 0.9689$
- $L = 4$ - - - $y = -19.75x + 15.16$ $R^2 = 0.9661$
- $L = 6$ -·-· $y = -11.01x + 12.12$ $R^2 = 0.6788$
- $L = 8$ ······ $y = -7.83x + 4.55$ $R^2 = 0.4927$
- $L = 10$ ······ $y = -8.22x + 9.96$ $R^2 = 0.6479$

(b) Relationship between the mineral distribution and specimen strength

- 0.1 —— $y = -0.986x + 17.58$ $R^2 = 0.877$
- 0.15 - - - $y = -0.809x + 16.23$ $R^2 = 0.955$
- 0.2 -·-· $y = -0.557x + 13.86$ $R^2 = 0.769$
- 0.25 ······ $y = -0.448x + 13.86$ $R^2 = 0.845$
- 0.3 ······ $y = -0.582x + 12.39$ $R^2 = 0.913$
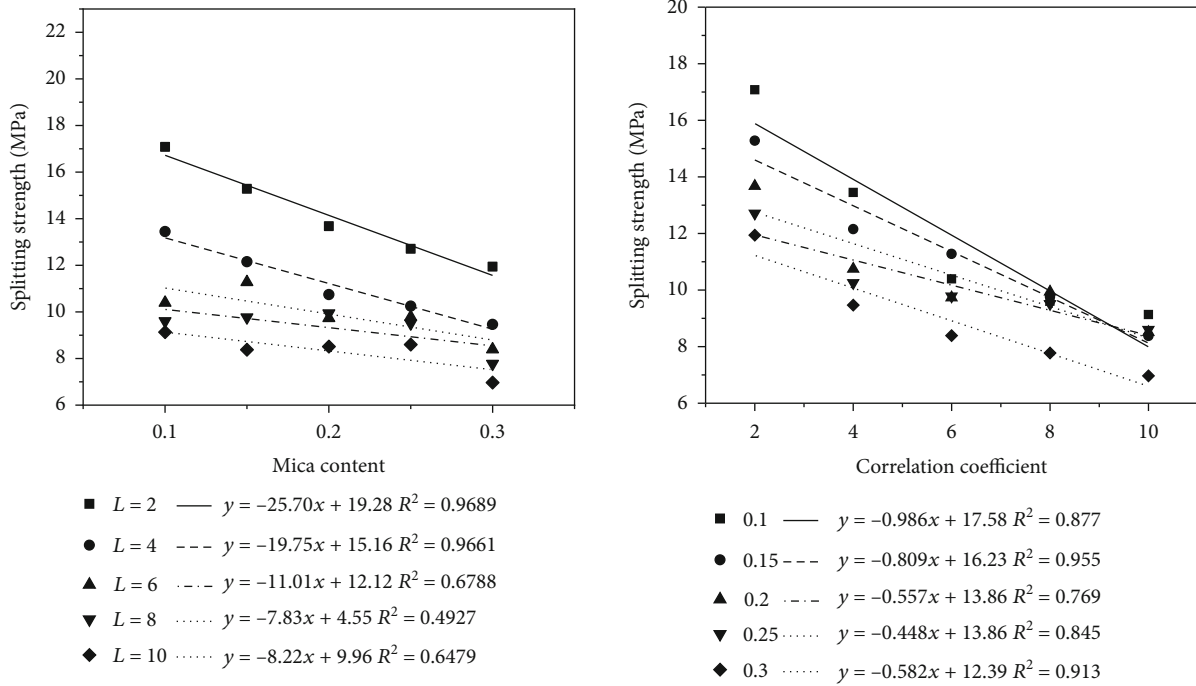
FIGURE 9: Relationship between different mineral fabrics and specimen strength.

Figure 11, but this correlation is slightly low when $L = 6$ and 8. It is analyzed that the strength of the two groups of specimens changes greatly with the mica content, while the section fractal changes slightly with the mica content; the reason is that the failure position in the specimen is relatively uniform without obvious change. This strong correlation can be obtained by linear fitting the two groups of parameters, as shown in Figure 11. It can be seen that there is an obvious linear relationship between the strength of the specimen and its section fractal when $L = 2, 4, 10$.

On the other hand, for mica content of $x = 10\%$, 15%, 20%, 25%, and 30%, the correlation between the fractal of the cross-section and the strength of the specimens is -0.813, -0.5883, -0.5918, -0.8774, and -0.76601, and the average value is -0.7293, which is higher than the fractal value. It is found that this correlation is low when $x = 15\%$ and 20%, and the larger or smaller mica component content will produce relatively stable fractures. When the aggregation degree

becomes large enough, the stable state of each failure will be destroyed to obtain a relatively stable fractal growth. The fitting results of the relationship between fractal and strength are shown in Figure 11; when the mica content is small, the composition of the fracture is less affected. The linear fitting results show that the fractal value of the cross-section has a linear relationship with the strength of the specimen, whose linearity is obvious at the lower or higher degree of polymerization.

Based on the above fitting curve, it can be known that the above formula can be used for low or high mica content and low or high mineral aggregation distribution.

6. Test Verification

By means of numerical simulation and image calculation, the relationship between the fractal dimension and the strength of the specimen under the condition of different fabrics is
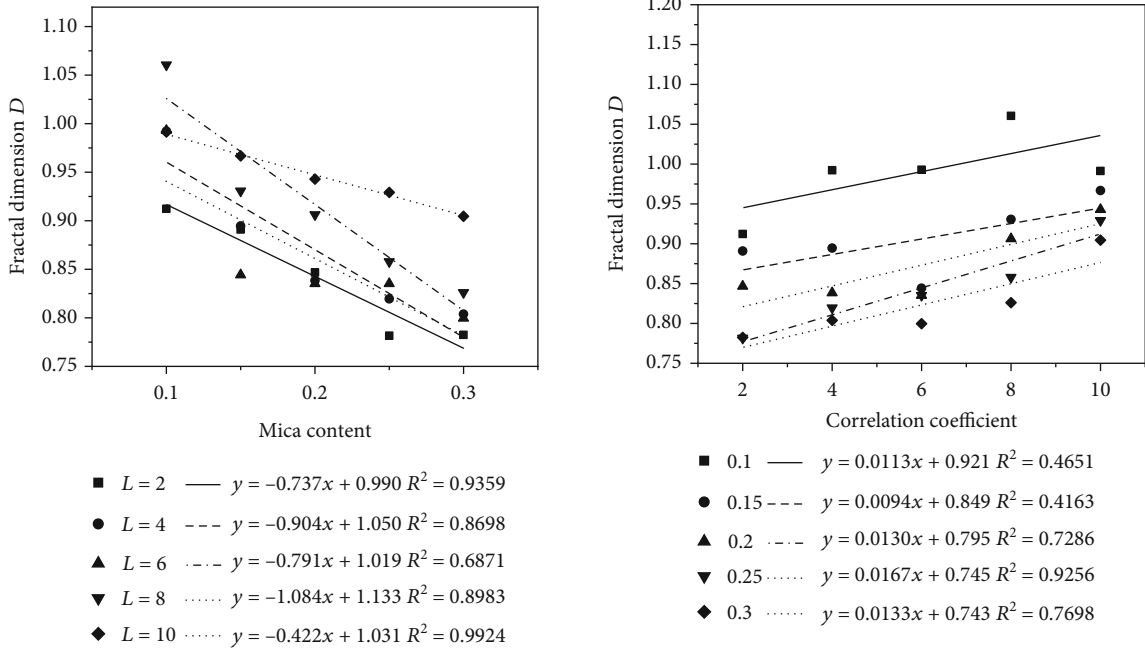
(a) Relationship between mica content and specimen strength

(b) Relationship between the mineral distribution and specimen strength

FIGURE 10: Fractal relationship between different mineral fabrics and specimen section.
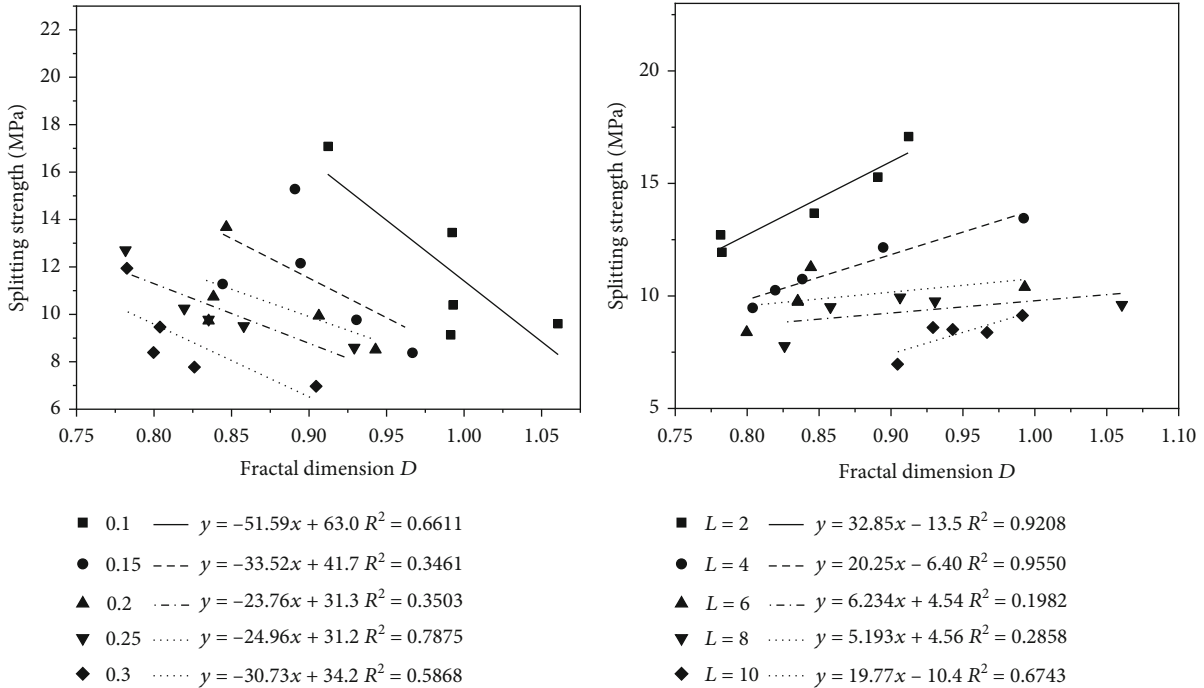
FIGURE 11: Relationship between fracture fractal and specimen strength under different fabric parameters.

obtained. Furthermore, this relationship will be verified through the corresponding indoor test.

6.1. Indoor Splitting Test. In order to obtain a complete granite section that is the same as the numerical test above, the Brazilian splitting tensile test method recommended by the international standard is used to test the specimen. The test equipment is shown in Figure 12.

(1) The surface distribution and content of the granite slab can be observed (the content can be accurately obtained by means of threshold division of numerical
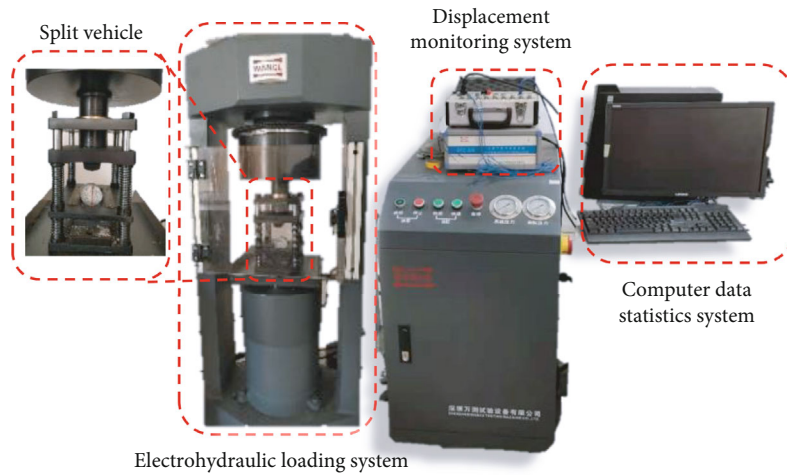
Figure 12: Wance electrohydraulic servo press.
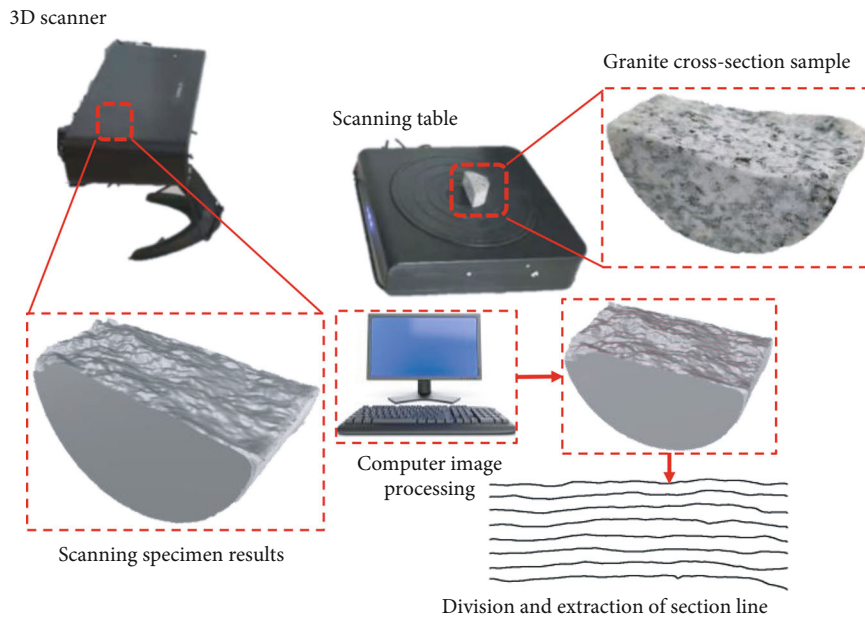
Figure 13: Fractal acquisition of granite specimen section.

image processing) to determine the distribution of mineral fabric

(2) The standard specimen is obtained by cutting the specimen into $\Phi 50 \, mm \times 25 \, mm$

(3) Place the test piece on the vehicle for loading. The peak load is defined as the tensile strength

6.2. Section Fractal Calculation. The fractal dimension of the section is calculated. The profile of the section can be obtained by using convenient binocular stereo image technology [60]. In this experiment, to guarantee accuracy, the Xinlin 3D laser scanner is adopted to obtain the section morphology; by slicing the 3D model, the fractal results are obtained from the section lines of several groups of sections.

Finally, the fractal results of the section are obtained by taking the average value of the results.

(1) After splitting, the specimen surface was observed, and the residual debris on the surface was removed

(2) The specimen with cross-section is scanned in three dimensions to obtain the profile information of the section

(3) The scanned specimen was imported into rhinoceros for adjustment, and its surface was segmented with equal width of 3 mm. Finally, 8 section lines were obtained

(4) The average value of 8 section lines was calculated by fractal, as shown in Figure 13

6.3. Validation of Results. Four groups of tests have been carried out, in which the mica content of the test piece is about 10%, and the distribution of components in different aggregation areas is on the same granite slab, which can be divided into three kinds of polymerization conditions: high, medium, and low. The fractal values of the test section are 0.9512, 0.9521, 0.9679, and 1.0153. When x is 10%, the fitting curve of different distributions is $y = -51.59x + 63.0$. The calculated strength values should be 13.92 MPa, 13.88 MPa, 13.07 MPa, and 10.62 MPa, respectively, while the actual measured strength values are 14.53 MPa, 12.67 MPa, 10.91 MPa, and 9.71 MPa, respectively. It can be seen that the numerical strength and the experimental strength have great consistency, and they all decrease with the increase of fractal value; the error ratios are -4.19%, 9.55%, 19.79%, and 9.37%, respectively, and the overall fluctuation is within 30%. The results show that other factors such as structural joints can lead the strength of rock samples to change, and they are not fully taken into account. It is proved that this method can predict the rock strength through the fractal and fabric of the rock section on a certain scale.

7. Discussion

The test results and test verification show that there is a certain linear relationship between the fractal value of the granite section and its strength under certain fabric conditions. According to the results, the component content and mineral aggregation have a strong fitting linear relationship with the strength and fractal section of the specimen. A parameter is defined to integrate the two groups of different parameters to make the strength and fractal section of the specimen show a more obvious correlation by adjusting the parameter. The corresponding formula is obtained.

8. Conclusion

Based on the requirements of hydraulic pressure strength and fracture analysis of the fracture water zone in hydraulic fracturing construction, considering the difference of rock component distribution and mineral content, numerical models of different fabrics are constructed to carry out the splitting test, and the fractal quantitative solution of its section is carried out.

(1) Based on the spatial correlation function and discrete element numerical simulation, the granite specimens with different fabrics can be reconstructed effectively to study further the mechanical problems combined with various monitoring methods

(2) The numerical test results show that there is an obvious linear relationship between the fabric of granite and the strength and the fractal value of the section; the strength of the specimen decreases with the increase of mica content, and the unit fractal value of the section decreases with the increase of mica content for the same polymerization degree. For the same mica content, the strength of specimens decreases with the increase of different polymerization degrees. The fractal of the fracture surface increases with the increase of mineral aggregation

(3) The results of numerical and physical tests show that when the specimen is distinguished to a certain extent; the strength of the specimen shows a linear relationship with the unit fractal value of the section under specific conditions. The strength of the specimen with the section can be roughly predicted by judging the fractal value of the section and the composition of the specimen, and the predicted value fluctuates within 30%.

Data Availability

(1) The (figure) data used to support the findings of this study are included within the article. (2) The (table) data used to support the findings of this study are included within the article

Conflicts of Interest

The authors declare that they have no conflicts of interest.

References

[1] H. Zhang, Z. Wan, and D. Elsworth, "Failure behavior of hot-dry-rock (HDR) in enhanced geothermal systems: macro to micro scale effects," *Geofluids*, vol. 2020, Article ID 8878179, 13 pages, 2020.

[2] J. Yang, H. Lian, and L. Li, "Fracturing in coals with different fluids: an experimental comparison between water, liquid CO_2, and supercritical CO_2," *Scientific Reports*, vol. 10, no. 1, p. 18681, 2020.

[3] K. M. Ajayi and S. J. Schatzel, "Transport model for shale gas well leakage through the surrounding fractured zones of a longwall mine," *International Journal of Mining Science and Technology*, vol. 30, no. 5, pp. 635–641, 2020.

[4] Z. Lei, Y. Zhang, Z. Hu et al., "Application of water fracturing in geothermal energy mining: insights from experimental investigations," *Energies*, vol. 12, no. 11, p. 2138, 2019.

[5] J. Yang, H. Lian, and V. P. Nguyen, "Study of mixed mode I/II cohesive zone models of different rank coals," *Engineering Fracture Mechanics*, vol. 246, 2021.

[6] J. Yang, H. Lian, and L. Li, "Investigating the effect of confining pressure on fracture toughness of CO_2-saturated coals," *Engineering Fracture Mechanics*, vol. 242, article 107496, 2021.

[7] Z. Liu, S. Wang, H. Ye et al., "Experimental study on the effects of pre-cracks, fracturing fluid, and rock mechanical characteristics on directional hydraulic fracturing with axial pre-cracks," *Geomechanics and Geophysics for Geo-Energy and Geo-Resources*, vol. 7, no. 2, pp. 7–29, 2021.

[8] Y. G. Zhang, Z. Zhang, S. Xue, R. Wang, and M. Xiao, "Stability analysis of a typical landslide mass in the Three Gorges Reservoir under varying reservoir water levels," *Environmental Earth Sciences*, vol. 79, no. 1, 2020.

[9] Y. G. Zhang, Y. L. Xie, Y. Zhang, J. Qiu, and S. Wu, "The adoption of deep neural network (DNN) to the prediction of soil liquefaction based on shear wave velocity," *Bulletin of*

Engineering Geology and the Environment, vol. 80, no. 6, pp. 5053–5060, 2021.

[10] Z. Liu, X. Ren, X. Lin, H. Lian, L. Yang, and J. Yang, "Effects of confining stresses, pre-crack inclination angles and injection rates: observations from large-scale true triaxial and hydraulic fracturing tests in laboratory," *Rock Mechanics and Rock Engineering*, vol. 53, no. 4, pp. 1991–2000, 2020.

[11] Y. Nie, G. Zhang, J. Wen, S. Li, and D. Zhou, "Cyclic injection to reduce hydraulic fracture surface roughness in glutenite reservoirs," *International Journal of Rock Mechanics and Mining Sciences*, vol. 142, p. 104740, 2021.

[12] L. Sousa, "Petrophysical properties and durability of granites employed as building stone: a comprehensive evaluation," *Bulletin of Engineering Geology and the Environment*, vol. 73, no. 2, pp. 569–588, 2014.

[13] L. M. O. Sousa, "The influence of the characteristics of quartz and mineral deterioration on the strength of granitic dimensional stones," *Environmental Earth Sciences*, vol. 69, no. 4, pp. 1333–1346, 2013.

[14] I. Rigopoulos, B. Tsikouras, P. Pomonis, and K. Hatzipanagiotou, "Correlations between petrographic and geometrical properties of ophiolitic aggregates from Greece," *Bulletin of Engineering Geology and the Environment*, vol. 73, no. 1, pp. 1–12, 2014.

[15] I. Rigopoulos, B. Tsikouras, P. Pomonis, and K. Hatzipanagiotou, "Petrographic investigation of microcrack initiation in mafic ophiolitic rocks under uniaxial compression," *Rock Mechanics and Rock Engineering*, vol. 46, no. 5, pp. 1061–1072, 2013.

[16] Y. Nara, "Effect of anisotropy on the long-term strength of granite," *Rock Mechanics and Rock Engineering*, vol. 48, no. 3, pp. 959–969, 2015.

[17] S. P. Morgan, C. A. Johnson, and H. H. Einstein, "Cracking processes in Barre granite: fracture process zones and crack coalescence," *International Journal of Fracture*, vol. 180, no. 2, pp. 177–204, 2013.

[18] S. S. Lim, C. D. Martin, and U. Åkesson, "In-situ stress and microcracking in granite cores with depth," *Engineering Geology*, vol. 147-148, pp. 1–13, 2012.

[19] S. Qi, H. Lan, D. Martin, and X. Huang, "Factors controlling the difference in Brazilian and direct tensile strengths of the Lac du Bonnet granite," *Rock Mechanics and Rock Engineering*, vol. 53, no. 3, pp. 1005–1019, 2020.

[20] M. Sajid, J. Coggan, M. Arif, J. Andersen, and G. Rollinson, "Petrographic features as an effective indicator for the variation in strength of granites," *Engineering Geology*, vol. 202, pp. 44–54, 2016.

[21] W. Yin, Z. Feng, and Y. Zhao, "Effect of Grain Size on the Mechanical Behaviour of Granite Under High Temperature and Triaxial Stresses," *Rock Mechanics and Rock Engineering*, vol. 54, no. 2, pp. 745–758, 2021.

[22] H. Xie and J.-a. Wang, "Direct fractal measurement of fracture surfaces," *International Journal of Solids and Structures*, vol. 36, no. 20, pp. 3073–3084, 1999.

[23] D. Huang, X. Chang, Y. Tan, K. Fang, and Y. Yin, "From rock microstructure to macromechanical properties based on fractal dimensions," *Advances in Mechanical Engineering*, vol. 11, no. 3, 2019.

[24] J. Zhang, L. Yu, H. Jing, and R. Liu, "Estimating the effect of fractal dimension on representative elementary volume of randomly distributed rock fracture networks," *Geofluids*, vol. 2018, Article ID 7206074, 13 pages, 2018.

[25] Y. Li and R. Huang, "Relationship between joint roughness coefficient and fractal dimension of rock fracture surfaces," *International Journal of Rock Mechanics and Mining Sciences*, vol. 75, pp. 15–22, 2015.

[26] Z. Z. Zhang, "Fractal dimension of fracture surface in rock material after high temperature," *Advances in Materials Science and Engineering*, vol. 2015, Article ID 468370, 6 pages, 2015.

[27] S. J. Chen, W. C. Zhu, Q. L. Yu, and X. G. Liu, "Characterization of anisotropy of joint surface roughness and aperture by variogram approach based on digital image processing technique," *Rock Mechanics and Rock Engineering*, vol. 49, no. 3, pp. 855–876, 2016.

[28] M. Min, B.-S. Jiang, M.-M. Lu, J.-K. Long, and Q. Zhang, "An improved strain-softening model for Beishan granite considering the degradation of elastic modulus," *Arabian Journal of Geosciences*, vol. 13, no. 6, 2020.

[29] P. Li, X. Zhao, Z. Guo, and L. Ma, "Variation of strength parameters of Beishan granite under triaxial compression," *Chinese Journal of Rock Mechanics and Engineering*, vol. 36, no. 7, pp. 1599–1610, 2017.

[30] D. J. Xue, L. Gao, L. Lu et al., "An acoustic emission-based cluster damage model for simulating triaxial compression behaviors of granite," *Rock Mechanics and Rock Engineering*, vol. 53, no. 9, pp. 4201–4220, 2020.

[31] Y. G. Zhang, J. Tang, Z. Y. He, J. Tan, and C. Li, "A novel displacement prediction method using gated recurrent unit model with time series analysis in the Erdaohe landslide," *Natural Hazards*, vol. 105, no. 1, pp. 783–813, 2021.

[32] Y. G. Zhang and L. Yang, "A novel dynamic predictive method of water inrush from coal floor based on gated recurrent unit model," *Natural Hazards*, vol. 105, no. 2, pp. 2027–2043, 2021.

[33] W. Chen, H. Konietzky, C. Liu, and X. Tan, "Hydraulic fracturing simulation for heterogeneous granite by discrete element method," *Computers and Geotechnics*, vol. 95, pp. 1–15, 2018.

[34] J. Shang, "Rupture of veined granite in polyaxial compression: insights from three-dimensional discrete element method modeling," *Journal of Geophysical Research: Solid Earth*, vol. 125, no. 2, 2020.

[35] H. Feng, L. Tianyong, and G. Xiaoye, "Study on the macro-micro failure mechanism of granite and its geometry effect under the different conditions of confining pressure by discrete element," *Journal of the China Coal Society*, vol. 44, no. 3, pp. 923–932, 2019.

[36] J. Hamdi, L. Scholtès, M. Souley, and M. al Heib, "Effect of discretization at laboratory and large scales during discrete element modelling of brittle failure," *International Journal of Rock Mechanics and Mining Sciences*, vol. 100, pp. 48–61, 2017.

[37] Z. Xuepeng, G. Wang, and J. Yujing, "Simulation research on granite compression test based on particle discrete element model," *Rock and Soil Mechanics*, vol. 35, Supplement 1, pp. 99–105, 2014.

[38] S. Chen, Z. Q. Yue, and L. G. Tham, "Digital image-based numerical modeling method for prediction of inhomogeneous rock failure," *International Journal of Rock Mechanics and Mining Sciences*, vol. 41, no. 6, pp. 939–957, 2004.

[39] C. Shi, W. Yang, J. Yang, and X. Chen, "Calibration of micro-scaled mechanical parameters of granite based on a bonded-particle model with 2D particle flow code," *Granular Matter*, vol. 21, no. 2, 2019.

[40] G. Ma, W. Zhou, R. A. Regueiro, Q. Wang, and X. Chang, "Modeling the fragmentation of rock grains using computed tomography and combined FDEM," *Powder Technology*, vol. 308, pp. 388–397, 2017.

[41] T. Xinwei, Z. Yuande, and Z. Chuhan, "A mesomechanical model with spatial correlation scale character and its application," *Rock and Soil Mechanics*, vol. 33, no. 7, pp. 2021–2026, 2012.

[42] T. Xinwei, H. Wenmin, Z. Yuande et al., "Experimental and meso-scale numerical modeling of splitting tensile behavior of weathered granites from South China," *Engineering Mechanics*, vol. 34, no. 6, pp. 246–256, 2017.

[43] X. Tang, Y. Zhou, C. Zhang, and J. Shi, "Study on the heterogeneity of concrete and its failure behavior using the equivalent probabilistic model," *Journal of Materials in Civil Engineering*, vol. 23, no. 4, pp. 402–413, 2011.

[44] X. Tang, X.-B. Yang, and Y.-D. Zhou, "An efficient algorithm for spatially-correlated random fields generation and its applications on the two-phase material," *Solid State Communications*, vol. 182, pp. 30–33, 2014.

[45] D. O. Potyondy, *A grain-based model for rock: approaching the true microstructure*, Rock Mechanics in the Nordic Countries, Kongsberg, Norway, 2010.

[46] Z. Yu, Y. Gao, S. Wu et al., "An equivalent crystal model for mesoscopic behavior of rock," *Chinese Journal of Rock Mechanics and Engineering*, vol. 34, no. 6, pp. 511–519, 2014.

[47] X. F. Li, Q. B. Zhang, H. B. Li, and J. Zhao, "Grain-based discrete element method (GB-DEM) modelling of multi-scale fracturing in rocks under dynamic loading," *Rock Mechanics and Rock Engineering*, vol. 51, no. 12, pp. 3785–3817, 2018.

[48] Y. Lv, H. Li, X. Zhu et al., "Discrete element method simulation of random Voronoigrain-based models," *Cluster Computing-the Journal Of Networks Software Tools and Applications*, vol. 20, no. S1, pp. 335–345, 2018.

[49] E. Ghazvinian, M. S. Diederichs, and R. Quey, "3D random Voronoi grain-based models for simulation of brittle rock damage and fabric-guided micro-fracturing," *Journal of Rock Mechanics and Geotechnical Engineering*, vol. 6, no. 6, pp. 506–521, 2014.

[50] D. O. Potyondy, "A grain-based model for rock: approaching the true microstructure," in *Rock Mechanics in the Nordic Countries 2010, Kongsberg, Norway, June 9–12, 2010*, pp. 225–234, Norwegian Group for Rock Mechanics, 2010.

[51] H. Hofmann, T. Babadagli, J. S. Yoon, A. Zang, and G. Zimmermann, "A grain based modeling study of mineralogical factors affecting strength, elastic behavior and micro fracture development during compression tests in granites," *Engineering Fracture Mechanics*, vol. 147, pp. 261–275, 2015.

[52] N. Bahrani, P. K. Kaiser, and B. Valley, "Distinct element method simulation of an analogue for a highly interlocked, non-persistently jointed rockmass," *International Journal of Rock Mechanics and Mining Sciences*, vol. 71, pp. 117–130, 2014.

[53] X. Hu, N. Xie, Q. Zhu, L. Chen, and P. C. Li, "Modeling damage evolution in heterogeneous granite using digital image-based grain-based model," *Rock Mechanics and Rock Engineering*, vol. 53, no. 11, pp. 4925–4945, 2020.

[54] T. Yin, S. Zhang, X. Li, and L. Bai, "A numerical estimate method of dynamic fracture initiation toughness of rock under high temperature," *Engineering Fracture Mechanics*, vol. 204, pp. 87–102, 2018.

[55] B. Shu, M. Liang, S. Zhang, and J. Dick, "Numerical modeling of the relationship between mechanical properties of granite and microparameters of the flat-joint model considering particle size distribution," *Mathematical Geosciences*, vol. 51, no. 3, pp. 319–336, 2019.

[56] J. Qiu, L. Luo, X. Li, D. Li, Y. Chen, and Y. Luo, "Numerical investigation on the tensile fracturing behavior of rock-shotcrete interface based on discrete element method," *International Journal of Mining Science and Technology*, vol. 30, no. 3, pp. 293–301, 2020.

[57] H. Lin, W. H. Kang, J. Oh, I. Canbulat, and B. Hebblewhite, "Numerical simulation on borehole breakout and borehole size effect using discrete element method," *International Journal of Mining Science and Technology*, vol. 30, no. 5, pp. 623–633, 2020.

[58] R. Abousleiman, G. Walton, and S. Sinha, "Understanding roof deformation mechanics and parametric sensitivities of coal mine entries using the discrete element method," *International Journal of Mining Science and Technology*, vol. 30, no. 1, pp. 123–129, 2020.

[59] G. du, S. Chen, and Z. Li, "Study on the tensile strength and crack development of granite crystal models with different fabrics," *Geofluids*, vol. 2021, Article ID 5533113, 15 pages, 2021.

[60] S. K. Singh, S. Raval, and B. Banerjee, "A robust approach to identify roof bolts in 3D point cloud data captured from a mobile laser scanner," *International Journal of Mining Science and Technology*, vol. 31, no. 2, pp. 303–312, 2021.

Research Article

Experimental and Numerical Investigation on Basic Law of Dense Linear Multihole Directional Hydraulic Fracturing

Xin Zhang (ID) **and Yuqi Zhang** (ID)

School of Mines, China University of Mining and Technology, Xuzhou 221116, China

Correspondence should be addressed to Xin Zhang; tyzyqhzx@163.com

Using the dense linear multihole to control the directional hydraulic fracturing is a significant technical method to realize roof control in mining engineering. By combining the large-scale true triaxial directional hydraulic fracturing experiment with the discrete element numerical simulation experiment, the basic law of dense linear holes controlling directional hydraulic fracturing was studied. The results show the following: (1) Using the dense linear holes to control directional hydraulic fracturing can effectively form directional hydraulic fractures extending along the borehole line. (2) The hydraulic fracturing simulation program is very suitable for studying the basic law of directional hydraulic fracturing. (3) The reason why the hydraulic fracture can be controlled and oriented is that firstly, due to the mutual compression between the dense holes, the maximum effective tangential tensile stress appears on the connecting line of the drilling hole, where the hydraulic fracture is easy to be initiated. Secondly, due to the effect of pore water pressure, the disturbed stress zone appears at the tip of the hydraulic fracture, and the stress concentration zone overlaps with each other to form the stress guiding strip, which controls the propagation and formation of directional hydraulic fractures. (4) The angle between the drilling line and the direction of the maximum principal stress, the in situ stress, and the hole spacing has significant effects on the directional hydraulic fracturing effect. The smaller the angle, the difference of the in situ stress, and the hole spacing, the better the directional hydraulic fracturing effect. (5) The directional effect of synchronous hydraulic fracturing is better than that of sequential hydraulic fracturing. (6) According to the multihole linear codirectional hydraulic fracturing experiments, five typical directional hydraulic fracture propagation modes are summarized.

1. Introduction

Conventional hydraulic fracturing can effectively change the internal structure of coal rock reservoirs to significantly improve the permeability of coal rock. At the same time, the hard roof above the coal seam is weakened to prevent the dynamic disaster caused by the sudden collapse of the roof. At present, this technology has been widely used in mines [1–11]. The geometric morphology of hydraulic fracture is the core of hydraulic fracturing construction design. Many studies showed that the initiation and propagation of hydraulic fractures are controlled by the three-dimensional in situ stress field. When the stress field is fixed, the orientation of the maximum tangential effective tensile stress on the borehole wall is fixed [12, 13], which makes the hydraulic

fractures usually initiate and propagate perpendicular to the direction of the minimum principal stress [14–17]. This provides a foundation for the mechanism and application of hydraulic fracturing.

As the initiation and expansion of hydraulic fractures are mainly controlled by far-field in situ stress, some limitations are found while using conventional hydraulic fracturing technology to solve underground related problems, such as roof cutting and pressure release engineering to automatically form the gob-side entry in the working face of an underground coal mine [18], gob management, gob-side entry retaining, and vertical fracture of hardtop coal [19]. The required direction of hydraulic fracture propagation in these projects is usually not consistent with that under the in situ stress field, which means the expansion of hydraulic fractures

in the suspended roof and coal seam needs to be accurately controlled to guarantee the effectiveness of directional fracture treatment [20, 21]. Therefore, directional hydraulic fracturing technology becomes the research topic.

In order to realize the directional expansion of hydraulic fractures, it is necessary to change the stress distribution of surrounding rock by artificial measures to make the maximum effective tensile stress appear first in the direction to be oriented, which can guide the expansion of hydraulic fractures and form the dominant fracture surface. At present, scholars have proposed the following four methods on this technology [19, 22, 23]:

Directional hydraulic fracturing by water jet preslotting [24–28]: this method uses the hydraulic slotting device to artificially prefabricate cracks on the borehole wall to change the stress distribution of the borehole wall, making the borehole crack along the preslotting direction. Relevant studies show that preslotting has an obvious directional effect on the initiation of hydraulic fracture. But with the increase of the distance, the propagation of hydraulic fracture gradually turns to the direction of the maximum principal stress, suggesting that a large range of directional fracture cannot be achieved, and its effective range is very limited.

Directional hydraulic fracturing method controlled by guiding hole [29, 30]: multiple guiding boreholes are arranged around the injection hole, which can significantly promote the internal stress distribution of the reservoir and effectively avoid local stress concentration. At the same time, it can also play the role of auxiliary free surface in the process of hydraulic fracture expansion. In addition, the mechanical properties of the rock bridge between the injection hole and the guiding hole are significantly reduced, which makes the hydraulic fracture more easily seep and expand along the direction of the guiding hole. The more guiding holes, the better the directional propagation effect and the larger the propagation range. Therefore, to achieve directional hydraulic fracture in coal and rock strata, a large amount of engineering and cost is required to arrange enough number of guiding holes.

Directional hydraulic fracturing guided by a guiding groove [31–34]: as the first directional hydraulic fracturing method, it was developed by the Polish General Institute of mining research to weaken the hard roof of the coal mine. The stress concentration of the annular groove leads the borehole to crack along the slotting direction. However, due to the limited stress concentration at the tip of the circular groove, its effect on the initiation and propagation of hydraulic fracture is limited, as well as its application.

Directional hydraulic fracturing controlled by dense linear multihole [29, 35, 36]: plenty of parallel dense linear boreholes are arranged in the specified direction inside the rock in advance. Then, water is injected into these boreholes simultaneously. Under the action of pore water pressure, the skeleton stress between boreholes is redistributed, and the effective tensile stress is formed in the direction of the drilling line [37, 38]. Thus, the hydraulic fracture can overcome the limitation of the far-field in situ stress, and the hydraulic fractures can be initiated and expanded along the wellbore line to achieve the directional fracturing of rock eventually. This method is superior, and the engineering

quantity is small with high efficiency. Compared with the above three methods, it is easier to implement and operate, so this method has gradually become the focus of scholars.

It is an effective method to realize directional hydraulic fracturing by using dense linear multiholes, which has positive significance for the directional treatment of the hard roof, directional transfer of stress, prevention of rockburst, and improvement of gas drainage rate [39–41]. However, research on laws of the initiation and propagation of the directional hydraulic fractures controlled by multihole is limited and needs to be further studied. In addition, the mechanism of dense linear boreholes affecting the distribution of the stress field in the rock mass to realize the directional propagation of hydraulic fractures is not clear. With the continuous progress of computer technology and numerical simulation algorithms, the combination of experimental research and numerical simulations provides a feasible solution to solve these problems mentioned [42–46]. At present, there are three popular numerical simulation methods used to research hydraulic fracturing [47–49]: the finite element method (FEM), extended finite element method (XFEM), and discrete element method (DEM). The basic idea of the FEM is to discretize the elastic body into an equivalent system of small elements [50]. In this method, the crack boundary coincides with the mesh nodes, and a mesh reconstruction method is used to simulate the crack propagation. The hydraulic fracturing model established by this method requires less calculation and has high efficiency. However, the hydraulic fracture can only extend along a preset path, and the FEM cannot simulate the deflection of hydraulic fractures or the formation process of a complex fracture network [51, 52]. The XFEM is based on the FEM and introduces a shape function to represent the discontinuity of the displacement field [53–55], so the description of the discontinuous displacement field is completely independent of the mesh boundary. This method can simulate fracture propagation along any path without grid reconstruction. This is advantageous in the analysis and calculation of fracture problems and greatly improves the calculation efficiency. The disadvantage of the XFEM is that the simulation of microhydraulic fracture propagation needs further development. The main idea of the DEM is to use an explicit algorithm to calculate the motion of particles or blocks, that is, update the motion and contact state of particles in each calculation [56, 57]. When the contact force exceeds its bearing limit, the material will demonstrate shear dislocation, compression shear failure, tensile failure, and other rock fracture phenomena [58, 59]. The channel formed between particles can be used to simulate the fluid flow in a pipe. Because the DEM does not have to satisfy the continuity condition, the DEM is very suitable for simulating the initiation and propagation of microcracks in rock. Considering that this paper mainly focuses on the micromechanism of directional hydraulic fracture propagation, the discrete element simulation method is more suitable.

In this paper, the experimental test and a DEM numerical simulation using particle flow code (PFC^{2D}) were combined to investigate the laws of the initiation and propagation of

directional hydraulic fracturing controlled by the dense linear multihole. Besides, the sensitivity analysis of the geological condition and hydraulic fracturing condition affecting the directional effect and accuracy was carried out. The research results can provide theoretical guidance for the implementation of directional hydraulic fracturing in coal mines.

2. Particle Flow Method

2.1. Parallel Bond Model. A parallel bonding model has not only standard stiffness and tangential stiffness but also normal tensile strength and shear strength [56]. It consists of two elements: linear model and parallel bond. The parallel bonding model can be compared to a set of springs arranged on rock particles (Figure 1). Under the action of external force, there is force and displacement between particles. If tensile and shear strength of parallel bond element exceeds σ_{max} or τ_{max}, the parallel bonds break, and the bond material and its associated forces, moments, and stiffness will be removed from the model, and only the linear model will be available. The parameters shown in the figure represent the mesoparameters of the parallel bond model, where k_n refers to the normal stiffness of particle element, k_s represents the tangential stiffness of particle element, g_s refers to the spacing between particles, μ represents the friction coefficient between particle elements, $\overline{\sigma_c}$ refers to the normal strength of parallel bond, $\bar{\Phi}$ represents the friction angle of rock, and $\bar{c}$ refers to the cohesion of rock [42, 60–62].

2.2. Fluid-Solid Coupling Model. The fluid-solid coupling model assumes that the geometric space between adjacent particles is the seepage channel of liquid, and the fluid form of liquid is plate flow (Figure 2). The adjacent seepage channels are connected to form a closed "domain." In the calculation process, the water pressure in the "domain" is continuously updated and acts on the particles.

The liquid flow of the domain is computed as follows [63]:

$$q = \frac{a^3}{12\mu} \frac{p_2 - p_1}{L},\qquad(1)$$

where q represents the liquid flow, μ represents the dynamic viscosity, $p_2 - p_1$ is the pressure difference between two adjacent areas, L is the length of the pipe, and a refers to the width of the connecting "pipe."

The change of pore fluid pressure is calculated as follows:

$$\Delta p = \frac{K_f}{V_d}\left(\sum q\Delta t - \Delta V_d\right),\qquad(2)$$

where K_f refers to the bulk modulus, V_d is the apparent volume of the domain, $\sum q$ represents the total flow of the domain from the surrounding pipes, and Δt refers to the calculation time step:

$$F_i = pn_is,\qquad(3)$$
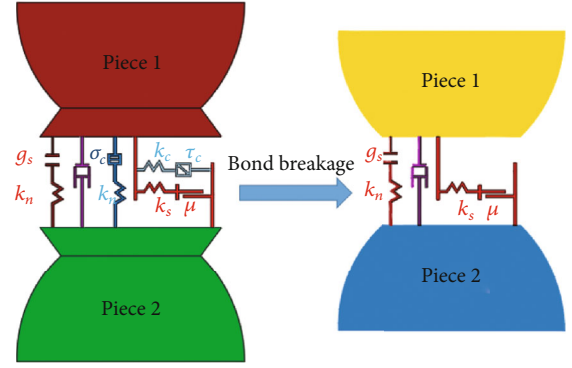
FIGURE 1: Parallel bond model: (a) parallel bond; (b) bond failure [30].

where n_i is the external average unit vector of the connecting line between adjacent particles, s is the distance from the center of the corresponding particle to the contact point, and p is the change of fluid pressure in each time step.

In addition, because of the explicit algorithm, in order to ensure the stability of the numerical model, the pressure change caused by water flow must be less than the disturbance pressure:

$$\Delta t = \frac{2rV_d}{NK_fka^3},\qquad(4)$$

where N is the number of pipes connected to a domain and r is the average radius of particles around a domain. In addition, in order to ensure the stability of the whole computing domain, the global time step must be the minimum of all local time steps.

3. Dense Linear Multihole Directional Hydraulic Fracturing Experimental Investigation

3.1. Test Block Preparation and Experimental System. In the experiment, a 500 mm × 500 mm × 500 mm cement mortar block is used as the sample to replace the coal rock mass (Figure 3). The physical and mechanical parameters of the test block are shown in Table 1. Three linearly distributed boreholes are prefabricated on the cube test block, named H1, H2, and H3, respectively. The angle between the direction of the linear borehole and the direction of maximum principal stress (σ_1) is 15°. The distance between two adjacent boreholes is 141 mm. The test block adopts a borehole packer with an outer diameter of 18 mm. There is another naked drill hole at 100 mm in length from the end of the borehole packer. In addition, a large-scale true triaxial hydraulic fracturing experimental system is applied in the test (Figure 4). The experimental system consisted of a bench frame, a loading system, and a monitoring system.

3.2. Morphology of Dense Linear Multihole Directional Hydraulic Fracture. According to the scheme shown in Table 2, directional hydraulic fracturing controlled by the dense linear multihole was carried out on the coal rock mass.
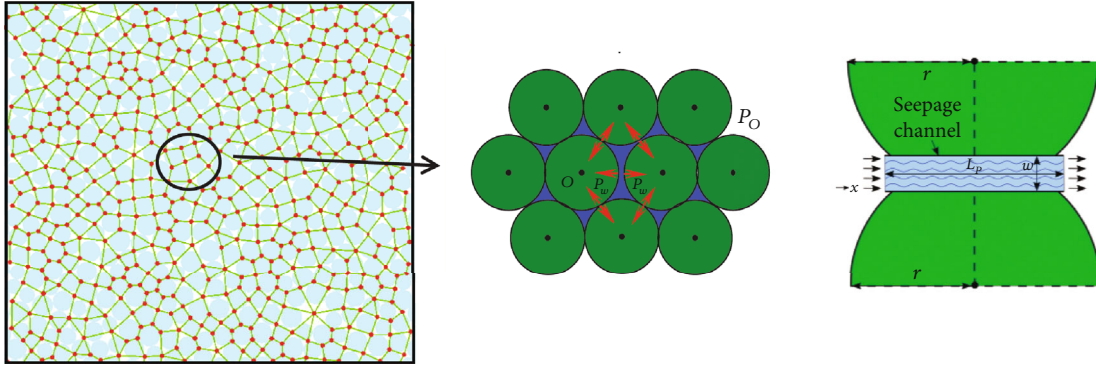
FIGURE 2: Pipeline and domain in PFC^{2D} [30].
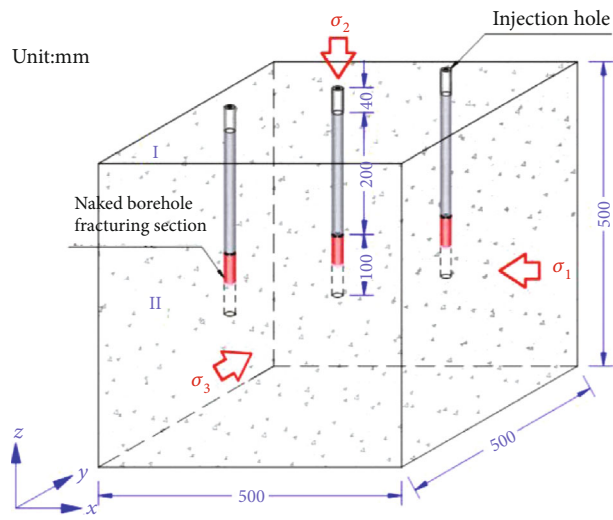
(a) The cement mortar test block
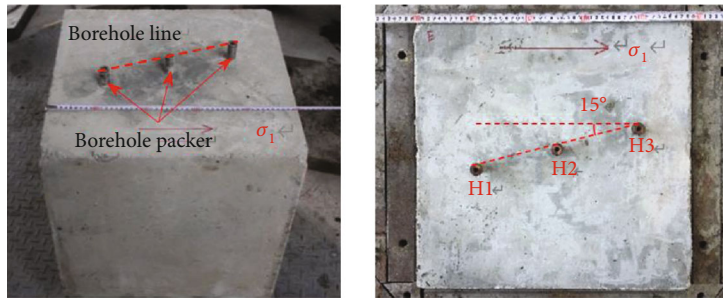
(b) Test block placement in the pressurized frame

FIGURE 3: Manufacture of specimens [64].

TABLE 1: Physical and mechanical parameters of the cement mortar.

Porosity ϕ (%)	Permeability K (mD)	Uniaxial compressive strength σ_c (MPa)	Modulus of elasticity E (GPa)	Tensile strength σ_t (MPa)	Cohesion c (MPa)	Angle of internal friction φ (°)	Fracture toughness K_{1c} (N·mm$^{3/2}$)
13.79	1.13	15.85	0.92	1.65	2.5443	31.29	13.23
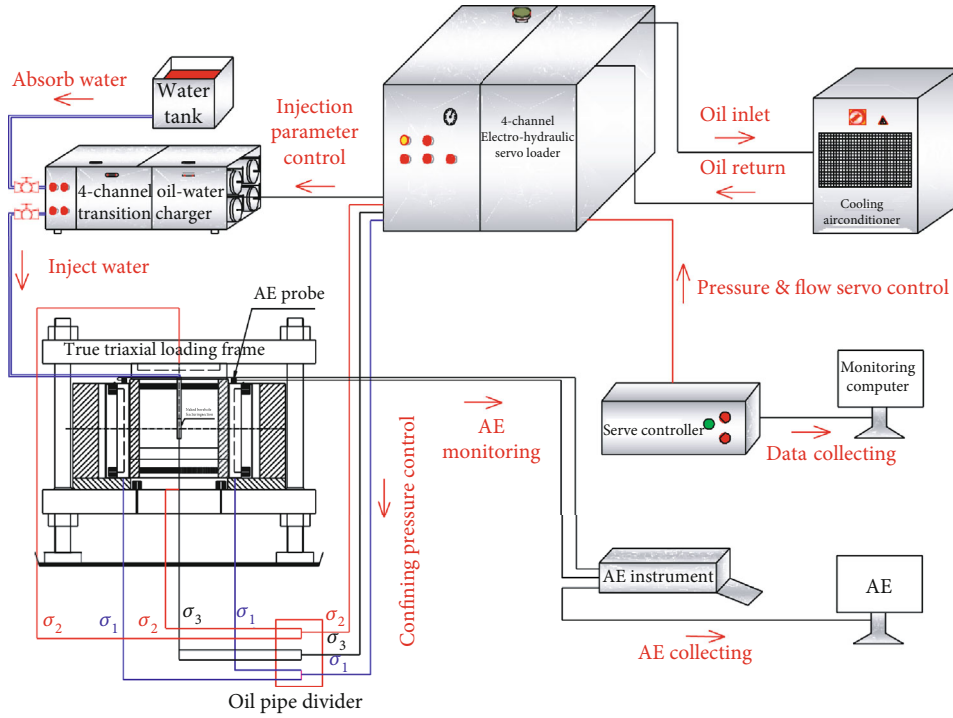
FIGURE 4: True triaxial hydraulic fracturing test system.

TABLE 2: Experimental scheme of directional hydraulic fracturing controlled by dense linear multihole.

| Test name | Principal stress (MPa) | | | Borehole spacing (mm) | Arrangement angle of boreholes (°) | The injection rate (ml/min) | Pumping mode |
	σ_1	σ_2	σ_3				
1-1 (laboratory test)	7	5	3	141	15	50	Synchronous
1-2 (simulation test)	7		3	141	15	50	Synchronous

After a large amount of water leakage from the loading frame, the experiment stopped.

After the loading plate is opened, there are visible hydraulic fractures on the upper surface and side of the test block (Figure 5), and the directional hydraulic fractures on the upper surface extend to the edge of the test block along the borehole line direction, and the directional effect is obvious.

Among them, hydraulic fracture on the leftwing of H1 initiated and expanded along the direction of maximum in situ stress, while that of the rightwing of H1 expanded along the direction of the borehole line and intersected with the H2 borehole. The hydraulic fracture on the leftwing of H2 extended along the direction of the borehole line, but it did not intersect with the hydraulic fracture on the rightwing of H1, forming a rock bridge area between them. The hydraulic fractures on the H2 rightwing and H3 leftwing both propagated along the direction of the borehole line and finally intersected smoothly. The hydraulic fracture on the H3 rightwing propagated to the boundary of the test block along the direction of maximum principal stress.

By observing the hydraulic fracture trajectory in each borehole, it was found that in borehole H1-H3, the hydraulic fractures were obviously initiated and expanded along the direction of the borehole line, while they were initiated and expanded basically along the direction of the maximum principal stress outside H1-H3. The fracture trajectory occurred with an obvious deflection at H1 and H3. On the whole, the directional hydraulic fracture surface was approximately a folding failure surface (Figure 6), which also suggested that the initiation and propagation of hydraulic fracture were affected by the far-field stress and the coupling stress between boreholes.

After cutting the test block along the trajectory of directional hydraulic fracture, it can be found that the directional fracture surface was formed in the H1-H3 section and a two-layered fracture surface appeared. The fracture surface I was formed by the expansion of hydraulic fractures on both wings of H1, and fracture surface II was formed by the expansion of hydraulic fractures on both wings of H2. The area between the two fracture surfaces is the rock bridge area mentioned above. The expansion range of fracture surface I was relatively small. The intensive fluctuation of the fracture surface I indicates that the hydraulic fracture expanded with obvious deflection, and the orientation effectiveness was poor. However, the second fracture zone covered the whole
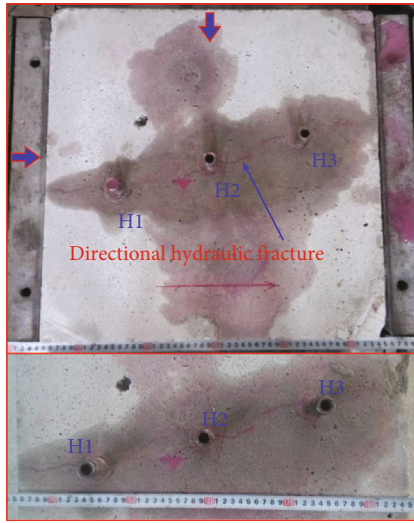
FIGURE 5: Propagation morphology of directional hydraulic fracturing [64].

FIGURE 7: Laboratory test and numerical simulation of the stress-strain curve and final fracture mode of the intact specimen [30].

DEM simulation samples consistent with the laboratory test results, a numerical model with a length of 100 mm and a width of 50 mm was established to calibrate the mechanical parameters (Figure 7). The microparameters were adjusted repeatedly until the stress-strain curve and the final fracture mode of the simulated specimen were consistent with the laboratory test. Table 3 shows the microscopic parameters of the simulated sample. The calibration results show that the selection of mesoparameters is reasonable.

The rock parameters obtained above were used for numerical modeling. As Figure 8 shows, the size of the square model is 500 mm in length and 500 mm in width, which contains approximately 14683 particles. The fluid injection point is located in the center of the borehole. The angle between the drilling line and the direction of the maximum principal stress is also 15°. The confining pressure of the test block was loaded by applying a stress constraint on the boundary (wall) of the model.

FIGURE 6: The integrated morphology of the failure plane [64].

block, and the fracture surface II showed a large expansion range and good orientation, indicating that the directional effect of the hydraulic fracture in the middle borehole was stronger than that in the surrounding borehole. This is because the stress coupling degree between the middle boreholes is the highest.

4. Numerical Investigation of Dense Linear Multihole Directional Hydraulic Fracturing

4.1. Calibration of Numerical Model Parameters. To guarantee the mechanical properties and failure characteristics of

4.2. Morphology of Directional Hydraulic Fracture. According to the scheme shown in Table 2, the simulation results are shown in Figure 9. The hydraulic fractures in the three boreholes are initiated and propagated along the direction of the drilling line. The hydraulic fracture of the H1 leftwing extended to the edge of the test block along the maximum main stress direction, while the hydraulic fracture of the H1 rightwing extended a short distance along the maximum main stress direction and then turned to the borehole line with obvious turning points in the fracture trajectory. Finally, they intersected with that of the H2. The hydraulic fracture of the H2 leftwing extended to H1 along the borehole line, but it did not intersect with the hydraulic fracture of the H1 rightwing, forming a rock bridge. The hydraulic fractures of H2 rightwing and H3 leftwing both extend in the direction of the drilling line and finally merged smoothly. Hydraulic fracture of H3 rightwing extended to the edge of test block along

TABLE 3: Micromechanical parameters of simulated samples [30].

Particle parameters					Parallel bonding parameters				
(GPa)	k_n/k_s	μ	R_{max}/R_{max}	ρ (g·cm^{-3})	$\bar{E}_c$ (GPa)	$\bar{k}_n/\bar{k}_s$	$\bar{\sigma}_c$ (MPa)	$\bar{c}$ (MPa)	$\bar{\lambda}$
1.51	1	0.1	1.66	2.65	1.51	1	5.4	12.7	1

FIGURE 8: Test block for laboratory test and numerical simulation.

the direction of maximum principal stress. The shape of directional hydraulic fracture in the numerical simulation was very consistent with that of the laboratory test, which fully verifies the rationality of the particle flow numerical simulation test.

5. The Mechanism of Directional Hydraulic Fracturing Controlled by Dense Linear Multihole

The simulation results were furtherly analyzed to explore the directional fracture mechanism. In this section, the mechanism of dense linear multihole controlling the directional hydraulic fracturing from the fracture initiation stage and fracture propagation stage was analyzed.

5.1. Initiation Stage of Hydraulic Fracture. According to the theory of hydraulic fracturing, the resistance that hydraulic fracture needs to overcome is the least when it propagates along the direction perpendicular to the minimum principal stress, which means the direction perpendicular to the minimum principal stress in the far-field stress field is the dominant propagation direction. When the water injection hole is excavated, due to the constraint of the far-field stress field, the borehole wall will occur compression deformation, resulting in the stress concentration effect around the wellbore. If multiple boreholes are arranged on the same straight line, due to the mutual compression between multiple boreholes, the stress concentration between boreholes affected by the superposition of boreholes will be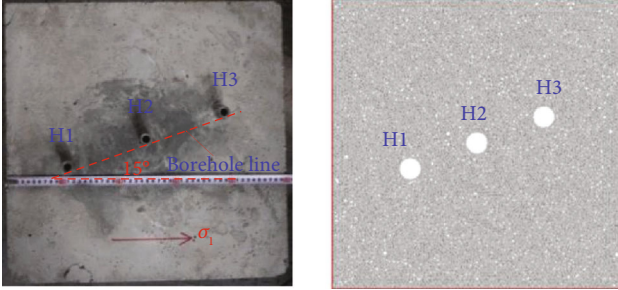 significantly higher than that of single boreholes, and the tangential tensile stress field perpendicular to the centerline of boreholes is generated. With the injection of high-pressure water, the pore water pressure gradient is formed on the hole wall, which creates a new additional stress field around the borehole, and the additional stress field will be superimposed on the surrounding rock stress formed after excavation.

It is assumed that the stress in the original reservoir rock mass is uniformly distributed. In this study, the complex three-dimensional stress problem is simplified as a two-dimensional stress model. The additional stress can be calculated by the thick-walled cylinder formula. The stress of surrounding rock mass can be calculated as follows [65]:

$$
\begin{cases}
\sigma_r = \dfrac{a^2(b^2 - r^2)}{r^2(b^2 - a^2)}p = \dfrac{a^2}{r^2}p, \\[2mm]
\sigma_\theta = -\dfrac{a^2(b^2 + r^2)}{r^2(b^2 - a^2)}p = -\dfrac{a^2}{r^2}p,
\end{cases}
\tag{5}
$$

where p represents the water pressure, a is the radius of the borehole, and b refers to the outer diameter.

According to equation (5), it can be found that in the process of hydraulic fracturing, the tangential tensile stress perpendicular to the borehole line will concentrate in the rock mass, and its stress intensity fluctuates periodically with the change of distance (Figure 10). The closer the borehole hole is, the higher the stress intensity is, and the tensile stress is the largest at the intersection of the borehole center line and the borehole wall. Therefore, with the continuous accumulation of water pressure in the hole, the water pressure in the direction of the borehole line will first overcome the tensile strength of the rock and cause a fracture; thus, the hydraulic fracture begins to germinate. That explains why the hydraulic fracture is most likely to initiate along the borehole line, when the directional hydraulic fracturing controlled by dense linear multihole is used.

5.2. Propagation Stage of Hydraulic Fracture. By extracting the maximum principal stress distribution data, the dynamic evolution of the stress field in the test block can be obtained and shown in Figure 11.

After the borehole wall cracked, the high-pressure water entered into the hydraulic fracture and penetrated the boundary area of the fracture tip, forming the pore pressure gradient. At this time, the stress was disturbed by the hydraulic fracturing, and the stress disturbance field appeared around the hydraulic fracture, where the tensile disturbance stress concentrated in the tip of the hydraulic fracture, and the compressive stress was distributed on both sides of the hydraulic fracture. The stress disturbance field superimposed the original stress field of surrounding rock, forming a new stress distribution field in the boundary area of the fracture tip and leading to the deflection of the direction of the maximum principal stress along the propagation path in front of the hydraulic fracture. However, because the size and scope of the tensile disturbance stress generated by the fracture tip were limited, the stress disturbance fields around different

(b)
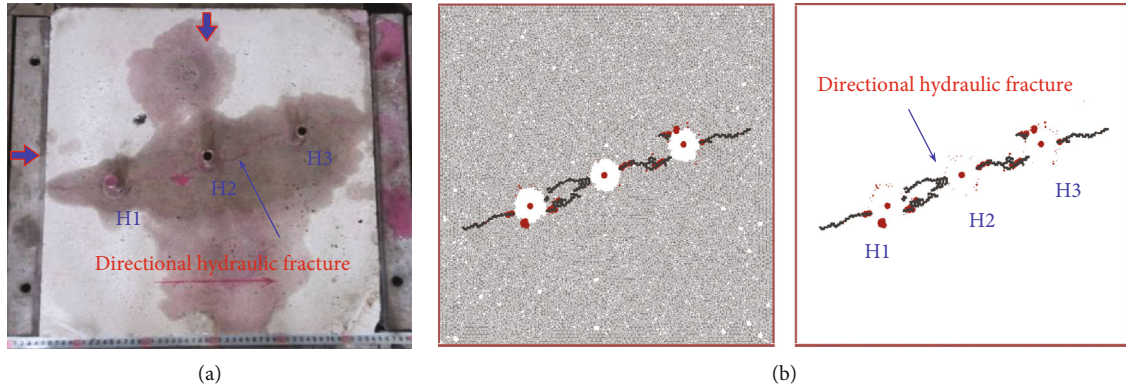
FIGURE 9: Comparison of laboratory test and simulation test: (a) laboratory test directional hydraulic fracture [30, 64]; (b) simulated test directional hydraulic fracture.
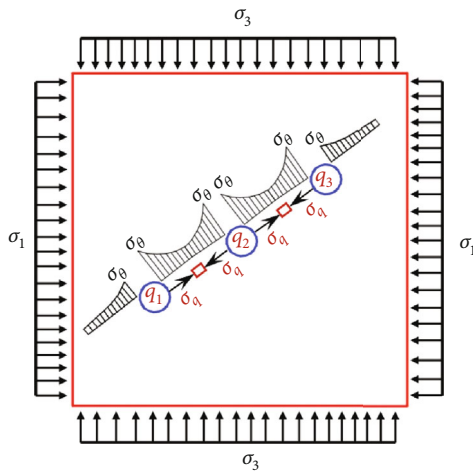
FIGURE 10: Distribution of tangential stress of multihole linear codirectional hydraulic fracturing.

hydraulic fracture tips did not superimpose with each other, making the far-field in situ stress still dominate the key factor of hydraulic fracture propagation direction.

With the continuous injection of high-pressure water, the length of hydraulic fracture increased, and the size and range of disturbed tensile stress at the tip of hydraulic fracture gradually increased. At this time, the influence of the far in situ stress field on hydraulic fracture propagation was weakened. The superposition and fusion of different tensile stress disturbance fields resulted in the formation of a new maximum principal stress concentration strip between adjacent boreholes, which is named "guided fracturing control zone between boreholes." The maximum principal stress strip showed an " ⌐_ " shape and connected the tips of adjacent hydraulic fractures, which promoted the hydraulic fractures in the guided fracturing control area to expand along the borehole line (Figure 12). In addition, multiple maximum principal stress concentration strips developed along the borehole line and paralleled to each other.

With the further increase of hydraulic fracture length, the range and internal stress of the maximum principal stress

concentration zone between boreholes also increased. It can be seen that the shape of the stress strip also changed from " ⌐_ " to " _⌐ " to " ⌐_ ". In the process of morphological change, the propagation direction of hydraulic fracture also changed continuously. In the expansion process, the hydraulic fracture in each borehole not only deflected as a whole and tended to expand along the borehole line but also locally deflected around the borehole axis, which made these hydraulic fractures intersected and fused to form a directional fracture surface along the borehole axis and realize the directional fracture of rock reservoir. In addition, after the adjacent hydraulic fractures merge with each other, the maximum principal stress strip gradually decreased and disappeared.

6. Analysis of Influencing Factors of the Multihole Linear Directional Hydraulic Fracture Propagation

When directional hydraulic fracturing controlled by dense linear multihole is carried out in the coal mine [66–72], the in situ stress conditions, borehole arrangement angle, borehole spacing, and borehole pumping mode will significantly affect the shape and orientation accuracy of the directional hydraulic fracture, so this section will carry out sensitivity analysis for the above factors.

6.1. Discussion: Angle between the Line of the Borehole and the Direction of Maximum Principal Stress. According to the scheme shown in Table 4, four groups of arrangement angles of boreholes θ are set, and the angles are 15, 45, 60, and 75, respectively. The final test results are shown in Figure 13. When the value of θ was 15°, except for hydraulic fracture of the H3 rightwing extended along the direction of maximum main stress, the hydraulic fractures of other holes all extended along the direction of the borehole line. The hydraulic fractures of the H2 leftwing and the H1 rightwing expanded and gradually fused, and the hydraulic fracture of the H2 rightwing was connected with the H3. In addition, the hydraulic fracture of the H3 leftwing turned obviously, forming a rock bridge with the hydraulic

(a) The dynamic expansion process of the directional hydraulic fracture

(b) The dynamic evolution of stress field in the test block
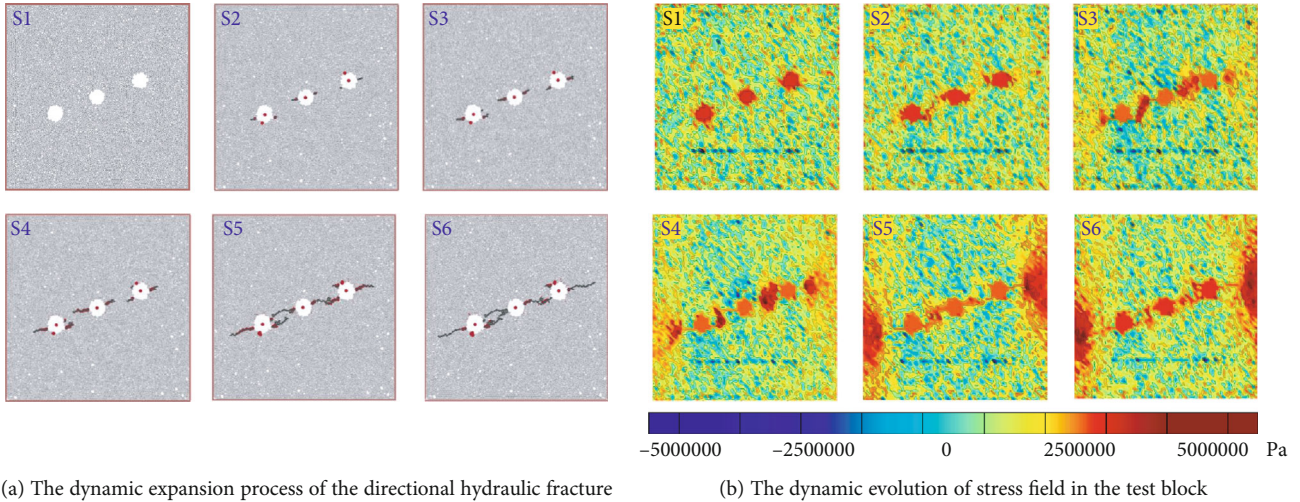
FIGURE 11: Hydraulic fracture propagation stage.
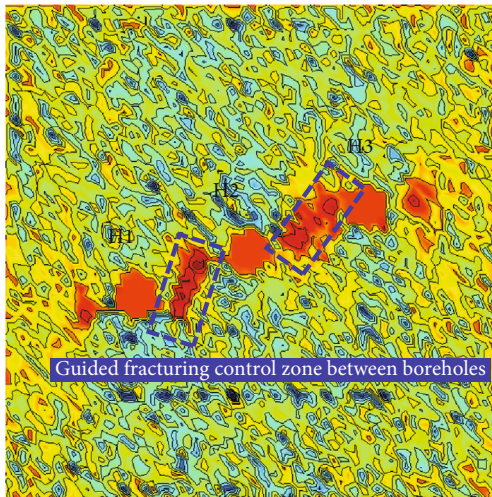
FIGURE 12: The shape and distribution of the guided fracturing control zone between boreholes.

fracture of H2 rightwing and resulting in a directional hydraulic fracture crossing each borehole without obvious bifurcation phenomenon.

When the value of θ was 45°, the hydraulic fractures of each borehole initiate along the direction of the maximum principal stress σ_1 and extend for a short distance. With different hydraulic fractures approaching each other, the propagation direction changed, and the hydraulic fractures expanded along the borehole line. Finally, the hydraulic fractures intersected with adjacent injection holes. In addition, it should be noted that the hydraulic fractures on both sides of different boreholes did not fuse. Thus, multiple rock bridge areas were formed, and the fracture morphology was more tortuous and rough, forming a "ladder"-shaped directional hydraulic fracture connecting each borehole with obvious stratification.

When the value of θ was 60°, the hydraulic fractures of the three boreholes initiated and expanded along the direc-

tion of σ_1. Under the influence of coupling stress between holes, the propagation direction of hydraulic fractures in each borehole gradually approached the borehole line from the direction of the maximum principal stress with a small deflection angle. Although the hydraulic fractures tended to connect with each other, the directional hydraulic fractures were not formed in the end.

When the value of θ was 75°, the hydraulic fractures of the three boreholes initiated and propagated along the direction of the maximum principal stress σ_1 without deflection.

The three main hydraulic fractures are parallel to each other, and the propagation behavior of hydraulic fractures is basically determined by the in situ stress field. In addition, there is an obvious stress shadow effect. Multiple fractures compete with each other, and the fracture propagation trajectories repel each other. The lateral hydraulic fracture will deflect to the outside due to the action of the medial hydraulic fracture. The medial hydraulic fracture is squeezed under the influence of the induced stress field of the outer hydraulic fracture, and the width and length of the fracture become narrower, which seriously affects the effect of hydraulic fracturing.

By comparing the directional hydraulic fracture morphology under different arrangement angles of boreholes θ, it can be found that with the increase of the angle, the directional effect and accuracy gradually weaken. When the angle increased to a certain extent, the directional effect disappeared, and the directional hydraulic fracture was not formed. When the directional hydraulic fractures were 30° and 45°, it was found that the orientation accuracy of directional hydraulic reduced within a certain range. However, the angle between the formed directional fractures and the direction of maximum principal stress significantly increased, and the effect range of the directional hydraulic fractures in the reservoir was also significantly improved. In addition, if the arrangement angle of boreholes θ is too large, it is difficult to form directional hydraulic fractures, and there will be an obvious stress shadow effect, which seriously affects the effect of conventional hydraulic fracturing.

TABLE 4: Experimental scheme of directional hydraulic fracturing.

Test name	Principal stress (MPa)			Borehole spacing (mm)	Arrangement angle of boreholes (°)	The injection rate (ml/min)	Pumping mode
	σ_1	σ_2	σ_3				
2-1	7		3	120	15	50	Synchronous
2-2	7		3	120	45	50	Synchronous
2-3	7		3	120	60	50	Synchronous
2-4	7		3	120	75	50	Synchronous
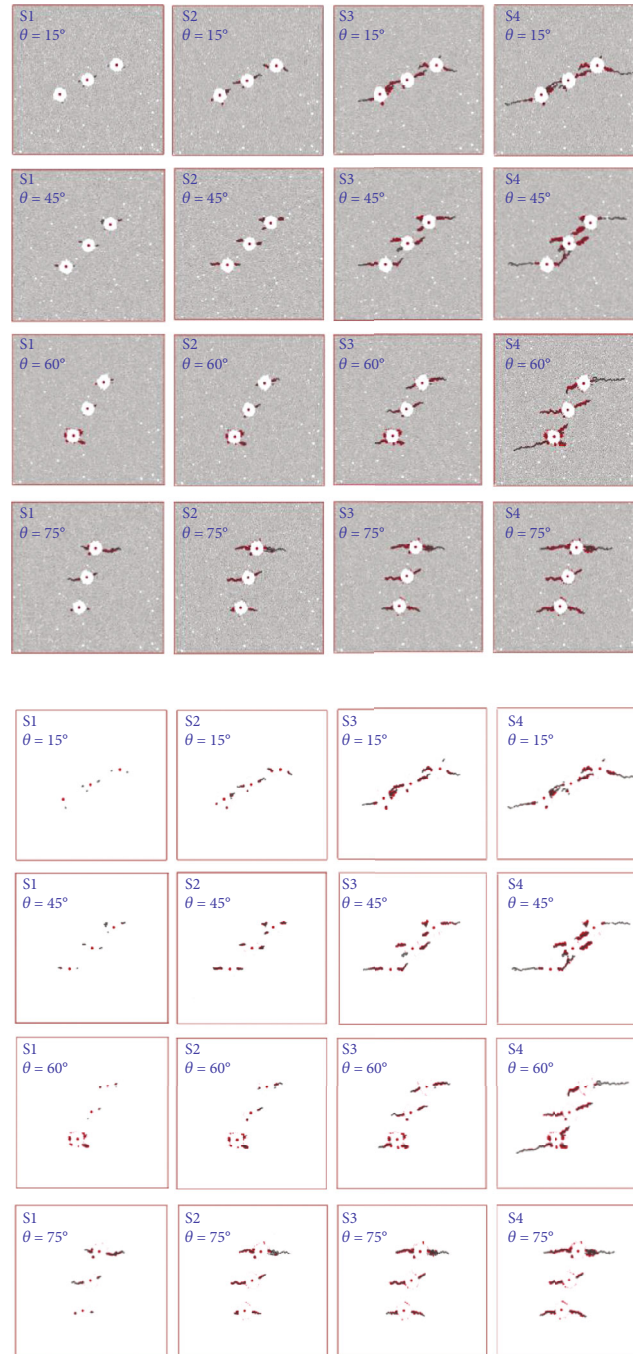
FIGURE 13: Initiation and propagation process of directional hydraulic fractures at different angles between the direction of borehole line and maximum principle stress σ_1.

TABLE 5: Experimental scheme of directional hydraulic fracturing.

Test name	Principal stress (MPa)			Borehole spacing (mm)	Arrangement angle of boreholes (°)	The injection rate (ml/min)	Pumping mode
	σ_1	σ_2	σ_3				
3-1	7		1	141	15	50	Synchronous
3-2	7		3	141	15	50	Synchronous
3-3	7		5	141	15	50	Synchronous

FIGURE 14: Initiation and propagation process of directional hydraulic fractures at different principle stress differences.

TABLE 6: Experimental scheme of directional hydraulic fracturing.

Test name	Principal stress (MPa)			Borehole spacing (mm)	Arrangement angle of boreholes (°)	The injection rate (ml/min)	Pumping mode
	σ_1	σ_2	σ_3				
4-1	7		3	105	15	50	Synchronous
4-2	7		3	141	15	50	Synchronous
4-3	7		3	176	15	50	Synchronous

6.2. Discussion: The Principal Stress Difference. According to the scheme shown in Table 5, three different horizontal in situ stress differences 2, 4, and 6 MPa were set, and the test results are shown in Figure 14.

When the value of $\Delta\sigma$ was 2 MPa, the hydraulic fractures of the three boreholes initiated and expanded along the direction of the borehole line, and the hydraulic fractures of the adjacent boreholes finally fused each other to form a linear directional hydraulic fracture coplanar with all the injection holes. The directional hydraulic fracture surface was smooth and flat with obvious directivity and high orientation accuracy.

When the value of $\Delta\sigma$ was 4 MPa, the hydraulic fractures on both sides of H3 extended to the edge of the test block along the direction of the maximum principal stress, and the hydraulic fractures on both sides of H1 and H2 extended along the direction of the borehole line and finally approached the adjacent boreholes to form directional hydraulic fractures. The directional hydraulic fractures of each hole did not fuse, and the formed rock bridge area showed an obvious stratification phenomenon.

When the value of $\Delta\sigma$ was 6 MPa, the hydraulic fractures of each borehole basically initiated and expanded along the direction of the maximum principal stress. In the expansion process, the hydraulic fractures slightly deflected and paralleled to each other, and no directional hydraulic fractures were formed, indicating the poor directional effect.

In conclusion, the principal stress difference has a significant effect on directional hydraulic fracturing. With the increase of principal stress difference, the effect and accuracy of orientation become worse. The hydraulic fracture propagation direction of each borehole gradually deviates from the borehole line, and the angle between the maximum principal stress and the hydraulic fracture propagation direction gradually decreases. Hydraulic fractures are more difficult to fuse and easy to form rock bridge area. When the stress difference is greater than a certain extent, the directional effect is completely invalid. The hydraulic fractures are parallel to each other, which cannot achieve the goal of directional fracturing.

6.3. Discussion: Borehole Spacing. According to the scheme shown in Table 6, three groups of different borehole spacing D were set, and the borehole spacing is 105, 141, and 176 mm. The final test results are shown in Figure 15.

When the value of D was 105 mm, the hydraulic fractures in the directional fracturing section (H1-H3) obviously initiated and expanded along the borehole line direction and finally intersected with each other and approached adjacent injection holes to form a directional hydraulic fracture. For the range outside the directional fracturing section (H1-H3), the hydraulic fractures extended to the edge of the test block along the direction of the maximum principal stress. The directional fracture surface was coplanar with all injection holes. It was smooth and flat with obvious directivity and without other bifurcation and stratification.

When the value of D was 141 mm, the hydraulic fractures of the H1 leftwing and the H3 rightwing extended to the edge of the test block along the direction of maximum principal stress σ_1 and then extended along the direction of the borehole line with an obvious turning point in the fracture trajectory. The hydraulic fractures of H2 finally extended to two adjacent holes along the borehole line and did not intersect with the adjacent hydraulic fractures, forming a rock bridge in the oblique direction of σ_1. Besides, there is delamination in directional hydraulic fracture.

When the value of D was 176 mm, the hydraulic fractures of the three boreholes all initiated and expanded along the direction of the maximum principal stress. After expanding for a certain distance, the direction of expansion deflected. However, due to the long distance between the boreholes, the coupling stress between the boreholes was weak and the degree of deflection was small, and finally, there was no directional fracture formed.

With the increase of hole spacing, the directional fracture zone became more difficult to be formed by overlapping the stress disturbance zones at the tip of hydraulic fractures. The coupling stress between holes was smaller, making it more difficult for hydraulic fractures of different boreholes to intersect. The stratification phenomenon and the number of rock bridges formed in the process of hydraulic fracture intersection significantly increased, and the directional effect and accuracy were reduced.

6.4. Discussion: Borehole Pumping Mode. During the hydraulic fracturing construction in the coal mine, due to the pipeline loss and the difference in the strength of rock around the borehole, the initiation of hole wall cracking was not synchronous. In order to reveal the influence of borehole pumping mode on directional hydraulic fracturing, the test scheme is shown in Table 7, and three different pumping modes were constructed, including the priority of middle hole, the priority of outer hole, and the simultaneous initiation of three holes, respectively. The test results are shown in Figure 16.

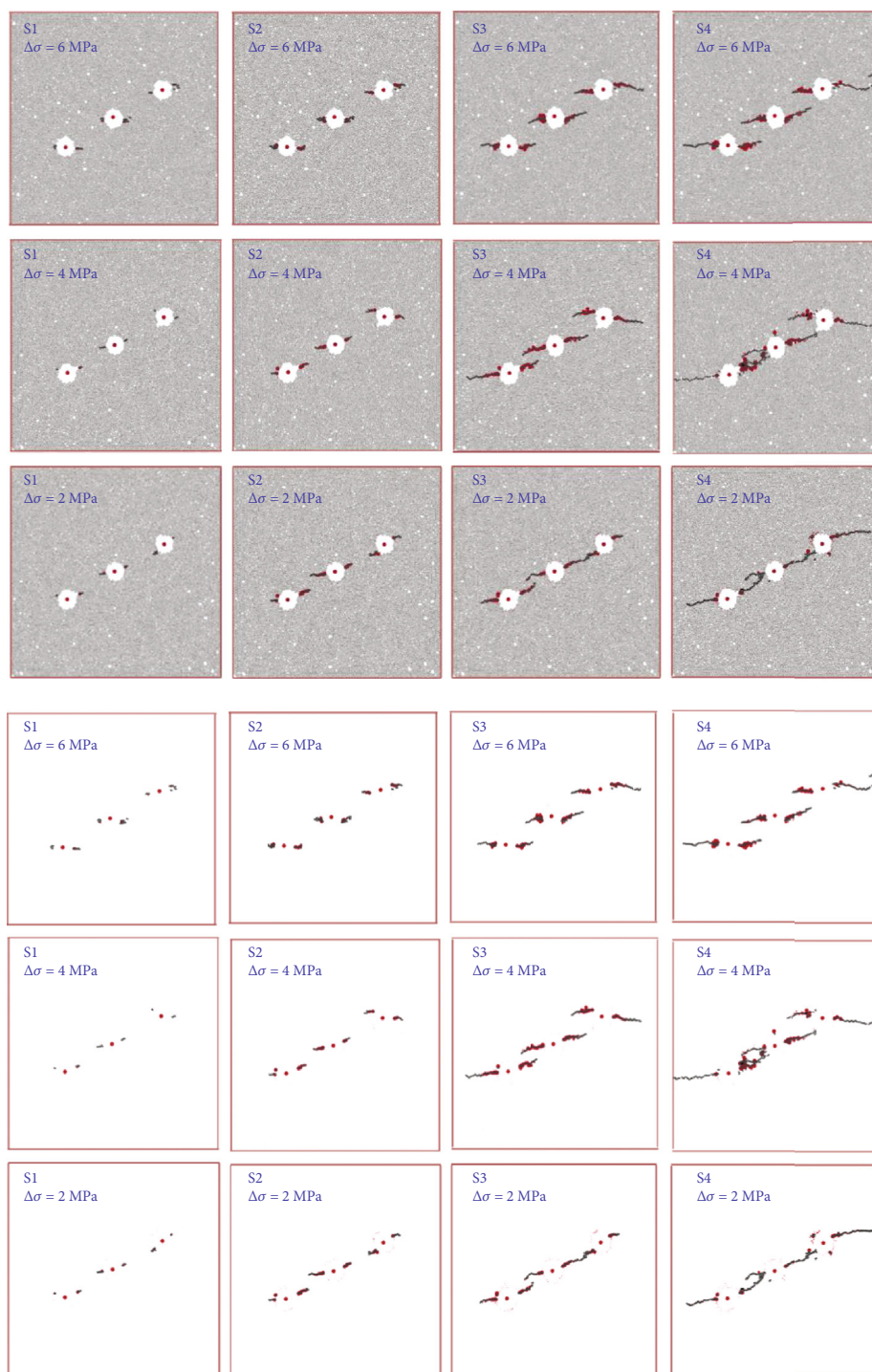When the middle borehole cracked first, the hydraulic fractures initiated along the borehole line and expanded along the direction of the maximum principal stress. After
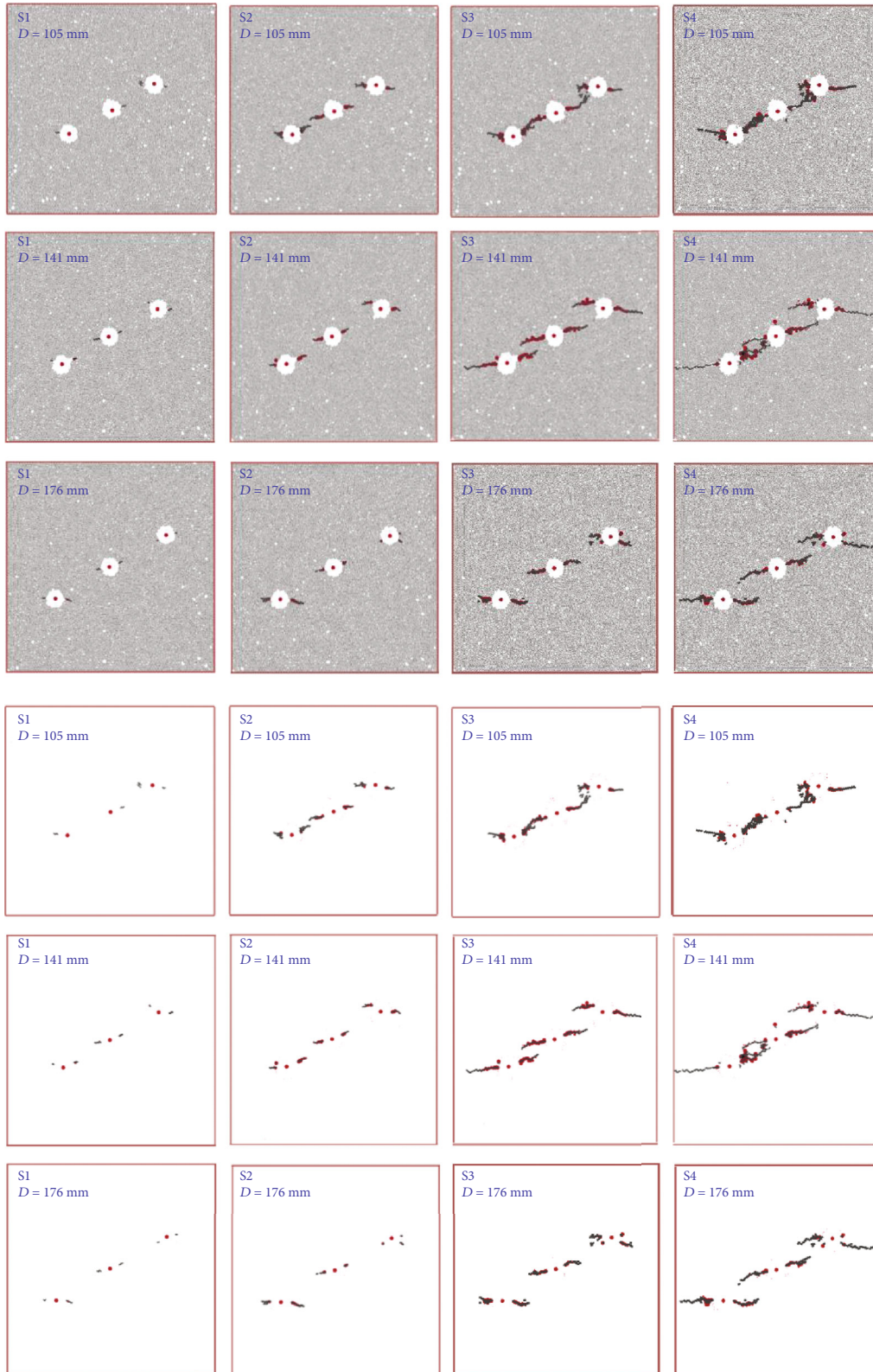
FIGURE 15: Initiation and propagation process of directional hydraulic fractures at different borehole spacing.

4000 time steps, the water began to be injected into the outer borehole. The hydraulic fractures of H1 leftwing and H3 rightwing extended to the edge of the test block along the direction of the maximum principal stress. The hydraulic fractures of the H1 rightwing and H3 leftwing initiated and expanded along the borehole line. Under the effect of the

TABLE 7: Experimental scheme of directional hydraulic fracturing.

Test name	Principal stress (MPa)			Borehole spacing (mm)	Arrangement angle of boreholes (°)	The injection rate (ml/min)	Pumping mode
	σ_1	σ_2	σ_3				
5-1	7		5	141	15	50	Sequence (1)
5-2	7		5	141	15	50	Sequence (2)
5-3	7		5	141	15	50	Synchronous
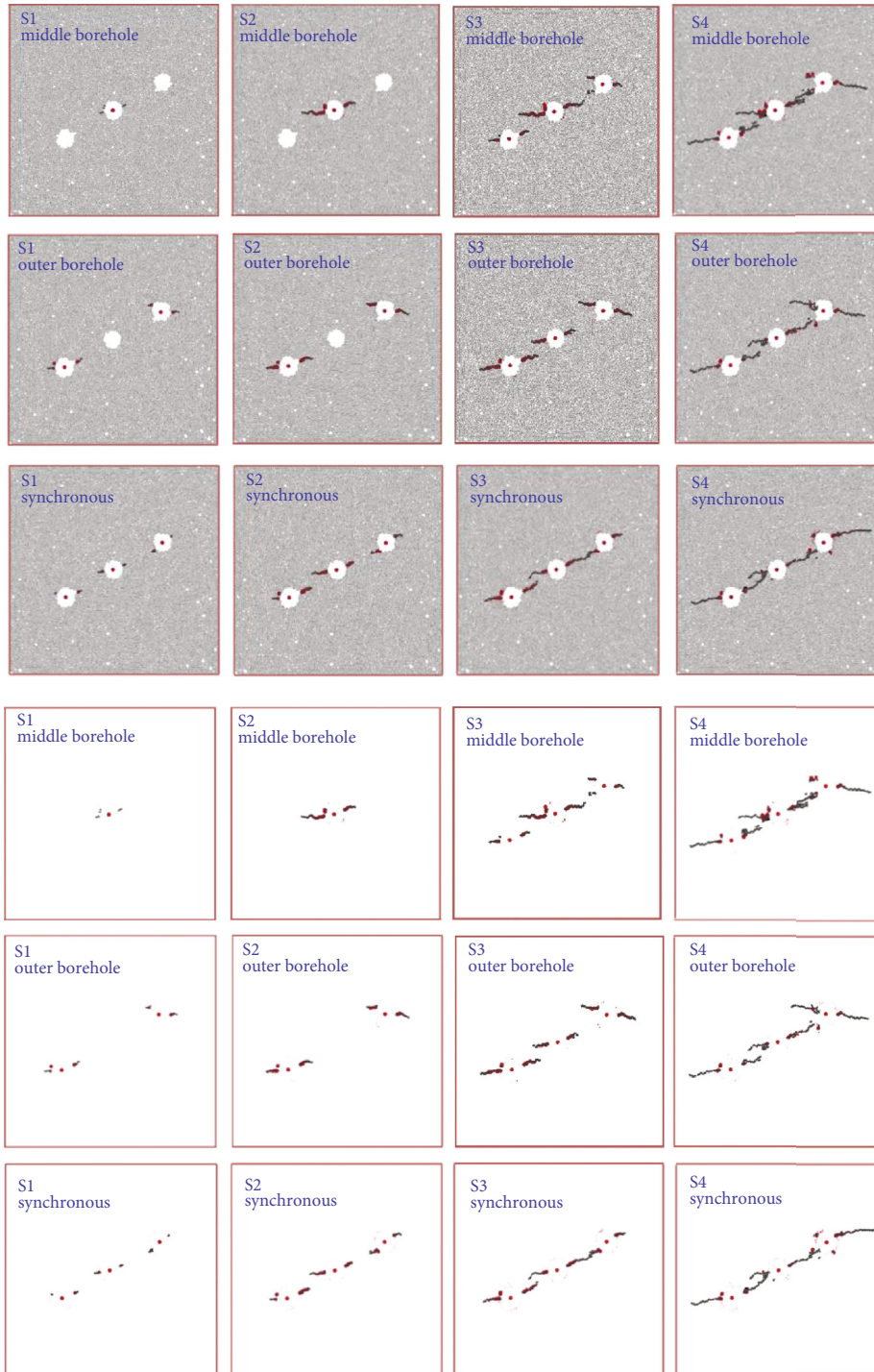
FIGURE 16: Initiation and propagation process of directional hydraulic fractures at borehole pumping mode.
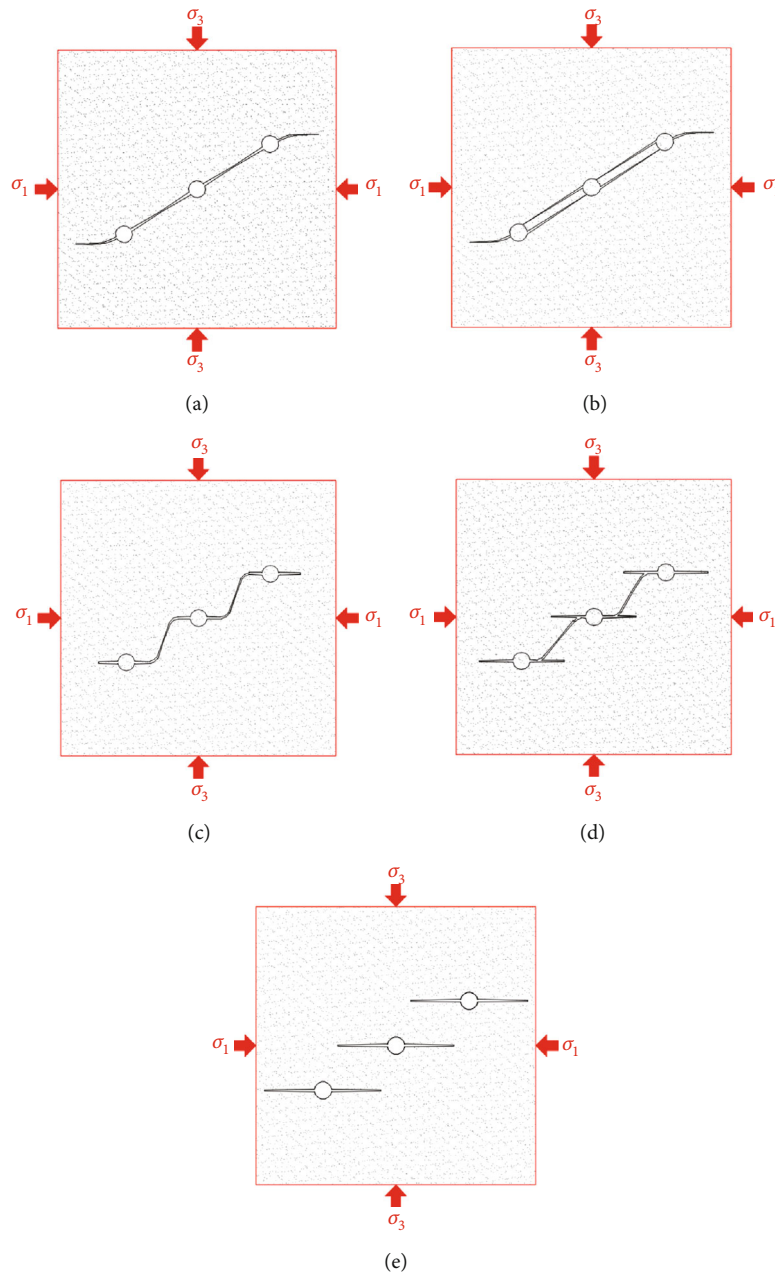
Figure 17: Dense linear multihole directional hydraulic fracture propagation modes.

hydraulic fractures of adjacent boreholes, the hydraulic fractures of two H2 wings deflected and expanded along the borehole line. Among them, hydraulic fractures of H2 rightwing and H3 leftwing were fused, and hydraulic fracture of H2 leftwing connected with that of the H1, forming a rock bridge between H2 leftwing and H1 rightwing and a stratified directional hydraulic fracture.

When the outer boreholes cracked first, the hydraulic fractures of the two holes initiated and expanded along the direction of the maximum principal stress. After 4000 time steps, the water began to be injected into the middle hole, and the hydraulic fractures of two H2 wings initiated and expanded along the borehole line, finally connecting the

adjacent boreholes. During the expansion process, the hydraulic fractures of the three holes did not intersect, forming rock bridges on the directional hydraulic fracture surface.

When the three boreholes started to crack simultaneously, the hydraulic fractures initiated and expanded along the direction of the borehole line, and the directional hydraulic fractures were formed by the fusion of the hydraulic fractures in the adjacent drilling holes. These fractures were smooth and flat in shape, with obvious directivity and good directional effect but without an obvious turn in the expansion.

In a word, the fracturing mode significantly affects directional hydraulic fracturing. If the sequence fracturing mode is

adopted, the coupling stress effect between the holes will be relatively poor, making it difficult to form the directional fracturing strip inside the test block. The formed directional fracture surface will be prone to stratification, the directional hydraulic fracture trajectory will become more tortuous, and the directional effect and accuracy are not as good as synchronous fracturing.

7. Dense Linear Multihole Directional Hydraulic Fracture Propagation Modes

According to the strength of directional effect and directional accuracy, the following five typical hydraulic fracture propagation behavior modes are finally extracted:

Mode 1: hydraulic fractures of adjacent boreholes intersect smoothly along the drilling line to form a linear directional hydraulic fracture, the fracture morphology is similar to "/". In this mode, the effect and accuracy of hydraulic fracture orientation are the best (Figure 17(a)).

Mode 2: the hydraulic fractures extend along the borehole line and connect with adjacent boreholes, but the hydraulic fractures of each borehole do not intersect, and a rock bridge is formed between different hydraulic fractures obliquely in direction (a). The shape of directional hydraulic fractures is similar to "//" (Figure 17(b)).

Mode 3: the hydraulic fracture first extends along the direction of the maximum principal stress σ_1 for a certain distance, then turns to expand along the drilling line direction and intersect with each other, forming a ladder-shaped directional hydraulic fracture, similar to "⌐⌐_" (Figure 17(c)).

Mode 4: the hydraulic fracture of the outer borehole propagates along the direction of the maximum principal stress, and the hydraulic fracture of the middle borehole propagates along the direction of the borehole line and communicates with the adjacent outer borehole; the shape of directional hydraulic fractures is similar to "⟋" (Figure 17(d)).

Mode 5: the hydraulic fractures of each hole expand along the direction of the maximum principal stress σ_1. In the process of expansion, the hydraulic fractures do not deflect and are parallel to each other, forming "≡"-shaped hydraulic fractures, and the orientation effect is the worst (Figure 17(e)). All the above hydraulic fracture propagation modes are reflected in the previous sections.

8. Conclusion

The experimental results demonstrate the following:

(1) When directional hydraulic fracturing controlled by dense linear multihole drilling was carried out, due to the coupled effect between boreholes, the hydraulic fracture propagation tends to intersect and run through and finally forms the directional failure plane along the direction of the connecting line of boreholes, which effectively realizes the directional failure of rock strata

(2) The results show that the directional effect is mainly concentrated in the internal dense boreholes. The hydraulic fractures of the external dense boreholes basically extend along the direction of the maximum principal stress, so the directional effect is poor. In addition, the numerical simulation results are in good agreement with the laboratory test results, which fully verifies the effectiveness and rationality of the directional hydraulic fracturing numerical simulation model based on the two-dimensional discrete element numerical software (PFC^{2D})

(3) After arranging the dense boreholes in the rock, the maximum tangential tensile stress is generated in the direction perpendicular to the drilling line due to the mutual extrusion of boreholes, so the borehole wall along the drilling line direction is most prone to crack initiation. With the increase of the length of the hydraulic fracture, the disturbed stress concentration areas will overlap each other and form the maximum principal stress band, which makes the hydraulic fracture deflect further towards the borehole line

(4) The angle (θ) between the borehole line and the direction of the maximum principal stress, the principal stress difference ($\Delta\sigma$), and the hole spacing (D) have significant effects on the directional hydraulic fracturing effect. The smaller the angle, the difference value of the in situ stress, and the hole spacing, the better the directional hydraulic fracturing effect. In addition, the directional effect of synchronous hydraulic fracturing is better than that of sequential hydraulic fracturing

(5) According to the multihole linear codirectional hydraulic fracturing experiments, five typical directional hydraulic fracture propagation modes are summarized: (1) directional hydraulic fracture completely along the drilling line, (2) directional hydraulic fractures that connect boreholes but do not intersect, (3) propagation forming a ladder pattern of directional hydraulic fracture, (4) directional hydraulic fracture propagation both along the borehole line and parallel to the direction of maximum principal stress, and (5) parallel hydraulic fractures extending completely along the direction of maximum principal stress

Nomenclature

E_c: Elastic modulus (GPa)
v: Poisson's ratio
k_n: Normal stiffness of particle element (N/m)
k_s: Tangential stiffness of particle element (N/m)
μ: Friction coefficient between particle elements
ρ: Particle unit density (kg/m^3)
σ_1: Maximum horizontal geostress (MPa)
σ_3: Minimum horizontal geostress (MPa)
p: Water pressure (MPa)
c_0: Cohesion of rock (MPa)
Φ: Friction angle of rock (°)

G_F: The initial fracture energy (N/m)
G_f: The dissipation energy (N/m)
$R_{\max}$:   Maximum particle radius (mm)
$R_{\min}$:   Minimum particle radius (mm)
$\bar{E}_c$:   Elastic modulus of particle element (GPa)
$\bar{k}_n$:   Normal stiffness of parallel bond (N/m)
$\bar{k}_s$:   Tangential stiffness of parallel bond (N/m)
$\bar{\sigma}$:   Normal strength of parallel bond (MPa)
$\Delta\sigma$:   The principal stress difference (definition of this paper) (MPa)
D: Borehole spacing (definition of this paper) (mm)
$\bar{\tau}$:   Shear strength of parallel bond (MPa)
q: Fluid volume rate (m^3/s)
w: Pipe width (mm)
L: Length of pipe (m)
N: Number of pipelines connecting the domain
K_f: Bulk modulus of fracturing fluid (GPa)
v: Injection rate of fracturing fluid (ml/min)
A: Cross-sectional area of fluid flow (m^2)
ΔP: Change of liquid pressure in river domain (MPa)
ΔV_d: Volume change of domain caused by volume force (m^3)
V_d: Apparent volume of river domain (m^3)
w_0:   Residual width of pipe (mm)
F_i: Normal contact force under current load (N)
g_s: Spacing between particles (mm)
μ: Dynamic viscosity (Pa·s)
k: Macropermeability of sample (mD)
a: Radius of the borehole (m)
b: Outer diameter (m)
θ: Angle between the line of the borehole and the direction of maximum principal stress (definition of this paper) (°).

Data Availability

All the data have been included in the manuscript.

Conflicts of Interest

The authors declare no conflict of interest.

Acknowledgments

References

[1] Cong Lin, Jianqiang Deng, Yaoru Liu, Qiang Yang, and Hongfei Duan, "Experiment simulation of hydraulic fracture in colliery hard roof control," *Journal of Petroleum Science & Engineering*, vol. 138, pp. 265–271, 2016.

[2] B. Huang, J. Liu, and Q. Zhang, "The reasonable breaking location of overhanging hard roof for directional hydraulic fracturing to control strong strata behaviors of gob-side entry," *International Journal of Rock Mechanics and Mining Sciences*, vol. 103, pp. 1–11, 2018.

[3] Y. Wang, J. Yang, M. He et al., "Test of a liquid directional roof-cutting technology for pressure-relief entry retaining mining," *Journal of Geophysics and Engineering*, vol. 16, no. 3, pp. 620–638, 2019.

[4] B. Huang, Y. Wang, and S. Cao, "Cavability control by hydraulic fracturing for top coal caving in hard thick coal seams," *International Journal of Rock Mechanics and Mining Sciences*, vol. 74, pp. 45–57, 2015.

[5] L. You, Y. Kang, Q. Chen, C. Fang, and P. Yang, "Prospect of shale gas recovery enhancement by oxidation-induced rock burst," *Natural Gas Industry B*, vol. 4, no. 6, pp. 449–456, 2017.

[6] C. Zhai, M. Li, C. Sun, J. Zhang, W. Yang, and Q. Li, "Guiding-controlling technology of coal seam hydraulic fracturing fractures extension," *International Journal of Mining Science and Technology*, vol. 22, no. 6, pp. 831–836, 2012.

[7] Q. He, F. T. Suorineni, and J. Oh, "Review of hydraulic fracturing for preconditioning in cave mining," *Rock Mechanics and Rock Engineering*, vol. 49, no. 12, pp. 4893–4910, 2016.

[8] J. Fan, L. Dou, H. He et al., "Directional hydraulic fracturing to control hard-roof rockburst in coal mines," *International Journal of Mining Science and Technology*, vol. 22, no. 2, pp. 177–181, 2012.

[9] X. Sun, C. Zhao, Y. Zhang, F. Chen, S. Zhang, and K. Zhang, "Physical model test and numerical simulation on the failure mechanism of the roadway in layered soft rocks," *International Journal of Mining Science and Technology*, vol. 31, no. 2, pp. 291–302, 2021.

[10] C. Mark, "An updated empirical model for ground control in U.S. multiseam coal mines," *International Journal of Mining Science and Technology*, vol. 31, no. 2, pp. 163–174, 2021.

[11] D. W. H. Su, P. Zhang, H. Dougherty, M. van Dyke, and R. Kimutis, "Longwall mining, shale gas production, and underground miner safety and health," *International Journal of Mining Science and Technology*, vol. 31, no. 3, pp. 523–529, 2021.

[12] M. K. Hubbert and D. Willis, "Mechanics of hydraulic fracturing," *Transactions of the AIME*, vol. 18, no. 1, pp. 369–390, 1972.

[13] B. Haimson and C. Fairhurst, "Hydraulic fracturing in porous-permeable materials," *Journal of Petroleum Technology*, vol. 21, no. 7, pp. 811–817, 1969.

[14] J. Huang, D. V. Griffiths, and S. W. Wong, "Initiation pressure, location and orientation of hydraulic fracture," *International Journal of Rock Mechanics and Mining Sciences*, vol. 49, pp. 59–67, 2012.

[15] P. C. Papanastasiou, "A coupled elastoplastic hydraulic fracturing model," *International Journal of Rock Mechanics and Mining Sciences*, vol. 34, no. 3-4, pp. 240.e1–240.e15, 1997.

[16] M. K. Rahman and A. H. Joarder, "Investigating production-induced stress change at fracture tips: implications for a novel hydraulic fracturing technique," *Journal of Petroleum Science & Engineering*, vol. 51, no. 3-4, pp. 185–196, 2006.

[17] A. G. Olovyanny, "Mathematical modeling of hydraulic fracturing in coal seams," *Journal of Mining Science*, vol. 41, no. 1, pp. 61–67, 2005.

[18] M. He, G. Zhu, and Z. Guo, "Longwall mining "cutting cantilever beam theory" and 110 mining method in China–the third mining science innovation," *Journal of Rock Mechanics and Geotechnical Engineering*, vol. 7, no. 5, pp. 483–492, 2015.

[19] J. Liu, C. Liu, and Q. Yao, "Mechanisms of crack initiation and propagation in dense linear multihole directional hydraulic fracturing," *Shock and Vibration*, vol. 2019, no. 9, Article ID 7953813, 15 pages, 2019.

[20] X. Cheng, G. Zhao, Y. Li, X. Meng, and Q. Tu, "Key technologies and engineering practices for soft-rock protective seam mining," *International Journal of Mining Science and Technology*, vol. 30, no. 6, pp. 889–899, 2020.

[21] J. Tian, D. Xu, and T. Liu, "An experimental investigation of the fracturing behaviour of rock-like materials containing two V-shaped parallelogram flaws," *International Journal of Mining Science and Technology*, vol. 30, no. 6, pp. 777–783, 2020.

[22] L. Weiyong and H. Changchun, "Numerical simulation of the fracture propagation of linear collaborative directional hydraulic fracturing controlled by pre-slotted guide and fracturing boreholes," *Engineering Fracture Mechanics*, vol. 235, article 107128, 2020.

[23] W. Lu and C. He, "Numerical simulation of the laws of fracture propagation of multi-hole linear co-directional hydraulic fracturing," *Energy Exploration & Exploitation*, vol. 39, no. 3, pp. 903–926, 2021.

[24] B. Huang, Q. Cheng, X. Zhao, and C. Kang, "Hydraulic fracturing of hard top coal and roof for controlling gas during the initial mining stages in longwall top coal caving: a case study," *Journal of Geophysics and Engineering*, vol. 15, no. 6, pp. 2492–2506, 2018.

[25] X. Zhang, Y. Zhang, and B. Huang, "Investigation of the Fracturing Effect Induced by the Disturbing Stress of Hydrofracturing Using the Bonded-particle Model," *Geofluids*, vol. 2021, article i.d 9988748, 2021.

[26] B. Lin and C. Shen, "Coal permeability-improving mechanism of multilevel slotting by water jet and application in coal mine gas extraction," *Environmental Earth Sciences*, vol. 73, no. 10, pp. 5975–5986, 2015.

[27] Y. Liu, B. Xia, and X. Liu, "A novel method of orienting hydraulic fractures in coal mines and its mechanism of intensified conduction," *Journal of Natural Gas Science & Engineering*, vol. 27, Part P1, pp. 190–199, 2015.

[28] Q. Zou and B. Lin, "Fluid–solid coupling characteristics of gas-bearing coal subjected to hydraulic slotting: an experimental investigation," *Energy & Fuels*, vol. 32, no. 2, pp. 1047–1060, 2018.

[29] Y. Cheng, Y. Lu, Z. Ge, L. Cheng, J. Zheng, and W. Zhang, "Experimental study on crack propagation control and mechanism analysis of directional hydraulic fracturing," *Fuel*, vol. 218, pp. 316–324, 2018.

[30] X. Zhang, Y. Zhang, and T. Zhang, "Experimental and numerical investigation on hydraulic fracture propagation law of composite rock materials considering the disturbing stress effect," *Geofluids*, vol. 2021, Article ID 9920633, 20 pages, 2021.

[31] J. Deng, Q. Yang, Y. Liu, Y. Liu, and G. Zhang, "3D finite element modeling of directional hydraulic fracturing based on deformation reinforcement theory," *Computers and Geotechnics*, vol. 94, pp. 118–133, 2018.

[32] J. Q. Deng, C. Lin, Q. Yang, Y. R. Liu, Z. F. Tao, and H. F. Duan, "Investigation of directional hydraulic fracturing based on true tri-axial experiment and finite element modeling," *Computers and Geotechnics*, vol. 75, pp. 28–47, 2016.

[33] Q. He, F. T. Suorineni, T. Ma, and J. Oh, "Parametric study and dimensional analysis on prescribed hydraulic fractures in cave mining," *Tunnelling and Underground Space Technology*, vol. 78, pp. 47–63, 2018.

[34] B. Zhang, J. Liu, S. G. Wang et al., "Impact of the distance between pre-existing fracture and wellbore on hydraulic fracture propagation," *Journal of Natural Gas Science and Engineering*, vol. 57, pp. 155–165, 2018.

[35] X. Liu, Z. Qu, T. Guo et al., "An innovative technology of directional propagation of hydraulic fracture guided by radial holes in fossil hydrogen energy development," *International Journal of Hydrogen Energy*, vol. 44, pp. 5286–5302, 2019.

[36] T. Guo, Z. Rui, Z. Qu, and N. Qi, "Experimental study of directional propagation of hydraulic fracture guided by multi-radial slim holes," *Journal of Petroleum Science and Engineering*, vol. 166, pp. 592–601, 2018.

[37] B. Lenoach, "The crack tip solution for hydraulic fracturing in a permeable solid," *Journal of the Mechanics and Physics of Solids*, vol. 43, no. 7, pp. 1025–1043, 1995.

[38] C. A. Tang, L. G. Tham, P. K. K. Lee, T. H. Yang, and L. C. Li, "Coupled analysis of flow, stress and damage (FSD) in rock failure," *International Journal of Rock Mechanics and Mining Sciences*, vol. 39, no. 4, pp. 477–489, 2002.

[39] D. G. Gong, Z. Q. Qu, T. K. Guo, Y. Tian, and K. H. Tian, "Variation rules of fracture initiation pressure and fracture starting point of hydraulic fracture in radial well," *Journal of Petroleum Science and Engineering*, vol. 140, pp. 41–56, 2016.

[40] M. M. Hossain and M. K. Rahman, "Numerical simulation of complex fracture growth during tight reservoir stimulation by hydraulic fracturing," *Journal of Petroleum Science & Engineering*, vol. 60, no. 2, pp. 86–104, 2008.

[41] B. Xian, B. Xia, Y. Zhang, Q. Xiao, L. Cao, and Z. Chen, "Technical analysis on radial horizontal well for development of coalbed methane of low coal rank," *Coal Geology & Exploration*, vol. 38, pp. 25–29, 2010.

[42] J. Zhou, L. Zhang, A. Braun, and Z. Han, "Numerical modeling and investigation of fluid-driven fracture propagation in reservoirs based on a modified fluid-mechanically coupled model in two-dimensional particle flow code," *Energies*, vol. 9, no. 9, p. 699, 2016.

[43] X. P. Zhang and Q. Zhang, "Distinction of crack nature in brittle rock-like materials: a numerical study based on moment tensors," *Rock Mechanics and Rock Engineering*, vol. 50, no. 10, pp. 2837–2845, 2017.

[44] Q. Zhang and X. P. Zhang, "A numerical study on cracking processes in limestone by the b-value analysis of acoustic emissions," *Computers and Geotechnics*, vol. 92, pp. 1–10, 2017.

[45] L. Zhang, J. Zhou, A. Braun, and Z. Han, "Sensitivity analysis on the interaction between hydraulic and natural fractures based on an explicitly coupled hydro-geomechanical model in PFC2D," *Journal of Petroleum Science & Engineering*, vol. 167, pp. 638–653, 2018.

[46] X. Liu, Z. Qu, T. Guo, Y. Sun, Z. Wang, and E. Bakhshi, "Numerical simulation of non-planar fracture propagation in multi-cluster fracturing with natural fractures based on lattice methods," *Engineering Fracture Mechanics*, vol. 220, p. 106625, 2019.

[47] Z. Chen, "Finite element modelling of viscosity-dominated hydraulic fractures," *Journal of Petroleum Science & Engineering*, vol. 88-89, pp. 136–144, 2012.

[48] S. Salimzadeh and N. Khalili, "A three-phase XFEM model for hydraulic fracturing with cohesive crack propagation," *Computers and Geotechnics*, vol. 69, pp. 82–92, 2015.

[49] J. Q. Bao, E. Fathi, and S. Ameri, "A coupled finite element method for the numerical simulation of hydraulic fracturing with a condensation technique," *Engineering Fracture Mechanics*, vol. 131, no. 2, pp. 269–281, 2014.

[50] M. J. Hunsweck, Y. Shen, and A. J. Lew, "A finite element approach to the simulation of hydraulic fractures with lag," *International Journal for Numerical and Analytical Methods in Geomechanics*, vol. 37, no. 9, pp. 993–1015, 2013.

[51] J. Q. Bao, E. Fathi, and S. Ameri, "Uniform investigation of hydraulic fracturing propagation regimes in the plane strain model," *International Journal for Numerical and Analytical Methods in Geomechanics*, vol. 39, no. 5, pp. 507–523, 2015.

[52] S. Ouyang, G. F. Carey, and C. H. Yew, "An adaptive finite element scheme for hydraulic fracturing with proppant transport," *International Journal for Numerical Methods in Fluids*, vol. 24, no. 7, pp. 645–670, 1997.

[53] T. Belytschko and T. Black, "Elastic crack growth in finite elements with minimal remeshing," *International Journal for Numerical Methods in Engineering*, vol. 45, no. 5, pp. 601–620, 1999.

[54] E. Gordeliy and A. Peirce, "Coupling schemes for modeling hydraulic fracture propagation using the XFEM," *Computer Methods in Applied Mechanics and Engineering*, vol. 253, pp. 305–322, 2013.

[55] N. Mos, J. Dolbow, and T. Belytschko, "A finite element method for crack growth without remeshing," *International Journal for Numerical Methods in Engineering*, vol. 46, no. 1, pp. 131–150, 1999.

[56] P. A. Cundall, "A computer model for simulating progressive large-scale movements in blocky rock systems," *Proceedings of the International Symposium on Rock Mechanics*, vol. 1, no. ii-b, pp. 11–18, 1971.

[57] P. A. Cundall and O. D. L. Strack, "A discrete numerical model for granular assemblies," *Geotechnique*, vol. 30, no. 3, pp. 331–336, 2008.

[58] X. P. Zhang and L. N. Y. Wong, "Cracking processes in rock-like material containing a single flaw under uniaxial compression: a numerical study based on parallel bonded-particle model approach," *Rock Mechanics and Rock Engineering*, vol. 45, no. 5, pp. 711–737, 2012.

[59] X. P. Zhang and L. N. Y. Wong, "Crack initiation, propagation and coalescence in rock-like material containing two flaws: a numerical study based on bonded-particle model approach," *Rock Mechanics and Rock Engineering*, vol. 46, no. 5, pp. 1001–1021, 2013.

[60] J. Zhou, L. Zhang, Z. Pan, and Z. Han, "Numerical studies of interactions between hydraulic and natural fractures by smooth joint model," *Journal of Natural Gas Science and Engineering*, vol. 46, pp. 592–602, 2017.

[61] Q. Zhang and X. P. Zhang, "The crack nature analysis of primary and secondary cracks: a numerical study based on moment tensors," *Engineering Fracture Mechanics*, vol. 210, pp. 70–83, 2018.

[62] N. Cho, C. D. Martin, and D. C. Sego, "A clumped particle model for rock," *International Journal of Rock Mechanics and Mining Sciences*, vol. 44, no. 7, pp. 997–1010, 2007.

[63] J. Bear, *Dynamics of Fluids in Porous Materials*, Elsevier Science, 1972.

[64] X. Zhao, B. Huang, and Z. Wang, "Experimental investigation on the basic law of directional hydraulic fracturing controlled by dense linear multi-hole drilling," *Rock Mechanics and Rock Engineering*, vol. 51, no. 6, pp. 1739–1754, 2018.

[65] W. Lu, N. Shan, X. Zhang, and X. Liang, "Effect of strain-dependent hydraulic conductivity of coal rock on groundwater inrush in mining," *Geofluids*, vol. 2020, no. 1, Article ID 8887392, 15 pages, 2020.

[66] Y. G. Zhang, Z. Zhang, S. Xue, R. Wang, and M. Xiao, "Stability analysis of a typical landslide mass in the Three Gorges Reservoir under varying reservoir water levels," *Environmental Earth Sciences*, vol. 79, no. 1, 2020.

[67] Y. G. Zhang, J. Tang, Z. Y. He, J. K. Tan, and C. Li, "A novel displacement prediction method using gated recurrent unit model with time series analysis in the Erdaohe landslide," *Natural Hazards*, vol. 105, no. 1, pp. 783–813, 2021.

[68] Y. G. Zhang, J. Tang, R. P. Liao et al., "Application of an enhanced BP neural network model with water cycle algorithm on landslide prediction," *Stochastic Environmental Research and Risk Assessment*, vol. 35, no. 6, pp. 1273–1291, 2021.

[69] Y. G. Zhang, Y. L. Xie, Y. Zhang, J. B. Qiu, and S. X. Wu, "The adoption of deep neural network (DNN) to the prediction of soil liquefaction based on shear wave velocity," *Bulletin of Engineering Geology and the Environment*, vol. 80, no. 6, pp. 5053–5060, 2021.

[70] Y. G. Zhang, J. Qiu, Y. Zhang, and Y. Wei, "The adoption of ELM to the prediction of soil liquefaction based on CPT," *Natural Hazards*, vol. 107, no. 1, pp. 539–549, 2021.

[71] Y.-G. Zhang, X.-Q. Chen, R.-P. Liao et al., "Research on displacement prediction of step-type landslide under the influence of various environmental factors based on intelligent WCA-ELM in the s," *Natural Hazards*, vol. 107, no. 2, pp. 1709–1729, 2021.

[72] Y. Zhang, J. B. Qiu, Y. G. Zhang, and Y. L. Xie, "The adoption of a support vector machine optimized by GWO to the prediction of soil liquefaction," *Environmental Earth Sciences*, vol. 80, no. 9, 2021.

WILEY | Hindawi

Research Article

Experimental and Numerical Investigation on Hydraulic Fracture Propagation Law of Composite Rock Materials considering the Disturbing Stress Effect

Xin Zhang [iD],[1] **Yuqi Zhang** [iD],[1] **and Tao Zhang** [iD][2]

[1]*School of Mines, China University of Mining and Technology, Xuzhou, China*
[2]*State Key Laboratory for Geomechanics and Deep Underground Engineering, China University of Mining and Technology, Xuzhou, China*

Correspondence should be addressed to Xin Zhang; tyzyqhzx@163.com

The stress disturbance effect will significantly affect the propagation path of hydraulic fractures in the composite rock reservoir. To reveal the influence mechanism of stress disturbance effect on the hydraulic fracture propagation, several groups of laboratory tests and simulation tests were carried out. The test results showed that the hydraulic fracture tip formed a disturbing stress field because of the pore water pressure. Before the hydraulic fracture was extended to the bedding plane, the bedding plane had been damaged under stress disturbance, and the disturbed fracture zone was formed. The propagation mode of hydraulic fracture at the bedding plane was highly sensitive to the formation of the disturbed fracture zone. The sensitivity is mainly reflected from two aspects. (1) Under the action of the hydraulic fracture tip disturbance stress, many microfractures are generated and penetrated into the disturbance fracture zone on the bedding plane. This behavior is accompanied by energy dissipation causing the bedding plane material to be significantly softened, and the energy required for hydraulic fracture propagation is reduced dramatically. (2) The formation of the disturbed fracture zone improves the degree of fragmentation of the bedding plane, and the permeability of the local area increases significantly, forming the dominant circulation path. The higher the development of the disturbed fracture zone, the greater the hydraulic fracture propagation tendency along the bedding plane. According to the formation characteristics of the bedding plane disturbed fracture zone, the author proposed a nonlinear fracture model of the bedding plane disturbed fracture zone and established the hydraulic fracture propagation path criterion. This paper further analyzed the influencing factors of the disturbed fracture zone's formation conditions and found that the bedding plane's cementation strength was the main factor affecting the development degree of the disturbed fracture zone.

1. Introduction

The reservoir rock mass of oil, natural gas, and unconventional natural gas reservoirs comprises various rock materials, discontinuous structural planes, and microfractures. When hydraulic fracturing is applied to a composite rock reservoir, the existence of a weak bedding plane will significantly affect the extension path of hydraulic fractures [1]. How to control the propagation of hydraulic fractures in such reservoirs is a critical problem in a hydraulic fracturing design [2–5].

In recent years, relevant scholars have carried out many experiments on the interaction mechanism between hydraulic fractures and rock bedding planes [6–9]. The research results show that under the condition of different bedding plane strength [10], in situ geo stress coefficient [11], the material difference [12, 13], injection pressure, and rheological and viscous characteristics of fracturing fluid [14–16], hydraulic fractures will form three modes: (1) expanding along the bedding plane, (2) expanding along the bedding plane and crossing the bedding plane, and (3) crossing the bedding plane. These three kinds of propagation modes can

be observed in relevant hydraulic fracturing tests and reservoir microseismic monitorization [17]. With the research deepening, some scholars carried out experiments on microcrack propagation mechanism and found that [18–20]; when the fracture approached the bedding plane, the disturbing stress field at the fracture tip would lead to the early failure of the bedding plane and form the microfracture zone, which was called Cooke-Garden cracking effect [21]. This early bedding plane fracture zone has a significant trapping effect on fracture propagation [22, 23]. However, at present, the research on this effect mainly focuses on surface crack propagation under a single stress state. By contrast, the research on fracture propagation under complex stress of fluid-solid coupling is rare, and it is helpful to reveal the mechanical mechanism of hydraulic fracture propagation at the bedding plane of composite rock material and is an effective means to solve the problem of reservoir reconstruction.

At present, the mechanical mechanism of the development of hydraulic fracture at the composite rock bedding plane is mainly divided into the following two aspects: firstly, based on the linear elastic mechanic's theory, taking the two-dimensional plane fracture as the research object and assuming a constant static pressure in the hydraulic fracture ignore the induced stress in the direction of perpendicular to the fracture [24]. The Mohr-Coulomb failure criterion is used to analyze the tensile failure caused by tensile stress acting on the fracture [25], and the shear slip failure caused by the shear stress acting on the fracture is considered through the linear friction theory [26]. Secondly, based on the linear elastic fracture mechanics, the analytical model of induced stress distribution at the fracture tip is established to provide the basis for judging whether the hydraulic fracture initiated or expanded [27]. The above research provides a useful reference for revealing the hydraulic fracture propagation mode and propagation path at the bedding plane, but there are still some deficiencies as follows: (1) both analytical criteria are based on the assumption that the rock bedding plane is completely cemented and ignored the change of stress field distribution and damage to materials caused by disturbed stress of hydraulic fracture. (2) Relevant scholars have revealed the morphological characteristics of actual hydraulic fractures by drilling cores [28]. Many microfractures or secondary fractures formed at the tip of actual hydraulic fractures reflect the morphological characteristics of complex clusters of small-sized fractures, which is inconsistent with the conventional understanding of wing hydraulic fractures. Therefore, the traditional hydraulic fracturing theory [29] based on elastic-plastic mechanics and linear elastic fracture parameters can not adequately describe the hydraulic fracture morphology and propagation law. At present, it is necessary to establish a nonlinear fracture model as the theoretical basis of the new hydraulic fracturing model to understand the hydraulic fracture extension mode comprehensively.

Most of the hydraulic fracturing experiments are also realized by direct observation of the internal hydraulic fracture morphology of the text block by the naked eye and microscope. Due to the closed confining pressure loading environment in the hydraulic fracturing test, it is difficult to observe the bedding fracture zone and the dynamic hydraulic fracture propagation process under the existing technology. Although the formation process of the fracture zone can be monitored by associated acoustic emission equipment (AE) [30–33], there is a significant disadvantage of determining the dynamic propagation process of hydraulic fracture only by the distribution range of acoustic emission events because the damage process of bedding plane is a quasistatic process with low energy release rate and long formation time, which is difficult to monitor. Moreover, it is difficult to distinguish whether the bedding fracture zone's formation is caused by stress induction or direct invasion of fracturing fluid. Thus, the distribution of the stress field in the test block can not be obtained. So, many studies in this part only focus on the macrophenomenon but the lack of research on the mesomechanism of the event restricts the understanding of the hydraulic fracture propagation mechanism and the formation mechanism of the hydraulic fracture network. Therefore, the particle flow calculation method proposed by Dr. Cundall based on the discrete element theory is used to tackle this problem [34, 35], whose modelled failure process is very consistent with the real failure of rock compared with other methods. It can monitor the dynamic fracture propagation process [36, 37]. It has been widely used in many geotechnical engineering research fields, such as rock mechanics tests, underground space excavation, slope engineering, and mining engineering. The fluid-structure coupling model established by PFC software can genuinely reproduce the hydraulic fracturing process and benefit from observing the hydraulic fracture morphology, which is an effective method to study the interaction between hydraulic fracture and bedding plane [38].

To sum up, this paper described the formation characteristics of bedding fracture zone under stress disturbance effect and the interaction mechanism between hydraulic fracture and bedding microfracture zone. A nonlinear fracture model of a disturbed fracture zone was proposed. The judgment criterion of the propagation path at the hydraulic fracture bedding plane considering the stress disturbance effect was improved. The sensitivity analysis of the influencing factors of the disturbance effect was carried out.

2. Particle Flow Method

Relevant research results have proved that the parallel bond model can simulate the fracture initiation and propagation of rock under different stress conditions, and it is in good agreement with the results of laboratory tests and theoretical analysis [35]. Besides, the channel formed between broken rigid bodies can be used to simulate fluid flow in pipes. Based on the fluid-solid coupling algorithm proposed by Cundall in 2000, after continuous improvement by relevant scholars, the fluid-solid coupling problem can be better simulated and calculated [39–45].

2.1. Parallel Bond Model. The particle discrete element method is based on Newton's second law and force-displacement rule to determine the motion of particles and the force on the contact surface. Its core is the contact characteristics of particles, that is, the constitutive contract law.
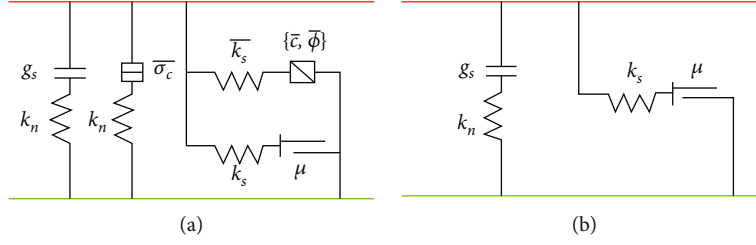
FIGURE 1: Parallel bond model: (a) parallel bond and (b) bond failure (stiffness, damping, and friction).

The constitutive contact model is described by a mesomodel and parameters which characterize the stiffness, damping, and friction (Figure 1). A parallel bonding model is similar to a group of springs, which are evenly arranged on the adjacent area of two contact particles. It has not only standard stiffness and tangential stiffness but also normal tensile strength and shear strength, which can transfer the force and moment between particles. If maximum stresses exceed the corresponding bond strength [46], the parallel bond will break, and the bond material and its associated forces, moments, and stiffness will be removed from the model, and only the linear model will be available. The failure criterion is closer to the real rock failure condition [38–40].

Force displacement laws for contact force and momentum in the BPM are, respectively, computed as follows [46]:

$$F_c = F_l + F_d + F_b, \tag{1}$$

$$M_c = M_b, \tag{2}$$

$$M_b = M_n^b n_i + M_s^b t_j, \tag{3}$$

where F_l refers to the linear force and F_d denotes the hysteretic damping force [47], which is applied to dissipate energy of the system for each particle in each calculation step, and F_b represents the parallel bond force and M_b stands for the parallel bond moment.

The parallel bond force and moment of parallel bond element are computed as follows:

$$F_i = F^n n_i + F^s t_j, \tag{4}$$

$$M_i = M^n n_i + M^s t_j, \tag{5}$$

where F^n and F^s denote the normal and tangential bond forces, respectively, and M^n and M^s are the torque.

According to the beam bending theory, the maximum tensile stress σ_c and shear stress τ_c acting on the parallel bond can be obtained from

$$\sigma_{\max} = \frac{F^n}{A} + \frac{|M^s|R}{I}, \tag{6}$$

$$\tau_{\max} = \frac{|F^s|}{A}, \tag{7}$$

where A and I are the area and moment of inertia of parallel bonded cross section, respectively.

When tensile and shear strength of parallel bond element exceed $\sigma_{\max}$ or $\tau_{\max}$, the parallel bonds break [47].

2.2. Fluid-Solid Coupling Model. In the program, the fluid-solid coupling is realized by assuming the geometric space of particle-particle contact as the parallel plate channel of fluid flow (Figure 2(b)). The adjacent parallel plate fluid channels in the model are connected to form a closed "domain" model (Figure 2(a)). In the calculation process, the water pressure in the "domain" is continuously updated and acts on the particles. The seepage flow q between the connected domains is determined by the hydraulic gap a width of the connecting "pipe," the water pressure p_1 and p_2 of the "domain" and the dynamic viscosity μ of the fluid [48], as shown in

$$q = \frac{a^3}{12\mu} \frac{p_2 - p_1}{L}, \tag{8}$$

where $p_2 - p_1$ is the pressure difference between two adjacent areas; L is the length of the pipe and its value is the sum of the radius of particles connected with the calculated contact; and a it is determined by the contact force between particles.

In the calculation time step Δt, the change of pore fluid pressure is calculated by the bulk modulus of fluid.

$$\Delta p = \frac{K_f}{V_d}\left(\sum q\Delta t - \Delta V_d\right), \tag{9}$$

where K_f is bulk modulus, V_d is the apparent volume of the domain, and $\sum q$ is the total flow of the domain from the surrounding pipes.

$$F_i = pn_i s, \tag{10}$$

where n_i is the external average unit vector of the connecting line between adjacent particles, s is the distance from the center of the corresponding particle to the contact point, and p is the change of fluid pressure in the basin in each time step.

In addition, because of the explicit algorithm, in order to ensure the stability of the numerical model, the pressure change caused by water flow must be less than the disturbance pressure:

$$\Delta t = \frac{2rV_d}{NK_f ka^3}, \tag{11}$$

(a)   (b)
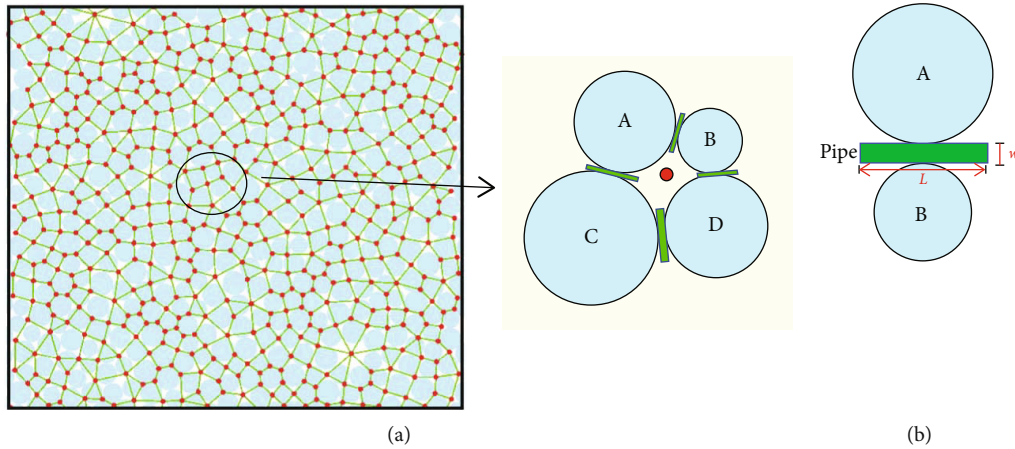
FIGURE 2: Pipeline and domain in PFC^{2D}: (a) fluid grid—solid green circle represents solid particles, middle area of particles represents drainage basin; solid red circle represents basin center, and green line segment represents pipeline; (b) domain and pipe—W and L: the width and length of pipelines are shown, respectively.

where N is the number of pipes connected to a domain and r is the average radius of particles around a domain. In addition, in order to ensure the stability of the whole computing domain, the global time step must be the minimum of all local time steps.

3. Experimental Program and Calibration of Numerical Model Parameters

3.1. Preparation of Test Block. It is difficult to sample, cut, and transport the test block containing bedding planes in the coal mine. In addition, the mechanical property of cement mortar with fixed material ratio is steady and its discrete is low, which meets the requirements of the experiments. In the experiments, cement mortar test blocks were used to simulate hydraulic fracturing on site. No. 32.5 cement, filtered fine sand, and freshwater with a mass ratio of 3.5 : 1 : 0.3 were mixed with casting test blocks. The bedding planed pouring method was used to pour the sample into the particular steel mold of $300 \times 300 \times 300$ mm. The specific process is shown in Figure 3. The air-dried composite rock material sample is shown in Figure 4. The mechanical strength of the test block was tested by sampling. The main experimental parameters are as follows: the compressive strength is 15.85 MPa, the average tensile strength is 1.65 MPa, Poisson's ratio is 0.18, cohesion is 2.94 MPa, tensile strength is 0.28 MPa at bedding plane, cohesion is 0.30 MPa at bedding plane, and the porosity of test block is 0.14 (Table 1).

To make the mechanical properties and failure characteristics of DEM simulation samples consistent with the indoor test results (Figure 4), a numerical model with a length of 100 mm and a width of 50 mm was established to calibrate the model parameters. The minimum particle radius R_{min} is 0.64 mm, and the ratio of maximum particle radius to a minimum particle radius is 1.66. In this model, the particle radius is uniformly distributed in this range, and the porosity is 0.14. The microparameters were adjusted repeatedly until the stress-strain curve and the final fracture mode of the simulated specimen were consistent with the laboratory test.

Table 2 shows the microscopic parameters of the simulated sample. Table 3 shows the comparison of the parameters of the laboratory test and numerical simulation. Figure 5 shows the contrast of the stress-strain curve and the final fracture mode of the complete specimen.

As shown in Figure 5, the simulated stress-strain curve is in good agreement with the curve in the experimental test (it should be noted that PFC cannot reflect the sample compaction stage). The peak strength of the indoor test sample is 15.85 MPa, and that of numerical simulation is 15.94 MPa, with a difference of 0.09. The results proved that the parameters in Table 2 were reasonable. To obtain the tensile strength of the bedding plane of the composite rock material test block, the shear experiments were carried out on the sample. Figure 6 shows the failure morphology of test blocks in the experiment. In the process of mechanical parameters testing, multiple shear failure planes occur in the test block without a bedding plane. No obvious weak plane exists in the test block. The shear failure planes occur along the bedding plane in test blocks with a prefabricated bedding plane. The number of associated fractures is also small. A weakening effect of bedding planes exists in the shear experiments. According to the Mohr-Coulomb criterion, the tensile strength of the bedding plane can be calculated, and the value is 1/5.8 of the matrix rock mass. The mechanical property of simulated bedding planes is similar to this typical rock bedding plane [49]. Therefore, the test blocks can be used to simulate bedding planes.

The rock parameters above were used to model composite rock mass materials, as shown in Figure 4. The modelling size of the square model is 300 mm in length and 300 mm in width, which contains about 12787 particles. The material is divided into three areas. To distinguish the bedding planes, the middle area's colour is set to be black, and the two outer areas are arranged as grey. The fluid injection point is located in the center of the model. The distance between the two bedding planes and the center of the injection point is 68 mm. The confining pressure is loaded by applying constraint stress on the boundary (wall) of the model. In addition, the
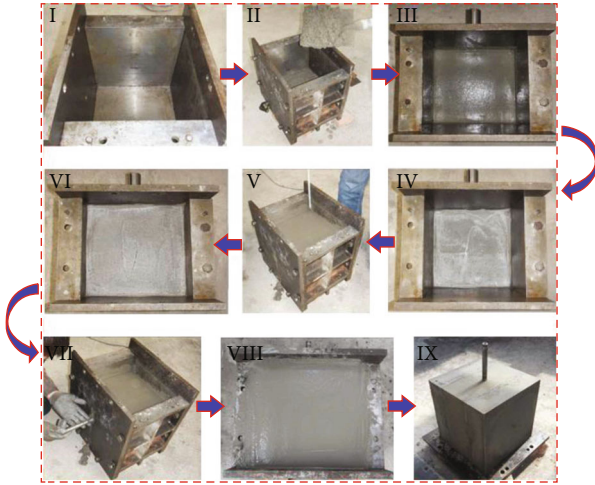
FIGURE 3: The preparation process of the test block containing bedding planes. (I) Putting down for casting. (II) Adding cement mortar and vibrating. (III) Start air drying. (IV) After air drying. (V) Start air drying the second bedding plane. (VI) The air drying of the second bedding plane is finished. (VII) Install the hole sealer. (VIII) The third layer is finished, and air drying was started. (IX) The test block is finished [49].

fluid viscosity, fluid bulk modulus, and model permeability used in the model are consistent with laboratory tests (Table 4).

3.2. Hydraulic Fracture Morphology of Composite Rock Materials

3.2.1. Test System and Scheme. As shown in Figure 7, the 500 mm × 500 mm × 500 mm true triaxial hydraulic fracturing experimental system was used for the hydraulic fracture propagation test of composite rock. Three channels of the four-channel electrohydraulic servo loader control the confining pressure accurately, and the other channel controls the oil-water loading converter to control the loading of water pressure.

According to the test scheme shown in Table 5, this part will monitor the dynamic hydraulic fracture propagation process and study the formation process of a bedding fracture zone (BFZ) in hydraulic fracturing of composite rock mass materials.

3.2.2. Analysis of the Spatial Form of Hydraulic Fracture. The laboratory test results are shown in Figures 8(a) and 8(b). The hydraulic fracture was roughly parallel to the direction of the maximum principal stress σ_1. When the hydraulic fracture extended to the left bedding plane, part of the fracturing fluid turned to the bedding plane and expanded along the bedding plane. The other part of the fracturing fluid continued to spread along the direction of the maximum principal stress, forming "≠"-shaped cross fractures on the bedding plane. When the hydraulic fracture extended to the right bedding plane, the hydraulic fracture directly turned and expanded along the bedding plane, forming a "T"-shaped cross fracture. Compared with the hydraulic fracture morphology of

homogeneous rock material shown in Figure 8(d), the hydraulic fracture propagation path of composite rock material presented a significant difference, indicating that the existence of the bedding plane is the key factor affecting the propagation path of hydraulic fracture. Besides, compared with Figure 8(c), it was found that the hydraulic fracture morphology and hydraulic fracture propagation mode of simulation results were in good agreement with the indoor test.

A large range of watermark in the right bedding plane indicated that the bedding plane was opened, and the fracturing fluid penetrated the bedding plane after the hydraulic fracture extended to the bedding plane while the right bedding plane was not stained (Figure 9(a)). It was shown that the dyed particles could not enter the small opening of the hydraulic fracture during the fracturing fluid expanding along the bedding plane. The main hydraulic fracture opening was 0.54 mm, the bedding plane hydraulic fracture opening was 0.09 mm, and the opening ratio was 6 in the indoor test (Figure 9(c)), which was 0.50 mm, 0.08 mm, and 6.25 mm, respectively, in the simulation test (Figure 9(d)), showing a high consistency between the results of hydraulic fracture opening and the indoor test, fully proving the rationality of the simulation test. Therefore, the simulation can be applied to observe the dynamic propagation process of hydraulic fracture and the interactive response process between the hydraulic fracture and bedding plane in the next section.

4. Dynamic Fracture Propagation Law of Composite Rock Hydraulic Fracture under the Fracturing Effect Induced by Disturbing Stress of Hydrofracturing

This part will analyze the dynamic propagation process of hydraulic fracture based on the verified particle flow model in section 3.2.2 and investigate the development characteristics of the bedding plane fracture zone (BFZ) as well as the interactive law between hydraulic fracture and bedding plane in the process of hydraulic fracturing.

The simulation results are shown in Figure 10. The dynamic hydraulic fracture propagation process can be divided into two stages (HF1 as an example). The first stage (Figure 10, Steps 1, 2, and 3) is that after the hydraulic fracture was initiated, the main hydraulic fracture gradually approached the bedding plane until they intersect. It should be noted that in this stage, the fracturing fluid did not invade the bedding plane. The second stage (Figure 10, Steps 4, 5, and 6) is that after the main hydraulic fracture intersected with the bedding plane, the fracturing fluid invaded into the bedding plane until the hydraulic fracturing was completed.

It can be known from the first stage that hydraulic fractures were initiated in the 140° and 320° directions of the injection hole, and the continuous expansion of the microcracks gradually formed the macrohydraulic fracture. When the HF1 fracture tip was 24 mm away from the I-bedding plane, microcracks were initiated at the I-bedding plane.
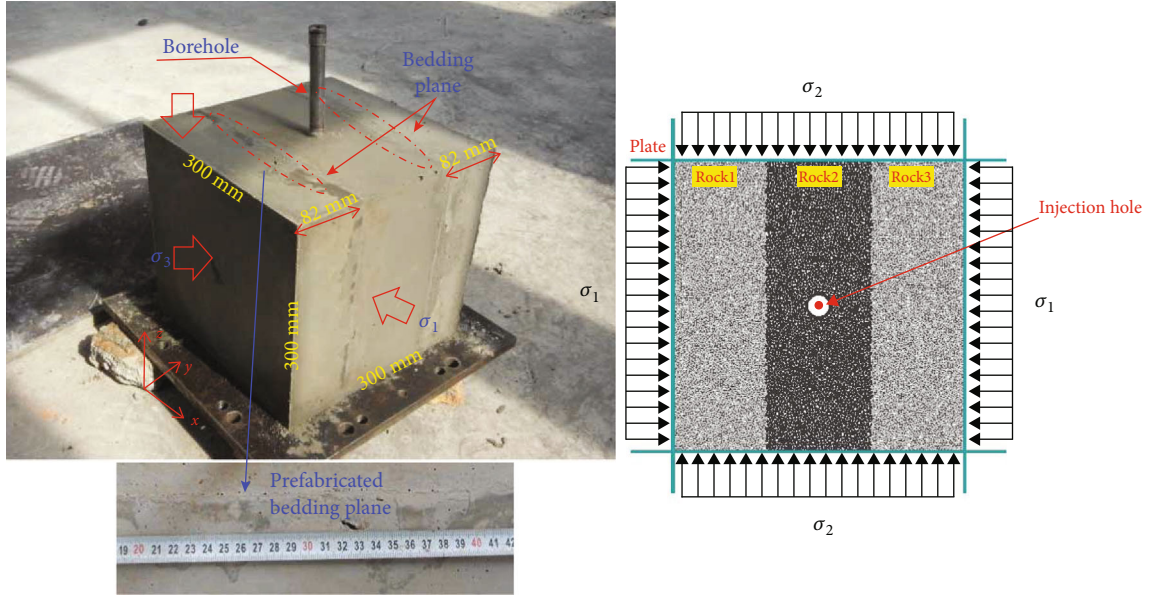
FIGURE 4: Three-dimensional diagram and simulation diagram of composite rock material test block with bedding (unit: mm).

TABLE 1: Physical and mechanical parameters of the cement mortar.

Porosity ϕ (%)	Permeability K (mD)	Uniaxial compressive strength σ_c (MPa)	Modulus of elasticity E (GPa)	Tensile strength σ_t (MPa)	Cohesion c (MPa)	Angle of internal friction φ (°)	Fracture toughness K_{1c} (N·mm$^{3/2}$)
13.79	1.13	15.85	0.92	1.65	0.30	31.29	13.23

TABLE 2: Micromechanical parameters of simulated samples.

Particle parameters					Parallel bonding parameters				
E_c (GPa)	k_n/k_s	μ	R_{max}/R_{max}	ρ (g·cm^{-3})	$\bar{E}_c$ (GPa)	$\bar{k}_n/\bar{k}_s$	$\bar{\sigma}_c$ (MPa)	$\bar{c}$ (MPa)	$\bar{\lambda}$
1.51	1	0.1	1.66	2.65	1.51	1	5.4	12.7	1

TABLE 3: Comparison of parameters between laboratory test and numerical simulation test.

Value type	Density ρ (g·cm^{-3})	Young's modulus E (GPa)	Uniaxial compressive strength σ_c (MPa)	Poisson's ratio	Porosity
Experimental value	2.65	0.92	15.85	0.18	0.14
Simulation value	2.65	0.90	15.94	0.18	0.14

The reason is that the disturbing stress field in front of the hydraulic fracture tip induced the tensile failure of the bedding plane.

According to the model stress field shown in Figure 11, it can be seen that the particles in the test block were in a compression state (black area) under the action of confining pressure. As hydraulic fracture propagated, a tensile load area was formed at the hydraulic fracture tip, the stress disturbance area (red zone). With the hydraulic fracture expanding, the compressive stress field at the front end of the hydraulic fracture tip shrank, and the tensile stress field gradually increased. The range of the tensile stress field was far greater than the permeable range of fracturing fluid. Under the influence of the disturbance stress at the hydraulic fracture tip, the stress state around the bedding plane was always in dynamic change, and the bedding plane broke, reflecting the fractur-

ing effect induced by disturbing stress of hydrofracturing. Besides, in the process of hydraulic fracture propagation, the red area at the front of the hydraulic fracture tip expanded continuously, indicating that the disturbing tensile stress perpendicular to the hydraulic fracture propagation direction increased steadily. The continuously deepening of the black area on both sides of the hydraulic fracture suggested that the disturbing compressive stress on both sides of the hydraulic fracture parallel to the propagation direction increased continuously.

With the extension of the hydraulic fracture to the bedding plane, the tensile disturbance stress on the bedding plane furtherly increased, and the tensile failure occurred continuously. In the damage-concentrated area, the different scale microcracks extended and fused. The superposition of microcracks at all levels formed the bedding plane fracture
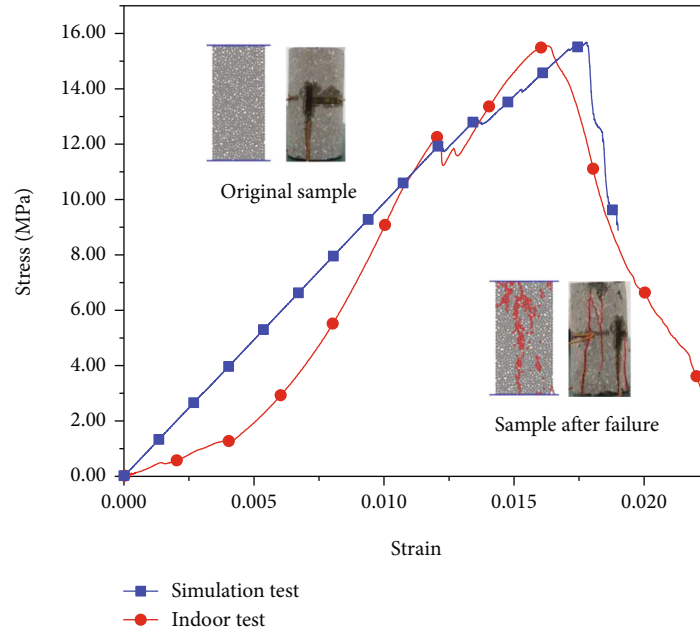
FIGURE 5: Laboratory test and numerical simulation of the stress-strain curve and final fracture mode of the intact specimen.

(a) Test block without a bedding plane (b) Test block with a bedding plane
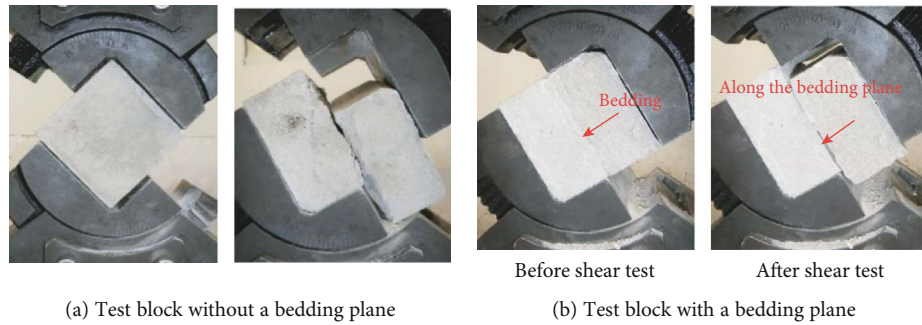
FIGURE 6: Morphology of test blocks after damage [49].

TABLE 4: Parameters in the process of hydraulic fracturing.

Fracturing parameters		Particle flow model	Laboratory test
μ_v (pa·s)	Viscosity coefficient of fracturing fluid	$135 \cdot 10^{-3}$	$135 \cdot 10^{-3}$
K_f (GPa)	Bulk modulus of fracturing fluid	10	10
K (mD)	Permeability	65.1762	65.1762

zone. It should be noted that the fractures in the numerical simulation had a hierarchical feature of multiple secondary microcracks. Therefore, a single microfracture in the simulation results represented the aggregation of multiple secondary fractures. In the first stage, the fracture zones were all generated by the disturbance stress, and it was called bedding disturbance fracture zone (BFZ).

In the second stage, after HF1 extended to the I-bedding plane, the hydraulic fracture was fused with the disturbance fracture zone of the bedding plane. HF1 had branch fractures; one branch spread along the fused fracture zone and penetrated to the rock mass on both sides along the bedding

plane. One of the branches passed through the bedding plane and entered into the left rock mass. At this time, the II-bedding plane, 24.8 mm away from the HF2 fracture tip, also fractured for the first time under the stress disturbance effect. The bedding plane's distance to the fracture tip was almost the same when the fracture occurred on both sides of the bedding planes. After that, HF2 extended to the II-bedding plane, and the hydraulic fracture fused with the fracture zone. The HF2 propagation direction deflected and expanded along the bedding plane from the maximum principal stress direction, which further communicated the original discontinuous bedding plane disturbance fracture zone. The
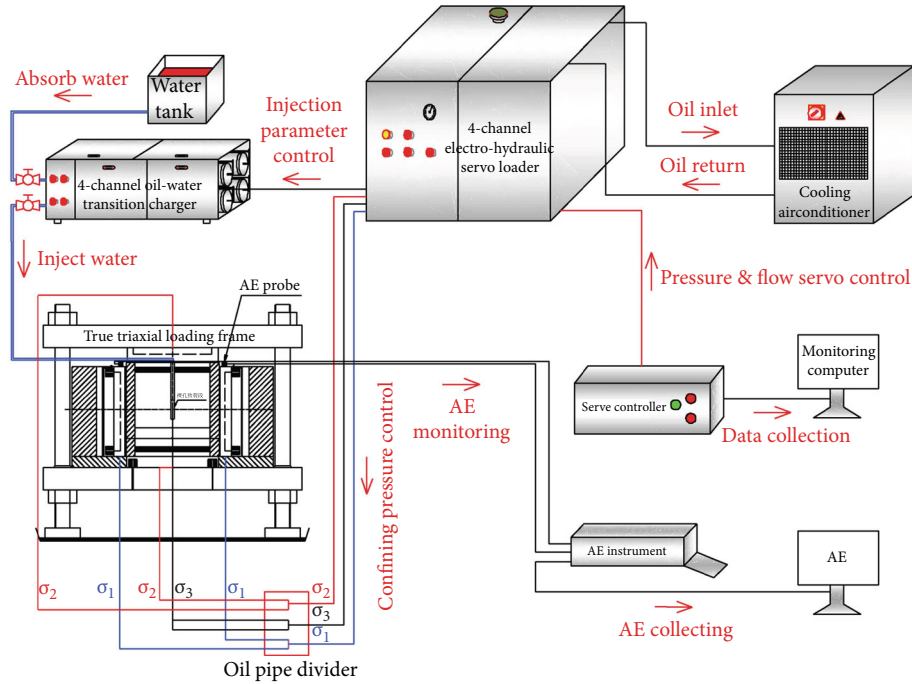
(a)
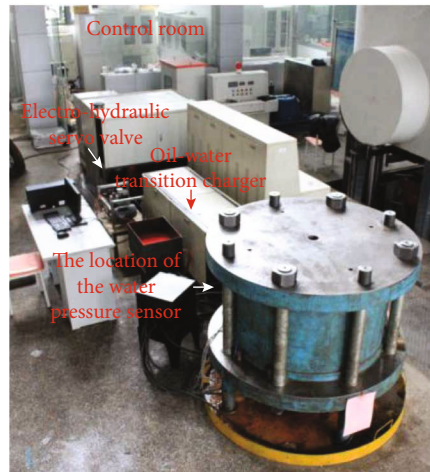
(b)

FIGURE 7: True triaxial hydraulic fracturing test system: (a) schematic diagram of test system and (b) field test system diagram.

TABLE 5: Experimental scheme for hydraulic fracturing of composite rock materials.

Test name	Confining pressure (MPa)			In situ stress coefficient	Bedding plane cementation strength (MPa)	The injection rate of fracturing fluid (m^{-3}/min)
	σ_1	σ_2	σ_3			
1-1 (indoor test)	6	4.5	3	0.5	0.28	0.0005
1-2 (simulation test)	6		3	0.5	0.28	0.0005

disturbance fracture zone captured the hydraulic fracture, and the hydraulic fracture propagated along the bedding plane; finally, the hydraulic fracturing experiment was completed. By observing the propagation path of HF1 and HF2, it can be found that the propagation path of hydraulic fractures on the bedding plane was consistent with the bedding plane disturbance fracture zone in the first stage, showing that the propagation path of hydraulic fractures at the

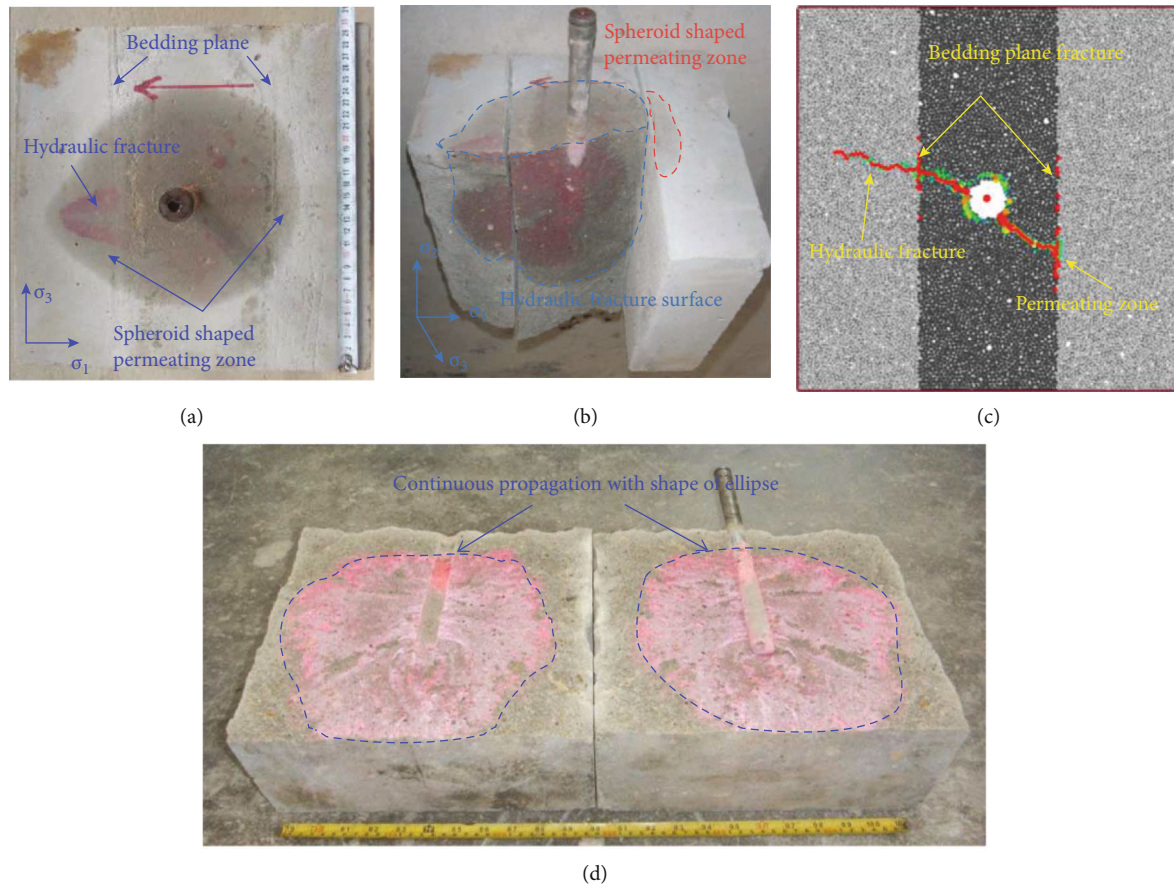(a)   (b)   (c)

(d)

FIGURE 8: Hydraulic fracture morphology: (a) top view of the fracturing test block; (b) front view of fracturing test block; (c) simulated fracture diagram; (d) hydraulic fracture morphology of homogeneous rock [49].

bedding plane was highly sensitive to the disturbance fracture zone formed. In other words, the stress disturbance effect significantly affected the propagation path of hydraulic fractures.

At present, hydraulic fracturing experimental research mainly focuses on the second stage. The effect of stress disturbance on the propagation path of hydraulic fractures in the first stage is ignored, leading to the contradiction between theoretical results and experimental phenomena. The particle flow research method proposed in this paper can effectively solve this problem. In Section 4, the fault model of the disturbed fracture zone at the bedding plane will be described, and the correlation between the development characteristics of the disturbed fracture zone and the hydraulic fracture extension mode can be revealed.

5. Mechanism Study on the Fracturing Effect Induced by Disturbing Stress of Hydrofracturing

Based on the above experimental study on the effect of stress disturbance, this part will propose the fracture model of the bedding disturbed fracture zone (BFZ) and the criteria for

determining hydraulic fractures' propagation path at the bedding plane.

5.1. Nonlinearity Fracture Model of Bedding Plane Disturbed Fracture Zone. Before establishing the fracture model, this part first analyzed the formation characteristics of the bedding disturbance fracture zone (BFZ). Under the influence of the stress disturbance effect, many microcracks were generated on the bedding plane, making the bedding plane rock material's fracture energy significantly decrease. As shown in Figure 12(a), when the accumulated dissipated energy of microcracks reached the fracture energy, the macrofracture surface of unit length was produced in the bedding plane. Based on nonlinear rock fracture mechanics, the fracture process zone (FPZ) was formed at the tip of the rock fracture in the process of fracture propagation [50, 51]. With the accumulation of the number of microcracks in the fracture process, the fracture per unit length would be generated when the dissipated energy reached the rock's fracture energy. The original fracture length was further increased [52]. The formation process and propagation behavior of the bedding disturbed fracture zone (BFZ) were highly consistent with those of the propagation fracture process zone (FPZ). Therefore, the formation mechanism of the bedding

(a)

(b)

(c)

(d)

(e)
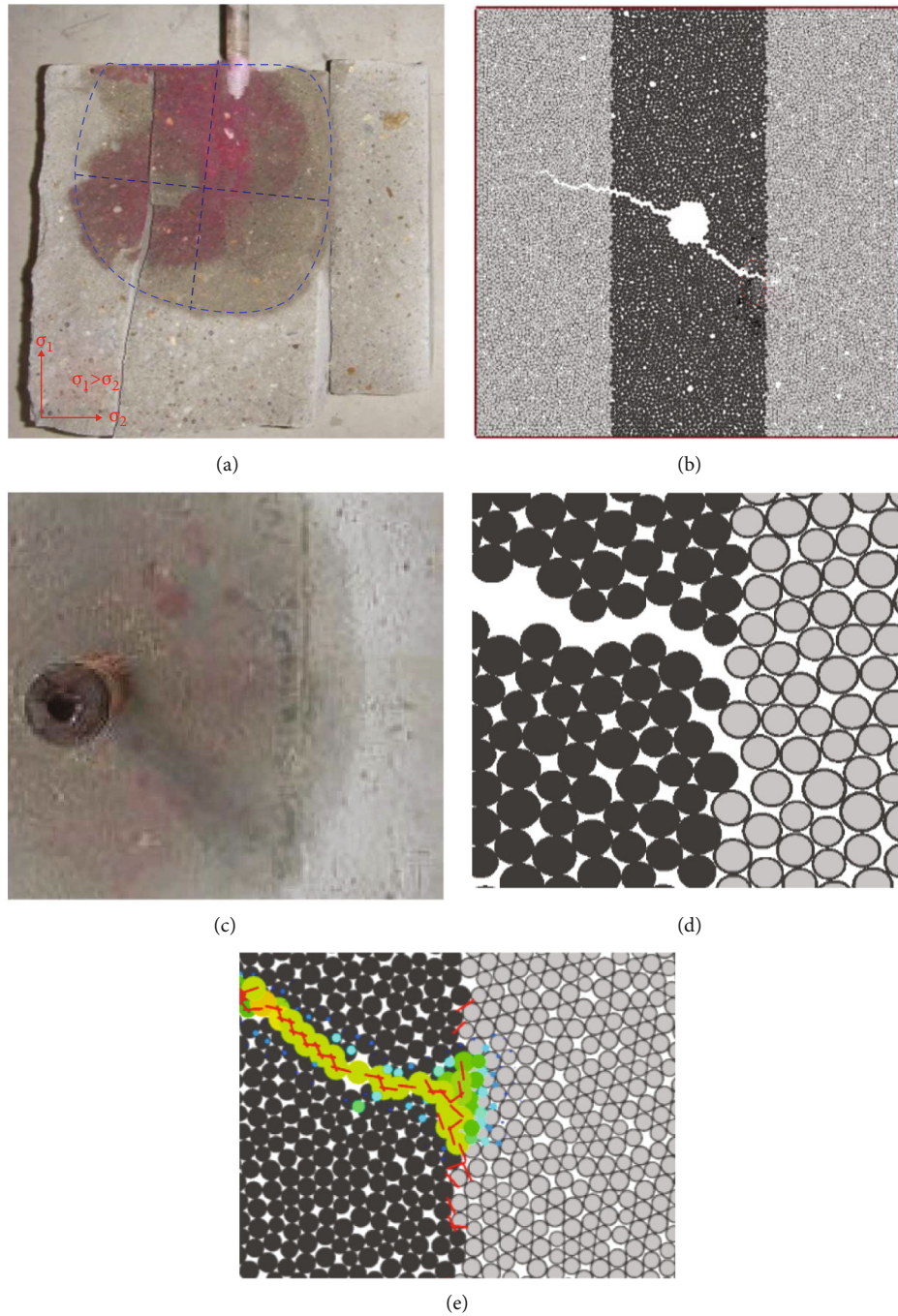
FIGURE 9: Comparison of laboratory test and simulation test: (a) laboratory test hydraulic fracture propagation plane [49]; (b) simulated test hydraulic fracture; (c) dyeing condition of test block; (d) simulated hydraulic fracture opening; (e) fracturing fluid permeability path at the bedding plane.

disturbance fractured zone (BFZ) can be explained by the fracture process zone's formation mechanism (FPZ).

Dugdale [53] has shown that the mechanical characteristics of the fracture process zone (FPZ) can be characterized by an equivalent fracture with cohesive force distributed (Figure 12(a)); that is, when the maximum tensile stress on both sides of a coherent fracture per unit length reached the critical tensile strength σ_t of cohesive fracture, the coherent fracture began to soften, and the fracture process zone developed; in the softening process, the cohesion of cohesive fracture $\sigma_t(w)$ decreased, the fracture opening displacement $w(x)$ increased until the fracture opening displacement reached the limit opening displacement of forming real fracture surface $w_{\max}$, then the cohesion disappeared, and the fracture process zone was fully developed; finally, the actual fracture surface per unit length was produced. Therefore, according to the
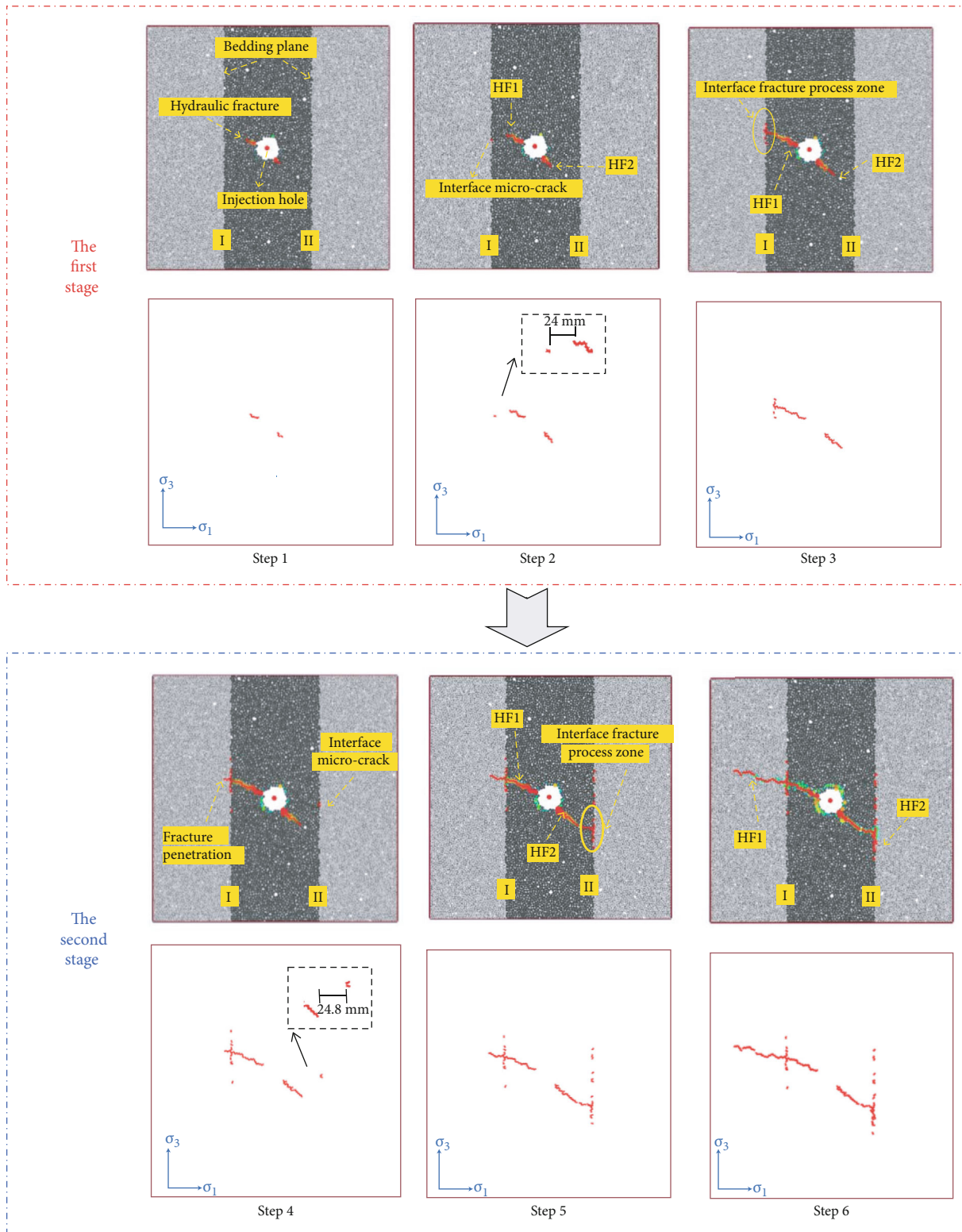
FIGURE 10: Dynamic propagation process of hydraulic fracture and the formation process of bedding plane fracture zone.

mechanical characteristics of the fracture process zone (FPZ), the bedding disturbed fracture zone (BFZ) can be characterized as a cohesive fracture to establish the fracture model of the disturbed bedding fracture zone (BFZ) [54, 55].

Based on the established fracture model, the initial fracture energy G_F (equation (12)) of the bedding plane can be expressed as the total integral area under $\sigma_t - w$ curve in the process of unit length cohesive fracture from
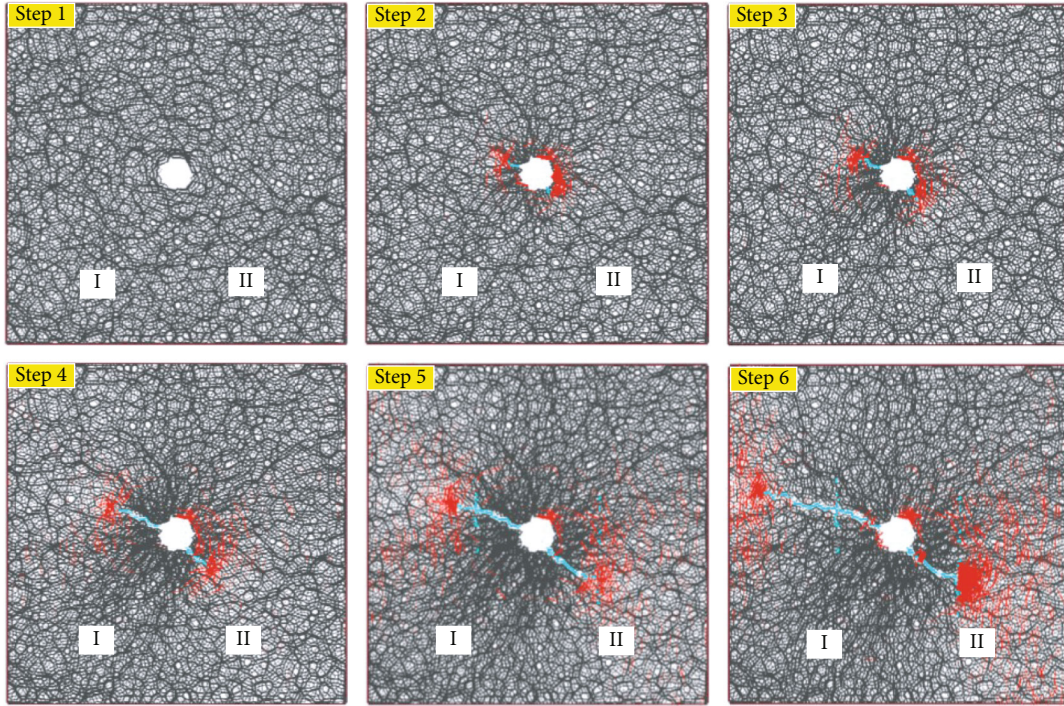
FIGURE 11: Internal stress distribution of test block during hydraulic fracturing (red lines: tension stress chain; black lines: compressive stress chain; blue lines: hydraulic fractures).

softening to forming real fracture surface [50, 51] (Figure 12(b)):

$$G_F = \int_0^{w_{\max}} \sigma_t(w)dw. \tag{12}$$

When the unit length cohesive fracture was in the softening stage and not fully opened, the integral area under the $\sigma_t - w$ curve was the dissipation energy G_f (equation (13)). The dissipation energy generated from the energy dissipation during the formation of microfractures can be used to characterize the fracturing effect induced by disturbing stress of hydrofracturing on the damage of the bedding plane.

$$G_f = \int_0^{w(x_1)} \sigma_t(w)dw. \tag{13}$$

When the hydraulic fracture just extended to the bedding plane, the energy required G_F' for the formation of actual fracture surface under the action of stress disturbance can be expressed as follows:

$$G_F' = G_F - G_f = \int_{w(x_1)}^{w_{\max}} \sigma_t(w)dw, \tag{14}$$

where $w_{\max}$ is a constant. According to equation (14), the fracture opening displacement $w(x)$ and the fracture opening energy G_F' are combined; it can be seen that the influ-

ence of stress disturbance on the hydraulic fracture propagation path is mainly reflected in the following two aspects:

(1) Energy dissipation occurred in the formation of microcracks [56, 57]. During the hydraulic fracturing process, the microcracks in the bedding plane accumulated continuously under the influence of the stress disturbance effect. The energy required for fracture opening per unit length decreased, which reduced the fracture energy of bedding rock. So, the propagation resistance of fracturing fluid along the bedding plane decreased, and the tendency of hydraulic fracture propagation along the bedding plane increased

(2) Under the impact of the fracturing effect induced by disturbing stress of hydrofracturing, many microfractures propagated and penetrated each other [1, 50] to form the bedding fracture zone. The fracture zone formation aggravated the degree of fragmentation and the opening degree of the bedding plane, improving the bedding plane's local permeability [58], and forming the dominant seepage path, which makes the tendency of propagation along the bedding surface significantly improved

The above conclusions reveal the mechanism that the fracturing effect induced by disturbing stress of hydrofracturing significantly affects the fracture propagation path from the theoretical framework of nonlinear rock fracture.

(a)

(b)
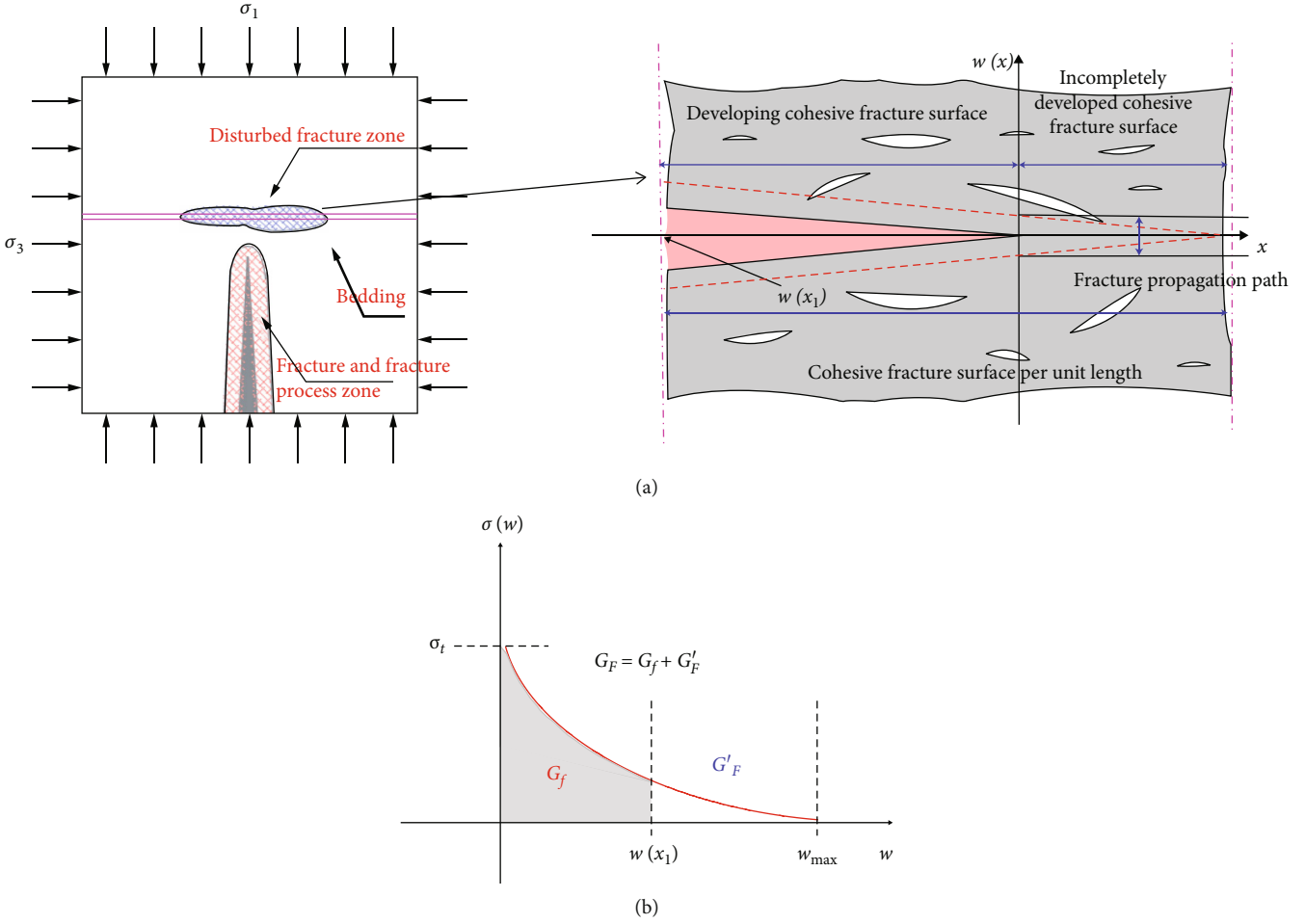
FIGURE 12: Fracture propagation mechanism: (a) cohesive fracture model of disturbed fracture zone at bedding plane (BFZ); (b) softening law of cohesive fracture.

5.2. Criteria for Determining the Propagation Path of Hydraulic Fractures at the Bedding Plane of Composite Rock Materials.

Under the condition of plane strain, for the composite rock material whose bedding plane is perpendicular to the fracture propagation direction, the driving force G_P (equation (15)) for the hydraulic fracture propagation to continues to enter the rock mass along the original path can be expressed as follows [59–61]:

$$G_P = A_{11} n \left(\lambda^{-3/4} K_I^2 + \lambda^{-1/4} K_{II}^2 \right), \quad (15)$$

$$n = \left[\frac{1 + \rho}{2} \right]^{1/2}, \quad (16)$$

where K_I and K_{II} are the stress intensity factors of fracture tip type I and type II. The sum of two-dimensional elastic parameters can express the stress state in the material under plane strain condition:

$$\lambda = \frac{A_{11}}{A_{22}},$$
$$\rho = \frac{(2A_{12} + A_{66})}{(2\sqrt{A_{12}A_{22}})}, \quad (17)$$

where A_{ij} is the material parameter.

The stress intensity factor of the fracture tip can be expressed as follows when the hydraulic fracture deflects to the bedding plane:

$$\left. \begin{array}{l} K_I^t = c_{11} \lambda^{-3/8} K_I + c_{12} \lambda^{-1/8} K_{II} \\ K_{II}^t = c_{21} \lambda^{-1/8} K_I + c_{22} \lambda^{1/8} K_{II} \end{array} \right\}, \quad (18)$$

where c_{ij} is the parameter determined by the elastic parameter ρ.

At this time, the driving force required for the hydraulic fracture to fully deflect along the bedding plane can be expressed as follows [59–61]:

$$G_K = A_{22} n \left(\lambda^{-3+4} K_I^{t2} + \lambda^{1+4} K_{II}^{t2} \right), \quad (19)$$

FIGURE 13: Two methods for judging the interactive coalescence mode of hydraulic fracturing fracture and bedding plane: (a) the impact of stress disturbance is considered; (b) the fracturing effect induced by disturbing stress of hydrofracturing is not considered (Taleghani's fracture path criterion [62]).

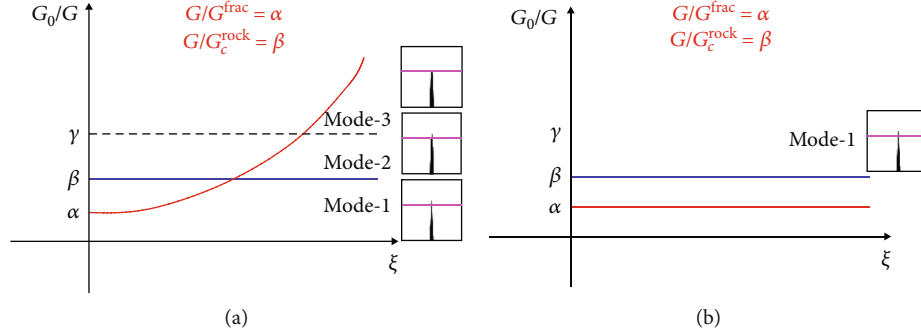where K_I^{t2} and K_{II}^{t2} are the stress intensity factors of fracture tip type I and type II. For the composite rock material $A_{11} = A_{22}$, the elastic parameter is 1.

Based on the energy analysis method, Taleghani's fracture path criterion [62] was improved, and a new criterion was proposed to determine the propagation path of hydraulic fractures, as shown in

$$\begin{cases} \dfrac{G_K}{G_c^{\text{frac}}} > \dfrac{G_P}{G_c^{\text{rock}}} \text{ fracture propagation along the bedding plane,} \\[3mm] \dfrac{G_K}{G_c^{\text{frac}}} < \dfrac{G_P}{G_c^{\text{rock}}} \text{ fracture propagation through layer,} \end{cases}$$

(20)

where G_K and G_P are the driving force of hydraulic fracture propagation along with different directions, G_c^{rock} is the energy required for critical fracture of intact matrix rock, and G_c^{frac} is the energy required for the failure of bedding material under the effect of hydraulic fracture stress disturbance. Combined with equation (20), it can be concluded that $G_c^{\text{frac}} = G_F'$. The above formula indicates that if there is enough driving force for hydraulic fracture propagation, the hydraulic fracture is most likely to propagate along the path with the most significant energy ratio. At this time, the energy required for hydraulic fracture propagation is the minimum. It should be noted that G_c^{frac} is a variable in the hydraulic fracturing process due to the damage of the bedding surface caused by the stress disturbance effect; its value continuously changes. Although the matrix is also affected by the disturbance stress at the fracture tip, the matrix strength is much higher than the bedding plane strength, so the stress disturbance effect of the fracture tip hardly causes matrix material damage; G_c^{rock} can be regarded as a constant.

According to the formation mechanism of the bedding disturbed fracture zone (BFZ), the longer the duration of the stress disturbance on the bedding plane is, the weaker the formation cementation strength is, and the greater the disturbance stress at the tip of hydraulic fracture will be, inducing more microcracks in the disturbed fracture zone, and the effect of stress disturbance will become stronger

and required less energy for the ultimate failure of bedding plane. Compared with Taleghani's fracture path criterion [62], G_c^{frac} in equation (20) proposed in this paper is a variable. The new criterion takes the fracturing effect caused by the stress disturbance at the hydraulic fracture tip into account to deal with the bedding plane damage and supplement the softening impact of bedding microfracture zone and, at the same time, pays attention to the whole dynamic process of hydraulic fracture propagation, and the judgment results are more in line with the real hydraulic fracture propagation situation.

According to equation (20), it can be found that the hydraulic fracture propagates in the composite rock material with multiple bedding planes, leading to a long time for hydraulic fractures to extend to the far bedding plane, so the duration of the stress disturbance effect is longer. The disturbed fracture zone's development degree in the far bedding plane is higher than that in the near bedding plane. With the development degree of disturbed fracture zone rising, G_c^{frac} decreases. There will be a situation that $G_K/G_c^{\text{frac}} < G_P/G_c^{\text{rock}}$ changes into $G_K/G_c^{\text{frac}} > G_P/G_c^{\text{rock}}$, indicating with the increase of the number of bedding planes, the propagation mode of hydraulic fracture changed from through bedding plane to along bedding plane. By contrast, it is challenging to realize the transformation from $G_K/G_c^{\text{frac}} > G_P/G_c^{\text{rock}}$ to $G_K/G_c^{\text{frac}} < G_P/G_c^{\text{rock}}$ without changing the driving force, which means it is difficult to change the propagation mode of hydraulic fracture from along bedding plane to through bedding plane. This conclusion reasonably explains why fractures are challenging to break through multiple bedding planes and eventually lead to limited hydraulic fracturing scope in large-scale composite reservoirs' fracturing operation. Also, it is the most effective way to solve the above problems. The method is to increase the hydraulic fracturing displacement, that is, to improve the driving force to achieve the ideal hydraulic fracturing range.

5.3. Evolution of Hydraulic Fracture Extension Mode under the Fracturing Effect Induced by Disturbing Stress of Hydrofracturing. Figure 13 shows the changing curve of the internal energy ratio of rock material with stress disturbance effect based on equation (20). The comparison curve can
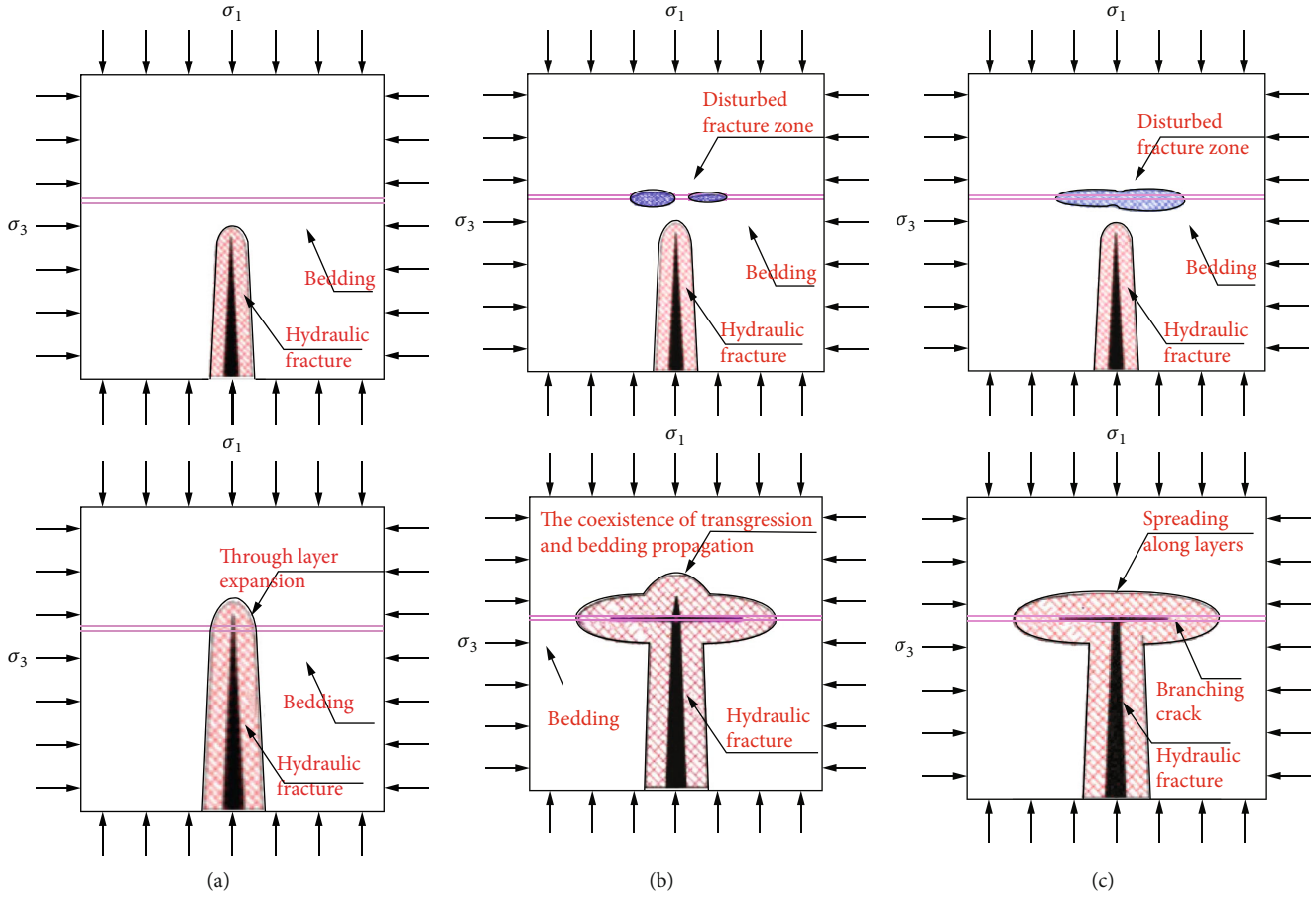
FIGURE 14: The influence of stress disturbance effect on the propagation path of hydraulic fracture in bedding plane: (a) mode 1 directly penetrates the stratum ("/"); (b) mode 2 penetrates along and pass through the bedding plane ("≠"); (c) mode 3 propagates completely along the bedding plane ("T").

TABLE 6: Experimental scheme for hydraulic fracturing of composite rock materials.

Test name	Confining pressure (MPa)			In situ stress coefficient	Bedding plane cementation strength (MPa)	The injection rate of fracturing fluid (m^{-3}/min)
	σ_1	σ_2	σ_3			
2-1	4		3	0.25	0.28	0.0005
2-2	4		3	0.25	0.84	0.0005
2-3	6		3	0.5	0.28	0.0005
2-4	6		3	0.5	0.84	0.0005

more intuitively reflect the influence of stress disturbance effect on bedding plane hydraulic fracture propagation. Suppose the value of initial G_K/G_c^{frac} of composite rock material sample is α; the amount of initial G_P/G_c^{rock} is β, where $\beta > \alpha$; the propagation mode of hydraulic fracture at the interface is through bedding plane extension (mode 1). Without considering the stress disturbance of hydraulic fracture (Taleghani's fracture path criterion), the value of G_K/G_c^{frac} and G_P/G_c^{rock} will be a constant; that is, the hydraulic fracture will always propagate through the bedding plane. But after considering the fracturing effect, the energy ratio of the bed-

ding plane G_K/G_c^{frac} will continuously increase with the increase of stress disturbance effect, as the red curve is shown. When α was between β and γ, the hydraulic fracture extended along and passed through the bedding plane (mode 2). When α was higher than γ, the hydraulic fracture ultimately propagated along the bedding plane (mode 3); that is, with the increase of stress disturbance effect, the hydraulic fracture propagation mode changes from mode 1 to mode 2 and mode 3 (Figure 14).

This phenomenon has been verified in the actual construction process. During the thin interbed hydraulic
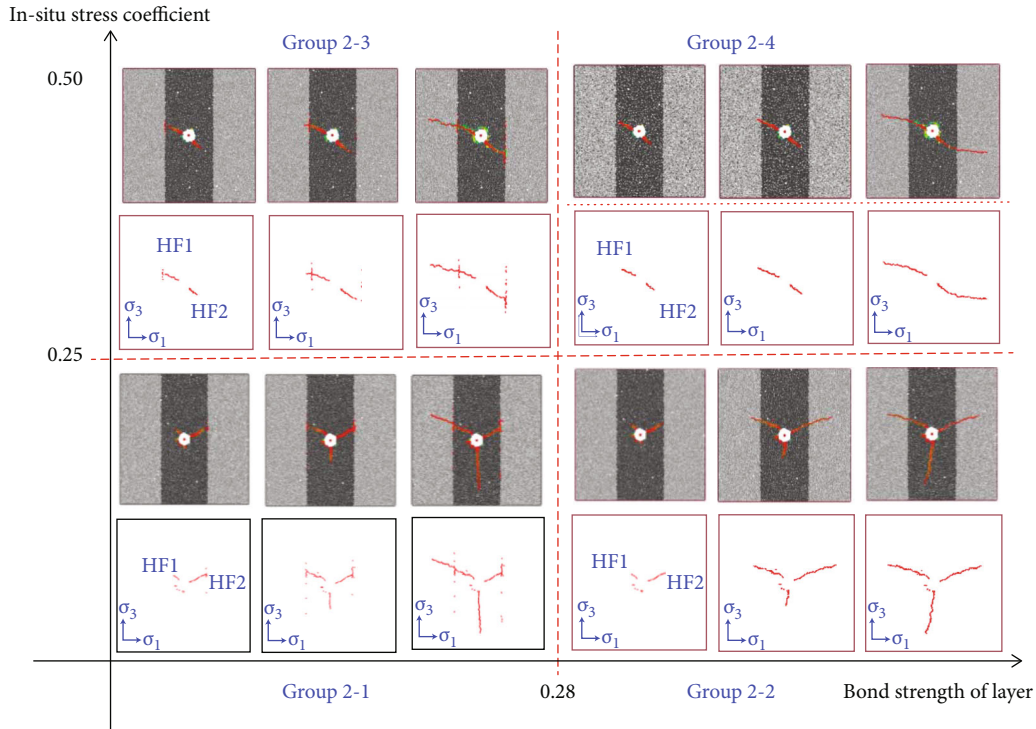
FIGURE 15: Schematic diagram of hydraulic fracture propagation and bedding plane disturbance fracture zone development under different conditions.

fracturing, it is difficult for hydraulic fractures to pass through multiple bedding planes at a fixed injection rate. If the injection hole is far away from the bedding plane, the hydraulic fracture is easy to expand along the bedding plane. In addition, the operation results show that hydraulic fracturing with a low injection rate is beneficial to activate the bedding plane and other natural weak surfaces. This is because the fracturing fluid has sufficient time to cause the initiation, development, expansion, and fusion of microfractures. If the injection rate is too large, the hydraulic fracturing effect may be reduced, and this conclusion is consistent with the experimental results of Guo and other scholars [63]; that is, by increasing the duration of the effect, the hydraulic fracturing effect caused by stress disturbance can be improved. Besides, to achieve an ideal hydraulic fracturing, variable injection rate hydraulic fracturing is usually used to make the fracturing fluid generate a pressure pulse in the hydraulic fracture and activate more primary fractures to improve the effect of hydraulic fracture stress disturbance by pulse damage effect.

6. Analysis of Influencing Factors of Hydraulic Fracture Propagation Based on Stress Disturbance Effect

Based on the above test results, this part will carry out sensitivity analysis on the bedding plane disturbance fracture zone's formation conditions. According to the test scheme shown in Table 6, the damage evolution law of bedding frac-

ture zone (BFZ) under different in situ stress and bedding plane cementation strength is described.

According to the sampling scheme shown in Table 6, the samples were divided into two groups, one group with an in situ stress coefficient of 0.25 and the other group with an in situ stress coefficient of 0.5 for a hydraulic fracturing test of composite rock materials. The test results are shown in Figure 15. In group 2-1, three major hydraulic fractures were initiated in the directions of 20°, 205°, and 280° of the injection hole, HF1 penetrated along and passed through the I-bedding plane, forming a "≠" cross fracture pattern. HF2 propagated completely along the II-bedding plane, forming a "T" cross fracture pattern. In the process of HF1 and HF2 approaching the bedding plane, the disturbed fracture zone was formed on the bedding plane. In the 2-2 group, HF1 and HF2 passed through the bedding plane, forming a "/" cross fracture pattern. In group 2-3, there were two major hydraulic fractures in the direction of 135° and 270° of the injection hole. HF1 penetrated along and passed through the I-bedding plane, forming a "≠" cross fracture pattern. HF2 propagated completely along the II-bedding plane, forming a "T" cross fracture pattern. The extension pattern of hydraulic fracture was similar to group 2-1. The disturbed fracture zone appeared on the bedding plane. In the 2-4 group, HF1 and HF2 passed through the bedding plane, forming a "/" cross fracture pattern. The extension pattern of hydraulic fracture was similar to group 2-2.

The results show that in situ stress significantly affects the initiation direction and overall shape of hydraulic fractures but has no obvious effect on the disturbed fracture zone's development degree. Under the same in situ stress
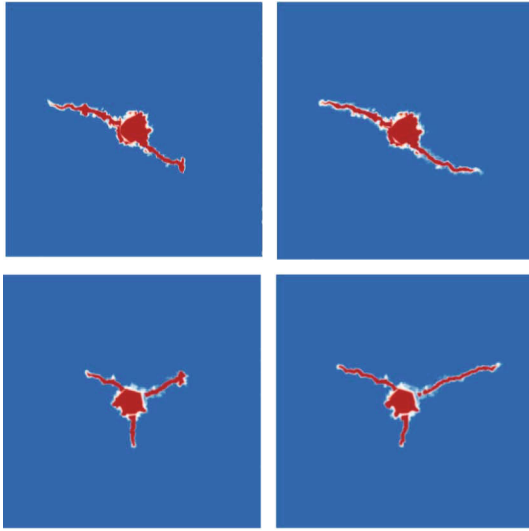
FIGURE 16: Distribution of permeability zone in materials under different conditions (red area is high permeability zone, and blue area is low permeability zone).

conditions, the hydraulic fracture interaction mode at the strong and weak bedding planes is obviously different. When the bedding plane strength was 0.84 MPa, the two sides of the bedding plane appeared "/" extension mode. When the bedding plane strength was 0.28 MPa, the two sides of the bedding plane appeared "≠" and "T" extension mode. There existed disturbance fracture zones induced by hydraulic fracture tip stress disturbance in the weak bedding plane group, while the disturbance fracture zone is not obvious in the strong bedding plane group, suggesting that the fracturing effect induced by disturbing stress of hydrofracturing is highly sensitive to the bedding plane cementation strength. This finding is consistent with the previous experimental results [49].

Figure 16 shows the permeability distribution in the test block during the hydraulic fracturing process. Each group shows that the hydraulic fracture just extends to the bedding plane, but the fracturing fluid does not intrude into the bedding plane. In the weak bedding plane group, the bedding plane fracture zone formed the dominant flow path, and the hydraulic fracture extended along the bedding plane. There was no disturbance fracture zone in the strong bedding plane group, and the hydraulic fracture propagation was basically unaffected by the bedding plane, and the original propagation direction was maintained. The bedding plane disturbance fracture zone induced by the stress disturbance effect significantly affected the hydraulic fracture's extended mode at the bedding plane. This phenomenon is entirely consistent with the evolution law of the extension mode at the hydraulic fracture of the bedding plane considering the stress disturbance effect discussed in the previous section. The conclusion of this section further verifies the correctness and scientific of the criteria in Section 5.2.

In conclusion, based on the hydraulic fracturing test results of composite rock materials, two optimization

schemes for hydraulic fracturing of composite rock reservoirs can be proposed: (1) for the composite rock reservoirs with poor continuity and low cementation strength, with the increase of hydraulic fracture extension length, the injection rate should be increased in real time. High hydraulic fracture propagation speed can reduce the disturbance effect of hydraulic fracture tip stress, reduce the damage caused by weak surface, and avoid hydraulic fracture propagation along with the bedding plane, resulting in a broad range of unfractured area. (2) For the composite rock reservoirs with strong continuity and high cementation strength, an alternate pump injection method can be used to set a short period of stop injection and pressure holding time in the hydraulic fracturing cycle to make the bedding plane fractures develop enough time and expand the volume of reservoir hydraulic fracturing.

7. Conclusion

The main conclusions are as follows:

(1) Based on the simulation test of the dynamic propagation of hydraulic fractures in composite rock materials, it is concluded that the disturbed tensile stress field is formed in front of the hydraulic fracture tip. With the continuous expansion of hydraulic fracture, the scope of the disturbing stress field is expanding. The formation process of the bedding fractured zone can be divided into two stages. The first stage is from the starting point of hydraulic fracture initiation, through the extension of hydraulic fractures to the bedding plane as the endpoint. The stress disturbance induces the disturbed fracture zone at the tip of hydraulic fractures. In the second stage, when the hydraulic fracture extends to the bedding plane, the fracturing fluid enters into the bedding plane, and the bedding plane is damaged

(2) Based on the experimental results, it is found that the fracturing effect of stress disturbance significantly affects the extension mode of the hydraulic fracture of the bedding plane. Through the establishment of the bedding plane disturbed fracture zone model, its influence is mainly reflected from the following two points: (1) the formation of the disturbance fracture zone in the first stage improves the degree of fragmentation and permeability of the bedding plane and forms the dominant flow path. (2) The formation of microfractures is accompanied by energy dissipation. The resistance of hydraulic fracture propagation along the bedding plane is greatly reduced, and the tendency of hydraulic fracture propagation along the bedding plane is increased

(3) A nonlinearity fracture model of the bedding disturbed fracture zone is proposed, and the hydraulic fracture path judgment criterion considering the fracturing effect induced by disturbing stress of hydrofracturing is given. With the improvement of

the fracturing effect caused by stress disturbance, the development degree of disturbed fracture zone will be improved, the energy ratio of hydraulic fracture propagation along the bedding plane is increased, and hydraulic capture fracture will be enhanced continuously. The extension pattern of hydraulic fractures has also changed

(4) It is found that the stress disturbance effect is highly sensitive to the bedding plane cementation strength. Based on the test results, two optimization schemes for the hydraulic fracturing operation of composite rock reservoirs are proposed

Symbols

E_c: Elastic modulus
v: Poision's ratio
k_n: Normal stiffness of particle element
k_s: Tangential stiffness of particle element
μ: Friction coefficient between particle elements
ρ: Particle unit density
σ_1:   Maximum horizontal geostress
σ_3:   Minimum horizontal geostress
p: Water pressure
c_0:   Cohesion of rock
Φ: Friction angle of rock
G: Energy release rate for fracture propagation
G_F: The initial fracture energy
G_f: The dissipation energy
G_c^{frac}:   Energy release rate of bedding plane boundary fault
G_c^{rock}:   Critical fracture energy release rate of rock
$R_{\max}$:   Maximum particle radius
$R_{\min}$:   Minimum particle radius
$\bar{E}_c$:   Elastic modulus of particle element
$\bar{k}_n$:   Normal stiffness of parallel bond
$\bar{k}_s$:   Tangential stiffness of parallel bond
$\bar{\sigma}$:   Normal strength of parallel bond
$\bar{\tau}$:   Shear strength of parallel bond
Q: Fluid volume rate
w: Pipe width
L: Length of pipe
N: Number of pipelines connecting the domain
K_f: Bulk modulus of fracturing fluid.
v: Injection rate of fracturing fluid
A: Cross sectional area of fluid flow
ΔP: Change of liquid pressure in river domain
ΔV_d: Volume change of domain caused by volume force
V_d: Apparent volume of river domain
w_0:   Residual width of pipe
F_i: Normal contact force under current load
k: Macropermeability of sample
g_s: Spacing between particles.

Data Availability

All the data have been included in the manuscript.

Conflicts of Interest

The authors declare no conflict of interest.

Authors' Contributions

References

[1] S. C. Blair, R. K. Thorpe, and F. E. Heuze, *Laboratory observations of the effect of geological discontinuities on hydrofracture propagation*, Proc. 30th U.S. Symp. on Rock Mech, 1989.

[2] B. Hou, R. Zhang, Y. Zeng, W. Fu, Y. Muhadasi, and M. Chen, "Analysis of hydraulic fracture initiation and propagation in deep shale formation with high horizontal stress difference," *Journal of Petroleum Science and Engineering*, vol. 170, pp. 231–243, 2018.

[3] Z. Zhang, H. Wang, B. Deng, M. Li, and D. Zhang, "Field investigation of hydraulic fracturing in coal seams and its enhancement for methane extraction in the Southeast Sichuan Basin, China," *Energies*, vol. 11, no. 12, p. 3451, 2018.

[4] K. M. Ajayi and S. J. Schatzel, "Transport model for shale gas well leakage through the surrounding fractured zones of a longwall mine," *International Journal of Mining Science and Technology*, vol. 30, no. 5, pp. 635–641, 2020.

[5] B. Xia, X. Zhang, B. Yu, and J. Jia, "Weakening effects of hydraulic fracture in hard roof under the influence of stress arch," *International Journal of Mining ence & Technology*, vol. 28, no. 6, pp. 951–958, 2018.

[6] J. Xie, J. Tang, R. Yong et al., "A 3-D hydraulic fracture propagation model applied for shale gas reservoirs with multiple bedding planes," *Engineering Fracture Mechanics*, vol. 228, p. 106872, 2020.

[7] Z. Liu, X. Ren, X. Lin, H. Lian, L. Yang, and J. Yang, "Effects of confining stresses, pre-crack inclination angles and injection rates: observations from large-scale true triaxial and hydraulic fracturing tests in laboratory," *Rock Mechanics and Rock Engineering*, vol. 53, no. 4, pp. 1991–2000, 2020.

[8] Z. Liu, S. Wang, H. Ye et al., "Experimental study on the effects of pre-cracks, fracturing fluid, and rock mechanical characteristics on directional hydraulic fracturing with axial pre-cracks," *Geomechanics and Geophysics for Geo-Energy and Geo-Resources*, vol. 7, no. 2, 2021.

[9] J. Yang, H. Lian, and L. Li, "Fracturing in coals with different fluids: an experimental comparison between water, liquid CO_2, and supercritical CO_2," *Scientific Reports*, vol. 10, no. 1, p. 18681, 2020.

[10] T. G. Fan and G. Q. Zhang, "Laboratory investigation of hydraulic fracture networks in formations with continuous orthogonal fractures," *Energy*, vol. 74, pp. 164–173, 2014.

[11] N. R. Warpinski, R. A. Schmidt, and D. A. Northrop, "In-situ stresses: the predominant influence on hydraulic fracture containment," *Journal of Petroleum Technology*, vol. 34, no. 3, 2013.

[12] H. Gu and X. Weng, *Criterion for fractures crossing frictional interfaces at non-orthogonal angles*, Us Rock Mechanics Symposium & Us-canada Rock Mechanics Symposium, 2010.

[13] M. Sarmadivaleh and V. Rasouli, "Modified Reinshaw and Pollard Criteria for a non-orthogonal cohesive natural interface intersected by an induced fracture," *Rock Mechanics and Rock Engineering*, vol. 47, no. 6, pp. 2107–2115, 2014.

[14] B. C. Haimson and F. H. Cornet, "ISRM suggested methods for rock stress estimation—part 3: hydraulic fracturing (HF) and/or hydraulic testing of pre-existing fractures (HTPF)," *International Journal of Rock Mechanics and Mining Sciences*, vol. 40, no. 7-8, pp. 1011–1020, 2003.

[15] E. M. Llanos, R. G. Jeffrey, R. Hillis, and X. Zhang, "Hydraulic fracture propagation through an orthogonal discontinuity: a laboratory, analytical and numerical study," *Rock Mechanics and Rock Engineering*, vol. 50, no. 8, pp. 2101–2118, 2017.

[16] Z.-L. Zhou, G. Q. Zhang, H. R. Dong, Z. B. Liu, and Y. X. Nie, "Creating a network of hydraulic fractures by cyclic pumping," *International Journal of Rock Mechanics and Mining Sciences*, vol. 97, pp. 52–63, 2017.

[17] T. L. Blanton, *An experimental study of interaction between hydraulically induced and pre-existing fractures*, Paper presented at the SPE Unconventional Gas Recovery Symposium, Pittsburgh, Pennsylvania, 1982.

[18] N. Dutler, M. Nejati, B. Valley, F. Amann, and G. Molinari, "On the link between fracture toughness, tensile strength, and fracture process zone in anisotropic rocks," *Engineering Fracture Mechanics*, vol. 201, pp. 56–79, 2018.

[19] J. Ning, J. Wang, Y. Tan, and Q. Xu, "Mechanical mechanism of overlying strata breaking and development of fractured zone during close-distance coal seam group mining," *International Journal of Mining Science and Technology*, vol. 30, no. 2, pp. 207–215, 2020.

[20] G. Wang, X. Qin, D. Hang, and Z. Liu, "Study on seepage and deformation characteristics of coal microstructure by 3D reconstruction of CT images at high temperatures," *International Journal of Mining Science and Technology*, vol. 21, no. 2, pp. 175–185, 2020.

[21] J. Cook and J. E. Gordon, "A mechanism for the control of crack propagation in all-brittle systems," *Proceedings of the Royal Society A: Mathematical, Physical and Engineering ence*, vol. 282, no. 1391, pp. 508–520, 1964.

[22] J. Yang, H. Lian, and L. Li, "Investigating the effect of confining pressure on fracture toughness of CO2-saturated coals," *Engineering Fracture Mechanics*, vol. 242, no. 6266, article 107496, 2020.

[23] J. Yang, H. Lian, and V. P. Nugyen, "Study of mixed mode I/II cohesive zone models of different rank coals," *Engineering Fracture Mechanics*, vol. 246, article 107611, 2021.

[24] I. N. Sneddon, "The distribution of stress in the neighbourhood of a crack in an elastic solid," *Proceedings of the Royal Society A*, vol. 187, no. 1009, pp. 229–260, 1946.

[25] A. G. Olovyanny, "Mathematical modeling of hydraulic fracturing in coal seams," *Journal of Mining Science*, vol. 41, no. 1, pp. 61–67, 2005.

[26] Y. Wang and M. B. Dusseault, "Borehole yield and hydraulic fracture initiation in poorly consolidated rock strata—part I. impermeable media," *International Journal of Rock Mechanics and Mining Science and Geomechanics Abstracts*, vol. 28, no. 4, pp. 235–246, 1991.

[27] G. R. Irwin, "Analysis of stresses and strains near end of a crack traversing a plate," *Journal of Applied Mechanics*, 1956.

[28] S. Rassenfoss, "A look into what fractures really look like," *Journal of Petroleum Technology*, vol. 70, no. 11, pp. 28–36, 2018.

[29] A. Ghassemi and Q. Zhang, "A transient fictitious stress boundary element method for porothermoelastic media," *Engineering Analysis with Boundary Elements*, vol. 28, no. 11, pp. 1363–1373, 2004.

[30] I. Matsunaga, H. Kobayashi, S. Sasaki, and T. Ishida, "Studying hydraulic fracturing mechanism by laboratory experiments with acoustic emission monitoring," *International Journal of Rock Mechanics and Mining Science and Geomechanics Abstracts*, vol. 30, no. 7, pp. 909–912, 1993.

[31] T. Dahm, G. Manthei, and J. Eisenblätter, "Automated moment tensor inversion to estimate source mechanisms of hydraulically induced micro-seismicity in salt rock," *Tectonophysics*, vol. 306, no. 1, pp. 1–17, 1999.

[32] N. R. Warpinski and J. Du, "Source-mechanism studies on microseismicity induced by hydraulic fracturing," in *Paper presented at the SPE Annual Technical Conference and Exhibition*, Florence, Italy, 2010.

[33] S. Stanchits, J. Burghardt, and A. Surdi, "Hydraulic fracturing of heterogeneous rock monitored by acoustic emission," *Rock Mechanics and Rock Engineering*, vol. 48, no. 6, pp. 2513–2527, 2015.

[34] P. A. Cundall, "A computer model for simulating progressive large-scale movements in blocky rock systems," *Proc.int.symp.On rock fracture*, vol. 1, no. ii-b, pp. 11–18, 1971.

[35] P. A. Cundall and D. O. Potyondy, "A bonded-particle model for rock," *International Journal of Rock Mechanics and Mining Sciences*, vol. 41, no. 8, pp. 1329–1364, 2008.

[36] R. Abousleiman, G. Walton, and S. Sinha, "Understanding roof deformation mechanics and parametric sensitivities of coal mine entries using the discrete element method," *International Journal of Mining Science and Technology*, vol. 30, no. 1, pp. 123–129, 2020.

[37] H. Lin, W. H. Kang, J. Oh, I. Canbulat, and B. Hebblewhite, "Numerical simulation on borehole breakout and borehole size effect using discrete element method," *International Journal of Mining Science and Technology*, vol. 30, no. 5, pp. 623–633, 2020.

[38] X. Zhao and R. Paul Young, "Numerical modeling of seismicity induced by fluid injection in naturally fractured reservoirs," *Geophysics*, vol. 76, no. 6, pp. WC167–WC180, 2011.

[39] J. Zhou, L. Zhang, A. Braun, and Z. Han, "Numerical modeling and investigation of fluid-driven fracture propagation in reservoirs based on a modified fluid-mechanically coupled model in two-dimensional particle flow code," *Energies*, vol. 9, no. 9, p. 699, 2016.

[40] J. Zhou, L. Zhang, Z. Pan, and Z. Han, "Numerical studies of interactions between hydraulic and natural fractures by smooth joint model," *Journal of Natural Gas Science and Engineering*, vol. 46, pp. 592–602, 2017.

[41] Y. Zhang, J. Qiu, Y. Zhang, and Y. Wei, "The adoption of ELM to the prediction of soil liquefaction based on CPT," *Natural Hazards*, vol. 107, no. 1, pp. 539–549, 2021.

[42] Y. Zhang, Y. Zhang, J. Qiu, S. Wu, and S. Wu, "The adoption of deep neural network (DNN) to the prediction of soil liquefaction based on shear wave velocity," *Bulletin of Engineering Geology and the Environment*, 2021.

[43] Y. Zhang, R. P. Liao, J. L. Wan et al., "Research on displacement prediction of step-type landslide under the influence of various environmental factors based on intelligent WCA-ELM in the Three Gorges Reservoir Area," *Natural Harzard*, 2021.

[44] Y. Zhang, J. Tang, R. P. Liao et al., "Application of an enhanced BP neural network model with water cycle algorithm on landslide prediction," *Stochastic Environmental Research and Risk Assessment*, 2020.

[45] Y. Zhang, J. Tang, Z.-y. He, J. Tan, and C. Li, "A novel displacement prediction method using gated recurrent unit model with time series analysis in the Erdaohe landslide," *Natural Hazards*, vol. 105, no. 1, pp. 783–813, 2021.

[46] X. P. Zhang, P. Q. Ji, Q. S. Liu, Q. Liu, Q. Zhang, and Z. H. Peng, "Physical and numerical studies of rock fragmentation subject to wedge cutter indentation in the mixed ground," *Tunnelling and Underground Space Technology*, vol. 71, pp. 354–365, 2018.

[47] N. Cho, C. D. Martin, and D. C. Sego, "A clumped particle model for rock," *International Journal of Rock Mechanics and Mining Sciences*, vol. 44, no. 7, pp. 997–1010, 2007.

[48] J. Bear, "Dynamics of fluids in porous media," *Soil Science*, vol. 10, no. 2, pp. 162-163, 1972.

[49] B. Huang and J. Liu, "Experimental investigation of the effect of bedding planes on hydraulic fracturing under true triaxial stress," *Rock Mechanics and Rock Engineering*, vol. 50, no. 10, pp. 2627–2643, 2017.

[50] A. Hillerborg, M. Modéer, and P. E. Petersson, "Analysis of crack formation and crack growth in concrete by means of fracture mechanics and finite elements," *Cement and Concrete Research*, vol. 6, no. 6, pp. 773–781, 1976.

[51] M. F. Ashby and C. G. Sammis, "The damage mechanics of brittle solids in compression," *Pure and Applied Geophysics*, vol. 133, no. 3, pp. 489–521, 1990.

[52] J. Labuz, S. P. Shah, and C. H. Dowding, "The fracture process zone in granite: evidence and effect," *International Journal of Rock Mechanics and Mining Science and Geomechanics Abstracts*, vol. 24, no. 4, pp. 235–246, 1987.

[53] D. S. Dugdale, "Yielding of steel sheets containing slits," *Journal of the Mechanics and Physics of Solids*, vol. 8, no. 2, pp. 100–104, 1960.

[54] Y. K. Xing, G. Zhang, T. Luo, Y. Jiang, and S. Ning, "Hydraulic fracturing in high-temperature granite characterized by acoustic emission," *Journal of Petroleum Science and Engineering*, vol. 178, pp. 475–484, 2019.

[55] Y. K. Xing, G. Zhang, B. Wan, and H. Zhao, "Subcritical fracturing of sandstone characterized by the acoustic emission energy," *Rock Mechanics and Rock Engineering*, vol. 52, no. 7, pp. 2459–2469, 2019.

[56] K. Otsuka and H. Date, "Fracture process zone in concrete tension specimen," *Engineering Fracture Mechanics*, vol. 65, no. 2-3, pp. 111–131, 2000.

[57] E. N. Landis and L. Baillon, "Experiments to relate acoustic emission energy to fracture energy of concrete," *Journal of Engineering Mechanics-Asce*, vol. 128, no. 6, pp. 698–702, 2002.

[58] G. Simpson, Y. Guéguen, and F. Schneider, "Permeability enhancement due to microcrack dilatancy in the damage regime," *Journal of Geophysical Research-Atmospheres*, vol. 106, no. B3, pp. 3999–4016, 2001.

[59] J. W. Hutchinson and Z. G. Suo, "Mixed mode cracking in layered materials," *Advances in Applied Mechanics*, vol. 29, pp. 63–191, 1992.

[60] X. Hao, W. du, Y. Zhao et al., "Dynamic tensile behaviour and crack propagation of coal under coupled static- dynamic loading," *International Journal of Mining Science and Technology*, vol. 30, no. 5, pp. 659–668, 2020.

[61] L. Gao, F. Gao, Z. Zhang, and Y. Xing, "Research on the energy evolution characteristics and the failure intensity of rocks," *International Journal of Mining Science and Technology*, vol. 30, no. 5, pp. 705–713, 2020.

[62] A. Taleghani and J. Olson, "Analysis of multistranded hydraulic fracture propagation: an improved model for the interaction between induced and natural fractures," in *Paper presented at the SPE Annual Technical Conference and Exhibition*, New Orleans, Louisiana, 2009.

[63] T. Guo, S. Zhang, Z. Qu, T. Zhou, Y. Xiao, and J. Gao, "Experimental study of hydraulic fracturing for shale by stimulated reservoir volume," *Fuel*, vol. 128, no. 14, pp. 373–380, 2014.

WILEY | Hindawi

Research Article

Study on the Tensile Strength and Crack Development of Granite Crystal Models with Different Fabrics

Guangsheng Du [1,2] **Shijiang Chen** [1,2] **and Zhihao Li** [1,2]

[1]*Institute of Mining Research, Inner Mongolia University of Science and Technology, Baotou, 014010 Inner Mongolia, China*
[2]*Key Laboratory of Mining Engineering of Inner Mongolia, Baotou, 014010 Inner Mongolia, China*

Correspondence should be addressed to Shijiang Chen; chenshijiang_2003@163.com

According to the relationship between the development of hydraulic fracture and the distribution of different rock and mineral fabrics, digital image technology was used in this study based on the discrete element particle flow method. An SCGM numerical model, which can control fabric and refine mesoscopic crystal defects, was constructed. The tensile strength test of granite specimens with different component contents and polymerization conditions was conducted, with the monitorization of damaged cracks. The test results showed that (1) the SCGM model could construct a model of a crystal structure containing variable components and polymerization, to achieve numerical experiments of different parameters; (2) compared with previous models, the SCGM model can reflect internal stress change of a specimen with the variation of the structure. At the same time, the contained crystal structure can characterize different failure modes such as intergranular cracks of different components, grain boundary cracks of the same component, and transgranular cracks, which were in good agreement with the actual failure state of granite; (3) the mica content of the specimen and its strength presented a linear relationship of $y = -14.723x + 12.642$. The degree of polymerization of the components and the strength of the specimens were both affected by the accumulation of microcracks and stress concentration, which appeared to increase first and then decrease. When the specimen was broken, the number of microcracks and the degree of polymerization of the components also increased first and then decreased. The SCGM model can construct a numerical model of granite with arbitrary fabric and crystal structure and provide a hydraulic fracturing analysis method.

1. Introduction

In recent years, as an important technical means in oil, gas, and hot dry rock exploitation, hydraulic fracturing technology has been widely used. In fact, in the construction process, the physical and mechanical properties of the rock itself have a great impact on the construction of hydraulic fracturing. Xia et al. [1–4] studied the crack propagation path of samples of heterogeneous rock with different microfractures by CT scanning 3D imaging technology, and it was found that the fractures of hydraulic fracturing were easy to generate along with the natural fractures and joints to interact with each other, forming complex network fractures. Therefore, the study of the relationship between the distribution of rock fab-

ric and the fracture distribution can further promote understanding the hydraulic fracturing mechanism.

However, the failure mechanism of rock is very complicated. On the one hand, naturally formed cracks and pores within the rock have different effects on the rock's failure process; on the other hand, in the rock, various mineral components and crystals have different physical and mechanical properties [5, 6]. As shown in Figure 1, many scholars have interpreted the micromechanical damage inside the rock from the aspects of structure shape, size, and position of the mineral aggregation, crystal orientation, and grain boundary geometry to reveal rock strength characteristics and failure laws. Rock strength is suggested to be closely related to its microstructure [7, 8].
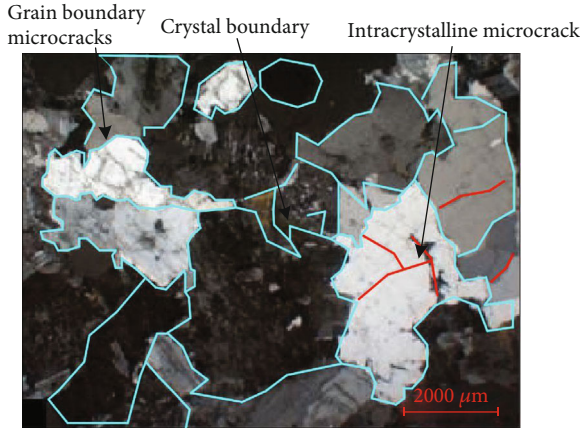
Figure 1: Micrograph of granite.

The fact is that the uniqueness of the rock structure makes it difficult to repeat the rock test accurately and control a specific variable of rock structure to study other influencing factors. Using the numerical simulation method to construct reusable rock samples for numerical experiments has become an effective method to solve rock mechanics problems.

In recent years, scholars have widely used discrete element numerical simulation technology to simulate rock mechanics tests because of its ability to effectively simulate the transfer relationship of internal rock forces. However, establishing a numerical model fitting the actual rock conditions best has been the focus of current research [9–12].

Many scholars have studied the mineral content and composition distribution of rock based on the discrete element method [13–24], which means identifying the surface information of the granite using digital image processing technology and importing it into numerical software in the form of vectorization to conduct a series of numerical experiments. It is proved that this method can reproduce the positional relationship between different fabrics of natural rock specimens to a great extent, making the numerical test results more realistic. By calibrating parameters through macroscopic experiments and considering the strength and modulus differences of different components, Jinzhao et al. [25] used digital image processing technology and other methods to construct a more consistent PFC numerical model containing different fabric information. Then, the peak strength and elastic modulus of rock were discussed. Although this method can effectively establish a numerical model consistent with the actual situation, it can only analyze a single specimen.

There are certain differences between the rock masses in the project and the experimental specimens, and it is not easy to obtain a specimen fully meeting the test requirements. Therefore, many scholars tried to fit the relationship between rock strength and internal microstructure using one or several functional relationships [26]. Considering the scale of spatial correlation based on the spatial correlation model, Tang et al. [27–30] analyzed the different continuous or aggregated components of rock and gave numerical images describing the aggregation form of different components of

rock to build a numerical model that can adjust the distribution of rock components through parameters.

However, the rock crystal structure and internal joints and fissures were not fully considered in the previous modelling. Aiming at the mechanical properties of the crystal structure and the discontinuous surface inside the rock, Lv et al. [31, 32] used the Voronoi method to generate a numerical model in which the crystal structure and content can be controlled to analyze the relationship between the crystal grain size and the rock strength characteristic. This model is widely used in the formation of crystals of rocks. Cho et al. [33–36] proposed that the bonding state between the crystal grains in the rock is different from the mechanical state inside the crystal and introduced a massive cluster model to simulate the internal crystal structure. It was indicated that the cluster model could better express the mechanical relationship formed by the massive crystal structure inside the rock, but the particles in a clump cannot move and rotate in this model.

In fact, although a single component exhibits relatively uniform property, there are still differences, such as the arrangement of crystal structures and Poisson's ratios during crystallization. Considering the changes inside the crystal and the structure on the crystal boundary, Potyondy and Zhou et al. [37, 38] established a grain-based model (equivalent crystalline model) (GBM) composed of PBM and a smooth joint model. In this model, the internal components of the crystal are constructed by PBM, and SJM constructs the bonding relationship between the unit cells, making it more accurately reflect the mechanical relationship between the crystal and structure of the rock to study the relationship between the crystal size and rock strength characteristics. Li et al. and Zhang et al. [39, 40] combined the digital image technology and this numerical model to construct a particle flow numerical model, discussed and analyzed the advantages and rationality of the GBM model, and verified the effectiveness of the numerical model constructed by the model.

After reviewing previous research, it is easy to find that while constructing a numerical model, the refinement and the parameter controllability of the model were not fully considered. In this paper, a spatial correlation coefficient was adopted to rebuild the component structure of the rock surface through quantitative parameters (discretion of component distribution, component content). Simultaneously, the Voronoi model was used to construct the internal crystal structure of different components in which the particle size can be controlled. Then, the microfracture grid was imported through the improved GBM model to simulate the real defects, such as the naturally formed component boundary crystal structure of microcracks in the rock. Finally, a new modelling method of Spatially Correlated Grains Model (SCGM), which can adjust the internal parameters and describe the structure of the internal rock joints and fractures more accurately, was proposed and used to construct a numerical model to test the strength of granite specimens with different fabric characteristics. By comparing and analyzing the tensile strength of the specimens with different component content and distribution, the fracture
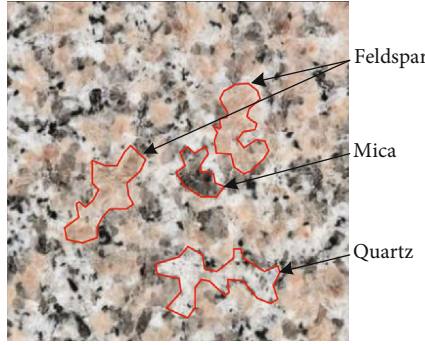
FIGURE 2: Actual granite image.

development law is further analyzed, providing a more accurate numerical method for the fracture analysis of hydraulic fracturing.

2. Construction of Numerical Model SCGM

In this study, PFC was used to conduct model construction and calculation. First, the component distribution was constructed through the spatial correlation function; secondly, the Voronoi model was used to construct the component's internal crystals; finally, the GBM model import method was used to construct the microcracks of the model specimen. The specific method is as follows.

2.1. Construction of Component Distribution of Model Specimens. Due to the influence of natural diagenesis processes, component distribution and physical and mechanical properties of rock materials are not entirely random; typically, different components and their properties show a certain degree of continuity and relevance in space. Figure 2 shows the section of natural granite; it can be seen that the inside of the same component keeps consistent in a large space. Tang et al. [27–30] introduced spatial correlation functions to describe these spatial distribution properties, which can be obtained by transforming the random field's spatial correlation function. With this method, image models of different component contents and distributions can be constructed to study heterogeneous materials and the influence of different spatial correlation coefficients on materials' mechanical properties. The results showed that this method was an effective method to construct the component distribution of granite specimens.

In this section, the spatial correlation function was used to construct the granite fabric. The steps are as follows.

(1) First, construct a random array, which is a matrix with two different label numbers. In this experiment, a 500×500 matrix A with the element of $a_{i,j}$ was constructed, and the label numbers were 1 and -1, respectively. Keeping A unchanged, the calculated structure based on A in the subsequent calculations has relative position stability

(2) Select the spatial correlation function that conforms to the generation state of such aggregated rocks:

$$f(d) = e^{-d/L}, \tag{1}$$

where d is the selected calculation distance; L represents the spatial aggregation length, and it can indicate the degree of aggregation between the two regions when the value of d remains unchanged. The smaller the L, the less the random field is affected by this function, which means that the original random state is maintained; otherwise, the state of aggregating will appear to a certain area. The rock fabric distribution affected by different material types and generation conditions can be obtained by changing this value. In this experiment, rock images with different spatial correlation degrees of $L = 4, 6, 8,$ and 10 were generated for different rock aggregation conditions, as shown in Figure 3

(3) Construct component spatial array for a given degree of aggregation. Multiply the elements in array A by the correlation function $f(d)$ and parameter C following the distance relationship, and superimpose them to obtain the array B containing spatial correlation information according to the distance relationship. In this case, it means that the points within d of a certain point are superimposed in the form of this distribution. Since the distribution characteristics of discrete points in a certain area are the same, the superposition will form a clustering effect. When the distance between the points is too large, the calculation amount will increase, and the influence on the aggregation point becomes small. Therefore, a reasonable calculation range needs to be selected. Tang et al. [30] analyzed the selected area of the function. Points within the distance $d = 45$ were used for calculation in this paper. Array B can be constructed as follows:

$$b_{i,j} = \sum_{p=-n}^{n} \sum_{q=-n}^{n} cd(p,q) \cdot a_{i+p,j+q} f(d(p,q)), \tag{2}$$

where array C is a variable coefficient indicating the degree of influence on an aggregation area under different distances. The smaller the distance, the closer the value of $cd(p,q)$ to 1

(4) Multicomponent distribution space construction of model specimens. It is suggested that the greyscale distribution of the granite surface image approximately conforms to the normal distribution, and the array calculated in this experiment also conforms to this characteristic. As shown in Figure 3, by adopting the technique of dividing granite components by the image grey threshold value and using the low-intensity component biotite as a reference, the generated images were divided into biotite with content $x = 10\%$, 15%, 20%, 25%, and 30% when the corresponding feldspar and quartz content was gradually reduced. Then, the values in the matrix were divided into the form of Equation (3), and each division adopted the same set of matrices to make the
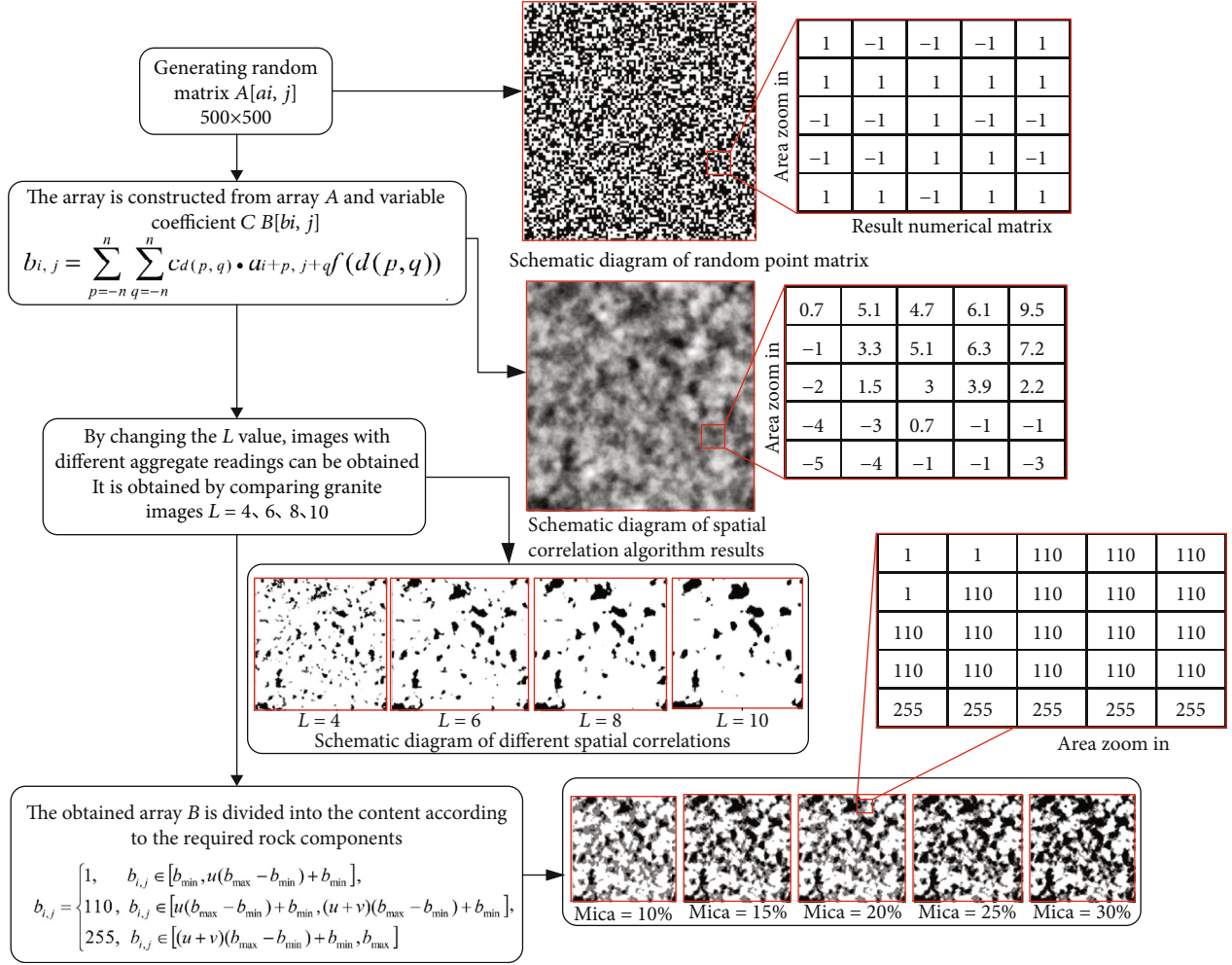
FIGURE 3: The construction process of the component distribution of the model specimen.

generated new matrix consistent with its image structure, which means that the position of mica, quartz, and other minerals in the image changed little except that their content area was expanded. Alternatively, a part of smaller blocks newly appeared within the threshold, as shown in Figure 3:

$$
b_{i,j} = \begin{cases} 1, & b_{i,j} \in [b_{\min}, u(b_{\max} - b_{\min}) + b_{\min}], \\ 110, & b_{i,j} \in [u(b_{\max} - b_{\min}) + b_{\min}, (u + v)(b_{\max} - b_{\min}) + b_{\min}], \\ 255, & b_{i,j} \in [(u + v)(b_{\max} - b_{\min}) + b_{\min}, b_{\max}], \end{cases}
$$

(3)

where $b_{i,j}$ represents the element value in the generated matrix, $b_{\max}$ and $b_{\min}$ are the maximum and minimum values in the matrix, u is the percentage of mica content, and v is the percentage of quartz content (Table 1)

2.2. Crystal Construction of Model Specimen. In the study of rock mesoscale, it is found that under the impact of loading, rock failure can be categorized into three types, including grain boundary cracks of different components, large crystal

TABLE 1: The content of different components in the generated image.

Component			Content		
Mica	10%	15%	20%	25%	30%
Quartz	40%	37.5%	35%	32.5%	30%
Feldspar	50%	47.5%	45%	45.5%	40%

cracks of the same composition, and transgranular cracks [41, 42]. The main factors leading to rock failure include the internal discontinuous surface, their distribution, and the ultimately formed stress concentration. Therefore, it is not enough to only discuss the composition distribution of the rock. The grain boundary cracks of different compositions and the large crystal cracks of the same composition need to be represented separately. The Voronoi crystal generation method is widely used to simulate the generation of crystals such as rocks, which is used to generate a crystal particle model within the composition region above so as to adjust the average size. Combining the component boundaries of the image and the crystal grains within the component, a model simultaneously considering the component
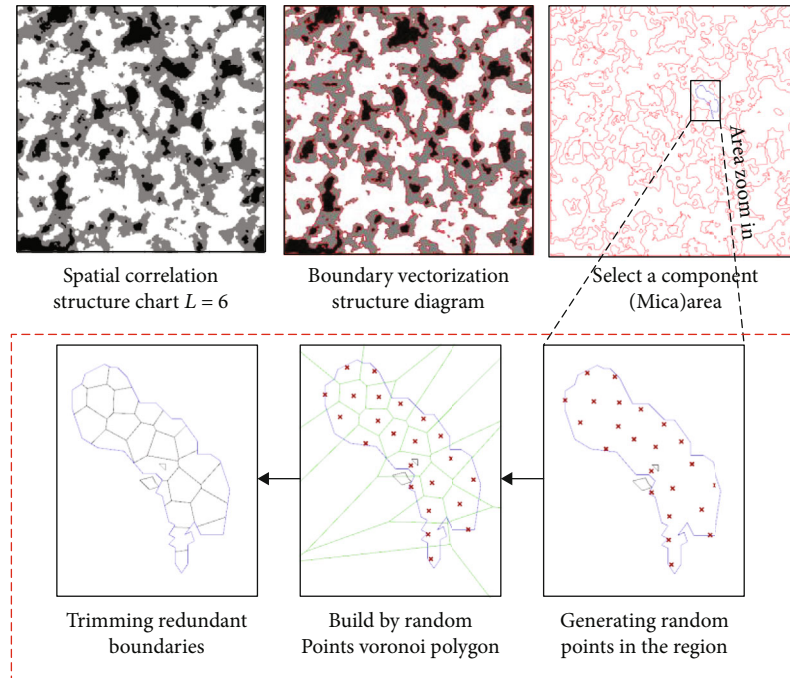
Figure 4: Generation diagram of the internal crystal structure in a certain area.

structure relationship and the crystal discontinuous surface relationship was generated. The vector structure model generation steps are as follows:

(1) Recognize the image containing spatial correlation information, and component content was divided and calibrated with grey values of 1, 110, and 255; that is, the positions with an abrupt change of grey value are segmented at the component boundary, and the segmentation position is closed as a region (Figure 4)

(2) Construct the unit cell structure inside the divided components, import the vectorized boundary into the drawing software Rhinoceros to adjust the size, and remove the unnecessary boundary

(3) By acquiring and observing the real granite surface images, the average radius of feldspar, quartz, and mica crystals was determined as 1.6 mm, 1.5 mm, and 0.9 mm; then, uniformly distributed random points matching area scales were generated to construct the internal crystal structure of the components according to the Voronoi polygon rule, as shown in Figure 4

2.3. Construction of Microcracks in Model Specimens. In order to describe the discontinuous crystals in rocks, Potyondy proposed the SJM model, which can simulate the sliding state with a certain amount of overlap after the strength is lost. Li et al. and Zhang et al. [39, 40] used the GBM model to construct a refined numerical model conforming to the distribution of the granite surface structure and carried out an analysis of the mesoscopic mechanical structure of the image components to explain the relationship between the mesoscopic mechanical properties and the macroscopic failure of rocks. Therefore, the GBM model is used to build a granite numerical model, as shown in Figure 5.

2.4. SCGM Model Generation Process. Based on the research on the strength of different rock fabrics and the refined construction of rock crystal structure models, the SCGM model was constructed by combining the above three sections, as shown in Figure 6.

The specific process is as follows:

(1) Generate granite surface images with different distributions and component structures through spatial correlation functions

(2) Divide the obtained image into vectorization (connect each component block to form a closed area)

(3) Generate a Voronoi model to represent crystal particles through random points in each closed area

(4) Firstly, generate a uniform specimen in the PFC2d software, and then, import the vectorized image to group the different components in order by layer

(5) Import the images containing crystal grain boundaries into the software to group the models and parameters in the order of layers

(6) Adjust the mesoscopic parameter

2.5. Parameter Calibration of PFC Numerical Model. In order to match the results of the numerical test with the actual rock
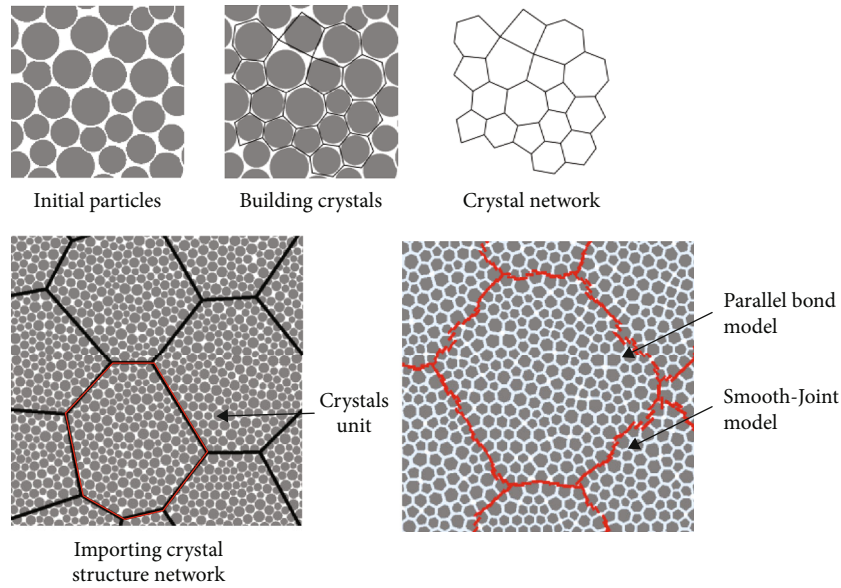
Figure 5: Generation diagram of new GBM model.

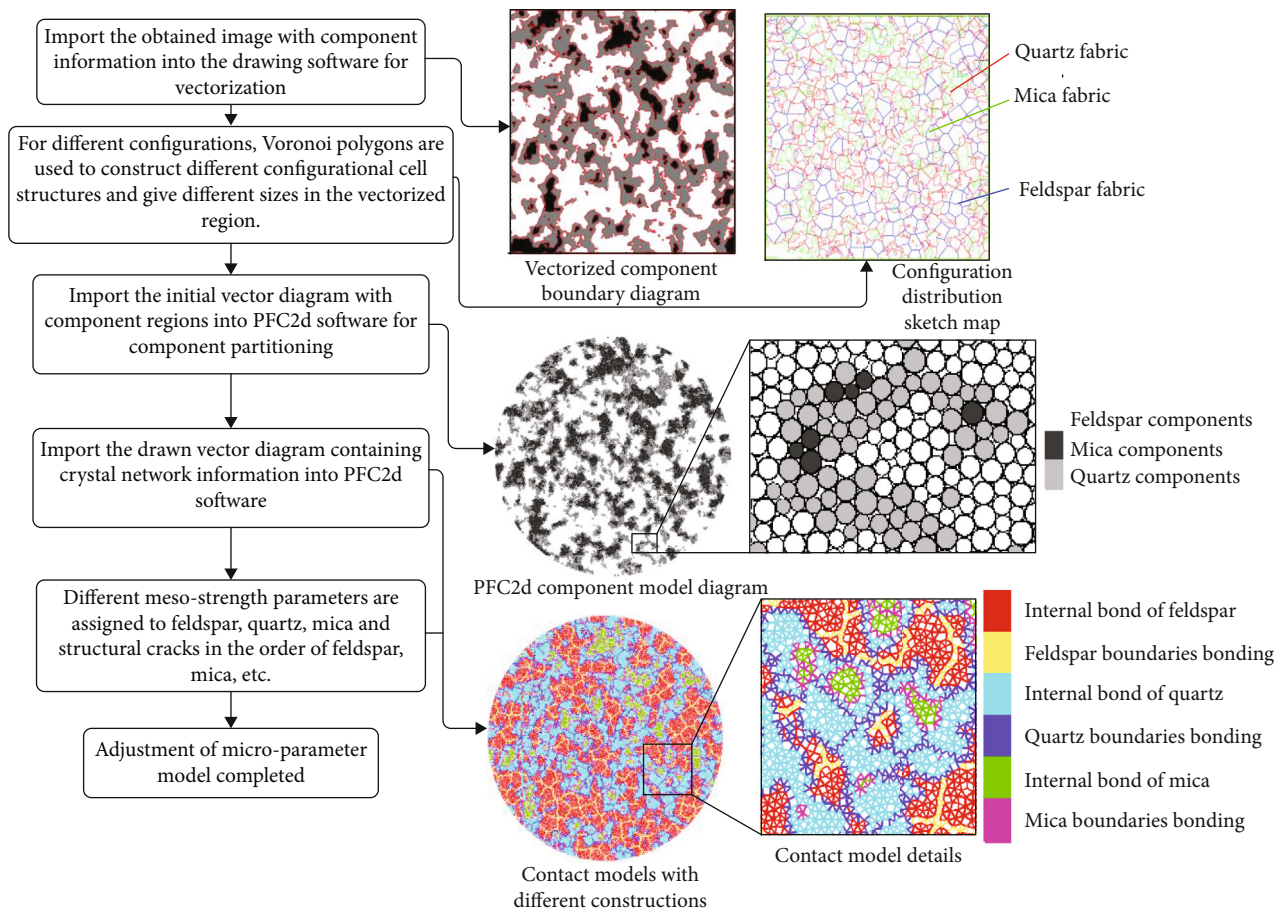Figure 6: Generation process of SCGM model.

failure better, it is necessary to calibrate parameters in the numerical model. The calibration method in this paper is to match the strength and the elastic modulus in the actual physical test within a certain range [43–48]. Considering the internal structure of the rock, the strength between rock crystals was set to be 40% of the internal strength of rock

TABLE 2: Mesoscopic parameters of particles of different components.

Mineral component	Parameters						
	Minimum radius (mm)	Radius ratio	Density (kg/m^3)	Elastic modulus (GPa)	Stiffness ratio	Friction coefficient	Void ratio
Feldspar			2750	45	1.5	0.6	
Quartz	0.15	1.66	2650	61	1.5	0.7	0.025
Mica			3100	20	2.5	0.3	

TABLE 3: Mesoscopic parameters of different component contact models.

Mineral component	Parameters					
	Volumetric modulus (GPa)	Stiffness ratio	Tensile limit (MPa)	Cohesion force (MPa)	Friction angle (°)	Friction coefficient
Feldspar	45	1.5	53.2	53.0	15	
Quartz	61	1.5	68.2	60.1	17	0.67
Mica	20	2.5	23.1	25.1	17	
Feldspar structure	40	1.5	20.5	23.1	16	
Quartz structure	40	1.5	25.1	22.5	15	0.85
Mica structure	40	2.5	10.5	12.1	15	

crystals referring to the study of Hu et al. [49–51]. Simultaneously, referring to the strength differences between different minerals in the rock, the strength ratio of feldspar, quartz, and mica inside the granite was set as $0.8 : 1 : 0.3$. In order to ensure high accuracy of the matched parameters, the component distribution of the real granite specimen was obtained through digital image processing, (Tables 2 and 3) the matching process is shown in Figure 7, and the result is shown in Figure 8.

3. Validation of Tensile Test of SCGM Numerical Model Specimen

The SCGM model was constructed and tested following the above scheme, and the result data was collected. The numerical simulation adopted the same scheme as the indoor test and monitored the tensile strength of the rock using the Brazilian split test. The stress distribution changes of heterogeneous specimens, the influence of the crystal structure on the failure of specimens, and the influence of different structural parameters on the development of cracks after specimens were broken were described, respectively.

3.1. Fabric Impact Analysis. While analyzing the initial Brazilian split tensile strength, the specimen was regarded as a homogeneous specimen, so the stress distribution on the surface was in the symmetric and uniform state [52, 53], as shown in Figure 9. However, the internal stress distribution of the specimen is affected by many factors, such as the different modulus of different components, the sliding, and stress concentration of the discontinuous surface. These factors cause the internal stress to nonlinearly change with the loading position, as shown in Figure 9. It can be seen that the internal stress of the rock was not smooth along the loading axis but showed a certain irregular change with the composition when the rock end was subjected to the load. Larger ten-

sile stress appeared near the lower right in the x-direction stress diagram; a certain amount of feldspar and quartz was distributed at this position, which is corresponding to the fabric distribution of the actual specimen; at the same time, because their strength and modulus are higher than mica, it will not instantly produce microdestruction and dislocation under load. In contrast, a large amount of elastic energy was accumulated, and deformation appeared to gradually form tensile stress in this direction. There was a large amount of mica component on the upper part of the test piece, which had low strength and small tangential deformation. It is easy to produce partial tension cracks and form partial sliding, making it not form effective tensile stress but apparent compressive stress. It can be clearly seen from the structural diagram that the distribution of stress is highly correlated with the corresponding relationship between the fabric in the specimen.

3.2. Crystal Structure Impact Analysis. Due to the convenience of the spatial correlation function, Wenmin [54] constructed a numerical model with different correlation coefficients and discussed the influence of different correlation coefficients and anisotropy parameters on the strength and failure state of the specimen. However, only the strength parameters of different mineral components were discussed in the numerical model, but the internal structural problems were not analyzed in detail. There are a large number of cracks and voids in the natural rock mass, especially the internal crystal interface that needs to be paid attention to. In this paper, the constructed model considered the crystal network structure of different components; Brazil splitting tests were performed on two different models. As shown in Figure 10, under the same mesoscopic parameter, the strength of the SCGM model was lower than that of the PBM model, about 87% of the strength of the PBM model, and the deformation was not much different. As shown in Figure 11, the two models showed obvious differences in
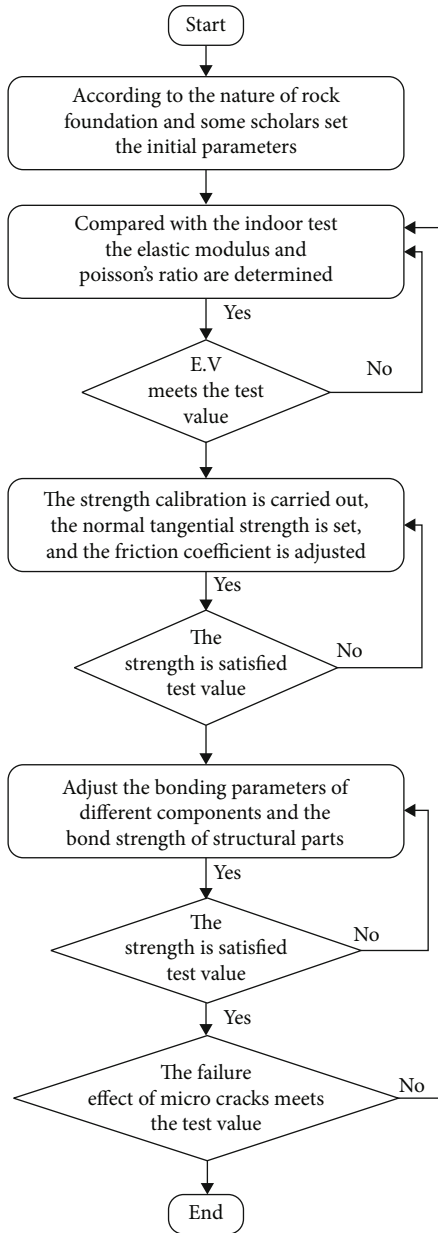
Figure 7: Calibration process of mesoscopic parameters in the numerical model.

the development of the damage cracks; at a certain special location in the same composition area, damage cracks in the SCGM model occurred obvious deflection because of a crystal interface, which is more consistent with the actual situation. During the failure process, the development of cracks in the SCGM model can better reflect the changes in the natural structure of the rock under force, and the model will produce grain boundary cracks of different components, large crystal cracks of the same composition, transgranular cracks, and more obvious secondary cracks. However, the PBM model cannot reflect these characteristics.

3.3. Realization of Tensile Test of Arbitrary Rock Fabric. The construction of a refined numerical model is of great significance to the study of rock mechanics. By identifying the

structure image of the rock surface component and constructing the model based on this, semicircular surface structure load strength of 16 granites was analyzed and compared with that of the structure generated by Voronoi. The real rock structure can be obtained by modelling using the original rock surface image, which helps the analysis of a single rock specimen. However, this method has many limitations while performing the horizontal comparison, such as analysis of the same component content in different locations, analysis of different component content in the same location, and controlling component changes and crystal size. As shown in Figure 12, the SCGM model can solve these problems more effectively. The spatial correlation function image can set the distribution and content of granite components, and the Voronoi model can set different grain sizes. It can be seen that the cracks tend to be more stable during the development process as the dispersion of the component distribution decreased; for the $L = 4$ specimen, the mica was more discretely arranged in the specimen; then, the cracks would develop in multiple directions during the loading process. As the L value increased, the composition distribution and the low-strength structure tended to be stable. At this time, the development direction of the cracks gradually becomes single. As the content of mica increased, the percentage of low-strength structures also increased, and the number of microcracks when the specimen was damaged also increased. Moreover, many apparent cracks break along the crack network structure.

In previous studies, it has been shown that the failure of rocks is mainly caused by the expansion and development of internal microcracks, which eventually converge into larger macrocracks. Therefore, the strength of the rock has an apparent relationship with the crack state. On the one hand, the development status of cracks is related to the distribution of different components in the rock; on the other hand, it also correlates with each component's content. For these two influencing factors, the SCGM model was used to construct granite specimens with different discrete distributions and component contents, and split tests were carried out to analyze the relationship between the different fabric contents and the distribution of granite strength and cracks.

In this experiment, the parameters of spatial correlation coefficient $L = 4$, 6, 8, and 10 (that is, the dense distribution of different components) were selected, and different component contents $x = 10\%$, 15%, 20%, 25%, and 30% were constructed in each spatial correlation coefficient by referring to the mica; the peak strength of each specimen was counted. Because of the smallest particles, a certain error will occur while constructing the model. Therefore, all models have performed 10 tests under the condition of different random seeds. The result is shown in Figures 13 and 14.

It can be seen from Figure 13 that for all distribution states of the component, as the mica content increased, the peak tensile strength all showed a downward trend with a relatively obvious linear change. By fitting the average value of the peak strength change and the mica content, the function of the variation law of the peak strength under different mica contents was obtained, $y = -14.723x + 12.642$, $R^2 = 0.9444$,
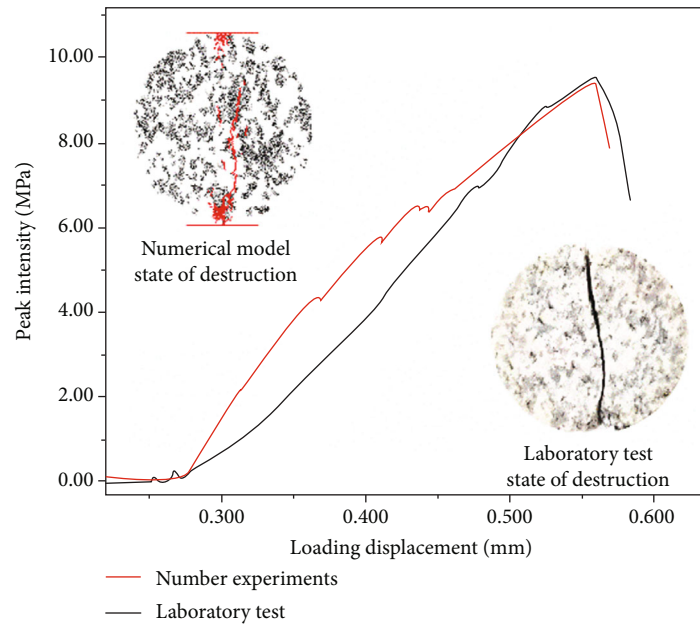
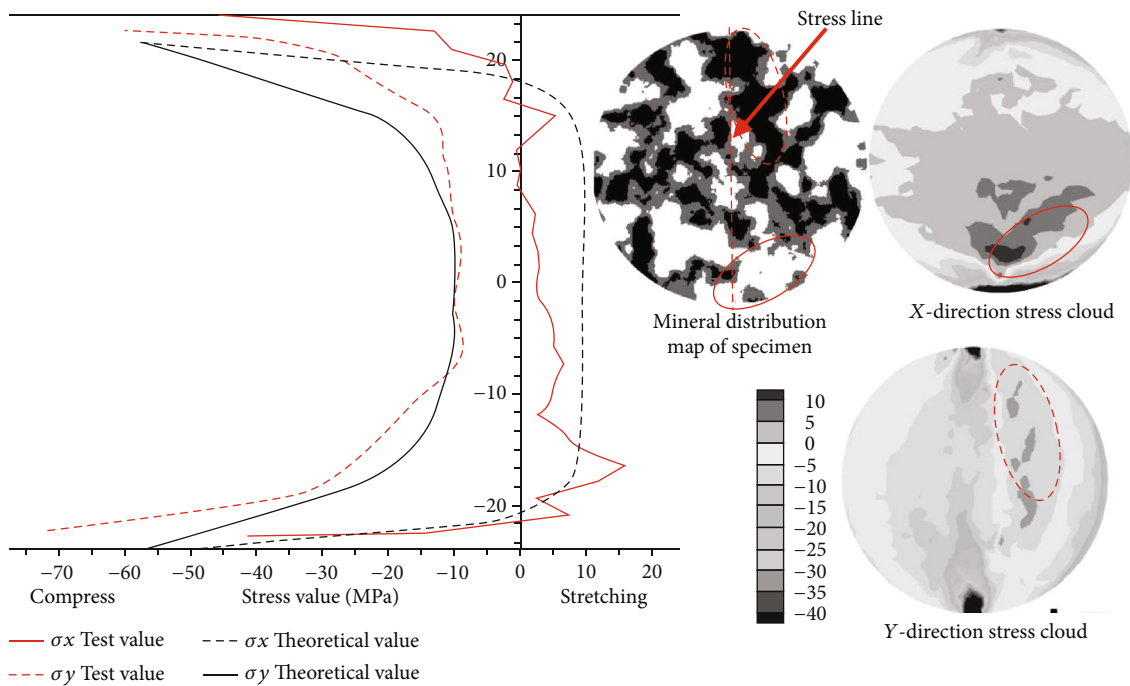FIGURE 8: Calibration results of mesoscopic parameter in the numerical model.

FIGURE 9: Schematic diagram of stress distribution along the loading direction.

where x is the mica content and y is the peak strength. However, there were certain fluctuations during the decline; this is because although the consistency of the recomposition distribution of the test piece was maintained, a certain change in the external morphology would produce a certain articulated surface to make the test piece stable under a certain structure with the increase of the mica content; moreover, although the Voronoi structure in different component structures was established with the same method and parameters, the initial

scattered point positions were randomly distributed, which led to certain volatility, but the tensile strength of the specimen decreased as the mica content increased.

It can be seen from Figure 14 that the strength of the specimen apparently first increased and then decreased with the value of L, which became obvious when the mica was 10%, 20%, and 30%. The average strength of the specimens with $L = 4$, 6, 8, and 10 was 9.706 MPa, 10.156 MPa, 9.908 MPa, and 9.228 MPa. Through comparative analysis,
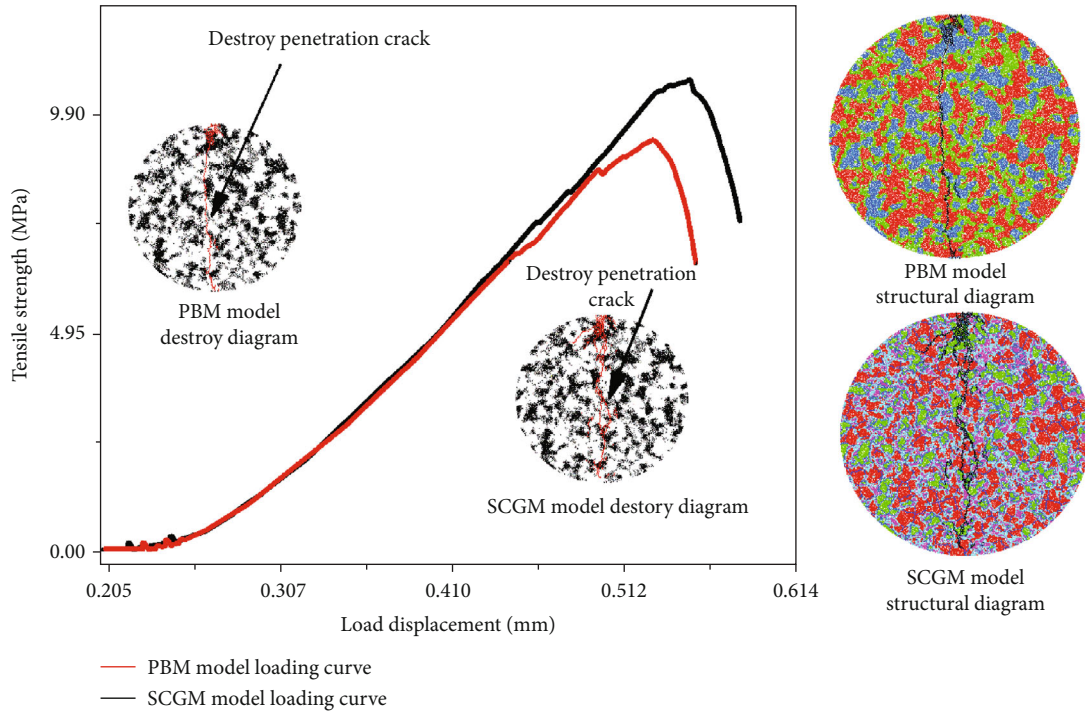
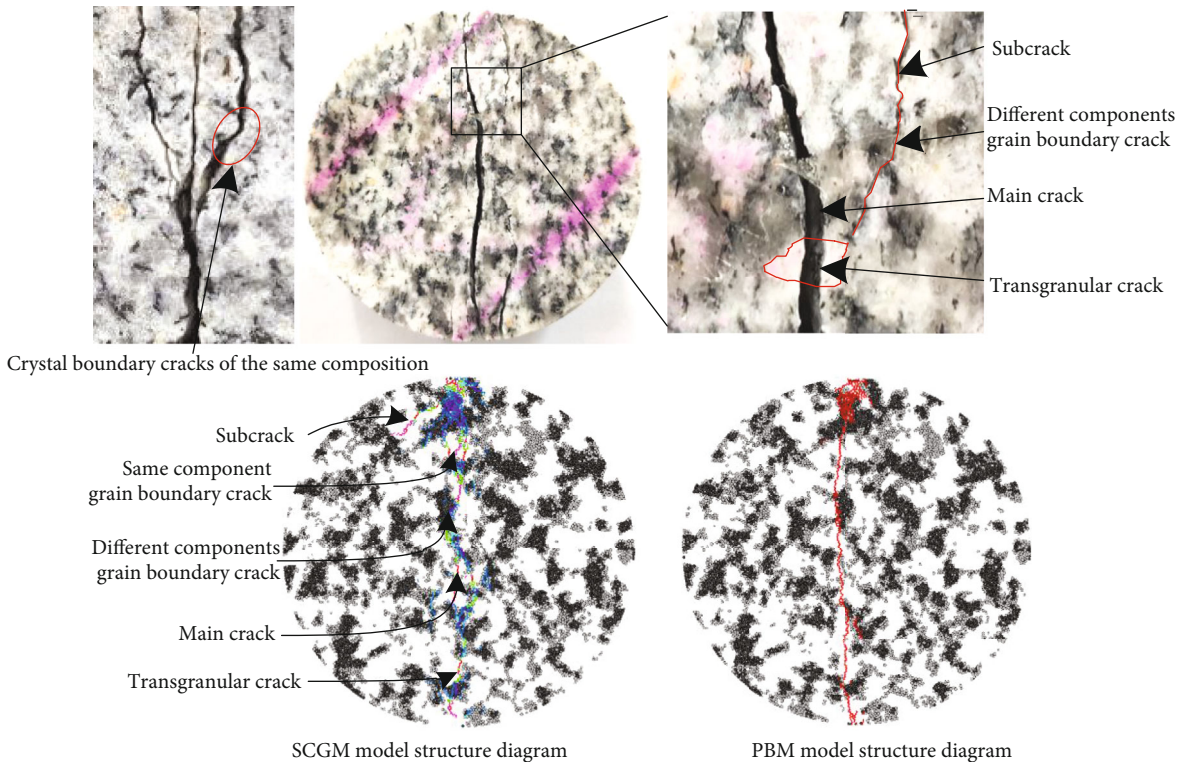Figure 10: Brazil split test results of SCGM and PBM models.

Figure 11: Modelling and actual splitting effect of spatial correlation function structure crystal.

it is found that the main reason for this phenomenon is that when L was small, the low-strength parts such as mica and its joints and cracks were distributed throughout the specimen; with the same content, the more scattered the distribu-

tion, the longer the length of the boundary joints. At this time, the strength of the whole specimen was weaker. On the contrary, when a large number of components were gathered, the length of the boundary joint decreased, and
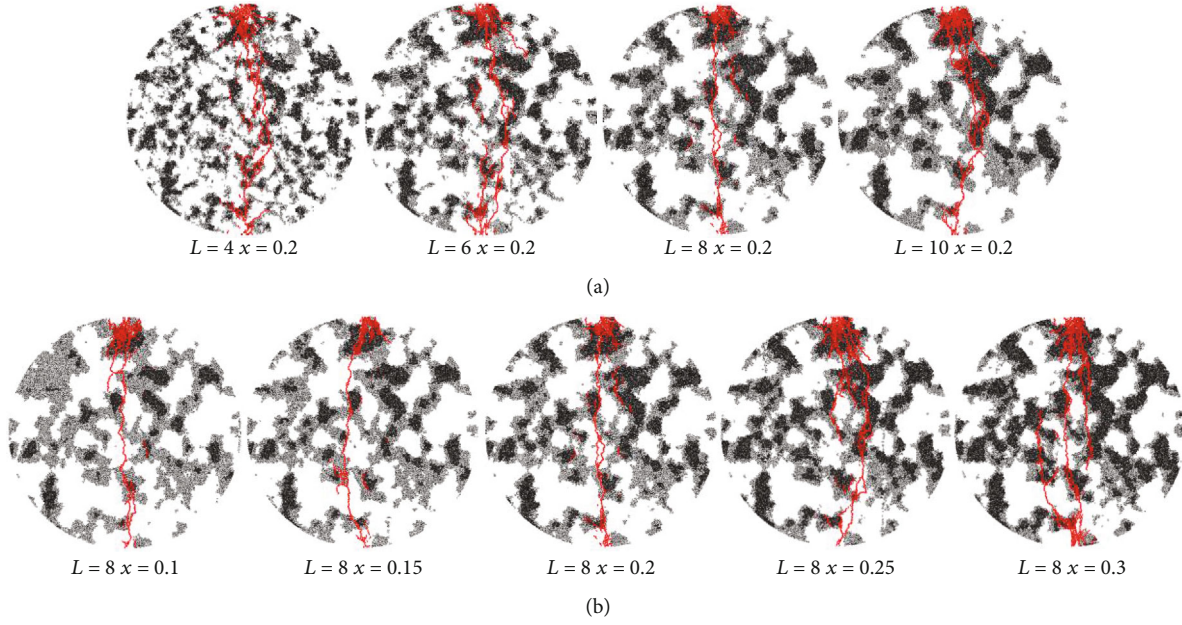
(a)

(b)

FIGURE 12: Brazil split test results with different structural parameters and component contents. (a) Fracture development diagram of specimens with different spatial correlation coefficients. (b) Fracture development diagram of specimens with different component contents.
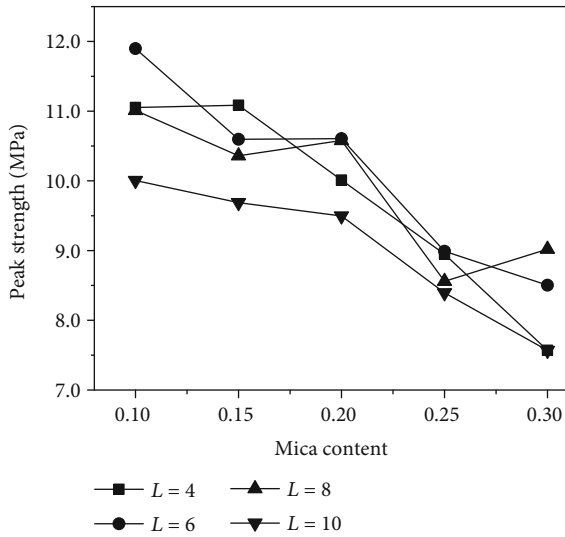

FIGURE 13: The relationship between the peak strength and the content of mica.

FIGURE 14: The relationship between the peak strength and the change of L.

the specimen's overall strength increased. When the mica content was $x = 20\%$, and $L = 4, 6, 8,$ and 10, the mica boundaries were 15.34%, 12.31%, 10.45%, and 9.83%, respectively. The boundary content obviously gradually decreased, but the strength of the specimens first increased and then decreased, which means that when the mica component was sufficiently large, a certain degree of stress concentration advantage will be formed, resulting in a decrease in its strength. Combining the above two reasons, the peak strength of the specimen first increased and then decreased with the value of L.

3.4. Analysis of the Relationship between Crack Development and Fabric. The macroscopic failure and instability of rock
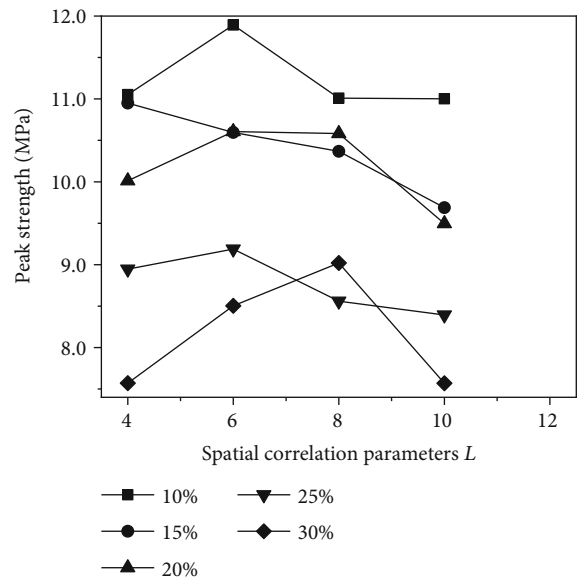
can be attributed to the gradual development and growth of internal microcracks under loading and finally converged into larger microcracks which causes the rock to fail eventually. Therefore, the analysis of internal rock fractures is helpful to understand the destruction mechanism furtherly.

The microfracture was monitored through the crack generation program of the PFC software. The principle is to set the monitoring distance between particles and the strength between particles. When the external load identification force reached this strength, a crack will be recorded. The particle size determines the crack size, which follows a normal

distribution with the size between 0.15 and 0.256 mm in this test; therefore, the crack size is also within this range. During the monitorization, the cracks of different components were grouped and performed statistics. As shown in Figure 15, regardless of the degree of polymerization, the number of cracks in the specimen and mica content showed a trend of increasing first and then decreasing with a peak state when mica content was 20%. The reason is that on the one hand, as the mica content increased, the number of low-strength components increased, and the total number of cracks increased; on the other hand, as the content increased, a large number of low-strength mica gathered to form stress concentration, leading to a rapid rupture of the specimen and making the cracks unable to develop to a large scale for when the number of cracks decreased.

The total number of cracks was counted as 5601, 5734, 5085, and 4797 when $L = 4$, 6, 8, and 10 are, respectively, showing the trend of increasing first and then decreasing. On the one hand, the number of cracks reflects the required destruction energy, and it can remain stable when more cracks have been generated, which means more energy is absorbed; on the other hand, it means that the structural stability of the area is high, and for many microcracks, it is still difficult to form macroscopic damage. Therefore, the specimen is stable with higher strength when $L = 6$, as shown in Figure 14.

As shown in Figure 16, as the value of L increased, the distribution of cracks gradually shifted from the external crystal to the destruction of the inside crystal. The proportion of cracks in the structural cracks decreased as the L value increased. The internal strength of the crystal was greater than the intercrystal structure strength. When there were more cracks in the crystal, more force and energy were required. This is also a fundamental reason for the nonlinear relationship between the strength of the specimen and the L value. By monitoring the cracks between the different component structures in Figure 17, it can be found that the cracks of the feldspar structure increased with the increase of L, and the proportions of the structural cracks of the quartz and mica both decreased with the increase of L. Numerically, it can be seen that the main contribution of the proportion of structural cracks in the whole specimen is provided by the proportion of structural cracks in mica, but its fluctuation is affected by the combined effects of the three components.

4. Discussion

Experiments showed that the SCGM model was used to construct the numerical test piece so that the structure of the component boundary and the discontinuous surface between the crystal particles within the component can be generated inside the model, and the quantitative construction of the component structure of the crystal model was realized at the same time. However, there is a problem worthy of being discussed: the determination of the strength parameters of the structure between different rock components. At present, the method of referring to the actual failure of the specimen and the peak strength elastic modulus
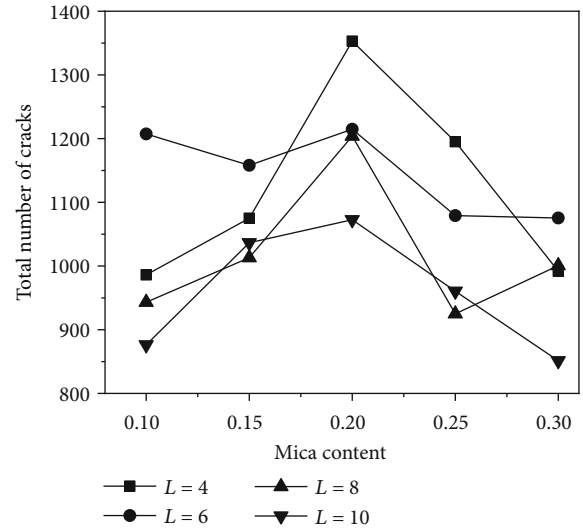

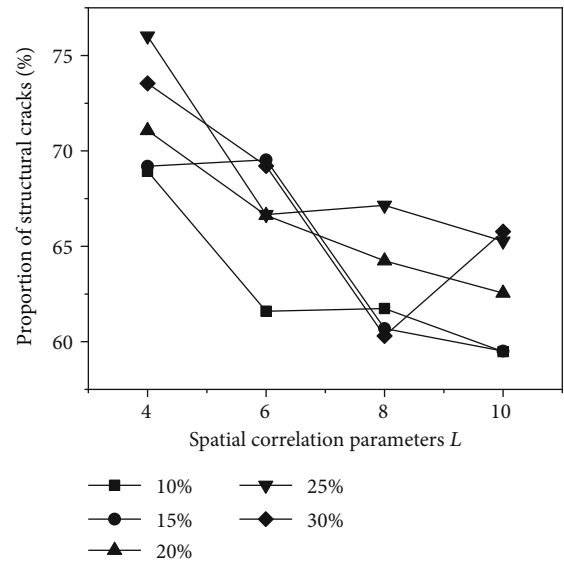Figure 15: The relationship between the number of cracks and the content of mica.

Figure 16: The relationship between the proportion of microcracks and the L value.

is usually used, but in fact, the value of the strength between different components of rock has always been in a fuzzy state. Some scholars choose a certain weakening factor α between 0 and 1 to reflect the reduction of its strength based on experience. When the timing α and other component parameters are double-calibrated, there may be multiple sets of solutions; that is, the final rock strength represented by different α and its corresponding strength parameters are consistent. Therefore, with the help of the SCGM model and more actual parameters, calibration and analysis of α parameters are of great significance. It can further advance the analysis and research of rock fracture development.
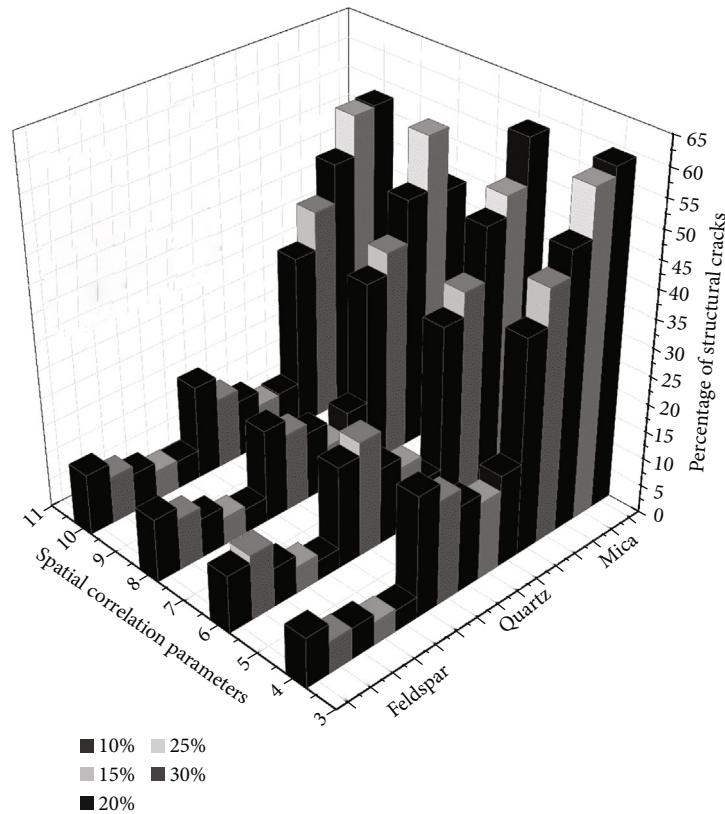
FIGURE 17: The relationship between the content of microcracks in different components and the *L* value.

5. Conclusion

Considering the fracture development of different fabric granite during hydraulic fracturing, the spatial correlation function was used to construct a digital image of the granite surface, which solved quantitating testing of the rock structure. Besides, a numerical model containing the internal crystal structure of the rock was constructed through the Voronoi model and the GBM import method. The newly formed SCGM model has more evident advantages in representing the fracture development of rock failure. Combining the advantage of the SCGM model, the relationships between the distribution and content of the internal components of the granite and its tensile strength were analyzed, as well as the cracks developed in the boundary structure and the crystal. The results are as follows.

(1) The spatial correlation function can generate a granite surface image with a controllable structure content by adjusting the parameters. Combining this method with the discrete element numerical model of the internal crystal structure, a numerical model of the granite with adjustable structural parameters can be constructed more accurately to perform numerical experiments

(2) Compared with the homogeneous model, internal stress of the SCGM model changed with the structure

distribution, which was more consistent with the actual rock specimen. Compared with the PBM model, the internal crystal structure constructed by the new model can better reflect the internal mechanical relationship of rock. Compared with laboratory experiments, the model with internal crystals showed intergranular cracks of different components, grain boundary cracks of the same composition, and transgranular cracks when granite fails. Compared with actual granite image modelling, the method had strong controllability and can construct accurate models for different discrete situations and component contents

(3) The Brazilian splitting numerical experiments of different fabrics showed that the strength of the specimen decreased significantly with the increase of the mica component content and showed a linear change $y = -14.723x + 12.642$; the strength of the specimen increased with the increase of the spatial correlation coefficient L, showing a certain trend of increasing first and then decreasing. By monitoring the cracks in the failure process, the total number of cracks showed the trend of first increasing and then decreasing with the increase of the internal mica content. Moreover, it existed a clear peak when the mica content was 20%; on the crystal interface, the ratio of cracks to the total cracks decreased with the increase

of *L*, and the result was more obviously affected by the mica component

(4) The test results show a significant correlation between fracture development and fabric distribution of different fabric rocks under external load, and corresponding technologies should be adopted for different fabric rocks in hydraulic fracturing

Data Availability

(1) The picture data used to support the findings of this study are included within the article. (2) The chart data used to support the findings of this study are included within the article. (3) The flow chart data used to support the findings of this study are included within the article.

Conflicts of Interest

The authors declare that they have no conflicts of interest.

References

[1] B. W. Xia, X. Zhang, B. Yu, and J. Jia, "Weakening effects of hydraulic fracture in hard roof under the influence of stress arch," *International Journal of Mining Science and Technology*, vol. 28, no. 6, pp. 951–958, 2018.

[2] Z. Yushi, Z. Shicheng, Z. Tong, Z. Xiang, and G. Tiankui, "Experimental investigation into hydraulic fracture network propagation in gas shales using CT scanning technology," *Rock Mechanics and Rock Engineering*, vol. 49, no. 1, pp. 33–45, 2016.

[3] J. He, C. Lin, X. Li, Y. Zhang, and Y. Chen, "Initiation, propagation, closure and morphology of hydraulic fractures in sandstone cores," *Fuel*, vol. 208, pp. 65–70, 2017.

[4] Z. H. Wang, W. G. Ren, Y. L. Tan, and H. Konietzky, "Experimental and numerical study on hydromechanical coupled deformation behavior of Beishan granite considering permeability evolution," *Geofluids*, vol. 2020, Article ID 8855439, 14 pages, 2020.

[5] D. Krajcinovic, "Damage mechanics: accomplishments, trends and needs," *International Journal of Solids and Structures*, vol. 37, no. 1-2, pp. 267–277, 2000.

[6] R. Prikryl, "Some microstructural aspects of strength variation in rocks," *International Journal of Rock Mechanics & Mining Sciences*, vol. 38, no. 5, pp. 671–682, 2001.

[7] A. Luque, E. Ruiz-Agudo, G. Cultrone, E. Sebastián, and S. Siegesmund, "Direct observation of microcrack development in marble caused by thermal weathering," *Environment and Earth Science*, vol. 62, no. 7, pp. 1375–1386, 2011.

[8] R. Peng, Y. Ju, J. G. Wang, H. Xie, F. Gao, and L. Mao, "Energy dissipation and release during coal failure under conventional triaxial compression," *Rock Mechanics and Rock Engineering*, vol. 48, no. 2, pp. 509–526, 2015.

[9] G. Ma, C. Zhou, X. Chang, and Z. Wei, "Continuous-discontinuous coupling analysis for whole failure process of rock," *Chinese Journal of Rock Mechanics and Engineering*, vol. 30, pp. 2444–2455, 2011.

[10] R. Abousleiman, G. Walton, and S. Sinha, "Understanding roof deformation mechanics and parametric sensitivities of coal mine entries using the discrete element method," *International Journal of Mining Science and Technology*, vol. 30, no. 1, pp. 123–129, 2020.

[11] R. Cao, H. Lin, and P. Cao, "Strength and failure characteristics of brittle jointed rock-like specimens under uniaxial compression: digital speckle technology and a particle mechanics approach," *International Journal of Mining Science and Technology*, vol. 28, no. 4, pp. 669–677, 2018.

[12] J. Qiu, L. Luo, X. Li, D. Li, Y. Chen, and Y. Luo, "Numerical investigation on the tensile fracturing behavior of rock-shotcrete interface based on discrete element method," *International Journal of Mining Science and Technology*, vol. 30, no. 3, pp. 293–301, 2020.

[13] Y. G. Zhang, J. Qiu, Y. Zhang, and Y. Wei, "The adoption of ELM to the prediction of soil liquefaction based on CPT," *Natural Hazards*, vol. 107, 2021.

[14] Y. G. Zhang, J. Tang, R. P. Liao et al., "Application of an enhanced BP neural network model with water cycle algorithm on landslide prediction," *Stochastic Environmental Research and Risk Assessment*, vol. 46, 2020.

[15] S. Lv, S. Wang, R. Li, G. Li, M. Yuan, and J. Wang, "Prediction of coal structure using particle size characteristics of coalbed methane well cuttings," *International Journal of Mining Science and Technology*, vol. 29, no. 2, pp. 209–216, 2019.

[16] Y. G. Zhang and L. N. Yang, "A novel dynamic predictive method of water inrush from coal floor based on gated recurrent unit model," *Natural Hazards*, vol. 105, no. 2, pp. 2027–2043, 2021.

[17] Y. G. Zhang, Z. Zhang, S. Xue, R. Wang, and M. Xiao, "Stability analysis of a typical landslide mass in the Three Gorges Reservoir under varying reservoir water levels," *Environmental Earth Sciences*, vol. 79, no. 1, 2020.

[18] J. Tian, D. Xu, and T. Liu, "An experimental investigation of the fracturing behaviour of rock-like materials containing two V-shaped parallelogram flaws," *International Journal of Mining Science and Technology*, vol. 30, no. 6, pp. 777–783, 2020.

[19] Y. G. Zhang, S. Y. Zhu, J. K. Tan, L. D. Li, and X. J. Yin, "The influence of water level fluctuation on the stability of landslide in the Three Gorges Reservoir," *Arabian Journal of Geosciences*, vol. 13, no. 17, p. 845, 2020.

[20] Z. Tao, Y. Shu, X. Yang, Y. Peng, Q. Chen, and H. Zhang, "Physical model test study on shear strength characteristics of slope sliding surface in Nanfen open-pit mine," *International Journal of Mining Science and Technology*, vol. 30, no. 3, pp. 421–429, 2020.

[21] Y. G. Zhang, Y. Zhu, W. Q. Zhang, and H. Liu, "Analysis of deformation characteristics and stability mechanisms of typical landslide mass based on the field monitoring in the Three Gorges Reservoir, China," *Journal of Earth System Science*, vol. 128, no. 1, article 1036, 2019.

[22] Y. G. Zhang, X. Q. Chen, R. P. Liao et al., "Research on displacement prediction of step-type landslide under the influence of various environmental factors based on intelligent WCA-ELM in the Three Gorges Reservoir Area," *Natural Harzard*, vol. 109, article 4655, 2021.

[23] S. Chen, Z. Q. Yue, and L. G. Tham, "Digital image-based numerical modeling method for prediction of inhomogeneous rock failure," *International Journal of Rock Mechanics and Mining Sciences*, vol. 41, no. 6, pp. 939–957, 2004.

[24] C. Shi, W. Yang, J. Yang, and X. Chen, "Calibration of micro-scaled mechanical parameters of granite based on a bonded-

particle model with 2D particle flow code," *Granular Matter*, vol. 21, no. 2, article 889, 2019.

[25] L. Jinzhao, J. Xu, and H. Dayong, "Particle flow simulation of granite deformation and failure process considering the actual distribution of mesoscopic components," in *Proceedings of National Engineering Geology Annual Conference 2015*, pp. 84–89, Beijing: China, 2015.

[26] G. Ma, W. Zhou, R. A. Regueiro, Q. Wang, and X. Chang, "Modeling the fragmentation of rock grains using computed tomography and combined FDEM," *Powder Technology*, vol. 308, no. 308, pp. 388–397, 2017.

[27] T. Xinwei, Z. Yuande, and Z. Chuhan, "A meso mechanical model with spatial correlation scale character and its application," *Rock and Soil Mechanics*, vol. 33, no. 7, pp. 2021–2026, 2012.

[28] T. Xinwei, H. Wenmin, and Z. Yuande, "Experimental and meso-scale numerical modeling of splitting tensile behavior of weathered granites from south China," *Engineering Mechanics*, vol. 34, no. 6, pp. 246–256, 2017.

[29] X. Tang, Y. Zhou, C. Zhang, and J. Shi, "Study on the heterogeneity of concrete and its failure behavior using the equivalent probabilistic model," *Journal of materials in civil engineering*, vol. 23, no. 4, pp. 402–413, 2011.

[30] X. Tang, X. Yang, and Y. Zhou, "An efficient algorithm for spatially-correlated random fields generation and its applications on the two-phase material," *Solid State Communications*, vol. 182, pp. 30–33, 2014.

[31] Y. Lv, H. Li, X. Zhu, and W. Liu, "Discrete element method simulation of random Voronoi grain-based models," *Cluster Computing*, vol. 20, no. 1, pp. 335–345, 2017.

[32] E. Ghazvinian, M. S. Diederichs, and R. Quey, "3D random Voronoi grain-based models for simulation of brittle rock damage and fabric-guided micro-fracturing," *Journal of Rock Mechanics and Geotechnical Engineering*, vol. 6, no. 6, pp. 506–521, 2014.

[33] J. Yang, H. Lian, and L. Lid, "Investigating the effect of confining pressure on fracture toughness of CO_2-saturated coals," *Engineering Fracture Mechanics*, vol. 242, article 107496, 2021.

[34] J. Yang, H. Lian, and V. P. Nguyen, "Study of mixed mode I/II cohesive zone models of different rank coals," *Engineering Fracture Mechanics*, vol. 246, article 107611, 2021.

[35] J. Yang, H. Lian, and L. Li, "Fracturing in coals with different fluids: an experimental comparison between water, liquid CO_2, and supercritical CO_2," *Scientific Reports*, vol. 10, no. 1, article 18681, 2020.

[36] N. Cho, C. D. Martin, and D. C. Sego, "A clumped particle model for rock," *International Journal Of Rock Mechanics And Mining Sciences*, vol. 44, no. 7, pp. 997–1010, 2007.

[37] D. O. Potyondy, "A grain-based model for rock: approaching the true microstructure," in *Proceedings of rock mechanics in the Nordic Countries*pp. 9–12, Kongsberg, Norway, 2010.

[38] Y. Zhou, Y. T. Gao, S. C. Wu, Q. Yan, and H. Sun, "An equivalent crystal model for mesoscopic behavior of rock," *Chinese Journal of Rock Mechanics and Engineering*, vol. 34, no. 3, pp. 511–519, 2015.

[39] X. F. Li, Q. B. Zhang, H. B. Li, and J. Zhao, "Grain-based discrete element method (GB-DEM) modelling of multi-scale fracturing in rocks under dynamic loading," *Rock Mechanics and Rock Engineering*, vol. 51, no. 12, article 1566, pp. 3785–3817, 2018.

[40] Y. Zhang, L. N. Y. Wong, and K. K. Chan, "An extended grain-based model accounting for microstructures in rock deformation," *Journal of Geophysical Research: Solid Earth*, vol. 124, no. 1, pp. 125–148, 2019.

[41] S. P. Morgan, C. A. Johnson, and H. H. Einstein, "Cracking processes in Barre granite: fracture process zones and crack coalescence," *International Journal of Fracture*, vol. 180, no. 2, pp. 177–204, 2013.

[42] S. S. Lim, C. D. Martin, and U. Åkesson, "In-situ stress and microcracking in granite cores with depth," *Engineering Geology*, vol. 147-148, pp. 1–13, 2012.

[43] H. Zhang, M. Tu, H. Cheng, and Y. Tang, "Breaking mechanism and control technology of sandstone straight roof in thin bedrock stope," *International Journal of Mining Science and Technology*, vol. 30, no. 2, pp. 259–263, 2020.

[44] H. Lin, W. H. Kang, J. Oh, I. Canbulat, and B. Hebblewhite, "Numerical simulation on borehole breakout and borehole size effect using discrete element method," *International Journal of Mining Science and Technology*, vol. 30, no. 5, pp. 623–633, 2020.

[45] H. J. Wang, D. A. Liu, W. L. Gong, and L. Li, "Dynamic analysis of granite rockburst based on the PIV technique," *International Journal of Mining Science and Technology*, vol. 25, no. 2, pp. 275–283, 2015.

[46] H. Hofmann, T. Babadagli, J. S. Yoon, A. Zang, and G. Zimmermann, "A grain based modeling study of mineralogical factors affecting strength, elastic behavior and micro fracture development during compression tests in granites," *Engineering Fracture Mechanics*, vol. 147, pp. 261–275, 2015.

[47] N. Bahrani, P. K. Kaiser, and B. Valley, "Distinct element method simulation of an analogue for a highly interlocked, non-persistently jointed rockmass," *International Journal of Rock Mechanics and Mining Sciences*, vol. 71, pp. 117–130, 2014.

[48] Y. Wu, Y. Xu, X. Zhang et al., "Experimental study on vacuum preloading consolidation of landfill sludge conditioned by Fenton's reagent under varying filter pore size," *Geotextiles and Geomembranes*, vol. 49, no. 1, pp. 109–121, 2021.

[49] X. Hu, N. Xie, Q. Zhu, L. Chen, and P. C. Li, "Modeling damage evolution in heterogeneous granite using digital image-based grain-based model," *Rock Mechanics and Rock Engineering*, vol. 53, no. 11, article 2191, pp. 4925–4945, 2020.

[50] T. Yin, S. Zhang, X. Li, and L. Bai, "A numerical estimate method of dynamic fracture initiation toughness of rock under high temperature," *Engineering Fracture Mechanics*, vol. 204, pp. 87–102, 2018.

[51] B. Shu, M. Liang, S. Zhang, and J. Dick, "Numerical modeling of the relationship between mechanical properties of granite and microparameters of the flat-joint model considering particle size distribution," *Mathematical Geosciences*, vol. 51, no. 3, pp. 319–336, 2019.

[52] E. Komurlu, A. Kesimal, and S. Demir, "Experimental and numerical study on determination of indirect (splitting) tensile strength of rocks under various load apparatus," *Canadian Geotechnical Journal*, vol. 53, no. 2, pp. 360–372, 2016.

[53] Y. G. Huang, L. G. Wang, Y. L. Lu, J. R. Chen, and J. H. Zhang, "Semi-analytical and numerical studies on the flattened Brazilian splitting test used for measuring the indirect tensile strength of rocks," *Rock Mechanics and Rock Engineering*, vol. 48, no. 5, pp. 1849–1866, 2015.

[54] H. Wenmin, *Study on Deformation and Fracture-Damage Mechanism of Rock Based on the Spatial Correlation Characteristics*, South China University of Technology, 2018.